

**COORDINATION-DRIVEN MULTI-COMPONENT SELF-ASSEMBLY OF DISCRETE
AND POLYMERIC COORDINATION ARCHITECTURES AND THEIR APPLICATIONS
IN CATALYSIS, CO₂ CAPTURE AND FIXATION, AND SENSING**

*A thesis submitted for the partial fulfilment of
doctoral degree in Chemical Sciences*

By

**Vijay Gupta
PH13011**

under the supervision of

Professor Sanjay K. Mandal



Department of Chemical Sciences,
Indian Institute of Science Education and Research (IISER) Mohali,
Knowledge city, Sector 81, SAS Nagar, Manauli PO, Mohali 140306, Punjab, India.

March, 2019

***DEDICATED to
TO ALL MY RESPECTED TEACHERS,
LOVING FRIENDS and
FAMILY MEMBERS***

Declaration

I hereby declare that the matter embodied in this thesis is the result of investigations carried out by me under the supervision of Prof. Sanjay K. Mandal at the Department of Chemical Sciences, Indian Institute of Science Education and Research (IISER) Mohali, SAS Nagar Mohali, India. This work has not been submitted in part or in full for a degree, a diploma, or a fellowship to any other university or institute. Whenever contributions of others are involved, every effort is made to indicate this clearly, with due acknowledgment of collaborative research and discussions. Any omission that might have occurred due to oversight or error in judgment is regretted. This thesis is a bona fide record of original work done by me and a complete bibliography of the books and journals referred to is given at the end of the thesis.

Vijay Gupta

Date:

Place:

In my capacity as the supervisor of the candidate's thesis work, I certify that the above statements by the candidate are true to the best of my knowledge.

Dr. Sanjay K. Mandal

Date:

Place:

Acknowledgments

It is my pleasure to express my sincere appreciation to each and every one, who have contributed in their own way for the completion of this fruitful and unforgettable journey.

First and foremost, I would like to acknowledge IISER Mohali and UGC for providing me with a research fellowship to carry out this work and I am indebted to IISER Mohali for the state-of-art infrastructure for my research. I would like to express my sincere gratitude to my research supervisor, Professor Sanjay K. Mandal, for his excellent guidance, incredible support and valuable suggestions to carry out this research work. Without his guidance, the completion of this work would never have been possible. It was due to his encouragement during my tenure in the MOCN lab that I began the path of this research in the first place. Dr. Mandal was consistently supportive throughout my time in the group, and had always made himself available for guidance and advice. I will always be thankful for his wisdom, knowledge, and deep concern. He is one of the hardest working people I know and has set an example that I hope to follow in the years to come. The joy and enthusiasm he has for his research was a source of constant motivation for me, even during the tough times during this work.

I am also especially grateful to my dissertation committee: Dr. Ramesh Ramachandran and Dr. K. R. Shmasunder. Throughout the years they have provided valuable insights based on their years of research experience and exposure to the scientific community. They were never short on constructive comments and encouragement.

I am also thankful to Prof. N. Sathyamurthy and Prof. Debi P. Sarkar, former Directors, IISER Mohali, for providing the infrastructure and central research facilities (NMR, X-ray, HRMS and Library) facilities at IISER Mohali. I acknowledge Prof. K. S. Viswanathan and Dr. S. Arulananda Babu, former and current Head of the Department, Chemical Sciences, IISER Mohali, for granting me to use various departmental facilities.

I am highly thankful to my current and former lab members, Dr. Sadhika Khullar and Dr. Navnita Kumar (for building the initial base of research for the entire group), Dr. Sandeep Kashyap and Biswajit Laha (many fruitful discussions and training of instruments and experimental set-ups) Datta Markad, Gouri Chakraborty, Prasenjit Das, Shradha Gandhi, Smriti Thakur, Alisha Gogia and Sheeba Khan their support and cooperation and creating a good work atmosphere in the group. I would never forget the beautiful moments shared with the project students (Gaurav Verma, Karan, Nitish, Sandhya, and Manpreet) and summer

students (Sujeeth, Priyakshi, Kaushik, Gaurav, Neeraj, Sunny Das, Shibna, Justin, Jigyasa, Shubashini, Annapurna, Shelly, Razia, Jagdeep, Monika and Zinnia).

I also wish to thank Mr. Bahadur, Mr. Mangat, Mr. Satwinder, Mr. Prahlad, Mr. Vishal and Mr. Ganesh (lab assistants of chemistry teaching lab) for their help.

I would like to thank my all my best friends especially Dr. Badri Parshad, Dr. Vinod Khatri and Sanjay Chauhan, who always have been a source of constant support and motivation. I am also thankful to Dr. Naveen Malik, Dr. Kuldeep Jaishwal, Dr. Ramarao Parela, Dr. Rajkumar, Dr. Nayyer Aslam Ahmad, Ajay Yadav, Nitin Mudgil, Amit, Narender, Mayank, Bharat, Neha, Rekha and Radha for their love, care and support at different stages of my life.

I owe a lot to my family members, especially my father, my uncle and my brother, who encouraged and helped me at every stage of my personal and academic life, and longed to see this achievement come true.

I would like to acknowledge my hostel friends Ankit Yadav, Yuvraj Vaishnav, Sajal Nawaria, Vishal Kataria, Harshit Jain, PBD and Ivan for always being at my side ready to go anytime and creating cheerful and funny environment in the hostel.

I would like to take this opportunity to thank all my teachers, particularly Sh. K. L. Bhatia, Mrs. Richa Kalra and Dr. Khalid Hussain, who have influenced my life in some way or the other.

Last but not the least, I thank the Almighty for giving me the courage, energy and dedication to accomplish this journey.

List of Figures

Chapter I (Introduction)

- Figure 1.1** (a) Openings at different angles provided by simple organic and inorganic precursors and (b) represents the cis-capping strategy to control the infinite polymeric networks
- Figure 1.2** Combination of various building units for accessing 2D (left) and 3D (right) supramolecular architectures by directional bonding approach. (Adopted from reference 11)
- Figure 1.3** Schematic representation of the definition of 1D, 2D or 3D coordination polymers
- Figure 1.4** Different bis(alkylnitrilo)copper(I) structures: one-dimensional chains sustained by succinonitrile (SUC), two-dimensional grid structures with glutaronitrile (GLU), and three-dimensional networks made of adiponitrile (ADI) linkers
- Figure 1.5** Chronology of advances in coordination chemistry of extended structures
- Figure 1.6** A schematic representation showing the synthesis and various applications of the coordination architectures
- Figure 1.7** A schematic diagram representing different catalytic sites in coordination architectures
- Figure 1.8** Global greenhouse gas emission sources in 2004 of which approximately 77% are represented by CO₂ emissions
- Figure 1.9** Structures of the neutral poly(pyridyl) ligands
- Figure 1.10** Structures of the anionic carboxylate linkers

Chapter III (Results and Discussion)

- Figure 3.1** Dicarboxylate linkers utilized for the synthesis of coordination architectures
- Figure 3.2** Single crystal X-ray structure of molecular squares **1** and **4**; (a and d) ORTEP views of the asymmetric units in **1** and **4**, respectively; (b and e) Ball-and-stick presentation of **1** and **4**, respectively; and (c and f) dimensions of the molecular squares **1** and **4**, respectively
- Figure 3.3** Single crystal X-ray structure of molecular squares **5**, **9** and **10**; (a d and g) ORTEP view of the asymmetric units in **5**, **9** and **10**, respectively; (b, e and f) Ball-and-stick presentation of **5**, **9** and **10**, respectively; and (c, f and i) the dimensions of the molecular squares **5**, **9** and **10**, respectively
- Figure 3.4** View of bifurcated intramolecular hydrogen bonding (a and c) and packing arrangement (c and d) for representative examples from both sets of molecular squares; a and c for **1** and b and d for **5**, respectively

- Figure 3.5** Powder X-ray diffraction patterns of the as synthesized molecular square **1**, **4**, **5**, **9** and **10** compared with the simulated powder patterns obtained from single crystal structures
- Figure 3.6** Powder X-ray diffraction pattern of the as synthesized samples of (left) **1-4** and (right) **5-10** compared to the simulated powder patterns obtained from the single crystal structures of **1** and **5**, respectively
- Figure 3.7** TGA scans for **1-4** (left) and **5-10** (right)
- Figure 3.8** Example of integration in ^1H NMR spectrum for the calculation of product yield in Knoevenagel condensation reaction of benzaldehyde with malononitrile (entry 1, Table 3.2)
- Figure 3.9** Plot of % yield versus catalyst amount (left) and time (right) for the Knoevenagel condensation reaction of benzaldehyde and malononitrile catalysed by **1** and **5**
- Figure 3.10** Yields for Knoevenagel condensation reaction of benzaldehyde and malononitrile catalysed by **1-10**
- Figure 3.11** Yield for three consecutive cycles of Knoevenagel condensation reaction of benzaldehyde and malononitrile catalysed by **1** and **5**
- Figure 3.12** FTIR spectra (top) and PXRD pattern (bottom) of **1** and **5** taken before and after catalysis experiments.
- Figure 3.13** Proposed catalytic cycle for the Knoevenagel condensation of benzaldehyde with malononitrile catalysed by **1-10**
- Figure 3.14** (a,b) Change in emission spectra of **4** and **10** dispersed in an aqueous medium upon incremental addition of the NB solution (2 mM) (Insets showing the blue emission and its disappearance under UV light, before and after NB addition, respectively) and (c,d) Stern-Volmer (SV) plot for NB of **4** and **10**. The relative fluorescence intensities are linear with NB concentration in the range of 0- 0.035 mM, $I_0/I = 1 + 84.026[\text{NB}]$ ($R^2 = 0.998$) for **4** and $I_0/I = 1 + 95.032[\text{NB}]$ ($R^2 = 0.992$) for **10**
- Figure 3.15** A comparison of 3D Stern-Volmer plot of different nitro analytes for **4** and **10**
- Figure 3.16** Two possible structural isomers (a) connected molecular squares and (b) fused hexagons, by the self-assembly of metal ions, bis(tridentate) ligands and carboxylate linkers
- Figure 3.17** Structural description for **11**; (a) view of the asymmetric unit and the coordination environment around the Mn(II) center, (b) view of 1D polymeric structure and (c) formation of 2D supramolecular architecture via the strong hydrogen bonding by lattice DMF molecules ($\text{O}_{\text{DMF}} \dots \text{HPy}$ 2.689 Å)
- Figure 3.18** Structural description for **11a**; (a) view of the asymmetric unit and the coordination environment around the Mn(II) center, (b) view of overall 1D polymeric structure
- Figure 3.19** Simplified representation of the structural isomers (a) **11** and (b) **11a**, respectively

- Figure 3.20** Powder X-ray diffraction pattern of the as-synthesized sample of **11a**, compared with the simulated powder X-ray diffraction pattern, obtained from the single crystal X-ray diffraction data
- Figure 3.21** Structural description for **12**; (a) view of the asymmetric unit and the coordination environment around the Mn(II) center, (b) view of 1D polymeric structure and (c) formation of 2D supramolecular architecture via the strong hydrogen bonding by lattice DMF molecules ($O_{DMF} \dots H_{Py}$ 2.700 Å and $O_{DMF} \dots H_{Me}$ 2.680 Å)
- Figure 3.22** Structural description for **13**; (a) view of the asymmetric unit and the coordination environment around the Mn(II) center, (b) view of 1D polymeric structure and (c) simplified view of the 1D polymeric structure formed by fused hexagons
- Figure 3.23** Powder X-ray diffraction pattern of the as-synthesized sample of **12** (left) and **13** (right), compared with their respective simulated powder X-ray diffraction pattern, obtained from the single crystal X-ray diffraction data
- Figure 3.24** Structural description for **14** and **15**; (a and c) represents the asymmetric units and the coordination environment around the Mn(II) center in **14** and **15**, respectively and (b and d) perspective views of 1D polymeric structures in **14** and **15**, respectively
- Figure 3.25** Simplified representation of the polymeric structures in (a) **14** and (b) **15**, respectively
- Figure 3.26** View of the discrete dimetallic linear complex formed in **16**
- Figure 3.27** Powder X-ray diffraction pattern of the as-synthesized sample of **14-16**, compared with their respective simulated powder X-ray diffraction pattern, obtained from the single crystal X-ray diffraction data
- Figure 3.28** Structural description for **17**; (a) asymmetric unit and coordination environment around the Cd(II) centers, (b) perspective view of metal-carboxylate 1D polymeric chain in **17** and (c) a view of hydrogen bonded supramolecular architecture showing 0D Cd(II)-tpen complex encapsulated into the Cd(II)-carboxylate chains
- Figure 3.29** Powder X-ray diffraction (PXRD) pattern of **17** compared with the simulated powder pattern obtained from the single crystal data
- Figure 3.30** Structural description for **18**; (a) asymmetric unit and coordination environment around the Cd(II) centers, (b) perspective view of 1D polymeric chain in **18** and (c) simplified representation of the polymeric chain composed of fused hexagons
- Figure 3.31** Structural description for **19**; (a) asymmetric unit and coordination environment around the Cd(II) centers, (b) perspective view of 1D polymeric chain in **19** and (c) simplified representation of the polymeric chain composed of fused hexagons
- Figure 3.32** Powder X-ray diffraction (PXRD) pattern of as-synthesized samples of (a) **18** and (b) **19** compared with the simulated powder pattern obtained from the single crystal data

- Figure 3.33** Structure description for **20**; (a) coordination environment around the Zn(II) center, (b) view of 1D polymeric chain, (c) node and linker type representation for **20** and (d) packing of 1D chains in crystal lattice
- Figure 3.34** Structure description for **21-23**; (a,b and c) shows the 2D sheet structures in **21**, **22** and **23**, respectively, (d) a paddle wheel SBU common in all cases represented as a simplified 4-connected node and (e and f) are simplified node and linker representation and space fill representations, showing 2-fold interpenetration into the frameworks
- Figure 3.35** Structure description for **24**; (a) representation of the 2D sheet structures in **24**, (b) AB-AB type stacking of the 2D sheets in **24**; different 2D sheets are shown in different colors. (c and d) simplified node and linker representation showing non interpenetration 2D sheets stacked in AB-AB fashion and (e) a schematic representation of the AB-AB stacking of 2D sheets
- Figure 3.36** Structure description for **25**; (a) perspective view of the 3D framework, (b) simplified node and linker representation showing 4-c uni-nodal sqc5-CdSO₄ type topology, (c) representation of the colonolly surfaces; dark blue represents the outer surface while sky blue represents the inner surface and (d) N₂ sorption isotherm for **25** collected at 77 K, inset shows the mean pore diameter in **25**
- Figure 3.37** BET surface area (left) and Langmuir surface area (right) of **25** obtained from the N₂ adsorption isotherm at 77 K
- Figure 3.38** Powder X-ray diffraction (PXRD) pattern of as-synthesized samples of **20-25**, compared with the simulated powder pattern obtained from the single crystal data
- Figure 3.39** (a) Thermogravimetric profile for **20-25** and (b) variable temperature powder X-ray diffraction patterns for **25**, indicating thermal robustness and retention of phase purity and crystallinity upon thermal activation
- Figure 3.40** Structure description for **26**; (a) asymmetric unit in **26**, (b) perspective view of an overall 2D framework containing tetracarboxylato bridged dimanganese paddle wheel core SBUs and (c and d) simplified node and linker representation and space fill representation showing two-fold interpenetration into the framework
- Figure 3.41** Structure description for **27**; (a) asymmetric unit and coordination around the Mn(II) centers in **27**, (b) perspective view of an overall 2D framework containing bis and triscarboxylato bridged dimanganese cores and (c) simplified node and linker representation showing 4-connected uninodal sql topology, where tetranuclear manganese cluster is simplified as 4-connected node
- Figure 3.42** Asymmetric unit and coordination environment around the metal centers in (a) **28** and (b) **29**
- Figure 3.43** Perspective view of the overall 2D structure in **28** which is isostructural to the framework in **29**, where the N-donor bpee ligand has been replaced with N-donor azopy ligand

- Figure 3.44** Structural description for **31**; (a) Asymmetric unit and coordination environment around Mn(II), (b) perspective view of the overall 3D structure in **31** and (c) representation of the μ -aqua bis-carboxylato bridged dimanganese core in **31**
- Figure 3.45** Powder X-ray diffraction (PXRD) pattern of as-synthesized samples of **26-30**, compared with the simulated powder pattern obtained from the single crystal data
- Figure 3.46** (a) Thermogravimetric profile for **26-30** and (b) variable temperature powder X-ray diffraction patterns for **26**, indicating thermal robustness and retention of phase purity and crystallinity up to 300 °C
- Figure 3.47** (a) Plot of χT vs. T for **26**; the solid line is the best fit to the experimental data and (b) Magnetization M per Mn(II) ion versus field H at 2 K for **26**
- Figure 3.48** Structure description for **32-34**; (a,b and c) shows the 2D sheet structures in **32**, **33** and **34**, respectively, (d) simplified representation of the paddle wheel SBU, dmsdba²⁻ and pillar ligands as 4-connected node and bent and linear linkers, respectively and (e) an overall node and linker type representation 4-connected sql topology with 2-fold interpenetration into the frameworks
- Figure 3.49** Structure description for **35** and **36**; (a and b) perspective view of the 3D structure obtained in case of **35** and **36**, respectively and (c) simplified node and linker type representation for **35** and **36** exhibiting 4-connected uni-nodal net sqc5 topology with 2-fold interpenetration into the frameworks
- Figure 3.50** Powder X-ray diffraction (PXRD) pattern of as-synthesized samples of **31** and **32-36**, compared with the simulated powder pattern obtained from the single crystal data of **26** and **32-36**, respectively
- Figure 3.51** Thermogravimetric profile for **31-36**
- Figure 3.52** Structure description for **37**; (a) Asymmetric unit and the coordination environment around the metal center, (b) view of the 1D framework; coordinated DMF molecules are shown in space fill representation and (c) represents the interpenetration into the 1D polymeric chains to generate the overall 2D framework
- Figure 3.53** Structure description for **38**; (a) Asymmetric unit and the coordination environment around the metal center, (b) view of the 1D framework; coordinated water molecules are shown in space fill representation and (c) represents the interpenetration into the 1D polymeric chains to generate the overall 2D framework
- Figure 3.54** Powder X-ray diffraction (PXRD) pattern of as-synthesized and desolvated samples of (a) **37** and (b) **38**, compared with the simulated powder pattern obtained from the single crystal data of **37** and **38**, respectively
- Figure 3.55** Thermogravimetric profile for the as-synthesized and desolvated samples of (a) **37** and (b) **38**, respectively
- Figure 3.56** Progress of the reaction with time in presence of catalyst (a) **37** and (b) **38** (solid lines) and after separating the catalyst from the reaction mixture (dotted lines) for Knoevenagel condensation reaction of benzaldehyde with malononitrile

- Figure 3.57** Conversion for three consecutive cycles of Knoevenagel condensation reaction of benzaldehyde and malononitrile catalysed by **37** and **38**
- Figure 3.58** FTIR and powder X-ray diffraction pattern of the catalyst (a and c) **37** and (b and d) **38**, before and after three cycles of Knoevenagel Condensation reaction
- Figure 3.59** (a) FTIR and (b) powder X-ray diffraction pattern of the catalyst **38**, before and after three cycles of Biginelli reaction
- Figure 3.60** Structure description for **39**; (a) View of the asymmetric unit and the coordination environment around the Cd (II) center, (b) perspective view of the 2D framework. Lattice DMF molecules present in the 1D channels have been shown as space-fill model, (c and d) representation of the 2-fold screw axis and 2-fold rotation axis along crystallographic b and c axis, respectively and (e) space-fill representation of the 2D framework viewed along the a-axis
- Figure 3.61** Simplified node and linker representation for **39**, indicating 4-connected uninodal net, sql topology
- Figure 3.62** Solid State Circular Dichroism (CD) Spectrum for **39**
- Figure 3.63** Structure description for **40**; (a) View of the asymmetric unit and the coordination environment around the Cd (II) center, (b) metal-carboxylate helical chains with opposite handedness and (c) perspective view of the 3D framework along b-axis, showing 1D open channels
- Figure 3.64** Simplified node and linker type representation for **40**; (a) $\text{Cd}_2(\text{COO})_4$ dinuclear core and the ligands dmsdba and 1,5-ND-4-Py simplified as 6-connected node and bent and linear linkers, respectively, (b) View of the overall 6-connected uni-nodal topology and (c) metal-carboxylate helical chains with opposite handedness
- Figure 3.65** Powder X-ray diffraction (PXRD) pattern of as-synthesized and desolvated samples of (a) **39** and (b) **40**, compared with the simulated powder pattern obtained from the single crystal data of **39** and **40**, respectively
- Figure 3.66** Thermogravimetric profile for the as-synthesized and desolvated samples of (a) **39** and (b) **40**, respectively
- Figure 3.67** BET and Langmuir surface area of obtained from the CO_2 adsorption isotherm for (a and c) **39** and (b and d) **40**, respectively
- Figure 3.68** CO_2 sorption isotherms at different temperatures for (a) **39**, (b) **40** and variation of isosteric heat of adsorption for CO_2 with respect to surface coverage for (c) **39** and (d) **40**, respectively
- Figure 3.69** (a) PXRD pattern of **39** before and after catalysis experiments and (b) conversion for three consecutive cycles of (i) Knoevenagel condensation reaction of benzaldehyde and malononitrile and (ii) Strecker reaction of benzaldehyde with aniline and trimethylsilyl cyanide, catalysed by **39**

- Figure 3.70** Progress of the reaction with time in presence of catalysts **39** (solid lines) and after separating the catalyst from the reaction mixture (dotted lines) for (left) Knoevenagel condensation reaction of benzaldehyde with malononitrile and (right) Strecker reaction of benzaldehyde with aniline and trimethyl silyl cyanide
- Figure 3.71** Plausible mechanism for the Knoevenagel condensation and the Strecker reactions catalyzed by **39**
- Figure 3.72** Different conformations of the dicarboxylate linker observed in (a) **37**, (b) **38**, (c) **39** and (d) **40**, respectively
- Figure 3.73** Coordination environment around the metal center in (a) **41** and (b) **42**, respectively
- Figure 3.74** Perspective view of the 3D frameworks in case of (a) **41** and (b) **42**, respectively
- Figure 3.75** Simplified node and linker type representation for **41** and **42**; (a-d) Zn(II) and Cd(II) centers, and the ligands 4-tpom and dmsdba²⁻, represented as 4-connected nodes and a bent linker, respectively, (e and f) overall node and linker representation for **41** and **42**, respectively, showing 4-connected uninodal net NbO; 4/6/c2; sqc35 topology in each case
- Figure 3.76** Powder X-ray diffraction patterns for the as-synthesized samples of (a) **41** and (b) **42** compared with their respective simulated powder patterns obtained from the single crystal data
- Figure 3.77** Thermogravimetric profile and variable temperature powder X-ray diffraction patterns for (a and c) **41** and (b and d) **42**, indicating their thermal stability and retention of crystallinity and phase purity at higher temperatures
- Figure 3.78** BET and Langmuir surface area of obtained from the CO₂ adsorption isotherm for (a and c) **41** and (b and d) **42**, respectively
- Figure 3.79** CO₂ sorption isotherms at different temperatures for (a) **41** and (b) **42**, respectively
- Figure 3.80** Fitting (purple solid lines) of the CO₂ adsorption isotherms for (a) **41** and (b) **42**, measured at different temperatures using the virial method and (c and d) represents the variation of isosteric heat of adsorption with respect to surface coverage for **41** and **42**, respectively
- Figure 3.81** CO₂ adsorption isotherms compared with the adsorption isotherms of N₂ and CH₄ at 273 K and 298 K for (a) **41** and (b) **42**
- Figure 3.82** H₂ sorption isotherms for (a) **41** and (b) **42** at 77 K and 1 bar pressure
- Figure 3.83** Progress of the cycloaddition reaction of CO₂ with epichlorohydrin, catalyzed by **41**, monitored by ¹H NMR spectroscopy
- Figure 3.84** (a) conversion for three consecutive cycles for the cycloaddition reaction of CO₂ with epichlorohydrin, (b) PXRD pattern of **41** before and after catalysis experiments and of (c) progress of the reaction with time in presence of catalysts (solid lines) and after separating the catalyst from the reaction mixture (dotted lines) for cycloaddition reaction of CO₂ with epichlorohydrin

- Figure 3.85** Proposed reaction mechanism for the cycloaddition of CO₂ with epoxides, catalyzed by **41**.
- Figure 3.86** Perspective view of the (a) coordination environment around the Zn(II) center and (b) overall 3D framework in **43**
- Figure 3.87** Perspective view of the (a) coordination environment around the Cd(II) center and (b) overall 2D framework in **44**
- Figure 3.88** Simplified node and linker representation for (a) **41** and (b) **43** and (c and d) shows Zn(II) and 4-tpom or 3-tpom as 4-connected nodes and relative orientations and dihedral angles between the phenyl rings containing carboxylic acid groups in dmsdba²⁻ in case of **41** and **43**, respectively
- Figure 3.89** Simplified node and linker representation for (a) **44** and (b) Cd-4-tpom-obba complex and (c and d) shows the 3-tpom and 4-tpom ligands as 4-connected nodes and dihedral angles between the phenyl rings containing carboxylic acid groups in obba²⁻ in case of **44** and Cd-4-tpom-obba complex, respectively
- Figure 3.90** Powder X-ray diffraction patterns for the as-synthesized samples of (a) **43** and (b) **44** compared with their respective simulated powder patterns obtained from the single crystal data
- Figure 3.91** Thermogravimetric profile for (a) **43** and (b) **44**, respectively
- Figure 3.92** (a) Comparison of N₂ (77 K) and CO₂ (195 K) sorption isotherms at low temperatures and (b and c) BET and Langmuir surface area of obtained from the CO₂ adsorption isotherm for **43**
- Figure 3.93** (a) CO₂ sorption isotherms for **43** collected at different temperatures, (b) Fitting (purple solid lines) of the CO₂ adsorption isotherms using the virial method, (c) variation of isosteric heat of adsorption with respect to surface coverage and CO₂ adsorption isotherms for **43** compared with the adsorption isotherms of N₂ and CH₄ at 273 K and 298 K, respectively
- Figure 3.94** (a) conversion for three consecutive cycles for the cycloaddition reaction of CO₂ with epichlorohydrin and three component Strecker reaction of benzaldehyde, aniline and trimethylsilyl cyanide, catalyzed by **43**, (b) PXRD pattern of **43** before and after catalysis experiments and (c and d) progress of the reaction with time in presence of catalysts (solid lines) and after separating the catalyst from the reaction mixture (dotted lines) for cycloaddition reaction of CO₂ with epichlorohydrin and Strecker reaction of benzaldehyde with aniline and trimethylsilyl cyanide, respectively
- Figure 3.95** (a) coordination environment around the metal centers and (b) perspective view of the overall 3D framework in **45**
- Figure 3.96** Simplified node and linker type representation for (a) the dimetallic Cd₂O₂ SBU and (b) H₃mstba as 4-connected and 3-connected node, respectively, (c and d) represents

the overall 3,4-connected bi-nodal net sqc5591 topology without and with twofold interpenetration into the framework of **45**

- Figure 3.97** Structural description for **46** and **47**; (a and b) coordination environment around the metal center in **46** and **47**, respectively, (c) double layered sheet structure in **46** and **47** and (d) view of 2D metal carboxylate sheet structure in both the frameworks
- Figure 3.98** Simplified representation of the metal center, H₃mstba and linear pillar ligand as 4- and 3-connected nodes and a linear linker, respectively and the overall 3,4-connected bi-nodal network topology with twofold interpenetration into the framework of **46** and **47**
- Figure 3.99** Powder X-ray diffraction patterns for the as-synthesized samples of (a) **45**, (b) **46** and (c) **47** compared with their respective simulated PXRD patterns obtained from their single crystal data
- Figure 3.100** Thermogravimetric profile for **45-47**
- Figure 3.101** Structure description for **48**; (a) The coordination environment around the Co (II) center showing the paddle-wheel secondary building unit (SBU), (b) fully deprotonated ligand tcps⁴⁻ coordinated to the eight cobalt atoms, (c) connections of a paddle wheel SBU, via tcps⁴⁻ and 4,4'-bipyridine linker, (d) a perspective view of the doubly interpenetrated 3D porous framework along the a-axis and (e) an enlarged view of the rhombus and triangular channels shown with the help of dummy balls of different colors
- Figure 3.102** (a) simplified node and linker representation of the ligands H₄tcps, bpy and Co₂(COO)₄ cluster, (b) the overall (4,6)-connected 2-nodal net, sqc422 topology and (c) view of the two fold interpenetration into the framework of **48**
- Figure 3.103** (a) Powder X-ray diffraction of the as-synthesized and activated sample of **48**, compared with the simulated powder pattern, (b) Diffuse reflectance UV-Vis spectra of **48** (red line) and H₄tcps (green line); inset: KM function vs. energy (eV) of **48** and H₄tcps
- Figure 3.104** (a) Thermogravimetric profiles of **48** (as-synthesized and desolvated). (b) In-situ variable temperature powder pattern of the as synthesized sample of **48** and (b) the powder X-ray diffraction pattern of the as synthesized sample after soaking in water at room temperature and in boiling water, indicating the thermal robustness and water stability of **48**
- Figure 3.105** (a and b) CO₂ and H₂ sorption isotherm for **48** at 195 K and 77 K. Filled circles and open circles indicate the adsorption and desorption points, respectively, (c and d) BET and Langmuir surface area of obtained from the CO₂ adsorption isotherm
- Figure 3.106** (a) CO₂ sorption isotherms for **48** collected at different temperatures, (b) comparison of CO₂ sorption isotherm with that of CH₄ and N₂ at 273 K and 298 K, respectively. (c) Fitting (purple solid lines) of the CO₂ adsorption isotherms using the virial method and (d) variation of isosteric heat of adsorption with respect to surface coverage

- Figure 3.107** Binary mixture adsorption isotherms and selectivities for CO₂/N₂ (15/85) mixture and CO₂/CH₄ (50/50) mixtures at 298 K (a and b) and 273 K (c and d), respectively
- Figure 3.108** Coordination environment around the metal centers in (a) **49** and (b) **50**, (c) view of the metal carboxylate clusters forming 1D linear chain in **49**, (d) metal carboxylate clusters bridged by the neutral bpy ligands and (e) representation of overall 3D structure formed in **49**. The structural features of **50** are similar to that of **49**
- Figure 3.109** Powder X-ray diffraction of the as-synthesized samples of (a) **49**, (b) **50** compared with their respective simulated powder patterns and (c) thermogravimetric profiles for **49** and **50**
- Figure 3.110** Coordination environment around the metal centers in (a) **51** and (b) **52**, (c) perspective view of the overall 3D framework and (d) two-fold interpenetration into the framework of **51**. Two different networks are shown in different colors
- Figure 3.111** (a) simplified node and linker representation of the dimetallic SBU, ligands H₄tcpu and 3-bpdc, (b) representation of the (4,5)-connected 2-nodal network topology without and (c) with twofold interpenetration into the framework of **51**
- Figure 3.112** Powder X-ray diffraction of the as-synthesized samples of (a) **51**, (b) **52** compared with their respective simulated powder patterns and (c) thermogravimetric profiles for **51** and **52**
- Figure 3.113** (a and b) BET and (c and d) Langmuir surface area obtained from the CO₂ adsorption isotherms for **51** and **52**, respectively
- Figure 3.114** (a and b) CO₂ sorption isotherms collected at different temperatures and (c and d) variation of isosteric heat of adsorption with respect to surface coverage for **51** and **52**, respectively
- Figure 3.115** Comparison of quenching percentages of different nitroanalytes (upon addition to 100 mL in each case) by **51** and **52**, respectively
- Figure 3.116** Change in emission intensities of (a) **51** and (b) **52** dispersed in aqueous methanol upon incremental addition of TNP solution and (c and d) linear fitting of Stern-Volmer plots for **51** and **52** in the low concentration region
- Figure 3.117** 3D-Stern-Volmer plot of different nitro-analytes for (a) **51** and (b) **52** showing high selectivity for TNP in each case
- Figure 3.118** Bar plot of percentage decrease in emission intensity of (a) **51** and (b) **52** before and after the addition of different analytes (40 μL) followed by same amount of 2,4,6-TNP (40 μL). (Red bar represent the emission intensity by pristine **51** or **52**, blue bar represents the percent emission intensity after addition of different analytes (**51** or **52** + analyte) and green bar represents the percent emission intensity after TNP addition (**51** or **52** + analyte + 2,4,6-TNP); A: NB; B: 4-NT; C: 1,3-DNB; D: 2,4-DNT; E: 2,4,6-TNT; F: 4-NP; G: 2-NP; H: 2,4-DNP).

- Figure 3.119** Structure description for **53**; (a) coordination environment around the metal center and perspective view of the overall 3D framework (b) without interpenetration and (c) with two-fold interpenetration into the framework
- Figure 3.120** Simplified node and linker type representation for **53**; (a) the metal center, carboxylate linker tcps^{4-} and 4-tpom shown as 4-connected nodes and overall 4-connected uni-nodal dia; sqc6 network topology (b) without interpenetration and (c) with two-fold interpenetration
- Figure 3.121** (a) Powder X-ray diffraction pattern of the as-synthesized samples of **53** compared with their respective simulated powder patterns and (b) thermogravimetric profiles for **53**
- Figure 3.122** (a) CO_2 sorption isotherms for **53** collected at different temperatures, (b) comparison of CO_2 sorption isotherm with that of CH_4 and N_2 at 273 K and 298 K, respectively. (c) Fitting (purple solid lines) of the CO_2 adsorption isotherms using the virial method and (d) variation of isosteric heat of adsorption with respect to surface coverage
- Figure 3.123** Binary mixture adsorption isotherms and selectivities for CO_2/N_2 (15/85) mixture and CO_2/CH_4 (50/50) mixtures at 298 K (a and b) and 273 K (c and d), respectively by **53**
- Figure 3.124** (a) coordination environment around the metal center (a) Zn1, (b) Zn2 and (c) perspective view of the overall 3D framework in **54**
- Figure 3.125** Simplified node and linker type representation for **54**; (a) the metal centers Zn1 and Zn2, carboxylate linker tcps^{4-} and 3-tpom shown as 4-connected nodes and overall 4-connected uni-nodal network topology
- Figure 3.126** (a) Powder X-ray diffraction pattern of the as-synthesized samples of **54** compared with their respective simulated powder patterns and (b) thermogravimetric profiles for **54**
- Figure 3.127** (a) Comparison of N_2 sorption isotherms for **53** and **54**, (b) CO_2 sorption isotherms for **54** at different temperatures and (c and d) BET and Langmuir surface area obtained from the N_2 adsorption isotherm for **54**
- Figure 3.128** Structure description for **55**; (a) coordination environment around the metal centers, (b) perspective view of the 3D framework with open channels, (c) simplified node and linker type representation exhibiting a 3,8-connected 2-nodal : cut; sqc517 topology where (d) tetranuclear $\text{Zn}_4(\text{COO})_6$ cluster and organic ligand dmsbta^{4-} have been shown as an eight connected node and a pair of 3-connected node, respectively
- Figure 3.129** (a) Powder X-ray diffraction pattern of the as-synthesized samples of **55** compared with the simulated powder patterns and (b) thermogravimetric profiles for **55**, (c) temperature dependent powder X-ray diffraction and (d) PXRD pattern of **55** after soaking in different solvents

- Figure 3.130** (a) CO₂ sorption isotherms for **55** collected at different temperatures, (b) comparison of CO₂ sorption isotherm with that of N₂ and CH₄ and (c and d) Binary mixture adsorption isotherms and selectivities for CO₂/N₂ (15/85) mixture and CO₂/CH₄ (50/50) mixtures, respectively at 298 K
- Figure 3.131** The snapshot of CO₂ adsorption for **55** at 1 bar and 298 K, calculated using GCMC method. The green dashed line represents the interaction between the CO₂ molecule and the preferential binding sites into the framework. Color codes: blue, N; gray, C; red, O; green, Zn
- Figure 3.132** The snapshot of (a) CH₄ and (b) N₂ adsorption for **55** at 1 bar and 298 K, calculated using GCMC method. Color codes: blue, N; gray, C; red, O; white, H; green, Zn, (c) simulated adsorption isotherms for CO₂, CH₄ and N₂ on **55** at 298 K and 1 bar and (d) energy histogram for **55** in presence of CO₂, CH₄ and N₂
- Figure 3.133** Simulated adsorption isotherms for (a) CO₂/N₂ (50/50) and (c) CO₂/CH₄ (50/50) binary mixtures at 298 K and their energy histograms (b and d, respectively)
- Figure 3.134** (a) conversion for five consecutive cycles for the cycloaddition reaction of CO₂ with epichlorohydrin, catalyzed by **55**, (b) PXRD pattern of **55** before and after catalysis experiments and of (c) progress of the reaction with time in presence of catalyst (solid lines) and after separating the catalyst from the reaction mixture (dotted lines) for cycloaddition reaction of CO₂ with epichlorohydrin
- Figure 3.135** Plausible mechanism for the cycloaddition reactions of CO₂ with epoxides catalyzed by **55**
- Figure 3.136** Propylene oxide position in **55** generated from GCMC simulation using locate method
- Figure 3.137** Structure description of **56**; (a) coordination environment around the metal center, (b) perspective view of the 3D framework with open channels and (c) fourfold interpenetration into the framework
- Figure 3.138** Simplified node and linker type representation for **56**; (a) paddle wheel SBU and the ligand H₄tpstba shown as 4-connected nodes and overall 4,4-connected 2-nodal PtS topology (b) without interpenetration and (c) with fourfold interpenetration
- Figure 3.139** (a) Powder X-ray diffraction pattern of the as-synthesized samples of **56** compared with the simulated powder patterns and (b) thermogravimetric profiles for **56**

List of Schemes

Chapter III (Results and Discussion)

- Scheme 3.1** General synthesis of bpta, tpen, tpbn, tpxn and tpxn
- Scheme 3.2** General synthesis of H₂dmsdbs, H₃mstba and H₄tcps
- Scheme 3.3** Synthesis of H₄dmsbta
- Scheme 3.4** Synthesis of H₄tpsba
- Scheme 3.5** Different strategies for the synthesis of molecular squares
- Scheme 3.6** Synthesis of **1-4**
- Scheme 3.7** Synthesis of **5-10**
- Scheme 3.8** Synthesis of **11** and **11a**
- Scheme 3.9** Synthesis of **12** and **13**
- Scheme 3.10** Synthesis of **14, 15** and **16**
- Scheme 3.11** Synthesis of **17**
- Scheme 3.12** Synthesis of **18** and **19**
- Scheme 3.13** Representation of the pillaring strategy in paddle-wheel SBUs
- Scheme 3.14** Synthesis of **20-25**
- Scheme 3.15** Synthesis of **26-30**
- Scheme 3.16** Synthesis of **31-36**
- Scheme 3.17** Synthesis of **37** and **38**
- Scheme 3.18** Synthesis of **39** and **40**
- Scheme 3.19** Synthesis of **41** and **42**
- Scheme 3.20** Synthesis of **43** and **44**
- Scheme 3.21** Synthesis of **45**
- Scheme 3.22** Synthesis of **46** and **47**
- Scheme 3.23** Synthesis of **48**
- Scheme 3.24** Synthesis of **49** and **50**
- Scheme 3.25** Synthesis of **51** and **52**
- Scheme 3.26** Synthesis of **53**
- Scheme 3.27** Synthesis of **54**
- Scheme 3.28** Synthesis of **55**
- Scheme 3.29** Synthesis of **56**

List of Tables

Chapter III (Results and Discussion)

Table 3.1	Hydrogen bonding parameters in 1, 4, 5, 9 and 10
Table 3.2	Optimization for Knoevenagel reaction, catalyzed by 1 and 5
Table 3.3	Substrate scope for Knoevenagel reaction, catalyzed by 1 and 5
Table 3.4	Substrate scope for the Knoevenagel condensation reaction catalyzed by 37
Table 3.5	Substrate scope for the Knoevenagel condensation reaction catalyzed by 38
Table 3.6	Substrate scope for the three component Biginelli reaction catalyzed by 38
Table 3.7	Substrate scope for the Knoevenagel condensation reaction catalyzed by 39
Table 3.8	Substrate scope for the Strecker reaction catalyzed by 39
Table 3.9	Optimization for the cycloaddition reaction of CO ₂ with epichlorohydrin, catalyzed by 41
Table 3.10	Substrate scope for the cycloaddition of CO ₂ with epoxides, catalyzed by 41
Table 3.11	Substrate scope for the cycloaddition of CO ₂ with epoxides, catalyzed by 43
Table 3.12	Substrate scope for the Strecker reaction catalyzed by 43
Table 3.13	Cyclic carbonates obtained from the reaction of epoxides with CO ₂ catalyzed by 55

Appendix

Table A1	Crystallographic data and structure refinement parameters for 1 and 4
Table A2	Crystallographic data and structure refinement parameters for 5, 9 and 10
Table A3	Crystallographic data and structure refinement parameters for 11 and 11a
Table A4	Crystallographic data and structure refinement parameters for 12 and 13
Table A5	Crystallographic data and structure refinement parameters for 14, 15 and 16
Table A6	Crystallographic data and structure refinement parameters for 17, 18 and 19
Table A7	Crystallographic data and structure refinement parameters for 20, 21 and 22
Table A8	Crystallographic data and structure refinement parameters for 23, 24 and 25
Table A9	Crystallographic data and structure refinement parameters for 26 and 27
Table A10	Crystallographic data and structure refinement parameters for 28, 29 and 30
Table A11	Crystallographic data and structure refinement parameters for 32, 33 and 34
Table A12	Crystallographic data and structure refinement parameters for 35 and 36
Table A13	Crystallographic data and structure refinement parameters for 37 and 38
Table A14	Crystallographic data and structure refinement parameters for 39 and 40
Table A15	Crystallographic data and structure refinement parameters for 41 and 42

Table A16	Crystallographic data and structure refinement parameters for 43 and 44
Table A17	Crystallographic data and structure refinement parameters for 45 , 46 and 47
Table A18	Crystallographic data and structure refinement parameters for 48
Table A19	Crystallographic data and structure refinement parameters for 49 and 50
Table A20	Crystallographic data and structure refinement parameters for 51 and 52
Table A21	Crystallographic data and structure refinement parameters for 53 and 54
Table A22	Crystallographic data and structure refinement parameters for 55 and 56
Table A23	Selected Bond lengths (Å) for 1 and 4
Table A24	Selected Bond lengths (Å) for 5 , 9 and 10
Table A25	Selected Bond lengths (Å) for 11 and 11a
Table A26	Selected Bond lengths (Å) for 12 and 13
Table A27	Selected Bond lengths (Å) for 14 , 15 and 16
Table A28	Selected Bond lengths (Å) for 17 , 18 and 19
Table A29	Selected Bond lengths (Å) for 20 , 21 and 22
Table A30	Selected Bond lengths (Å) for 23 , 24 and 25
Table A31	Selected Bond lengths (Å) for 26 and 27
Table A32	Selected Bond lengths (Å) for 28 , 29 and 30
Table A33	Selected Bond lengths (Å) for 32 , 33 and 34
Table A34	Selected Bond lengths (Å) for 35 and 36
Table A35	Selected Bond lengths (Å) for 37 and 38
Table A36	Selected Bond lengths (Å) for 39 and 40
Table A37	Selected Bond lengths (Å) for 41 and 42
Table A38	Selected Bond lengths (Å) for 43 and 44
Table A39	Selected Bond lengths (Å) for 45 , 46 and 47
Table A40	Selected Bond lengths (Å) for 48
Table A41	Selected Bond lengths (Å) for 49 and 50
Table A42	Selected Bond lengths (Å) for 51 and 52
Table A43	Selected Bond lengths (Å) for 53 and 54
Table A44	Selected Bond lengths (Å) for 55 and 56
Table A45	Selected Bond angles (°) for 1 and 4
Table A46	Selected Bond angles (°) for 5 , 9 and 10
Table A47	Selected Bond angles (°) for 11 and 11a
Table A48	Selected Bond angles (°) for 12 and 13
Table A49	Selected Bond angles (°) for 14 , 15 and 16

Table A50	Selected Bond angles (°) for 17, 18 and 19
Table A51	Selected Bond angles (°) for 20, 21 and 22
Table A52	Selected Bond angles (°) for 23, 24 and 25
Table A53	Selected Bond angles (°) for 26 and 27
Table A54	Selected Bond angles (°) for 28, 29 and 30
Table A55	Selected Bond angles (°) for 32, 33 and 34
Table A56	Selected Bond angles (°) for 35 and 36
Table A57	Selected Bond angles (°) for 37 and 38
Table A58	Selected Bond angles (°) for 39 and 40
Table A59	Selected Bond angles (°) for 41 and 42
Table A60	Selected Bond angles (°) for 43 and 44
Table A61	Selected Bond angles (°) for 45, 46 and 47
Table A62	Selected Bond angles (°) for 48
Table A63	Selected Bond angles (°) for 49 and 50
Table A64	Selected Bond angles (°) for 51 and 52
Table A65	Selected Bond angles (°) for 53 and 54
Table A66	Selected Bond angles (°) for 55 and 56
Table A67	Q _{st} values of reported MOFs
Table A68	Adsorption selectivity of reported MOFs for CO ₂ /N ₂ (15:85) and CO ₂ /CH ₄ (50:50) at 1 bar
Table A69	Comparison of K _{sv} and Detection Limit for the sensing of TNP

Acronyms and Abbreviations

bpta	2-methyl-N,N-bis(pyridin-2-ylmethyl)propan-2-amine
tpen	N,N',N'',N'''-Tetrakis-(2-pyridylmethyl)ethane-1,2-diamine
tpbn	N,N',N'',N'''-Tetrakis-(2-pyridylmethyl)-1,4-diaminobutane
tphxn	N,N',N'',N'''-Tetrakis-(2-pyridylmethyl)-1,4-diaminohexane
tpxn	N,N'-(1,4-phenylenebis(methylene))bis(1-(pyridin-2-yl)-N-(pyridin-2-ylmethyl)methanamine)
bpy	4,4'-bipyridine
bpe	1,2-di(pyridin-4-yl)ethane
bpee	1,2-di(pyridin-4-yl)ethene
azopy	4,4'-azopyridine
bpp	1,3-di(pyridin-4-yl)propane
dpb	1,4-di(pyridin-4-yl)benzene
4-bpdb	bis-(4-pyridyl)-diazobutane
4-bpdh	bis-(4-pyridyl)-diazohexane
3-bpdb	bis-(3-pyridyl)-diazobutane
3-bpdh	bis-(3-pyridyl)-diazohexane
4-bpmp	1,4-bis(pyridin-4-ylmethyl)piperazine
3-bpmp	1,4-bis(pyridin-3-ylmethyl)piperazine
1,5-ND-4-Py	bis(pyridin-4-ylmethylene) naphthalene-1,5-diamine
1,5-ND-3-Py	bis(pyridin-3-ylmethylene) naphthalene-1,5-diamine
4-tpom	tetrakis(4-pyridyloxymethylene)methane
3-tpom	tetrakis(4-pyridyloxymethylene)methane
H ₂ dmsdba	4,4'-(dimethylsilanediyl)dibenzoic acid
H ₂ obba	4,4'-oxydibenzoic acid
H ₃ mstba	4,4',4''-(methylsilanetriyl)tribenzoic acid
H ₄ tcps	tetracarboxyphenyl silane
H ₄ dmsbta	5,5'-(4,4'-((dimethylsilanediyl)bis(4,1-phenylene))bis(1H-1,2,3-triazole-4,1-diyl))diisophthalic acid
H ₄ tpstba	4,4',4'',4'''-(4,4',4'',4'''-(tetraphenylsilane))tetrakis(1H-1,2,3-triazole-4,1-diyl))tetrabenzoic acid
B.p.	Boiling point
M.p.	melting point
MeOH	methanol
EtOH	ethanol
CHCl ₃	chloroform
DCM	dichloromethane
CH ₃ CN	acetonitrile
THF	tetrahydrofuran
DMF	N,N'-dimethylformamide
DMA	N,N'-dimethylacetamide
DEA	N,N'-diethylacetamide
DMSO	dimethylsulfoxide

CDCl ₃	deuterated chloroform
DMSO- <i>d</i> ₆	deuterated dimethylsulfoxide
NB	Nitrobenzene
1,3-DNB	1,3-dinitrobenzene
1,4-DNB	1,4-dinitrobenzene
4-NT	4-nitrotoluene
2,4-DNT	2,4-dinitrotoluene
2,4,6-TNT	2,4,6-trinitrotoluene
2-NP	2-nitrophenol
4-NP	4-nitrophenol
2,4-DNP	2,4-dinitrophenol
2,4,6-TNP	2,4,6-trinitrophenol
TMSCN	trimethylsilyl cyanide
TCTPM	4,4',4'',4'''-tetracyanotetraphenylmethane
TBAB	tetra Butyl ammonium bromide
diam	diammine
mea	monoethanolamine
BDC	benzene dicarboxylic acid
SV	Stern-Volmer
SF	selectivity factor
BET	Brunauer–Emmett–Teller
Qst	isosteric heat of adsorption
CC	Clausius Clapeyron
IAST	ideal adsorption solution theory
CCS	carbon capture and sequestration
atm	atmosphere
CCS	carbon dioxide capture and sequestration
CP	Coordination Polymer
MOF	Metal Organic Frameworks
IRMOF	iso-reticular Metal Organic Frameworks
ZIF	Zeolitic Imidazole Framework
MOCN	Metal Organic Coordination Networks
SCNs	Supramolecular Coordination Networks
MNP	metal nano particles
0D	zero dimensional
1D	one dimensional
2D	two dimensional
3D	three dimensional
SBU	secondary building unit
SC	Single Crystal
TLC	thin layer chromatography
FTIR	Fourier Transform Infrared
UV-Vis	Ultraviolet-Visible
FESEM	Field emission scanning electron microscopy

TGA	Thermogravimetric analysis
NMR	Nuclear magnetic resonance
PXRD	Powder X-ray diffractometry
SCXRD	Single crystal X-ray diffractometry

Contents

	Page
Declaration	iii
Acknowledgement	iv
List of Figures	vi
List of Schemes	xviii
List of Tables	xix
Acronyms and Abbreviations	xxii
Abstract	xxvi
Introduction	1
Experimental Section	19
Results and Discussion	49
Conclusions	221
References	227
Appendix	241
Publications	301
Vita	303

Abstract

For rapid advances and widespread interest in the study of macromolecules of nanoscopic dimensions, a fascinating growth in the field of supramolecular chemistry is observed over the past few decades. In this regard, with the pioneering work of Fujita et al. and Robson et al., coordination driven self-assemblies have gained considerable attention for the synthesis of discrete and polymeric structures with desired structural topologies. Coordination driven self-assembly, which proceeds via the simultaneous assembly of predetermined building blocks, provides a greater control over the rational design of coordination architectures as metal ligand coordination bonds are highly directional in nature. The design principle primarily depends on the judicious selection of metal ion/cluster and multitopic organic linkers, resulting in the formation of coordination architectures with targeted structural topologies and physicochemical properties.

This thesis work presents the strategic design of such architectures via multicomponent self-assembly of metal ion, neutral polypyridyl ligands and anionic carboxylate linkers in a one-pot self-assembly procedure without the need of any predesigned precursors. Their solid state structures (discrete or polymeric) have been established by single crystal X-ray diffraction analysis and their bulk phase purity has been supported by various analytical techniques like powder X-ray diffraction, FT-IR, UV-Vis spectroscopy, thermo gravimetric and elemental analysis. The structural diversity of these coordination architectures has been systematically studied by changing one variable at a time and this understanding has been further utilized in the tailor-made synthesis of coordination architectures for targeted applications. The utility of these materials in different areas, particularly in the field of (i) heterogeneous catalysis for some well-known organic transformations (Knoevenagel reaction, Strecker reaction and Biginelli reaction), (ii) selective carbon dioxide capture, separation and its chemical conversion into value-added cyclic carbonates by porous metal organic frameworks (MOFs) and (iii) sensing of nitroaromatic compounds by discrete molecular squares or by luminescent MOFs have been explored to further support the underlying strategy designed for the construction of these coordination architectures.

CHAPTER I

Introduction

In the past few decades, enormous efforts have been devoted to the construction of aesthetically appealing functional structures with sizes that approach nanoscopic dimensions. Further advances and widespread interest in the study of macromolecules have resulted a fascinating growth in the field of supramolecular chemistry. Today, the field of supramolecular chemistry has grown into a mature field of modern science whose interface with many disciplines have provided invaluable opportunities for crossing boundaries both inside and between the fields of chemistry, physics, and biology. Cooperative interactions are ubiquitous and plays the fundamental role in all aspects of supramolecular chemistry. When one has control over the synthesis of structures containing well defined cavities with deliberately designed cooperative interactions, supramolecular systems can be designed for targeted applications. The interest into the field of supramolecular chemistry started after the discovery of “crown ethers”, “cryptands”, and “spherands” by Charles John Pedersen,¹ Donald James Cram² and Jean-Marie Lehn³ in early 1960s, followed by their importance in the recognition process via non-covalent interactions such as hydrogen bonding, charge-charge, donor-acceptor, π - π and van der Waals etc. Synthetic organic chemists enjoy the luxury of having a large collection of reliable reactions for preparing small molecules, mesoscopic structures, and polymers. However, as the scale and complexity of target molecules increases, the step-wise synthesis of large discrete supramolecular structures becomes increasingly difficult.⁴ Metal–ligand bonding circumvents many of the difficulties associated with directional control afforded by predictable and well-defined coordination geometries of transition metal ions. The concept was established with the pioneered work of Makoto Fujita⁵ in 1990 for the synthesis of molecular square using a square planar metal complex (Figure 1.1). The cis-capping of the square planar metal complex provides the required coordination sites at 90° angle (which is a daunting task with organic building blocks) and controls the polymerization to form infinite framework structures. On the basis of various interactions used in the self-assembly process, supramolecular chemistry can be broadly classified into three main branches: (a) those that utilize H-bonding, (b) processes that uses noncovalent interactions such as ion–ion, ion-dipole, π - π stacking, van der Waals, and hydrophobic interactions, and (c) those that employ strong and directional metal-ligand bonds for the assembly process.

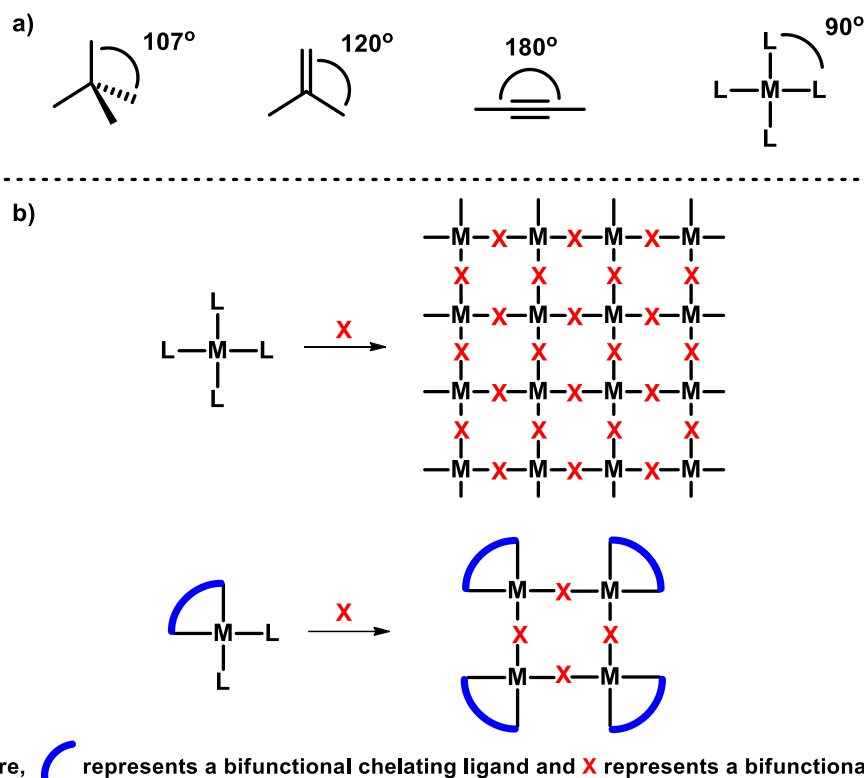


Figure 1.1. (a) Openings at different angles provided by simple organic and inorganic precursors and (b) represents the cis-capping strategy to control the infinite polymeric networks.

Coordination-driven self-assembly process has gained considerable attention over the other approaches for the rational design of such architectures^{6–16} as the metal ligand coordination bonds are much predictable and directional in nature. In addition, the ligand structure can be modulated in a desirable manner by established synthetic organic chemistry. The self-assembly process to design the metal based supramolecules offers an alternative to the classical organic route because it proceeds via the simultaneous assembly of pre-determined building blocks, resulting in well-defined, discrete supramolecular architectures. The strategy has been very much explored for designing molecules of desired dimensions ranging from a few cubic angstroms to over a cubic nanometer. Since the early pioneering work by Lehn¹⁷ and Sauvage¹⁸ on the feasibility and usefulness of coordination driven self-assembly in the formation of infinite helicates, grids, ladders, racks, knots, rings, catenanes, rotaxanes, and related species,^{19–23} several groups—those of Stang,^{9,10,12,14} Raymond,^{24–26} Fujita,^{6,11,13,27} Mirkin,^{16,28} Cotton,^{29,30} and others^{31–33}—have independently developed and exploited novel coordination based paradigms for the self-assembly of discrete metallacycles and metallacages with well-defined shapes and sizes. A diverse range of 2D (rhomboids, squares, rectangles, and triangles, etc.) and 3D (trigonal pyramids, trigonal prisms, cubes, cuboctahedra, double squares, adamantanoids, dodecahedra, etc.)

supramolecular architectures have been reported. The precursors to these architectures can be grouped as Lewis acidic metal complexes as “acceptors” and Lewis basic organic ligands as “donors”. Using different donor-acceptor combinations, various synthetic strategies have been employed for the metal-ligand coordination.^{8,10,12} Of the various synthetic strategies, the directional bonding approach, established by Fujita^{5,34} and Stang’s³⁵ group gives access to a wide variety of 2D and 3D supramolecular architectures. The basic structural requirements for this approach consist of structural rigidity and pre-defined bite angle of the complementary precursors with appropriate stoichiometry. In practice, many other factors are important and have a great influence on the experimental results, for instance the solvent choice, the temperature, precursor’s concentrations, the order of building blocks introduction, and/or the rate of mixing of the substrates. As shown in Figure 1.2, the symmetry and number of binding sites within each precursor unit guide the shape of the target assembly. The structural and functional features of these self-assembled structures result from the information stored in the components and their intrinsic properties that are dictated by the presence of functional groups.

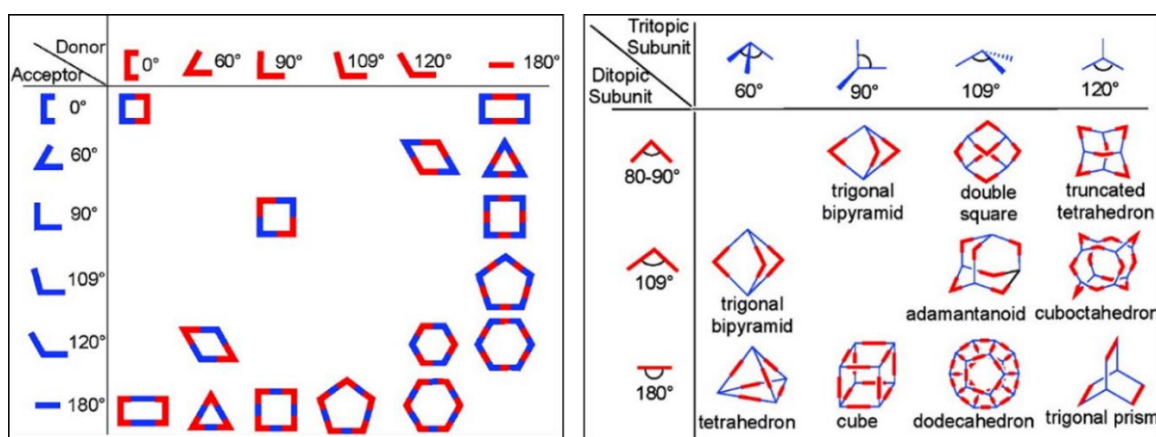


Figure 1.2. Combination of various building units for accessing 2D (left) and 3D (right) supramolecular architectures by directional bonding approach. (Adapted from reference 11).

There have been several reports in the literature which explains the design principles of these architectures based on either the different classes of building blocks (donors or acceptors) or based on different structures of the final architectures.³⁶⁻⁴⁸ Among the metal-mediated assembly of molecular polygons, molecular squares represent a special class of metallacycles because of their ease of preparation, conformational stability, and the distinctive properties they exhibit, and hence have gained extensive attention of the synthetic chemists. According to the directional bonding approach, a molecular square can be formed by the combination of a 90° corner unit with a linear bridging ligand. Thus, there are two complementary ways to design a molecular square: (a) by the combination of a 90°

metal-containing acceptor having two accessible *cis*-coordination sites with linear donor units and (b) by using a 180° linear metal-containing acceptor and a ligand with donor atoms at 90° to each other. Almost any transition metal with a square-planar, trigonal-bipyramidal, or an octahedral geometry can be used as a corner unit. However, transition metals with square-planar geometries are most widely used because *cis*-protected 90° metal corner units can be easily derived by blocking adjacent coordination sites with strong chelating ligands, leaving the other two sites accessible for ligand substitution. Since the pioneered work of Fujita et al.,⁵ a vast number of molecular squares have been reported utilizing this strategy.^{6–15,16,27} There have been several attempts in the literature to design functional molecular squares by using functional corner ligands or functional linkers. For example, in addition to the simple *cis*-protected corner ligands, titanocene,^{49,50} carbazole⁵¹ and fluxional thiocrown-based⁵² corner ligands in combination with a variety of ligand edges ranging from porphyrins,¹⁰ luminescent perylene diimides⁵³ and redox-active ferrocene derivatives¹⁰ to chiral linkers such as phosphine-functionalized binaphthols⁵⁴ have been utilized for the synthesis of cationic molecular squares. A set of neutral molecular squares have also been reported either by using divalent metal ions with neutral chelating bidentate ligands at the corners with anionic alkynyl linkers^{55–57} or by using divalent metal ions with anionic ligands at the corners with neutral linkers.^{58,59} A very different approach was explored by Cotton et al. by fusing the multiply bonded dimetallic angular building units (Mo_2^{4+} , Rh_2^{4+} or Ru_2^{5+}) with linear building units, such as dicarboxylates, for [4 + 4] self-assembled molecular squares.^{29,30} This area has been populated by several reports on many transition metal containing molecular squares in the literature.^{7,60–65} For various synthetic strategies employed, one important prerequisite is the use of pre-synthesized donor/acceptor counterparts with fixed directionalities in a two-component self-assembly process.

On the other hand, coordination polymers are the extended form of the discrete coordination architectures, where, the basic building blocks containing metal ions and organic ligands assemble infinitely leading to one-, two-, and three-dimensional networks (Figure 1.3), are commonly known as coordination polymers.^{66–71} The term “polymer” was first employed by J.J. Berzelius in 1833 to describe any compound that could be formulated as consisting of multiple units of a basic building block. In comparison to the organic polymers the term “coordination polymer” was defined by J. C. Bailar in 1964 for inorganic compounds that can be considered as polymeric species and established rules for the building and the required properties of new species involving metal ions and organic ligands. The basic requirement for the coordination polymer is that the ligand must be a bridging organic group

and the metal atoms must solely be bridged by this organic ligand at least in one extended dimension. Furthermore, at least one carbon atom must lie between the donor atoms. The last requirement excludes groups such as organyloxides (RO^-), organophosponates (RPO_3^{2-}) or organosulfonates (RSO_3^-), which bridge with their one “inorganic” end group only, from giving rise to coordination polymers. Also the metal-ligand assemblies where the metal is bridged by “inorganic” bridges, such as $-(\text{R,H})\text{O}-$, $-\text{Cl}-$, $-\text{CN}-$, $-\text{N}_3-$, $-(\text{R,O})\text{PO}_3-$ and $-(\text{R,O})\text{SO}_3-$ cannot be considered as coordination polymers.^{69,72}

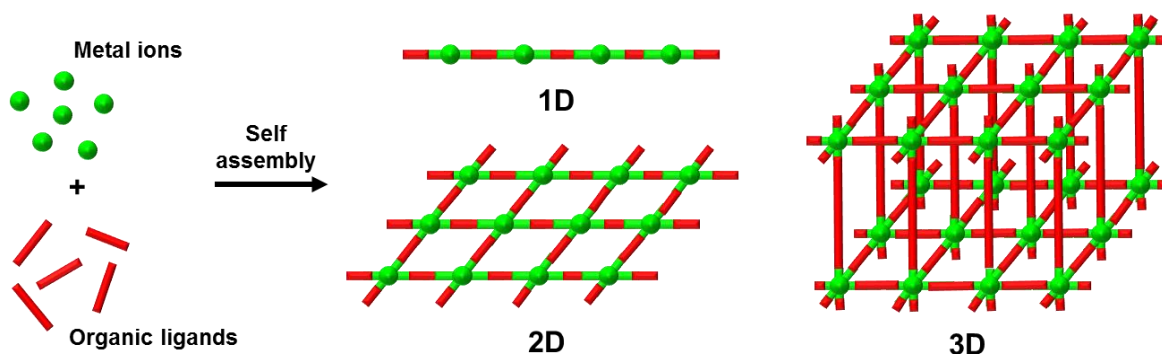


Figure 1.3. Schematic representation of 1D, 2D or 3D coordination polymers.

The development in the field of coordination chemistry of extended structures have gained considerable attention after the structural characterization of Prussian blue⁷³ in 1977 which was in use since early 1700s, and Hoffman clathrate,⁷⁴ which was first synthesized in 1897. It was found later that the structure of the Hofmann clathrate is composed entirely of inorganic constituents: square planar and octahedral Ni^{2+} ions linked by cyanide into a 2D square grid. Notably, the axial positions of the octahedral metal ions are occupied by ammonia ligands thus pushing the layers apart and creating voids that are accessible for the inclusion of organic guests. In 1959, Saito et al. reported the first bis(alkylnitrilo)copper(I) structures composed of tetrahedral $\text{Cu}(-\text{CN})_4$ units.⁷⁵⁻⁷⁷ These building units are connected through organic moieties of different lengths and thus propagate into extended networks of varying dimensions. Depending on the length and conformation of the dinitrile linker, one-dimensional chains in case of succinonitrile (SUC), two-dimensional grid structures in case of glutaronitrile (GLU) and three-dimensional networks in case of adiponitrile (ADI) were obtained (Figure 1.4). With this understanding of the geometric aspects of the bonding in coordination chemistry of extended networks, a hallmark discovery was reported by Hoskins and Robson in 1989 and provided an important rationale for the deliberate design and synthesis of extended nets.⁷⁸ In their contribution they utilized the tetrahedral single-metal building unit $\text{Cu}(-\text{CN})_4$ together with the tetrahedral organic linker 4,4',4'',4'''-

tetracyanotetraphenylmethane (TCTPM), to afford an infinite, non-interpenetrated, 3D framework with diamond net topology. Utilizing the simple design principles many coordination polymers with diamond-type, pts-type and alb- or ths-type framework topologies have been reported using tetrahedral, square planer and tritopic cyano based organic linkers, respectively.⁶⁶

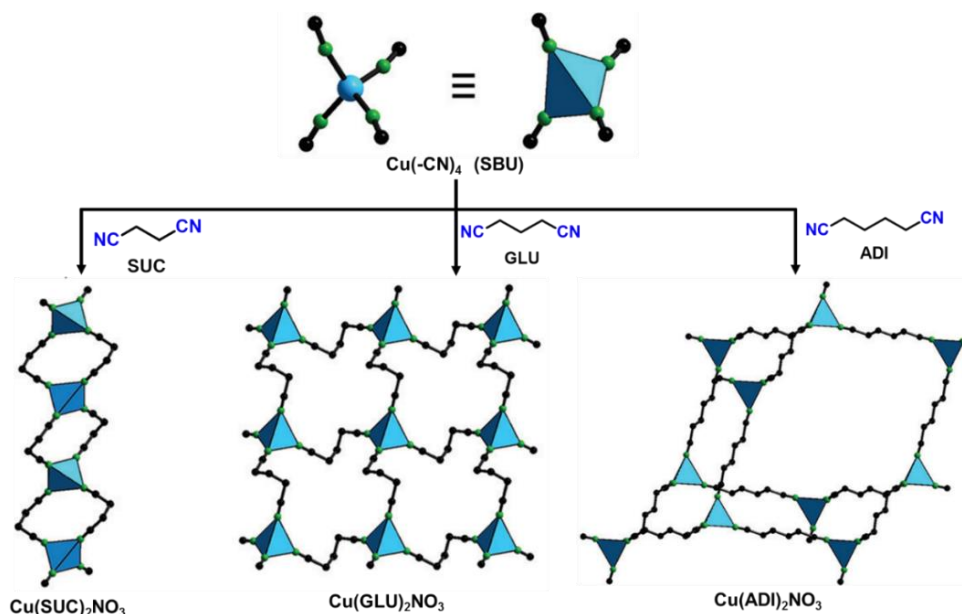


Figure 1.4. Different bis(alkylnitrilo)copper(I) structures: one-dimensional chains sustained by succinonitrile (SUC), two-dimensional grid structures with glutaronitrile (GLU), and three-dimensional networks made of adiponitrile (ADI) linkers.

Another inspiration for the design of this kind of materials composed of metal ions and organic linkers started with the modification of the original Hoffman clathrates. Several series of the analogous clathrates have been derived by appropriate replacements of the host moieties. These clathrates are designated with a general formula $\text{Cd}(\text{diam})\text{M}'(\text{CN})_4 \cdot n\text{G}$ where diam refers to diammine, an ambident diamine or monoethanolamine (mea), or a pair of unidentate mea's, $\text{M}'(\text{CN})_4$ is a square-planar or a tetrahedral tetracyanommetallate(II), and G is a small aromatic guest molecule.⁷⁹ In addition to the cyano-based organic linkers, the use of pyridyl based bifunctional linkers for the synthesis of such coordination polymers evolved after the first two-dimensional square grid network reported by Fujita et al.⁸⁰ The framework can be considered as an extended form of 4,4'-bipyridine based discrete molecular square reported by the same group.¹ It is composed of $\text{Cd}(\text{bpy})_2(\text{NO}_3)_2$ (bpy = 4,4'-bipyridine) and contains large guest filled voids that can render catalytic processes with respect to cyanosilylation. The bridging ability of pyridyl-based bifunctional linkers was further utilized for connecting Hoffman clathrates; it was found that the capping ammonia

ligands can be replaced by bis(pyridyl) linkers, thereby connecting the 2D layers to form 3D coordination architectures. Further progress in the field of coordination polymers based on cyano- and bis(pyridyl) organic ligands have resulted in the development of porous coordination polymers of varied dimensionalities and topologies. For example, a range of porous structures with diamond-like, ThSi_2 (*ths*) and primitive cubic (*pcu*) topology with open pores having about 50% empty space of the total unit cell volume have been reported.^{81–83} However, while considering these materials for practical applications, most of the porous structures were found to be unstable upon loss of guest molecules.

The instability issue underlined the need for developing strategies for making robust frameworks that exhibit permanent porosity so that they can be utilized for various applications. The instability of the cyano- and pyridyl-based coordination polymers was thought to be due to the weak bonding interactions between the linker and the metal center and the flexibility of the coordination sphere around the metal center. In order to design permanently porous structures, Yaghi and co-workers⁸⁴ reported the use of charged chelating carboxylate linker to lock the metal–ion positions in place and allow for robust metal–carboxyl clusters to be used as nodes in making extended structure. In contrast to the neutral donor linkers, the charged linkers provide much stronger bonding to the metal ion. Other advantage which is often observed is that the polynuclear metal–carboxyl clusters (also referred to as secondary building units, SBUs) had one kind of an overall coordination mode, ensuring the stiffness of the local geometry and thus the architectural robustness of the resulting framework. This kind of porous and robust structures were termed as metal organic frameworks (MOFs), which were defined as “crystalline compound consisting of metal ions or clusters coordinated to often rigid organic molecules to form two-, or three-dimensional structures that can be porous”. This different nomenclature for the metal organic structures was made on the basis of their structural aspects; the term coordination polymer very broadly encompasses all the extended structures based on metal ions linked into an infinite chain, sheet, or three-dimensional architecture by bridging ligands that usually contain carbon atom, whereas the term MOF is much more specific to be used for two- or three-dimensional networks. Chronology of advances in the coordination chemistry of extended structures is presented in Figure 1.5.

After establishing the permanent porosity and robustness of the 2D framework, the same group reported the first 3D extended framework, MOF-5 [$\text{Zn}_4\text{O}(\text{BDC})_3$], shortly after the discovery of the 2D MOF structure.⁸⁵ The 3D structure, constructed from octahedral $\text{Zn}_4\text{O}(-\text{COO})_6$ SBUs and BDC linkers, constituted the highest reported surface area for any

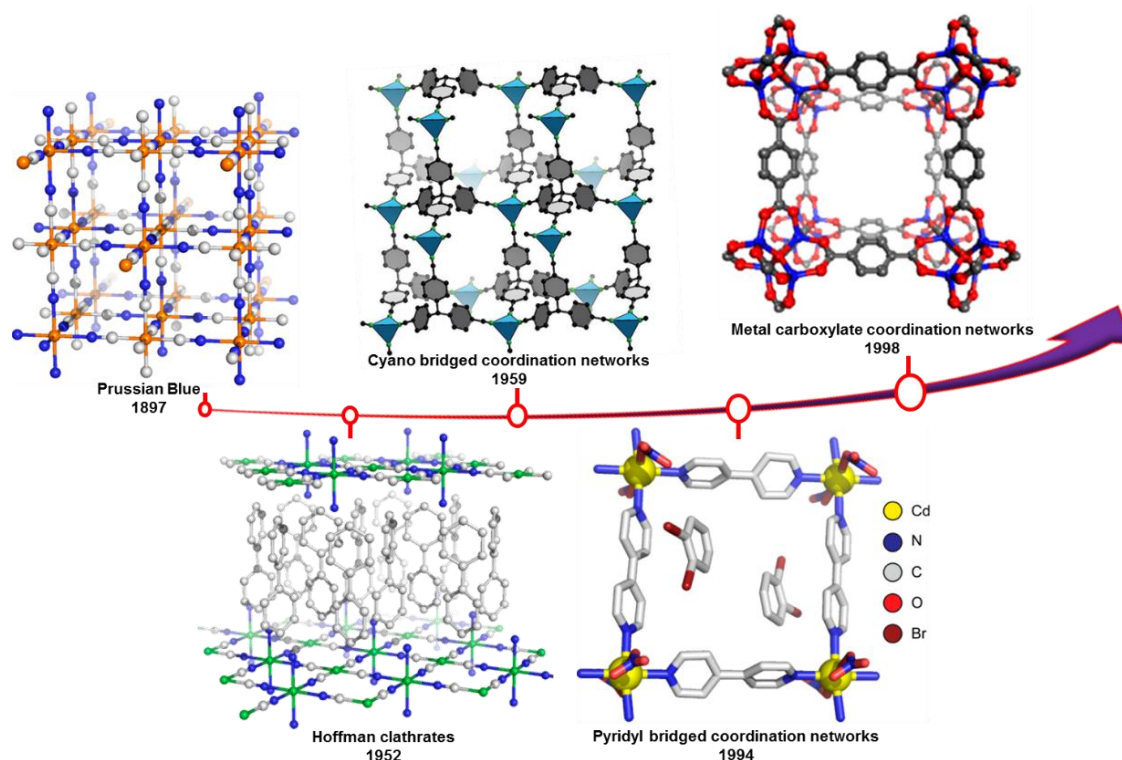


Figure 1.5. Chronology of advances in coordination chemistry of extended structures.

structure known at the time. The enormous popularity of this structure inspired the researchers towards a rapid development of MOF chemistry, which has come to entail the largest class of synthetic crystalline materials known today.^{86,87} It was shown that a series of MOF-5 prototypes could be obtained by using extended or functionalized BDC analogous as linkers.⁸⁸ A series of MOFs based on the same net or topology with different void volume and pore environment were reported and the concept was defined as isorecticular (from the Greek term “iso” meaning “same” and Latin “reticulum” meaning “net”) MOF (IRMOFs) synthesis. In addition to the linear BDC analogous, the concept of IRMOFs synthesis was further explored for the synthesis of functional MOF structures with different tritopic, tetratopic and hexatopic carboxylate linkers and different sets of metal carboxylate clusters as SBUs.⁸⁷

The interest in the coordination architectures started with the initial work of Fujita et al. and Robson et al. for the synthesis of coordination driven discrete and polymeric architectures, respectively. Both of these fields have attracted considerable scientific interest due to the discovery of ways for the tailor-made synthesis of a diverse range of 2D (rhomboids, squares, rectangles, and triangles, etc.) and 3D (trigonal pyramids, trigonal prisms, cubes, cuboctahedra, double squares, adamantanoids, dodecahedra, etc.) discrete and polymeric architectures. Coordination polymers (or MOFs) with high surface area have now taken an

important position in the porous-materials area and are added as a new category along with conventional inorganic and organic porous materials. Porous coordination polymers have an extra advantage of structural manipulations as per the requirements. For example, the inorganic part (SBU) provides regularity and rigidity and the porosity and functionality can be tuned by judicious selection of the organic linkers. Therefore, these materials display a large structural diversity based on various geometries of metal ion/cluster (node) and size, shape, and multifunctionality of the organic linkers.

Studies in the area of crystal engineering of coordination architectures have witnessed an upsurge in recent years not only because of their variety of intriguing architectures and topologies,^{10,12,89–92} but also because of their potential applications in areas that includes gas/vapour separation and storage,^{93–97} sensors,^{98–100} magnetism^{101,102} drug delivery,^{103–109} water treatment,¹¹⁰ heterogeneous catalysis^{111–116} and embedding of nano-particles (Figure 1.6).^{117–123} As discussed above, a lot of effort has been made in the rational design of these materials as the diverse properties of the coordination architectures are closely related to their structures, and could be modulated by tailoring their structures via crystal engineering.^{124–128} The diverse selection of organic ligands and inorganic nodes in constructing such coordination architectures has given an opportunity to build a library of discrete and polymeric architectures with varied dimensionalities and functionalities. Keeping in mind the above-mentioned factors, the synthesis of a series of discrete and polymeric coordination architectures using multicomponent self-assembly process are reported in work. Out of various synthetic methods available in literature (e.g. one pot self-assembly at ambient conditions, hydro/solvothermal, sonochemical, electrochemical and microwave) the ambient and hydro/solvothermal protocols for the synthesis of these coordination architectures have been mainly employed for the present work. Based on their underlying design strategy these materials are further utilized for various applications (Figure 1.6), which are discussed below.

Catalysis

In its classical definition, a catalyst is a substance that increases the rate of a reaction without being consumed considerably. The active site in the catalyst and its interaction with reactant(s), transition state(s), and product(s) define whether the desired reaction will proceed with a higher rate and selectivity at relatively milder conditions compared to the non-catalyzed reaction. A catalyst can work in a homogeneous and heterogeneous manner; both these sub disciplines have their own advantages and limitations. To bridge the gap

between these two sub disciplines of catalysis, intense research has been carried out over the last few decades in the quest for alternative systems. Coordination architectures have evolved as a relatively new class of materials that have the potential to become the ideal homo–hetero bridge.^{111–116,129–131}

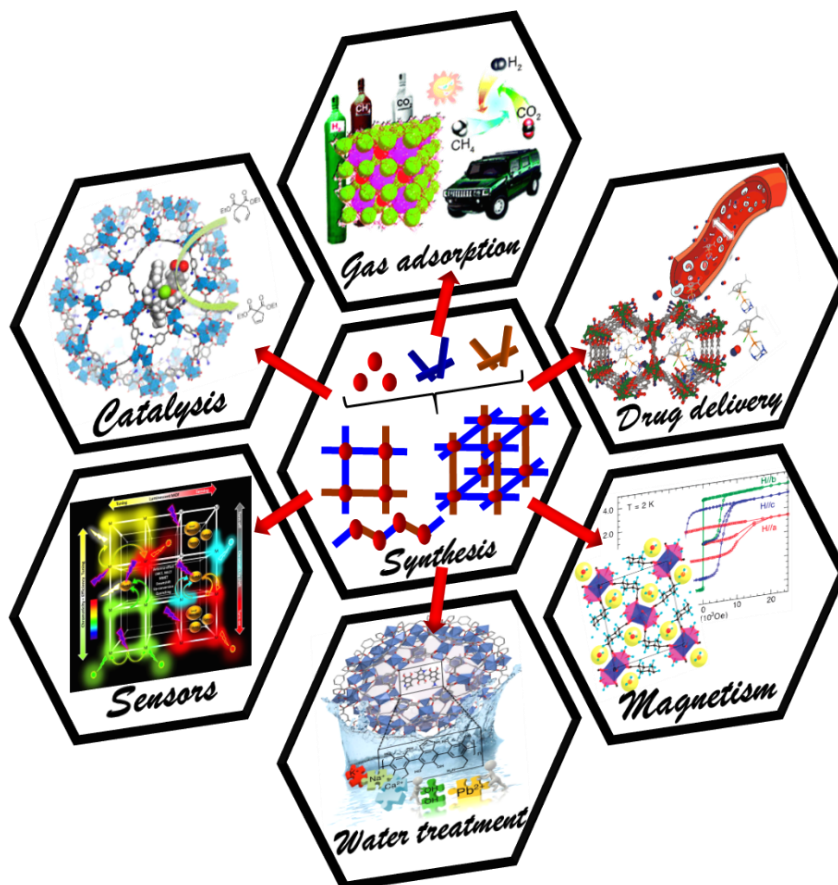


Figure 1.6. A schematic representation showing the synthesis and various applications of the coordination architectures.

However, the term ‘coordination architectures’ has been known since early 1950s; the first catalytic process within a coordination architecture was addressed through cyanosilylation of benzaldehyde and imines in 1994.⁸⁰ This inspired the researchers to explore the concept of coordination chemistry to design such architectures, which has led to numerous elegant examples. In general, the Lewis acid open metal site or Bronsted basic organic functional site acts as the active catalytic site in these architectures and it is not surprising that the design of such active sites is one of the main targets of catalyst engineering. Coordination architectures are very good candidates for this purpose because of their ease of structure tunability using various sets of the organic linker which provides the site for catalysis. As shown in Figure 1.7, multiple active sites can be incorporated into the coordination architectures.

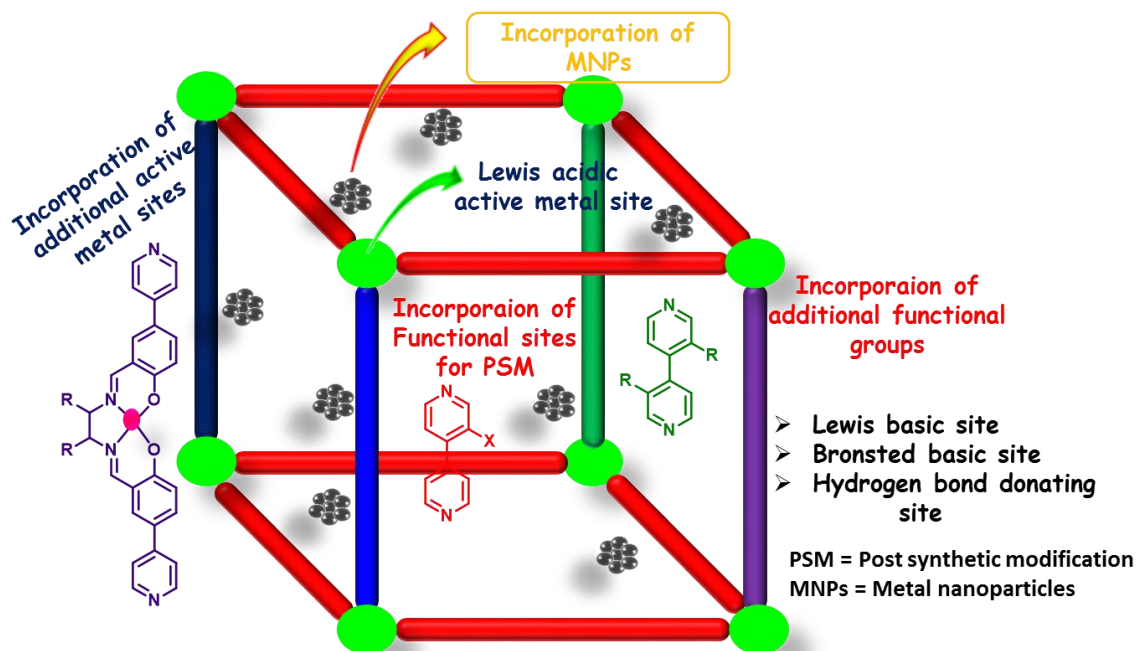


Figure 1.7. A schematic diagram representing different catalytic sites in a coordination architecture.

In addition to the open metal site, various basic and hydrogen bond donating sites can be incorporated by judicious ligand design. The available empty space and high surface area of some of these architectures provide the opportunity for embedding metal nanoparticles, which is an active area of research for designing catalysts with multiple active sites.^{117–123}

Sensing

A chemical sensor can be defined as a device that responds with perfect and instantaneous selectivity to a particular target chemical substance (analyte) present in any desired medium in order to produce a measurable signal output at any required analyte concentration. Chemical sensors are used for sensing diverse entities like explosives, toxic gases, neutral molecules, solvent molecules, temperature, pH, acids/bases, vapors, anions, cations, fungicides, fumigants, biological entities like cells, virus, antibodies, and pesticides etc.^{98,132–136} Sensing by these materials is strongly dependent on the molecular recognition and self-assembly of these chemical structures by various supramolecular interactions resulting in a change in the physical properties which is observed using different analytical techniques.^{137,138} Out of various analytical techniques used, fluorescence sensing has evolved as the most popular technique. It is based on the fluorescent-tagged molecules in the coordination architecture or using the lanthanides as metal center which can produce fluorescence after interacting with the organic ligand. Fluorescence is based on the property of some molecules which when hit by a photon, can absorb the energy of that photon to get

into an excited state. Upon relaxation from that excited state, the same molecule releases a photon (fluorescence emission). Any interference in this process results in a change in the fluorescence emission. There are four ways by which this change in the fluorescence emission can take place. First is *turn-on fluorescence* in which an enhancement in the fluorescence intensity (hyperchromic shift) takes place while the second is the *turn-off fluorescence* in which a decrease in the fluorescence intensity (hypochromic shift) is observed. Other two are the change in the λ_{\max} to the higher wavelength, known as *red shift* (bathochromic shift) and the change towards lower wavelength known as *blue shift* (hypsochromic shift). All these changes in the fluorescence are due to the different interactions of an external analyte or guest molecule with the framework which can trigger the electron or energy transfer between the framework and the analyte.^{100,139–141} Coordination architectures have evolved as very promising candidates as chemical sensors for the solution or vapour phase detection of various analytes.^{100,142–147} Importance of these materials have extensively increased because of their exceptional structure tunability and also because these materials can interact with different analytes due to the presence of different interaction sites which can be anchored using various design principles of coordination chemistry. Out of a range of different analytes, the sensing of small molecules such as nitro aromatics is an essential task to accomplish as these serve as potential pollutants and explosive materials used in terrorist activities. Coordination architecture have shown excellent potential for detecting a range of organic molecules and ions, however, still there is much room for improvement.

Carbon dioxide capture and conversion

Carbon dioxide (CO₂), as the major greenhouse gas, has been cited as the leading culprit, causing global warming and subsequent climate changes.^{96,148,149} During the last 10 years, the mean annual absolute CO₂ concentration has increased by 2.21 ppm per year and is responsible for about 83 % of the increase in radiative forcing over the past 5 years.¹⁵⁰ Therefore, it is of immense importance to develop such systems which can work successfully in the process of carbon dioxide capture and sequestration (CCS) thus can help in reducing the greenhouse emission. Human activities, mainly burning of fossil fuels are largely increasing the concentration of CO₂ in the atmosphere (Figure 1.8).

Since fossil fuels will remain to be the major energy source for many years and an immediate halt of CO₂ emission is not possible, a global effort has recently been devoted to developing new technologies and processes for the effective capture and sequestration of

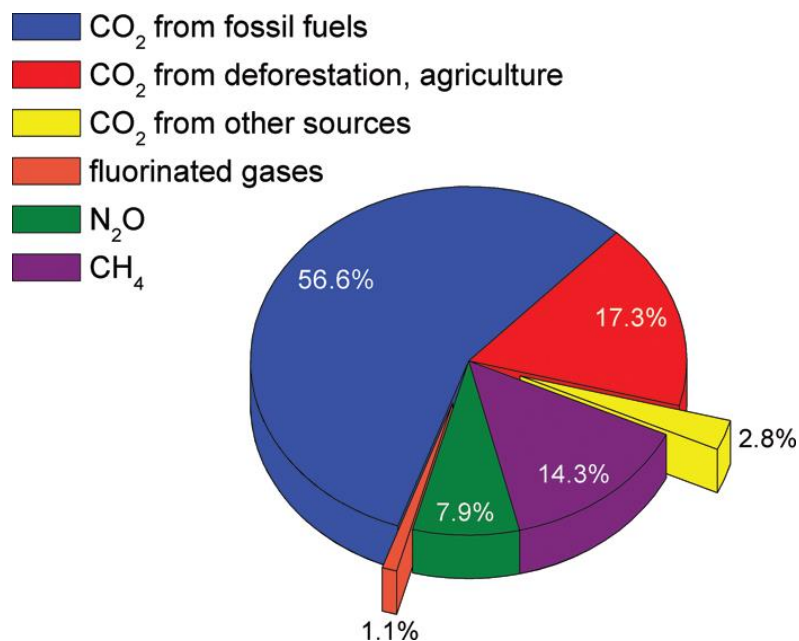


Figure 1.8. Global greenhouse gas emission sources in 2004 of which approximately 77% are represented by CO₂ emissions. (Adapted from reference 155).

CO₂ from post-combustion effluents, such as flue gas wastes Carbon capture and sequestration (CCS), where carbon dioxide is removed from industrial flue gases has attracted considerable attention as it is technologically feasible and could play a significant role in reducing greenhouse gas emissions.^{151–153} Numerous efforts have been made to develop effective methods and materials capable of CCS.⁹⁶ Recent works on numerous materials including aqueous absorbents like alkanolamine or ionic liquid-based wet scrubbing systems and solid porous adsorbent, such as, zeolites and activated carbons have demonstrated their potential for adsorption-based separation,^{96,154–157} but these CCS technologies still suffer from reusability and gas selectivity issues.

Adsorption of carbon dioxide is considered to be one of the most promising, competitive, and viable technologies for the commercial and industrial CCS applications because of its low energy requirement and broad applicability over a relatively wide range of temperature and pressure. Coordination architectures, particularly, metal organic frameworks as a new class of crystalline porous organic–inorganic hybrid materials have emerged as promising candidates for gas storage and separation applications, particularly in the area of carbon capture,^{96,158–162} and have therefore received significant attention as cost-effective and efficient carbon capture materials. For selective CO₂ capture/separation from other gases, like CO₂/N₂ (post-combustion), CO₂/H₂ (pre-combustion), CO₂/O₂ (air separation), and CO₂/CH₄ (natural gas purification), high porosity of the framework is not the only prerequisite, instead, several factors like (a) suitable pore sizes for their size-exclusive

effects, (b) functional sites and (c) several parameters of gases like kinetic diameters and their electric properties, i.e., quadrupole moment and polarization, are even much more important.^{151,163–174} Aiming at selective CO₂ capture into the MOFs, current efforts are largely devoted to enhance the CO₂ binding affinity in MOFs. Reported strategies include control over the pore size and shape,¹⁷¹ incorporation of open metal sites or donor/basic sites,^{175–177} and immobilization of polar functional groups (–NO₂, –NH₂, –OH, –COOH, –CONH₂, –SO₃H, –F, and –CF₃ etc.) in their pore surfaces.^{171,175–179}

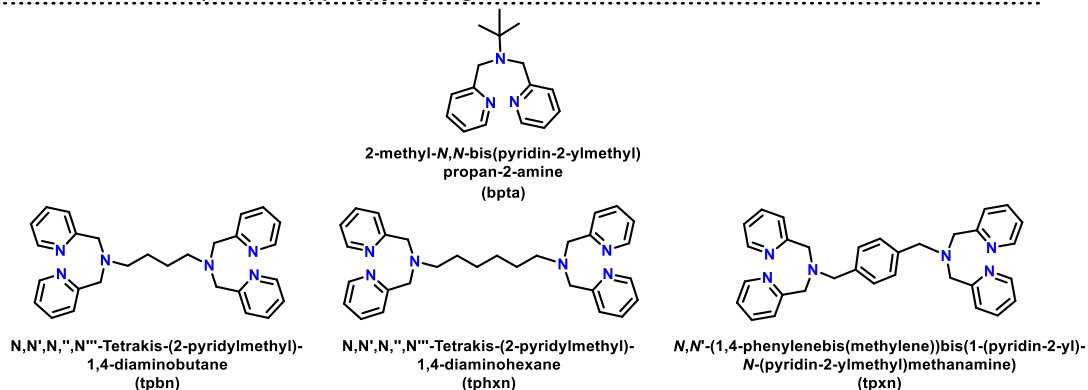
Beyond the well-studied CCS using sorbent materials, chemical transformation of CO₂ into value-added industrial products turns into an alternative yet sustainable means, given that CO₂ represents an abundant, nontoxic, and inexpensive C1 building block.^{180,181} In particular, the synthesis of cyclic carbonates from CO₂ and epoxides is of great promise because of high atom efficiency, and the generated carbonates can be broadly utilized as starting materials for electrolytes, polycarbonates, and aprotic polar solvents. However, because of the thermodynamic and kinetic stability of CO₂, the chemical fixation of CO₂ is not easy. Therefore, it is imperative and attractive to develop methods to activate and convert CO₂ catalytically to high-value chemicals. A variety of homogeneous and heterogeneous catalysts such as alkali-metal salts,¹⁸² transition metal complexes,¹⁸³ ionic liquids,¹⁸⁴ zeolites,^{185,186} metal oxides,¹⁸⁷ and so forth have been exploited to promote the efficient synthesis of cyclic carbonates from CO₂ and epoxides via cycloaddition reactions. In contrast to these mentioned catalysts, MOFs as heterogeneous catalysts have some advantages because of their high surface area, tunable pore size, and functionality. Although some MOFs have been considered as effective heterogeneous catalysts in the chemical conversion and fixation of CO₂,^{188–201} some factors such as the pore size effect of the frameworks towards reaction substrates should be well investigated during the processes of MOF-based CO₂ chemical conversion.

Scope and Significance of present work

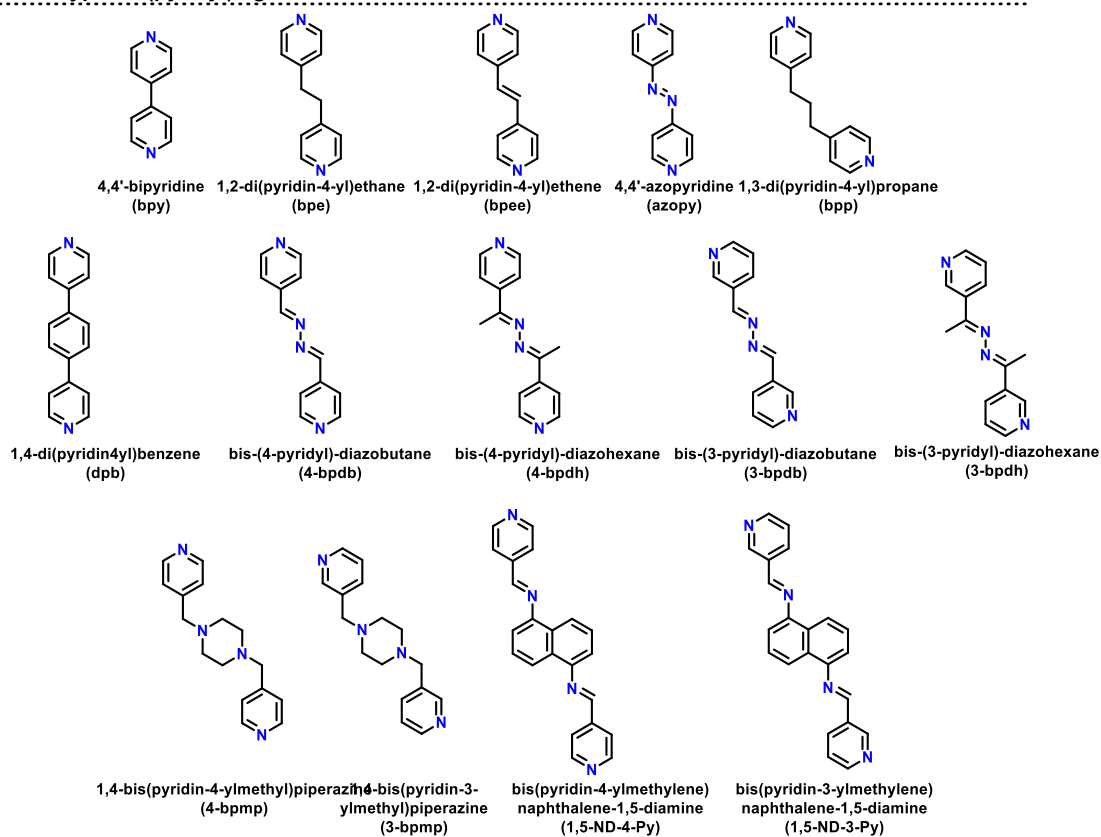
The thesis work presents the multi component self-assembly of discrete and polymeric coordination architectures using either ambient or hydro/solvothermal synthetic conditions. As the selection of organic ligand/linker is one of the most important criterion, the ligands and linkers used in this study have been classified into four different categories- (i) includes neutral tridentate and bis-tridentate capping ligands for the synthesis of discrete and polymeric coordination architectures, (ii) includes the rigid, flexible and functional pillar ligands and neutral tetradentate ligands for the synthesis of porous coordination polymers

with varied dimensionalities and functionalities, (iii) includes bent dicarboxylates, a tricarboxylate and a semi rigid tetrahedral tetracarboxylate linker used for the synthesis of

a) **Tridentate and bis(tridentate) polypyridyl ligands**



b) **Pillar-type bis(pyridyl) ligands**



c) **Tetra(pyridyl) ligands**

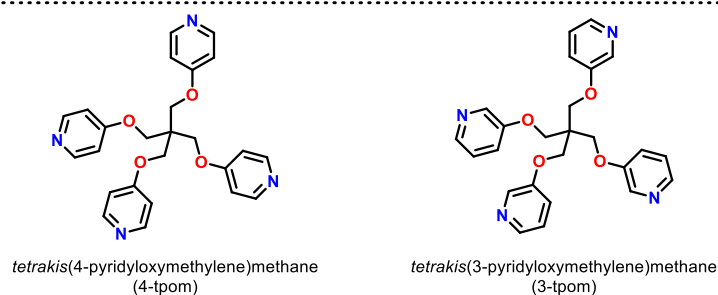


Figure 1.9. Structures of the neutral *poly*(pyridyl) ligands.

these coordination architectures and (iv) includes the functionalized carboxylate linkers for the synthesis of nitrogen-rich coordination polymers for enhanced carbon dioxide capture and separation. All these ligands have been synthesized in good yields and high purity. The chemical structures of the ligands used in this study are shown in Figures 1.9 and 1.10.

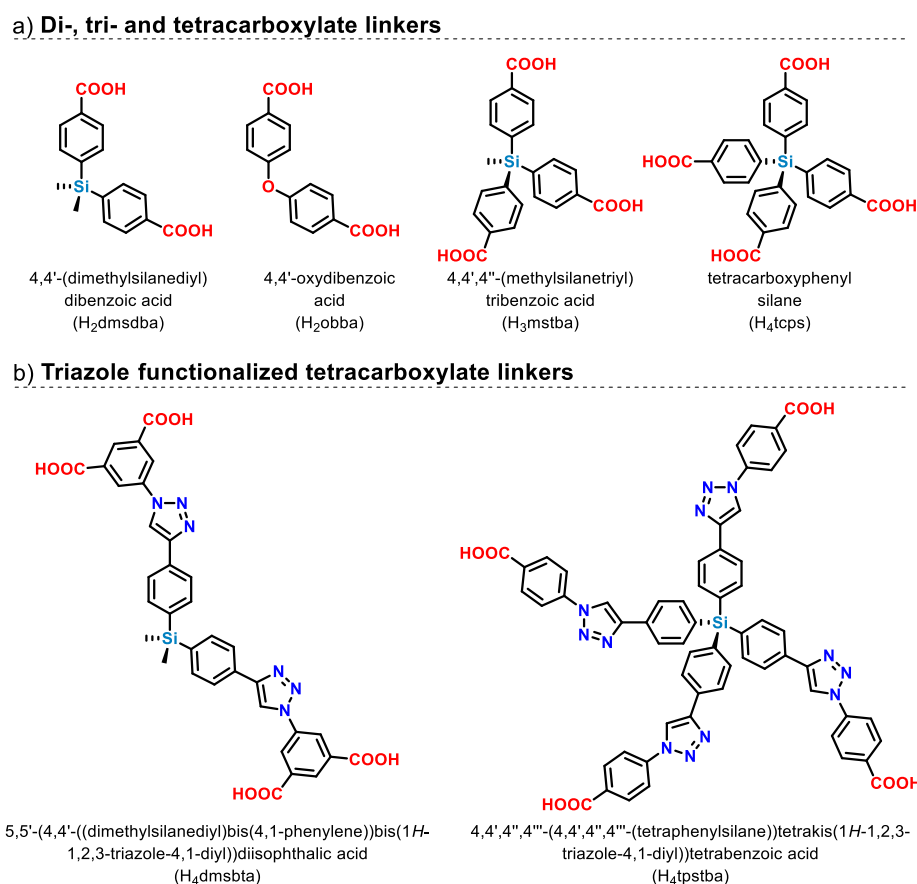


Figure 1.10. Structures of the anionic carboxylate linkers.

There are only few reports so far in the literature for the carboxylates shown in Figure 1.10. Furthermore, their synthetic accessibility has encouraged us to choose the silicon centered carboxylate linkers for this work. It is equally important to point out that the dicarboxylate linkers can be structurally modified to tricarboxylate and tetracarboxylate linkers for a systematic studies while keeping the other factors constant. Utilizing the combination of the carboxylate linkers and neutral polypyridyl ligands with various metal ions, the present work illustrates the controlled and tailored synthesis of coordination architectures of desired topology and functionality by judicious selection of organic ligands and metal ions. The work presents a new strategy for the synthesis of discrete molecular squares based on octahedral metal centers using multi-component self-assembly process without the need of pre-synthesized donor-acceptor counterparts. The selective adsorption and separation of carbon dioxide into the porous coordination architectures shows their significant role in the

gas purification for the environmental applications. The incorporation of catalytic active sites into the porous coordination architectures shows their significant role as heterogeneous catalysts for various organic transformations and catalytic chemical fixation of the carbon dioxide into value added chemicals and utilization of the greenhouse carbon dioxide gas as an abundant C1 building block. Further, the ligand functionalization into the framework structures illustrates the impact of functional sites for enhanced carbon dioxide uptake capacity and selectivity.

CHAPTER II

Experimental Section

2.1 Materials and Methods

All chemicals and solvents used for synthesis were obtained from commercial sources and were used as received, without further purification, unless specifically mentioned. All reactions involving *n*-BuLi were carried out in oven-dried glassware and were performed under an inert atmosphere of nitrogen. Di-ethyl ether and tetrahydrofuran (THF) were dried by distillation over sodium metal prior to use.

2.2 Physical Measurements

NMR spectra of the synthesized ligands were obtained in deuterated solvents at 25 °C on a Bruker ARX-400 spectrometer; chemical shifts are reported relative to the residual solvent signals. Each sample was prepared by taking 5-10 mg of the compound in approx. 0.5 mL of the deuterated solvent. Each data obtained was analyzed and plotted using either TOPSPIN software by Bruker or Spinworks.

Melting points (M.p.) were measured on a *Büchi Melting and Boiling Point apparatus*. All melting points have been measured in open melting point capillaries.

FTIR spectra were measured in the range of 4000-400 cm⁻¹ on a Perkin-Elmer Spectrum I spectrometer with samples prepared as KBr pellets.

Elemental analysis (C, H, N) was carried out using either a Leco-USA Tru Spec CHNS micro version 2.7x analyzer at IISER Mohali or Mettler CHNS analyzer at NIPER Mohali.

Thermogravimetric analysis was carried out from 25 to 500 °C (at a heating rate of 10 °C/min) under dinitrogen atmosphere on a Shimadzu DTG-60. The sample to be analyzed was weighed using an analytical balance, put in a pan and weighed again using the micro balance of the instrument to avoid any discrepancy. The data obtained were analyzed using TA 60 software.

UV-Vis spectra of the compounds in different solvents were recorded in an Agilent Technologies Cary60 UV-Vis spectrophotometer using a cuvette of path length 10 mm. solid state reflectance of solid samples were recorded in cary5000 UV-Vis spectrophotometer using KBr medium.

Florescence emission spectra were obtained using a Horiba Scientific Fluorolog 3

Spectrophotometer with stirring mode with a cuvette of 10 mm path length. To obtain the spectra a slurry of compound was prepared in a particular solvent by stirring for 15 minutes.

Powder X-ray diffraction data were recorded on a Rigaku Ultima IV diffractometer equipped with a 3 KW sealed tube Cu K α X-ray radiation (generator power settings: 40 kV and 40 mA) and a DTex Ultra detector using parallel beam geometry (2.5° primary and secondary solar slits, 0.5° divergence slit with 10 mm height limit slit). Each sample grounded into a fine powder using a mortar and a pestle was placed on a glass sample holder for room temperature measurement while on a copper sample holder for variable temperature measurement. The data were collected over an angle range 5° to 50° (5° to 40° for VT-PXRD) with a scanning speed of 2° per minute with 0.02° step.

Single crystal X-ray analysis were performed by initial crystal evaluation and data collection were performed on a Kappa APEX II diffractometer equipped with a CCD detector (with the crystal-to-detector distance fixed at 60 mm) and sealed-tube monochromated Mo K α radiation using the program APEX2.²⁰² By using the program SAINT²⁰² for the integration of the data, reflection profiles were fitted, and values of F^2 and $\sigma(F^2)$ for each reflection were obtained. In some cases, a lot of efforts were invested to recollect data sets with new crystals a few times but no better data sets that are used here could be obtained. Data were also corrected for Lorentz and polarization effects. The subroutine XPREP²⁰² was used for the processing of data that included determination of space group, application of an absorption correction (SADABS),²⁰² merging of data, and generation of files necessary for solution and refinement. Using Olex2,²⁰³ the structure was solved with the ShelXT²⁰⁴ structure solution program using Intrinsic Phasing and refined with the ShelXL²⁰⁵ refinement package using least squares minimization. The space group was chosen based on systematic absences and confirmed by the successful refinement of the structure. Positions of most of the non-hydrogen atoms were obtained from a direct method solution. Several full-matrix least-squares/difference Fourier cycles were performed, locating the remainder of the non-hydrogen atoms. In some cases, the solvents molecules were highly disordered. Therefore, the Olex2²⁰³ masking program was used to remove the diffused electron density due to the disordered solvent molecules. In order to obtain reasonable thermal parameters compared to other atoms, the lowest residual factors and optimum goodness of fit with the convergence of refinement, occupancy factors of some of the atoms were adjusted accordingly. The occupancy factors of some of the atoms were adjusted to obtain favorable thermal parameters. All non-hydrogen atoms in each case

were refined with anisotropic displacement parameters except where mentioned. Every attempt has been made to account for the electron densities above $1 \text{ e } \text{Å}^{-3}$ in each case. The residual electron density above this value in some cases are either due to the electron densities split over different positions due to the disordered lattice solvent molecules or the ghost peaks very close to the metal centers. Crystallographic parameters and basic information pertaining to data collection and structure refinement for all compounds are summarized in appendix. All figures were drawn using and MERCURY V 3.10.2²⁰⁵ and DIAMOND V 3.2²⁰⁶ hydrogen bonding parameters were generated using PLATON.^{207,208}

Gas/Vapour sorption measurements were recorded for pressures in the range 0–1.2 bar by the volumetric method using a BELSORP instrument. Each solid sample was transferred to pre-weighed analysis tubes, which were capped with transeals and evacuated by heating at a temperature between 110-150 °C (based on thermal profile obtained from TGA) under dynamic vacuum until an outgas rate of less than 2 mTorr min^{-1} (0.27 Pa min^{-1}) was achieved (ca. 12-24 h). The evacuated analysis tubes containing the degassed sample was then carefully transferred to an electronic balance and weighed again to determine the mass of sample. The tube was then placed back on the analysis port of the gas adsorption instrument. The outgas rate was again confirmed to be less than 2 mTorr min^{-1} (0.27 Pa min^{-1}). For all isotherms, warm and cold free-space (dead volume) correction measurements were performed using ultra-high-purity He gas (UHP grade 5.0, 99.999% purity). The change of the pressure was monitored and the degree of adsorption was determined by the decrease in pressure at the equilibrium state via computer controlled automatic operations that are set up at the start of each measurement. Oil-free vacuum pumps and oil-free pressure regulators were used for all measurements to prevent contamination of the samples during the evacuation process or of the feed gases during the isotherm measurements.

2.3 Synthesis of Ligands

The neutral N-donor capping ligands (**bpta**, **tpen**, **tpbn**, **tpxn** and **tpxn**), or bidentate pillar ligands (**dpb**, **4-bpdb**, **4-bpdh**, **3-bpdb**, **3-bpdh**, **4-bpmp**, **3-bpmp**, **1,5-ND-4-Py** and **1,5-ND-3-Py**) or tetradentate (**4-tpom** and **3-tpom**) were synthesized following literature procedures.^{209–229} The carboxylate linkers **H₂dmsdba**, **H₃mstba** and **H₄tcps** were synthesized by following the literature procedures with slight modifications.^{230–233} The triazole functionalized tetracarboxylate linkers **H₄dmsbta** and **H₄tpstba** were synthesized by the azide-alkyne cycloaddition using well known Click chemistry.^{234–238}

General procedure for H₂dmsdba, H₃mstba and H₄tcps. A solution of n-BuLi and dry

THF was made in a 250 mL Schlenk flask and cooled to $-78\text{ }^{\circ}\text{C}$ under a nitrogen atmosphere. The solution equivalent amount of $\text{Me}_n\text{Si}(\text{PhBr})_{4-n}$ in THF was added dropwise to the flask at $-78\text{ }^{\circ}\text{C}$ with a positive flow of nitrogen gas. After stirring the reaction mixture for 1 h, a large excess of crushed dry ice was added to it maintaining this temperature for 1 h. It was then allowed to warm slowly to room temperature and stirred for further 12 h. The reaction was quenched by adding 1N aqueous HCl solution and stirred for 20 mins. The organic phase was separated, washed with water and brine solution and dried over anhydrous Na_2SO_4 . Removal of THF under reduced pressure gave a white residue which was recrystallized using ethyl acetate-hexane mixture to afford the corresponding carboxylic acids as a white solid.

H2dmsdba: Yield: 68%, selected FTIR peaks (KBr, cm^{-1}): 1688, 1596, 1549, 1502, 1415, 1293, 1091, 829, 758, 711, 498. ^1H NMR (400 MHz, δ ppm, $\text{DMSO}-d_6$): 7.93 (d, $J=8$, 4H), 7.65 (d, $J=8$, 4H), 0.59 (s, 6H). ^{13}C NMR (100 MHz, δ ppm, $\text{DMSO}-d_6$): 167.7, 143.6, 134.5, 131.9, 128.9, -2.6.

H3mstba: Yield: 75%, selected FTIR peaks (KBr, cm^{-1}): 1692, 1598, 1551, 1498, 1415, 1291, 1092, 829, 754, 709, 502. ^1H NMR (400 MHz, δ ppm, $\text{DMSO}-d_6$): 7.97 (d, $J=8$, 6H), 7.61 (d, $J=8$, 6H), 0.93 (s, 3H). ^{13}C NMR (100 MHz, δ ppm, $\text{DMSO}-d_6$): 167.7, 140.8, 135.5, 132.4, 129.1, -3.8.

H4tcps: Yield: 70%, selected FTIR peaks (KBr, cm^{-1}): 1690, 1595, 1553, 1499, 1416, 1290, 1093, 830, 754, 709, 504. ^1H NMR (400 MHz, δ ppm, $\text{DMSO}-d_6$): 8.02 (d, $J=8$, 8H), 7.63 (d, $J=8$, 8H). ^{13}C NMR (100 MHz, δ ppm, $\text{DMSO}-d_6$): 167.6, 138.0, 136.5, 132.9, 129.3.

Procedure for H4dmsbta. It was synthesized using the following multi-step synthetic procedure.

Step 1: bis(4-bromophenyl)dimethylsilane. It was synthesized according to the reported procedure.²³²

Step 2: dimethylbis(4-((trimethylsilyl)ethynyl)phenyl)silane. It was synthesized according to literature reported method with slight modifications. In an oven dried 25 mL round bottom flask, 3.7 g (10 mmol) of bis(4-bromophenyl)dimethylsilane, 280 mg (0.4 mmol) of $[\text{Pd}(\text{PPh}_3)_2\text{Cl}_2]$, 150 mg (0.8 mmol) of copper(I) iodide and 260 mg (1 mmol) of triphenylphosphine was taken along with 5 mL of dry THF and 20 mL triethylamine. To this solution, 4.2 mL (30 mmol, 2.5 eq.) of TMS-acetylene was added and the reaction mixture was stirred at room temperature under N_2 environment. The reaction was monitored by TLC. After 24 hours the spot due to the starting material was completely disappeared. The insoluble substance was filtered off and washed with ethyl acetate. The combined filtrate

was dried over sodium sulphate and evaporated to give the crude solid which was purified by column chromatography over silica gel using ethyl acetate/hexane (0-5 %) as eluent to give the product as a pale yellow solid (2.8 g, yield: 70%). ¹H NMR (400 MHz, δ ppm, CDCl₃): 7.45 (d, J = 8 Hz, 4H), 7.42 (d, J = 8 Hz, 4H), 0.55 (s, 6H), 0.27 (s, 18 H). ¹³C NMR (100 MHz, δ ppm, CDCl₃): 138.57, 133.91, 131.11, 123.85, 105.05, 94.98, -0.02, -2.60.

Step 3: bis(4-ethynylphenyl)dimethylsilane. The terminal alkyne was obtained by the deprotection of the TMS bond using potassium carbonate. In a 250 mL round bottom flask a solution of 2 g (4.95 mmol) of TMS protected alkyne, dimethylbis(4-((trimethylsilyl)ethynyl)phenyl)silane in 150 mL DCM/Methanol (1:1) mixture was made and 1.5g (10 mmol) of dry K₂CO₃ was added to this solution. The reaction mixture was stirred at room temperature for 5-6 h. The reaction was monitored by TLC using hexane as eluent. The deprotected product was obtained after 5 h. The solvent was evaporated and 30 mL of water was added to the crude solid. The product was extracted with DCM (40 mL + 20 mL). The organic layer was collected and dried over sodium sulphate and evaporated to give the pure product as a white solid. (1.2 g, yield: 93%). ¹H NMR (400 MHz, δ ppm, CDCl₃): 7.49 (d, J = 8 Hz, 4H), 7.47 (d, J = 8 Hz, 4H), 3.13 (s, 2H), 0.57 (s, 6H). ¹³C NMR (100 MHz, δ ppm, CDCl₃): 138.90, 134.00, 131.35, 122.90, 83.62, 77.87, 2.64.

Step 4: dimethyl 5-azidoisophthalate. In a 250 mL round bottom flask 2 g (9.56 mmol) of dimethyl-5-aminoisophthalate was added along with 100 mL of 6 N HCl solution. The suspension thus obtained was cooled to 0 °C. To this solution, a previously cooled aqueous solution of 700 mg (10 mmol) of sodium nitrite (NaNO₂) was slowly added and stirred at this temperature for 30 minutes. An aqueous solution of 650 mg (10 mmol) of sodium azide (NaN₃) was then slowly added to the reaction mixture at 0 °C. After the complete addition the temperature was allowed to rise slowly to room temperature and the reaction mixture was stirred overnight. The white precipitate thus formed was filtered and washed with copious water and dried in air to get the pure product as white solid (2.1 g, yield: 93%). ¹H NMR (400 MHz, δ ppm, CDCl₃): 8.46 (s, 1H), 7.89 (s, 2H), 3.98 (s, 6H). ¹³C NMR (100 MHz, δ ppm, CDCl₃): 165.41, 141.26, 132.28, 126.90, 124.04, 52.66.

Step 5: tetramethyl 5,5'-(4,4'-((dimethylsilanediyl)bis(4,1-phenylene))bis(1H-1,2,3-triazole-4,1 diyl))diisophthalate. To a solution containing 350 mg (1.35 mmol) of the terminal alkyne and 820 mg (3.5 mmol) of the dimethyl-5-azidoisophthalate in 50 mL THF and 15 mL water in a 100 mL round bottom flask, 125 mg (0.5 mmol) of copper sulphate pentahydrate and an excess of sodium ascorbate, 500 mg (2.5 mmol) was added. The

reaction mixture was heated to 60 °C and stirred for 3 days under nitrogen atmosphere. Then, 50 mL of DCM and 50 mL water was added to the reaction mixture and the organic layer was separated. The aqueous layer was again extracted with 20 mL DCM. The combined organic layer was collected and dried over sodium sulphate and concentrated under reduced pressure to get the yellow solid which was used as obtained for the next step. (0.90 g, yield: 91%). ¹H NMR (400 MHz, δ ppm, CDCl₃): 8.77 (s, 2H), 8.70 (s, 4H), 8.38 (s, 2H), 7.96 (d, J = 8 Hz, 4H), 7.69 (d, J = 8 Hz, 4H), 4.04 (s, 12H), 0.66 (s, 6H). ¹³C NMR (100 MHz, δ ppm, CDCl₃): 165.05, 148.86, 138.81, 137.41, 134.88, 132.50, 130.49, 130.35, 125.30, 125.00, 117.61, 52.92, 2.39. ESI-TOF-HRMS: m/z calcd. for C₃₈H₃₄N₆O₈Si: 731.2285, found: 731.2316 [M+H]⁺.

Step 6: H₄dmsbta. The corresponding acid was obtained by the hydrolysis of the ester group. 1 g (1.36 mmol) of methyl ester was dissolved in 50 mL THF and 100 mL water mixture and 400 mg of sodium hydroxide was added to the solution. The reaction mixture was stirred overnight at room temperature. THF was removed under reduced pressure and the remaining solution was filtered and acidified to pH 1 with dilute HCl. The yellow precipitate formed was filtered and washed with water and air dried. (0.87 g, yield: 94%). ¹H NMR (400 MHz, δ ppm, CDCl₃): 13.80 (s, 4H), 9.69 (s, 2H), 8.73 (s, 4H), 8.53 (s, 2H), 8.01 (d, J = 8 Hz, 4H), 7.70 (d, J = 8 Hz, 4H), 0.63 (s, 6H). ¹³C NMR (100 MHz, δ ppm, CDCl₃): 166.17, 147.99, 138.46, 137.55, 135.06, 133.66, 131.25, 129.80, 125.24, 124.88, 120.63, 2.22. ESI-TOF-HRMS: m/z calcd for C₃₄H₂₆N₆O₈Si: 675.1659, found: 675.1628 [M+H]⁺. Selected FTIR peaks (KBr, cm⁻¹): 3382, 1722, 1682, 1603, 1463, 1427, 1247, 1173, 1090, 812, 760, 663, 522.

Procedure for H₄tpstba. It was synthesized using the following multi-step synthetic procedure.

Step 1: tetrakis(4-bromophenyl)silane. It was synthesized according to the reported procedure.²³³

Step 2: tetrakis(4-((trimethylsilyl)ethynyl)phenyl)silane. It was synthesized according to the procedure discussed above. In an oven dried 25 mL round bottom flask 3.2 g (5 mmol) of tetrakis(4-bromophenyl)silane, 280 mg (0.4 mmol) of [Pd(PPh₃)₂Cl₂], 150 mg (0.8 mmol) of copper(I) iodide and 260 mg (1 mmol) of triphenylphosphine was taken along with 5 mL of dry THF and 20 mL triethylamine. To this solution, 4.2 mL (30 mmol, 6 eq.) of TMS-acetylene was added and the reaction mixture was stirred at room temperature under N₂ environment. The reaction was monitored by TLC. After 24 h the spot due to the starting material was completely disappeared. The insoluble substance was filtered off and washed

with ethyl acetate. The combined filtrate was dried over sodium sulphate and evaporated to give the crude solid which was purified by column chromatography over silica gel using ethyl acetate/hexane (0-5 %) as eluent to give the product as a pale yellow solid (2.65 g, yield: 75%). ¹H NMR (400 MHz, δ ppm, CDCl₃): 7.47 (d, J = 8 Hz, 8H), 7.42 (d, J = 8 Hz, 8H), -0.27 (s, 36 H). ¹³C NMR (100 MHz, δ ppm, CDCl₃): 135.98, 133.70, 131.32, 124.70, 104.73, 95.86, -0.06.

Step 3: tetrakis(4-ethynylphenyl)silane. The terminal alkyne was obtained by the deprotection of the TMS bond using potassium carbonate. In a 250 mL round bottom flask, a solution of 2.1g (3 mmol) of TMS protected alkyne, tetrakis(4-((trimethylsilyl)ethynyl)phenyl)silane in 150 mL DCM/Methanol (1:1) mixture was made and 2.3 g (15 mmol) of dry K₂CO₃ was added to this solution. The reaction mixture was stirred at room temperature for 5-6 h. The reaction was monitored by TLC using hexane as eluent. The deprotected product was obtained after 4 h. The solvent was evaporated and 50 mL of water was added to the crude solid. The product was extracted with DCM (50 mL + 25 mL). The organic layer was collected and dried over sodium sulphate and evaporated to give the pure product as a white solid. (1.1 g, yield: 87%). ¹H NMR (400 MHz, δ ppm, CDCl₃): 7.53 (d, J = 8 Hz, 8H), 7.49 (d, J = 8 Hz, 8H), 3.17 (s, 4H). ¹³C NMR (100 MHz, δ ppm, CDCl₃): 136.08, 133.90, 131.60, 123.85, 83.35, 78.61.

Step 4: methyl 4-azidobenzoate. To a 250 mL round bottom flask 1.5g (10 mmol) of methyl-4-aminobenzoate was added along with 100 mL of 6 N HCl solution. The suspension thus obtained was cooled to 0 °C. To this solution, a previously cooled aqueous solution of 700 mg (10 mmol) of sodium nitrite (NaNO₂) was slowly added and stirred at this temperature for 30 minutes. An aqueous solution of 650 mg (10 mmol) of sodium azide (NaN₃) was then slowly added to the reaction mixture at 0 °C. After the complete addition, the temperature was allowed to rise slowly to room temperature and the reaction mixture was stirred overnight. The white precipitate thus formed was filtered and washed with copious water and dried in air to get the pure product as white solid (1.5 g, yield: 85%). ¹H NMR (400 MHz, δ ppm, CDCl₃): 8.04 (d, J = 8 Hz, 2H), 7.07 (d, J = 8 Hz, 2H), 3.92 (s, 3H). ¹³C NMR (100 MHz, δ ppm, CDCl₃): 166.31, 144.74, 131.39, 126.64, 118.63, 52.16.

Step 5: tetramethyl 4,4',4'',4'''-(4,4',4'',4'''-(silanetetrayltetrakis(benzene-4,1-diyl)) tetrakis(1H-1,2,3-triazole-4,1-diyl))tetrabenzoate. 388 mg (0.9 mmol) of the terminal alkyne and 800 mg (4.5 mmol) of the methyl-4-azidobenzoate was added to a mixture of 150 mL THF and 50 mL water in a 250 mL round bottom flask. Then copper sulphate pentahydrate (125 mg, 0.5 mmol, 5 mL H₂O) and an excess of sodium ascorbate (500 mg,

2.5 mmol, 5 mL H₂O) was added to the above solution. The reaction mixture was heated to 50 °C and stirred for 3 days under nitrogen atmosphere. Then 50 mL of DCM and 50 mL water was added to the reaction mixture and the organic layer was separated. The aqueous layer was again extracted with 50 mL DCM. The combined organic layer was collected and dried over sodium sulphate and concentrated under reduced pressure to get the yellow solid. (0.92 g, yield: 90%). ¹H NMR (400 MHz, δ ppm, CDCl₃): 8.36 (s, 4H), 8.25 (d, J = 8 Hz, 8H), 8.00 (d, J = 8 Hz, 8H), 7.95 (d, J = 8 Hz, 8H), 7.77 (d, J = 8 Hz, 8H), 3.50 (s, 12H). ¹³C NMR (100 MHz, δ ppm, CDCl₃): 165.92, 148.51, 140.01, 137.05, 134.16, 131.43, 130.32, 125.52, 119.90, 118.85, 117.75, 52.53. ESI-TOF-HRMS: m/z calcd. for C₆₄H₄₈N₁₂O₈Si: 1141.3565, found: 1141.3514 [M+H]⁺.

Step 6: H4tpstba. The corresponding acid was obtained by the hydrolysis of the ester group. 800 mg (0.7 mmol) of methyl ester was dissolved in 50 mL THF and 100 mL water mixture and 300 mg of sodium hydroxide was added to the solution. The reaction mixture was stirred at room temperature overnight. THF was removed under reduced pressure and the remaining solution was filtered and acidified to pH 1 with dilute HCl. The yellow precipitate formed was filtered and washed with water and air dried. (650 mg, yield: 85%). ¹H NMR (400 MHz, δ ppm, DMSO-*d*6): 9.53 (s, 4H), 8.19 (d, J = 8 Hz, 8H), 8.13 (d, J = 8 Hz, 8H), 8.10 (d, J = 8 Hz, 8H), 7.75 (d, J = 8 Hz, 8H). ¹³C NMR (100 MHz, δ ppm, DMSO-*d*6): 166.87, 147.82, 139.96, 137.11, 133.82, 132.08, 131.62, 131.15, 125.71, 120.74, 120.22. ESI-TOF-HRMS: m/z calcd. for C₆₀H₄₀N₁₂O₈Si: 1085.2939, found: 1085.2954 [M+H]⁺. Selected FTIR peaks (KBr, cm⁻¹): 3402, 1721, 1685, 1605, 1462, 1435, 1248, 1171, 1091, 807, 766, 665, 521.

2.4 Synthesis of Metal Complexes

Stock solutions for crystallization. For using small quantities of ligands, stock solutions were first prepared and the required amount was taken by using calculated volume of the stock solutions. For example, a stock solution of 75 mg (0.25 mmol) of H₂dmsdba was made in 3 mL water using 20 mg (2 equivalent) of sodium hydroxide. For each crystallization experiment, 0.3 mL of this stock solution containing a solution of 7.5 mg (0.25 mmol) of H₂dmsdba with 2 equivalent of sodium hydroxide in 0.3 mL water was utilized.

[Mn₂(bpta)₂(dmsdba)₂(H₂O)₂] (1). 30 mg (0.1 mmol) of H₂dmsdba was dissolved in 1 mL DMF in a 10 mL round bottom flask. To this solution, a solution of 24.5 mg (0.1 mmol) of manganese acetate tetrahydrate and 25.5 mg (0.1 mmol) of bpta in 4

mL ethanol/water mixture (1:3) was slowly added at room temperature. After stirring for 15 min, a white precipitate appeared. The reaction mixture was stirred for another 8 h at room temperature to ensure complete precipitation of the product. A white solid was collected via filtration, washed with DMF and water, and air-dried. Yield: 30 mg (48%). Anal. Calcd for $C_{64}H_{74}N_6O_{10}Si_2Mn_2$ (MW 1252.38): Calc. %C, 61.32; %H, 5.95; %N, 6.70 and Found: %C, 60.95; %H, 5.88; %N, 6.61. Selected FTIR peaks (KBr, cm^{-1}): 3418 (br), 1591 (s), 1539 (s), 1393 (s), 1101 (m), 1017 (m), 809 (m), 763 (s), 714 (m).

[Co₂(bpta)₂(dmsdba)₂(H₂O)₂] (2). It was synthesized following the general procedure as for **1**, except that 25 mg (0.1 mmol) of cobalt acetate tetrahydrate was used in place of manganese acetate tetrahydrate. A pink solid was collected via filtration, washed with DMF and water, and air-dried. Yield 35 mg (55%). Anal. Calcd for $C_{64}H_{74}N_6O_{10}Si_2Co_2$ (MW 1260.36): Calc. %C, 60.93; %H, 5.91; %N, 6.66 and Found: %C, 60.35; %H, 5.85; %N, 6.55. Selected FTIR peaks (KBr, cm^{-1}): 3426 (br), 1590 (s), 1539 (s), 1393 (s), 1251 (m), 1101 (m), 809 (m), 763 (s), 714 (m).

[Ni₂(bpta)₂(dmsdba)₂(H₂O)₂] (3). It was synthesized following the general procedure as for **1**, except 25 mg (0.1 mmol) of nickel acetate tetrahydrate was used in place of manganese acetate tetrahydrate. A green solid was collected via filtration, washed with DMF and water, and air-dried. Yield 31 mg (49.6%). Anal. Calcd for $C_{64}H_{74}N_6O_{10}Si_2Ni_2$ (MW 1259.88): Calc. %C, 60.95; %H, 5.91; %N, 6.66 and Found: %C, 59.95; %H, 5.84; %N, 6.41. Selected FTIR peaks (KBr cm^{-1}): 3424 (br), 1590 (s), 1539 (s), 1394 (s), 1245 (m), 1101 (m), 809 (m), 763 (s), 716 (m).

[Cd₂(bpta)₂(dmsdba)₂(H₂O)₂] (4). It was synthesized following the general procedure as for **1**, except 27 mg (0.1 mmol) of cadmium acetate dihydrate was used in place of manganese acetate tetrahydrate. A white solid was collected via filtration, washed with DMF and water, and air-dried. Yield 40 mg (58%). Anal. Calcd for $C_{64}H_{74}N_6O_{10}Si_2Cd_2$ (MW 1367.32): Calc. %C, 56.16; %H, 5.45; %N, 6.14 and Found: %C, 56.20; %H, 5.22; %N, 6.21. Selected FTIR peaks (KBr cm^{-1}): 3424 (br), 1579 (s), 1531 (s), 1393 (s), 1250 (m), 1100 (m), 813 (m), 763 (s), 722 (m).

Method for crystallization: As all the compounds mentioned above are insoluble in common organic solvents, solvothermal technique was employed for their crystallization. 15 mg (0.05 mmol) of the H₂dmsdba was taken in a teflon reactor and dissolved in 0.4 mL of DMF. A solution of M(OAc)₂·xH₂O (0.05 mmol) (where M = Mn (**1**), Co (**2**), Ni (**3**) and Cd (**4**)) and 12.75 mg (0.05 mmol) of the bpta ligand in 1.6 mL ethanol/water (1:3) was

then added to this solution. The reactor was sealed in a stainless steel vessel and heated to 120 °C for 48 h in a programmable oven and then slowly cooled to room temperature at a rate of 4 °C/h. The crystals suitable for single crystal X-ray diffraction analysis were obtained in case of **1** and **4** only, while a polycrystalline material was obtained in case of **2** and **3**.

[Mn₂(bpta)₂(obba)₂(H₂O)₂] (5). It was synthesized following the general procedure as for **1**, except 26 mg (0.1 mmol) of H₂obba was used in place of H₂dmsdba. A white solid was collected via filtration, washed with DMF and water, and air-dried. Yield: 45 mg (76%). Anal. Calcd for C₆₀H₆₂N₆O₁₂Mn₂ (MW 1168.32): Calc. %C, 61.62; %H, 5.34; %N, 7.19 and Found: %C, 61.21; %H, 5.41; %N, 6.92. Selected FTIR peaks (KBr, cm⁻¹): 3407 (br), 1684 (s), 1596 (s), 1558 (s), 1495 (m), 1393 (s), 1297 (m), 1240 (s), 1160 (s), 1095 (m), 1016 (m), 873 (m), 784 (s), 758 (s), 650 (m).

[Co₂(bpta)₂(obba)₂(H₂O)₂] (6). It was synthesized following the general procedure as for **5**, except 25 mg (0.1 mmol) of cobalt acetate tetrahydrate was used in place of manganese acetate tetrahydrate. A pink solid was collected via filtration, washed with DMF and water, and air-dried. Yield: 50 mg (86%). Anal. Calcd for C₆₀H₆₂N₆O₁₂Co₂ (MW 1176.31): Calc. %C, 61.20; %H, 5.31; %N, 7.14 and Found: %C, 60.85; %H, 5.26; %N, 6.87. Selected FTIR peaks (KBr, cm⁻¹): 3415 (br), 1596 (s), 1557 (s), 1495 (m), 1393 (s), 1295 (m), 1242 (s), 1159 (s), 1095 (m), 1021 (m), 873 (s), 784 (s), 759 (s), 652 (m).

[Ni₂(bpta)₂(obba)₂(H₂O)₂] (7). It was synthesized following the general procedure as for **5**, except 25 mg (0.1 mmol) of nickel acetate tetrahydrate was used in place of manganese acetate tetrahydrate. A green solid was collected via filtration, washed with DMF and water, and air-dried. Yield: 50 mg (85%). Anal. Calcd for C₆₀H₆₂N₆O₁₂Ni₂ (MW 1175.83): Calc. %C, 61.23; %H, 5.31; %N, 7.14 and Found: %C, 60.88; %H, 5.22; %N, 6.74. Selected FTIR peaks (KBr, cm⁻¹): 3411 (br), 1596 (s), 1557 (s), 1496 (m), 1394 (s), 1293 (m), 1244 (s), 1159 (s), 1094 (m), 1024 (m), 874 (s), 784 (s), 761 (s), 654 (m).

[Cu₂(bpta)₂(obba)₂(H₂O)₂] (8). It was synthesized following the general procedure as for **5**, except 20 mg (0.1 mmol) of copper acetate monohydrate was used in place of manganese acetate tetrahydrate. A blue solid was collected via filtration, washed with DMF and water, and air-dried. Yield: 30 mg (51%). Anal. Calcd for C₆₀H₆₂N₆O₁₂Cu₂ (MW 1185.53): Calc. %C, 60.73; %H, 5.27; %N, 7.08 and Found: %C, 61.47; %H, 5.32; %N, 7.18. Selected FTIR peaks (KBr, cm⁻¹): 3412 (br), 1684

(s), 1597 (s), 1571 (w), 1497 (w), 1387 (s), 1292 (m), 1250 (s), 1160 (s), 1103 (w), 1011 (w), 877 (w), 857 (m), 782 (s), 653 (m).

[Zn₂(bpta)₂(obba)₂(H₂O)₂] (9). It was synthesized following the general procedure as for **5**, except 22 mg (0.1 mmol) of zinc acetate dihydrate was used in place of manganese acetate tetrahydrate. A white solid was collected via filtration, washed with DMF and water, and air-dried. Yield: 48 mg (80%). Anal. Calcd for C₆₀H₆₂N₆O₁₂Zn₂ (MW 1186.3): Calc. %C, 60.69; %H, 5.26; %N, 7.08 and Found: %C, 61.42; %H, 5.22; %N, 6.87. Selected FTIR peaks (KBr, cm⁻¹): 3410 (br), 1596 (s), 1557 (s), 1495 (m), 1393 (s), 1295 (m), 1242 (s), 1159 (s), 1097 (w), 1020 (w), 873 (m), 784 (s), 760 (s), 652 (m).

[Cd₂(bpta)₂(obba)₂(H₂O)₂] (10). It was synthesized following the general procedure as for **5**, except 27 mg (0.1 mmol) of cadmium acetate dihydrate was used instead of manganese acetate tetrahydrate. A white solid was collected via filtration, washed with DMF and water, and air-dried. Yield: 48 mg (75%). Anal. Calcd for C₆₀H₆₂N₆O₁₂Cd₂ (MW 1283.26): Calc. %C, 56.11; %H, 4.87; %N, 6.54 and Found: %C, 56.20; %H, 5.22; %N, 6.21. Selected FTIR peaks (KBr, cm⁻¹): 3415 (br), 1595 (s), 1558 (s), 1492 (m), 1388 (s), 1299 (w), 1237 (s), 1159 (s), 1096 (m), 1017 (m), 873 (m), 784 (s), 759 (s), 650 (m).

Method for crystallization: A solution of the 6.45 mg (0.025 mmol) of H₂obba in 0.2 mL DMF was placed in a narrow glass tube. A solution of (0.025 mmol) of M(OAc)₂·xH₂O (where M = Mn (**5**), Co (**6**), Ni (**7**), Cu (**8**), Zn (**9**) and Cd (**10**)) and 6.5 mg (0.025 mmol) of bpta ligand in 1 mL ethanol/water mixture (1:3) was added very carefully along the sides of the tube on the top of H₂obba solution and kept undisturbed. The crystals suitable for single crystal X-ray diffraction analysis were obtained in case of **5**, **9** and **10** only, while the crystals obtained in case of **6**, **7** and **8** were not good enough for single crystal X-ray diffraction analysis.

{[Mn₂(tpbn)(dmsdba)₂(H₂O)₂]·2DMF}_n (11). 30 mg (0.1 mmol) of H₂dmsdba was dissolved in 1 mL DMF in a 10 mL round bottom flask. To this solution, a solution of 24.5 mg (0.1 mmol) of manganese acetate tetrahydrate and 22.6 mg (0.05 mmol) of tpbn in 4 mL ethanol/water mixture (1:3) was slowly added at room temperature. After stirring for 15 min, a white precipitate appeared. The reaction mixture was stirred for another 8 h at room temperature to ensure complete precipitation of the product. A white solid containing mixture of **11** and {[Mn₂(tpbn)(dmsdba)₂(H₂O)₂]_n **11a** was collected via filtration, washed with DMF and water, and air-dried.

Combined yield for both isomers: 30 mg (48%). Selected FTIR peaks (KBr, cm^{-1}): 3401 (br), 1654 (m), 1602 (s), 1593 (s), 1538 (s), 1480 (m), 1384 (s), 1311 (m), 1250 (s), 1155 (m), 1099 (s), 1016 (s), 808 (s), 767 (s), 714 (s), 644 (m), 480 (m)

$\{[\text{Mn}_2(\text{tpbn})(\text{dmsdba})_2(\text{H}_2\text{O})_2]\}_n$ (11a). 30 mg (0.1 mmol) of H_2dmsdba was dissolved in 2 mL water by making the sodium salt of H_2dmsdba , using 2 equivalent of sodium hydroxide and mixed with a solution of 22.6 mg (0.05 mmol) of tpbn in 5 mL methanol. The resulting clear solution was subsequently added to a solution of 24.5 mg (0.1 mmol) of manganese acetate tetrahydrate in 3 mL water. An off white precipitate appeared immediately. The reaction mixture was further stirred for another 4 h at room temperature to ensure complete precipitation of the product. The off-white solid thus obtained was collected via filtration, washed with water and ethanol, and air-dried. Yield: 38 mg (63%). Anal. Calcd for $\text{C}_{60}\text{H}_{64}\text{N}_6\text{O}_{10}\text{Si}_2\text{Mn}_2$ (MW 1195.30): Calc. %C, 60.29; %H, 5.40; %N, 7.03 and Found: %C, 60.95; %H, 5.86; %N, 6.91. Selected FTIR peaks (KBr, cm^{-1}): 3400 (br), 1602 (s), 1594 (s), 1539 (s), 1478 (w), 1438 (m), 1385 (s), 1311 (w), 1257 (m), 1249 (m), 1157 (w), 1099 (s), 1050 (m), 1015 (m), 829 (w), 809 (s), 768 (s), 714 (s), 481 (w).

$\{[\text{Mn}_2(\text{tphxn})(\text{dmsdba})_2(\text{H}_2\text{O})_2]2\text{DMF}\}_n$ (12). It was synthesized following the same procedure as for **11**, except 24 mg (0.05 mmol) of tphxn was used in place of tpbn. After stirring for 15 min, a white precipitate appeared. The reaction mixture was stirred for another 8 h at room temperature to ensure complete precipitation of the product. A white solid thus obtained was collected via filtration, washed with DMF and water, and air-dried. Yield: 42 mg (68%). Anal. Calcd for $\text{C}_{68}\text{H}_{78}\text{N}_8\text{O}_{12}\text{Si}_2\text{Mn}_2$ (MW 1369.48): Calc. %C, 59.87; %H, 5.76; %N, 8.21 and Found: %C, 59.98; %H, 5.21; %N, 8.92. Selected FTIR peaks (KBr, cm^{-1}): 3422 (br), 1676 (m), 1604 (s), 1591 (s), 1537 (s), 1436 (m), 1386 (s), 1240 (m), 1099 (s), 1017 (m), 832 (m), 810 (s), 762 (s), 717 (m), 638 (m), 473 (m).

$\{[\text{Mn}_2(\text{tpxn})(\text{dmsdba})_2(\text{H}_2\text{O})_2]3\text{MeOH}\}_n$ (13). It was synthesized following the same procedure as for **11a**, except 25 mg (0.05 mmol) of tpxn was used in place of tpbn. After stirring for 15 min, a white precipitate appeared. The reaction mixture was stirred for another 8 h at room temperature to ensure complete precipitation of the product. A white solid thus obtained was collected via filtration, washed with DMF and water, and air-dried. Yield: 40 mg (64%). Anal. Calcd for $\text{C}_{67}\text{H}_{72}\text{N}_6\text{O}_{11}\text{Si}_2\text{Mn}_2$ (MW 1303.34): Calc. %C, 61.74; %H, 5.57; %N, 6.45 and Found: %C, 60.81; %H, 5.87; %N, 6.61. Selected FTIR peaks (KBr, cm^{-1}): 3418 (br),

1602 (m), 1583 (s), 1537 (s), 1443 (w), 1385 (s), 1379 (s), 1347 (w), 1251 (m), 1154 (m), 1097 (s), 1053 (m), 1017 (m), 957 (w), 812 (s), 763 (s), 719 (s), 707 (s), 577 (w), 477 (w).

Method for crystallization: In all three cases, the single crystals were obtained by slow diffusion technique. A solution of the 7.5 mg (0.025 mmol) of H₂dmsdba in 0.2 mL DMF was placed in a narrow glass tube. A solution of 6 mg (0.025 mmol) of manganese acetate tetrahydrate and 5.6 mg (0.0125 mmol) of tpbn (for **11**) or 6 mg (0.0125 mmol) of tpxn (for **12**) or 6.2 mg (0.0125 mmol) of tpxn (for **13**) ligand in 1 mL ethanol/water mixture (1:3) was added very carefully along the sides of the tube on the top of H₂dmsdba solution and kept undisturbed. In all cases, colourless crystals were obtained at the interface of the two solutions after 5-7 days. In case of tpbn, a mixture of **11** and **11a** was obtained. We have been fortunate to get the single crystal X-ray diffraction data for both the isomers. But unfortunately because of similar shape and size of both the crystal we have not been able to separate both the isomers to study their bulk properties. In order to get the single phase material, the crystallization was done in a different solvent combination. For this purpose, a solution of 6 mg (0.025 mmol) of manganese acetate in 0.2 mL water was placed in a narrow glass tube. A solution of 7.5 mg (0.025 mmol) of H₂dmsdba was made in 0.3 mL water using 2 equivalent of sodium hydroxide and added to a solution of 6 mg (0.0125 mmol) of tpbn in 1 mL methanol. The resulting clear solution was added very carefully along the sides of the tube on the top of manganese acetate solution using 1 mL methanol/water buffer (1:1) in between the two solutions. The tube was kept undisturbed at room temperature. Colourless crystals of **11a** suitable for single crystal X-ray diffraction analysis was obtained after 7 days.

{[Mn₂(tpbn)(obba)₂]}_n (14**).** 26 mg (0.1 mmol) of H₂obba was dissolved in 1 mL DMF in a 10 mL round bottom flask. To this solution, a solution of 24.5 mg (0.1 mmol) of manganese acetate tetrahydrate and 22.6 mg (0.05 mmol) of tpbn in 4 mL ethanol/water mixture (1:3) was slowly added at room temperature. After stirring for 15 min, a white precipitate appeared. The reaction mixture was stirred for another 8 h at room temperature to ensure complete precipitation of the product. The white solid thus obtained was collected via filtration, washed with DMF and water, and air-dried. Yield: 38 mg (70%). Anal. Calcd for C₅₆H₄₈N₆O₁₀Mn₂ (MW 1074.89): Calc. %C, 62.57; %H, 4.50; %N, 7.82 and Found: %C, 61.85; %H, 4.23; %N, 6.95. Selected FTIR peaks (KBr, cm⁻¹): 1607 (s), 1592 (s), 1557 (s), 1440 (m), 1412 (s),

1391 (s), 1311 (m), 1216 (s), 1155 (s), 1015 (s), 888 (m), 871 (s), 784 (m), 762 (s), 714 (m), 654 (s), 639 (m), 540 (m), 412 (m).

{[Mn₂(tphxn)(obba)₂(H₂O)₂]}_n (15). It was synthesized following the same procedure as for **14**, except 24 mg (0.05 mmol) of tphxn was used in place of tpbn. After stirring for 15 min, a white precipitate appeared. The reaction mixture was stirred for another 8 h at room temperature to ensure complete precipitation of the product. A white solid thus obtained was collected via filtration, washed with DMF and water, and air-dried. Yield: 37 mg (65%). Anal. Calcd for C₅₈H₅₆N₆O₁₂Mn₂ (MW 1138.97): Calc. %C, 61.16; %H, 4.96; %N, 7.38 and Found: %C, 60.84; %H, 4.26; %N, 6.98. Selected FTIR peaks (KBr, cm⁻¹): 3418 (br), 1605 (s), 1597 (s), 1560 (s), 1495 (s), 1431 (m), 1395 (s), 1388 (s), 1303 (w), 1241 (s), 1159 (s), 1095 (s), 1054 (m), 1017 (s), 873 (s), 784 (s), 759 (s), 701 (m), 651 (s), 629 (m), 506 (m), 411 (m).

{[Mn₂(tpxn)(obba)₂(H₂O)₄]·6H₂O·2EtOH}_n (16). 26 mg (0.1 mmol) of H₂obba was dissolved in 2 mL water by making the sodium salt of H₂obba, using 2 equivalent of sodium hydroxide and mixed with a solution of 25 mg (0.05 mmol) of tpxn in 5 mL ethanol. The resulting clear solution was subsequently added to a solution of 24.5 mg (0.1 mmol) of manganese acetate tetrahydrate in 3 mL water. White precipitate appeared immediately. The reaction mixture was further stirred for another 4 h at room temperature to ensure complete precipitation of the product. The white solid thus obtained was collected via filtration, washed with water and ethanol, and air-dried. Yield: 45 mg (71%). Anal. Calcd for C₆₄H₈₀N₆O₂₂Mn₂ (MW 1395.22): Calc. %C, 55.09; %H, 5.78; %N, 6.02 and Found: %C, 56.01; %H, 5.19; %N, 6.21. Selected FTIR peaks (KBr, cm⁻¹): 3386 (br), 1601 (s), 1571 (w), 1552 (s), 1544 (s), 1497 (m), 1444 (m), 1416 (s), 1379 (s), 1301 (m), 1241 (s), 1157 (s), 1085 (m), 1054 (s), 1014 (s), 879 (s), 766 (s), 649 (m), 414 (w).

Method for crystallization: A solution of the 6.5 mg (0.025 mmol) of H₂obba in 0.2 mL DMF was placed in a narrow glass tube. A solution of 6 mg (0.025 mmol) of manganese acetate tetrahydrate and 5.6 mg (0.0125 mmol) of tpbn (for **14**) and 6 mg (0.0125 mmol) of tphxn (for **15**) ligand in 1 mL ethanol/water mixture (1:3) was added very carefully along the sides of the tube on the top of H₂obba solution and kept undisturbed. Colourless crystals suitable for single crystal X-ray diffraction analysis were obtained after 3-5 days in both the cases.

A similar technique for crystallization was employed in case of **16** as well, with a slight modification. A solution of 6 mg (0.025 mmol) of manganese acetate in 0.2

mL water was placed in a narrow glass tube. A solution of 6.5 mg (0.025 mmol) of H₂obba was made in 0.3 mL water using 2 equivalent of sodium hydroxide and added to a solution of 6.2 mg (0.0125 mmol) of tpxn in 1 mL ethanol. The resulting clear solution was added very carefully along the sides of the tube on the top of manganese acetate solution using 1 mL ethanol/water buffer (1:1) in between the two solutions. The tube was kept undisturbed at room temperature. Colourless crystals suitable for single crystal X-ray diffraction analysis was obtained after 7 days.

{[Cd(tpen)₂(H₂O)][(Cd(dmsdba)₂]·6H₂O)_n (17). 30 mg (0.1 mmol) of H₂dmsdba was dissolved in 1 mL DMF in a 10 mL round bottom flask. To this solution, a solution of 26.6 mg (0.1 mmol) of cadmium acetate dihydrate and 21.2 mg (0.05 mmol) of tpen in 4 mL ethanol/water mixture (1:3) was slowly added at room temperature. After stirring for 15 min, a white precipitate appeared. The reaction mixture was stirred for another 8 h at room temperature to ensure complete precipitation of the product. The white solid thus obtained was collected via filtration, washed with DMF and water, and air-dried. Yield: 40 mg (61%). Anal. Calcd for C₅₈H₇₀N₆O₁₅Si₂Cd₂ (MW 1372.14): Calc. %C, 50.77; %H, 5.14; %N, 6.12 and Found: %C, 5.071; %H, 5.22; %N, 5.96. Selected FTIR peaks (KBr, cm⁻¹): 3421 (br), 1612 (w), 1578 (s), 1528 (s), 1498 (w), 1399 (s), 1249 (m), 1100 (s), 1018 (s), 829 (m), 813 (s), 765 (s), 725 (s), 660 (w), 553 (w), 481 (w).

Method for crystallization: The single crystals of the compound was obtained by slow diffusion technique. A solution of the 7.5 mg (0.025 mmol) of H₂dmsdba in 0.2 mL DMF was placed in a narrow glass tube. A solution of 6.6 mg (0.025 mmol) of cadmium acetate dihydrate and 5.3 mg (0.0125 mmol) of tpen ligand in 1 mL ethanol/water mixture (1:3) was added very carefully along the sides of the tube on the top of H₂dmsdba solution and kept undisturbed. Colourless crystals suitable for single crystal X-ray diffraction analysis was obtained at the interface of the two solutions after 3 days.

{[Cd₂(tpbn)(dmsdba)₂]·2H₂O)_n (18). 30 mg (0.1 mmol) of H₂dmsdba was dissolved in 1 mL DMF in a 10 mL round bottom flask. To this solution, a solution of 26.6 mg (0.1 mmol) of cadmium acetate dihydrate and 22.6 mg (0.05 mmol) of tpbn in 4 mL ethanol/water mixture (1:3) was slowly added at room temperature. After stirring for 15 min, a white precipitate appeared. The reaction mixture was stirred for another 8 h at room temperature to ensure complete precipitation of the product. The white solid thus obtained was collected via filtration, washed with DMF and water, and air-

dried. Yield: 46 mg (70%). Anal. Calcd for $C_{60}H_{64}N_6O_{10}Si_2Cd_2$ (MW 1310.18): Calc. %C, 55.00; %H, 4.92; %N, 6.41 and Found: %C, 54.21; %H, 4.65; %N, 6.61. Selected FTIR peaks (KBr, cm^{-1}): 3429 (br), 1602 (s), 1591 (s), 1534 (s), 1482 (m), 1442 (m), 1395 (s), 1313 (m), 1258 (w), 1249 (s), 1155 (m), 1099 (s), 1053 (m), 1017 (s), 833 (m), 814 (s), 765 (s), 726 (s), 641 (w), 473 (w).

$\{[Cd_2(tpbn)(obba)_2]\}_n$ (19). 26 mg (0.1 mmol) of H_2obba was dissolved in 1 mL DMF in a 10 mL round bottom flask. To this solution, a solution of 26.6 mg (0.1 mmol) of cadmium acetate dihydrate and 22.6 mg (0.05 mmol) of tpbn in 4 mL ethanol/water mixture (1:3) was slowly added at room temperature. After stirring for 15 min, a white precipitate appeared. The reaction mixture was stirred for another 8 h at room temperature to ensure complete precipitation of the product. The white solid thus obtained was collected via filtration, washed with DMF and water, and air-dried. Yield: 42 mg (70%). Anal. Calcd for $C_{56}H_{48}N_6O_{10}Cd_2$ (MW 1189.84): Calc. %C, 56.53; %H, 4.07; %N, 7.06 and Found: %C, 55.74; %H, 3.88; %N, 6.84. Selected FTIR peaks (KBr, cm^{-1}): 1603 (s), 1598 (s), 1573 (w), 1552 (s), 1483 (m), 1442 (m), 1406 (s), 1388 (s), 1313 (m), 1266 (m), 1215 (s), 1156 (s), 1095 (s), 1016 (s), 871 (s), 769 (s), 726 (s), 654 (s), 537 (m), 411 (m).

Method for crystallization: The single crystals of **18** and **19** were obtained by slow diffusion technique. A solution of 6.6 mg (0.025 mmol) of cadmium acetate dihydrate and 5.6 mg (0.0125 mmol) of tpbn ligand in 1 mL ethanol/water mixture (1:3) was added very carefully along the sides of the tube on the top of $H_2dmsdba$ solution (7.5 mg (0.025 mmol) of $H_2dmsdba$ in 0.2 mL DMF) in case of **18** and H_2obba solution (6.5 mg (0.025 mmol) of H_2obba in 0.2 mL DMF) in case of **19**, and kept undisturbed. In both cases, colourless crystals suitable for single crystal X-ray diffraction analysis was obtained at the interface of the two solutions after 3 days.

$\{[Zn_2(dmsdba)_2(H_2O)_2]\cdot 4H_2O\}_n$ (20). 30 mg (0.1 mmol) of $H_2dmsdba$ was dissolved in 1 mL DMF in a 10 mL round bottom flask. To this solution, a solution of 22 mg (0.1 mmol) of zinc acetate dihydrate in 4 mL ethanol/water mixture (1:3) was slowly added at room temperature. After stirring for 15 min, a white precipitate appeared. The reaction mixture was stirred for another 8 h at room temperature to ensure complete precipitation of the product. The white solid thus obtained was collected via filtration, washed with DMF and water, and air-dried. Yield: 25 mg (60%). Anal. Calcd for $C_{32}H_{40}O_{14}Si_2Zn_2$ (MW 835.58): Calc. %C, 46.00; %H, 4.83 and Found: %C, 47.89; %H, 5.88; %. Selected FTIR peaks (KBr, cm^{-1}): 3418 (br),

1658 (s), 1624 (s), 1604 (s), 1542 (s), 1498 (m), 1413 (s), 1308 (m), 1266 (m), 1252 (s), 1188 (m), 1100 (s), 1019 (m), 833 (s), 813 (s), 764 (s), 722 (s), 705 (m).

{[Zn₂(bpy)(dmsdba)₂]}_n (21). It was synthesized using the same procedure as for **20**, with the additional 4,4'-bipyridine (bpy) added as a pillar ligand. 30 mg (0.1 mmol) of H₂dmsdba was dissolved in 1 mL DMF in a 10 mL round bottom flask. To this solution, a solution of 22 mg (0.1 mmol) of zinc acetate dihydrate and 7.8 mg (0.05 mmol) of bpy in 4 mL ethanol/water mixture (1:3) was slowly added at room temperature. After stirring for 15 min, a white precipitate appeared. The reaction mixture was stirred for another 8 h at room temperature to ensure complete precipitation of the product. The white solid thus obtained was collected via filtration, washed with DMF and water, and air-dried. Yield: 30 mg (68%). Anal. Calcd for C₄₂H₃₆N₂O₈Si₂Zn₂ (MW 883.67): Calc. %C, 57.09; %H, 4.11; %N, 3.17 and Found: %C, 58.12; %H, 4.88; %N, 4.21. Selected FTIR peaks (KBr, cm⁻¹): 1636 (s), 1612 (s), 1543 (s), 1496 (m), 1411 (s), 1252 (m), 1220 (m), 1187 (w), 1099 (s), 1075 (m), 1019 (m), 831 (s), 813 (s), 765 (s), 721 (s), 644 (m), 494 (m).

{[Zn₂(4-bpdb)(dmsdba)₂]·DMF·2H₂O}_n (22). 30 mg (0.1 mmol) of H₂dmsdba was dissolved in 2 mL water by making the sodium salt of H₂dmsdba, using 2 equivalent of sodium hydroxide and mixed with a solution of 10.5 mg (0.05 mmol) of 4-bpdb in 5 mL ethanol. The resulting clear solution was subsequently added to a solution of 22.0 mg (0.1 mmol) of zinc acetate dihydrate in 3 mL water. A light yellow precipitate appeared immediately. The reaction mixture was further stirred for another 4 h at room temperature to ensure complete precipitation of the product. The light yellow solid thus obtained was collected via filtration, washed with water and ethanol, and air-dried. Yield: 35 mg (75%). Anal. Calcd for C₄₇H₄₉N₅O₁₁Si₂Zn₂ (MW 1046.85): Calc. %C, 53.92; %H, 4.72; %N, 6.69 and Found: %C, 54.71; %H, 4.87; %N, 6.31. Selected FTIR peaks (KBr, cm⁻¹): 1635 (s), 1616 (s), 1545 (s), 1497 (s), 1410 (s), 1308 (m), 1250 (s), 1186 (w), 1099 (s), 1031 (m), 1019 (m), 813 (s), 763 (s), 721 (s), 694 (m), 429 (m).

{[Zn₂(4-bpmp)(dmsdba)₂]·2DMF·2H₂O}_n (23). It was synthesized using the same procedure as for **21**, instead 13.5 mg (0.05 mmol) of 4-bpmp was used in place of bpy. The resulting off white solid thus obtained was collected via filtration, washed with DMF and water, and air-dried. Yield: 42 mg (71%). Anal. Calcd for C₅₄H₆₆N₆O₁₂Si₂Zn₂ (MW 1178.07): Calc. %C, 55.05; %H, 5.65; %N, 7.13 and Found: %C, 55.82; %H, 5.88; %N, 6.78. Selected FTIR peaks (KBr, cm⁻¹): 3418 (br),

1636 (s), 1620 (s), 1596 (s), 1544 (s), 1497 (m), 1408 (s), 1303 (m), 1251 (s), 1160 (m), 1099 (s), 1014 (s), 831 (s), 813 (s), 764 (s), 719 (s), 617 (w), 489 (m).

[[Zn₂(3-bpdh)(dmsdba)₂]₃EtOH₃H₂O]_n (24). It was synthesized using the same procedure as for **22**, instead 12 mg (0.05 mmol) of 3-bpdh was used in place of 4-bpdb ligand. The light yellow solid thus obtained was collected via filtration, washed with water and ethanol, and air-dried. Yield: 42 mg (72%). Anal. Calcd for C₅₂H₆₆N₄O₁₄Si₂Zn₂ (MW 1158.03): Calc. %C, 53.95; %H, 5.74; %N, 4.84 and Found: %C, 52.74; %H, 5.93; %N, 5.62. Selected FTIR peaks (KBr, cm⁻¹): 3401 (br), 1637 (s), 1598 (s), 1539(s), 1498 (m), 1410 (s), 1307 (w), 1250 (s), 1100 (s), 1057 (m), 1020 (m), 813 (s), 763 (s), 721 (s).

[[Zn₂(bpp)(dmsdba)₂]₃DMF₃H₂O]_n (25). It was synthesized using the same procedure as for **21**, instead 10 mg (0.05 mmol) of bpp was used in place of bpy. The resulting white solid thus obtained was collected via filtration, washed with DMF and water, and air-dried. Yield: 35 mg (69%). Anal. Calcd for C₄₈H₅₁N₃O₁₀Si₂Zn₂ (MW 1016.86): calc. %C, 56.70; %H, 5.06; %N, 4.13 and Found: %C, 55.32; %H, 4.73; %N, 5.21. Selected FTIR peaks (KBr, cm⁻¹): 3418 (br), 1638 (s), 1621 (s), 1596 (s), 1543 (s), 1498 (m), 1407 (s), 1305 (m), 1251 (s), 1186 (m), 1099 (s), 1033 (m), 1019 (m), 831 (s), 829 (s), 813 (s), 764 (s), 720 (s), 617 (w), 493 (m).

Method for crystallization: The single crystals of **20-25** were obtained by slow diffusion technique using different solvent combinations. For the crystallization of **20, 21, 23** and **25**, a solution of 7.5 mg (0.025 mmol) of H₂dmsdba in 0.2 mL DMF was placed in a narrow glass tube. A solution of 5.5 mg (0.025 mmol) of zinc acetate dihydrate (in case of **20**) or a solution of 5.5 mg (0.025 mmol) of zinc acetate dihydrate and 0.0125 mmol of the *bis*(pyridyl) ligands, 2 mg of bpy for **21**, 3.4 mg of 4-bpmp for **23** and 2.5 mg of bpp for **25** was added very carefully along the sides of the tube on the top of H₂dmsdba solution and kept undisturbed. In all cases, colourless crystals suitable for single crystal X-ray diffraction analysis were obtained at the interface of the two solutions after 5-7 days.

For the crystallization of **22** and **24**, a solution of 5.5 mg (0.025 mmol) of zinc acetate dihydrate in 0.2 mL water was placed in a narrow glass tube. A solution of 7.5 mg (0.025 mmol) of H₂dmsdba was made in 0.3 mL water using 2 equivalent of sodium hydroxide and added to a solution of 2.6 mg (0.0125 mmol) of 4-bpdb (in case of **22**) or 3 mg (0.0125 mmol) of 3-bpdh (in case of **24**) in 1 mL ethanol. The resulting clear solution was added very carefully along the sides of the tube on the top of zinc acetate

solution using 1 mL ethanol/water buffer (1:1) in between the two solutions. The tube was kept undisturbed at room temperature. Clear light yellow crystals suitable for single crystal X-ray diffraction analysis was obtained after 5-6 days.

{[Mn₂(bpy)(dmsdba)₂]_n (26)}. 30 mg (0.1 mmol) of H₂dmsdba was taken in a teflon reactor and dissolved in 0.4 mL of DMF. A solution of 24.5 mg (0.1 mmol) of manganese acetate tetrahydrate and 8 mg (0.05 mmol) of bpy in 1.6 mL ethanol/water (1:3) mixture was then added to this solution. The reactor was sealed in a stainless steel vessel and heated to 120 °C for 48 h in a programmable oven and then slowly cooled to room temperature at a rate of 4 °C/h. The colourless plate-like crystals suitable for single crystal X-ray diffraction analysis, thus obtained was collected via filtration, washed with DMF and water, and air dried. Yield: 27 mg (63%). Anal. Calcd for C₄₂H₃₆N₂O₈Si₂Mn₂ (MW 862.79): Calc. %C, 58.46; %H, 4.20; %N, 3.24 and Found: %C, 58.05; %H, 4.31; %N, 2.73. Selected FTIR peaks (KBr, cm⁻¹): 1619 (s), 1543 (s), 1410 (s), 1251 (s), 1219 (m), 1160 (m), 1098 (s), 1014 (s), 810 (s), 764 (s), 719 (s), 719 (m), 642 (m), 493 (m).

{[Mn₂(dpb)_{0.5}(dmsdba)₂]_n (27)}. It was synthesized using the same procedure as for **26**, instead 12 mg (0.05 mmol) of dpb was used in place of bpy. The colourless plate like crystals suitable for single crystal X-ray diffraction analysis, thus obtained was collected via filtration, washed with DMF and water, and air dried. Yield: 25 mg (60%). Anal. Calcd for C₄₀H₃₆NO₉Si₂Mn₂ (MW 840.74): Calc. %C, 58.39; %H, 4.17; %N, 1.70 and Found: %C, 60.15; %H, 5.02; %N, 2.31. Selected FTIR peaks (KBr, cm⁻¹): 3386 (br), 1651 (s), 1605 (s), 1587 (s), 1535 (s), 1498 (m), 1486 (m), 1399 (s), 1250 (m), 1187 (w), 1102 (s), 1006 (m), 812 (s), 768 (s), 715 (s), 673 (m), 578 (w), 484 (m).

{[Mn₃(bpee)(dmsdba)₃(H₂O)₂]·0.5bpee·DMF·H₂O}_n (28)}. It was synthesized using the same procedure as for **26**, instead 9.2 mg (0.05 mmol) of bpee was used in place of bpy. The colourless plate like crystals suitable for single crystal X-ray diffraction analysis, thus obtained was collected via filtration, washed with DMF and water, and air dried. Yield: 45 mg (61%). Anal. Calcd for C₆₉H₆₉N₄O₁₆Si₃Mn₃ (MW 1459.39): Calc. %C, 56.71; %H, 4.90; %N, 3.83 and Found: %C, 55.21; %H, 5.62; %N, 4.28. Selected FTIR peaks (KBr, cm⁻¹): 3432 (br), 1695 (s), 1606 (s), 1555 (m), 1419 (s), 1388 (s), 1313 (m), 1288 (s), 1253 (s), 1180 (m), 1096 (s), 1066 (m), 1014 (s), 829 (s), 799 (s), 758 (s), 707 (m), 549 (s), 502 (m).

[[Mn₃(azopy)(dmsdba)₃(H₂O)₂]·0.5azopy·DMF·2H₂O]_n (29). It was synthesized using the same procedure as for **26**, instead 9.2 mg (0.05 mmol) of azopy was used in place of bpy. The red block-shaped crystals suitable for single crystal X-ray diffraction analysis, thus obtained was collected via filtration, washed with DMF and water, and air dried. Yield: 48 mg (65%). Anal. Calcd for C₆₆H₆₉N₇O₁₇Si₃Mn₃ (MW 1481.36): Calc. %C, 53.51; %H, 4.69; %N, 6.62 and Found: %C, 51.82; %H, 4.12; %N, 7.24. Selected FTIR peaks (KBr, cm⁻¹): 3447 (br), 1700 (s), 1597 (s), 1542 (m), 1458 (w), 1411 (s), 1310 (w), 1280 (s), 1177 (m), 1108 (s), 1095 (s), 1016 (s), 835 (s), 800 (s), 761 (s), 704 (m), 676 (w), 548 (m).

[[Mn₂(bpe)(μ-OH₂)(dmsdba)₂]_n (30). It was synthesized using the same procedure as for **26**, instead 9.2 mg (0.05 mmol) of bpe was used in place of bpy. The colourless block shaped crystals suitable for single crystal X-ray diffraction analysis, thus obtained was collected via filtration, washed with DMF and water, and air dried. Yield: 32 mg (70%). Anal. Calcd for C₄₄H₄₂N₂O₉Si₂Mn₂ (MW 908.86): Calc. %C, 58.15; %H, 4.66; %N, 3.08 and Found: %C, 57.72; %H, 4.92; %N, 4.56. Selected FTIR peaks (KBr, cm⁻¹): 3418 (br), 1608 (s), 1588 (s), 1541 (s), 1429 (m), 1408 (s), 1335 (s), 1255 (m), 1248 (m), 1103 (s), 1017 (s), 814 (s), 803 (s), 775 (s), 764 (s), 712 (s), 516 (m).

[[Co₂(bpy)(dmsdba)₂]_n (31). It was synthesized using the same procedure as for **26**. 30 mg (0.1 mmol) of the H₂dmsdba was taken in a teflon reactor and dissolved in 0.4 mL of DMF. A solution of 25 mg (0.1 mmol) of cobalt acetate tetrahydrate and 8 mg (0.05 mmol) of bpy in 1.6 mL ethanol/water (1:3) was then added to this solution. The reactor was sealed in a stainless steel vessel and heated to 120 °C for 48 h in a programmable oven and then slowly cooled to room temperature at a rate of 4 °C/h. The violet precipitate thus obtained was collected via filtration, washed with DMF and water, and air dried. Yield: 32 mg (73%). Anal. Calcd for C₄₂H₃₆N₂O₈Si₂Co₂ (MW 870.78): Calc. %C, 57.93; %H, 4.17; %N, 3.22 and Found: %C, 56.71; %H, 4.82; %N, 4.22. Selected FTIR peaks (KBr, cm⁻¹): 1609 (s), 1544 (m), 1411 (s), 1251 (w), 1217 (w), 1098 (m), 833 (w), 811 (s), 763 (s), 721 (m), 494 (w).

[[Co₂(bpee)(dmsdba)₂]_n (32). It was synthesized using the same procedure as for **31**, instead 9.2 mg (0.05 mmol) of bpee was used in place of bpy. The pink plate-like crystals suitable for single crystal X-ray diffraction analysis, thus obtained was

collected via filtration, washed with DMF and water, and air dried. Yield: 30 mg (67%). Anal. Calcd for $C_{44}H_{38}N_2O_8Si_2Co_2$ (MW 896.82): Calc. %C, 58.93; %H, 4.27; %N, 3.12 and Found: %C, 57.18; %H, 4.86; %N, 4.02. Selected FTIR peaks (KBr, cm^{-1}): 1610 (s), 1541 (m), 1456 (w), 1411 (s), 1250 (m), 1219 (w), 1099 (s), 1026 (w), 829 (m), 812 (m), 762 (s), 718 (m), 549 (w).

$\{[Co_2(4\text{-bpdb})(dmsdba)_2]\}_n$ (33). It was synthesized using the same procedure as for **31**, instead 10.5 mg (0.05 mmol) of 4-bpdb was used in place of bpy. The violet block-shaped crystals suitable for single crystal X-ray diffraction analysis, thus obtained was collected via filtration, washed with DMF and water, and air dried. Yield: 32 mg (69%). Anal. Calcd for $C_{44}H_{38}N_4O_8Si_2Co_2$ (MW 924.83): Calc. %C, 57.14; %H, 4.14; %N, 6.06 and Found: %C, 58.52; %H, 4.82; %N, 6.72. Selected FTIR peaks (KBr, cm^{-1}): 1597 (s), 1533 (m), 1495 (w), 1399 (s), 1309 (w), 1248 (m), 1101 (s), 1019 (m), 812 (s), 764 (s), 719 (m), 494 (w).

$\{[Co_2(4\text{-bpmp})(dmsdba)_2]\cdot H_2O\}_n$ (34). It was synthesized using the same procedure as for **31**, instead 13.5 mg (0.05 mmol) of 4-bpmp was used in place of bpy. The violet plate- like crystals suitable for single crystal X-ray diffraction analysis, thus obtained was collected via filtration, washed with DMF and water, and air dried. Yield: 31 mg (62%). Anal. Calcd for $C_{48}H_{50}N_4O_9Si_2Co_2$ (MW 1000.97): Calc. %C, 57.60; %H, 5.03; %N, 5.60 and Found: %C, 58.35; %H, 5.82; %N, 6.21. Selected FTIR peaks (KBr, cm^{-1}): 3418 (br), 1616 (s), 1541 (m), 1410 (s), 1250 (m), 1099 (s), 1017 (w), 811 (m), 763 (s), 721 (m), 493 (w).

$\{[Co_2(azopy)(dmsdba)_2]\}_n$ (35). It was synthesized using the same procedure as for **31**, instead 9.2 mg (0.05 mmol) of azopy was used in place of bpy. The violet block-shaped crystals suitable for single crystal X-ray diffraction analysis, thus obtained was collected via filtration, washed with DMF and water, and air dried. Yield: 30 mg (67%). Anal. Calcd for $C_{42}H_{36}N_4O_8Si_2Co_2$ (MW 898.79): Calc. %C, 56.13; %H, 4.04; %N, 6.23 and Found: %C, 57.25; %H, 4.97; %N, 7.03. Selected FTIR peaks (KBr, cm^{-1}): 1609 (s), 1541 (w), 1411 (s), 1250 (m), 1099 (s), 1020 (w), 831 (m), 812 (m), 762 (s), 720 (m), 494 (w).

$\{[Co_2(bpp)(dmsdba)_2]\}_n$ (36). It was synthesized using the same procedure as for **31**, instead 10 mg (0.05 mmol) of bpp was used in place of bpy. The violet block-shaped crystals suitable for single crystal X-ray diffraction analysis, thus obtained was collected via filtration, washed with DMF and water, and air dried. Yield: 35 mg (76%). Anal. Calcd for $C_{45}H_{42}N_2O_8Si_2Co_2$ (MW 912.86): Calc. %C, 59.21; %H,

4.64; %N, 3.07 and Found: %C, 58.53; %H, 5.02; %N, 3.82. Selected FTIR peaks (KBr, cm^{-1}): Selected FTIR peaks (KBr, cm^{-1}): 1617 (s), 1542 (m), 1409 (s), 1259 (m), 1222 (w), 1098 (s), 1018 (m), 811 (s), 762 (s), 717 (m), 492 (w).

[[Cd₂(bpe)(dmsdba)₂(DMF)₂]]_n (37). 30 mg (0.1 mmol) of H₂dmsdba was dissolved in 1 mL DMF in a 10 mL round bottom flask. To this solution, a solution of 26.6 mg (0.1 mmol) of cadmium acetate dihydrate and 9.2 mg (0.05 mmol) of bpe in 4 mL ethanol/water mixture (1:3) was slowly added at room temperature. After stirring for 15 min, a white precipitate appeared. The reaction mixture was stirred for another 8 h at room temperature to ensure complete precipitation of the product. The white solid thus obtained was collected via filtration, washed with DMF and water, and air-dried. Yield: 38 mg (66%). Anal. Calcd for C₅₀H₅₄N₄O₁₀Si₂Cd₂ (MW 1151.98): Calc. %C, 52.13; %H, 4.72; %N, 4.86 and Found: %C, 51.23; %H, 5.51; %N, 5.72. Selected FTIR peaks (KBr, cm^{-1}): 1653 (s), 1613 (m), 1578 (s), 1526 (s), 1498 (m), 1400 (s), 1220 (m), 1099 (s), 1020 (m), 830 (m), 814 (s), 765 (s), 724 (s), 544 (m), 488 (w).

Method for crystallization: The single crystals of the compound was obtained by slow diffusion technique. A solution of 7.5 mg (0.025 mmol) of H₂dmsdba in 0.2 mL DMF was placed in a narrow glass tube. A solution of 6.7 mg (0.025 mmol) of cadmium acetate dihydrate and 2.3 mg (0.0125 mmol) of bpe was added very carefully along the sides of the tube on the top of H₂dmsdba solution and kept undisturbed. Colourless crystals suitable for single crystal X-ray diffraction analysis were obtained at the interface of the two solutions after 5 days.

[[Cd₂(4-bpdb)(dmsdba)₂(H₂O)₂·2H₂O]]_n (38). 30 mg (0.1 mmol) of H₂dmsdba was dissolved in 2 mL water by making the sodium salt of H₂dmsdba, using 2 equivalent of sodium hydroxide and mixed with a solution of 10.5 mg (0.05 mmol) of 4-bpdb in 5 mL ethanol. The resulting clear solution was subsequently added to a solution of 26.6 mg (0.1 mmol) of cadmium acetate dihydrate in 3 mL water. A light yellow precipitate appeared immediately. The reaction mixture was further stirred for another 4 h at room temperature to ensure complete precipitation of the product. The light yellow solid thus obtained was collected via filtration, washed with water and ethanol, and air-dried. Yield: 42 mg (76%). Anal. Calcd for C₄₄H₄₆N₄O₁₂Si₂Cd₂ (MW 1103.85): Calc. %C, 47.88; %H, 4.20; %N, 5.08 and Found: %C, 48.02; %H, 5.21; %N, 5.54. Selected FTIR peaks (KBr, cm^{-1}): 3370 (br), 1609 (s), 1575 (s), 1525 (s),

1498 (m), 1402 (s), 1309 (w), 1252 (m), 1143 (w), 1099 (s), 1019 (m), 814 (s), 763 (s), 727 (m), 688 (m), 518 (m).

Method for crystallization: A solution of 7.5 mg (0.025 mmol) of H₂dmsdba was made in 0.3 mL water using 2 equivalent of sodium hydroxide and added to a solution of 2.6 mg (0.0125 mmol) of 4-bpdb in 1 mL ethanol. The resulting clear solution was added very carefully along the sides of the tube on the top of cadmium acetate dehydrate solution using 1 mL ethanol/water buffer (1:1) in between the two solution. The tube was kept undisturbed at room temperature. Clear light yellow crystals suitable for single crystal X-ray diffraction analysis was obtained after 7 days.

{[Cd(bpp)(dmsdba)(H₂O)]·DMF}_n (39). A mixture of dicarboxylic acid, H₂dmsdba 30 mg (0.1 mmol), bpp 20 mg (0.1 mmol) and 31 mg (0.1 mmol) of cadmium nitrate tetrahydrate was dissolved in 3 mL DMF. To this solution 2 mL water was added and the clear solution was transferred to a glass vial. The glass vial was sealed and heated to 100 °C for 48 h. The colourless rod shaped crystals, thus obtained were filtered while hot to remove any unreacted ligands or metal salt from the product. The crystals were repeatedly washed with DMF followed by water and air-dried. Yield: 48 mg (69%), based on the metal salt. Anal. Calcd for C₃₂H₃₇N₃O₆SiCd (MW 700.13): Calc. %C, 54.89; %H, 5.33; %N, 6.00 and Found: %C, 55.05; %H, 6.10; %N, 5.88. Selected FTIR peaks (KBr, cm⁻¹): 3406 (br), 1669 (s), 1579 (s), 1530 (s), 1400 (s), 1307 (w), 1250 (m), 1225 (w), 1100 (s), 1017 (m), 812 (s), 767 (s), 724 (m), 659 (w), 509 (m).

{[Cd₂(1,5-ndp)(dmsdba)₂(THF)₂]·2THF}_n (40). 30 mg (0.1 mmol) of H₂dmsdba and 17 mg (0.05 mmol) of 1,5-ndp was dissolved in 5 mL THF in a 25 mL round bottom flask. A solution of 31 mg (0.1 mmol) of cadmium nitrate tetrahydrate in 5 mL methanol was then added very slowly to the above solution while stirring. A Yellow precipitate appeared immediately. The reaction mixture was further stirred for another 8 h at room temperature to ensure complete precipitation of the product. The yellow solid thus obtained was collected via filtration, washed with THF and methanol, and air-dried. Yield: 48 mg (66%). Anal. Calcd for C₇₈H₉₂N₄O₁₄Si₂Cd₂ (MW 1590.57): Calc. %C, 58.90; %H, 5.83; %N, 3.52 and Found: %C, 59.52; %H, 6.18; %N, 3.32. Selected FTIR peaks (KBr, cm⁻¹): 3392 (br), 1609 (s), 1578 (s), 1528 (s), 1500 (m), 1401 (s), 1317 (w), 1248 (m), 1189 (w), 1100 (s), 1061 (m), 1018 (m), 927 (w), 829 (s), 813 (s), 764 (s), 725 (s), 538 (m).

Method for crystallization: Single crystals of the compound was obtained by slow diffusion technique. A solution of 7.5 mg (0.025 mmol) of H₂dmsdba and 4.2 mg (0.0125 mmol) of 1,5-ndp was made in 1 mL THF and transferred to a narrow glass tube. A solution of 7.7 mg (0.025 mmol) of cadmium nitrate tetrahydrate in 0.5 mL methanol was then added very carefully along the sides of the tube on the top of the above solution using 1 mL THF/MeOH buffer (1:1) in between the two solutions. The tube was kept undisturbed at room temperature. Clear yellow crystals suitable for single crystal X-ray diffraction analysis was obtained after 7 days.

{[Zn₂(4-tpom)(dmsdba)₂]·DMF·2H₂O}_n (41). 30 mg (0.1 mmol) of the H₂dmsdba and 22 mg (0.05 mmol) of 4-tpom was taken in a teflon reactor and dissolved in 1 mL of DMF. A solution of 22 mg (0.1 mmol) of zinc acetate dihydrate in 4 mL ethanol/water (1:3) was then added to this solution. The reactor was sealed in a stainless steel vessel and heated in a programmable oven at 120 °C for 48 h followed by slow cooling to room temperature at a rate of 3-4 °C/hr. The colourless block shaped crystals thus obtained were collected via filtration, washed with DMF and then with water to remove the acetic acid by-product and air-dried. Yield: 45 mg (70%). Anal. Calcd for C₆₀H₆₃N₅O₁₅Si₂Zn₂ (MW 1281.10): Calc. %C, 56.25; %H, 4.96; %N, 5.47 and Found: %C, 55.92; %H, 4.58; %N, 5.83. Selected FTIR peaks (KBr, cm⁻¹): 3434 (br), 1664 (w), 1613 (s), 1542 (m), 1513 (m), 1468 (w), 1387 (s), 1293 (s), 1213 (s), 1100 (m), 1030 (s), 830 (m), 810 (s), 764 (s), 723 (m), 538 (m).

{[Cd₂(4-tpom)(dmsdba)₂]·4DMF·H₂O}_n (42). 30 mg (0.1 mmol) of the H₂dmsdba and 22 mg (0.05 mmol) of 4-tpom was taken in a teflon reactor and dissolved in 1 mL of DMF. A solution of 26.6 mg (0.1 mmol) of cadmium acetate dihydrate in 4 mL ethanol/water (1:3) was then added to this solution. The reactor was sealed in a stainless steel vessel and heated in a programmable oven at 120 °C for 48 h followed by slow cooling to room temperature at a rate of 3-4 °C/hr. The colourless block shaped crystals thus obtained were collected via filtration, washed with DMF and then with water to remove the acetic acid by-product and air-dried. Yield: 52 mg (65%). Anal. Calcd for C₆₉H₈₂N₈O₁₇Si₂Cd₂ (MW 1576.43): Calc. %C, 52.57; %H, 5.24; %N, 7.11 and Found: %C, 52.83; %H, 5.62; %N, 6.89. Selected FTIR peaks (KBr, cm⁻¹): 3411 (br), 1668 (w), 1607 (s), 1576 (m), 1526 (m), 1509 (m), 1466 (w), 1397 (s), 1291 (s), 1212 (s), 1100 (m), 1023 (s), 829 (m), 812 (s), 764 (s), 725 (m), 537 (m).

{[Zn₂(3-tpom)(dmsdba)₂]·EtOH·3H₂O}_n (43). 30 mg (0.1 mmol) of the H₂dmsdba and 22 mg (0.05 mmol) of 3-tpom was taken in a teflon reactor and dissolved in 1 mL of DMF. A solution of 22 mg (0.1 mmol) of zinc acetate dihydrate in 4 mL ethanol/water (1:3) was then added to this solution. The reactor was sealed in a stainless steel vessel and heated in a programmable oven at 120 °C for 48 h followed by slow cooling to room temperature at a rate of 3-4 °C/hr. The colourless block shaped crystals thus obtained were collected via filtration, washed with DMF and then with water to remove the acetic acid by-product and air-dried. Yield: 42 mg (66%). Anal. Calcd for C₅₉H₆₄N₄O₁₆Si₂Zn₂ (MW 1272.09): Calc. %C, 55.70; %H, 5.10; %N, 4.41 and Found: %C, 56.02; %H, 5.46; %N, 4.82. Selected FTIR peaks (KBr, cm⁻¹): 3430 (br), 1624 (s), 1601 (m), 1576 (s), 1548 (m), 1482 (m), 1435 (s), 1390 (s), 1369 (s), 1283 (s), 1244 (s), 1190 (w), 1101 (s), 1056 (m), 1018 (m), 829 (m), 814 (s), 772 (s), 760 (s), 722 (m), 697 (m), 642 (w).

{[Cd₂(3-tpom)(obba)₂]·(H₂O)_n (44). 26 mg (0.1 mmol) of the H₂obba and 22 mg (0.05 mmol) of 3-tpom was taken in a teflon reactor and dissolved in 1 mL of DMF. A solution of 31 mg (0.1 mmol) of cadmium nitrate tetrahydrate in 4 mL ethanol/water (1:3) was then added to this solution. The reactor was sealed in a stainless steel vessel and heated in a programmable oven at 120 °C for 48 h followed by slow cooling to room temperature at a rate of 3-4 °C/hr. The colourless block shaped crystals thus obtained were collected via filtration, washed with DMF and then with water and air-dried. Yield: 40 mg (66%). Anal. Calcd for C₅₃H₄₂N₄O₁₅Cd₂ (MW 1199.81): Calc. %C, 53.06; %H, 3.55; %N, 4.65 and Found: %C, 53.21; %H, 3.46; %N, 4.91. Selected FTIR peaks (KBr, cm⁻¹): 3431 (br), 1684 (w), 1631 (w), 1597 (s), 1575 (m), 1542 (m), 1482 (m), 1435 (m), 1401 (s), 1277 (s), 1245 (s), 1195 (m), 1161 (s), 1058 (m), 1010 (m), 881 (s), 779 (s), 697 (m), 664 (m), 636 (m).

{[Cd₃(mstba)₂(H₂O)₆]·H₂O}_n (45). A mixture of tricarboxylic acid, H₃mstba 40.6 mg (0.1 mmol) and 46.2 mg (0.15 mmol) of cadmium nitrate tetrahydrate was dissolved in 3 mL DMF. To this solution 2 mL ethanol/water mixture (1/1) was added and the clear solution was transferred to a glass vial. The glass vial was sealed and heated to 100 °C for 48 h, followed by slow cooling to room temperature. The colourless block shaped crystals, thus obtained were filtered and washed repeatedly with DMF followed by water and air-dried. Yield: 43 mg (68 %). Anal. Calcd for C₄₄H₄₄O₁₉Si₂Cd₃ (MW 1270.21): Calc. %C, 41.60; %H, 3.49 and Found: %C, 43.02; %H, 4.51. Selected FTIR peaks (KBr, cm⁻¹): 3402 (br), 1663 (m), 1594 (s), 1576 (s),

1537 (s), 1528 (s), 1498 (m), 1469 (m), 1415 (s), 1307 (w), 1244 (m), 1191 (w), 1101 (s), 1019 (s), 857 (s), 799 (s), 766 (s), 742 (s), 724 (m), 704 (m), 537 (m).

{[NH₂(CH₃)₂]₂[Cd₂(bpy)(mstba)₂]₂·8DMF·2H₂O}_n (46). A mixture of tricarboxylic acid, H₃mstba 40.6 mg (0.1 mmol), 30.8 mg (0.1 mmol) of cadmium nitrate tetrahydrate and 8 mg (0.05 mmol) of bpy was dissolved in 5 mL DMF. To this solution 3 mL ethanol/water mixture (1/1) was added and the clear solution was transferred to a glass vial. The glass vial was sealed and heated to 100 °C for 48 h, followed by slow cooling to room temperature. The colourless needle shaped crystals, thus obtained were filtered and washed repeatedly with DMF followed by water and air-dried. Yield: 58 mg (61%). Anal. Calcd for C₈₂H₁₁₄N₁₂O₂₂Si₂Cd₂ (MW 1900.84): Calc. %C, 51.81; %H, 6.04; %N, 8.84 and Found: %C, 50.35; %H, 5.14; %N, 10.21. Selected FTIR peaks (KBr, cm⁻¹): 3412 (br), 1654 (m), 1595 (s), 1576 (m), 1537 (s), 1498 (m), 1413 (s), 1244 (m), 1220 (w), 1101 (s), 1019 (m), 856 (s), 799 (s), 766 (s), 742 (s), 724 (m), 630 (m), 536 (m).

{[NH₂(CH₃)₂]₂[Cd₂(azopy)(mstba)₂]₂·4DMF·2H₂O}_n (47). It was synthesized using the same procedure as for **46**, except 9.2 mg (0.05 mmol) of azopy was used instead of bpy. The red coloured block shaped crystals, thus obtained were filtered and washed repeatedly with DMF followed by water and air-dried. Yield: 62 mg (76 %). Anal. Calcd for C₇₀H₈₆N₁₀O₁₈Si₂Cd₂ (MW 1636.48): Calc. %C, 51.38; %H, 5.30; %N, 8.56 and Found: %C, 51.82; %H, 5.83; %N, 9.82. Selected FTIR peaks (KBr, cm⁻¹): 3400 (br), 1654 (m), 1592 (s), 1576 (m), 1534 (s), 1500 (m), 1403 (s), 1307 (w), 1245 (m), 1191 (w), 1102 (s), 1018 (s), 860 (s), 796 (s), 766 (s), 742 (s), 725 (m), 704 (m), 537 (m).

{[Co₂(bpy)(tcps)]₂·0.5DMF·H₂O}_n (48). A mixture of tetracarboxylic acid, H₄tcps 51.2 mg (0.1 mmol), 15.6 mg (0.1 mmol) of bpy and 58.2 mg (0.2 mmol) of cobalt nitrate hexahydrate was taken in a teflon reactor along with 10 mL solvent mixture of DMF/EtOH/H₂O (1/1/3). The teflon vessel was sealed in a stainless-steel vessel and heated to 120 °C for 48 h. The mixture was allowed to cool down to room temperature at a rate of 4 °C/h. Violet plate-like crystals, thus obtained was filtered and washed with DMF and ethanol and air dried to get the as synthesized compound. Yield: 60 mg (77%). Anal. Calcd for C_{39.5}H_{29.5}N_{2.5}O_{9.5}SiCo₂, (MW 836.5): Calc. %C, 56.6; %H, 3.5; %N, 4.2 and Found: %C, 57.2; %H, 3.7; %N, 4.6. Selected FTIR peaks (KBr, cm⁻¹): 1681 (s), 1618 (s), 1542 (m), 1498 (w), 1399 (s), 1384 (s), 1259 (w), 1217 (w), 1097 (m), 1018 (w), 811 (m), 770 (m), 725 (s), 481 (w).

{[Cd₂(bpy)(tcps)]·(H₂O)}_n (49). A mixture of tetracarboxylic acid, H₄tcps 25.6 mg (0.05 mmol), 8 mg (0.05 mmol) of bpy was dissolved in 3 mL DMF. To this clear solution 30.8 mg (0.1 mmol) of cadmium nitrate hexahydrate was added and stirred for 10 minutes to obtain a clear solution. To this solution 2 mL ethanol/water mixture (1/1) was added and the clear solution was transferred to a glass vial. The glass vial was sealed and heated to 100 °C for 48 h, followed by slow cooling to room temperature. The colourless needle shaped crystals, thus obtained were filtered and washed repeatedly with DMF followed by water and air-dried. Yield: 33 mg (73 %). Anal. Calcd for C₃₈H₂₆N₂O₉SiCd₂ (MW 907.53): Calc. %C, 50.29; %H, 2.89; %N, 3.09 and Found: %C, 51.54; %H, 3.23; %N, 3.78. Selected FTIR peaks (KBr, cm⁻¹): 3412 (br), 1654 (m), 1601 (s), 1533 (m), 1393 (s), 1256 (w), 1099 (s), 1017 (m), 850 (m), 811 (m), 744 (m), 730 (s), 706 (m), 559 (m).

{[Cd₂(azopy)(tcps)]·DMF·H₂O}_n (50). It was synthesized using the same procedure as for **49**, except 9.2 mg (0.05 mmol) of azopy was used instead of bpy. The red block-shaped crystals, thus obtained were filtered and washed repeatedly with DMF followed by water and air-dried. Yield: 35 mg (69%). Anal. Calcd for C₄₁H₃₃N₅O₁₀SiCd₂ (MW 1008.64): Calc. %C, 48.82; %H, 3.30; %N, 6.94 and Found: %C, 48.07; %H, 4.21; %N, 7.58. Selected FTIR peaks (KBr, cm⁻¹): 3410 (br), 1654 (s), 1578 (s), 1528 (s), 1393 (s), 1098 (s), 1017 (m), 858 (m), 773 (m), 730 (s), 706 (m), 559 (m).

{[Cd₂(3-bpdb)_{0.5}(tcps)(H₂O)₂]·4EtOH·3H₂O}_n (51). 51.2 mg (0.1 mmol) of H₄tcps was dissolved in 5 mL water by making the sodium salt of H₄tcps, using 4 equivalent of sodium hydroxide and mixed with a solution of 21 mg (0.1 mmol) of 3-bpdb in 5 mL ethanol. The resulting clear solution was subsequently added to a solution of 61.6 mg (0.2 mmol) of cadmium nitrate tetrahydrate in 5 mL water. A light yellow precipitate appeared immediately. The reaction mixture was further stirred for another 4 h at room temperature to ensure complete precipitation of the product. The light yellow solid thus obtained was collected via filtration, washed with water and ethanol, and air-dried. Yield: 95 mg (78%). Anal. Calcd for C₄₂H₅₅N₂O₁₇SiCd₂ (MW 1112.80): Calc. %C, 45.33; %H, 4.98; %N, 2.52 and Found: %C, 46.34; %H, 5.22; %N, 3.21. Selected FTIR peaks (KBr, cm⁻¹): 3412 (br), 1654 (m), 1580 (s), 1528 (s), 1496 (m), 1397 (s), 1253 (m), 1095 (s), 1018 (s), 858 (m), 774 (s), 731 (s), 703 (m), 559 (m), 483 (w).

Method for crystallization: Single crystal of the compound was obtained by slow diffusion technique. A solution of 6.4 mg (0.0125 mmol) of H₄tcps was made in 0.3 mL water using 4 equivalent of sodium hydroxide and added to a solution of 2.6 mg (0.0125 mmol) of 4-bpdb in 1 mL ethanol. The resulting clear solution was added very carefully on the top of cadmium nitrate tetrahydrate solution in 0.5 mL water kept in a narrow glass tube using 1 mL ethanol/water buffer (1:1) in between the two solutions. The tube was kept undisturbed at room temperature. Clear light yellow crystals suitable for single crystal X-ray diffraction analysis was obtained after 7 days.

{[Cd₂(3-bpdh)_{0.5}(tcps)(H₂O)(DMF)]·5DMF}_n (52). A mixture of tetracarboxylic acid, H₄tcps 25.6 mg (0.05 mmol), 12 mg (0.05 mmol) of 3-bpdh was dissolved in 3 mL DMF. To this clear solution, 30.8 mg (0.1 mmol) of cadmium nitrate hexahydrate was added and stirred for 10 minutes to obtain a clear solution. To this solution 2 mL ethanol/water mixture (1/1) was added and the clear solution was transferred to a glass vial. The glass vial was sealed and heated to 100 °C for 48 h, followed by slow cooling to room temperature. The light yellow needle shaped crystals, thus obtained were filtered and washed repeatedly with DMF followed by water and air-dried. Yield: 45 mg (63%). Anal. Calcd for C₅₃H₆₇N₈O₁₅SiCd₂ (MW 1309.26): Calc. %C, 48.63; %H, 5.16; %N, 8.56 and Found: %C, 48.82; %H, 4.69; %N, 9.23. Selected FTIR peaks (KBr, cm⁻¹): 3365 (br), 1652 (s), 1578 (s), 1527 (s), 1495 (s), 1391 (s), 1191 (s), 1095 (s), 1044 (w), 1017 (m), 858 (m), 772 (s), 729 (s), 704 (s), 557 (m), 475 (m).

{[Ni₂(4-tpom)(tcps)]·3DMF·H₂O}_n (53). A mixture of tetracarboxylic acid, H₄tcps 25.6 mg (0.05 mmol), 22 mg (0.05 mmol) of 4-tpom and 25 mg (0.1 mmol) of nickel acetate tetrahydrate was taken in a teflon reactor along with 5 mL solvent mixture of DMF/EtOH/H₂O (1/1/3). The teflon vessel was sealed in a stainless-steel vessel and heated to 120 °C for 72 h. The mixture was allowed to cool down to room temperature at a rate of 3 °C/h. Green block-shaped crystals, thus obtained was collected via filtration, washed with DMF and ethanol and air dried to get the as synthesized compound. Yield: 47 mg (72%). Anal. Calcd for C₆₂H₆₃N₇O₁₆SiNi₂, (MW 1307.67): Calc. %C, 56.95; %H, 4.86; %N, 7.50 and Found: %C, 55.62; %H, 4.21; %N, 8.72. Selected FTIR peaks (KBr, cm⁻¹): 3412 (br), 1659 (s), 1609 (s), 1576 (s), 1530 (s), 1509 (s), 1467 (w), 1388 (s), 1289 (s), 1211 (s), 1099 (s), 1028 (s), 829 (m), 774 (m), 729 (s), 540 (m).

{[Zn₂(3-tpom)(tcps)]·3DMF}_n (54). A mixture of tetracarboxylic acid, H₄tcps 25.6 mg (0.05 mmol), 22 mg (0.05 mmol) of 4-tpom and 22 mg (0.1 mmol) of zinc acetate dihydrate was taken in a teflon reactor along with 5 mL solvent mixture of DMF/EtOH/H₂O (1/1/3). The teflon vessel was sealed in a stainless-steel vessel and heated to 120 °C for 72 h. The mixture was allowed to cool down to room temperature at a rate of 3 °C/h. The colourless plate-like crystals, thus obtained was collected via filtration, washed with DMF and ethanol and air dried to get the as synthesized compound. Yield: 47 mg (72%). Anal. Calcd for C₆₂H₆₁N₇O₁₅SiZn₂ (MW 1303.03): Calc. %C, 57.15; %H, 4.72; %N, 7.52 and Found: %C, 58.23; %H, 5.56; %N, 8.61. Selected FTIR peaks (KBr, cm⁻¹): 3422 (br), 1601 (s), 1577 (s), 1541 (m), 1495 (w), 1484 (w), 1432 (m), 1389 (s), 1278 (m), 1244 (m), 1195 (w), 1100 (s), 1019 (m), 803 (m), 773 (m), 731 (s), 702 (m), 647 (w), 551 (m).

{[Zn₂(dmsbta)(H₂O)]·4H₂O}_n (55) 35 mg (0.05 mmol) of the tetracarboxylic acid, H₄dmsbta was taken in a teflon vessel and dissolved in 2 mL diethylacetamide (DEA). To this solution 30 mg (0.1 mmol) of zinc nitrate hexahydrate was added along with 2 mL water. The teflon vessel was sealed in a stainless-steel reactor and heated to 120 °C for 3 days followed by slow cooling to room temperature at a rate of 2 °C/h. Colourless plate-like crystals thus obtained was filtered and washed with fresh DMA for three times and then with ethanol and air dried at room temperature to get the as synthesized compound. Yield: 35 mg (78%). Anal. Calcd for C₃₄H₃₂N₆O₁₃SiZn₂ (MW 891.50): Calc. %C, 45.81; %H, 3.62; %N, 9.43 and Found: %C, 45.23; %H, 4.46; %N, 10.23. Selected FTIR peaks (KBr, cm⁻¹): 3413 (br), 1624 (s), 1583 (s), 1566 (s), 1452 (m), 1415 (s), 1386 (m), 1246 (m), 1121 (m), 1093 (m), 1059 (m), 1033 (m), 814 (s), 776 (s), 757 (m), 728 (w), 511 (w).

{[Cu₂(tpstba)(H₂O)₂]·20(DMF)}_n (56) 27 mg (0.025 mmol) of the tetracarboxylic acid, H₄tpstba was taken in a glass vial and dissolved in 2 mL dimethylformamide (DMF). To this solution 10 mg (0.05 mmol) of copper acetate monohydrate was added and stirred for 5 minutes to get the clear solution. To this clear solution 1 mL of water was added. The glass vial was sealed and heated to 100 °C for 48 h, followed by slow cooling to room temperature. The green block-shaped crystals thus obtained was filtered and washed with fresh DMF for three times and then with ethanol and air dried at room temperature to get the as synthesized **57**. Yield: 30 mg (44%). Anal. Calcd for C₁₂₀H₁₈₀N₃₂O₃₀SiCu₂ (MW 2706.09): Calc. %C, 53.26; %H, 6.70; %N, 16.56 and Found: %C, 53.89; %H, 5.92; %N, 17.20. Selected FTIR peaks (KBr, cm⁻¹): 3399 (br), 1657 (s), 1604 (s), 1556 (s), 1515 (m),

1436 (m), 1406 (s), 1387 (s), 1228 (m), 1172 (m), 1115 (s), 1032 (s), 992 (s), 781 (s), 745 (m), 718 (m), 538 (m).

CHAPTER III

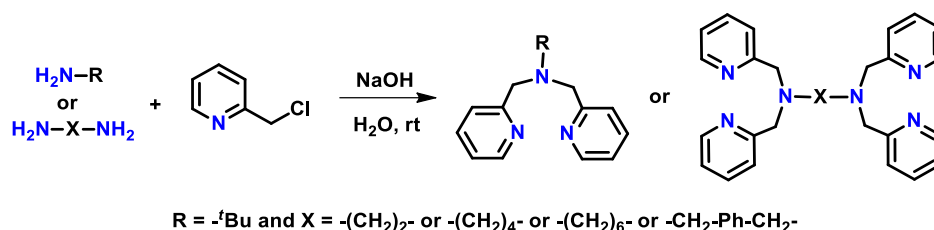
Results and discussion

This chapter is divided into four major sections: coordination architectures derived from (a) bent dicarboxylates, (b) tricarboxylates, (c) semi-rigid tetrahedral tetracarboxylate and (d) triazole functionalized carboxylates. Apart from this, the sections (a) and (c) are further classified into different subsections based on the ligand systems. The important fundamental characteristics of these coordination architectures include the number of binding sites available on the metal ion/clusters, the relative orientation of these binding sites, the number of Lewis-basic sites on a linker, the mode of coordination of these sites, and the relative angularity of these sites, which directs the topology and functionality of coordination architectures. The topology and functionality of the coordination architectures can be controlled by appropriate choice of the metal center, ligand and linkers.^{126,239–243} In terms of crystal engineering, an effective route for the synthesis of novel coordination architectures with attractive topological structures is the employment of mixed ligands.²⁴⁴ Keeping the above factors in mind, various poly pyridyl-based ligands (capping or pillar ligands) and carboxylate linkers have been synthesized using either the literature method or with some modifications in the reported procedures. Considering the multi component self-assembly, combinations of these precursors (metal ions, poly-pyridyl ligands and carboxylate linkers) results in the formation of various discrete or polymeric coordination architectures with different dimensionality and functionality. In this section, syntheses of these architectures have been discussed followed by their characterizations and applications. Most of these coordination architectures have been structurally characterized by single crystal X-ray diffraction analysis and their structural features have been well corroborated by a combination of various analytical techniques such as like elemental analysis, UV-Vis and FTIR spectroscopy, fluorescence spectroscopy, powder X-ray diffraction and thermo-gravimetric analysis.

Syntheses of Ligands. All the ligands were synthesized using either the literature method or with some modifications in the reported procedures. The polypyridyl capping ligands (tridentate **bpta** or bis-tridentate **tpen**, **tpbn**, **tpxn**, **tpxn**) were synthesized by substitution reaction between mono- or diammine and picolylchloride in an aqueous medium using equivalent amount of sodium hydroxide (Scheme 3.1). In all cases the solid product thus formed was isolated via filtration except for **bpta** and **tpen** where the product was extracted using DCM. The pillars ligands **4-bpdb**, **4-bpdh**, **3-bpdb**, **3-bpdh**, **1,5-ND-4-Py** and **1,5-**

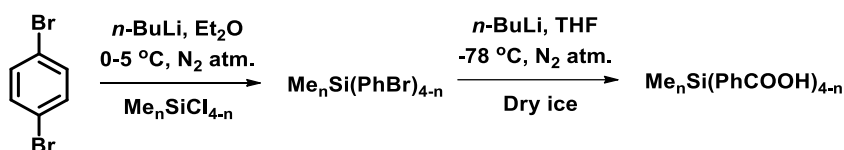
ND-3-Py were synthesized by condensation reaction of hydrazine or corresponding diammines with corresponding aldehyde or ketone. The ligand **dpb** and **4-bpmp** or **3-bpmp** was synthesized by coupling reaction of 1,4-dibromobenzene with pyridine-4-boronic acid and by substitution reaction between pyrazine and the corresponding picolyl chlorides, respectively. These ligands were thoroughly characterised by NMR and HRMS techniques and used as is with out any purification.

Scheme 3.1. General synthesis of bpta, tpen, tpbn, tphxn and tpxn.



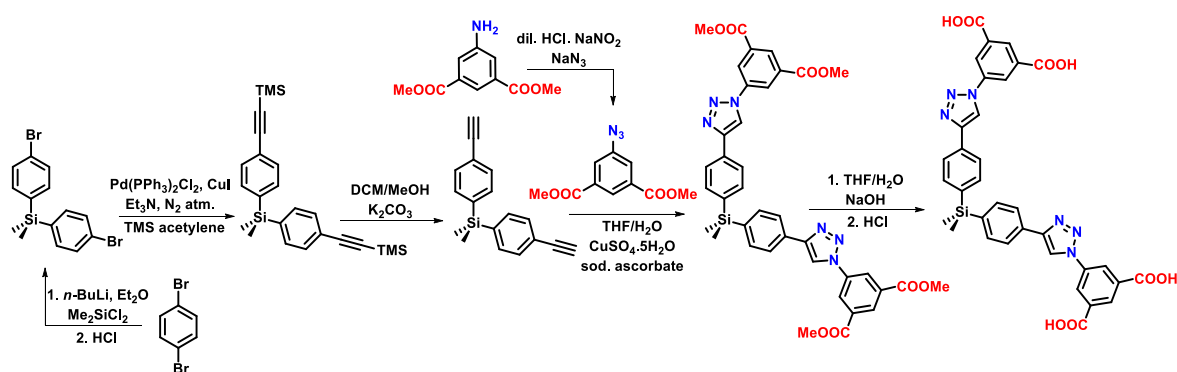
The di-, tri- or tetracarboxylate linkers (**H₂dmsdbs**, **H₃mstba** and **H₄tcps**) were synthesized in two step procedure, starting with 1,4-dibromobenzene in each case (Scheme 3.2). The first step involves the halogen exchange reaction with one eq. of *n*-BuLi to generate the nucleophile, followed by its reaction with the electrophilic dichlorodimethyl-, trichloromethyl- or tetrachlorosilane to generate bis(4-bromophenyl)dimethyl-, tris(4-bromophenyl)(methyl)- or tetrakis(4-bromophenyl)silane derivatives. The second step again involves the halogen exchange reaction to generate the nucleophile which on reaction with electrophilic carbon dioxide and further acidification with dil. HCl produces the corresponding carboxylic acid derivatives in good yield.

Scheme 3.2. General synthesis of H₂dmsdbs, H₃mstba and H₄tcps.

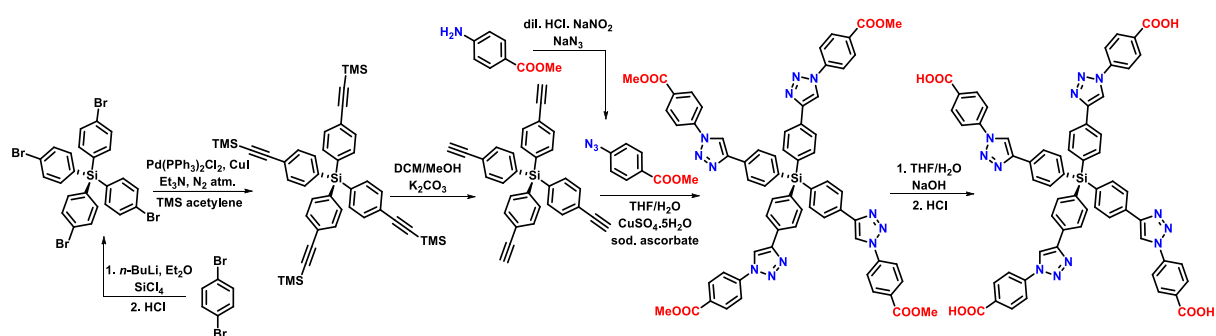


The triazole functionalized carboxylate linkers (**H₄dmsbta**, and **H₄tpsba**) were synthesized by using the versatile Click reaction for azide-alkyne cycloaddition. The azide and alkyne precursors were synthesized by modifying the literature procedures (Scheme 3.3 and 3.4).

Scheme 3.3. Synthesis of H₄dmsbta.



Scheme 3.4. Synthesis of H₄tpsba.



3.1 COORDINATION ARCHITECTURES DERIVED FROM BENT DICARBOXYLATES

In the crystal engineering of coordination architectures, out of various organic ligands/linkers the N- and O-donor ligands have been considered as the best combination.²⁴⁴ The O-donor being the carboxylates have gained considerable attention because of strong metal carboxylate binding. However, a series of carboxylate linkers have been explored for the synthesis of various coordination architectures; the architectures with bent dicarboxylates are not much explored. There are only a few dicarboxylates reported in the literature (Figure 3.1), out of which **H₂dmsdba** is comparatively less explored and being synthetically accessible attract our attention for its utilization in the synthesis of coordination architectures. Further, it can be modified to tri- and tetracarboxylic acid derivatives for comparative studies. In this section the chemistry of coordination architectures with this dicarboxylate linker has been explored. The section has been further divided into two major subsections; a) coordination driven self-assembly of discrete molecular squares and b) coordination driven self-assembly of polymeric architectures,

which has been further divided into two sections based on the strategies employed for the synthesis of these polymeric architectures.

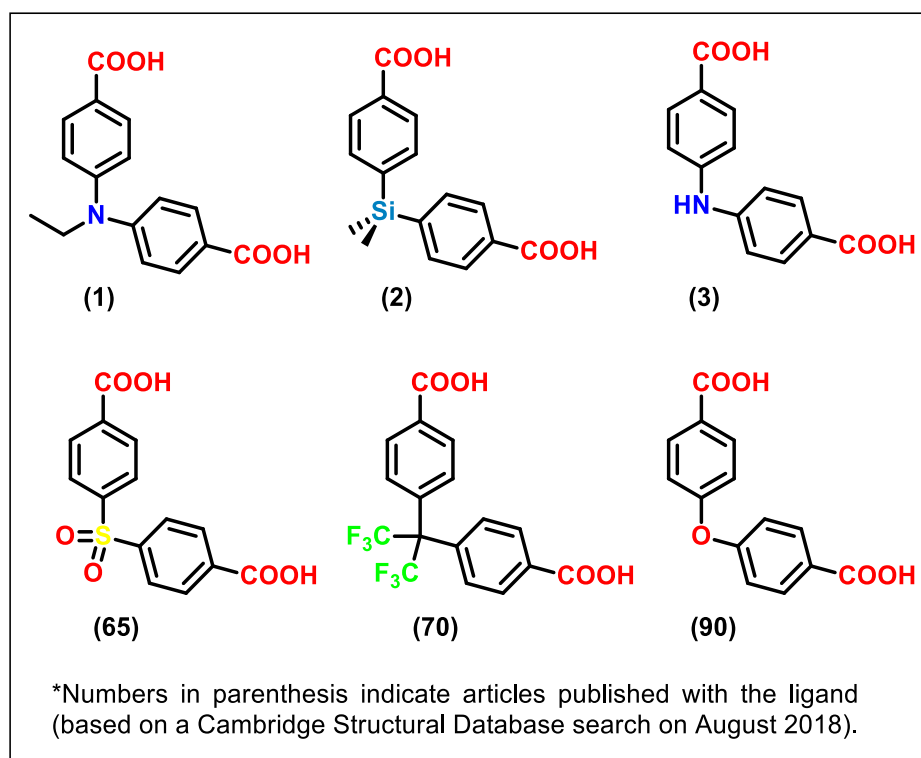


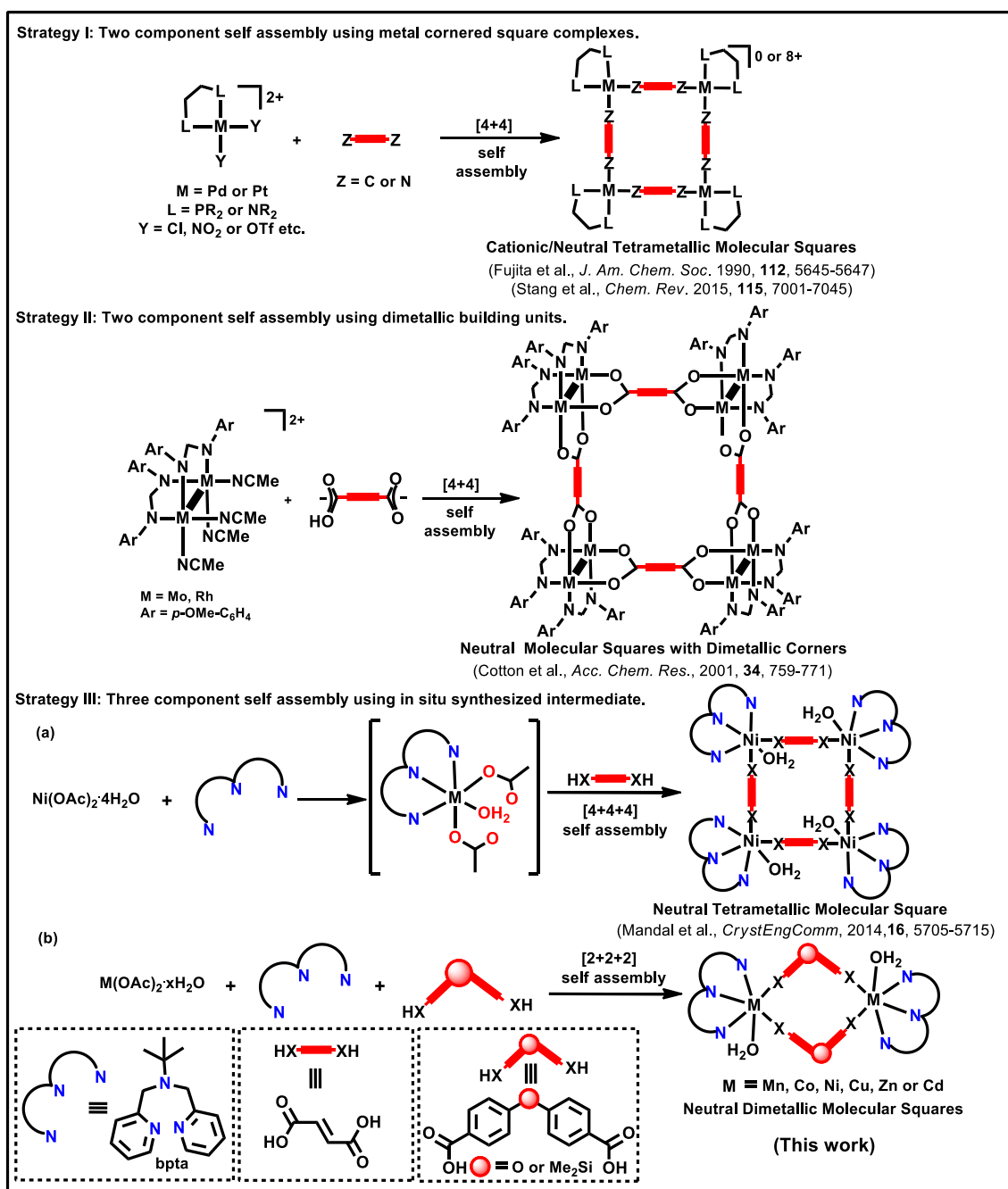
Figure 3.1. Dicarboxylate linkers utilized for the synthesis of coordination architectures reported in the literature.

3.1.1 Coordination driven self-assembly of molecular squares

In the past few decades, enormous efforts have been devoted to the construction of aesthetically appealing metallocyclic structures, such as molecular triangles, squares, rectangles, prisms and cages, by connecting the multitopic organic linkers with transition metal centers through coordination-driven self-assembly processes.^{6,8–16,245,246} Thus, coordination chemistry has emerged as an effective and versatile tool for the design and construction of such metallocyclic structures as the metal-ligand coordination bonds are stronger and more directional than non-covalent interactions such as hydrogen bonds and π - π interactions. One of the metallocycles, molecular squares, is the result of a [4+4] self-assembly of two types of building units (linear and angular), where linear building units possess two active functional end groups that are oriented at an angle of 180° from each other and angular building units have labile end groups positioned in cis orientation (about 90°) to each other. On the other hand, a [2+2] combination of two different 90° angular building units can also generate molecular squares. With the first example of a [4+4] self-assembly reported by Fujita et al.¹⁶ for palladium based cationic molecular squares, Stang

et al.³⁵ established the chemistry of platinum and palladium based molecular squares. Utilizing this approach, many groups have reported numerous examples, notably chiral molecular squares constructed by Lin et al.;⁵⁴ for example, neutral molecular squares were synthesized either by using divalent metal ions with neutral chelating bidentate ligands at

Scheme 3.5. Different strategies for the synthesis of molecular squares.

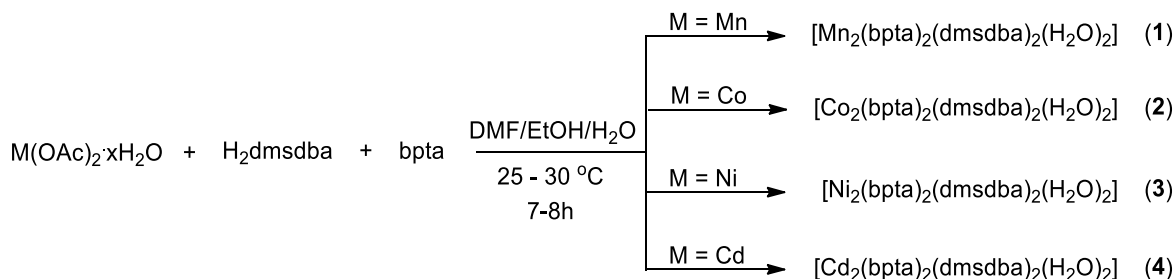


the corners with anionic alkynyl linker⁵⁵⁻⁵⁷ or by using divalent metal ion with anionic ligands at the corners with neutral linkers.^{58,59} A very different approach (see Strategy II, Scheme 3.5) was explored by Cotton et al. by fusing the multiply bonded dimetallic angular

building units (Mo_2^{4+} , Rh_2^{4+} or Ru_2^{5+}) with linear building units, such as dicarboxylates, for [4+4] self-assembled molecular squares.^{29,246,247} However, the area has been populated by several reports, majority of which focus on the use of pre-synthesized square planar metal complexes with fixed directionalities. There are very few reports of molecular squares based on octahedral metal complexes. In this section, we have explored the syntheses of such molecular squares of octahedral metal complexes using [4+4+4] self-assembly of three components (metal acetate, polypyridyl capping ligand and dicarboxylate). A generalized schematic representation for this approach in combination with the reported strategies to synthesize molecular squares is shown in Scheme 3.5.

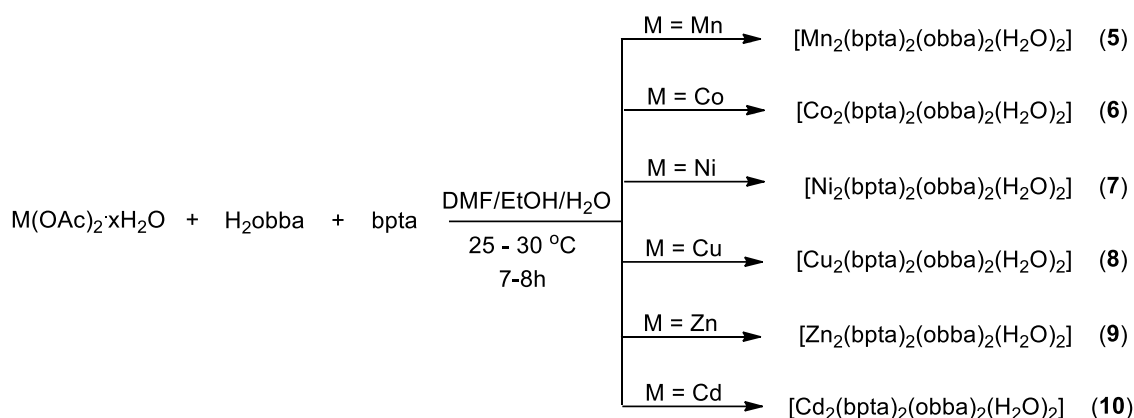
For this purpose, we chose a tridentate capped ligand, bpta which surrounds and protect the three binding sites of metal ion leaving behind three opening at 90° to each other. Inspired from our previous work on tetrametallic Ni_4 molecular square using polypyridyl ancillary ligand and linear carboxylates this study was extended for bent dicarboxylate which can span between two such metal units to form the molecular squares in a highly selective manner. The bent dicarboxylate, H_2dmsdba was used in combination with different metal salts and tridentate capping ligand, bpta to synthesize molecular squares **1-4** (Scheme 3.6).

Scheme 3.6. Synthesis of **1-4**.



The utility of the capping ligand bpta was further explored for the synthesis of molecular squares **5-10** using another bent dicarboxylate H_2obba (Scheme 3.7). All the molecular squares **1-10** were synthesized by one pot self-assembly of the corresponding metal salt, bpta ligand and respective dicarboxylic acid (in a 1:1:1 ratio) in a mixture of DMF/EtOH/ H_2O (in a 1/1/3 volume ratio) under ambient conditions. In all cases, the product was obtained as a precipitate which was filtered and washed with DMF and water to remove any traces of acetic acid by-product. Single crystals of all compounds were obtained either by solvothermal or by slow diffusion techniques. Based on the FTIR and PXRD data, the solid isolated from the self-assembly of components in each case was exactly the same as the crystals obtained by either of the two techniques mentioned above.

Scheme 3.7. Synthesis of **5-10**.



Single crystal structure analysis. Our efforts resulted in the formation of suitable crystals for **1**, **4**, **5**, **9** and **10** for single crystal X-ray studies. Crystals suitable for **1** and **4** were obtained by the solvothermal method and those for **5**, **9** and **10** by the slow diffusion technique. X-ray diffraction analysis reveals that dinuclear compounds **1** and **4** are isostructural. Both the compounds crystallize in the triclinic $P\bar{1}$ space group having an inversion center at the middle of the molecular square. The asymmetric unit contains one metal ion, Mn(II) in **1** and Cd(II) in **4**, one tridentate bpta ligand, one carboxylate linker and one water molecule coordinated to the metal centre (Figure 3.2a and d). Three nitrogen atoms of the bpta ligand bind to each metal ion in facial mode, leaving three open sites for one water molecule and two carboxylate groups of two different dmsdba²⁻. The two bent dicarboxylate ligands, which binds in a monodentate fashion, spans between the two metal ions forming a molecular square motif (Figure 3.2b and e). The geometry around the metal center in both cases is distorted octahedron. Dimensions of the squares (Si...Si, metal...metal and Si...metal) are shown in Figure 3.2c and f. The average M-N (2.26-2.40 Å) and M-O (2.13-2.23 Å) bond lengths are in the usual range for this kind of complexes.^{249,250} The crystallographic information pertaining to data collection and structure refinement parameters, selected bond distances and angles are listed in Table A1, A23 and A45, respectively.

Compounds **5**, **9** and **10** are isostructural to **1** and **4**. The coordination environment around the metal centres is N3O3 type. All three compounds crystallize in the triclinic $P\bar{1}$ space group having an inversion center at the middle of the molecular square. The asymmetric unit contains one metal ion, (Mn(II) in **5**, Zn(II) in **9**, and Cd(II) in **10**), one tridentate bpta ligand, one carboxylate linker (obba²⁻) and one water molecule coordinated to the metal center. (Figure 3.3a, d and g) In all compounds, metal center is in a distorted octahedral

geometry, which is reflected from the cisoid angles $[72.75(7) - 109.86(7)^\circ]$ in (**5**), $[74.96(10) - 106.25(10)^\circ]$ in (**9**) and $[71.58(8) - 109.99(8)^\circ]$ in (**10**). The coordination environment of the metal centers in **5**, **9** and **10** is similar to those of **1** and **4**. The two carboxylates from two obba²⁻ molecules span in between the two metal ions forming a molecular square as shown in Figure 3.3b, e and h. Dimensions of the squares are shown in Figure 3.3c, f and i, where the distances are measured from O...O, metal...metal and O...metal.

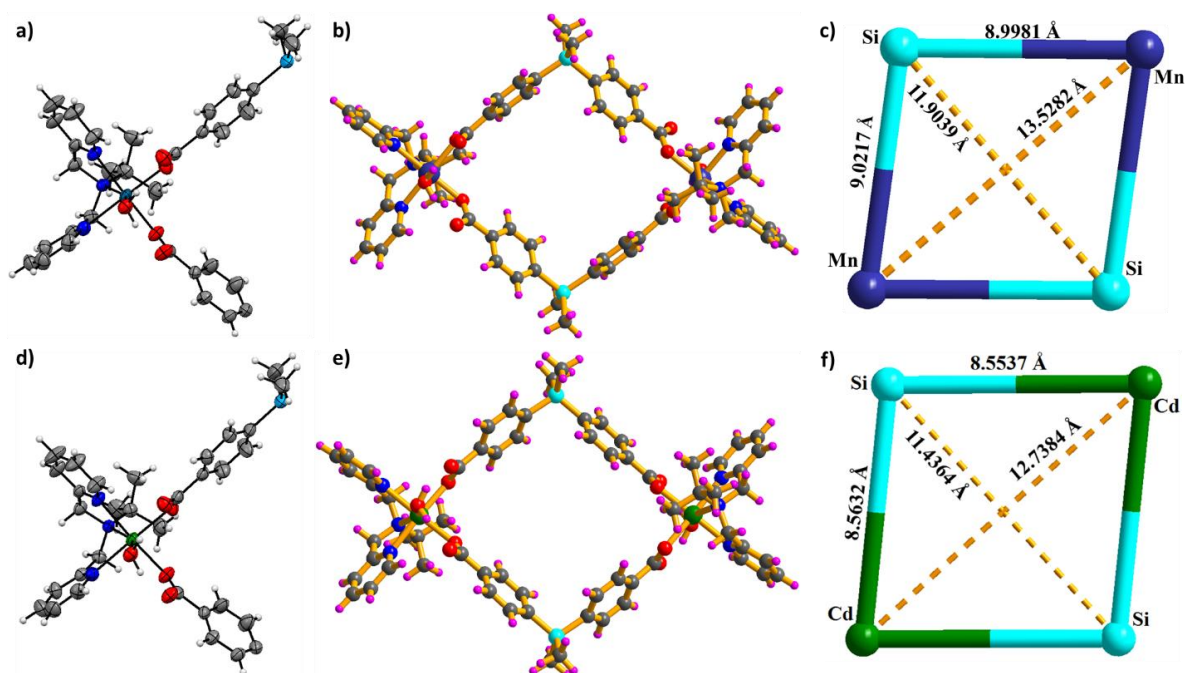


Figure 3.2. Crystal structure of molecular square **1** and **4**; (a and d) ORTEP views of the asymmetric units in **1** and **4**, respectively; (b and e) Ball-and-stick presentation of **1** and **4**, respectively; and (c and f) dimensions of the molecular squares **1** and **4**, respectively.

The average M-N and M-O bond lengths are in the usual range for this kind of complexes.^{249,250} The crystallographic information pertaining to data collection and structure refinement parameters, selected bond distances and angles are listed in Table A2, A24 and A46, respectively. All these molecular squares contain one coordinated water molecule on each metal center, which shows bifurcated hydrogen bonding, where it is strongly and intra-molecularly hydrogen bonded to the uncoordinated oxygen atom of the carboxylate group forming two 6-membered rings ($R_1^1(6)$). All hydrogen bonding parameters are listed in Table 3.1. These molecular squares are stacked in an eclipsed fashion leaving the available pore size unaltered for host-guest chemistry and catalysis. The Hydrogen bonding pattern and the packing arrangement for the representative examples from both set of molecular squares is shown in Figure 3.4.

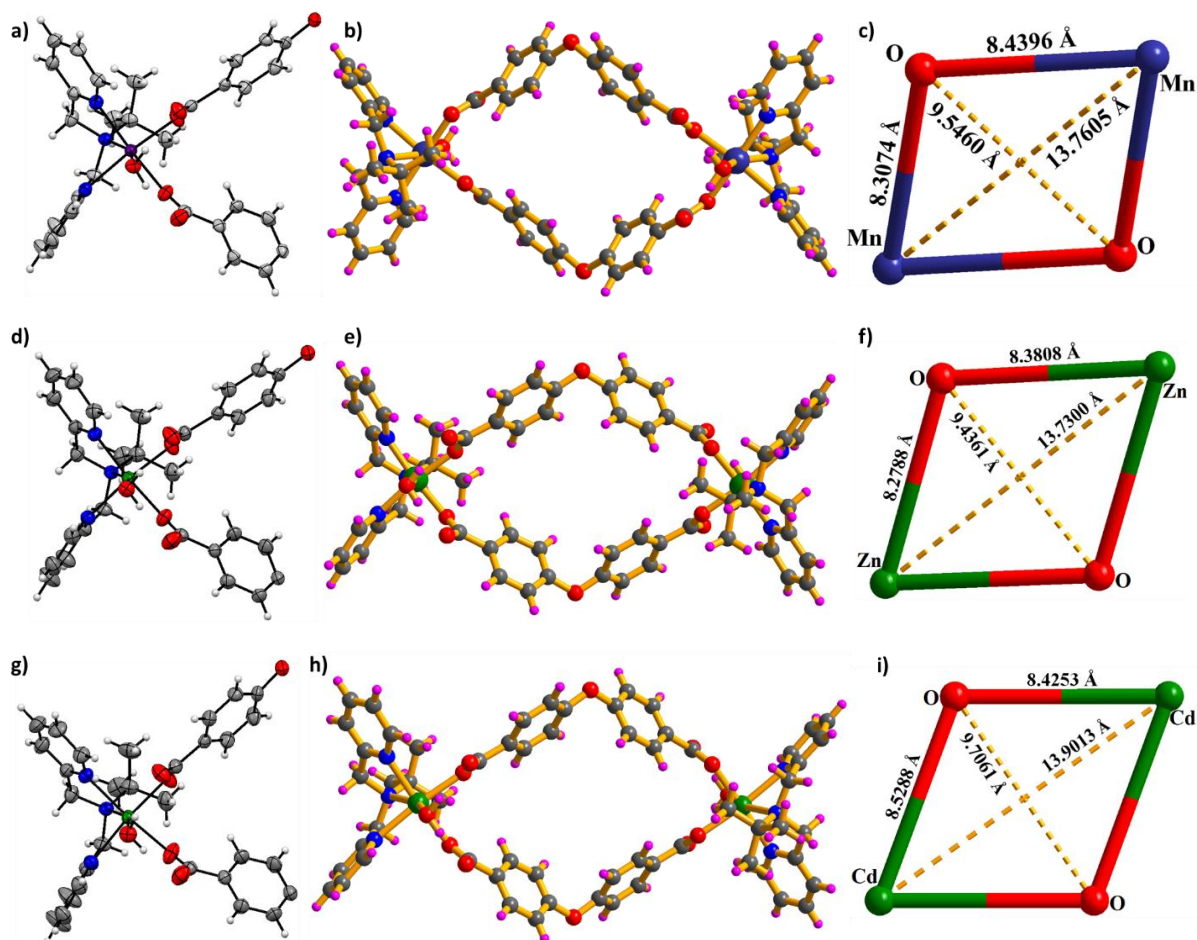


Figure 3.3. Single crystal X-ray structure of molecular squares **5**, **9** and **10**; (a d and g) ORTEP view of the asymmetric units in **5**, **9** and **10**, respectively; (b, e and f) Ball-and-stick presentation of **5**, **9** and **10**, respectively; and (c, f and i) the dimensions of the molecular squares **5**, **9** and **10**, respectively.

FTIR and PXRD analysis. FTIR spectra of **1-10** were recorded in the solid state at room temperature as KBr pellets. All complexes show a band in the region of 3400 and 3410 cm^{-1} , which is a characteristic feature for the O-H stretching frequency of coordinated water molecule as evident from their crystal structures. The bands at 1591 and 1393 cm^{-1} in **1**, 1591 and 1393 cm^{-1} in **2**, 1591 and 1394 cm^{-1} in **3**, 1578 and 1396 cm^{-1} in **4**, are due to the asymmetric and symmetric stretching modes of the carboxylate groups of dmsdba^{2-} , respectively. The asymmetric and symmetric stretching modes of the carboxylate groups of obba^{2-} were found at 1597 and 1391 cm^{-1} in **5**, 1596 and 1393 cm^{-1} in **6**, 1596 and 1393 cm^{-1} in **7**, 1597 and 1387 cm^{-1} in **8**, 1596 and 1393 cm^{-1} in **9**, 1595 and 1389 cm^{-1} in **10**, respectively. The difference in the asymmetric and symmetric stretching frequencies of the carboxylate group in **1-10** is approximately 200 cm^{-1} , which is indicative of monodentate binding of the carboxylate to the metal center ($\Delta\nu < 200 \text{ cm}^{-1}$ and $\Delta\nu \geq 200 \text{ cm}^{-1}$ are

indicative of bidentate and monodentate binding of the carboxylates to the metal centers)²⁵¹ corroborating with their single crystal structures.

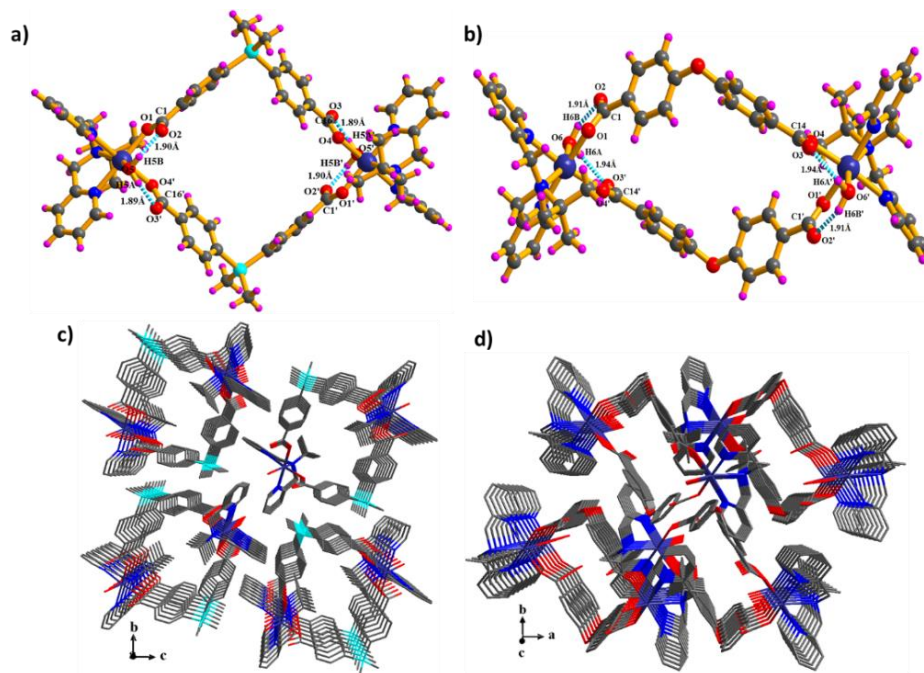


Figure 3.4. View of bifurcated intramolecular hydrogen bonding (a and c) and packing arrangement (c and d) for representative examples from both sets of molecular squares; a and c for **1** and b and d for **5**, respectively.

Table 3.1. Hydrogen bonding parameters in **1**, **4**, **5**, **9** and **10**.

Compound	D-H-A	d(D-H)/Å	d(H-A)/Å	d(D-A)/Å	D-H-A/°
1	O5-H5A-O3'	0.89	1.89	2.630(17)	140.0
	O5-H5B-O2	0.89	1.90	2.661(18)	143.7
4	O4-H4A-O5	0.87	1.81	2.484(3)	135.8
	O4-H4B-O2	0.85	1.79	2.512(3)	141.8
5	O6-H6A-O3'	0.88	1.94	2.702(2)	143.9
	O6-H6B-O2	0.88	1.91	2.681(2)	145.8
9	O1-H1A-O4	0.89	1.80	2.675(4)	170.5
	O1-H1B-O3'	0.84	1.84	2.661(4)	165.5
10	O6-H6A-O3'	0.88	1.94	2.696(3)	143.2
	O6-H6B-O2	0.88	1.99	2.726(3)	140.7

To confirm whether the single crystal structure corresponds to the bulk material or not, powder X-ray diffraction patterns were recorded for **1-10** at room temperature. As can be seen in Figure 3.5, the experimentally obtained powder patterns match exactly with the

simulated powder patterns (obtained from the single crystal data). This confirms that the single crystal and bulk material are the same. It also confirms the phase purity of the bulk sample. Additionally, experimental powder patterns of **2** and **3** are similar to the simulated powder pattern of **1**, indicating **2** and **3** are isostructural with **1**. Similarly, **6-8** were found to be isostructural with **5**, **9** and **10** (Figure 3.6).

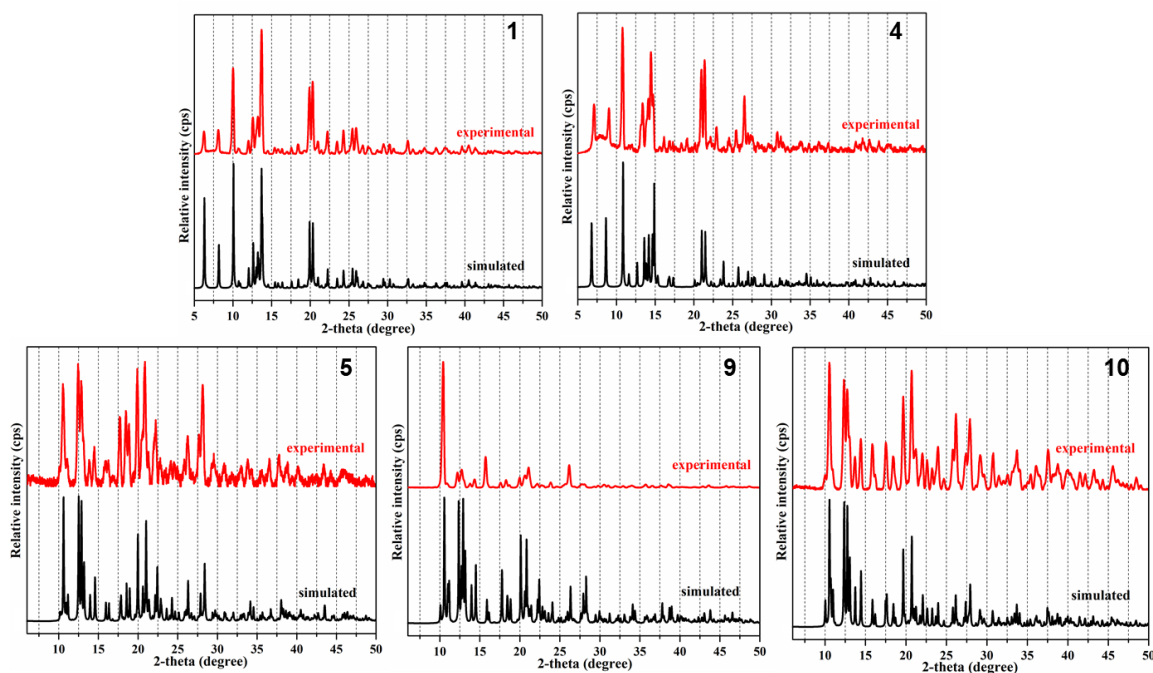


Figure 3.5. Powder X-ray diffraction patterns of the as synthesized molecular square **1**, **4**, **5**, **9** and **10** compared with the simulated powder patterns obtained from single crystal structures.

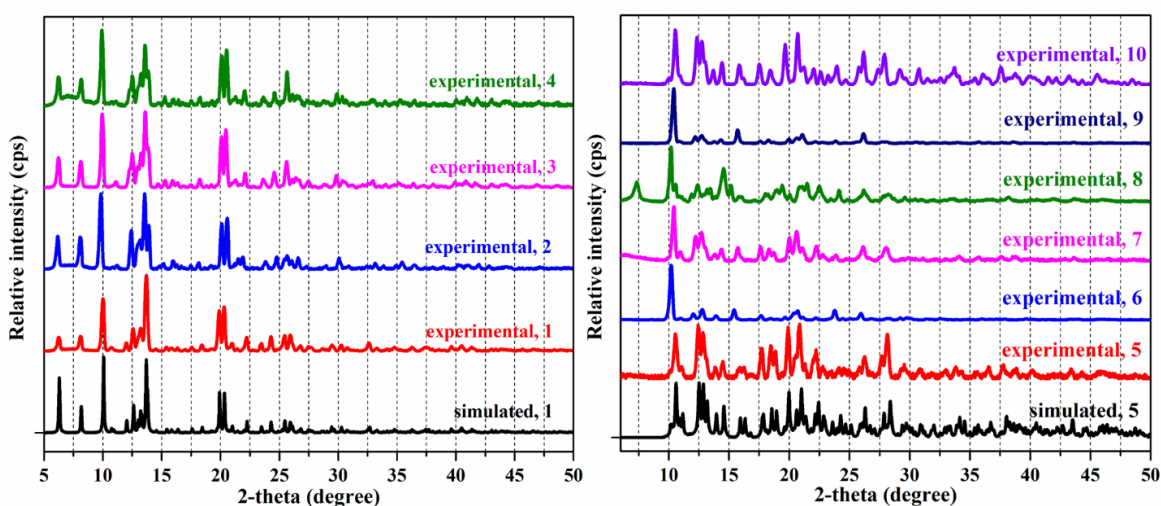


Figure 3.6. Powder X-ray diffraction pattern of the as synthesized samples of (left) **1-4** and (right) **5-10** compared to the simulated powder patterns obtained from the single crystal structures of **1** and **5**, respectively.

Framework Stabilities and Thermal Properties. In addition to bulk phase purity and isostructural relationship confirmed by powder X-ray diffraction, the high chemical stability

of **1-10** in various solvents is verified by matching the powder patterns of each compound immersed in different solvents for 24 h with the respective powder patterns of the as-synthesized compounds.

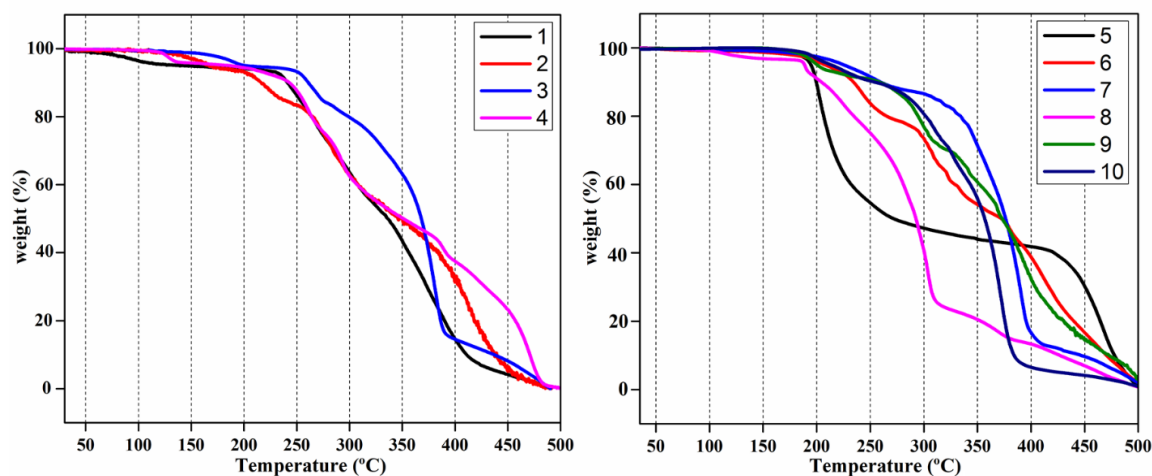


Figure 3.7. TGA scans for **1-4** (left) and **5-10** (right).

In order to understand the thermal stability and its structural variation as a function of temperature, thermogravimetric analysis (TGA) was carried out for the single-phase polycrystalline samples of **1-10** between 30-500 °C under dinitrogen atmosphere. All TGA scans are shown in Figure 3.7. From the multistep decomposition process observed for these compounds, it is clearly evident that the first weight loss in the temperature range of 100-200 °C in case of **1-4** corresponds to the loss of coordinated water molecules, corroborated by the crystal structures of **1** and **4**. A similar thermogravimetric profile was observed in case of **5-10**, where the initial weight loss in the temperature range of 100-200 °C corresponds to the loss of coordinated water molecules, corroborated by the crystal structures of **5**, **9** and **10**. The second weight loss was observed for all compounds in the temperature range of 200-300 °C due to the loss of ligands followed by continuous decomposition of the compounds. In addition to the isostructural relationship supported by the PXRD analysis, the similar thermal stability by TGA further confirms the isostructural relationship of **1-4** and **5-10**.

Catalysis Studies. The Knoevenagel condensation of aldehydes with active methylene compounds is one of the most useful C–C bond forming reactions to give rise to α,β -unsaturated compounds, valuable precursors of fine chemicals and biological compounds. This condensation is generally catalyzed by bases or Lewis acids.^{252,253} While various type of homo/heterogeneous catalysts (discrete or polymeric coordination compounds) have been developed for such organic transformation, there is still a considerable interest in

developing shape persistent discrete complexes with well-defined geometry, and chemical and thermal stability. Thus, the catalytic activity of the representative compounds **1** and **5** were tested as solid heterogeneous catalysts in the Knoevenagel condensation of malononitrile with various aldehydes. In a typical reaction, a mixture of benzaldehyde (10 μ L, 0.10 mmol), malononitrile (10 mg, 0.15 mmol), and catalyst (3.6 mg of **1** or **5**, 3 mol %) was placed in a capped glass vial, and then 1 mL of solvent was added to it. The mixture was stirred at 25-30 $^{\circ}$ C for 60 minutes. The product was extracted using ethyl acetate and filtered to remove any catalyst. Evaporation of the solvent under reduced pressure gives the crude product, which was re-dissolved in CDCl_3 and analysed by ^1H NMR spectroscopy. Both ^1H NMR spectra and related calculation of the percentage yield for **1** in water (entry 1, Table 3.2) are presented in Figure 3.8. Using benzaldehyde as the simplest substrate, it was found that both **1** and **5** provided high product yields in polar protic solvents compared to the non-polar solvents (entries 1–8, Table 3.2) under identical conditions (reaction time and temperature). Since the product yield was comparable with all polar protic solvents, therefore water was chosen as the solvent with consideration of green chemistry principles. Consequently, the optimization of reaction conditions (amount of catalyst and reaction time) was carried out in a model malononitrile-benzaldehyde system with **1** or **5** as the catalyst.

An increase in the amount of catalyst from 1.0 to 3.0 mol% enhances the product yield from 64 to 93%, but further increase in the amount of catalyst leads to no significant increase in the product Yield (entries 9–13, Table 3.2). To select the most appropriate reaction conditions, 2 mol% of catalyst was chosen and the reaction time was varied from 20-120 minutes (entries 14–19, Table 3.2). These results indicate that with 2 mol% catalyst yields about 98% of benzaldehyde into 2-benzylidenemalononitrile occurs (entry 18, Table 3.2) after 100 minutes and hence is chosen as the best reaction condition. A blank reaction carried out with benzaldehyde in absence of catalyst resulted a very low conversion (10%) of aldehyde into 2-benzylidenemalononitrile after 100 minutes (entry 21, Table 3.2). Moreover, the reaction did not give good yield when free ligand $\text{H}_2\text{L1}$ or $\text{H}_2\text{L2}$ was used instead of catalyst **1** or **5** (entry 20, Table 3.2), respectively. The catalytic activity of different metal acetates, used for the synthesis of **1-10**, was also checked. In all cases, very less product yield was obtained (entries 22–27, Table 3.2). The results indicate that catalysts **1** and **5** are much better than the metal salts or ligands under identical conditions.

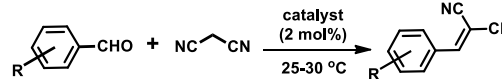
Table 3.2. Optimization for Knoevenagel reaction, catalyzed by **1** and **5**.¹⁸

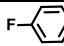
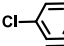
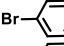
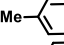
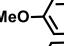
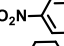
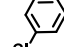
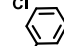
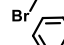
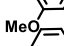
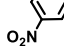
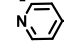

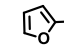
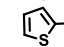
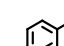
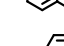


Entry	Solvent	Catalyst(mol%)		Time ^b (min.)	% yield ^c		TON ^d	
		1	5		1	5	1	5
1	Water	3	3	60	93.5	92.5	31	31
2	MeOH	3	3	60	84.7	88.7	28	29
3	EtOH	3	3	60	90.1	92.3	30	30
4	DCM	3	3	60	35.6	42.5	11	14
5	CH ₃ CN	3	3	60	10.1	13.2	3	4
6	THF	3	3	60	75.2	78.3	25	26
7	Toluene	3	3	60	43.8	50.3	14	16
8	DMF	3	3	60	89.3	90.2	29	30
9	Water	1	1	60	65.2	66.7	65	66
10	Water	2	2	60	88.5	90.2	44	45
11	Water	3	3	60	93.5	92.5	31	31
12	Water	4	4	60	94.3	95.8	23	23
13	Water	5	5	60	98.2	98.8	19	19
14	Water	2	2	20	50.4	55.8	25	28
15	Water	2	2	40	69.8	77.4	35	39
16	Water	2	2	60	88.5	90.2	44	45
17	Water	2	2	80	94.2	94.6	47	47
18	Water	2	2	100	97.2	98.5	48	49
19	Water	2	2	120	98.3	99.2	49	49
20	Water	H ₂ L1 ^e	H ₂ L2 ^e	100	17.0	18.7	8	9
21	Water	f		100	10.2	f		
22	Water	Mn(OAc) ₂ ^g		100	39.0	19.5		
23	Water	Co(OAc) ₂ ^g		100	41.3	20.6		
24	Water	Ni(OAc) ₂ ^g		100	39.8	19.9		
25	Water	Cu(OAc) ₂ ^g		100	42.0	21.0		
26	Water	Zn(OAc) ₂ ^g		100	40.6	20.3		
27	Water	Cd(OAc) ₂ ^g		100	38.7	19.3		

^aReaction conditions: 10 μ L benzaldehyde (0.10 mmol), 10 mg malononitrile (0.15 mmol) and solvent 1 mL. ^bReaction time 20-120 minutes. ^caverage yield for a set of triplicate reactions calculated by ¹H NMR. ^dNumber of moles of product per mole of catalyst. ^e5 mol % was used. ^fNo catalyst was used. ^g5 mol % of the hydrated metal salts were used as catalyst.

Table 3.3. Substrate scope for Knoevenagel reaction, catalyzed by **1** and **5**.^d



Entry	Aldehyde	% yield ^b		TON ^c	
		1	5	1	5
1		96	98	48	49
2		>99	>99	50	50
3		>99	>99	50	50
4		71	75	35.5	37.7
5		54	55	27	27.5
6		>99	>99	50	50
7		89	92	44.5	46
8		90	89	45	44.5
9		60	62	30	31
10		>99	>99	50	50
11		64	65	32	32.5
12		71	70	35.5	35
13		72	74	36	37
14		70	72	35	36
15		56	60	28	30
16		50	50	25	25
17		20	20	10	10

^aReaction conditions: 0.10 mmol of aromatic aldehyde and 0.15 mmol of malononitrile was taken along with 1 mL water. ^baverage yield for a set of triplicate reactions, calculated by ¹H NMR. ^cNumber of moles of product per mole of **1** or **5**.

The effect of catalyst concentration on the product yield was also tested. A plot of % yield versus catalyst amount or time for the Knoevenagel condensation reaction of benzaldehyde and malononitrile with **1** and **5** is presented in Figure 3.9. Since both the representative compounds of each set showed similar activity, we further checked the catalytic activity of **2-4** and **6-10** for the Knoevenagel condensation of malononitrile with benzaldehyde under the optimized reaction conditions. In all cases, 95-100% conversion was obtained. These are summarized in a plot between percent yields versus compound used (Figure 3.10). The catalytic activity obtained is comparable with the discrete or polymeric coordination architectures.^{113,254-257}

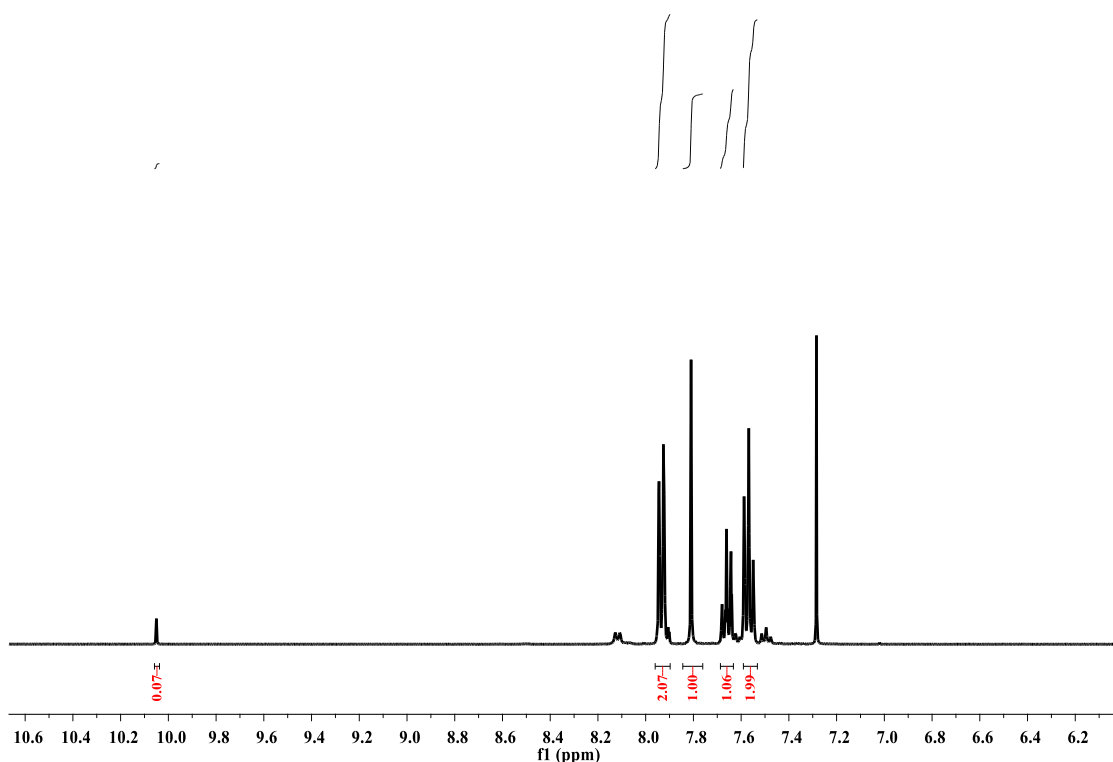


Figure 3.8. Example of integration in ¹H NMR spectrum for the calculation of product yield in Knoevenagel condensation reaction of benzaldehyde with malononitrile (entry 1, Table 3.2).

Calculation of the product yield in the Knoevenagel condensation reaction of benzaldehyde with malononitrile catalyzed by 1

Total amount of compounds at the end (see figure 3.8): Unreacted benzaldehyde (10.05 ppm) + 2-benzylidenemalononitrile (7.81 ppm) = 0.07 + 1.00 = 1.07.

Yield of 2-benzylidenemalononitrile = $(1/1.07) * 100 = 93.45 \%$.

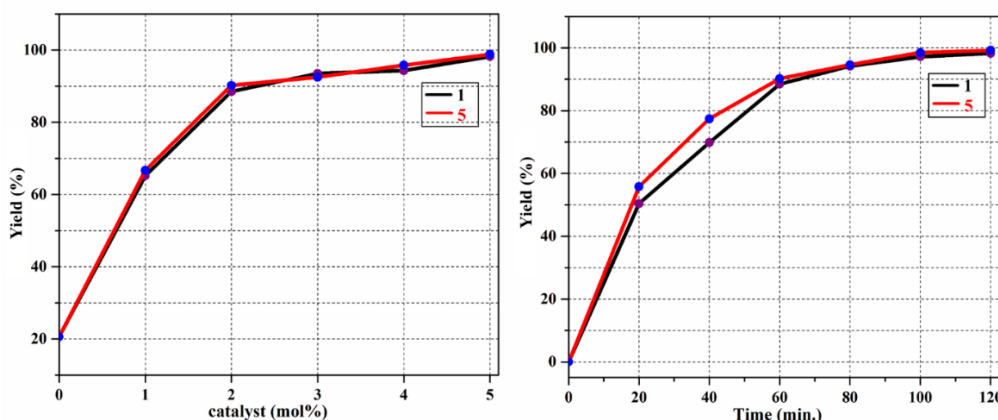


Figure 3.9. Plot of % yield versus catalyst amount (left) and time (right) for the Knoevenagel condensation reaction of benzaldehyde and malononitrile catalysed by 1 and 5.

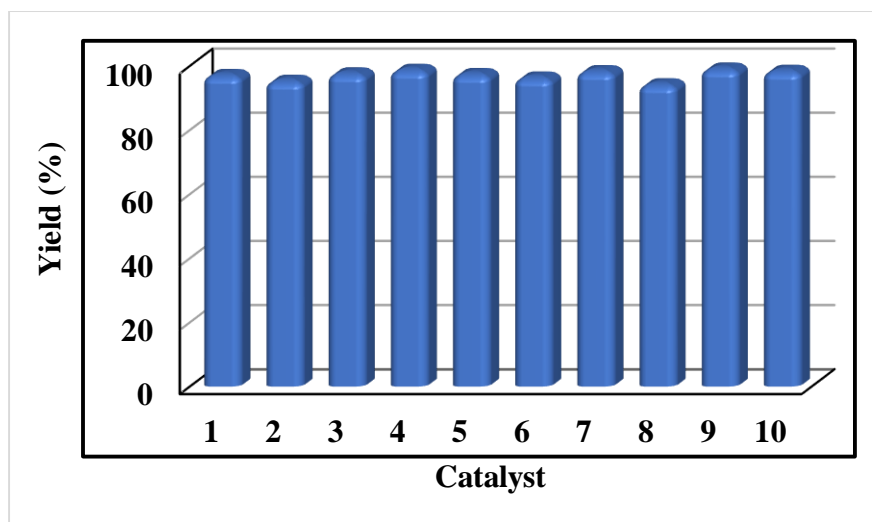


Figure 3.10. Yields for Knoevenagel condensation reaction of benzaldehyde and malononitrile catalysed by **1-10**.

In order to demonstrate the versatility of the catalysts, the catalytic activity of **1** and **5** was also investigated with different types of substituted aromatic aldehydes in the reaction with malononitrile. It gave the corresponding α,β -unsaturated compounds in good-to-excellent yields. The results are summarized in Table 3.3. The nitro substituted aromatic aldehydes gave the maximum yield (entries 6 and 10, Table 3.3) while the lowest yield (entry 5, Table 3.3) was obtained for p-methoxybenzaldehyde. This trend unveils the strong accelerating influence of electron-withdrawing nitro group in contrast to an electron donating moiety for a reaction involving nucleophilic attack at the carbonyl group. The stronger is the electron-withdrawing ability of the substituent, the faster is the activation of aldehyde for nucleophilic attack at the carbonyl group and hence higher is the yield.

To determine the recyclability of the catalyst, it was isolated after the reaction by filtration from the aqueous phase and washed with methanol and reactivated by heating under vacuum conditions. Both catalysts **1** and **5** were recycled in three consecutive experiments, and their activity did not show appreciable change (Figure 3.11). Based on FTIR spectra and PXRD data of the catalyst recorded before and after the reaction, no loss of crystallinity or phase purity of the catalyst was observed (Figure 3.12). Further, to check no leaching of the catalyst into the product stream, the reaction mixture after 20 minutes of reaction time was separated from the catalyst by extracting the organics with ethyl acetate and provided with the same reaction condition. The yield of the product did not change significantly. These experiments indicate that the catalyst essentially remains intact and does not leach out during the catalytic process.

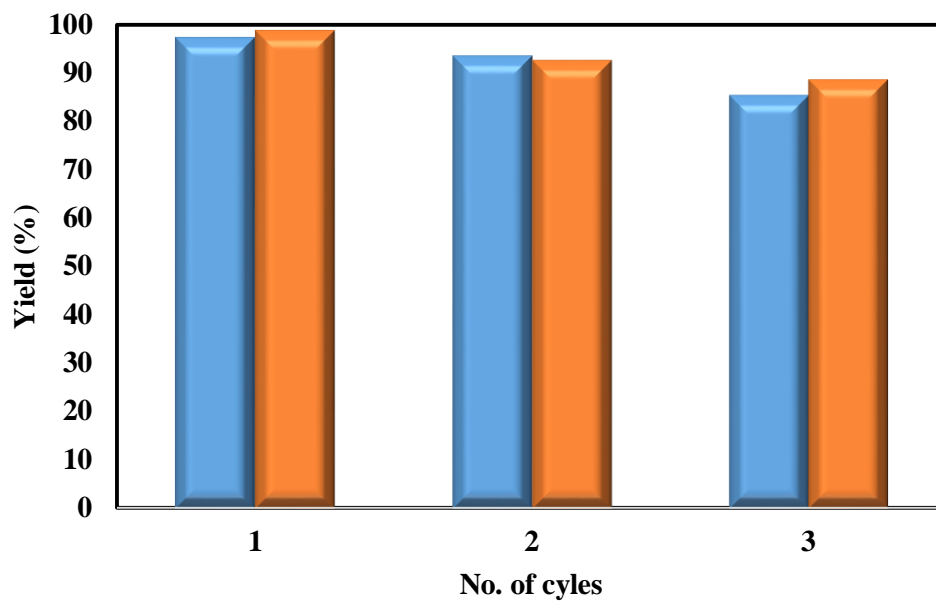


Figure 3.11. Yield for three consecutive cycles of Knoevenagel condensation reaction of benzaldehyde and malononitrile catalyzed by **1** and **5**.

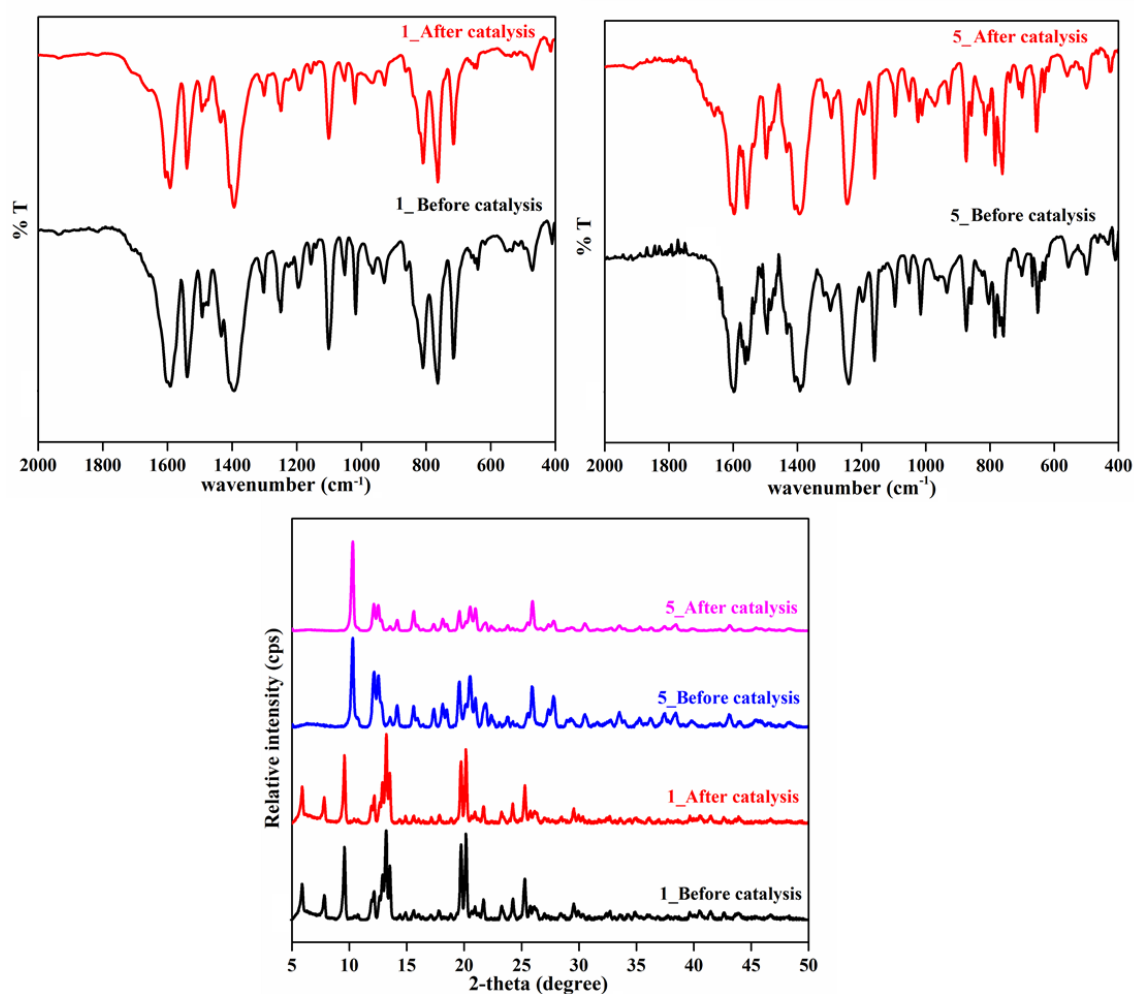


Figure 3.12. FTIR spectra (top) and PXRD pattern (bottom) of **1** and **5** taken before and after catalysis experiments.

Based on the studies described above, a possible mechanism of Knoevenagel condensation catalyzed by **1-10** is presented in Figure 3.13 on the basis of reported proposals.^{258–261} The metal center (Lewis acidic site) interacts with the carbonyl group of the benzaldehyde, resulting in polarization of this group, which in turn increases the electrophilic character of the carbonyl carbon atom. This polarization accounts for attack by the nucleophile (malononitrile). The interaction of a cyano group of malononitrile with the Lewis acid site increases the acidity of the methylene group, which further enhances the deprotonation of malononitrile. The basic sites (carboxylate-O or amide-O) can abstract the proton from the methylenic group to generate the corresponding nucleophilic species, which attack the carbonyl group of benzaldehyde resulting in the C–C bond formation followed by dehydration.

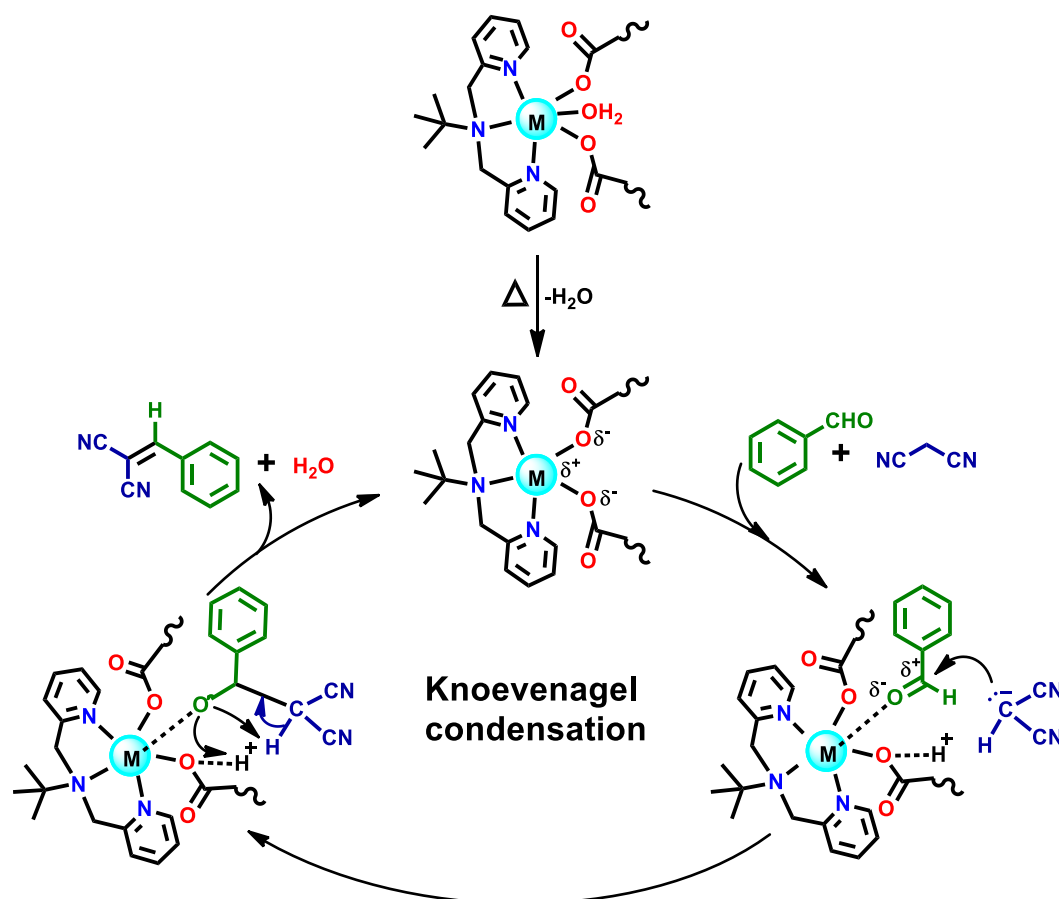


Figure 3.13. Proposed catalytic cycle for the Knoevenagel condensation of benzaldehyde with malononitrile catalyzed by **1-10**.

Luminescence properties. The design and construction of metallocycles and metallocages have attracted considerable attention for their wide applications in fluorescence detection of metal ions, anions, or small molecules. In order to study the luminescence properties of **1-10** and the respective free ligands, their solid-state reflectance spectra were first recorded

at room temperature. H₂L1 and **1-4** exhibited a strong and broad absorption with λ_{max} 250 nm while H₂L2 and **5-10** exhibited a strong and broad absorption with λ_{max} 270 nm corresponding to $\pi-\pi^*$ transitions. On the basis of these data, emission properties of the Cd(II) compounds, **4** and **10**, with a d^{10} configuration were studied. On excitation at 270 nm, the emission spectra of **4** and **10** exhibit a strong feature at 422 and 413 nm, respectively. Compared to H₂L1 and H₂L2, the emission bands of **4** and **10** show significant red shifts (58 nm in **4** and 98 nm in **10**), which can be attributed to the metal-ligand charge transfer. In order to understand the effect of organic solvents on their emission properties, emission spectra of **4** and **10** were recorded in different solvents such as water (H₂O), ethanol (EtOH), acetonitrile (CH₃CN), chloroform (CHCl₃), acetone, dimethylformamide (DMF) and nitrobenzene upon excitation at the same wavelength. It is significant to observe that **4** and **10** show different emission intensities in different solvents; with shifts in the emission wavelength due to change in polarity of the solvents.²⁶² The maximum intensity for **4** was obtained in water while **10** gave the maximum intensity in acetonitrile. Although a variation in the luminescence response was observed for different solvents, both **4** and **10** exhibit very strong emission intensities in water and are therefore suitable for sensing studies in this solvent. Among all the solvents, the emission intensity of **4** and **10** was totally quenched in nitrobenzene (NB). This is because of the electron-withdrawing ability of the nitro group that facilitates an electron transfer from the excited state of **4** and **10** to the electron-deficient nitrobenzene, restricting the self-relaxation to the ground state.²⁶³ This type of solvent-dependent quenching behavior is of great interest towards nitrobenzene sensing and thus further experiments with NB were performed in more detail. Fluorescence titration experiment was performed with suspensions of **4** or **10** in water by the incremental addition of 2 mM stock solution of nitrobenzene (NB) (from 10 μ L to 300 μ L). As shown in Figure 3.14, the luminescence intensities of **4** and **10** decrease gradually as the concentration of NB increases and at 26 ppm of NB, the fluorescence intensity was almost completely quenched (96% for (**4**) and 90% for (**10**)). The quenching efficiency, defined by $(I_0 - I)/I_0 \times 100 \%$, where I_0 and I are the luminescence intensities of **4** or **10** before and after the addition of NB, respectively, was estimated to be 35% for 1 ppm of NB, 77% for 5 ppm of NB and 92% for 9 ppm of NB for **4**. A similar trend for quenching efficiency was observed for **10**. The result has further been analysed using the Stern-Volmer (SV) equation: $I_0/I = 1 + K_{\text{SV}}[A]$, where I_0 and I are the luminescent intensities of the compound before and after addition of the NB, $[A]$ is the molar concentration of NB, and K_{SV} is the quenching constant (mM^{-1}). A good linear correlation exists between the fluorescence quenching

efficiency and the concentration of nitrobenzene over the range of 0–0.035 mmol (Figure 3.14). The K_{SV} values were found to be $0.84 \times 10^2 \text{ mM}^{-1}$ for **4** and $0.95 \times 10^2 \text{ mM}^{-1}$ for **10**. These are moderate among the values reported for coordination polymers^{264,265} but are much higher compared to the self-assembled adduct,²⁶⁶ indicating efficient fluorescence quenching of nitrobenzene by **4** and **10**. For example, the coordination polymers $\{[\text{Cd}_2(\text{HL})_2(\text{bibp})_2] \cdot 3\text{H}_2\text{O}\}_n$ and $\{[\text{Zn}(\text{tta})_{0.5}(\text{m-bimb})] \cdot \text{H}_2\text{O}\}_n$ (where, H_3L is tris(*p*-carboxyphenyl)phosphane oxide, H_4tta is terphenyl-4,2'',5'',4'-tetracarboxylic acid, *bibp* is 4,4'-bis(imidazol-1-yl)biphenyl and *m-bimb* is 1,3-bis(imidazol-1-ylmethyl)benzene) have comparable K_{SV} values, $0.82 \times 10^2 \text{ mM}^{-1}$ and $1.1 \times 10^2 \text{ mM}^{-1}$, respectively. On the other hand, the K_{SV} value was found to be 2.7 mM^{-1} for the hydrogen bonded $[\text{2HL}]^{2+} \cdot [\text{CdCl}_4]^{2-}$ adduct, where *L* is 4'-methylenebis(2,6-diethyl-*N*-(naphthalen-1-ylmethyl)aniline).

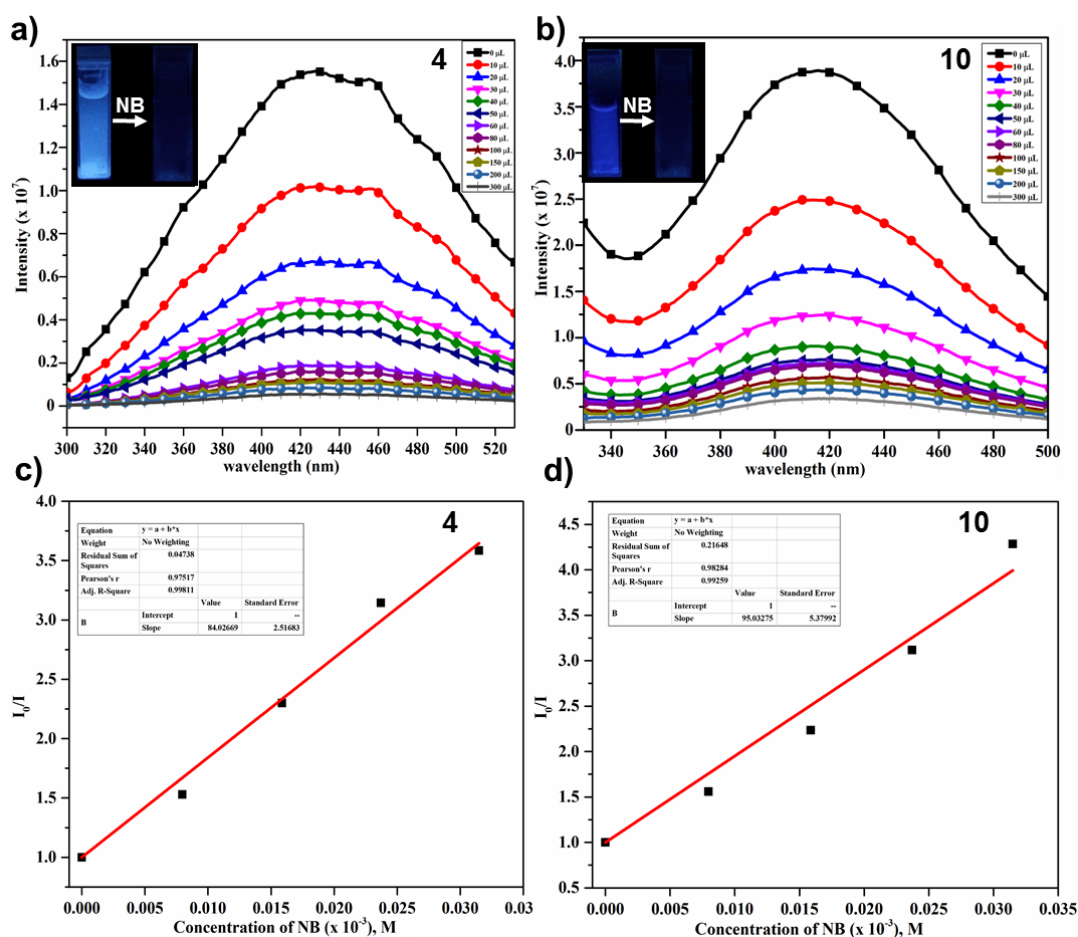


Figure 3.14. (a,b) Change in emission spectra of **4** and **10** dispersed in an aqueous medium upon incremental addition of the NB solution (2 mM) (Insets showing the blue emission and its disappearance under UV light, before and after NB addition, respectively) and (c,d) Stern-Volmer (SV) plot for NB of **4** and **10**. The relative fluorescence intensities are linear with NB concentration in the range of 0 – 0.035 mM, $I_0/I = 1 + 84.026[\text{NB}]$ ($R^2 = 0.998$) for **4** and $I_0/I = 1 + 95.032[\text{NB}]$ ($R^2 = 0.992$) for **10**.

Quenching of the luminescence intensities of **4** and **10** upon the incremental addition of nitrobenzene can be explained on the basis of electrostatic interaction between NB and the molecular squares.¹⁰⁰ To understand the effect of size and electron withdrawing effect of the nitro group, the fluorescence responses of **4** and **10** were measured with other nitro aromatic compounds, such as 1,3-dinitrobenzene (1,3-DNB), 1,4-dinitrobenzene (1,4-DNB) and 2,4,6-trinitrotoluene (2,4,6-TNT). As expected, these three nitro aromatics act as fluorescence quenchers for **4** and **10**. However, even with more electron withdrawing groups attached to them, their fluorescence quenching efficiencies are lower than that of NB. The order of K_{SV} values for the four quenchers is NB > 2,4,6-TNT > 1,3-DNB \geq 1,4-DNB. This trend of quenching efficiencies might be due to the combined effect of the size of the nitro analytes and the number of electron withdrawing nitro groups attached to the benzene ring.

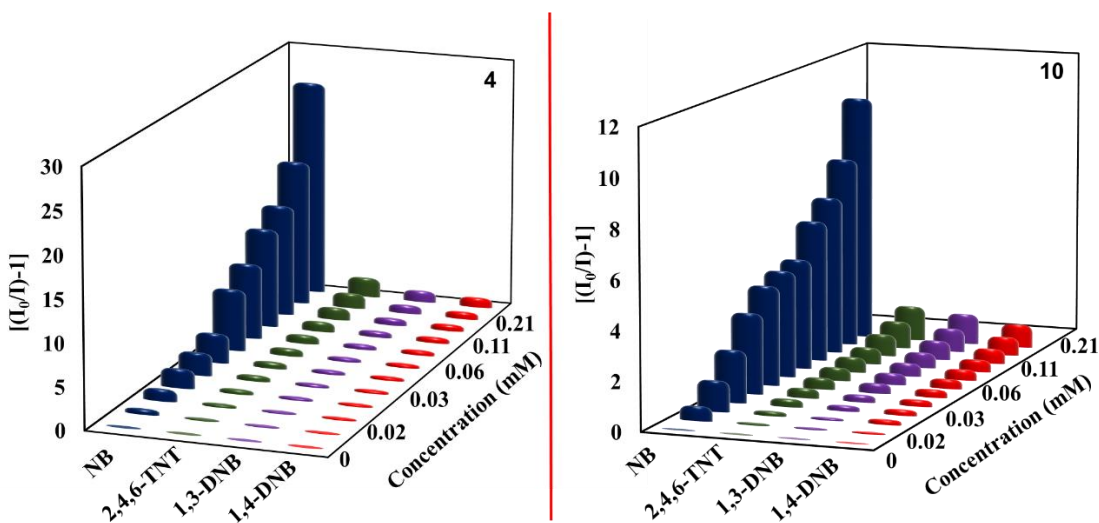


Figure 3.15. A comparison of 3D Stern-Volmer plot of different nitro analytes for **4** and **10**.

A comparison of 3D Stern-Volmer plots of different nitro analytes for **4** and **10** is shown in Figure 3.15. The ratio between K_{SV} values of NB and other nitro aromatics is defined as the selectivity factor (SF),²⁶⁷ which is generally used to evaluate the selectivity. The SF values for 2,4,6-TNT, 1,3-DNB and 1,4-DNB over NB are 0.221, 0.131 and 0.110 for **4** and 0.122, 0.0853 and 0.0894 for **10**, respectively. This suggests that both **4** and **10** have very good selectivity towards NB detection in aqueous medium.

In summary, **1-10**, has laid a foundation for the strategy in developing new molecular squares by the three-components in a [2+2+2] self-assembly process. This synthetic strategy used to construct the molecular squares have been generalized with different metal centers and their catalytic activity (due to the presence of Lewis-acidic open metal sites) and

remarkable photo-physical properties have been established by Knoevenagel condensation reaction and selective detection of nitrobenzene via the fluorescence quenching mechanism.

3.1.2 Coordination driven self-assembly of polymeric architectures

The phrase, “coordination polymers” was first appeared in the early 1960s, and since then extensive advancements have been reported to the chemistry of coordination polymers. Versatile synthetic strategies have been developed for the self-assembly of target structures. The key to success is the design of the molecular building blocks which direct the formation of the desired architectural, chemical, and physical properties of the resulting architectures. In addition to the two central components, connectors and linkers, coordination polymers consist of other auxiliary components, such as blocking ligands, counter anions, and nonbonding guests or template molecules. Various combinations of these components afford various specific structural motifs. For the synthesis of such specific structural architectures, we have used the dicarboxylate ($H_2dmsdba$) in combination with different transition metal ions to obtain such 1D, 2D or 3D coordination polymers using either multidentate polypyridyl ligands or bidentate pillar ligands. The judicious selection of the ligands structures has been shown to control the dimensionality and functionality of the resulting frameworks.

3.1.2.1 Architectures through connected polygons (squares and hexagons)

Transition metals are very well known for their diverse oxidation states and coordination preferences, giving rise to various coordination geometries. Because of this reason the transition-metal ions have been extensively utilized as versatile connectors in the construction of coordination polymers. In addition to the utilization of such naked metal ions, the use metal-complex connectors have the advantage of offering control of the bond angles and restricting the number of coordination sites; sites that are not required can be blocked by chelating ligands and thus leave specific binding sites for linkers. Inspired from our previous work on the polypyridyl tridentate capping ligand **bpta**, for the synthesis of discrete molecular squares, we thought of extending the dimensionality by ligand modifications keeping all other factors or components constant. For this purpose, we have used a series of bis(tridentate) ligands (**tpen**, **tpbn**, **tphxn** and **tpxn**) where two tridentate capping sites are separated by aliphatic or aromatic spacers; **tpen**, **tpbn** and **tphxn** differ by different number of carbon atom in the methylene chain spacer, 2 in **tpen**, 4 in **tpbn**, 6 in **tphxn** and **tpxn** have a rigid xylyl spacer between two tridentate capping sites.

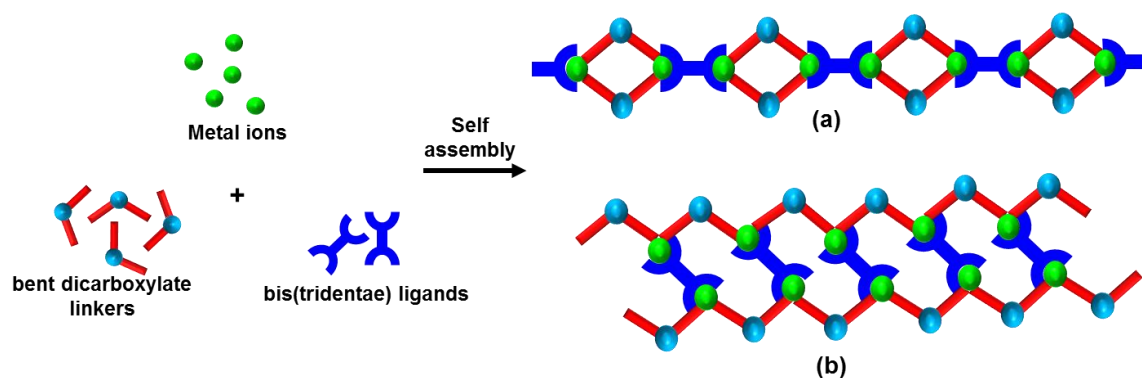


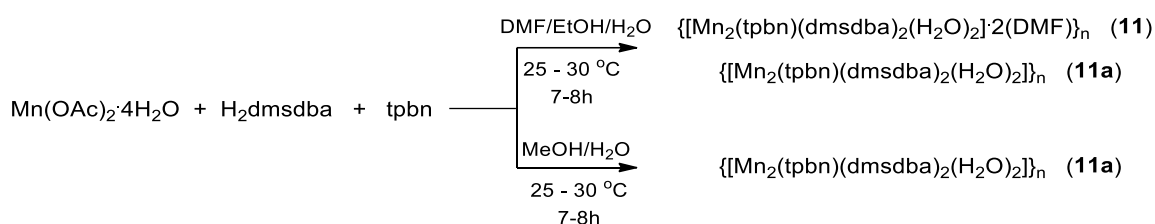
Figure 3.16. Two possible structural isomers (a) connected molecular squares and (b) fused hexagons, by the self-assembly of metal ions, bis(tridentate) ligands and carboxylate linkers.

Chemical structures of the ligands used are shown in Figure 1.9a. Based on the results obtained in the previous section, two possibilities can be predicted for the resulting architectures while using bis tridentate ligands in combination of bent dicarboxylate linkers. As shown in Figure 3.16, the resulting polymeric architecture can be formed by connected molecular squares or by fused hexagons. In the present section, we have studied the effect of different spacers in bis(tridentate) ligands and reaction conditions to the final coordination architectures.

Mn(II) Chemistry

In order to study the effect of the spacer length and rigidity/flexibility of the bis(tridentate) polypyridyl ligands on the resulting coordination architecture, a series of coordination architectures have been synthesized by varying one variable at a time. By using Mn(II) as metal centre and keeping the metal and carboxylate linkers constant, the spacer chain length/flexibility of the bis(tridentate) polypyridyl ligands was varied and two sets of coordination architectures were synthesized (Scheme 3.8-3.10); the first set includes the self-assembly of Mn(II) and H₂dmsdba with three different bis(tridentate) ligands (tpbn, tphxn and tpxn), whereas for the second set a different dicarboxylate linker (H₂obba) having similar geometry was used in combination with Mn(II) and bis(tridentate) ligands. The effect of reaction conditions and selection of the ligand structure has been discussed and optimized to get the coordination architectures with either of the possible structure (Figure 3.16).

Single crystal structure analysis. Single crystals suitable for single crystal X-ray diffraction analysis was obtained by the slow diffusion technique in each case. A mixture of products was obtained when a mixture of DMF/EtOH/H₂O was used for the self-assembly process.

Scheme 3.8. Synthesis of **11** and **11a**.

The two compounds thus obtained not only differ in their molecular formula (with DMF as lattice solvent in **11** or no lattice solvent in **11a**), but also are the structural isomers of one another. We have been fortunate to get the single crystal X-ray diffraction data for both the isomers, but due to similar crystals shape, size as well as colour, we have not been able to separate both the isomers manually for the study of bulk phase properties. Both isomers crystallize in triclinic system with $P\bar{1}$ space group in each case with different unit cell parameters ($a = 9.17 \text{ \AA}$, $b = 14.46 \text{ \AA}$, $c = 14.84 \text{ \AA}$, $\alpha = 100.33^\circ$, $\beta = 103.91^\circ$, $\gamma = 99.75^\circ$ for **11** and $a = 8.53 \text{ \AA}$, $b = 12.93 \text{ \AA}$, $c = 14.71 \text{ \AA}$, $\alpha = 104.53^\circ$, $\beta = 94.21^\circ$, $\gamma = 102.96^\circ$ for **11a**). In both cases Mn(II) is in a distorted octahedral geometry where from a total of six coordination sites three are occupied by three nitrogen atoms of the polypyridyl capping site. Three nitrogen atoms of the capping site occupies the facial positions of the octahedral geometry in each case.

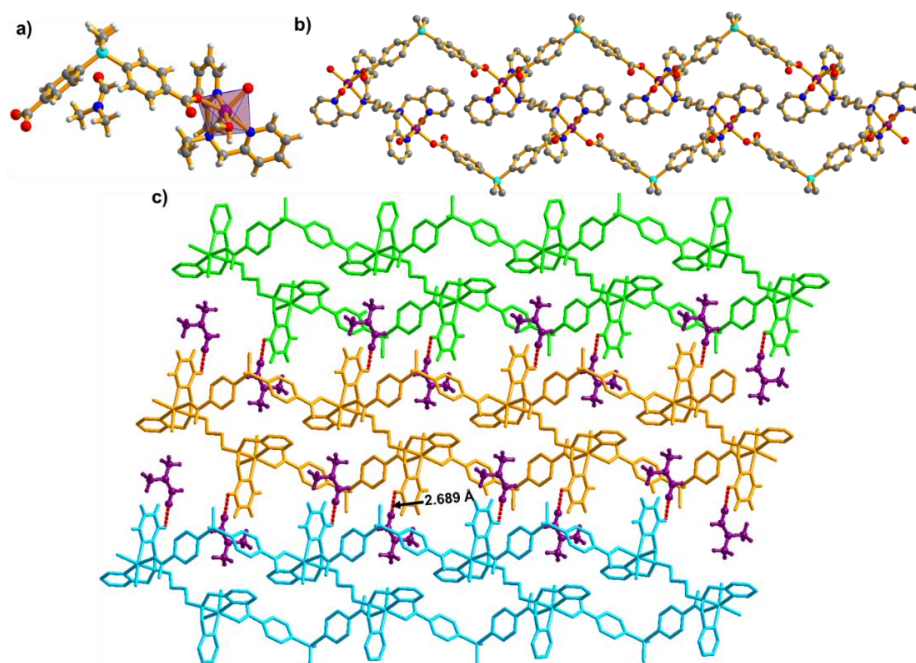


Figure 3.17. Structural description for **11**; (a) view of the asymmetric unit and the coordination environment around the Mn(II) center (the other lattice DMF is highly disordered and hence the diffused electron density was squeezed out during structure refinement), (b) view of 1D polymeric structure and (c) formation of 2D supramolecular architecture via the strong hydrogen bonding by lattice DMF molecules ($\text{O}_{\text{DMF}} \dots \text{H}_{\text{Py}}$ 2.689 \AA).

Two sites are occupied by two oxygen atoms of two different carboxylate groups of **dmsdba**²⁻ which binds in a monodentate binding mode and sixth one is occupied by oxygen atom of the coordinated water molecule. The asymmetric unit in both cases is same which consists of one Mn(II) ion, one dicarboxylate, one coordinated water molecule and one-half of the bis(tridentate) ligand, except one lattice DMF molecule in case of **11**. The asymmetric unit along with the coordination environment around the Mn(II) center in **11** and **11a** is shown in Figure 3.17a and 3.18a, respectively. The average Mn-O (2.1 Å) and Mn-N (2.2 Å) bond lengths in both cases are in the range of the values reported for this kind of complexes.^{249,250} Prominent distortions from the octahedral geometry in both cases are evident from the bond angle values in respective cases. All the crystallographic information pertaining to data collection and structure refinement parameters, selected bond lengths and bond angles are listed in Table A3, A25 and A47, respectively. In both cases the asymmetric unit extends only in one direction resulting in the formation of 1D polymeric structures (Figure 3.17b and 3.18b).

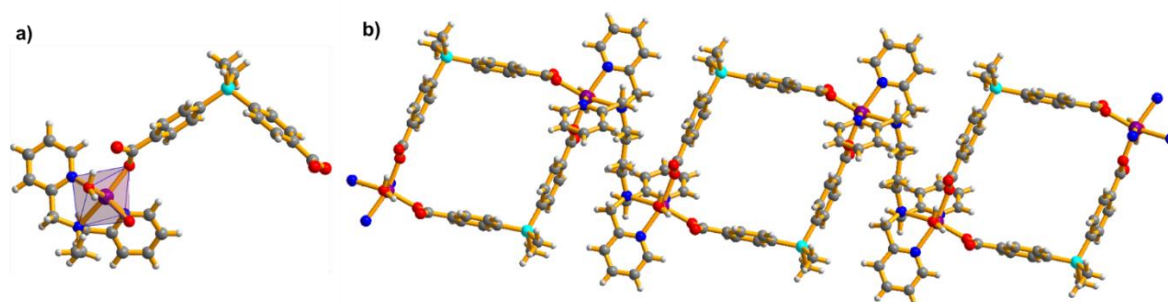


Figure 3.18. Structural description for **11a**; (a) view of the asymmetric unit and the coordination environment around the Mn(II) center, (b) view of overall 1D polymeric structure.

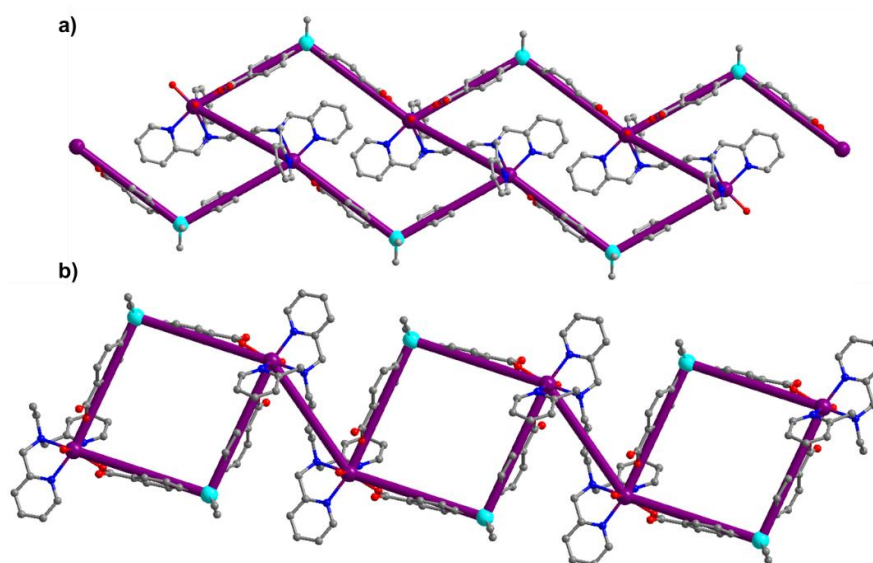


Figure 3.19. Simplified representation of the structural isomers (a) **11** and (b) **11a**, respectively.

*Comparison of the structural isomers **11** and **11a**.* As shown in Figure 3.17b and 3.18b, both **11** and **11a** forms the 1D polymeric structures; the arrangement of various structural units, has resulted into the formation of structural isomers. In case of **11**, the 1D polymeric architecture is formed by fused hexagons, whereas the polymeric architecture in **11a** is a result of connected molecular squares. The different square motifs are connected to one other by the bis(tridentate) ligand, which is acting as a span between two such square motifs. A simplified representation of both the isomers is shown in Figure 3.19. In addition to this difference, the 1D chains in **11** are further extended via the strong hydrogen-bonding interactions by the lattice DMF molecules to afford an overall 2D supramolecular architecture (Figure 3.17c). The O6 atom of lattice DMF interacts with the H25 of one of the pyridyl ring of the ligand tpbn via strong Hydrogen bonding interaction. The C-H \cdots O distance and \angle C-H \cdots O for the Hydrogen bonded O6 and H25 is found to be 2.689 Å and 125.15°, respectively.

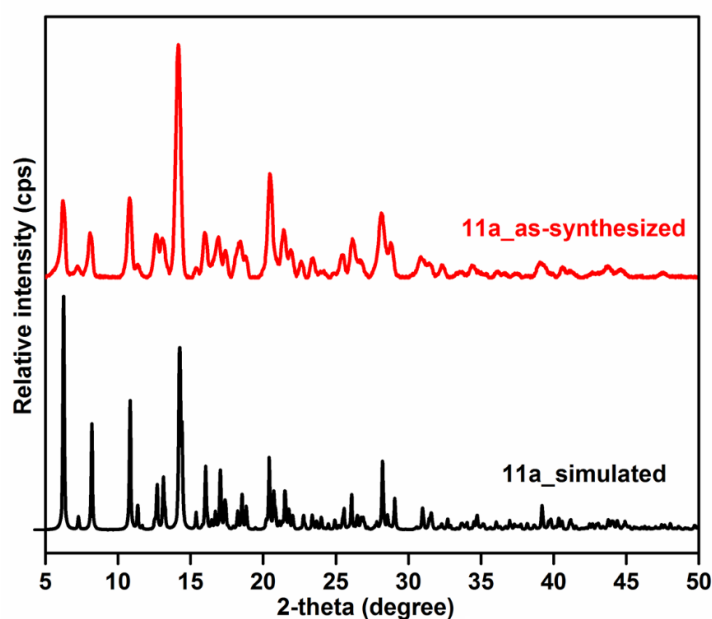


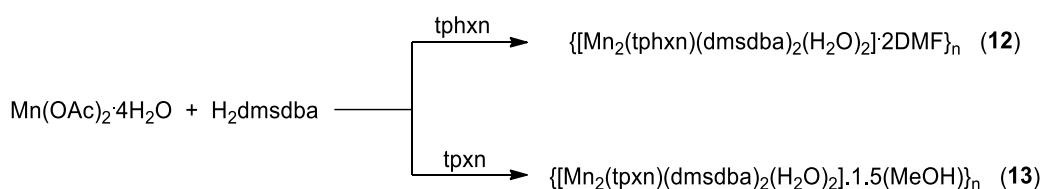
Figure 3.20. Powder X-ray diffraction pattern of the as-synthesized sample of **11a**, compared with the simulated powder X-ray diffraction pattern, obtained from the single crystal X-ray diffraction data.

In our attempts of isolating both the isomers in pure form for their bulk phase studies, we have been able to isolate **11a** as single isomer, by varying the reaction conditions. It was found that a change in the solvent combination from DMF/EtOH/H₂O mixture to MeOH/H₂O mixture has resulted in the predominate formation of **11a**, which has been also characterized by single crystal X-ray diffraction analysis and the bulk phase purity has been established by powder X-ray diffraction analysis. As shown in Figure 3.20 the powder X-

ray diffraction pattern of the bulk sample of **11a**, matches exactly with the simulated powder X-ray diffraction pattern of **11a**, obtained from the single crystal X-ray diffraction data. In addition the sharp signals due to asymmetric (ν_{asym}) and symmetric (ν_{sym}) stretching of the carboxylates at 1593 cm^{-1} and 1385 cm^{-1} in the FTIR spectra of **11a**, supports the monodentate binding ($\Delta\nu = 208\text{ cm}^{-1}$) of the carboxylate,²⁵¹ as indicated from the single crystal structure.

In order to further study the effect of spacer chain length/flexibility on the structural diversity of such coordination polymers, two more coordination polymers were synthesized (Scheme 3.9) using **tphxn** and **tpxn** as *bis*(tridentate) ligands. The two ligands differ in the nature of the spacer in between the two tridentate capping sites; for **tphxn** the spacer consists of an aliphatic chain of six carbon atoms, whereas **tpxn** consists of a comparatively rigid xylyl spacer in between the two tridentate capping sites.

Scheme 3.9. Synthesis of **12** and **13**.



Single crystal structure analysis. Single crystals X-ray diffraction analysis reveal that, **12** crystallizes in a triclinic crystal system with $P\bar{1}$ space group, whereas **13** crystallizes in a monoclinic crystal system with $C2/c$ space group. Irrespective of the different crystal systems and nature of the spacer both **12** and **13** forms similar kind of 1D polymeric structure. The asymmetric unit in cases of **12** consists of one Mn(II) ion, one dicarboxylate, one coordinated water molecule, one-half of the **tphxn** ligand and one lattice DMF molecule whereas the asymmetric unit in cases of **13** consists of one Mn(II) ion, one dicarboxylate, one-half of the **tpxn** ligand and one and half molecules of methanol as lattice solvents. The coordination environment around the metal center in each case is N3O3 type with distorted octahedral geometry. The six coordination sites in **12** are occupied by three nitrogen atoms from one of the capping site of the **tphxn** ligand, two oxygen atoms from carboxylate group of **dmsdba**²⁻ and one oxygen atom from the coordinated water molecule, whereas in case of **13**, three coordination sites are occupied by three nitrogen atoms of one capping site of **tpxn**, and other three coordination sites are occupied by the oxygen atoms of the carboxylate groups of **dmsdba**²⁻, where one of the carboxylates binds in a bidentate chelated fashion and the other in a monodentate fashion. The asymmetric unit and the

coordination environment around the Mn(II) center in each case are shown in Figure 3.21a and 3.22a, respectively. The average Mn-O and Mn-N bond lengths are in the range of values reported for this kind of complexes.^{249,250} All the crystallographic information pertaining to data collection and structure refinement parameters, selected bond lengths and bond angles are listed in Table A4, A26 and A48, respectively.

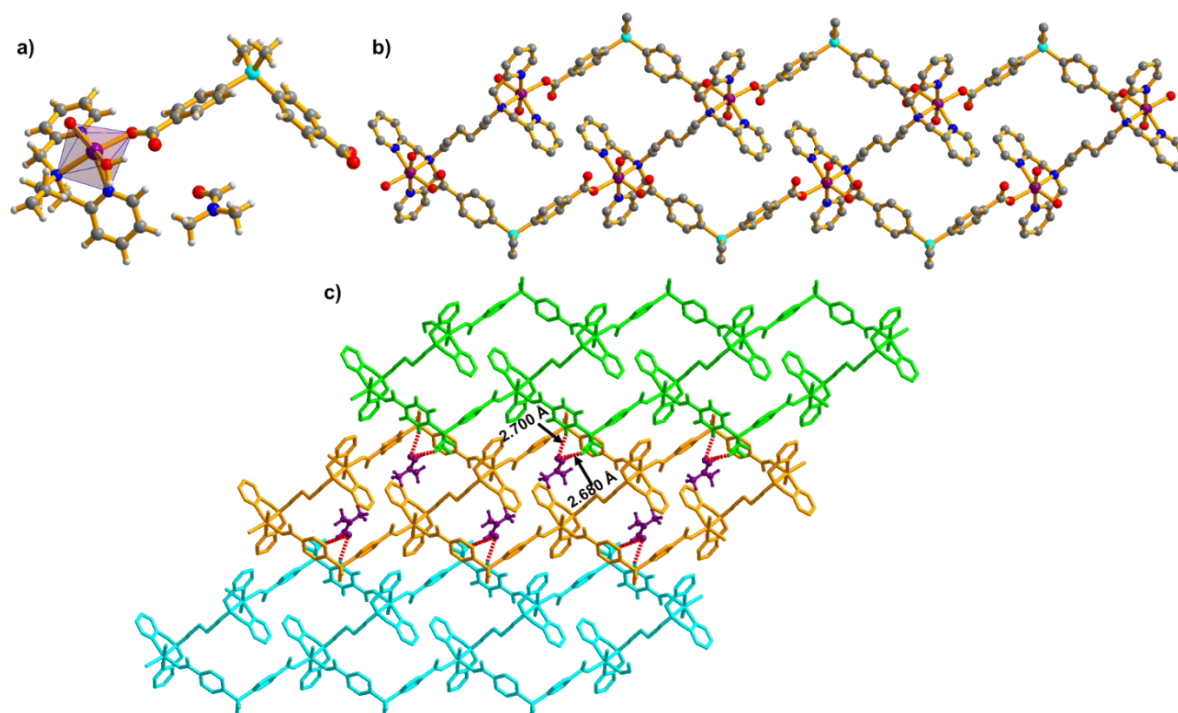


Figure 3.21. Structural description for **12**; (a) view of the asymmetric unit and the coordination environment around the Mn(II) center, (b) view of 1D polymeric structure and (c) formation of 2D supramolecular architecture via the strong hydrogen bonding by lattice DMF molecules ($O_{\text{DMF}} \cdots H_{\text{Py}} 2.700 \text{ \AA}$ and $O_{\text{DMF}} \cdots H_{\text{Me}} 2.680 \text{ \AA}$).

As shown in Figure 3.21c, the lattice DMF present in the crystal lattice takes part in the hydrogen bonding with the 1D polymeric chains in **12** and results in the formation of a 2D supramolecular framework. The O6 of the lattice DMF is Hydrogen bonded with the H11 of one of the pyridyl ring of the ligand tpbn and H8 of the dmsdba²⁻. The C-H \cdots O distance and \angle C-H \cdots O for the Hydrogen bonded O6 and H11 is found to be 2.700 Å and 144.53°, whereas the The C-H \cdots O distance and \angle C-H \cdots O for the Hydrogen bonded O6 and H8 is found to be 2.680 Å and 145.57°, respectively. On the other hand, the lattice methanol present in the crystal structure of **13** does take part in the formation of hydrogen bonded supramolecular network. A simplified representation of the 1D polymeric structure formed by fused hexagons is shown in Figure 3.22c

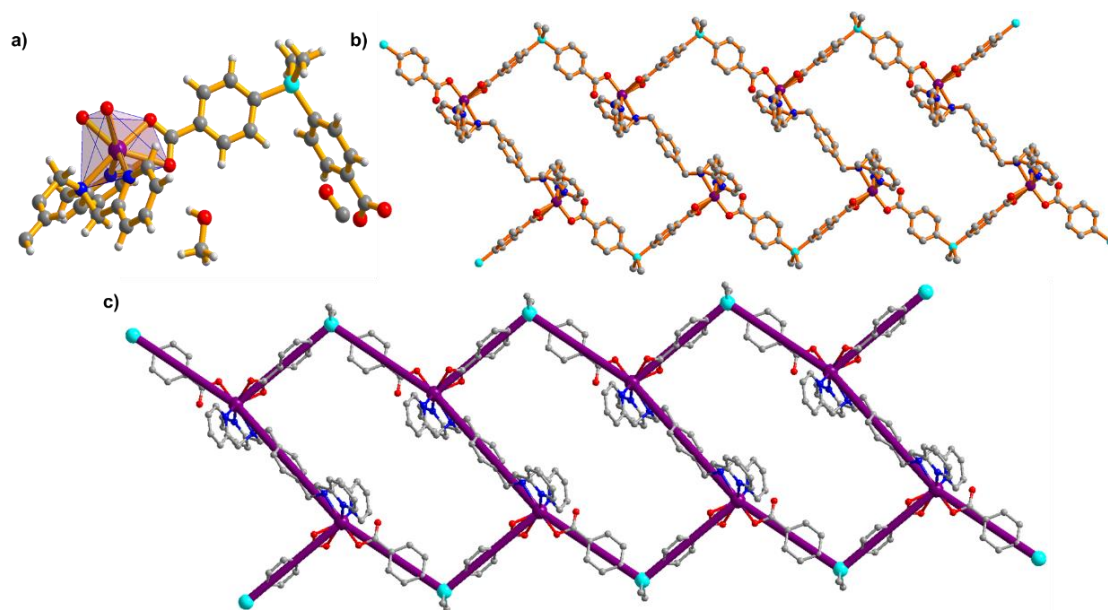


Figure 3.22. Structural description for **13**; (a) view of the asymmetric unit and the coordination environment around the Mn(II) center, (b) view of 1D polymeric structure and (c) simplified view of the 1D polymeric structure formed by fused hexagons.

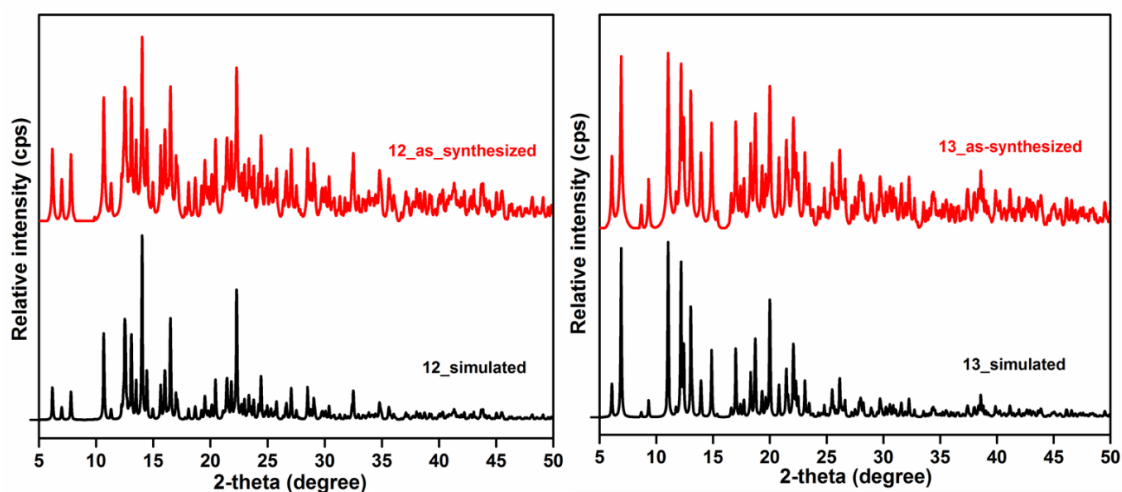


Figure 3.23. Powder X-ray diffraction pattern of the as-synthesized sample of **12** (left) and **13** (right), compared with their respective simulated powder X-ray diffraction pattern, obtained from the single crystal X-ray diffraction data.

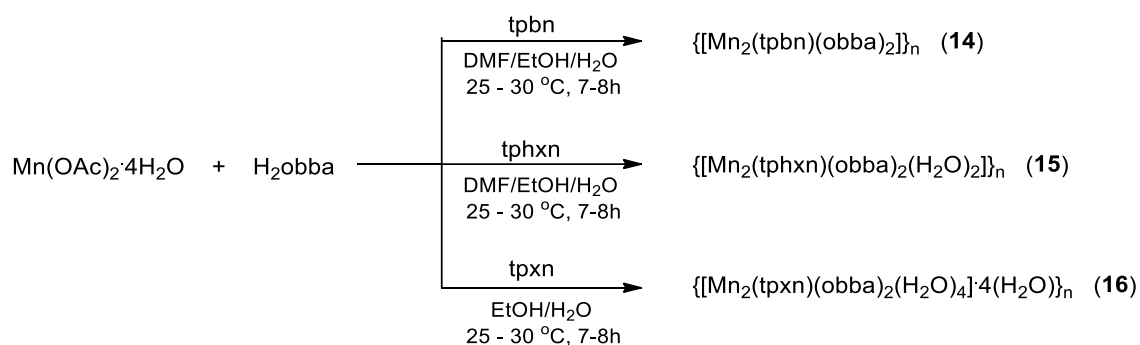
In order to study the effect of reaction conditions on the formation of either possible structural isomer in case of **12** and **13**, various reaction parameters (solvent and temperature) were tested, but in all cases predominate formation of single-phase polycrystalline material has occurred which was tested by the powder X-ray diffraction analysis of the resulting material (Figure 3.23).

In order to confirm different binding modes of carboxylates in both cases the FTIR spectra of **12** and **13** was recorded in the solid state at room temperature as KBr pellets. The sharp signals due to asymmetric (ν_{asym}) and symmetric (ν_{sym}) stretching of the carboxylates in

case of **12** appeared at 1604 cm^{-1} and 1386 cm^{-1} ($\Delta\nu = 208\text{ cm}^{-1}$), whereas in case of **13**, the signal due to asymmetric (ν_{asym}) and symmetric (ν_{sym}) stretching appeared at 1602 cm^{-1} and 1379 cm^{-1} ($\Delta\nu = 221\text{ cm}^{-1}$) and 1583 cm^{-1} and 1385 cm^{-1} ($\Delta\nu = 198\text{ cm}^{-1}$). The observation of the difference in their asymmetric and symmetric stretching frequencies (i.e. $\Delta\nu$ value) in the FTIR spectra, clearly indicate the monodentate binding of the carboxylate to the metal center in case **12** and two kind of (monodentate as well as bidentate) binding of the carboxylate in cases of **13**.²⁵¹

The study was further extended to see the effect of carboxylate geometry to the resulting polymeric architecture. Keeping all other variables constant, a comparatively flexible bent dicarboxylate (**H₂obba**) was used in combination and another set of coordination polymer have been synthesized (**Scheme 3.10**) and well characterized by a combination of different analytical techniques.

Scheme 3.10. Synthesis of **14**, **15** and **16**.



Single crystal structure analysis. Single crystals X-ray diffraction analysis reveal that, as expected **14** and **15** forms 1D polymeric architectures similar to what was observed for **11-13** but in case of **16** a discrete dimetallic complex was obtained. The structure of **14** crystallizes in a $P2_1/c$ space group with monoclinic crystal system whereas **15** and **16** crystallizes in a triclinic crystal system with $P\bar{1}$ space group. The asymmetric unit in **14** and **15** consists of one Mn(II) ion, one dicarboxylate (**obba**²⁻) and one-half of the **tpbn** (in **14**) or **tphxn** (in **15**) ligand. In addition the asymmetric unit in **15** consists of an extra water molecule coordinated to the Mn(II) center. On the other hand the asymmetric unit in case of **16** consists of one Mn(II) ion, one dicarboxylate (**obba**²⁻), one-half of the **tpxn** ligand and total of five water and one methanol molecules, where two water molecules are coordinated to the Mn(II) center and other three water molecules and one methanol occupy the lattice positions. The Mn(II) center in all cases is in an distorted octahedral N3O3 environment, where from a total of six coordination sites, three are occupied by nitrogen

atoms of one of capping site of the tpbn (in **14**) or tphxn (in **15**) or tpxn (**16**) ligand. The other three sites in **14** are occupied by oxygen atoms of the carboxylate groups of **obba**²⁻, where one of the carboxylates binds in a bidentate chelated fashion and the other in a monodentate fashion (Figure 3.24a) and in case of **15**, two sites are occupied by the oxygen atoms of the carboxylate groups of **obba**²⁻, and one is occupied by the oxygen atom of water molecule coordinated to the Mn(II) center (Figure 3.24c), whereas in case of **16** one of the site is occupied by oxygen atoms of the carboxylate groups of **obba**²⁻, and other two are occupied by oxygen atoms of two water molecule coordinated to the Mn(II) center. Prominent distortions from the regular octahedral geometries in each case is evident from the O-Mn-O or N-Mn-O or N-Mn-N bond angle values ranging from 54.49° to 125.50°. All the Mn-N and Mn-O bond lengths are in the usual range for this kind of complexes.^{249,250} All the crystallographic information pertaining to data collection and structure refinement parameters, selected bond lengths and bond angles are listed in Table A5, A27 and A49, respectively.

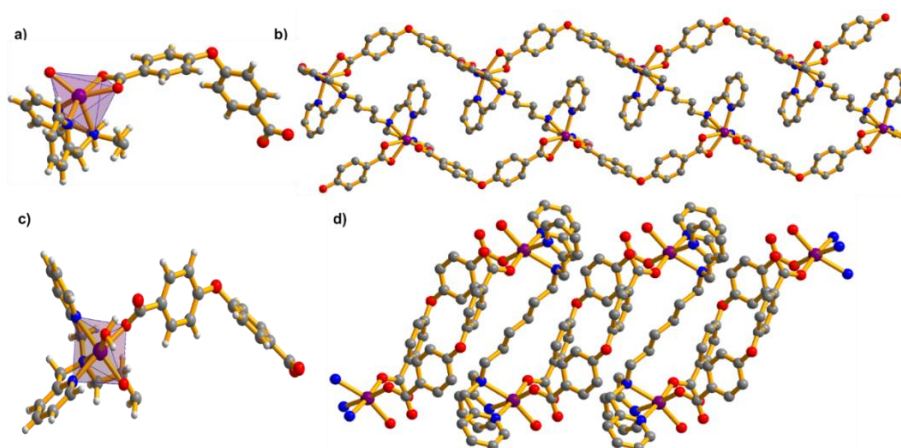


Figure 3.24. Structural description for **14** and **15**; (a and c) represents the asymmetric units and the coordination environment around the Mn(II) center in **14** and **15**, respectively and (b and d) perspective views of 1D polymeric structures in **14** and **15**, respectively.

As shown in Figure 3.24b and d, the asymmetric unit in both cases (**14** and **15**) further extends only in one direction to result an infinite 1D chain structure as expected with the strategy designed for this kind of polymeric structures. However, both **14** and **15** gives 1D polymeric structure; the structural arrangement of the components has resulted into the formation of polymeric structure in different possible ways. For example, the polymeric structure in **14**, can be considered as a result of fused hexagons whereas the polymeric structure in **15**, is a result of connected molecular squares. A simplified representation of both the structures is shown in Figure 3.25. The results are similar to what was observed in

case of **11** and **11a**, but it is interesting to note that unlike **11** where both isomers were obtained as a mixture, pure single-phase product was obtained in both cases. Unexpectedly, when **tpxn** was used in case of **16**, the asymmetric unit extends to give a discrete dimetallic linear complex (Figure 3.26). It should be also noted that attempts to study the effect of reaction conditions has also resulted in the formation of single-phase products in respective cases.

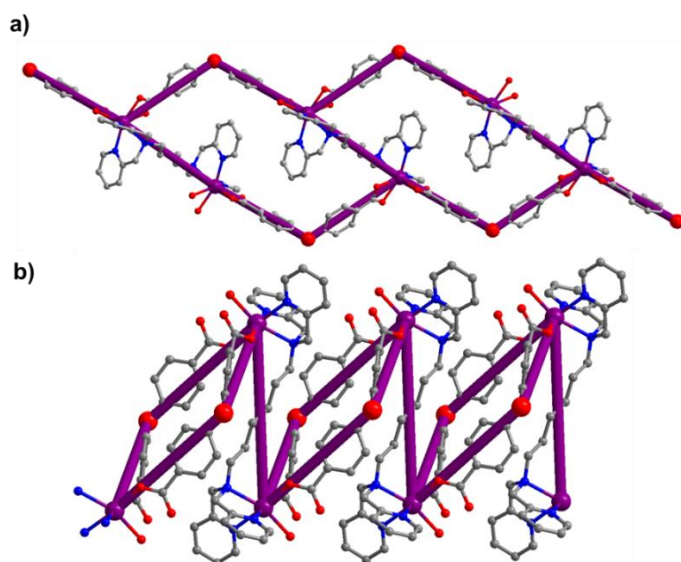


Figure 3.25. Simplified representation of the polymeric structures in (a) **14** and (b) **15**, respectively.

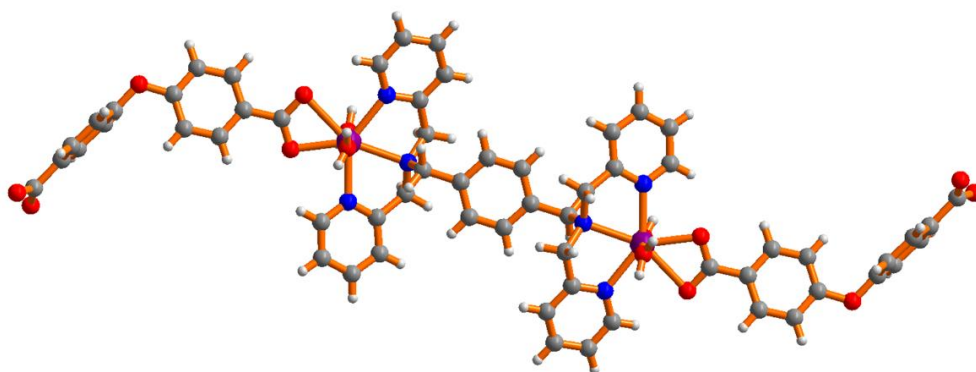


Figure 3.26. View of the discrete dimetallic linear complex formed in **16**.

In order to establish the phase purity of the resulting architectures powder X-ray diffraction (PXRD) patterns of the as-synthesized samples of **14-16** was recorded at room temperature. As can be seen in Figure 3.27, a very good agreement between the powder pattern of the as-synthesized samples of **14-16** and the simulated powder patterns obtained from the single crystal structure data, indicates the phase purity and the exclusive formation of particular structures in case of **14-16**. Further the FTIR spectra of **14-16** recorded in the solid state at room temperature confirm different binding modes of carboxylates in each case. The sharp

signals due to asymmetric (ν_{asym}) and symmetric (ν_{sym}) stretching of the carboxylates in case of **14** appeared at 1607 cm^{-1} and 1391 cm^{-1} ($\Delta\nu = 216\text{ cm}^{-1}$) and 1592 cm^{-1} and 1412 cm^{-1} ($\Delta\nu = 180\text{ cm}^{-1}$), indicate the two kind of carboxylate bindings (monodentate as well as bidentate), whereas in case of **15** and **16** these signal appeared at 1605 cm^{-1} and 1395 cm^{-1} ($\Delta\nu = 210\text{ cm}^{-1}$) and 1601 cm^{-1} and 1379 cm^{-1} ($\Delta\nu = 222\text{ cm}^{-1}$), respectively, which indicate monodentate binding of the carboxylate to the metal center in each case.²⁵¹

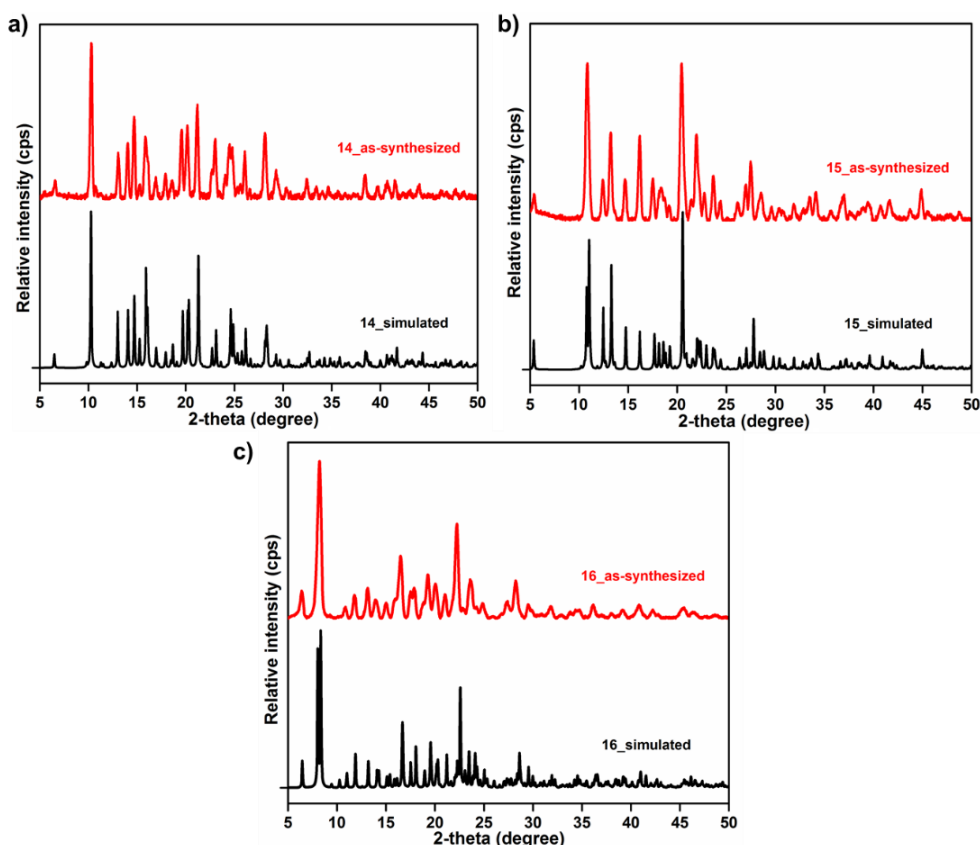


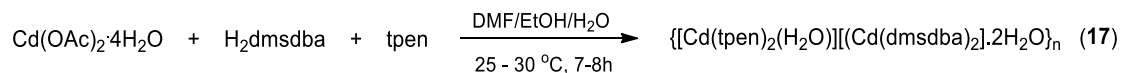
Figure 3.27. Powder X-ray diffraction pattern of the as-synthesized sample of **14-16**, compared with their respective simulated powder X-ray diffraction pattern, obtained from the single crystal X-ray diffraction data.

Cd(II) Chemistry

Different metal ions because of their own coordination preferences are known to play an important role in the structural diversity of the resulting coordination architectures.²⁶⁸ In this respect Cd(II), because of its extended coordination number has attracted much attention. Therefore, in order to support the utility of this ligand combinations (*bis*(tridentate) and bent dicarboxylates) to design such 1D coordination polymer (either possible isomer), we have expanded the study with **tpen** and **tpbn** ligands in combination with the bent dicarboxylates (**H₂dmsdba** or **H₂obba**) and Cd(II) as the metal center. As the first example in this series, **tpen** ligand was used in combination of **H₂dmsdba** and Cd(II)

metal center (Scheme 3.11), where in order to study the effect of spacer chain length, it has been reduced to two carbon chain in between the two tridentate capping sites in case of **tpen**.

Scheme 3.11. Synthesis of **17**.



Single crystal structure analysis. Single crystals X-ray diffraction analysis reveal that, **17** crystallizes in a triclinic crystal system with $P\bar{1}$ space group and consists of an anionic 1D linear chain of Cd(II) and **dmsdba**²⁻ which are further hydrogen bonded to each other to form 2D supramolecular framework. The six N-donors presents in tpen ligand wrap around a single metal centre coordinated with an extra water molecule to form a cationic 0D metal complex, which is encapsulated in the anionic 1D polymeric chains of metal-carboxylate via strong hydrogen bonding interactions. The asymmetric unit consists of two crystallographically independent Cd(II), one **tpen** ligand, two **dmsdba**²⁻ and a total of seven water molecules where one is coordinated to the Cd(II) and other six occupies the lattice positions. Both Cd1 and Cd2 are in an hepta-coordination environment, where from the seven coordination sites in case of Cd1 six are occupied by oxygen atoms of three carboxylates of two dmsdba²⁻ coordinated to Cd1 in a chelated fashion; fourth carboxylate group being non-coordinating. One of the coordinated carboxylate is in a chelated bridging mode, completing the seventh coordination site of Cd1, resulting in a Cd₂O₂ dimetallic cluster as repeat unit. In case of Cd2 the seven sites are occupied by six nitrogen atoms of the tpen ligand and one oxygen atom of the coordinated water molecule (Figure 3.28a). As shown in Figure 3.28b, the structure consists of Cd(II)-carboxylate 1D chains, where Cd₂O₂ cluster is acting as a node and are linked to each other by the dicarboxylate acting as linkers. Two of such carboxylate groups in the structure are deprotonated and does not bind with any metal center, resulting in an overall -2 charge on the 1D Cd(II)-carboxylate chains which is charge-balanced by the +2 charge on the 0D Cd(II)-tpen complex encapsulated into the 1D Cd(II)-carboxylate chains by the strong hydrogen-bonding interactions (Figure 3.28c). This results into an overall neutral hydrogen bonded supramolecular architecture. The average Cd-O (2.37 Å) and Cd-N (2.44 Å) bond lengths are in the usual range for this kind of complexes^{269,270} and the usual distortions from the regular geometries are evident from the bond angle value. All the crystallographic information pertaining to data collection and structure refinement parameters, selected bond

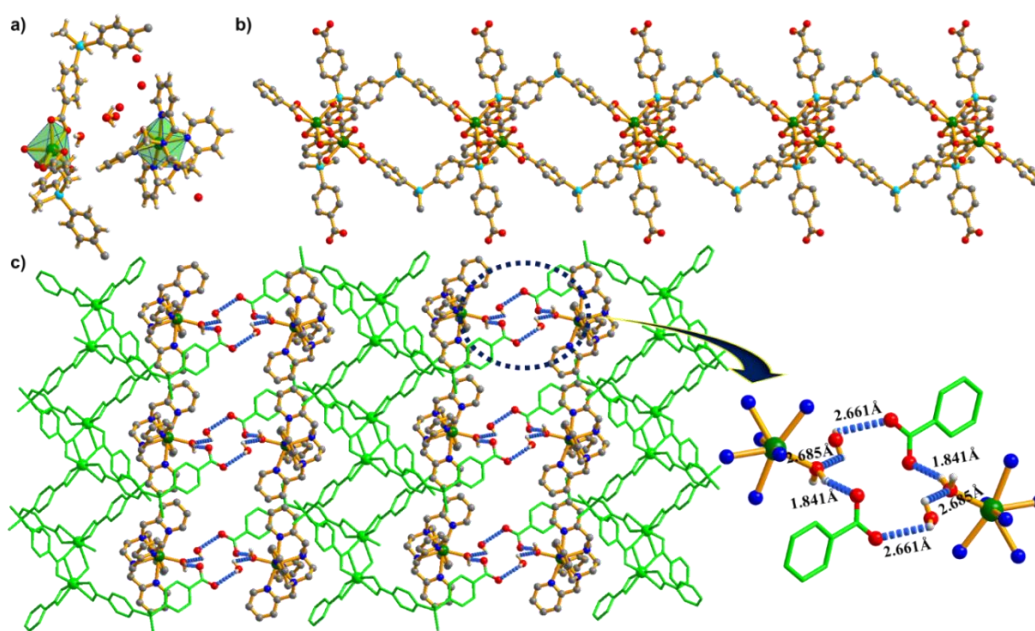


Figure 3.28. Structural description for **17**; (a) asymmetric unit and coordination environment around the Cd(II) centers, (b) perspective view of metal-carboxylate 1D polymeric chain in **17** and (c) a view of hydrogen bonded supramolecular architecture showing 0D Cd(II)-tpen complex encapsulated into the Cd(II)-carboxylate chains.

lengths and bond angles are listed in Table A6, A28 and A50, respectively. The structural features in **17** have been further supported by FTIR spectroscopic analysis. The signals due to asymmetric (ν_{asym}) and symmetric (ν_{sym}) stretching of the carboxylates at 1578 cm^{-1} and 1399 cm^{-1} ($\Delta\nu = 179\text{ cm}^{-1}$), confirms the bidentate chelated binding of the carboxylate to the metal center.²⁵¹ In addition, a very good agreement between the experimental powder X-ray diffraction (PXRD) pattern of the bulk sample and simulated powder pattern (Figure 3.29) confirms that the bulk sample represents the same structure as obtained from the single crystal X-ray diffraction analysis.

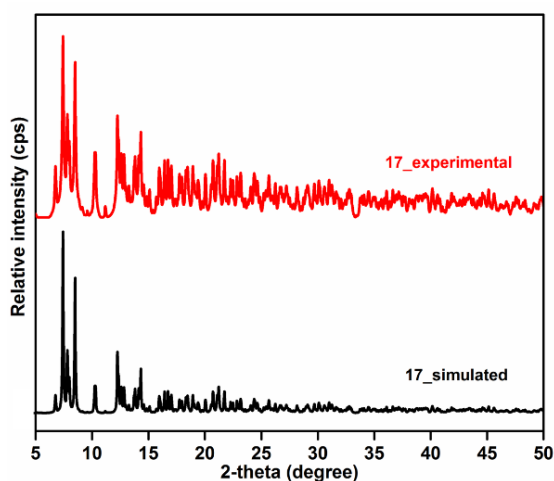
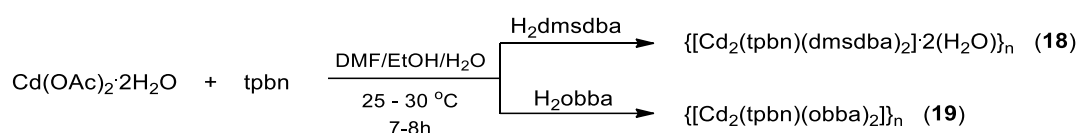


Figure 3.29. Powder X-ray diffraction (PXRD) pattern of **17** compared with the simulated powder pattern obtained from the single crystal data.

The result indicates that bis(tridentate) ligand **tpbn** with comparatively short spacer between the two tridentate capping sites does not spans between two metal centers, instead wrap around the metal center to block all the available coordination sites on the metal ion. This particular example suggests the requirement of the optimum spacer length between the two capping sites in bis(tridentate) ligand in order to synthesize such pre-designed 1D coordination polymers. After establishing the important role of the optimum spacer length, the study has been further extended to establish the design strategy for such coordination polymers by using **tpbn** ligand in combination with Cd(II) metal ions and previously used dicarboxylates (**dmsdba**²⁻ and **obba**²⁻). A set of two coordination polymers namely $\{[\text{Cd}_2(\text{tpbn})(\text{dmsdba})_2] \cdot 2(\text{H}_2\text{O})\}_n$ (**18**) and $\{[\text{Cd}_2(\text{tpbn})(\text{obba})_2]\}_n$ (**19**) (Scheme 3.12) were synthesized and characterized using different analytical techniques.

Scheme 3.12. Synthesis of **18** and **19**.



The coordination polymers **18** and **19** were synthesized at room temperature by reacting cadmium acetate, **tpbn** and **H₂dmsdba** or **H₂obba** in 2:1:2 ratio. In both the cases single crystal suitable for single crystal X-ray diffraction analysis were obtained by slow diffusion technique and the corresponding molecular formula was established by a combination of elemental analysis, TGA and single crystal X-ray diffraction analysis.

Single crystal structure analysis. Single crystals X-ray diffraction analysis reveal that, **18** and **19** crystallizes in triclinic and monoclinic crystal systems with $P\bar{1}$ and $P2_1/c$ space groups, respectively. Both consists of similar kind of 1D coordination polymers. The Cd(II) metal center in each case is in a N₃O₄ type hepta-coordination environment. The asymmetric unit consists of a Cd(II) metal center, one dicarboxylate (**dmsdba**²⁻ in case of **18** and **obba**²⁻ in case of **19**) and one half of the bis(tridentate) ligand, **tpbn**. In addition, a water molecule is also present in case of **18**, occupying the crystal lattice. As shown in Figure 3.30a and 3.31a, the seven coordination sites around the Cd(II) in both the cases are occupied by three nitrogen atoms of one of the capping site in **tpbn**, and remaining site are occupied by four oxygen atoms of the two carboxylate groups, which binds in a bidentate chelated fashion. This bidentate chelated binding of the carboxylates is evident from the FTIR spectra of **18** and **19**, where the signals due to asymmetric (ν_{asym}) and symmetric (ν_{sym}) stretching of the carboxylates at 1591 cm⁻¹ and 1395 cm⁻¹ ($\Delta\nu = 196 \text{ cm}^{-1}$) in **18** and 1598

cm^{-1} and 1406 cm^{-1} ($\Delta\nu = 192 \text{ cm}^{-1}$) in **19**, confirms the bidentate chelated binding of the carboxylate to the metal center.²⁵¹

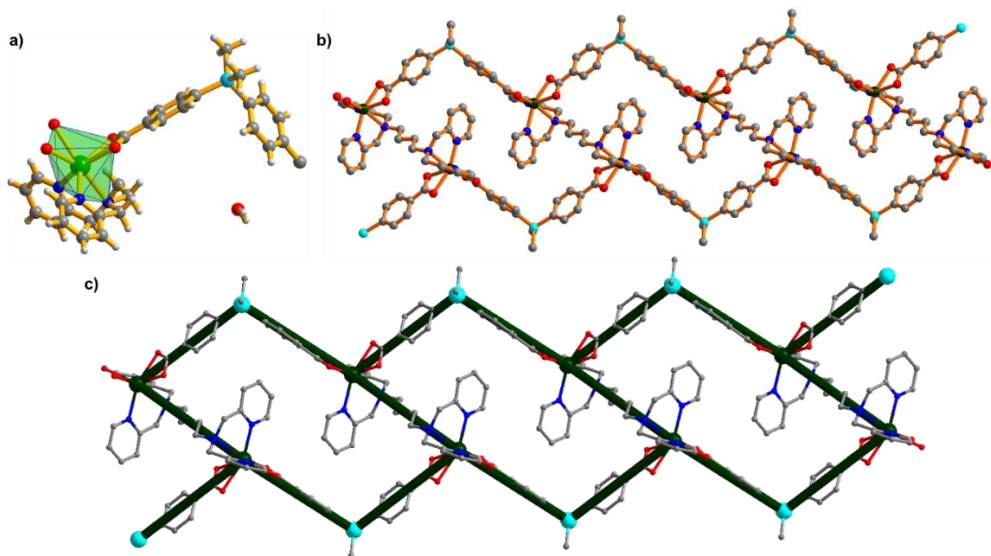


Figure 3.30. Structural description for **18**; (a) asymmetric unit and coordination environment around the Cd(II) centers, (b) perspective view of 1D polymeric chain in **18** and (c) simplified representation of the polymeric chain composed of fused hexagons.

The asymmetric unit further extends to give an overall 1D structure. In both the case similar kind of polymeric structure was obtained (Figure 3.30b and 3.31b). A simplified representation of the polymeric structures showing fused hexagons in **18** and **19** are shown in Figure 3.30c and 3.31c, respectively. The average Cd-O (2.43 \AA) and Cd-N (2.41 \AA) bond lengths are in the usual range for this kind of complexes^{269,270} and the usual distortions from the regular geometries are evident from the bond angle value. All the crystallographic information pertaining to data collection and structure refinement parameters, selected bond lengths and bond angles are listed in Table A6, A28 and A50, respectively.

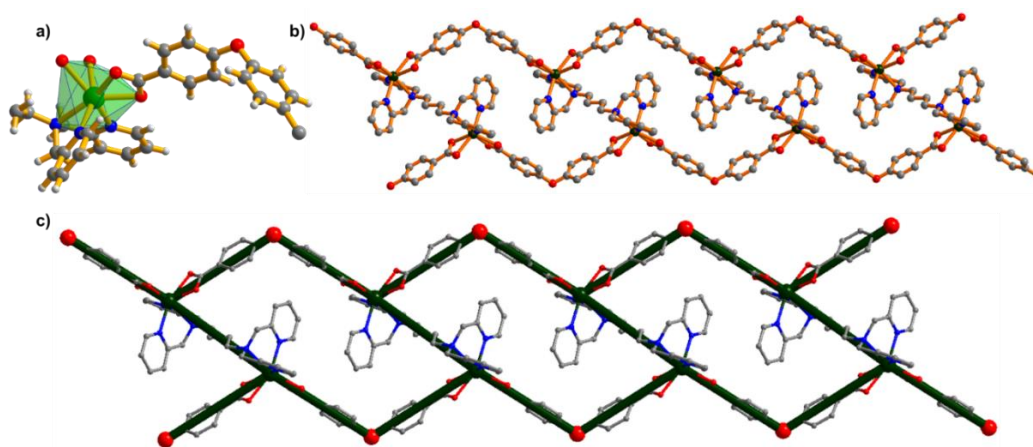


Figure 3.31. Structural description for **19**; (a) asymmetric unit and coordination environment around the Cd(II) centers, (b) perspective view of 1D polymeric chain in **19** and (c) simplified representation of the polymeric chain composed of fused hexagons.

In order to check whether the bulk sample represents the same material as obtained from the single crystal X-ray diffraction analysis or not, powder X-ray diffraction (PXRD) patterns of the as-synthesized samples of both **18** and **19** was recorded at room temperature. As can be seen in Figure 3.32, the obtained PXRD patterns in both cases are in very good agreement with the simulated powder patterns obtained from their single crystal structure data. This confirms that the single crystal and the bulk material are the same. It also confirms the phase purity of the bulk sample and exclusive formation of particular structural isomer in both the cases. Additionally, in an attempt to obtain the other possible structural isomers in both the cases by varying the reaction conditions, resulted in the formation of same isomer in all cases in a highly selective manner.

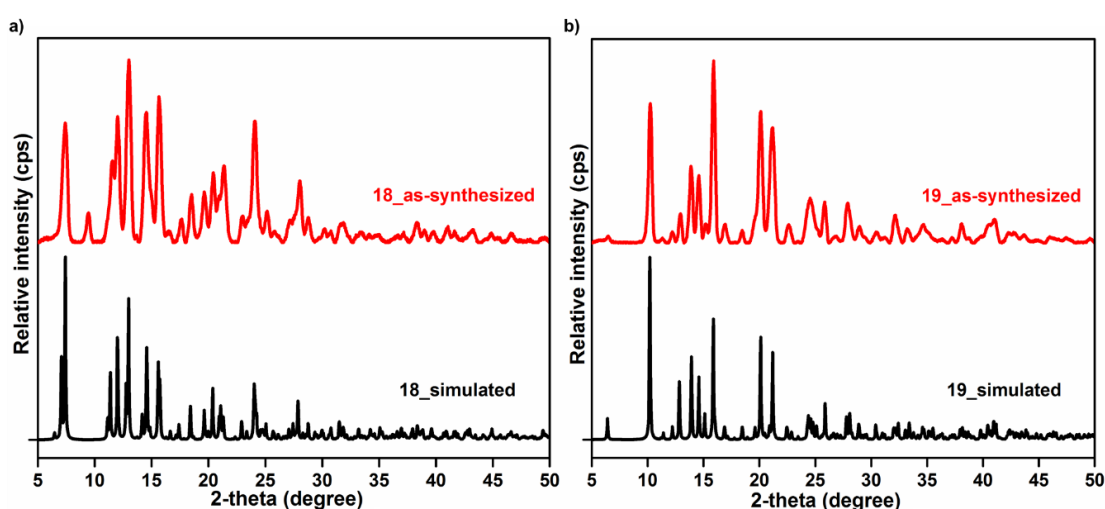


Figure 3.32. Powder X-ray diffraction (PXRD) pattern of as-synthesized samples of (a) **18** and (b) **19** compared with the simulated powder pattern obtained from the single crystal data.

With these examples **11-19**, we have established the utilization metal-complex connectors for the tailored synthesis of 1D coordination polymers using bis(tridentate) ligands. The capping sites provides a greater control of the bond angles and restrict the number of coordination sites by blocking at least three coordination sites of the metal center. The strategy has been optimized for the synthesis of either possible structural isomers by judicious selection of the bis(tridentate) ligand, metal ion, carboxylate linker or by varying the reaction conditions.

3.1.2.2 Architectures with bis(pyridyl) pillar ligands

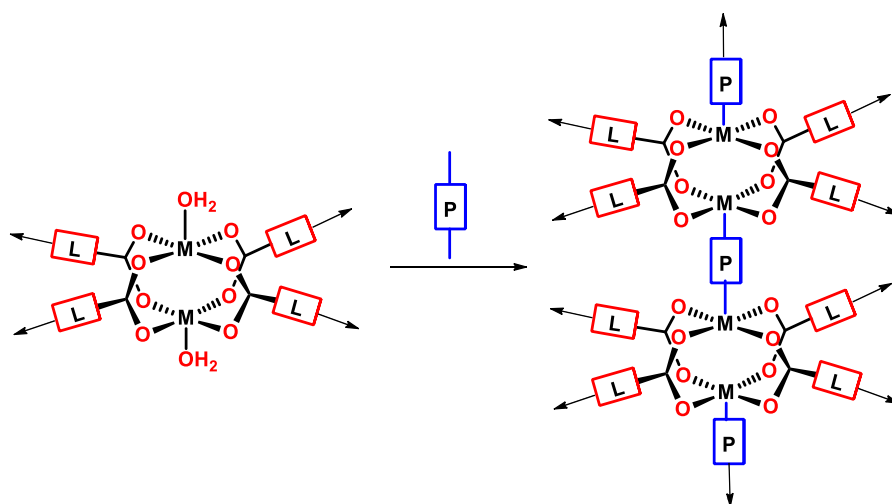
In terms of crystal engineering, an effective route for the synthesis of novel coordination polymers with attractive topological structures is the employment of mixed ligands. Primary reports on porous coordination polymers mainly focused on the use of metal nodes as connectors and carboxylate ligands as linkers.^{83,84,271} In continuation of the studies on

porous coordination polymers and to extend their applicability, the utilization of a second linker for higher tailoring of the structures was considered. This was the first step toward constructing pillar-layered mixed ligand coordination polymers. Introducing pillars into coordination polymers has opened new possibilities for researchers to better control the assembly of building blocks into frameworks with desired network properties. The first reports on pillar linkers utilized simple nitrogen donor ligands such as bpy²⁷² or DABCO.²⁷³ The increasing number of investigations in this field has led to the design of a series of rigid, flexible or functional pillar ligands; the chemical structure of some of them, used for the present work are shown in Figure 1.9. The judicious selection/modification of the pillar ligands can aid the fabrication of novel networks with desirable performance. Controlling the structural flexibility, interpenetration, chemical stability and functionality by judicious modifications on pillar backbone provides an opportunity to design polymeric architectures with optimal pore volumes and efficiencies. The present section illustrates the synthesis, stability and structural properties and improved applicability of such coordination polymers derived from various pillar ligands in combination of the bent dicarboxylate ligand (**H₂dmsdba**) and different metal ions.

Zn(II) Chemistry

In contrast to polymeric architectures with mononuclear connected nodes, those containing polynuclear metal–carboxyl clusters (also referred to as secondary building units, SBUs) have attracted much attention, as they provide stiffness of the local geometry and thus the architectural robustness of the resulting framework. In terms of the coordination chemistry

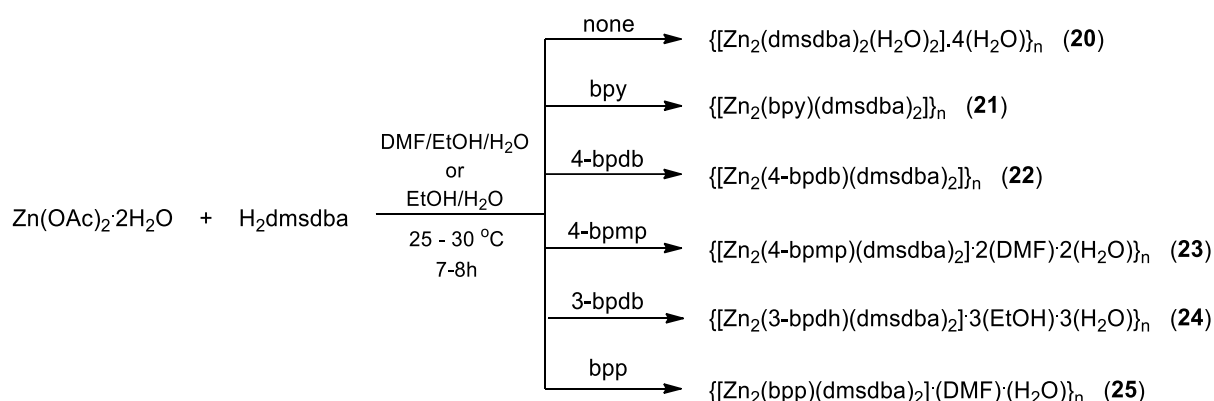
Scheme 3.13. Representation of the pillaring strategy in paddle-wheel SBUs.



where, L and P represents the carboxylate linker and pillar ligand, respectively

of Zn(II) metal ion in combination with carboxylate linkers it is well known to afford tetranuclear Zn_4O or dinuclear $Zn_2(COO)_4$ clusters as SBUs. The $Zn_2(COO)_4$ clusters also known as paddle-wheel SBU, have both the metal centers in a square pyramidal coordination geometry, where the axial positions, in general are occupied by coordinating solvent molecules, which can be replaced by bidentate pillar ligands to add up an extra dimensionality to the resulting pillared structure (Scheme 3.13). Because of the ability of Zn(II) metal ions to adopt the $Zn_2(COO)_4$ clusters SBUs with carboxylate linkers, it was chosen in combination of bent dicarboxylate linker **H₂dmsdba** and neutral N-donor pillar ligands to synthesize a set of coordination polymers **20-25** (Scheme 3.14). These examples present a control over the dimensionality and framework interpenetration into the coordination polymers by judicious selection of the pillar ligands.

Scheme 3.14. Synthesis of **20-25**.



All compounds were synthesized at room temperature by the reaction of zinc acetate, **H₂dmsdba** and different pillar ligands, except in case of **20**, where for an in-depth understanding of the pillaring strategy, a Zn(II)-carboxylate polymer was synthesized where no pillar ligand was used. In all cases the compounds were isolated as solid materials in good yields. Single crystals for structural characterizations were obtained by slow diffusion technique in all cases using different combinations. The molecular formula in each case was established by a combination of elemental analysis, TGA and single crystal X-ray diffraction analysis.

Single crystal structure analysis. Single crystals X-ray diffraction analysis reveals that **20** is a 1D coordination polymer. It crystallizes in a monoclinic crystal system with $C2/m$ space group. The asymmetric unit consists of two Zn(II), with half occupancy each, one **dmsdba**²⁻ and two water molecules which are coordinated to each metal center. As depicted in Figure

3.33a, the Zn(II) ions adopt a distorted square pyramidal geometry, two of such Zn(II) ions are bridged by carboxylate groups to make $Zn_2(COO)_4$ bimetallic cluster as SBU. Zn(II) is coordinated by four carboxyl oxygen atoms of carboxylate linker at equatorial positions and one oxygen atom from coordinated water molecule at axial positions. All of the Zn-O bond distances fall in the range of 1.946 Å-2.110 Å, which are in the usual range for this kind of complexes.²⁷⁰ All the crystallographic information pertaining to data collection and structure refinement parameters, selected bond lengths and bond angles are listed in Table A7, A29 and A51, respectively. As shown in Figure 3.33b, two of **dmsdba**²⁻ linkers spans between two $Zn_2(COO)_4$ SBUs to form a 1D polymeric structure. The polymeric structure can be simplified in the form of node and linkers, where bimetallic $Zn_2(COO)_4$ SBU can be considered as a node and **dmsdba**²⁻ as a bent linker. A simplified node and linker type representation is shown in Figure 3.33c. The packing arrangement of 1D polymeric chains in the crystal lattice shows that the different polymeric chains are stacked one above the other in an eclipsed fashion (Figure 3.33d). No interpenetration was observed in between the polymeric chains, which sometimes results in the structures with higher dimensionalities.

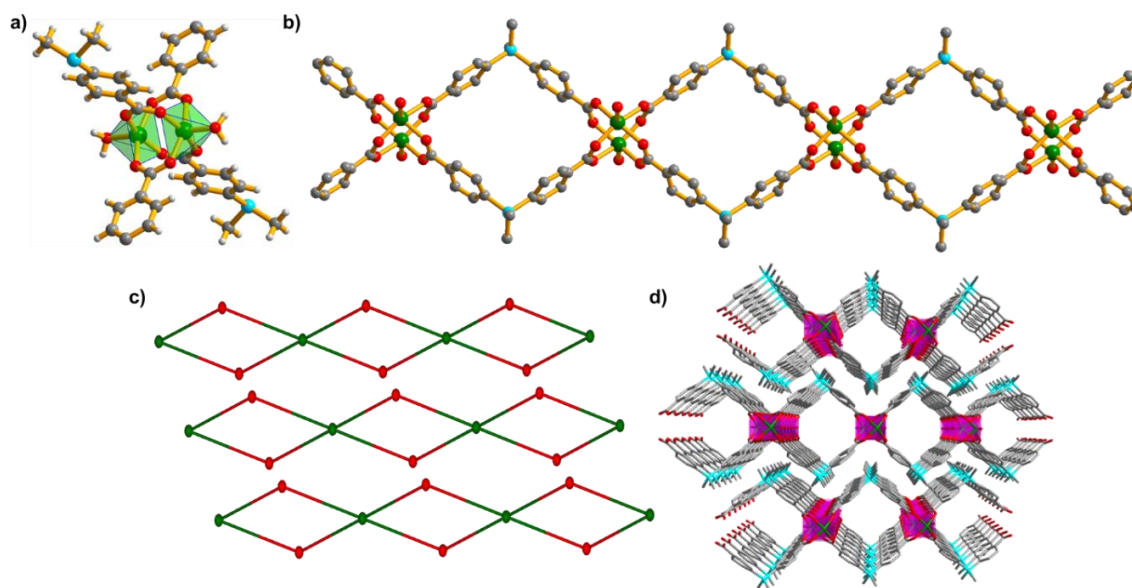


Figure 3.33. Structure description for **20**; (a) coordination environment around the Zn(II) center, (b) view of 1D polymeric chain, (c) node and linker type representation for **20** and (d) packing of 1D chains in crystal lattice.

The polymers **21**, **22** and **23** forms 2D sheet structures (Figure 3.34a-c). All of these crystallizes in triclinic crystal systems with $P\bar{1}$ space group. The asymmetric unit in case of **21** consists of one Zn(II), one **dmsdba**²⁻ and one half of the 4,4'-bipyridine (**bpy**), whereas **22** and **23** contains two Zn(II), two **dmsdba**²⁻ and one pillar ligand (**4-bpdb** in case of **22**

and **4-bmpm** in case of **23**). As depicted in Figure 3.34d, all three structures shares the same secondary building unit; $Zn_2(COO)_4$ bimetallic cluster, where each Zn(II) ions adopt a distorted square pyramidal geometry. Each Zn(II) is coordinated by four carboxyl oxygen atoms of carboxylate linker at equatorial positions and one nitrogen atom from the pillar ligand occupies the axial position. All of the Zn-O and Zn-N bond distances fall in the range of 2.019 Å-2.108 Å and 2.023 Å-2.050 Å, respectively, which are in the usual range for this kind of complexes.²⁷⁰

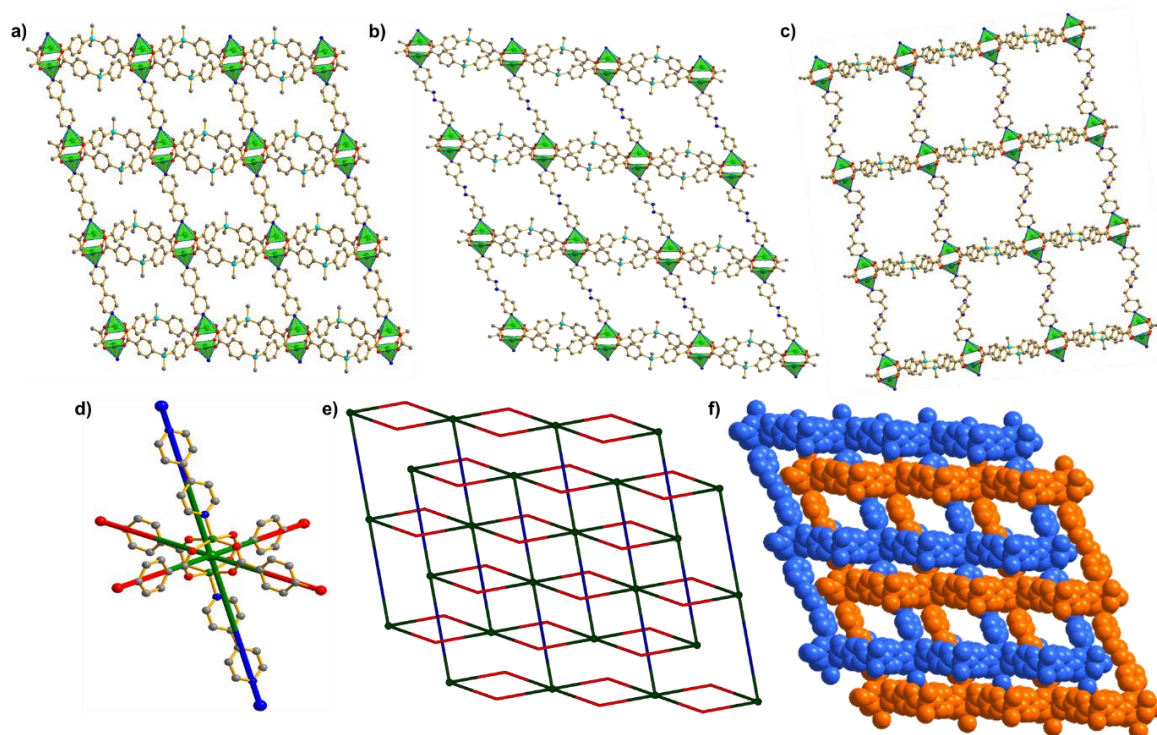


Figure 3.34. Structure description for **21-23**; (a,b and c) shows the 2D sheet structures in **21**, **22** and **23**, respectively, (d) a paddle wheel SBU common in all cases represented as a simplified 4-connected node and (e and f) are simplified node and linker representation and space fill representations, showing 2-fold interpenetration into the frameworks.

The prominent distortions from the regular square pyramidal geometries are evident from the bond angle values falling in the range of 85.20°-165.02°. All the crystallographic information pertaining to data collection and structure refinement parameters, selected bond lengths and bond angles for **21** and **22** are listed in Table A7, A29 and A51, respectively, whereas this information for **23** are listed in Table A8, A30 and A52, respectively. The polymeric structure can be simplified as node and linkers, where bimetallic $Zn_2(COO)_4$ SBU can be considered as a 4-connected node and the pillar ligands **bpy** or **4-bpdb** or **4-bmpm** and dicarboxylate linker **dmsdba**²⁻ can be considered as linear and bent linkers, respectively. Further examination of the node and linker representation reveals that the

frameworks in **21-23** exhibits a 4-connected uni-nodal net, sql (Shubnikov tetragonal plane net) topology, with Schläfli point symbol $\{4^4.6^2\}$ as determined by the TOPOS program.²⁷⁴ The simplified node and linker representation and a space fill representation of representative example is presented in Figure 3.34e and Figure 3.34f, respectively, indicating 2-fold interpenetration into the frameworks, which is a usual case when long pillar ligands are used to extend the dimensionality of the frameworks.

The polymers **24** crystallizes in triclinic crystal systems with $P\bar{1}$ space group. The asymmetric unit consists of two Zn(II), two **dmsdba**²⁻ and one **3-bpdh** ligand. It shares the same secondary building unit as in case of **21-23**. The coordination geometry around Zn(II) ions is distorted square pyramidal where each Zn(II) is coordinated by four carboxyl oxygen atoms of carboxylate linker at equatorial positions and one nitrogen atom from the pillar ligand (**3-bpdh**) occupies the axial position. The bimetallic Zn₂(COO)₄ paddle-wheel SBU further extends to form the overall 2D framework (Figure 3.35a). All of the Zn-O bond distances vary from 2.023 Å to 2.060 Å and the average Zn-N bond distances is 2.035 Å. The prominent distortions from the regular square pyramidal geometries can be seen from the bond angle values falling in the range of 86.36°-160.50°. All the crystallographic information pertaining to data collection and structure refinement parameters, selected bond lengths and bond angles are listed in Table A8, A33 and A54, respectively. More insight into the structure reveals that unlike **21-23**, it forms a non-interpenetrated framework, where different 2D sheets are stacked in an AB-AB fashion (Figure 3.35b). This can be due to the bulky methyl groups on to the ligand backbone which imparts sufficient steric hindrance and hence does not allow the framework interpenetration. The AB-AB stacking of the 2D sheets can be easily seen when the structure is simplified as node and linker type representation. As shown in Figure 3.35c and Figure 3.35d, the simplified node and linker representation clearly shows the AB-AB packing of the 2D sheets, where each sheet forms non-interpenetrated structures. A schematic representation of the AB-AB staking of 2D sheets is shown in Figure 3.35e. Further examination of the node and linker representation reveal that the framework exhibits the same topology as in the case of **21-23**.

The polymers **25** crystallizes in monoclinic crystal systems with $C2/c$ space group. The asymmetric unit consists of two Zn(II), two **dmsdba**²⁻ and one **bpp** ligand. Like previous examples it also contains the same bimetallic Zn₂(COO)₄ paddle-wheel core as secondary building unit which further extends in all 3 directions to give an overall 3D porous framework (Figure 3.36a). The increased dimensionality can be attributed due to the

conformational flexibility of the **bpp** ligand, where the Conformationally flexible $-(\text{CH}_2)_3-$ spacer between the two coordinating sites imparts conformational freedom to coordinate between different 2D-sheets. The distorted square

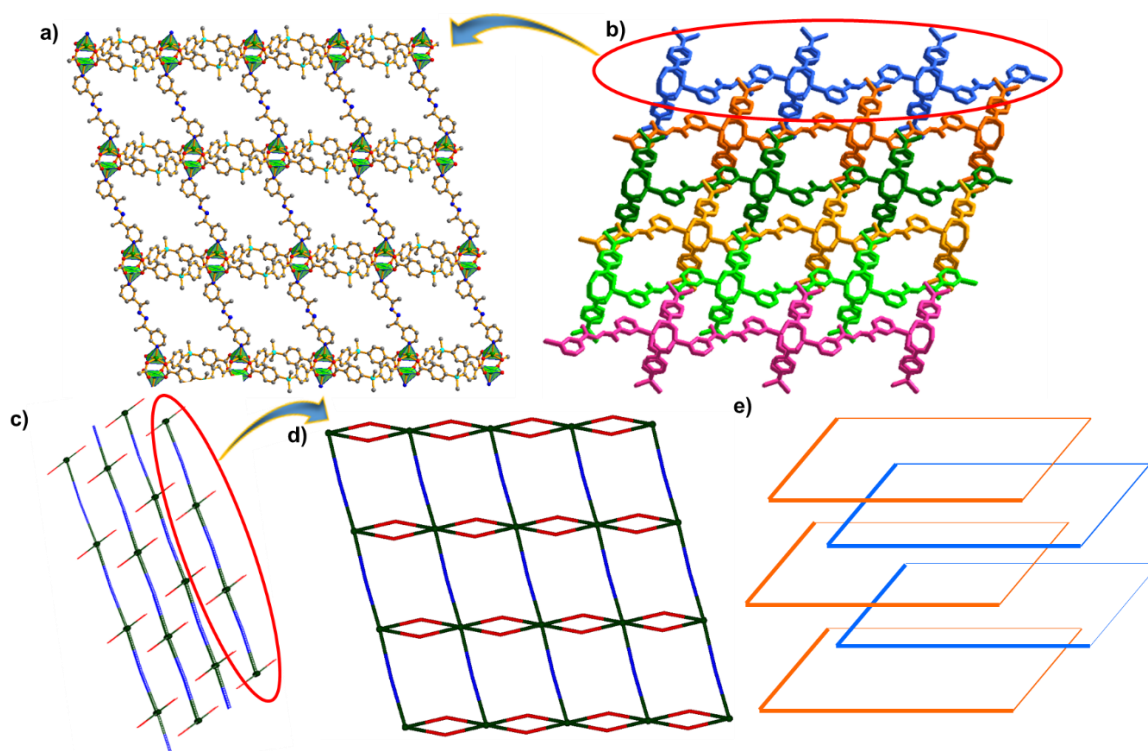


Figure 3.35. Structure description for **24**; (a) representation of the 2D sheet structures in **24**, (b) AB-AB type stacking of the 2D sheets in **24**; different 2D sheets are shown in different colors. (c and d) simplified node and linker representation showing non-interpenetration 2D sheets stacked in AB-AB fashion and (e) a schematic representation of the AB-AB stacking of 2D sheets.

pyramidal coordination geometry around Zn(II) centers is fulfilled by coordination with four carboxyl oxygen atoms of carboxylate linker at equatorial positions and one nitrogen atom from the pillar ligand (**bpp**) at the axial position. The average Zn-O (2.048 Å) and Zn-N (2.031 Å) bond distances are in the usual range for such type of complexes. The prominent distortions from the regular square pyramidal geometries can be seen from the bond angle values falling in the range of 86.07°-159.36°. All the crystallographic information pertaining to data collection and structure refinement parameters, selected bond lengths and bond angles are listed in Table A8, A30 and A52, respectively. Further insights into the structure reveals that the framework consists of 2-fold interpenetration into the structure which can be clearly expressed in a simplified node and linker representation of **25** (Figure 3.36b). Topological analysis by the TOPOS program²⁷⁴ on the node and linker representation of **25**, reveals that the framework exhibits the 4-connected uni-nodal net

sqc5, cadmium sulphate type topology with Schläfli point symbol $\{6^5.8\}$. Even after the interpenetration into the framework, the structure consists of potential voids filled with the

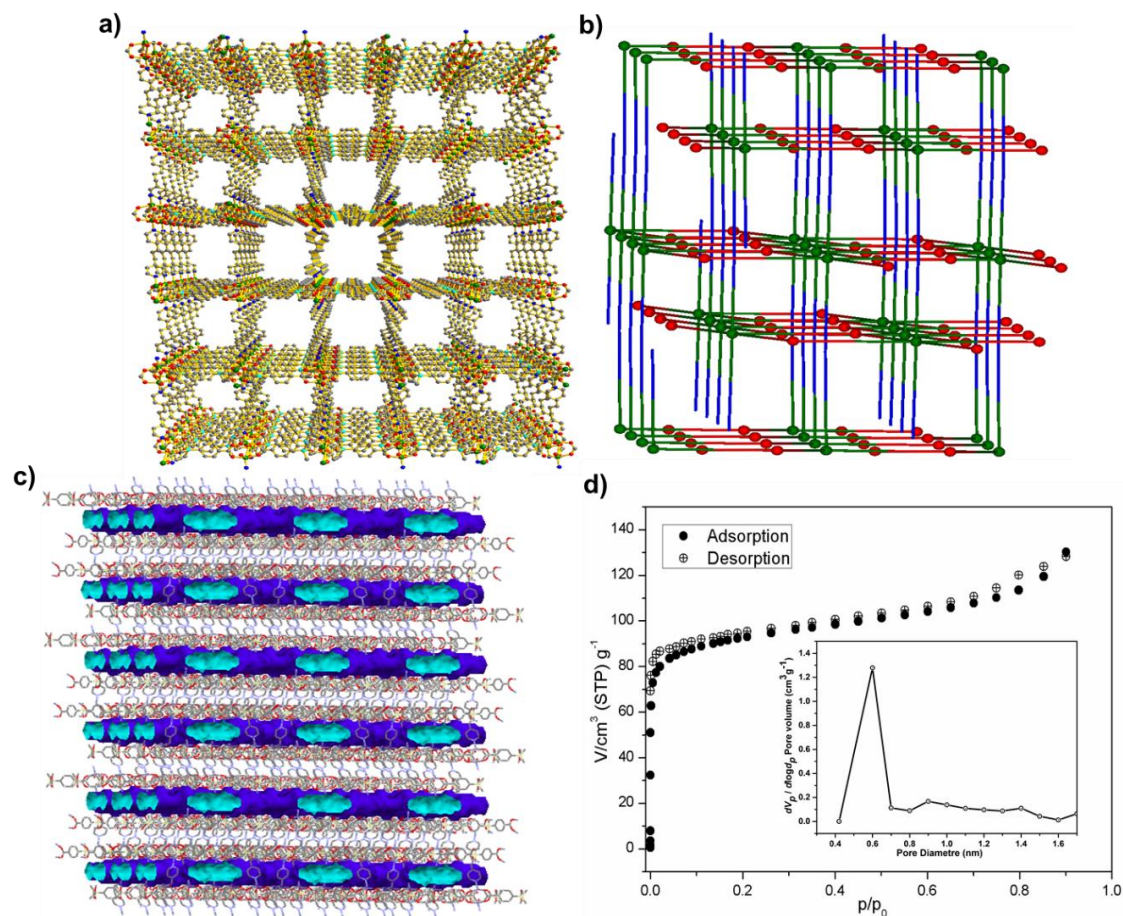


Figure 3.36. Structure description for **25**; (a) perspective view of the 3D framework, (b) simplified node and linker representation showing 4-c uni-nodal sqc5-CdSO₄ type topology, (c) representation of the colonolly surfaces; dark blue represents the outer surface while sky blue represents the inner surface and (d) N₂ sorption isotherm for **25** collected at 77 K, inset shows the mean pore diameter in **25**.

highly disordered solvent molecules. The diffused electron density due to the distorted solvent molecules was squeezed by using solvent masking option in Olex2 software²⁰³ during the structure refinement. The total solvent-accessible volume for **25** was estimated to be 17% (1631/9495 Å³ per unit cell volume) by the PLATON software.²⁷⁵

The establishment of permanent porosity in **25** was further investigated by nitrogen adsorption isotherm at 77 K. Prior to adsorption measurements, the sample (~100 mg) was activated by degassing at an elevated temperature of 393 K under vacuum conditions (20 mTorr) for 24 hours to generate the desolvated framework. The N₂ gas sorption isotherm for activated sample of **25** at 77 K and 1 bar pressure (Figure 3.36d) clearly indicates its microporous nature. Based on the N₂ adsorption data at 77 K, the Brunauer–Emmett–Teller

(BET) surface area and the Langmuir surface area were estimated to be $307 \text{ m}^2\text{g}^{-1}$ and $471 \text{ m}^2\text{g}^{-1}$, respectively (Figure 3.37). The average pore diameter was found to be 0.6 nm based on the N_2 adsorption measurement at 77 K (average pore diameter for microporous MOFs lies in the range of $0.4 - 1.0 \text{ nm}$).

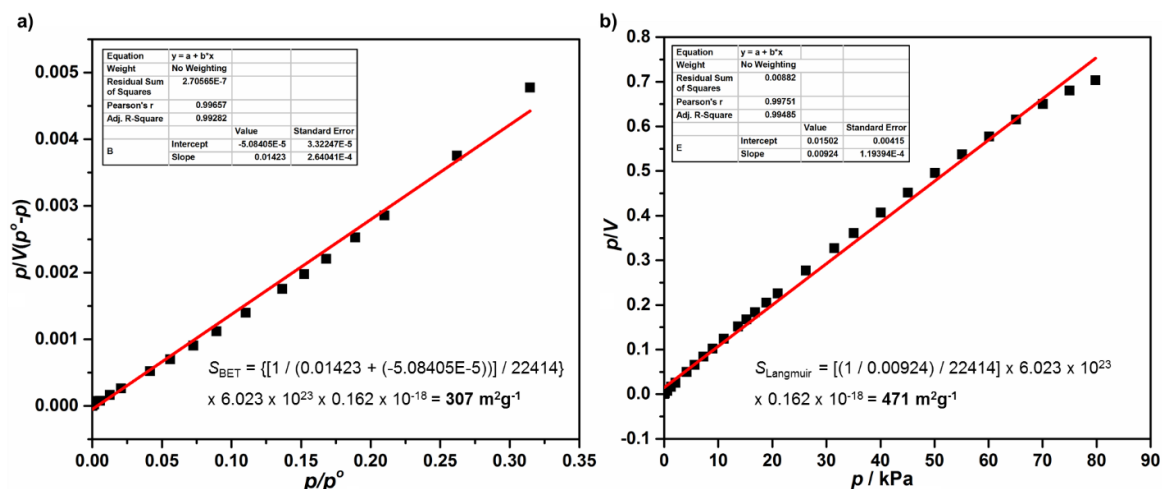


Figure 3.37. BET surface area (left) and Langmuir surface area (right) of **25** obtained from the N_2 adsorption isotherm at 77 K .

The value of τ parameter,²⁷⁶ which is an indicator for the deviation from the ideal square-pyramidal ($\tau = 0$) and trigonal bipyramidal ($\tau = 1$) geometries for five coordinate metal centers, was found to be in the range of 0 to 0.083 for **20-25**, which is again indicative of square pyramidal geometries around the metal center in all these cases.

FTIR and PXRD analysis. FTIR spectra of **20-25** were recorded in the solid state at room temperature as KBr pellets. The signals due to asymmetric (ν_{asym}) and symmetric (ν_{sym}) stretching of the carboxylates in their respective FTIR spectra appeared at 1614 cm^{-1} and 1413 cm^{-1} ($\Delta\nu = 201 \text{ cm}^{-1}$) in **20**, 1612 cm^{-1} and 1411 cm^{-1} ($\Delta\nu = 201 \text{ cm}^{-1}$) in **21**, 1616 cm^{-1} and 1410 cm^{-1} ($\Delta\nu = 206 \text{ cm}^{-1}$) in **22**, 1620 cm^{-1} and 1408 cm^{-1} ($\Delta\nu = 212 \text{ cm}^{-1}$) in **23**, 1614 cm^{-1} and 1410 cm^{-1} ($\Delta\nu = 204 \text{ cm}^{-1}$) in **24** and 1621 cm^{-1} and 1407 cm^{-1} ($\Delta\nu = 214 \text{ cm}^{-1}$) in **25**, respectively. The prominent shift in the asymmetric and symmetric stretching frequencies of the $-\text{C}=\text{O}$ group in **20-25** from free **H₂dmsdba** (1690 cm^{-1} and 1416 cm^{-1}) indicates strong binding of the carboxylates to the metal center and the values are in good agreement with the spectroscopic data for square pyramidal complexes with an NO_4 coordination environment.²⁷⁶ In order to confirm the bulk phase purity of **20-25**, powder X-ray diffraction patterns were recorded at room temperature. As can be seen in Figure 3.38, the experimentally obtained powder patterns of the bulk samples of **20-25** were

in very good agreement with the simulated powder patterns (obtained from the single crystal data). This confirms that in all cases the overall bulk materials represents the same structures

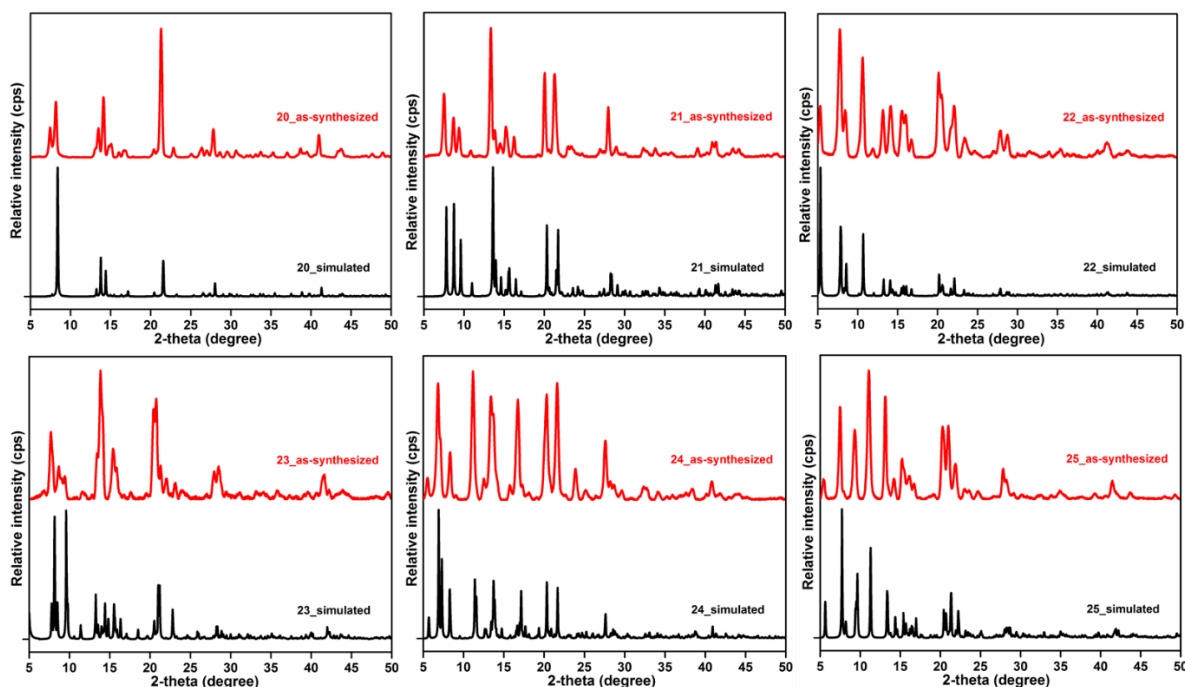


Figure 3.38. Powder X-ray diffraction (PXRD) pattern of as-synthesized samples of **20-25**, compared with the simulated powder pattern obtained from the single crystal data.

as obtained from the single crystal X-ray diffraction analysis.

Framework stabilities and thermal properties. In order to understand the thermal stability and structural variation as a function of temperature, thermogravimetric analysis (TGA) was carried out with the single-phase polycrystalline sample of **20-25** between 30-500 °C, under a dinitrogen atmosphere (Figure 3.39a). The TG plot shows that **20** is stable up to 400 °C, after the initial weight loss in the temperature range of 70 to 150 °C which is ascribed to the release of coordinated as well as lattice water molecules. No such weight loss could be seen in case of **21**, before degradation of the framework after 350 °C, indicating its good thermal stability. A similar trend was observed in case of **22**, which also did not show any weight loss before degradation of the framework after 320 °C. In contrast **23-25** exhibits low thermal stabilities, which shows the framework degradation after 250 °C. The initial weight loss before 250 °C can be ascribed to the lattice solvent molecules in **23-25**. Also, since **25** was also tested for its microporous nature by gas adsorption measurements; it is important to check for its thermal robustness and any phase transformation during thermal activation of the framework. Therefore, the thermal robustness and retention of phase purity and crystallinity was investigated by temperature dependent powder X-ray diffraction analysis (Figure 3.39b).

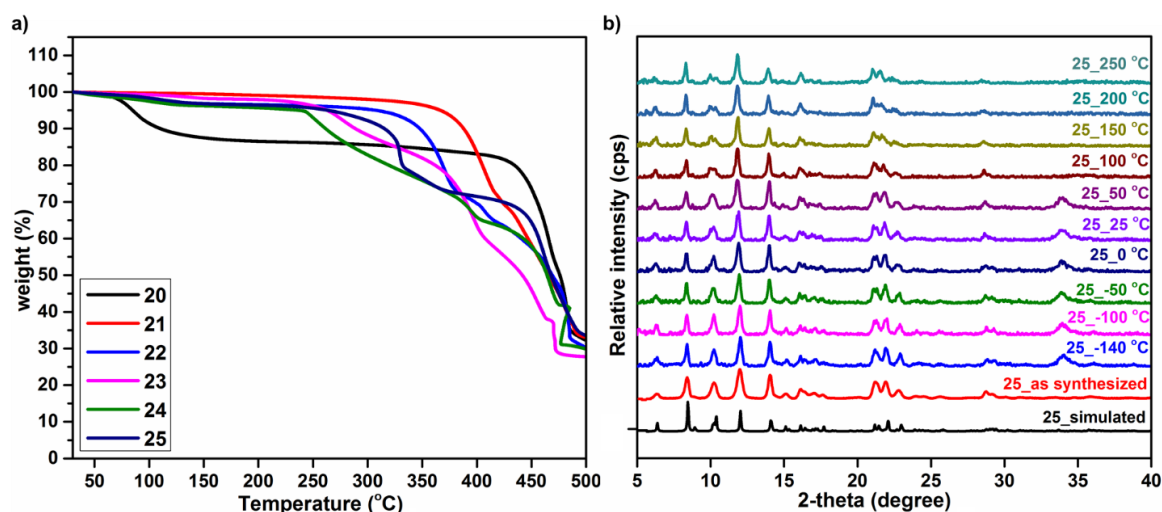


Figure 3.39. (a) Thermogravimetric profile for **20-25** and (b) variable temperature powder X-ray diffraction patterns for **25**, indicating thermal robustness and retention of phase purity and crystallinity upon thermal activation.

Control over dimensionality and framework interpenetration. The phenomenon of framework interpenetration or catenation is very common in pillar-layered coordination polymers. Attempts to increase the dimensionality or pore size enlargement using pillaring strategy usually results in the framework interpenetration. Obtaining a single network (non-interpenetrated) coordination architecture, which is a direct route to the highest porosity, has proven to be problematic in majority of cases, especially when long pillar ligands are used. This phenomenon decreases the accessible space and leads to close packing which imposes a severe limitation on efforts to expand surface area by employing longer pillar ligands for the framework structures. Although interpenetration is not always undesirable; a control over framework interpenetration by systematic ligand design/selection is a necessary to fabricate non-interpenetrated structures. In this study, the effect of ligands geometry on the final architecture has been investigated in a Zn(II)-carboxylate system. With a rigid **bpy** pillar ligand, a 2D polymeric structure has been obtained, where the 1D Zn(II)-carboxylate chains are connected by the pillar ligands to form overall 2D structures. Further the incorporation of longer and functionalized rigid and semi-rigid pillar ligands **4-bpdb** and **4-bpmp**, have resulted in the similar coordination architecture, where the pores are not accessible due to framework interpenetration. The shifting of the coordination site and incorporation of methyl groups into the pillar ligand **3-bpdh**, has resulted in the non-interpenetrated framework, where the methyl group provides enough steric hindrance, which prevents the interpenetration into the framework. On the other hand, the utilization of flexible pillar ligand **bpp** has resulted into the formation of a 3D framework, where the

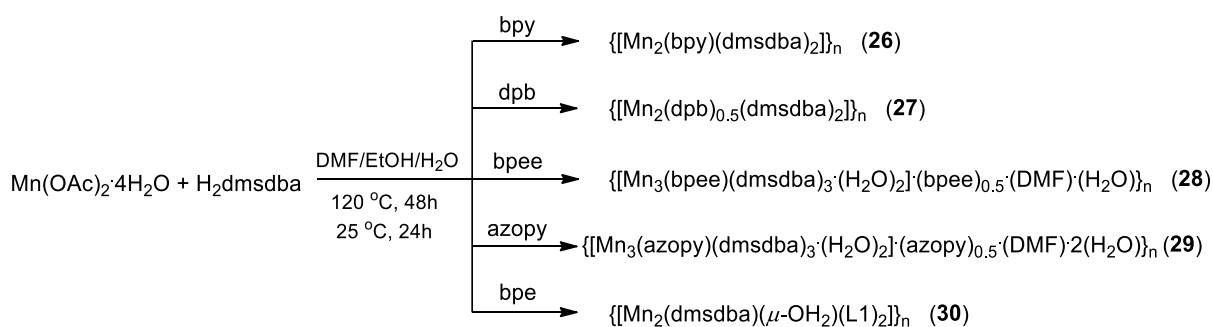
conformational flexibility of methylene chain spacer allows the binding sites to coordinate with the alternate layers. Therefore, the present study illustrates the important role of judicious selection of pillar ligands to control the dimensionality and interpenetration into the pillar-layered coordination architectures.

Mn(II) Chemistry

With numerous examples of Zn(II) and other heavier congeners, there are relatively a couple of examples for coordination architecture with $\text{Mn}_2(\text{COO})_4$ paddle-wheel core as secondary building unit. More importantly, Mn(II) being a paramagnetic center, the coordination polymers with such carboxylato bridged bimetallic SBUs can impart attractive properties due to the close metal-metal interactions. Therefore, in order to design such coordination polymers the pillar layer strategy has been further extended using Mn(II)-**dmsdba**²⁻ metal carboxylate system. In order to understand the effect of ligand geometry (rigidity or flexibility) on the formation of such bimetallic SBUs a set coordination polymer have been synthesized using rigid and flexible pillar ligands.

Solvothermal reaction of manganese acetate, **H₂dmsdba** and different pillar ligands in a solvent mixture of DMF/EtOH/H₂O has resulted in the formation of coordination polymers **26-30** (Scheme 3.15). The molecular formula in each case was established by a combination of elemental analysis, TGA and single crystal X-ray diffraction analysis.

Scheme 3.15. Synthesis of **26-30**.



Single crystal structure analysis. Single crystals for single crystal X-ray studies in each case were obtained from the solvothermal reactions. The studies reveal that **26** is a neutral polymer with centrosymmetrical tetracarboxylato bridged dimanganese repeat units. The dimetal repeat unit of **26** is similar to the repeat unit in **21**. The Mn...Mn distance is 3.005 Å and does not change upon cooling down to 100 K [2.989 Å]. Each Mn(II) center in dimanganese repeat unit lies in a distorted square-pyramidal coordination environment formed by four O atoms of four carboxylate groups of four different **dmsdba**²⁻ linkers, while

the apical position is occupied by the N atom of the pyridyl group **bpy** pillar ligand. As shown in Figure 3.40a, the asymmetric unit contains one Mn(II), one **dmsdba**²⁻ and one half of the pillar ligand **bpy**, which further extends to give the overall 2D framework (Figure 3.40b) similar to **21**. Both **21** and **26** are found to be isostructural. Further the two-fold interpenetration into the 2D sheets is similar to what was observed for **21**, which can be easily seen in the simplified node and linker representation and space fill representation for **26** (Figure 3.40c and d).

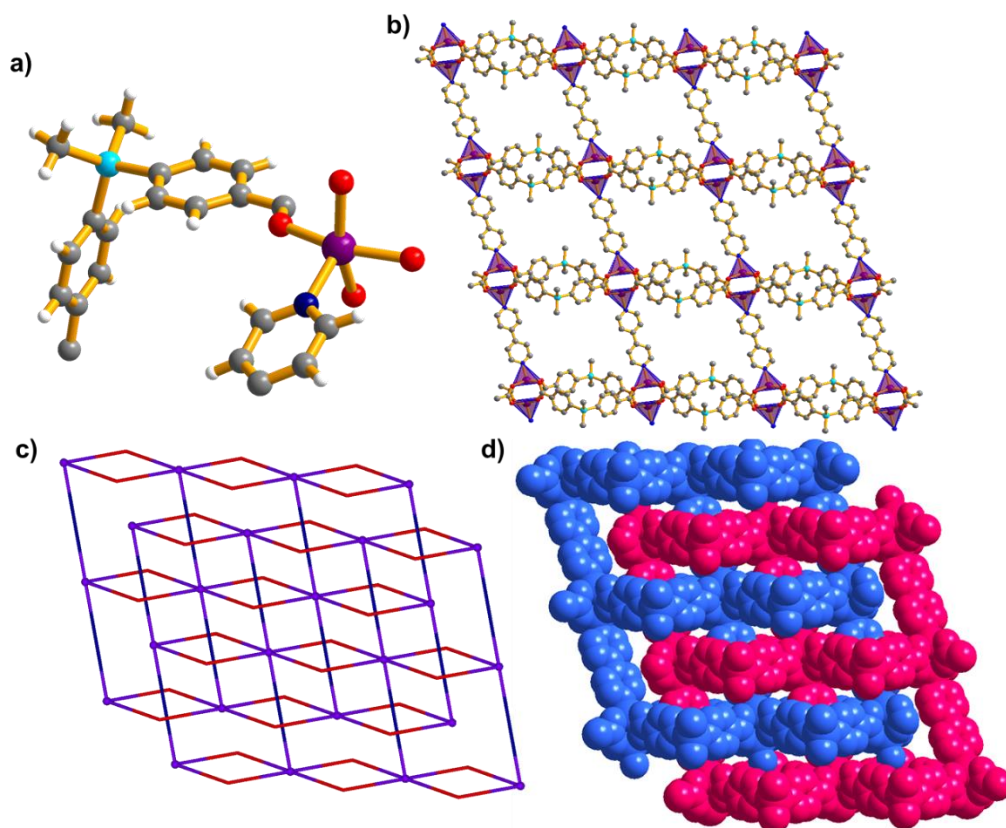


Figure 3.40. Structure description for **26**; (a) asymmetric unit in **26**, (b) perspective view of an overall 2D framework containing tetracarboxylato bridged dimanganese paddle wheel core SBUs and (c and d) simplified node and linker representation and space fill representation showing two-fold interpenetration into the framework.

The τ parameter for five coordinated Mn(II) center is found to be 0.025 for **26**. While the average Mn-O distance is 2.127 Å and the Mn-N bond length is 2.156 Å. Prominent distortions around the Mn(II) center are evident from the bond angles as well as the distance (2.215 Å) between the O atoms of the bridging carboxylate groups. Furthermore, the N-Mn-Mn angle is 156.5(2)° showing a large deviation from linearity. In the only other polymeric compound with the paddlewheel core containing the flexible neutral ligand 1,2-bis(4-pyridyl)ethane (**bpe**)²⁷⁷ compared to the rigid **bpy** linker in **26**, no such deviation is observed. Interestingly, a similar Mn···Mn distance (3.058 Å) observed in the **bpe**

example²⁷⁷ has been termed as a single bond. However, no magnetic measurements were carried out for this example. As it will be evident from further discussion below, the Mn···Mn distance in this example is also indicative of having no metal–metal bond (*vide infra*). Compared to the Cu···Cu distance of 2.64 Å in the dicopper system^{278,280} with no metal–metal bond where nine electrons are available per copper center, the Mn···Mn distance in **27** as well as through bridge super-exchange interactions as observed from the magnetic susceptibility measurements (*vide infra*) can be used to understand the extent of metal–metal bonding. Additionally, the theoretical calculations of such a core reported earlier²⁸⁰ for the anhydrous manganese(II) formate has the same Mn···Mn distance but there was no mentioning of metal–metal bonding in that complex; on the other hand, based on one of the reports²⁸¹ the Mn···Mn distance obtained for the +3/+3 system is 3.04 Å as well. Furthermore, in [Mn₂(tda)₂(bpy)₂] with a D_{3h} symmetry the metal–metal separation is 3.5 Å.²⁸² The order of the orbitals and the arrangement of the d-electrons in **26** for the prominent distortions around the metal centers, and the metal–metal distance can be understood if the bonding considerations reported earlier for the Mn(I) dimers²⁸³ are used. As described in the examples of Mn(I) dimers where the Mn···Mn distance is about 2.72 Å, the Mn–Mn single bond is mainly formed by the half-filled 4s orbitals of the Mn atoms. This distance in the Mn(I) examples is much shorter than that in Mn₂(CO)₁₀, 2.92 Å,²⁸⁴ where Mn exists in the zero oxidation state. All the crystallographic information pertaining to data collection and structure refinement parameters, selected bond lengths and bond angles are listed in Table A9, A31 and A53, respectively.

The polymeric structure in **27** consists of 2D sheets where the metal carboxylate tetranuclear Mn₄ clusters are pillared by the **dpb** ligand. It crystallizes in a triclinic crystal system with $P\bar{1}$ space group. The asymmetric unit consists two crystallographically independent Mn(II), two **dmsdba**²⁻ one half of the pillar ligand **dpb** and one water molecule coordinated to one of the metal center (Mn1) (Figure 3.41a). Each Mn(II) center lies in a distorted square-pyramidal coordination environment, where the five coordination sites around Mn1 are occupied by three carboxyl oxygen atoms of **dmsdba**²⁻, one oxygen from the coordinated water molecule and one nitrogen atom of the pillar ligand **dpb**. The coordination sites around Mn2 are occupied by five O atoms of carboxylate groups of **dmsdba**²⁻ linker. The two Mn(II) centers are bridged by three carboxylate groups resulting in triscarboxylato bridged dimanganese unit. In addition to this the two Mn2 ions are further bridged by two carboxylate groups resulting in biscarboxylato bridged dimanganese unit, therefore

resulting in an overall tetranuclear Mn_4 cluster as secondary building unit (Figure 3.41b). As shown in the simplified node and linker type representation (Figure 3.41c) for **27**, the tetranuclear Mn_4 clusters, which can be simplified as 4-connected node are further connected by eight dicarboxylate linkers **dmsdba**²⁻ and two pillar ligands **dpb**, resulting in an overall 2D pillar layered framework (Figure 3.41b).

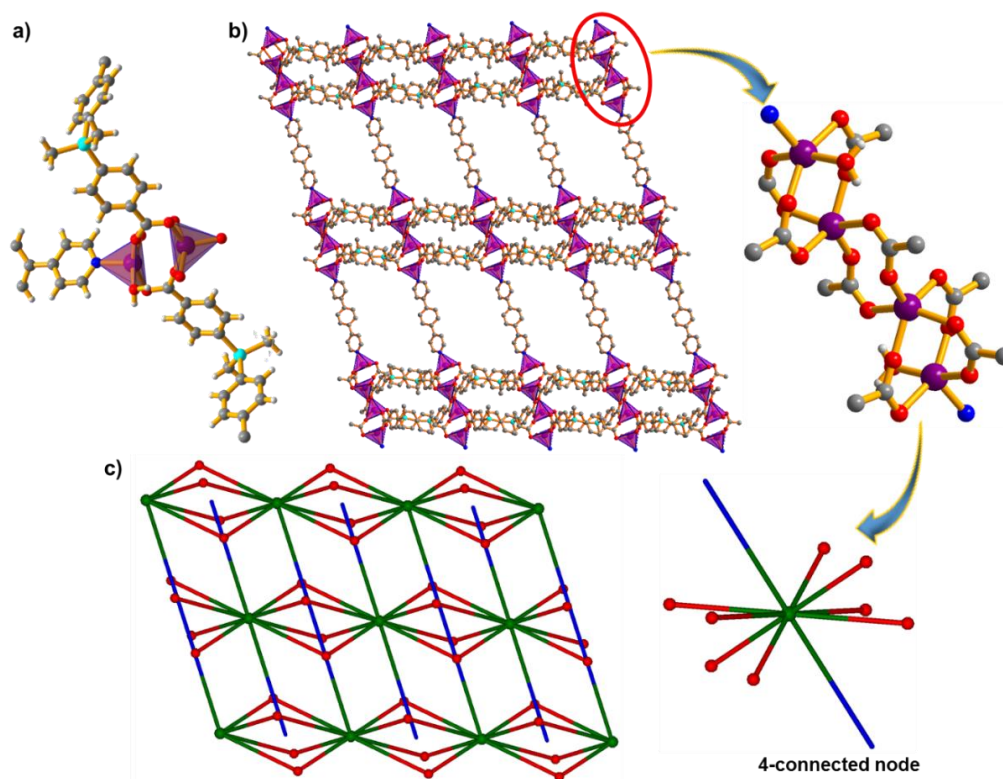


Figure 3.41. Structure description for **27**; (a) asymmetric unit and coordination around the Mn(II) centers in **27**, (b) perspective view of an overall 2D framework containing bis and triscarboxylato bridged dimanganese cores and (c) simplified node and linker representation showing 4-connected uninodal sql topology, where tetranuclear manganese cluster is simplified as 4-connected node.

Further examination of the simplified node and linker representation reveal that the framework exhibits the same 4-connected uni-nodal net, sql (Shubnikov tetragonal plane net) topology, with Schläfli point symbol $\{4^4.6^2\}$ as obtained for **21-24** and **26**, respectively. The τ parameter²⁷⁶ for five coordinate Mn1 and Mn2 is found to be 0.190 and 0.255, respectively. While the average Mn-O distance is 2.140 Å, the Mn-N bond length is 2.170 Å. The Mn \cdots Mn distance in triscarboxylato bridged (Mn1 \cdots Mn2) and biscarboxylato bridged (Mn2 \cdots Mn2) core is found to be 3.333 Å and 4.309 Å, respectively. Prominent distortions from the regular geometries around the metal centers are evident from the bond angle values ranging from 82.4° to 163.4° for Mn1 and 79.73° to 152.63° for Mn2, respectively. All the crystallographic information pertaining to data collection and structure

refinement parameters, selected bond lengths and bond angles are listed in Table A9, A31 and A53, respectively.

Single crystal analysis of **28** and **29** reveals that both are iso-structural and forms a 2D polymeric structure. Both crystallizes in monoclinic crystal system with $P2_1/n$ space group. The asymmetric unit in each case consists of three crystallographically independent Mn(II), three **dmsdba**²⁻ one and half of the pillar ligand **bpee** in case of **28** and **azopy** in case of **29**, where half of the pillar ligand is non-coordinating and occupies the lattice position in both cases along with one water and one DMF molecule. In addition, one of the Mn(II) consists of two coordinated water molecules in each case. The geometry around the metal centers (Mn1 and Mn2 in each case) is distorted square pyramidal whereas Mn3 is in a distorted octahedral geometry.

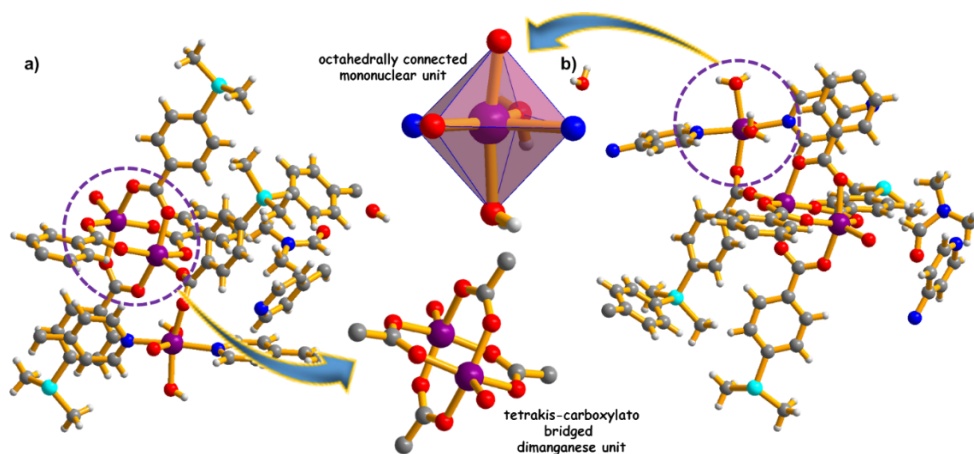


Figure 3.42. Asymmetric unit and coordination environment around the metal centers in (a) **28** and (b) **29**.

The five coordination sites around Mn1 and Mn2 are occupied by five carboxyl oxygen atoms of **dmsdba**²⁻ whereas, the six coordination sites around Mn3 are occupied by two carboxyl oxygen atoms, two nitrogen atoms from the pillar ligands **bpee** (in **28**) or **azopy** (in **29**) and two oxygen atoms from coordinated water molecules. The asymmetric unit and coordination environment around the metal center in **28** and **29** are shown in Figure 3.42. The τ parameter²⁷⁶ for five coordinated Mn1 and Mn2 is found to be 0.038 and 0.011 in **28** and 0.003 and 0.033 in **29**, respectively. The Mn-O bond lengths in lies in the range of 2.000 Å to 2.262 Å for **28** and 1.997 Å to 2.259 Å for **29**, whereas the average Mn-N bond length is 2.248 Å in **28** and 2.271 Å in **29**, respectively. The Mn...Mn distance in tetrakis-carboxylato bridged (Mn1...Mn2) dimanganese core is found to be 3.029 Å and 3.033 Å, in **28** and **29**, respectively. Prominent distortions from the regular geometries around the metal centers are evident from the bond angle values. All the crystallographic

information pertaining to data collection and structure refinement parameters, selected bond lengths and bond angles are listed in Table A10, A32 and A54, respectively.

The asymmetric unit in both the case is further extended to form an overall 2D polymeric structure (Figure 3.43). More insight into the formation of 2D sheet structure reveals that the dinuclear and mononuclear units are arranged in an alternate fashion where the carboxylate group occupying the axial position of the dinuclear core is acts as bridge between 1D metal carboxylate chains to give the 2D structure, whereas the ligand bpee and azopy in **28** and **29** does not act as pillar ligands to extend the dimensionality of the framework.

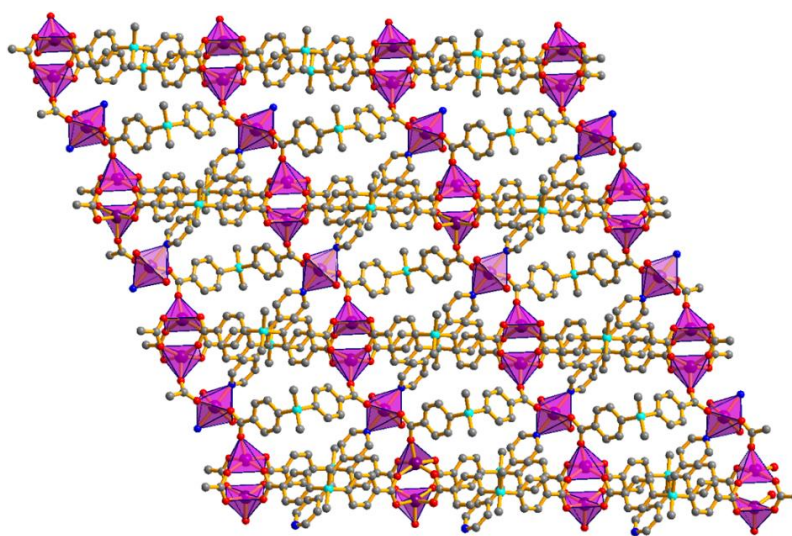


Figure 3.43. Perspective view of the overall 2D structure in **28** which is isostructural to the framework in **29**, where the N-donor bpee ligand has been replaced with N-donor azopy ligand.

The use of flexible ligand, bpe, in **30** has resulted in the formation of a 3D coordination architecture. It crystallizes in an orthorhombic crystal system with space group *Pbcn*. The asymmetric unit in contains one Mn(II), one **dmsdba**²⁻ one half of the pillar ligand **bpe** and one coordinated water molecules which is bridged between two Mn(II) centers resulting in the formation of μ -aqua bis-carboxylato bridged dimanganese SBU, which are linked through the fully deprotonated **dmsdba**²⁻ and neutral **bpe** ligand to form the overall 3D structure (Figure 3.44). The two Mn(II) centers of the dinuclear core are bridged by two carboxylate groups in a syn-syn coordination mode and an oxygen atom from a water molecule. The distorted octahedral coordination environment around the metal center is composed of four oxygen atoms of the carboxylate group, which occupies the equatorial positions of the octahedral geometry and two axial positions are occupied by the oxygen atom of the coordinated water molecule and nitrogen atom of the **bpe** ligand. The value of

Mn···Mn separation in μ -aqua bis-carboxylato bridged dimanganese core is found to be 3.772 Å, which is similar to the Mn···Mn distance of 3.739 Å²⁸⁵ and 3.78 Å,²⁸⁶ but is higher

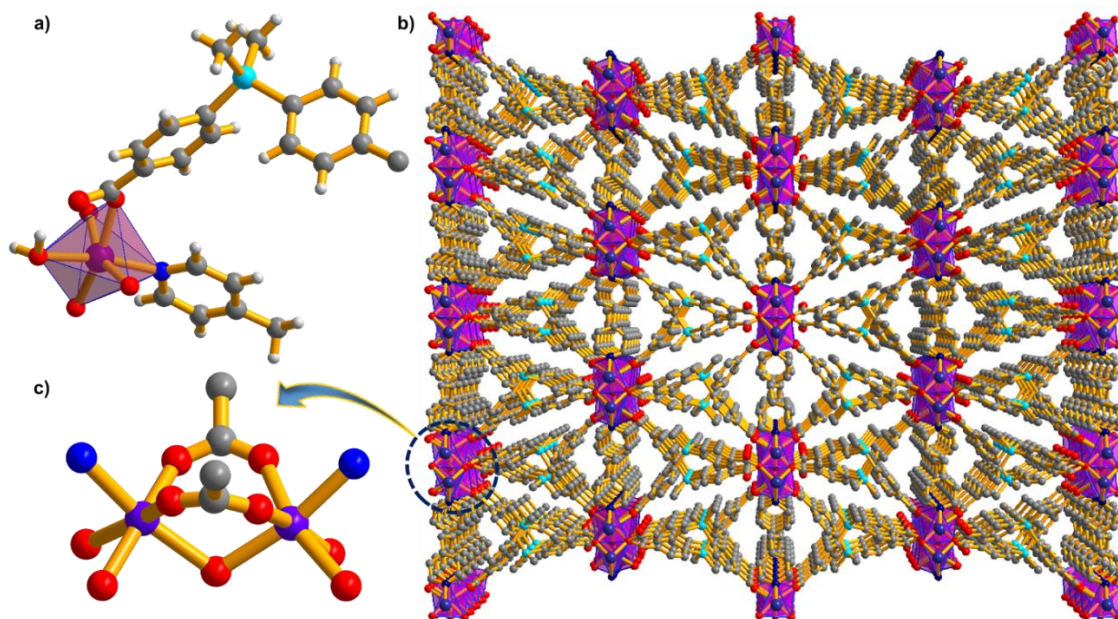


Figure 3.44. Structural description for **31**; (a) Asymmetric unit and coordination environment around Mn(II), (b) perspective view of the overall 3D structure in **31** and (c) representation of the μ -aqua bis-carboxylato bridged dimanganese core in **31**.

than the bond distance values (3.540 Å, 3.581 Å, 3.595 Å, 3.614 Å, 3.621 Å and 3.635 Å)^{282,287–290} reported for this kind of examples. The lengthening of the Mn···Mn separation in **30** with respect to that of the other examples can be attributed due to the longer values of the metal-to-aqua bonds (2.313 Å) in **30**. The average Mn-O_{carboxylate} bond length is found to be 2.153 Å and the Mn-N bond length is 2.273 Å. All the crystallographic information pertaining to data collection and structure refinement parameters, selected bond lengths and bond angles are listed in Table A10, A32 and A54, respectively. There are relatively a very few examples of coordination polymers with this type of core and the coordination polymers with this type of SBUs exhibits strong antiferromagnetic coupling in their magnetic susceptibility measurements indicating strong metal-metal interactions via small aqua and carboxylate bridges. Such core types have also have been studied, primarily as mimics of the active sites in many important enzymes.

FTIR and PXRD analysis. FTIR spectra of **26–30** were recorded in the solid state at room temperature as KBr pellets. The characteristic peaks due to asymmetric (ν_{asym}) stretching vibrations of the carboxylates in all cases were observed in the range of 1597–1619 cm^{-1} and symmetric stretching vibrations (ν_{sym}) in the range of 1399–1417 cm^{-1} . The difference in the asymmetric and symmetric stretching vibrations $\Delta\nu$ ($\nu_{\text{asym}} - \nu_{\text{sym}}$) in the range of 187–

209 cm^{-1} confirms its bridging binding mode.²⁵¹ Further, the prominent shift in the asymmetric and symmetric stretching frequencies of the $-\text{C}=\text{O}$ group in **26-30** from free **H₂dmsdba** (1690 cm^{-1} and 1416 cm^{-1}) indicates strong binding of the carboxylates to the metal center. In order to confirm the bulk phase purity and crystallinity of the as-synthesized **26-30**, powder X-ray diffraction patterns were recorded at room temperature for the as-synthesized samples of **26-30**. The experimental powder X-ray diffraction patterns for **26-30** confirm their crystallinity and the comparison with those simulated from single-crystal data, indicating that all were isolated as single-phase polycrystalline materials (Figure 3.45). **Framework stabilities and thermal properties.** In order to understand the thermal stability and structural variation as a function of temperature, thermogravimetric analysis (TGA) was carried out with the single-phase polycrystalline sample of **26-30** between 30-500 $^{\circ}\text{C}$, under a dinitrogen atmosphere (Figure 3.46a). The thermogravimetric profiles corroborate with the structures obtained from the single crystal analysis. No weight loss was observed until 250 $^{\circ}\text{C}$, except in the case of **28** and **29**, which exhibits weight loss in the temperature range of 50-120 $^{\circ}\text{C}$, which can be ascribed due to the loss of lattice solvents and neutral N-donor ligands present in the crystal lattice. After which no weight loss was observed up to 200 $^{\circ}\text{C}$ in case of **28**, and 250 $^{\circ}\text{C}$ in case of **29**.

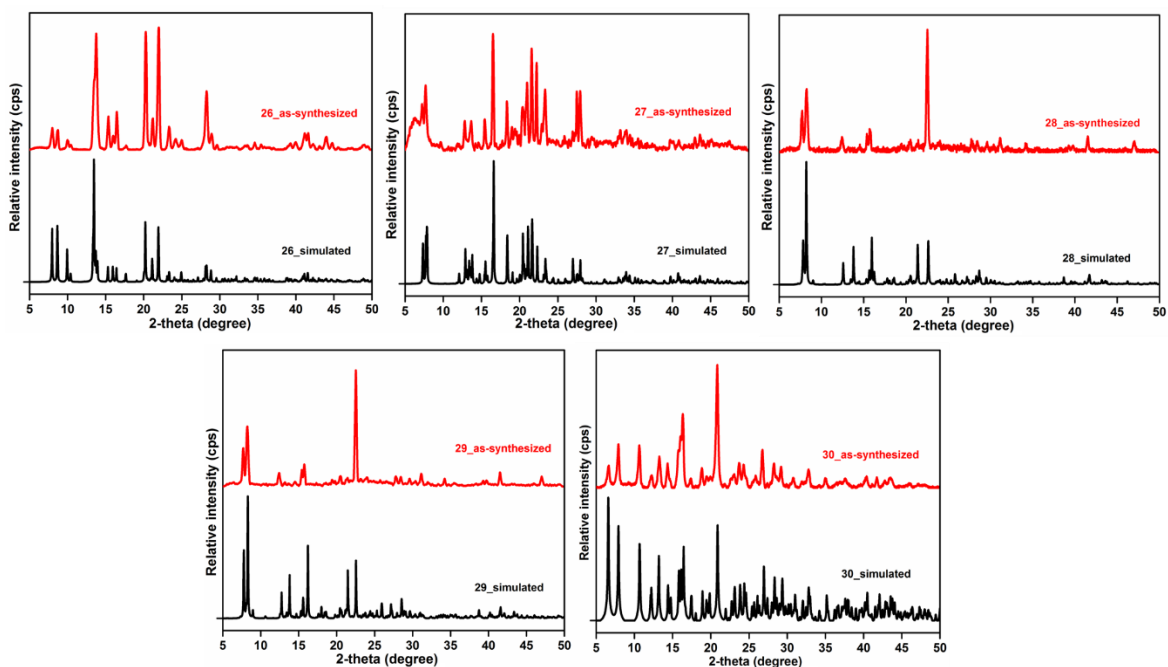


Figure 3.45. Powder X-ray diffraction (PXRD) pattern of as-synthesized samples of **26-30**, compared with the simulated powder pattern obtained from the single crystal data.

However, **26**, **27** and **30**, exhibits very good stability as can be seen in their thermogravimetric profile, the compound **26** shows an extraordinary thermal stability up to

340 °C as no weight loss can be seen in the TG profile. The high thermal stability and robustness of **26** was further investigated by temperature dependent powder X-ray diffraction analysis. As shown in Figure 3.46b, there was no change in the PXRD pattern of **26** even up to 300 °C. Thus, the variable temperature PXRD data further supports the thermal robustness of **26** and also indicates the retention of crystallinity and phase purity at higher temperatures.

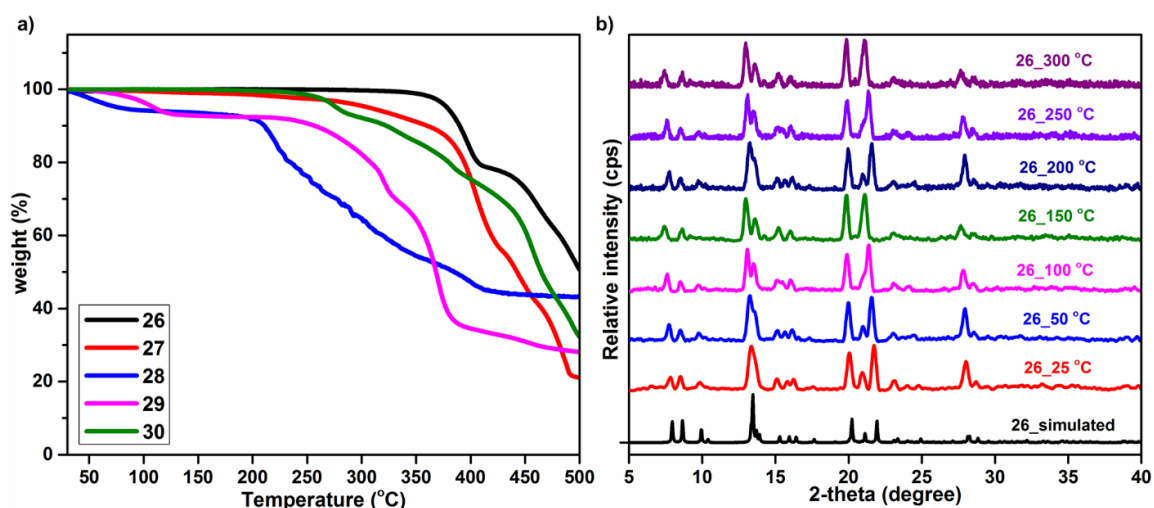


Figure 3.46. (a) Thermogravimetric profile for **26-30** and (b) variable temperature powder X-ray diffraction patterns for **26**, indicating thermal robustness and retention of phase purity and crystallinity up to 300 °C.

Magnetic properties. As this kind of compounds with carboxylato bridged diamanganese core are known to exhibit interesting magnetic properties, the magnetic susceptibility data of a polycrystalline powder sample of **26** was measured in the temperature range of 2–300 K. The effective magnetic moment per Mn atom is 5.13 μ_B at 300 K indicating that the Mn(II) ions are in a high spin state. However, this value is much smaller than the expected spin-only value for the non-interacting Mn(II) ions with five unpaired electrons each. This implies that an antiferromagnetic interaction between the metal centers is present. This is confirmed with the fact that the value of χT (6.58 $\text{cm}^3 \text{K}$ per Mn dimer mol at 300 K) decreases continuously down to 0.10 $\text{cm}^3 \text{K}$ per Mn dimer mol at 2 K (Figure 3.47a). Furthermore, it points to an $S = 0$ coupled ground state at 0 K for the dimeric subunit in 1. A good fit of the experimental data to $S = 5/2$ (per Mn) with a Bleaney-Bowers-like equation²⁹¹ yielded a magnetic coupling constant $2J = -12.4 \text{ cm}^{-1}$ with $g = 2.014$ ($H = -2JS_1S_2$). The $S = 0, 1,$ and 2 coupled states are the ones thermally populated up to 300 K. This value of $2J$ is similar to what were observed for discrete $[\text{Mn}_2^{\text{II}} (\mu\text{-O}_2\text{CR})_4\text{L}_2]$ complexes, where $R = (\text{C}_6\text{H}_5)_2\text{CH}$ or $(\text{C}_6\text{H}_5)_2\text{C}(\text{CH}_3)$ and $L = \text{quinoline}$,²⁹² and $R = (\text{CH}_3)_3\text{C}$

and L = 2,6-diaminopyridine;²⁹³ for $[\text{Mn}_2(\text{tda})_2(\text{bpy})_2]$,²⁸² a value of -8.2 cm^{-1} was observed due to a much longer Mn···Mn distance. On the other hand, the calculated value²⁷⁶ for anhydrous manganese(II) formate as the model was about -20.0 cm^{-1} with an Mn···Mn distance similar to that for **26**. It should be noted that the antiferromagnetic interactions in other dimanganese units with syn–syn carboxylates²⁹⁴ are much weaker as compared to the tetrakis-(carboxylato)-bridged cores; furthermore, this study adds to the limited number of examples in this category, only three out of the six compounds mentioned above have been studied for their magnetic behavior. In order to understand the magnetic properties of **26**, one can consider (a) the extensively studied d^9 - d^9 dicopper complexes with similar core structures that feature through bridge super exchange pathways,^{278,279} (b) the d^7 - d^7 dicobalt system where the magnetism has been interpreted in terms of weak metal–metal interactions between the two Co(II) ions based on the observation of temperature-dependence of the metal-metal distance,²⁹⁵ and (c) more importantly, broadly similar

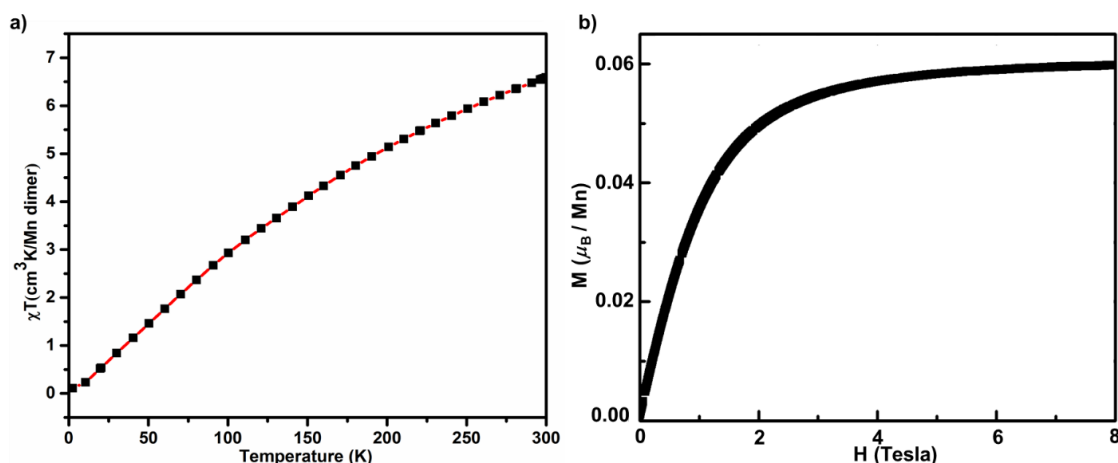


Figure 3.47. (a) Plot of χT vs. T for **26**; the solid line is the best fit to the experimental data and (b) Magnetization M per Mn(II) ion versus field H at 2 K for **26**.

magnetic behavior (but with much higher antiferromagnetic coupling constants, -40 to -55 cm^{-1}) observed for the dimanganese(I) systems²⁸³ where a single bond between the metal centers is found to be present from the pairing of the $4S^1$ electrons leaving the d^5 high spin configurations similar to the Mn(II) ions in **26** and other complexes. In the case of **26**, there is no change in the metal–metal interaction due to change in temperature indicating a through-bridge pathway (not through the metal–metal vector). The magnetization (M) versus field (H) data measured at 2 K for **26** is shown in Figure 3.47b. The saturation value M_s at the highest field observed for it is negligible compared to the expected value of about $5\mu_B$, probably due to an unavoidable minor paramagnetic impurity, and thus confirms further the correct description of the antiferromagnetic coupling in **26**.

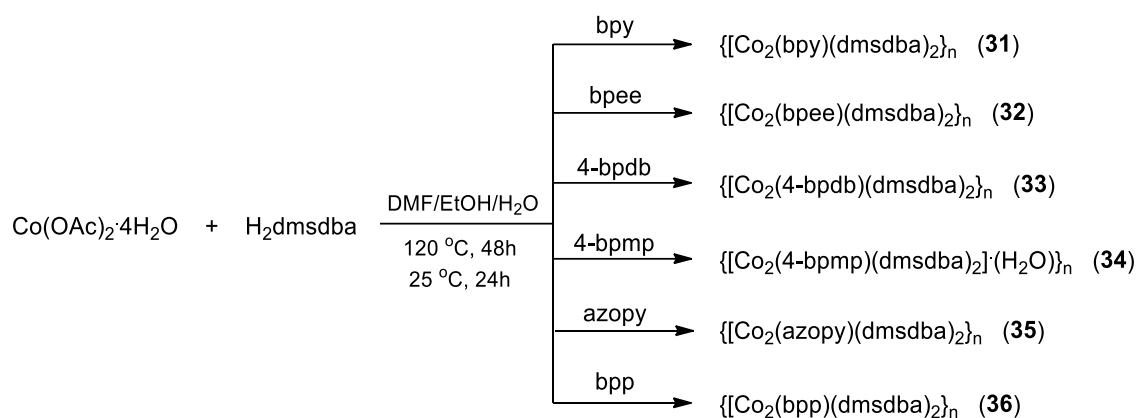
Effect of pillar ligands. In this study, the neutral N-donor pillar ligands with varied length and rigid/flexible geometries were used to show any effect on the formation of different dinuclear clusters of manganese in the Mn(II)-**dmsdba**²⁻ system under similar reaction conditions. In case of rigid **bpy** ligand a 2D pillar-layered framework with tetrakis(carboxylato) bridged dimanganese paddle wheel core as SBU was obtained. Extending the length of the pillar ligand by a rigid phenyl spacer has resulted in the formation of similar 2D interpenetrated framework with same topology but different SBU. Instead of a tetrakis(carboxylato) bridged dimanganese paddle wheel core as SBU in **26**, a tetra metallic Mn₄ cluster with bis and tris carboxylato bridged dimanganese subunits was obtained as SBU in case of **27**. Further imparting semi rigid pillar ligands (**bpee** or **azopy**) into the Mn(II)-**dmsdba**²⁻ system has resulted into the formation of a 2D framework with two different kind to SBUs, where two kind of SBUs (a tetrakis(carboxylato) bridged dimanganese paddle wheel subunit and a mononuclear subunit) are bridged to each other in an alternate fashion by the carboxylate linkers **dmsdba**²⁻. Both the compound **28** and **29** are isostructural having same asymmetric unit and coordination environment around the metal centers. Incorporation of a comparatively flexible pillar ligand **bpe** has resulted in an entirely different architecture. The structure of **29**, consists of a 3D non-interpenetrated framework with μ -aqua bis(carboxylato) bridged dimanganese core as SBU. However, in all cases the carboxylate linker **dmsdba**²⁻ binds to the metal center in a syn–syn fashion to form the dimetallic repeat units; the use of different pillar ligands with varied length and geometries has resulted in the formation of different kind of such dimetallic repeat units with different number and nature of the bridging units in between the two metal centers. The nature and number of such bridging units are of particular interest while studying close metal-metal interactions in such type of systems. Therefore, the role of the ligand geometries on the formation of such coordination polymers with bis, tris or tetrakis carboxylato bridged dimanganese repeat units is clearly demonstrated.

Co(II) Chemistry

In order to generalize the pillaring strategy on metal-**dmsdba**²⁻ system, the chemistry has been further extended on Co(II)-**dmsdba**²⁻ system. A set of coordination polymers **31-36** have been synthesized using different N-donor pillar ligands varying in their lengths, functionalities and conformational flexibility/rigidity of their structures. Solvothermal reaction of cobalt acetate tetrahydrate, **H₂dmsdba** and different pillar ligands in a solvent

mixture of DMF/EtOH/H₂O has resulted in the formation of coordination polymers **31-36** (Scheme 3.16).

Scheme 3.16. Synthesis of **31-36**.



In most of the cases (**32-36**) the structures have been established by their single crystal X-ray diffraction analysis and in case of **31**, where the single crystals could not be obtained the structures have been established by the combination of different analytical techniques. All the coordination polymers have been well characterized by FTIR, PXRD, TGA and elemental analysis. The molecular formula in each case was established by a combination of elemental analysis, TGA and single crystal X-ray diffraction analysis.

Single crystal structure analysis. Single crystals suitable for single crystal X-ray studies in each case were obtained from the solvothermal reactions. The study reveals that, **32-34** forms an isostructural 2D framework with tetrakis-carboxylato bridged dimetallic core as SBU, where the metal carboxylate 1D chains are pillared by the pillar ligands **bpee**, or **4-bpdb** or **4-bpmp** to form an overall 2D structure (Figure 3.48). The compounds crystallize in a triclinic crystal system with $P\bar{1}$ space group and the asymmetric unit in each case consists of two Co(II) atoms, two carboxylate linker **dmsdba**²⁻, and one pillar ligand, except in case of **34**, where an additional water molecule is also present in the crystal lattice. The carboxylate linker is fully deprotonated and binds to the metal atoms in a syn-syn bidentate bridging manner forming the tetrakis-carboxylato bridged dimetallic SBU. Each metal atom is in an NO₄ square pyramidal coordination environment, where four carboxyl oxygen atoms from four different **dmsdba**²⁻ occupies the four equatorial positions of the square pyramidal geometry and the apical position is occupied by the nitrogen atom of the N-donor pillar ligands. The metal to metal distance (Co...Co) in each case (2.873 Å in **32**, 2.818 Å in **33** and 2.834 Å in **34**) is shorter than those found in discrete and polymeric paddle wheel complexes but longer than the Co-Co single bond (2.3 Å) reported in dicobalt

tetrakis(formamidinate) complexes.²⁹⁶ The τ parameter for five coordinate Co1 and Co2 is found to be 0.061 and 0.060 in **32**, 0.014 and 0.022 in **33**, and 0.038 and 0.005 in **34**, respectively. The average Co-O bond distance in **32-34** lies in the range of 2.065 Å to 2.130 Å and Co-N bond distance lies in the range of 1.946 Å to 2.068 Å. Prominent distortions around the Co(II) center are evident from the bond angles as well as the distance (2.225 Å - 2.274 Å) between the O atoms of the bridging carboxylate groups. Upon simplification of the structures of **32-34** in the node and linker type representation, the tetrakis(carboxylato) bridged paddle wheel SBU can be considered as a four connecting node and the carboxylate linker and the pillar ligands can be considered as bent and linear linkers respectively. Further analysis of the node and linker type representation reveal that all three coordination polymers exhibit 4-connected uni-nodal net, sql (Shubnikov tetragonal plane net) topology, with Schläfli point symbol $\{4^4.6^2\}$, which is the same network topology as obtained for **21-24** and **26-27**, respectively. As shown in Figure 3.48 in all cases the structure exhibits 2-fold interpenetration into the framework. All the crystallographic information pertaining to data collection and structure refinement parameters, selected bond lengths and bond angles are listed in Table A11, A33 and A55, respectively.

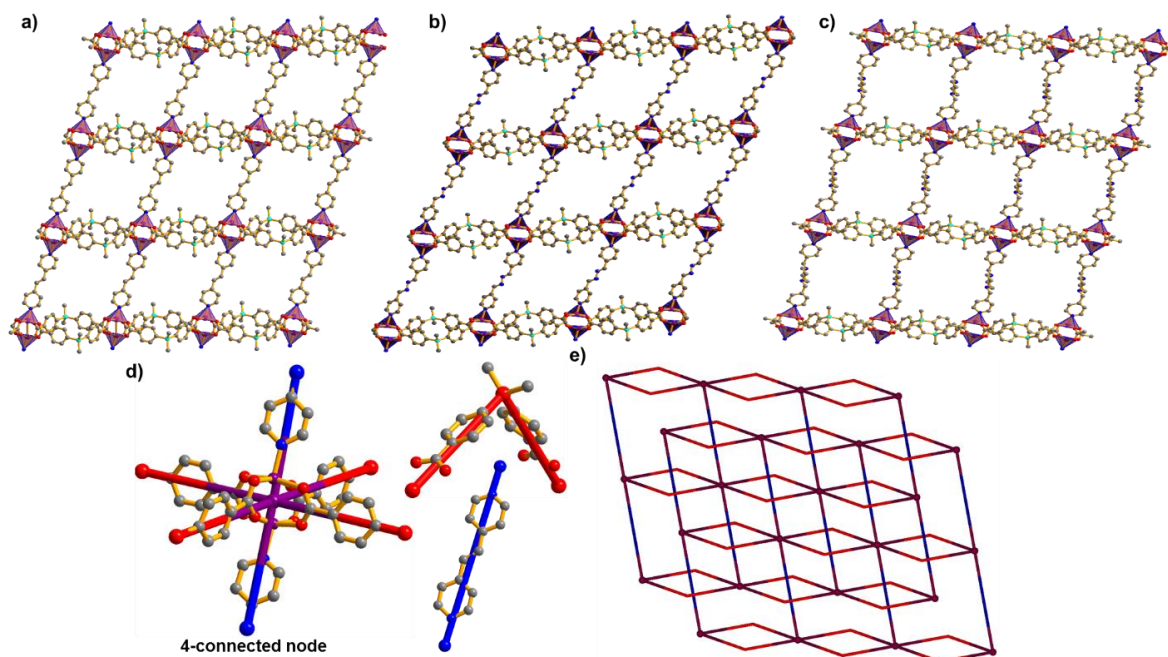


Figure 3.48. Structure description for **32-34**; (a,b and c) shows the 2D sheet structures in **32**, **33** and **34**, respectively, (d) simplified representation of the paddle wheel SBU, dmsdba^{2-} and pillar ligands as 4-connected node and bent and linear linkers, respectively and (e) an overall node and linker type representation 4-connected sql topology with 2-fold interpenetration into the frameworks.

Single crystal structural analysis for **35** and **36** reveals that both forms a 3D polymeric structure (Figure 3.49). The compound **35** crystallizes in a triclinic $P\bar{1}$ space group whereas

the compound **36** crystallizes in a monoclinic crystal system with $C2/c$ space group. The asymmetric unit in **35** consists of four Co(II) atoms, four carboxylate linker **dmsdba**²⁻, and two pillar ligand (**azopy**), whereas in case of **36**, it consists of two Co(II) atoms, two carboxylate linker **dmsdba**²⁻, and one pillar ligand (**bpp**). In both cases, the carboxylate linker binds to the metal atoms in a syn-syn bidentate bridging manner forming the same tetrakis(carboxylato) bridged dimetallic SBU as obtained in case of **32-34**. Each metal atom is also in the same NO₄ square pyramidal coordination environment, where four carboxyl oxygen atoms from four different **dmsdba**²⁻ occupies the four equatorial positions of the square pyramidal geometry and the apical position is occupied by the nitrogen atom of the N-donor pillar ligands (**azopy** or **bpp**), with only difference that the unlike **32-34**, **35** and **36** forms an overall 3D structure, which can be attributed due to the conformational flexibilities of the **azopy** or **bpp** pillar ligands. The metal to metal distance (Co...Co) in each case is similar to the distance observed in **32-34**. In addition to that all other structural parameters for tetrakis(carboxylato) bridged paddle wheel SBU like bond lengths, bond angles and τ values are also similar to the values observed in **32-34**.

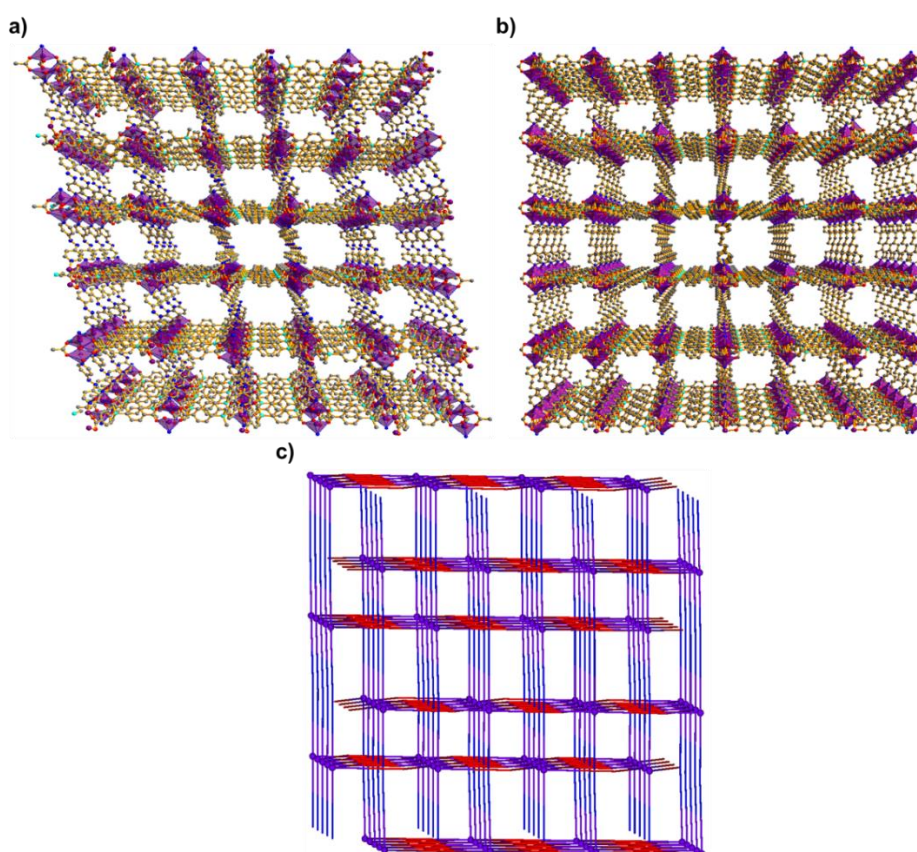


Figure 3.49. structure description for **35** and **36**; (a and b) Perspective view of the 3D structure obtained in case of **35** and **36**, respectively and (c) simplified node and linker type representation for **35** and **36** exhibiting 4-connected uni-nodal net sqc5 topology with 2-fold interpenetration into the frameworks.

All the crystallographic information pertaining to data collection and structure refinement parameters, selected bond lengths and bond angles are listed in Table A12, A34 and A56, respectively. As shown in Figure 3.49, the rather intricate 2-fold interpenetrated 3D structures of **35** and **36** can be simplified in the form of node and linker type representation, where paddle wheel SBU, and the carboxylate linker and pillar ligands can be considered as a 4-connected node and a bent and linear linkers, respectively to form an overall 3D structure which exhibits a 4-connected uni-nodal net sqc5, cadmium sulphate type topology as determined by the TOPOS²⁷⁴ program. The topological structural type observed is identical to the structural type observed for **25**.

FTIR and PXRD analysis. FTIR spectra of **31-36** were recorded in the solid state at room temperature as KBr pellets. The characteristic peaks due to asymmetric (ν_{asym}) and symmetric (ν_{sym}) stretching vibrations of the carboxylates in all cases shows significant shift from the asymmetric and symmetric -C=O stretch for free **H₂dmsdba** (1690 cm^{-1} and 1416 cm^{-1}). This indicates a strong binding of the carboxylates to the metal center in all cases. In addition, the difference in their ν values ($\Delta\nu = \nu_{\text{asym}} - \nu_{\text{sym}}$) further supports the syn-syn bridging bidentate binding of the carboxylates to the metal centers²⁵¹ as obtained from their single crystal structure analysis. The peaks due to asymmetric (ν_{asym}) and symmetric (ν_{sym}) stretching vibrations of the carboxylates for **31-36** were obtained at 1609 cm^{-1} and 1411 cm^{-1} , 1610 cm^{-1} and 1411 cm^{-1} , 1597 cm^{-1} and 1399 cm^{-1} , 1616 cm^{-1} and 1410 cm^{-1} , 1609 cm^{-1} and 1411 cm^{-1} and 1617 cm^{-1} and 1409 cm^{-1} , respectively. In order to confirm the bulk phase purity and crystallinity of the as-synthesized **31-36**, powder X-ray diffraction patterns were recorded at room temperature for the as-synthesized samples of **26-30**. The experimental powder X-ray diffraction patterns for **31-36** confirm their crystallinity and the comparison with those simulated from single-crystal data, indicating that all were isolated as single-phase polycrystalline materials (Figure 3.50). In addition, the experimental powder patterns of **31** is exactly similar to the simulated powder pattern of **26**, indicating the iso-structural relationship of **26** and **31**.

Framework stabilities and thermal properties. In order to understand the thermal stability and structural variation as a function of temperature, thermogravimetric analysis (TGA) was carried out with the single-phase polycrystalline sample of **31-36** between 30-500 °C, under a dinitrogen atmosphere (Figure 3.51). The thermogravimetric profiles corroborate with the structures obtained from the single crystal analysis. Compounds **32**, **34** and **35** exhibits moderate thermal stabilities up to 220 °C, whereas the compounds **31**, **33**

and **36** exhibits very high thermal stability. The thermogravimetric profile of **31** shows its extraordinary thermal stability as no weight loss was observed up to 340 °C; which is similar to the thermogravimetric profile for **26**. Therefore, in addition to the similar powder X-ray diffraction pattern in both the cases, the similar TG profile further supports the similar interpenetrated frameworks in **26** and **31**.

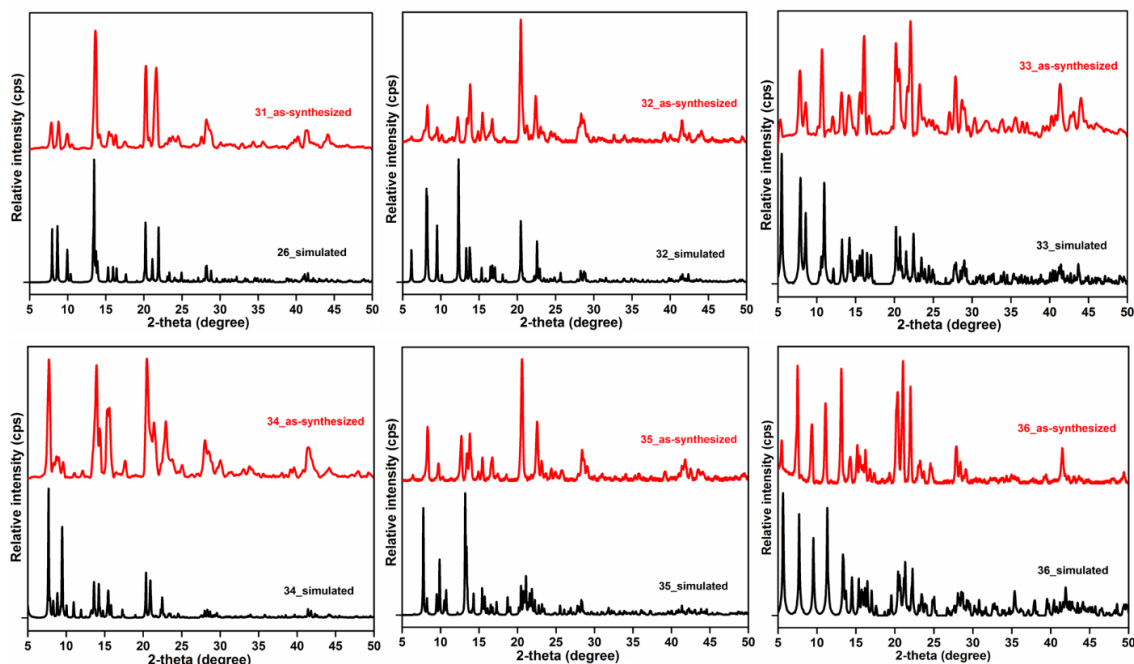


Figure 3.50. Powder X-ray diffraction (PXRD) pattern of as-synthesized samples of **31** and **32-36**, compared with the simulated powder pattern obtained from the single crystal data of **26** and **32-36**, respectively.

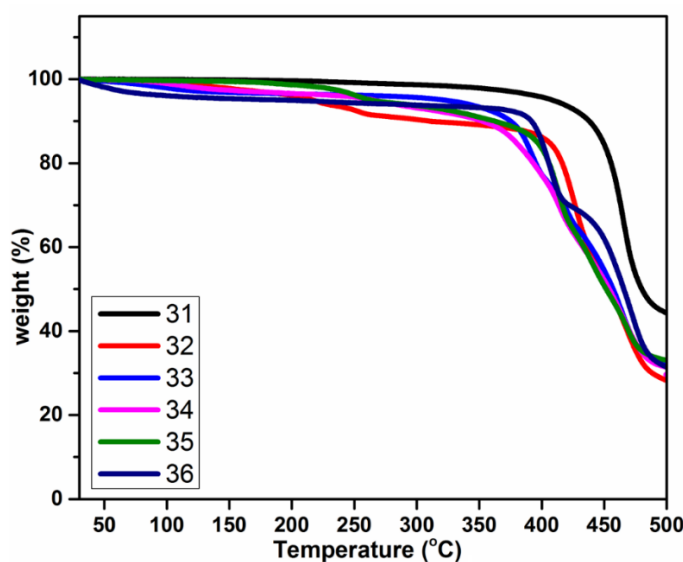


Figure 3.51. Thermogravimetric profile for **31-36**.

The thermogravimetric profiles of **33** and **36** shows that both the compounds are stable up to 320 °C and 370 °C, respectively as no weight loss can be seen in the thermogravimetric

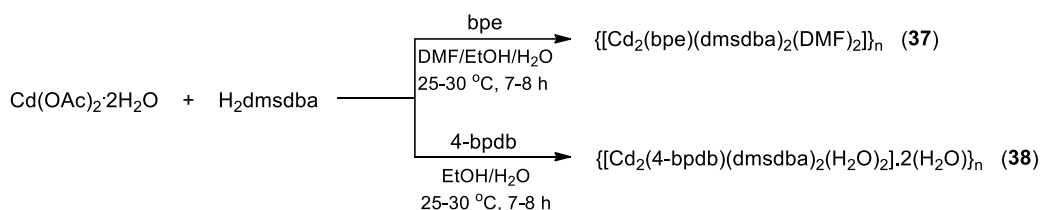
plots of **33** and **36** up to 320 °C and 370 °C, respectively before the framework decomposition.

Effect of rigidity/flexibility of the pillar ligand on the final architecture. In this study, the pillar-layered strategy has been further extended to synthesize mixed ligand coordination polymers and the effect of rigid or flexible N-donor pillar ligands has been studied in the Co(II)-**dmsdba**²⁻ system under similar reaction conditions. As expected, the rigid or semi-rigid pillar ligands coordinates between the 1D metal carboxylate chains to result in the formation of interpenetrated 2D coordination polymers, whereas in case of conformationally flexible ligands (azopy or bpp), the conformation flexibility of azo or methylene chain spacers adds up an extra dimensionality by allowing the coordinating pyridyl groups to bind to the alternative 2D sheets resulting in the formation of overall 3D structures.

Cd(II) Chemistry

As pointed out in the previous section (Section 3.1.2.1) that different metal ions are known for their own coordination preferences, which can play an important role in the structural diversity of the resulting coordination architectures.²⁶⁸ Therefore the study has been further extended to the Cd(II)-**dmsdba**²⁻ system, since cadmium is known to expand its coordination sphere from hexa- to hepta- or in some cases octa-coordination. By judicious design and selection of different N-donor ligands, a set of mixed ligand Cd(II) coordination polymers have been synthesized and the pillar ligand induced structural diversity and applications of these coordination polymers have been discussed.

Scheme 3.17. Synthesis of **37** and **38**.



Self-assembly of cadmium acetate, H₂dmsdba and different N-donor ligands **bpe** or **4-bpdb** at ambient conditions has resulted in the formation of $\{[\text{Cd}_2(\text{bpe})(\text{dmsdba})_2(\text{DMF})_2]\}_n$ (**37**) and $\{[\text{Cd}_2(4\text{-bpdb})(\text{dmsdba})_2(\text{H}_2\text{O})_2]\}_n$ (**38**) in good yields (Scheme 3.17). Their structures have been analyzed by single crystal X-ray diffraction analysis and their molecular formula has been established by a combination of elemental analysis, TGA and single crystal X-ray diffraction analysis

Single crystal structure analysis. Single crystals suitable for single crystal X-ray diffraction analysis in each case were obtained by the slow diffusion technique at room temperature using different solvent combinations. Compound **37** forms a 1D coordination polymer which crystallizes in a triclinic crystal system with $P\bar{1}$ space group. The asymmetric unit consists of one Cd(II) atoms, one carboxylate linker **dmsdba**²⁻, and one half of the neutral N-donor ligand **bpe** along with one molecule of DMF coordinated to the metal center (Figure 3.52a). The Cd(II) center is in a NO5 type coordination environment with a distorted octahedral geometry around the metal center. The coordination sites of the octahedral geometry are occupied by four oxygen atoms of the carboxyl groups of **dmsdba**²⁻, one oxygen atom from the coordinated DMF molecule and one nitrogen atom of the neutral N-donor ligand **bpe**. The carboxylate linker **dmsdba**²⁻ is fully deprotonated and arranged in the form of linear chain upon coordination to the metal center. Two of such chains are further connected by the pillar ligand **bpe**, resulting the overall structure (Figure 3.52b). The 1D polymeric chains are further interpenetrated (1D + 1D → 2D) into one another to generate the overall 2D framework (Figure 3.52c).

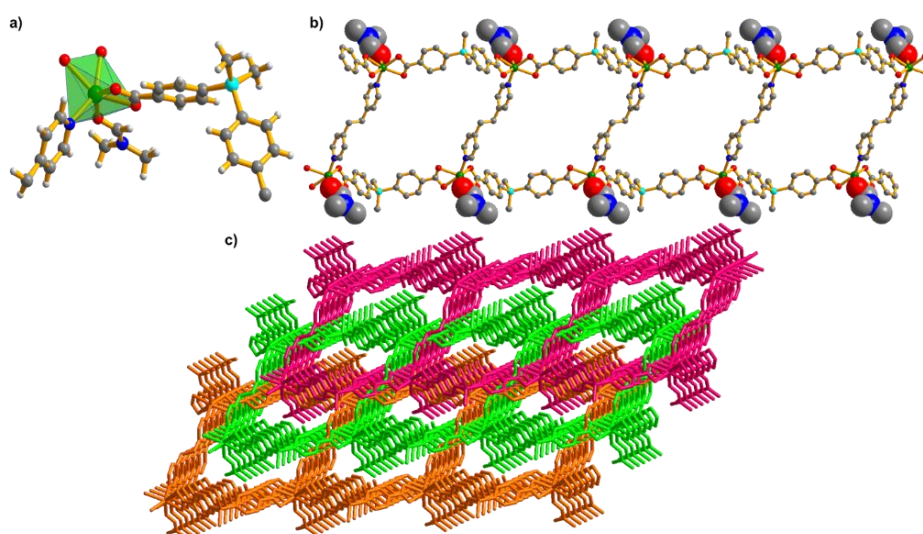


Figure 3.52. Structure description for **37**; (a) asymmetric unit and the coordination environment around the metal center, (b) view of the 1D framework; coordinated DMF molecules are shown in space fill representation and (c) represents the interpenetration into the 1D polymeric chains to generate the overall 2D framework in **37**.

Compound **38**, exhibits the similar structure as that of **37**, except that the instead of coordinated DMF in **37**, **38** consists of a water molecule coordinated to the metal center. In addition to it, there is also a water molecule in the crystal lattice. It also crystallizes in a triclinic $P\bar{1}$ space group. The asymmetric unit contains one Cd(II) atoms, one carboxylate linker **dmsdba**²⁻, and one half of the neutral N-donor ligand **4-bpdb** along with two water

molecule; one coordinated and one lattice water molecule (Figure 3.53a). The distorted octahedral geometry around the metal center is formed by four carboxyl oxygen atoms of the carboxylate linker **dmsdba**²⁻, one oxygen atom of the coordinated water molecule and one nitrogen atom of the N-donor ligand **4-bpdb**. The other structural features are similar to that of **37**. As shown in (Figure 3.53b) the asymmetric unit is further extended by the carboxylate linker **dmsdba**²⁻ and the ligand **4-bpdb** to generate the 1D polymeric structure which are further interpenetrated (1D + 1D → 2D) to form the overall 2D framework (Figure 3.53c).

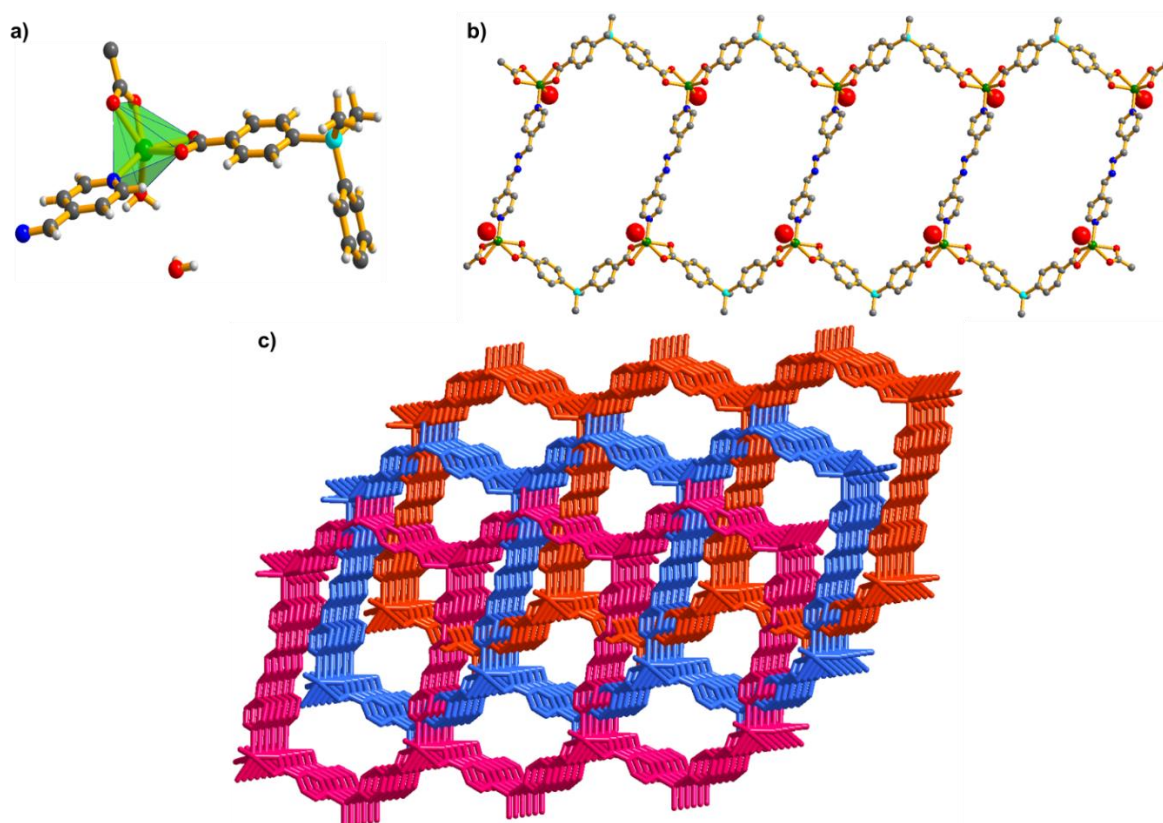


Figure 3.53. Structure description for **38**; (a) Asymmetric unit and the coordination environment around the metal center, (b) view of the 1D framework; coordinated water molecules are shown in space fill representation and (c) represents the interpenetration into the 1D polymeric chains to generate the overall 2D framework.

The Cd-O bond lengths in **37** and **38** lies in the range 2.257 Å to 2.390 Å and 2.239 Å to 2.437 Å, whereas the Co-N bond lengths are found to be 2.255 Å and 2.315 Å, respectively. These values are within the usual range for this kind of complexes. The prominent distortions from the regular geometries around the metal centers are evident from the bond angle value in each case. All the crystallographic information pertaining to data collection and structure refinement parameters, selected bond lengths and bond angles are listed in Table A13, A35 and A57, respectively.

FTIR and PXRD analysis. FTIR spectra of **37** and **38** was recorded in the solid state at room temperature as KBr pellets. The sharp peaks due to asymmetric (ν_{asym}) and symmetric (ν_{sym}) stretching vibrations of the carboxylates in **37** and **38** were observed at 1578 cm^{-1} and 1400 cm^{-1} for **37** and 1575 cm^{-1} and 1402 cm^{-1} for **38**. The difference in asymmetric and symmetric stretching vibrations ($\Delta\nu = 178\text{ cm}^{-1}$ and 173 cm^{-1} for **37** and **38**, respectively) indicates the chelated bidentate binding of the carboxylate to the metal center²⁵¹ as seen in their respective single crystal structures. In addition, significant shift from the asymmetric and symmetric -C=O stretch for free **H₂dmsdba** (1690 cm^{-1} and 1416 cm^{-1}) indicates a strong binding of the carboxylates to the metal center in both cases. A sharp peak at 1652 cm^{-1} in case of **37** can be ascribed due to the presence of coordinated DMF molecule in **37**. In order to confirm whether the single crystal structure corresponds to the bulk material or not, powder X-ray diffraction patterns were recorded at room temperature for **37** and **38**. The experimental powder X-ray diffraction patterns for **37** and **38** confirm their crystallinity and PXRD patterns of the as-synthesized and the desolvated samples in both the cases, when compared with their respective PXRD pattern simulated from single-crystal data, shows good agreement between the experimental and simulated data (Figure 3.54). This confirms the phase purity as well as retention of structural integrity upon thermal desolvation/activation.

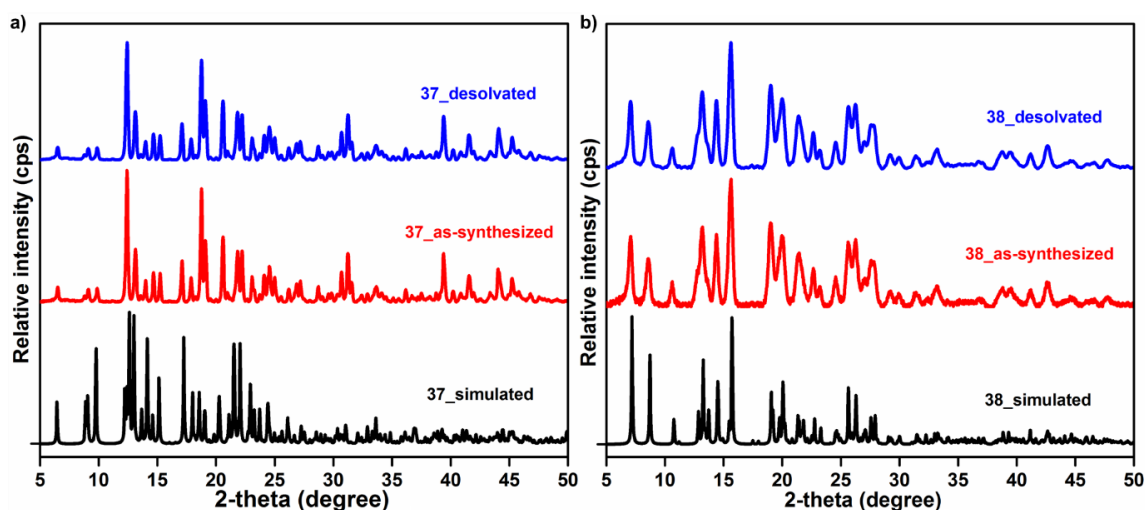


Figure 3.54. Powder X-ray diffraction (PXRD) pattern of as-synthesized and desolvated samples of (a) **37** and (b) **38**, compared with the simulated powder pattern obtained from the single crystal data of **37** and **38**, respectively.

Framework stabilities and thermal properties. In order to test the thermal stability and structural variation as a function of temperature, thermogravimetric analysis (TGA) was carried out with the single-phase polycrystalline sample of **37** and **38** between $30\text{--}500\text{ }^{\circ}\text{C}$,

under a dinitrogen atmosphere (Figure 3.55a). The thermogravimetric profiles corroborate with the structures obtained from the single crystal analysis. Compound **37** exhibits an initial weight loss of about 13 % in the temperature range of 120 °C to 180 °C, which is in good agreement due to the loss of coordinated DMF molecule (calculated 12.69 %). After which no weight loss was observed up to 300 °C before the framework degradation.

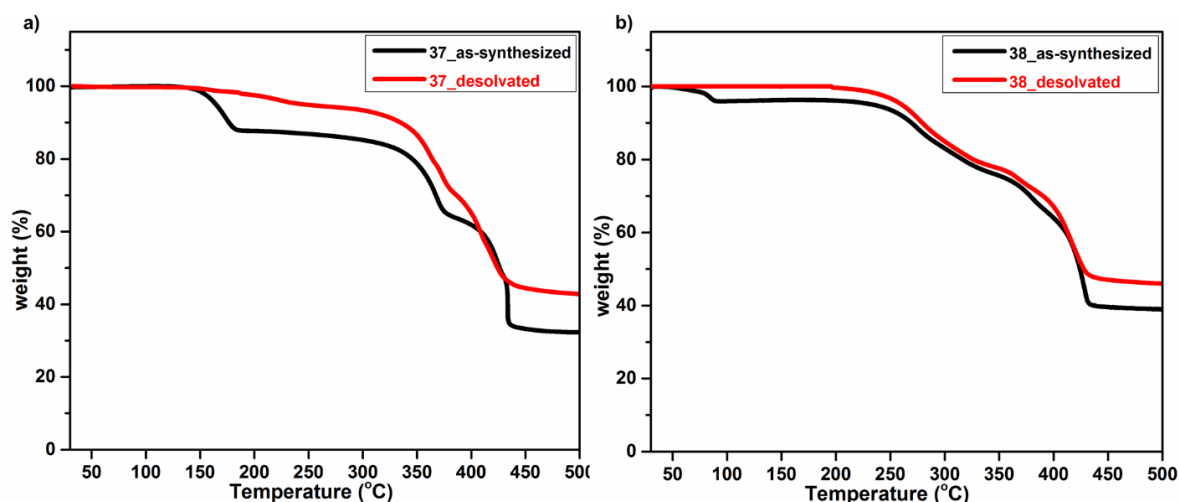


Figure 3.55. Thermogravimetric profile for the as-synthesized and desolvated samples of (a) **37** and (b) **38**, respectively.

Similarly, in the thermogravimetric profile for **38**, it exhibits an initial loss of about 6% in the temperature range of 50 °C to 100 °C, which is in good agreement due to the loss of two water molecules (ca. 6.54%). After which the compound exhibits stable behavior up to 220 °C, as no weight loss can be seen in the temperature range of 100 °C to 220 °C. After which it shows continuous weight loss which indicates framework degradation at higher temperature. In addition to the retention of phase purity and crystallinity after thermal desolvation/activation, the compounds are found to follow their thermal stability profiles. As seen in Figure 3.55, the desolvated samples of **37** and **38** follows the same thermogravimetric profiles, except that no weight loss can be seen due to the coordinated or lattice solvent molecules up to 300 °C and 220 °C, respectively before the framework degradation.

Catalysis Studies. Because of the presence of coordinatively unsaturated metal site which can act as potential Lewis acidic sites, both **37** and **38** were tested for their catalytic activity as an active heterogeneous catalyst for Lewis acid prompted reactions. The Knoevenagel condensation of aldehydes with active methylene compounds is one of the most useful C–C bond forming reaction having wide applications for the synthesis of several fine chemicals

and pharmaceuticals.²⁹⁷ Also, the product benzylidene malononitrile is well known for its biological activity.²⁹⁸ This condensation is generally catalyzed by bases or Lewis acids.^{252,299} While various type of homo/heterogeneous catalysts (discrete or polymeric coordination compounds) have been developed for such organic transformation, there is still a great demand to develop new types of catalysts based on cheap and environmentally tolerable metal complexes that could be easily recyclable (hence forming an heterogeneous system) and could show high efficiency under mild conditions. Thus, the catalytic activity of **37** and **38** was tested as solid heterogeneous catalysts in the Knoevenagel condensation of malononitrile with various aldehydes. Motivated by green chemistry principles the reaction was carried out with 3 mol% of compounds at room temperature in methanol solvent. Before the catalysis experiments, the compounds were activated by heating under vacuum conditions to generate the Lewis-acidic open metal sites. As shown in Figure 3.54 and 3.55, both the compounds maintain their structure integrity upon thermal activation. In a typical reaction, a mixture of benzaldehyde (10 μ L, 0.10 mmol), malononitrile (10 mg, 0.15 mmol), and catalyst (3 mol%) was placed in a capped glass vial, and then 1 mL of solvent was added to it. The mixture was stirred at 25-30 $^{\circ}$ C. The progress of the reaction was monitored by TLC analysis and the final conversion was calculated by 1 H NMR spectroscopy. Using benzaldehyde as the simplest substrate, the test reactions gave about 88% and 92% product conversions in case of **37** and **38**, respectively in 60 minutes. This good catalytic activity of **37** and **38** for Knoevenagel condensation encouraged us to extend the catalytic study to various other substituted aromatic aldehydes and active methylene compounds under identical reaction conditions. Inspired by the good catalytic activity, the versatility of **37** and **38** was further tested by the reaction of different types of substituted aromatic aldehydes and active methylene compounds. It gave the corresponding α,β -unsaturated compounds in good-to-excellent yields. The results are summarized in Table 3.4 and 3.5, respectively.

The results obtained for the Knoevenagel condensation reaction follows the same trend in both cases. It is clear from the Table 3.4 and 3.5 that the highest yield was obtained in case of substrates with electron withdrawing groups while a drop in the product conversion was obtained for the substrates with electron donating substituents. Thus, the reactivity trend unveils the strong accelerating influence of electron-withdrawing groups in contrast to an electron donating moiety for the reactions involving nucleophilic attack at the carbonyl group. The blank reaction between benzaldehyde and malononitrile carried out in the absence of catalyst **37** or **38** results in almost negligible conversions (21% and 15%,

Table 3.4. Substrate Scope for the Knoevenagel Condensation Reaction Catalyzed by **37**^a

Entry	Aldehyde	catalyst 37 (3 mol%)		Ar-CH=C(R ₁)(R ₂)
		R ₁ , R ₂	25-30 °C	
Entry	Aldehyde	R ₁ , R ₂	% yield ^b	TON ^c
1		R ₁ = R ₂ = CN	88	29.3
2		R ₁ = R ₂ = CN	98	32.6
3		R ₁ = R ₂ = CN	>99	33.0
4		R ₁ = R ₂ = CN	>99	33.0
5		R ₁ = R ₂ = CN	76	25.3
6		R ₁ = R ₂ = CN	56	18.6
7		R ₁ = R ₂ = CN	>99	33.0
8		R ₁ = R ₂ = CN	96	32.0
9		R ₁ = R ₂ = CN	92	30.6
10		R ₁ = R ₂ = CN	64	21.3
11		R ₁ = R ₂ = CN	>99	33.0
12		R ₁ = R ₂ = CN	21 ^d	7.0

^aReaction conditions: Aldehyde (0.1 mmol), active methylene compound (0.15 mmol) and reaction time: 60 minutes. ^bAverage percent yield for a set of triplicate runs, calculated by ¹H NMR of the crude products. ^cNumber of moles of product per mole of catalyst. ^dBlank reaction.

Table 3.5. Substrate Scope for the Knoevenagel Condensation Reaction Catalyzed by **38**^a

Entry	Aldehyde	catalyst 38 (3 mol%)		Ar-CH=C(R ₁)(R ₂)
		R ₁ , R ₂	25-30 °C	
Entry	Aldehyde	R ₁ , R ₂	% yield ^b	TON ^c
1		R ₁ = R ₂ = CN	92	30.6
2		R ₁ = R ₂ = CN	>99	33.0
3		R ₁ = R ₂ = CN	>99	33.0
4		R ₁ = R ₂ = CN	>99	33.0
5		R ₁ = R ₂ = CN	80	26.6
6		R ₁ = R ₂ = CN	60	20.0
7		R ₁ = R ₂ = CN	>99	33.0
8		R ₁ = R ₂ = CN	96	32.0
9		R ₁ = R ₂ = CN	94	31.3
10		R ₁ = R ₂ = CN	66	22.0
11		R ₁ = R ₂ = CN	>99	33.0
12		R ₁ = R ₂ = CN	15 ^d	5.0

^aReaction conditions: Aldehyde (0.1 mmol), active methylene compound (0.15 mmol) and reaction time: 60 minutes. ^bAverage percent yield for a set of triplicate runs, calculated by ¹H NMR of the crude products. ^cNumber of moles of product per mole of catalyst. ^dBlank reaction.

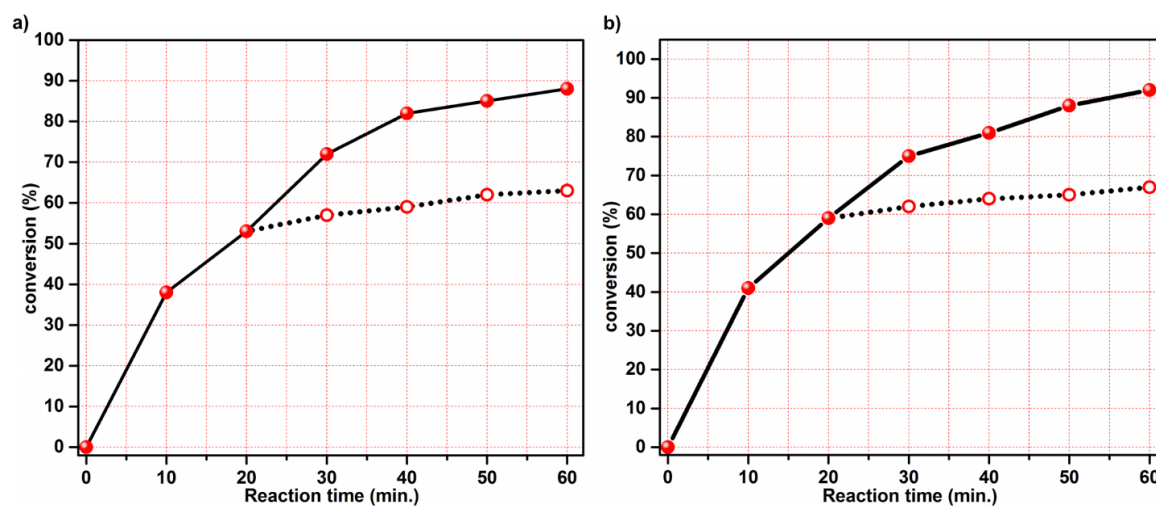


Figure 3.56. Progress of the reaction with time in presence of catalyst (a) **37** and (b) **38** (solid lines) and after separating the catalyst from the reaction mixture (dotted lines) for Knoevenagel condensation reaction of benzaldehyde with malononitrile

respectively) of condensation product, suggesting the requirement of a catalyst (entries 12, Table 3.4 and 3.5). Further, to rule out the possibility of leaching of the catalyst into the product stream, the catalyst was separated from the reaction mixture by centrifugation after

certain time and the supernatant was provided with the same reaction conditions. No significant conversion was obtained in both the cases (Figure 3.56), suggesting no contribution from leached species and the catalytic conversion was only being possible in the presence of the **37** or **38** confirming their heterogeneous nature.

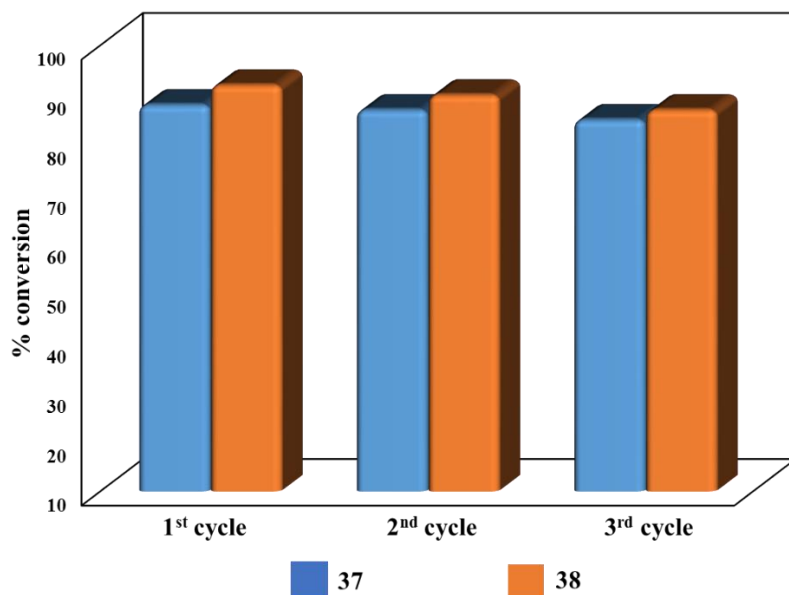


Figure 3.57. Conversion for three consecutive cycles of Knoevenagel condensation reaction of benzaldehyde and malononitrile catalysed by **37** and **38**.

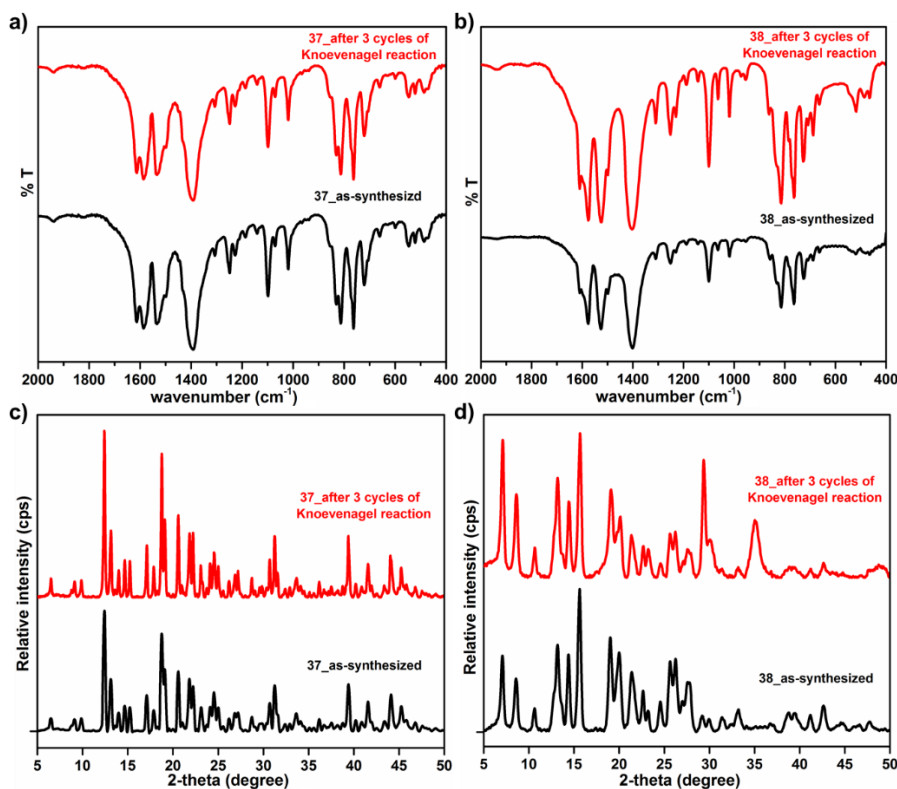


Figure 3.58. FTIR and powder X-ray diffraction pattern of the catalyst (a and c) **37** and (b and d) **38**, before and after three cycles of Knoevenagel Condensation reaction.

In addition to the heterogeneity of the catalyst **37** and **38**, both the catalysts were further studied for their recyclability. In order to determine the recyclability of the catalyst, the catalyst was isolated after the reaction by filtration and washed with methanol, dried under vacuum and reused for the consecutive experiments. Both catalysts **37** and **38** were recycled in three consecutive experiments, and their activity did not show appreciable change (Figure 3.57). Based on FTIR spectra and PXRD data of the catalysts **37** and **38**, recorded before and after the catalysis experiments, no loss of crystallinity or phase purity of the catalyst was observed even after three cycles of reactions (Figure 3.58). The mechanism of the catalytic cycle can be proposed similar to **1-10**.

In addition to the utility of **38**, as an active heterogeneous catalyst for Knoevenagel condensation reaction, it was further tested for its bifunctional catalytic activity towards three-component Biginelli reaction, due to the presence of azine functionality into the framework. In a typical reaction, a mixture of benzaldehyde (10 μ L, 0.10 mmol), ethyl acetoacetate (25 μ L, 0.20 mmol), and urea (10 mg, 0.15 mmol) was reacted at 50 $^{\circ}$ C in the presence of **38** (3 mol%) under a nitrogen atmosphere and solvent-free conditions. The progress of the reaction was monitored by TLC analysis and the final conversion was calculated by 1 H NMR spectroscopy. Inspired by the good catalytic activity of **38**, the study was further extended to several other derivatives. It gave the corresponding dihydropyrimidinone derivative in good yields. The results are summarized in Table 3.6.

It is clear from the Table 3.6 that both the substrates with electron withdrawing or electron releasing groups show similar reactivity as no much difference was obtained in the product conversion. For a control experiment a blank reaction was carried out between benzaldehyde, ethylacetoacetate and urea in the absence of catalyst. This results in almost negligible product conversions (10%, entry 15, Table 3.6), suggesting the active role of the catalyst. In order to determine the recyclability of the catalyst similar protocol was followed. The catalyst was isolated after the reaction by filtration, washed with methanol, dried under vacuum and reused for the next catalytic experiment. The catalyst was recycled in three consecutive experiments with a slight loss (~7-8%) in its catalytic activity (Figure 3.59). The retention of structural integrity, phase purity and crystallinity of the catalyst after three cycles of reactions was further confirmed by the FTIR and PXRD of the recovered catalyst. The mechanism for the catalytic reaction is similar to the reported proposals.³⁰⁰

Table 3.6. Substrate Scope for the three component Biginelli Reaction Catalyzed by **38**^a

Entry	R	carbonyl compound	X	yield ^b	TON ^c
1	H		O	88	29.3
2	<i>p</i> -F		O	91	30.0
3	<i>p</i> -Cl		O	88	29.3
4	<i>p</i> -Br		O	92	30.1
5	<i>p</i> -OMe		O	72	24.0
6	<i>p</i> -NO ₂		O	93	31.0
7	<i>m</i> -OMe		O	75	25.0
8	<i>m</i> -NO ₂		O	94	31.0
9	H		O	89	29.7
10	<i>p</i> -NO ₂		O	92	30.1
11	H		O	85	28.3
12	<i>p</i> -NO ₂		O	92	30.1
13	H		S	83	27.7
14	<i>p</i> -NO ₂		S	92	30.1
15	H		O	10 ^d	3.3

^aReaction conditions: Aromatic aldehyde (0.10 mmol), diketone (0.2 mmol) and urea or thiourea (0.15 mmol). The reaction was carried out in a sealed tube at 50 °C for 4h. ^bAverage percent yield for a set of triplicate runs, calculated by ¹H NMR of the crude products. ^cNumber of moles of product per mole of catalyst. ^dBlank reaction.

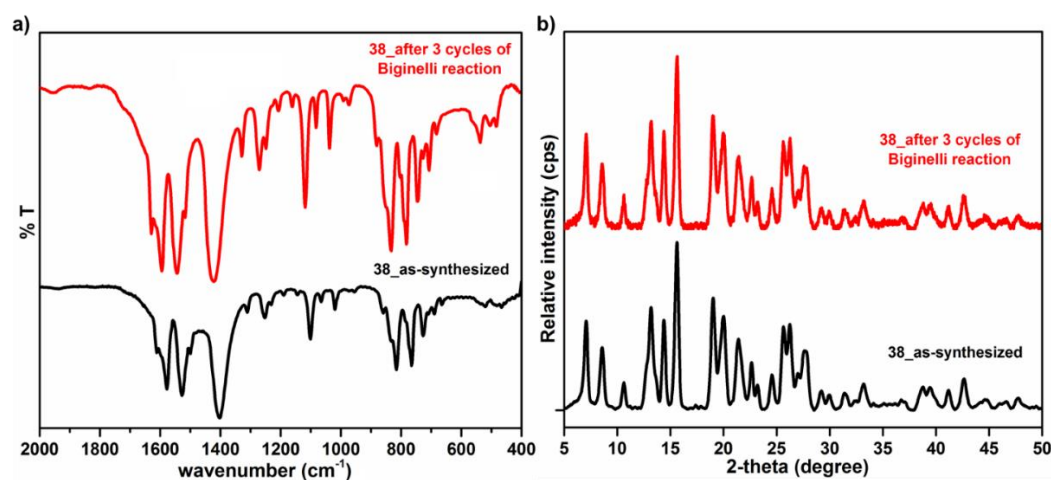
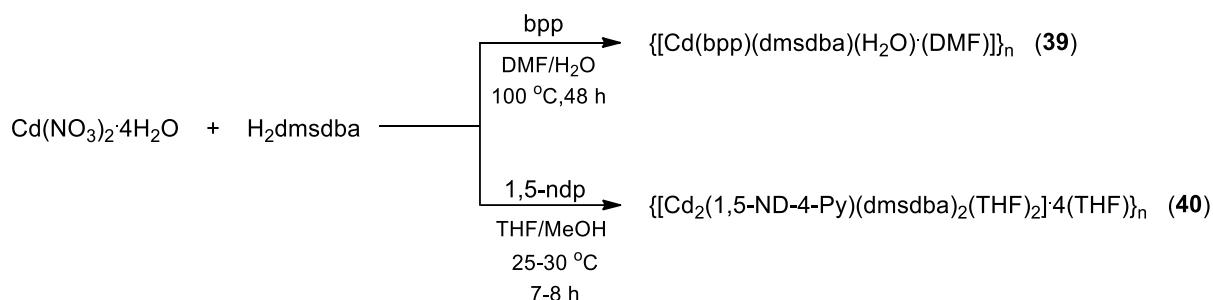


Figure 3.59. (a) FTIR and (b) powder X-ray diffraction pattern of the catalyst **38**, before and after three cycles of Biginelli reaction.

In order to further explore the structural diversity and applications of such Cd(II) coordination polymers, we have further utilized the conformationally flexible ligand **bpp** and an aromatic fluorophore tagged ligand **1,5-ND-4-Py**, with a naphthalene moiety into the ligand backbone to synthesize the coordination polymers $\{[\text{Cd}(\text{bpp})(\text{dmsdba})(\text{H}_2\text{O})]\cdot\text{DMF}\}_n$ (**39**) and $\{[\text{Cd}_2(1,5\text{-ND-4-Py})(\text{dmsdba})_2(\text{THF})_2]\cdot 2\text{THF}\}_n$ (**40**). The reaction of cadmium nitrate, **H₂dmsdba** and the neutral N-donor ligands **bpp** and **1,5-ND-4-Py** under solvothermal and ambient conditions has resulted in the formation of **39** and **40**, respectively in good yields (Scheme 3.18).

Scheme 3.18. Synthesis of **39** and **40**.



Both these compounds have been structurally characterized by single crystal X-ray diffraction analysis and their molecular formulas have been established by a combination of elemental analysis, thermogravimetric and single crystal X-ray diffraction analysis. Compound **39** represents a rare example of helically chiral MOF derived from achiral organic ligands and without the need of any chiral auxiliaries such as enantiopure solvents, additives, catalysts or a template. The chirality in these frameworks results from the spatial organization (e.g., helix) of achiral components, but the interpenetration of opposite-handed helices often yields nonporous and achiral structures. The other possibility is that the individual crystals can be homochiral through a process called spontaneous resolution. However, the bulk sample tends to be a conglomerate, an equal mixture of crystals with opposite handedness.

Single crystal structure analysis. Single crystal suitable for X-ray diffraction analysis in case of **39** were obtained by solvothermal reaction at 100 °C and in case of **40**, the single crystals were obtained by slow diffusion technique at room temperature. Single crystal X-ray diffraction analysis reveals that **39** crystallizes in the chiral space group $P2_12_12$ (space group no. 18) and has a 2D structure constructed from Cd–bpp–dmsdba²⁻ helical chains [Flack parameter = 0.001(7)]. As shown in Figure 3.60a, the asymmetric unit consists of

one Cd (II) ions, one **bpp**, one **dmsdba**²⁻ and one coordinated water molecule along with one lattice DMF molecule. The Cd center has a distorted pentagonal bipyramidal geometry with an N2O5 coordination environment due to binding of four oxygen atoms (O1, O2, O3, O4) from carboxylates of two different **dmsdba**²⁻ in a chelated fashion and one oxygen (O5) from coordinating water at the equatorial positions. The two apical positions are occupied by two nitrogen atoms (N1 and N2) from two different bis-pyridyl ligands (**bpp**). The chelated mode of carboxylate binding with the metal center is evident by the difference ($\Delta\nu = 179 \text{ cm}^{-1}$) in the asymmetric ($\nu = 1579 \text{ cm}^{-1}$) and symmetric ($\nu = 1400 \text{ cm}^{-1}$) carbonyl stretching of carboxylates in the FTIR spectrum of **39**. The Cd (II) centers act as a link between the helical chains giving rise to an overall 2D framework with 1D open channels with dimensions of $10.9 \times 12.1 \text{ \AA}^2$ ($7.1 \times 9.0 \text{ \AA}^2$ without van der Waals radii), which are filled with lattice DMF molecules (Figure 3.60b). The total potential solvent-accessible void volume for **39** was estimated to be 17.8% (577 \AA^3 out of the unit cell volume 3224 \AA^3) using the PLATON software.²⁷⁵ The dicarboxylate ligand (**dmsdba**²⁻) adopting a helical chain conformation, based on its connectivity with the Cd(II) centers in **39**, can be observed by considering the 2_1 screw axis along the b-axis (Figure 3.60c). On the other hand, the two-fold rotation axis along c-axis provides the overall connectivity of all components (Figure 3.60d). Furthermore, a space fill view of the framework shown in Figure 3.60e depicts the fusion of different 1D helical chains at the Cd(II) centers.

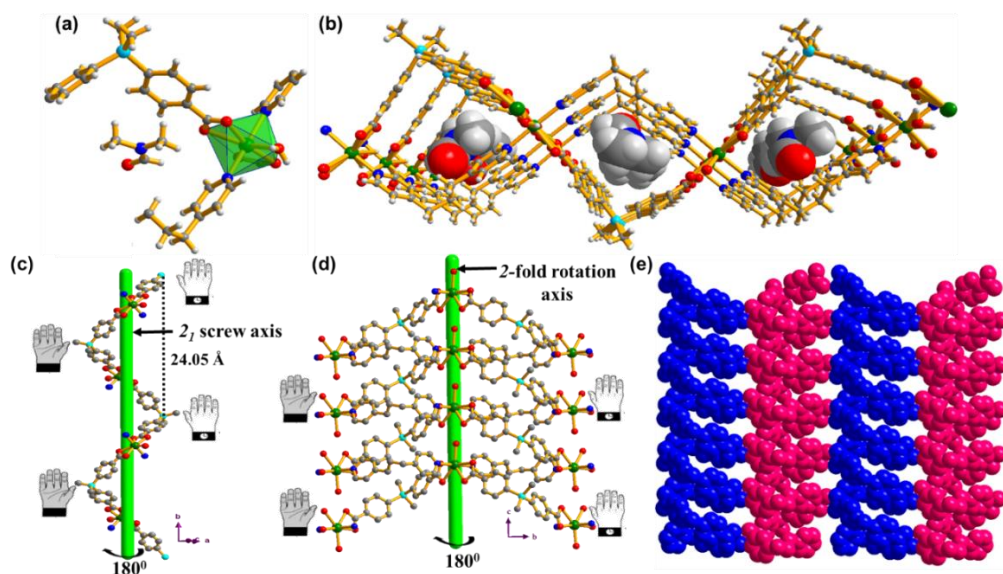


Figure 3.60. Structure description for **39**; (a) View of the asymmetric unit and the coordination environment around the Cd (II) center, (b) perspective view of the 2D framework in **39**. Lattice DMF molecules present in the 1D channels have been shown as space-fill model, (c and d) representation of the 2-fold screw axis and 2-fold rotation axis along crystallographic b and c axis, respectively and (e) space-fill representation of the 2D framework viewed along the a-axis.

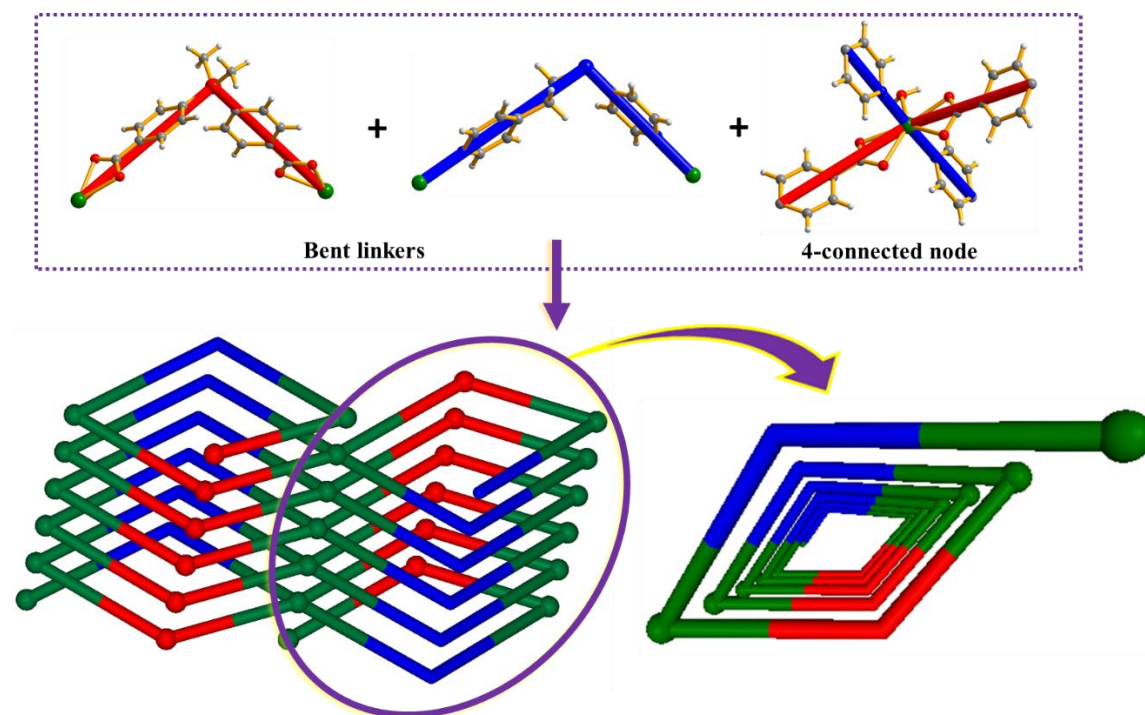


Figure 3.61. Simplified node and linker representation for **39**, indicating 4-connected uninodal net, *sql* topology.

To simplify the rather intricate structure of **39**, the Cd (II) center can be considered as a 4-connected node and the ligands **bpp** and **dmsdba**²⁻ as bent linkers. Further examination of the node and linker representation reveals that the framework exhibits a 4-connected uninodal net, *sql* topology, with Schläfli point symbol $\{4^4.6^2\}$ (Figure 3.61) as determined by the TOPOS program.²⁷⁴ Upon analysis of the structure, the metal center is not stereogenic and is not responsible for the chirality induction; thus, the V-shaped dicarboxylate **dmsdba**²⁻ and the conformationally flexible **bpp** adopt a helical arrangement when coordinated to the metal ion, giving rise to a chiral network. The helical chirality of the framework was further established with the help of solid-state circular dichroism (CD) measurement (Figure 3.62).

The Cd-O bond lengths lies in the range 2.307 Å to 2.456 Å, whereas the Co-N bond lengths are found to be 2.324 Å and 2.354 Å, respectively. These values are within the usual range for this kind of complexes.²⁷¹ The prominent distortions from the regular geometries around the metal centers are evident from the bond angle value in each case. All the crystallographic information pertaining to data collection and structure refinement parameters, selected bond lengths and bond angles are listed in Table A14, A39 and A60, respectively.

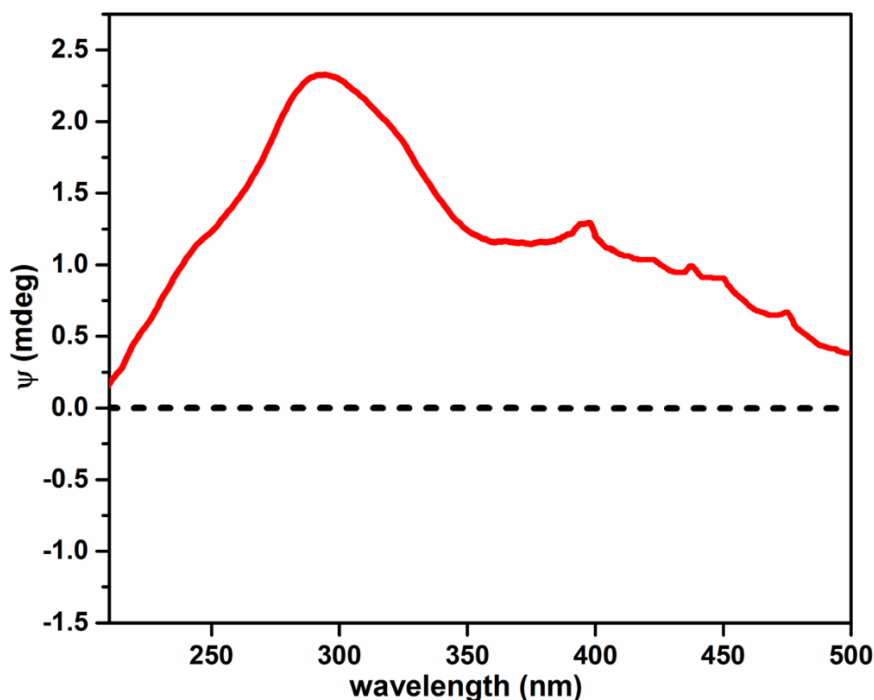


Figure 3.62. Solid State Circular Dichroism (CD) Spectrum for **39**.

Compound **40** crystallizes in a monoclinic crystal system with $C2/c$ space group. As shown in Figure 3.63a, the asymmetric unit consists of one Cd(II) ion, one carboxylate linker **dmsdba**²⁻, one half of the neutral N-donor ligand **1,5-ND-4-Py** and one THF molecule coordinated to the Cd(II) center along with disordered THF molecules in the crystal lattice. The dicarboxylate linker **dmsdba**²⁻ is fully deprotonated where one of the carboxylate binds in a chelated bidentate fashion and the other one binds in a syn-syn bridging bidentate fashion resulting in the formation of a biscarboxylato bridged dinuclear core as secondary building unit. Each Cd(II) is in a NO5 type distorted octahedral coordination environment, where the coordination sites around Cd(II) are occupied by four carboxyl oxygen atoms of **dmsdba**²⁻, one oxygen atom from coordinated THF molecule and one nitrogen atom of the neutral N-donor ligand.

The framework in **40** is composed of a dinuclear Cd₂(COO)₂ SBU which are bridged by four dicarboxylate linkers **dmsdba**²⁻ to form the right and left-handed metal carboxylate helical chains (Figure 3.63b). These left and right helical chains are fused at the Cd(II) center in an alternative fashion to form 2D metal carboxylate structure. The 2D metal carboxylate polymeric structure is further bridged by the neutral N-donor ligands to form the overall 3D framework (Figure 3.63c). As shown in Figure 3.63c, the framework consists of considerable open 1D channels along the b-axis of dimensions 10.23 x 13.76 Å² (6.03 x 10.6 Å² without van der Waals radii). The channels are filled with disordered solvent

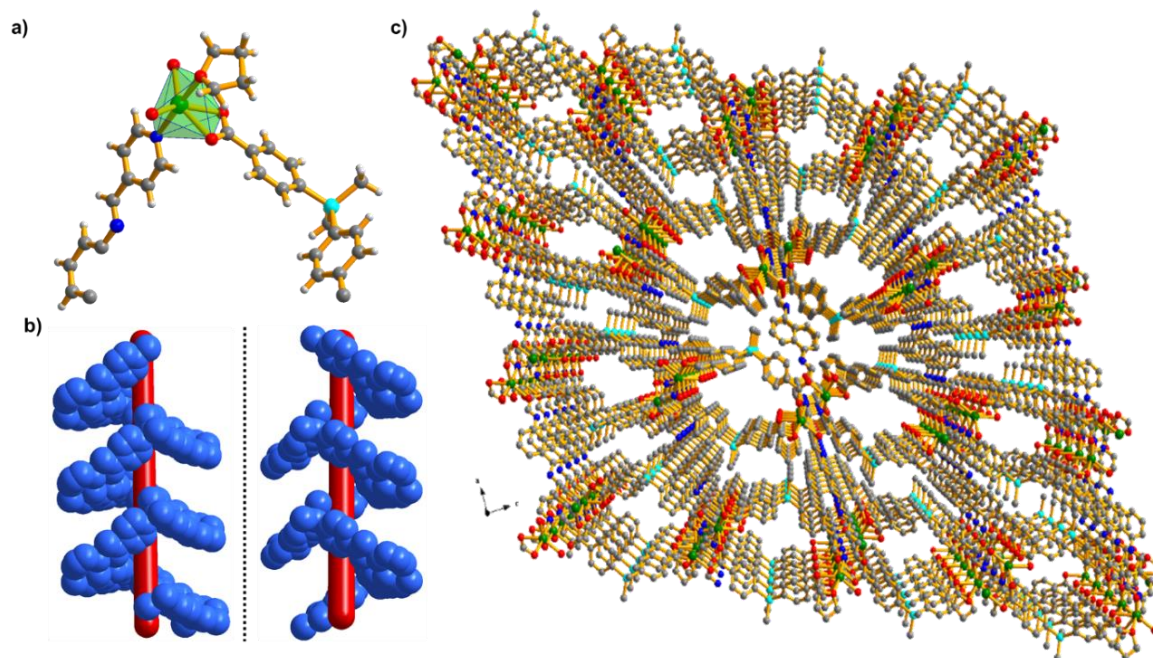


Figure 3.63. Structure description for **40**; (a) View of the asymmetric unit and the coordination environment around the Cd (II) center, (b) metal-carboxylate helical chains with opposite handedness and (c) perspective view of the 3D framework along b-axis, showing 1D open channels.

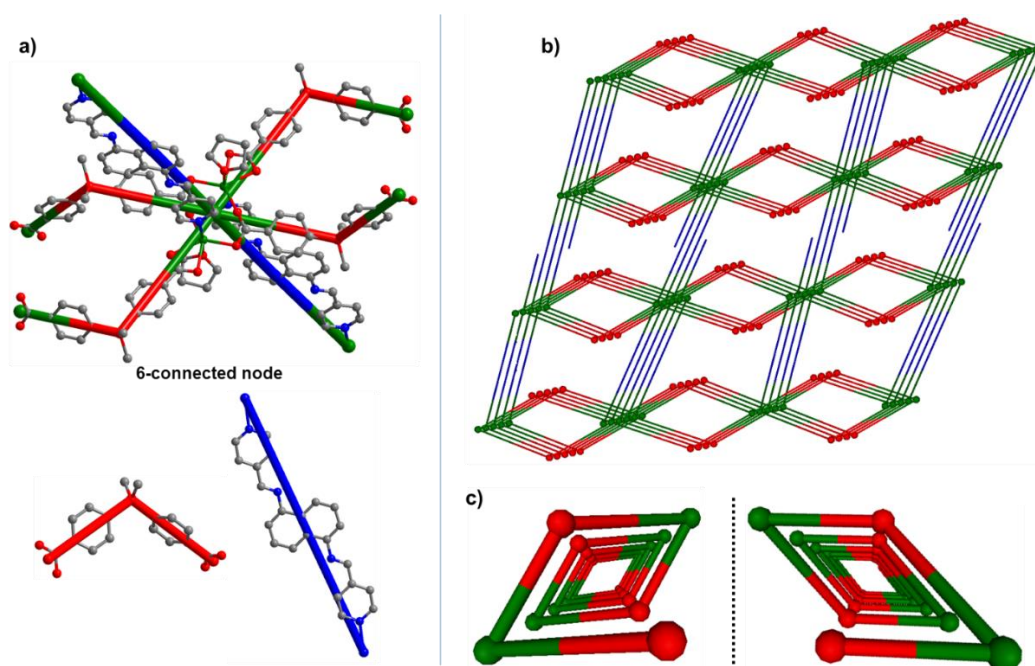


Figure 3.64. Simplified node and linker type representation for **40**; (a) $\text{Cd}_2(\text{COO})_4$ dinuclear core and the ligands dmsdba and 1,5-ND-4-Py simplified as 6-connected node and bent and linear linkers, respectively, (b) View of the overall 6-connected uni-nodal roa topology and (c) metal-carboxylate helical chains with opposite handedness.

molecules, which were removed using solvent masking option in Olex2 software²⁰³ during the structure refinement. The total solvent-accessible volume for **40** was estimated to be 32 % (2508/7760 \AA^3 per unit cell volume) by the PLATON software.²⁷⁵ The topological

analysis of **40** using TOPOS²⁷⁴ revealed that the Cd₂(COO)₂ SBUs can be viewed as six connected nodes and the ligands **dmsdba**²⁻ and **1,5-ND-4-Py** as bent and linear linkers (Figure 3.64a). Therefore, **40** can be envisioned as a 6-c uninodal net with roa (topos & RCSR.ttd) topology (Figure 3.64). The point symbol for the net is {4⁴.6⁶10.8}.

The Cd-O bond lengths lies in the range 2.196 Å to 2.403 Å, whereas the Co-N bond length is found to be 2.305 Å. These value lies within the usual range for this kind of complexes. The prominent distortions from the regular geometries around the metal centers are evident from the bond angle value in each case. All the crystallographic information pertaining to data collection and structure refinement parameters, selected bond lengths and bond angles are listed in Table A14, A36 and A58, respectively.

FTIR and PXRD analysis. FTIR spectra of **39** and **40** were recorded in the solid state at room temperature as KBr pellets. The sharp peaks due to asymmetric (ν_{asym}) and symmetric (ν_{sym}) stretching vibrations of the carboxylates in **39** at 1579 cm⁻¹ and 1401 cm⁻¹ with ($\Delta\nu = 178$ cm⁻¹) indicates the chelated bidentate binding mode of the carboxylate to the metal center as seen in the single crystal structures. A sharp peak at 1670 cm⁻¹ can be ascribed due to the presence of coordinated DMF molecule. The peaks due to asymmetric (ν_{asym}) and symmetric (ν_{sym}) stretching vibrations of the carboxylates in **40** were observed at 1579 cm⁻¹ and 1402 cm⁻¹. These values show significant shift from the asymmetric and symmetric -C=O stretch for free **H₂dmsdba** (1690 cm⁻¹ and 1416 cm⁻¹), which indicates strong binding of the carboxylates to the metal center in both cases. In order to the phase purity of the as-synthesized materials, powder X-ray diffraction patterns were recorded for **39** and **40** at room temperature. As shown in Figure 3.65, the experimentally obtained powder patterns for as-synthesized, solvent exchanged or desolvated one, were in good agreement with the simulated powder patterns (obtained from the single crystal data). This confirms the phase purity as well as retention of structural integrity upon thermal desolvation/activation in both the cases.

Framework stabilities and thermal properties. In order to test the thermal stability and structural variation as a function of temperature, thermogravimetric analysis (TGA) was carried out with the single-phase polycrystalline sample of **39** and **40** between 30-500 °C, under a dinitrogen atmosphere (Figure 3.66a). The thermogravimetric profiles corroborate with the structures obtained from the single crystal analysis. The as-synthesized sample of **39** exhibits an initial weight loss of about 12 % in the temperature range of 100 °C to 200 °C, which is in good agreement due to the loss of coordinated water and lattice DMF

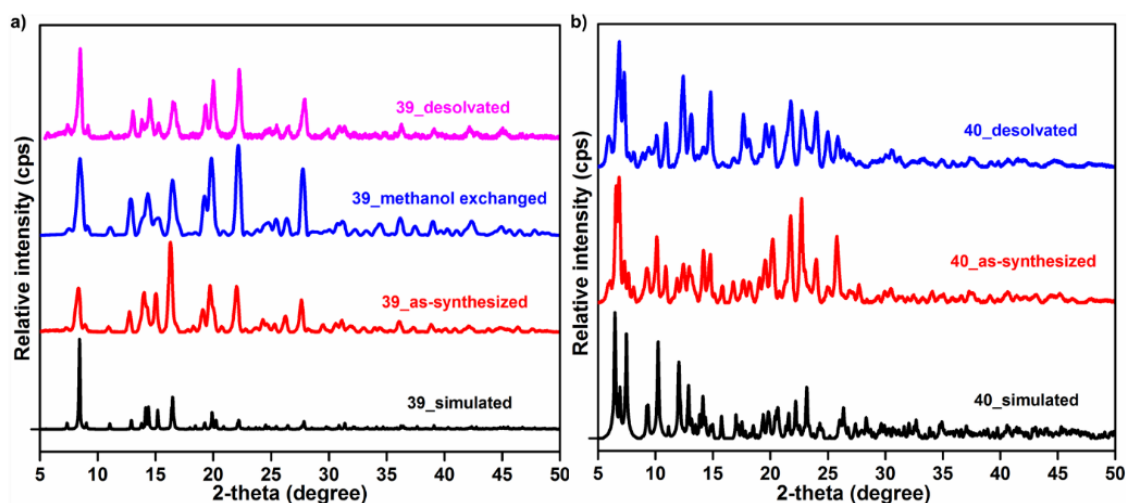


Figure 3.65. Powder X-ray diffraction (PXRD) pattern of as-synthesized and desolvated samples of (a) **39** and (b) **40**, compared with the simulated powder pattern obtained from the single crystal data of **39** and **40**, respectively.

molecule (calculated 12.9 %), whereas the methanol exchanged sample exhibits the weight loss of about 7 % which can be attributed to the loss of coordinated water and methanol (calculated 7.5 %). No appreciable weight loss in the TG profile for desolvated sample of **39**, indicates the removal of coordinated water molecule after framework activation. A similar TG profile was obtained for **40** also. As shown in (Figure 3.66b), initial weight loss of about 10 % in the temperature range of 60 °C to 120 °C can be ascribed due to the loss of coordinated THF molecule. No weight loss due to the lattice THF molecules was observed because of low boiling nature of THF which were escaped during sample drying. No weight loss in the TG profile for desolvated sample of **40**, indicates the removal of coordinated THF molecule after framework activation.

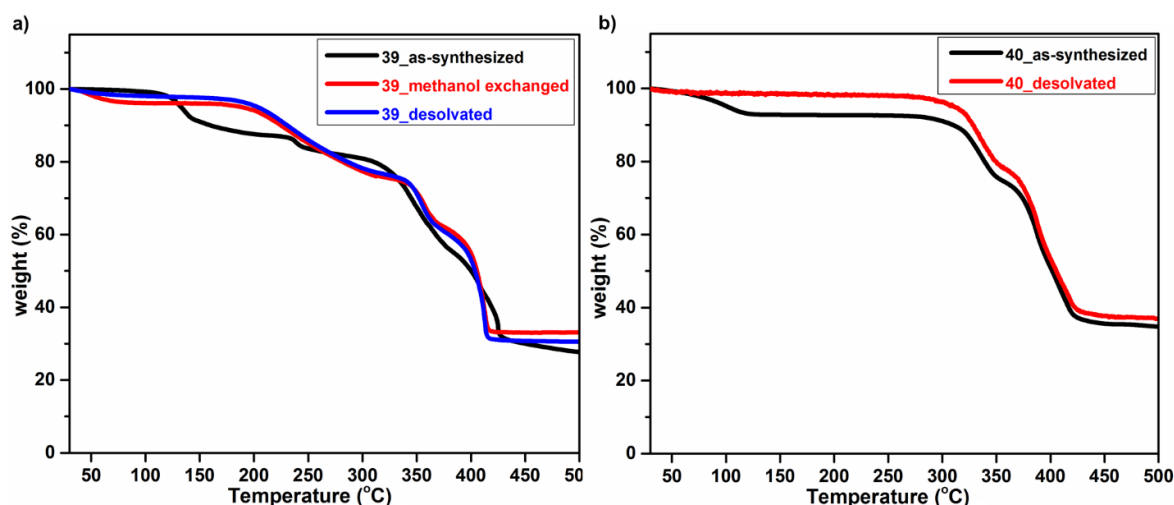


Figure 3.66. Thermogravimetric profile for the as-synthesized and desolvated samples of (a) **39** and (b) **40**, respectively.

Gas sorption studies. The coordinated and the guest solvent molecules can be removed by heating under vacuum conditions to obtain the desolvated/activated frameworks in both the cases. As mentioned before, the activated samples of **39** and **40** have open pores of about $10.9 \times 12.1 \text{ \AA}^2$ ($7.1 \times 9.0 \text{ \AA}^2$) and $10.23 \times 13.76 \text{ \AA}^2$ ($6.03 \times 10.6 \text{ \AA}^2$), respectively. The presence of open channels encouraged us to examine permanent porosity in both the compounds. Prior to adsorption measurements, the sample (~100 mg) was activated by degassing at an elevated temperature of 393 K under vacuum conditions (20 mTorr) for 24 hours to generate the desolvated frameworks. The loss of lattice solvents was confirmed by thermogravimetric and analysis (Figure 3.66). Furthermore, the PXRD pattern of the activated sample revealed that the original framework structure is retained after the activation process (Figure 3.65). The low temperature gas sorption measurements reveal that both the samples adsorb appreciable amount of CO_2 but very less amount of N_2 . The Brunauer-Emmett-Teller (BET) and the Langmuir surface area for **39** and **40** was estimated to be $61 \text{ m}^2\text{g}^{-1}$ and $109 \text{ m}^2\text{g}^{-1}$ for **39** and $67 \text{ m}^2\text{g}^{-1}$ and $76 \text{ m}^2\text{g}^{-1}$ for **40** respectively, based on the CO_2 adsorption measurement (Figure 3.67).

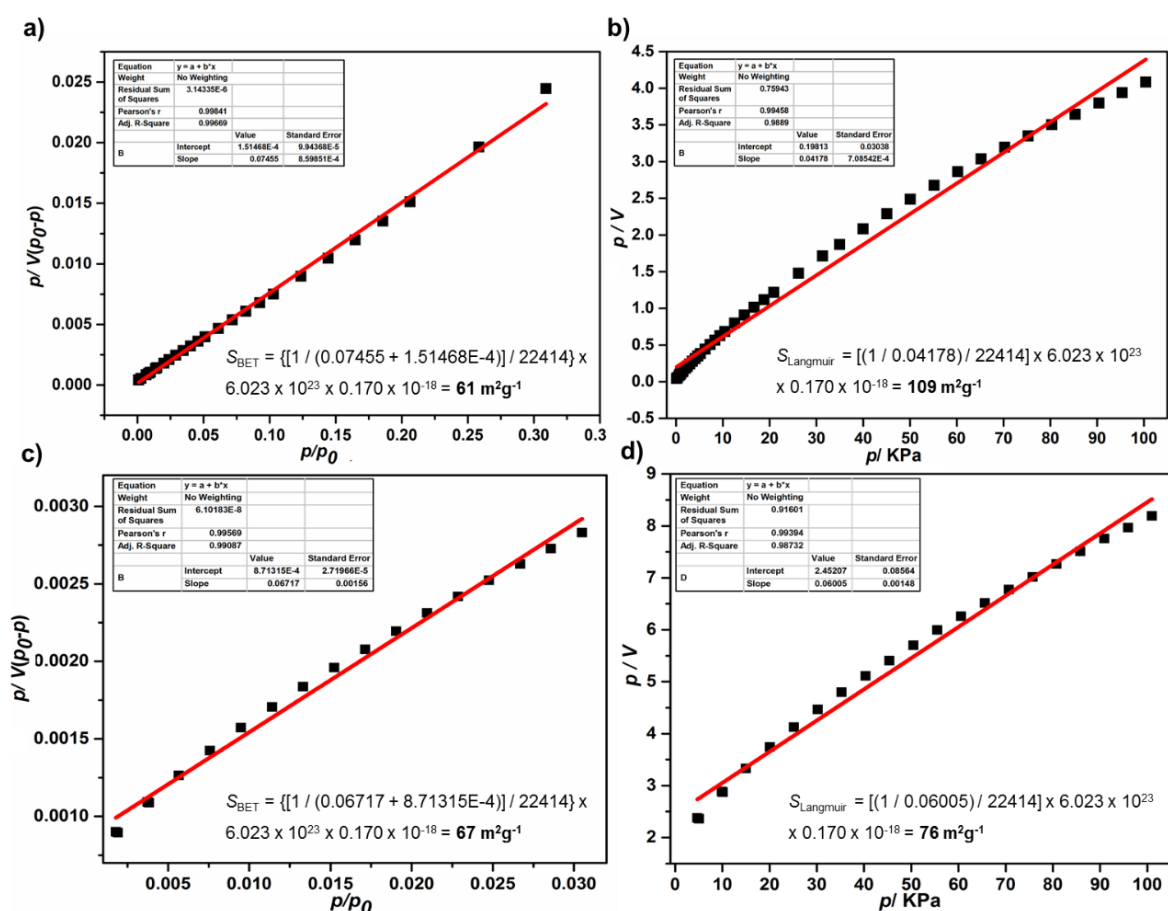


Figure 3.67. BET and Langmuir surface area of obtained from the CO_2 adsorption isotherm for (a and c) **39** and (b and d) **40**, respectively.

In order to determine the quantitative binding strength of CO₂ molecules with the framework, the isosteric adsorption enthalpy (Q_{st}) was calculated based on the Clausius-Clapeyron equation, using the adsorption isotherms collected at different temperatures (Figure 3.68). The Q_{st} value at zero loading was found to be ~25 kJ mol⁻¹ and ~28 kJ mol⁻¹, for **39** and **40**, respectively, indicating good binding affinity of CO₂ with the framework in both cases.

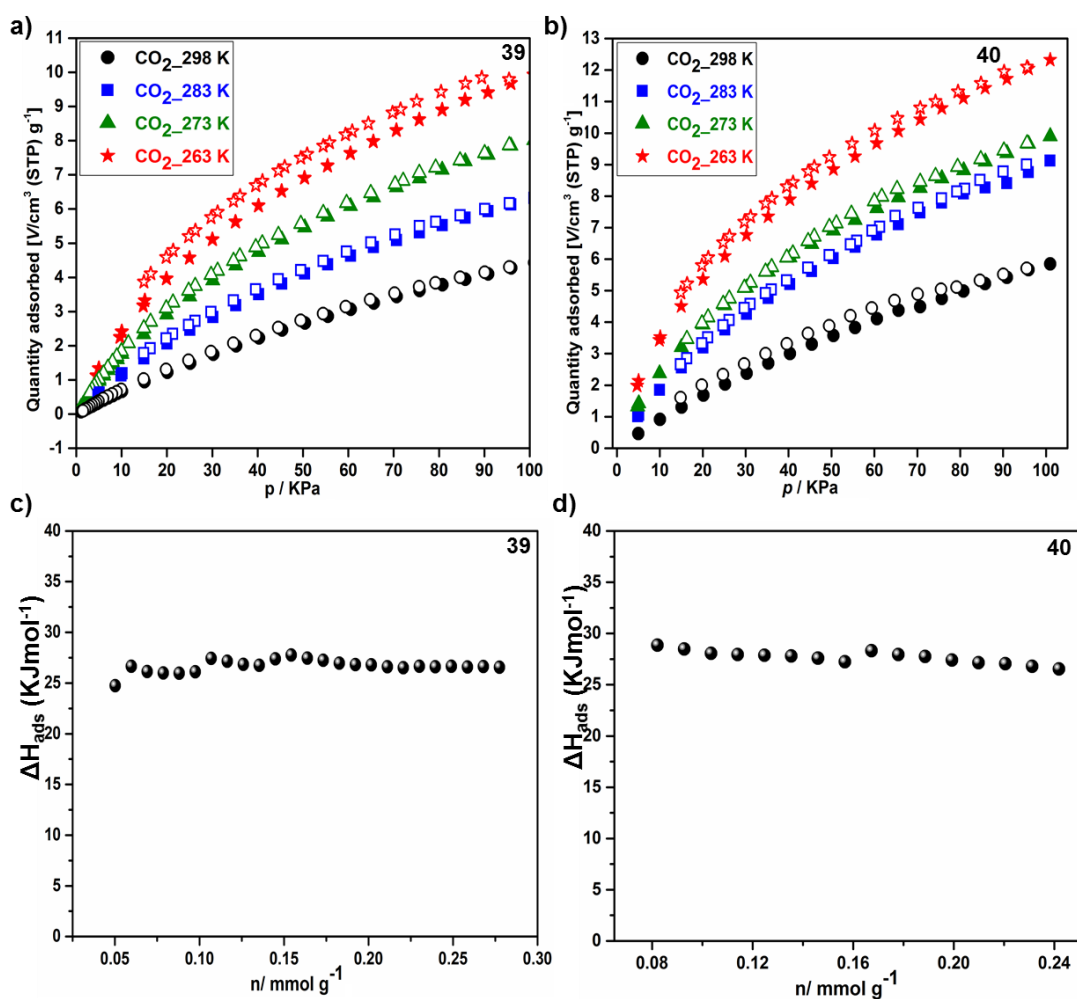


Figure 3.68. CO₂ sorption isotherms at different temperatures for (a) **39**, (b) **40** and variation of isosteric heat of adsorption for CO₂ with respect to surface coverage for (c) **39** and (d) **40**, respectively.

Catalysis Studies. Due to the microporous nature and coordinatively unsaturated metal site in **39**, it was tested for its catalytic activity as an active heterogeneous catalyst for Lewis acid promoted reactions. The Knoevenagel condensation and Strecker reactions are well known Lewis acid catalyze C-C and C-N bond forming reactions used for the synthesis of benzylidene malono-nitriles and α-aminonitriles, respectively.

To check the feasibility of **39** towards the Knoevenagel condensation reaction, the reaction between benzaldehyde and malononitrile was picked as a test reaction. Both the components were placed in a capped glass vial along with a catalytic amount (3 mol%) of **39**. The reaction was performed at room temperature using methanol as reaction medium. The progress of the reaction was monitored by TLC and the final conversion was calculated by ^1H NMR spectroscopy. Inspired by the good catalytic activity, the versatility of **39** was further tested by the reaction of different types of substituted aromatic aldehydes and active methylene compounds. It resulted the corresponding α,β -unsaturated cyano/ester derivatives in good-to-excellent yields. The results are summarized in Table 3.7.

Table 3.7. Substrate Scope for the Knoevenagel Condensation Reaction Catalyzed by **39**^a

Entry	Aldehyde	R ₁ , R ₂	% yield ^b	TON ^c
1		R ₁ = R ₂ = CN	80 ^d	26.6
2		R ₁ = R ₂ = CN	82 ^d	27.3
3		R ₁ = R ₂ = CN	88 ^d	29.3
4		R ₁ = R ₂ = CN	85 ^d	28.3
5		R ₁ = R ₂ = CN	82	27.3
6		R ₁ = R ₂ = CN	62	20.6
7		R ₁ = R ₂ = CN	>99	33
8		R ₁ = R ₂ = CN	96	32
9		R ₁ = R ₂ = CN	92	30.6
10		R ₁ = R ₂ = CN	64	21.3
11		R ₁ = R ₂ = CN	>99	33
12		R ₁ = CN, R ₂ = COOMe	78	26
13		R ₁ = CN, R ₂ = COOMe	64	21.3
14		R ₁ = CN, R ₂ = COOMe	92	30.6
15		R ₁ = R ₂ = CN	17 ^e	5.6

^aReaction conditions: Aldehyde (0.1 mmol), active methylene compound (0.15 mmol) and reaction time: 60 minutes. ^bAverage percent yield for a set of triplicate runs, calculated by ^1H NMR of the crude products. ^cNumber of moles of product per mole of catalyst. ^dIsolated yield. ^eBlank reaction.

Table 3.8. Substrate Scope for the Strecker Reaction Catalyzed by **39**^a

Entry	Aldehyde/ketone	% yield ^b	TON ^c
1		91 ^d	30.3
2		89 ^d	29.6
3		90 ^d	30
4		57 ^d	19
5		80 ^d	26.6
6		85 ^d	28.3
7		62	20.6
8		68	22.6
9		88	29.3
10		86	28.6
11		92	30.6
12		96	32
13		96	32
14		27 ^e	9

^aReaction conditions: Aldehyde/ketone (0.1 mmol), amine (0.1 mmol), TMSCN (0.12 mmol) and reaction time: 6 h. ^bAverage percent yield for a set of triplicate runs, calculated by ^1H NMR of the crude products. ^cNumber of moles of product per mole of catalyst. ^dIsolated yield. ^eBlank reaction.

There are reports where metal organic coordination polymers have been utilized for Strecker reaction, but the scope of d^{10} metal ion-based coordination polymers is very limited for this reaction.³⁰¹ Therefore, for a three-component Strecker reaction, benzaldehyde,

trimethylsilyl cyanide (TMSCN) and aniline were used as the test substrates, where 3 mol% of **39** was taken in a Schlenk tube pursued by the addition of all the reactants. The reaction was carried out under a solvent free condition at room temperature under N₂ atmosphere. The progress of the reaction was monitored by TLC and the final conversion was calculated by ¹H NMR spectroscopy. The catalytic activity of **39** was further tested for different substrates, especially for the more reluctant ketone derivatives (Table 3.8). The results obtained for both the Knoevenagel and Strecker reactions reveal that the substrates with electron withdrawing group gave the maximum conversion while a drop in the product conversion was obtained for the substrates with electron donating substituents. This trend reveals the strong accelerating impact of electron withdrawing groups rather than an electron releasing group for the reactions involving nucleophilic attack at electrophilic carbon of carbonyl or imine groups. The stronger is the electron withdrawing ability of the substituent, the faster is the activation of carbonyls or imines for nucleophilic attack at and consequently faster the reaction. In all cases, products were isolated and characterized by ¹H and ¹³C NMR spectroscopy to confirm their identity and purity. For control experiments a blank reaction was carried out in the absence of catalyst. In each case very little product conversions indicates the active role of the catalyst in both the reactions.

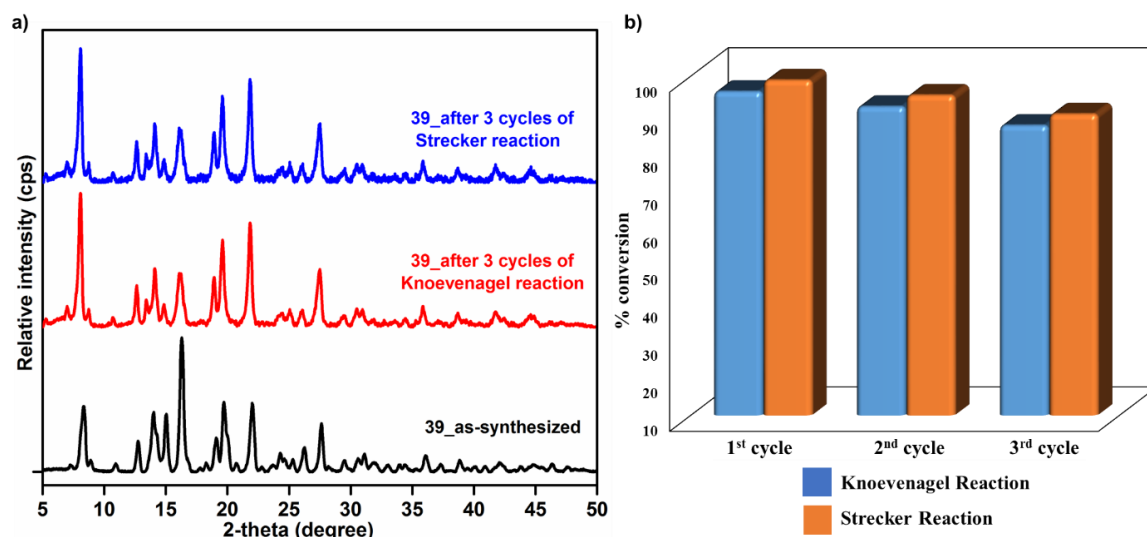


Figure 3.69. (a) PXRD pattern of **39** before and after catalysis experiments and (b) conversion for three consecutive cycles of (i) Knoevenagel condensation reaction of benzaldehyde and malononitrile and (ii) Strecker reaction of benzaldehyde with aniline and trimethylsilyl cyanide, catalysed by **39**.

In order to check its utility as a reusable catalyst, it was separated after the catalytic reaction by filtration, washed with chloroform and methanol, followed by drying under vacuum at 100 °C for 5 h to regenerate the active catalyst and reused for next catalytic experiment. In

both cases, no loss of crystallinity or phase purity of the catalyst was observed even after three cycles of reactions, as confirmed by the PXRD of the recovered catalyst (Figure 3.69a). Also, the catalyst can be reused up to three cycles in both cases with a slight loss (~8-10 %) in its catalytic activity (Figure 3.69b). Further, to check no leaching of the catalyst into the product stream, the catalyst was separated from the reaction mixture by centrifugation after certain time and the supernatant was provided with the same reaction conditions. No significant conversion was obtained (Figure 3.70) indicating heterogeneous nature of the catalyst and its active role as a catalyst in both the reactions. The efficiency of **39**, when compared to the catalytic activity of various coordination polymers that have been used as heterogeneous catalysts in the Knoevenagel and Strecker reactions is found to be comparable with the reported examples.^{252,256,301,302}

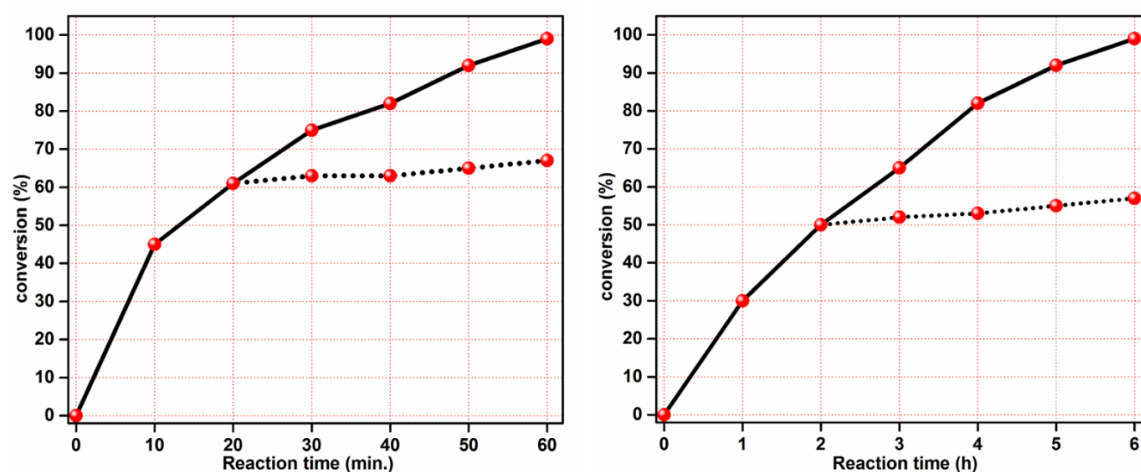


Figure 3.70. Progress of the reaction with time in presence of catalysts **39** (solid lines) and after separating the catalyst from the reaction mixture (dotted lines) for (left) Knoevenagel condensation reaction of benzaldehyde with malononitrile and (right) Strecker reaction of benzaldehyde with aniline and trimethyl silyl cyanide.

Based on the studies described above and on the basis of previous reports,^{302,303} plausible mechanisms are proposed and are shown in Figure 3.71. The open metal center (Lewis-acidic site) interacts with the O/N of the carbonyl/imine group (electrophile), resulting in polarization of these groups, which results in the enhancement of electrophilic character of the carbon atom of carbonyl or imine moieties. In addition, the O atom of the coordinated carboxylate group is known to impart basic character (Lewis-basicity) to the framework and can help in driving the reaction by activating the corresponding nucleophile.

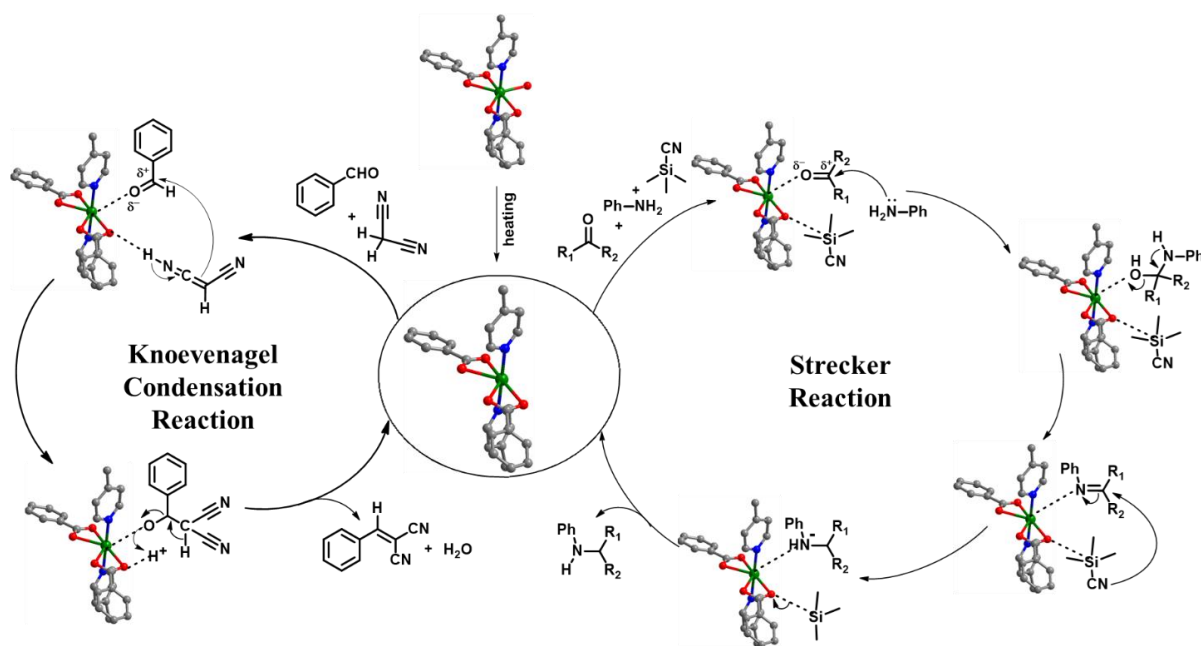


Figure 3.71. Plausible mechanisms for the Knoevenagel condensation and the Strecker reactions catalyzed by **39**.

Pillar ligand induced structural diversity and applications of coordination polymers. In this study, a set of four Cd(II)-coordination polymers have been synthesized using different pillar ligands. First two examples **37** and **38**, represents the isostructural frameworks, where the incorporation of azine functionalized ligand **4-bpdb** in case of **38**, imparts dual functionality to the framework. The Lewis-acidic open metal sites and Lewis-basic azo functionality into the framework makes it an efficient heterogeneous catalyst for Knoevenagel condensation reaction and three component Biginelli reaction. The introduction of the conformationally flexible ligand **bpp** in **39** has resulted in the formation of a helically chiral Cd(II) coordination polymer. This represents a special class of example where a chiral coordination polymer has been synthesized by the self-assembly of achiral components without the need of any chiral auxiliaries such as enantiopure solvents, additives, catalysts or a template. The helical chirality into the framework is due to the natural ability of V-shaped ligand (**H₂dmsdba**) to endorse a twisted conformation and the rotation freedom of Py-CH₂-CH₂-CH₂-Py bonds of the conformationally flexible ligand **bpp**, which adopts a helical arrangement when coordinated to the metal ion, giving rise to a chiral network. Further, the existence of exposed Lewis-acidic metal sites in **39** has been demonstrated by its heterogeneous catalytic activity towards the carbon-carbon (Knoevenagel condensation reaction) and carbon nitrogen (Strecker) bond forming reactions. The use of a long pillar ligand **1,5-ND-4-Py**, functionalized with aromatic fluorophore naphthyl group in case of **40**, has resulted in the formation of a 3D porous

framework with open metal sites. These kind of open frameworks, functionalized with aromatic fluorophores are known to impart interesting luminescence properties to the framework. All the factors play an important role in the structural diversity of these coordination polymers. In addition to the different conformational arrangement of N-donor ligands, the carboxylate linker also adopts different conformational arrangements, inducing the structural diversity in the resulting architectures. As shown in Figure 3.72, the angle between the two phenyl rings ($C_{Ph}-Si-C_{Ph}$) and the dihedral angle between the phenyl rings was different in all cases; maximum deviation the dihedral angle was observed in case of **40**.

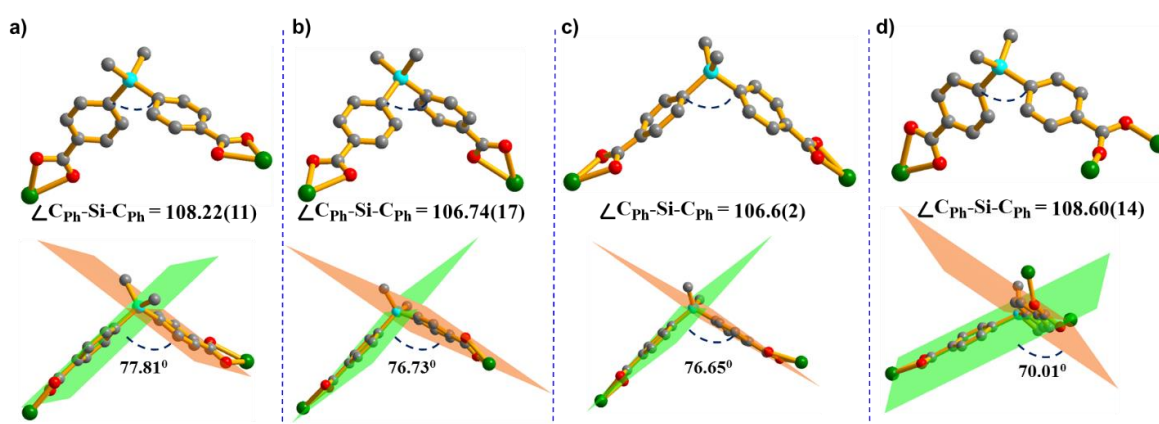


Figure 3.72. Different conformations of the dicarboxylate linker observed in (a) **37**, (b) **38**, (c) **39** and (d) **40**, respectively.

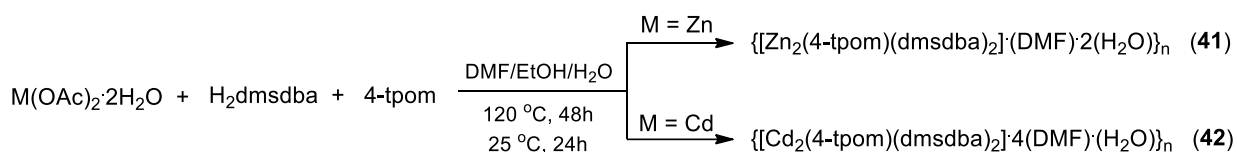
3.1.2.3 Architectures with semi-flexible tetra(pyridyl) ligands

In terms of coordination architectures comprised of mixed ligands, the polymers with flexible ligands exhibit more complex and unusual structures, as functional groups on the ligands offer variable configurations. Flexible pyridyl ligands, such as 1,2-bis-(4-pyridyl)-ethane (**bpe**), di(4-pyridyl)-ethylene (**dpe**), and 1,3-bis(4-pyridyl)-propane (**bpp**), often freely rotate to meet the requirement of flexible ligands in the self-assembly of such coordination polymers. As an important family of multidentate N-donor ligands, organic pyridyl ligands have been extensively employed in the preparation of coordination polymers with multidimensional networks and interesting properties. Among the flexible N-donor bridging ligands, tetrakis(4-pyridyloxy-methylene) methane (tpom) is a good candidate for the construction of coordination polymers with diverse structures. The ligand can serve as four connecting node and the four pyridyl arms can twist around the central quaternary carbon atom randomly. Various coordination polymers exhibiting different topologies and functional properties have been explored with tpom ligand in combination with rigid

polycarboxylate linkers, there are a limited reports for the coordination polymers with bent dicarboxylate linkers with tpom ligand. Therefore, the present section illustrates the synthesis, structural properties, stability and topology of coordination polymers of divalent transition metals with bent dicarboxylate (**H₂dmsdba**) and flexible tetradentate tpom ligand. In addition, the selective carbon dioxide adsorption properties and their catalytic properties for the chemical conversion of carbon dioxide into the cyclic carbonates have been studied.

The solvothermal reaction of zinc acetate or cadmium acetate with dicarboxylate linker (**H₂dmsdba**) and 4-tpom ligand has resulted in the formation of coordination polymers $\{[\text{Zn}_2(4\text{-tpom})(\text{dmsdba})_2] \cdot (\text{DMF}) \cdot 2(\text{H}_2\text{O})\}_n$ (**41**) and $\{[\text{Cd}_2(4\text{-tpom})(\text{dmsdba})_2] \cdot 4(\text{DMF}) \cdot (\text{H}_2\text{O})\}_n$ (**42**) (Scheme 3.19). Both the compounds have been structurally characterized by single crystal X-ray diffraction analysis and their molecular formulas have been established by a combination of elemental analysis, thermogravimetric and single crystal analysis.

Scheme 3.19. Synthesis of **41** and **42**.



Single crystal structure analysis Single crystal suitable for X-ray diffraction analysis in both cases were obtained by solvothermal reaction at 120 °C. Both **41** and **42** crystallizes in the monoclinic crystal system with C2/c space group and forms isostructural non-interpenetrated 3D frameworks. The asymmetric unit in **41** contains one Zn(II) ion, one **dmsdba**²⁻ and one-half of the tetradentate ligand 4-tpom, whereas in case of **42**, it consists of three Cd(II) ions, three carboxylate linkers **dmsdba**²⁻ and one and half of the tetradentate ligand 4-tpom. The coordination environment around the Zn(II) center in **41** and Cd(II) center in **42** is N2O4 type tetrahedral and N2O4 types distorted octahedral, where the four coordination sites of the tetrahedral geometry around the Zn(II) are occupied by two nitrogen atoms of the two pyridyl groups of the tetradentate ligand 4-tpom and two oxygen atoms of the carboxyl oxygen of two different **dmsdba**²⁻, which are coordinated to the metal center in a monodentate fashion (Figure 3.73a). The six coordination sites of the octahedral geometry around the Cd(II) in **42** are occupied by two nitrogen atoms of the two pyridyl groups of the tetradentate ligand 4-tpom and four oxygen atoms of the carboxyl oxygen of

two different **dmsdba**²⁻, which are coordinated to the metal center in chelated bidentate fashion (Figure 3.73b).

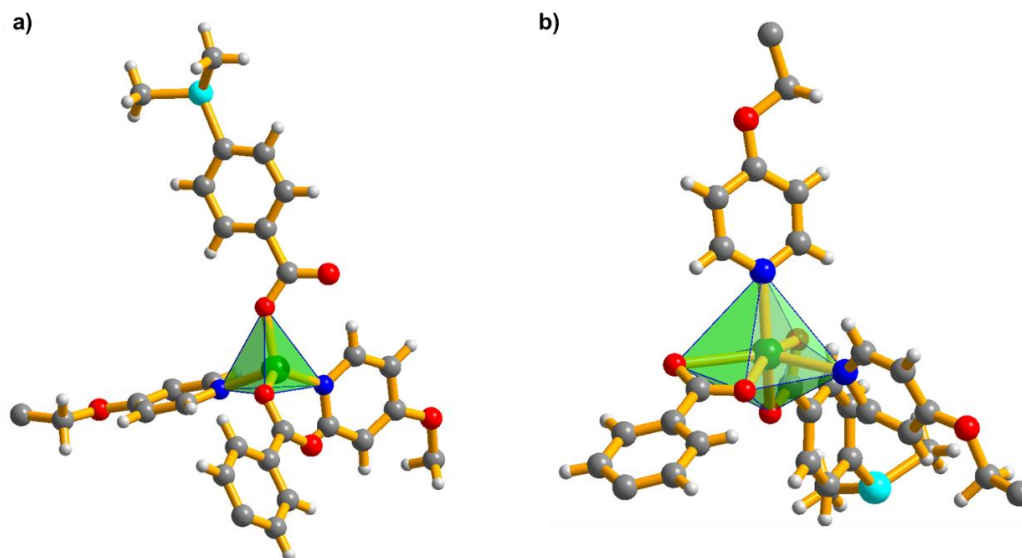


Figure 3.73. Coordination environment around the metal center in (a) **41** and (b) **42**, respectively.

The asymmetric unit in both cases is expanded by full span of the tetradentate pyridyl ligand and dicarboxylate linker to form the overall 3D frameworks (Figure 3.74). The structure consists of open channels filled with highly disordered solvent molecule. The diffused electron density due to these solvent molecules was squeezed out using solvent masking option in Olex2 software²⁰² during the structure refinement. The total potential solvent-accessible void volume was estimated to be 26 % (1675/6424 Å³ per unit cell volume) and 28 % (5696/20400 Å³ per unit cell volume) in **41** and **42**, respectively by the PLATON software.²⁷⁵ The pore wall in both cases are functionalized by the oxygen atoms of the tetrapyrridyl ligands. The various M-O and M-N bond lengths are in the usual range for this kind of complexes. The bond angle values lying in the range of 98.91° to 127.14° in case of **41** and 53.9° to 166.3° in case of **42** are indicative of prominent distortions from the regular geometries around the metal centers in both cases. All the crystallographic information pertaining to data collection and structure refinement parameters, selected bond lengths and bond angles are listed in Table A15, A37 and A59, respectively.

The structure in both the cases can be simplified as node and linker representation, where the ligand **4-tpom** and the metal centers (Zn(II) and Cd(II) in **41** and **42**) can be considered as 4-connecting nodes and the carboxylate linker **dmsdba**²⁻ can be considered as a bent linker (Figure 3.75). Further examination of the node and linker representation indicates that both the frameworks exhibit a 4-connected uninodal net NbO; 4/6/c2; sqc35 (topos &

RCSR.ttd) topology with Schläfli point symbol $\{6^4.8^2\}$, as determined by the TOPOS program.²⁷⁴

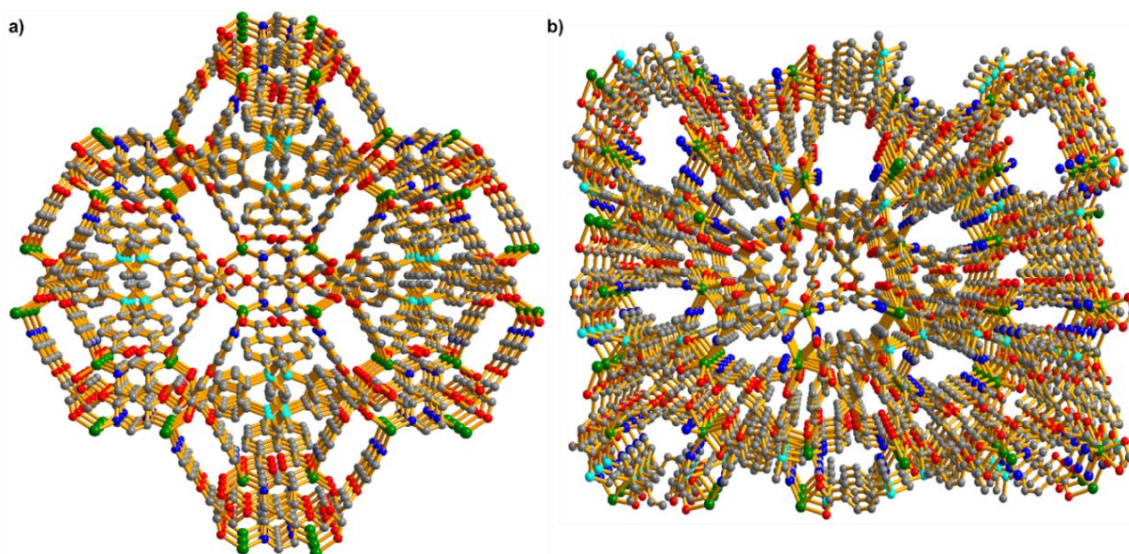


Figure 3.74. Perspective view of the 3D frameworks in case of (a) **41** and (b) **42**, respectively.

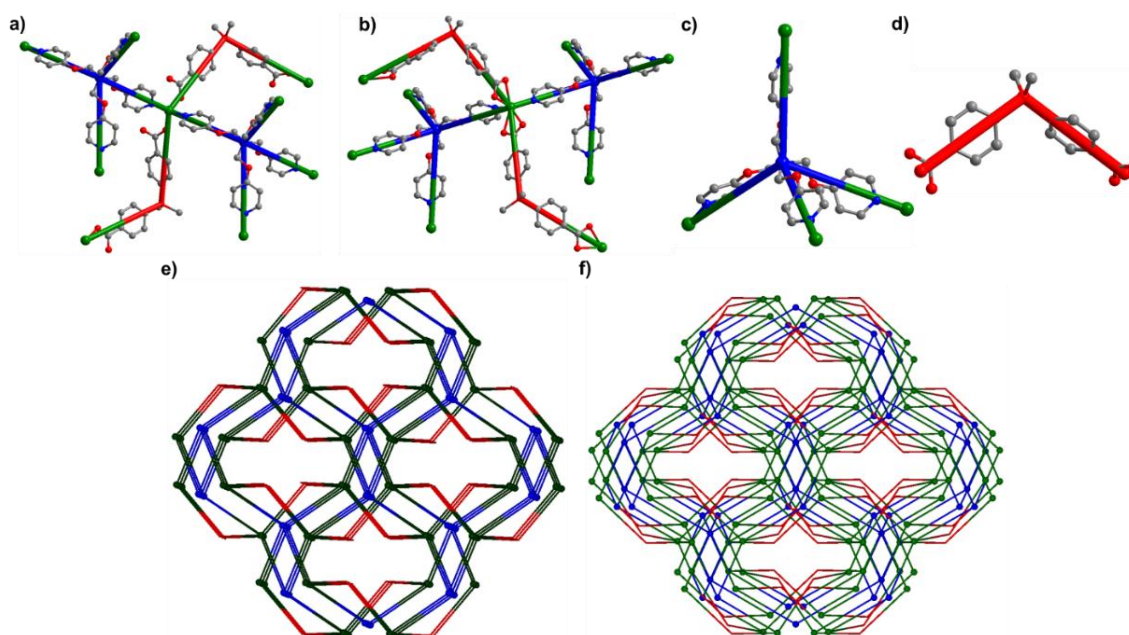


Figure 3.75. Simplified node and linker type representation for **41** and **42**; (a-d) Zn(II) and Cd(II) centers, and the ligands 4-tpom and dmsdba²⁻, represented as 4-connected nodes and a bent linker, respectively, (e and f) the overall 4-connected uninodal net NbO; 4/6/c2; sqc35 topology in **41** and **42**, respectively.

FTIR and PXRD analysis. FTIR spectra of **41** and **42** was recorded in the solid state at room temperature as KBr pellets. The sharp peaks due to asymmetric (ν_{asym}) and symmetric (ν_{sym}) stretching vibrations of the carboxylates appeared at 1613 cm^{-1} and 1388 cm^{-1} with ($\Delta\nu = 225 \text{ cm}^{-1}$) in **41** and 1605 cm^{-1} and 1398 cm^{-1} with ($\Delta\nu = 207 \text{ cm}^{-1}$) in **42**. The $\Delta\nu$

values in case of **41** and **42** are indicative of the monodentate and chelated bidentate binding of the carboxylate to the metal center in **41** and **42**, respectively. In addition to it, the sharp peaks at 1666 cm^{-1} and 1658 cm^{-1} in **41** and **42** can be ascribed due to the presence of lattice DMF molecules in the open channels. Further, the shift from the asymmetric and symmetric -C=O stretch for free **H₂dmsdba** (1690 cm^{-1} and 1416 cm^{-1}), indicates strong binding of the carboxylates to the metal center in both cases. In order to the phase purity of the as-synthesized materials, powder X-ray diffraction patterns were recorded for **41** and **42** at room temperature. As shown in Figure 3.76, the experimentally obtained powder patterns for as-synthesized compounds were in good agreement with the simulated powder patterns (obtained from the single crystal data). This confirms the crystallinity and phase purity of the as-synthesized **41** and **42**, respectively.

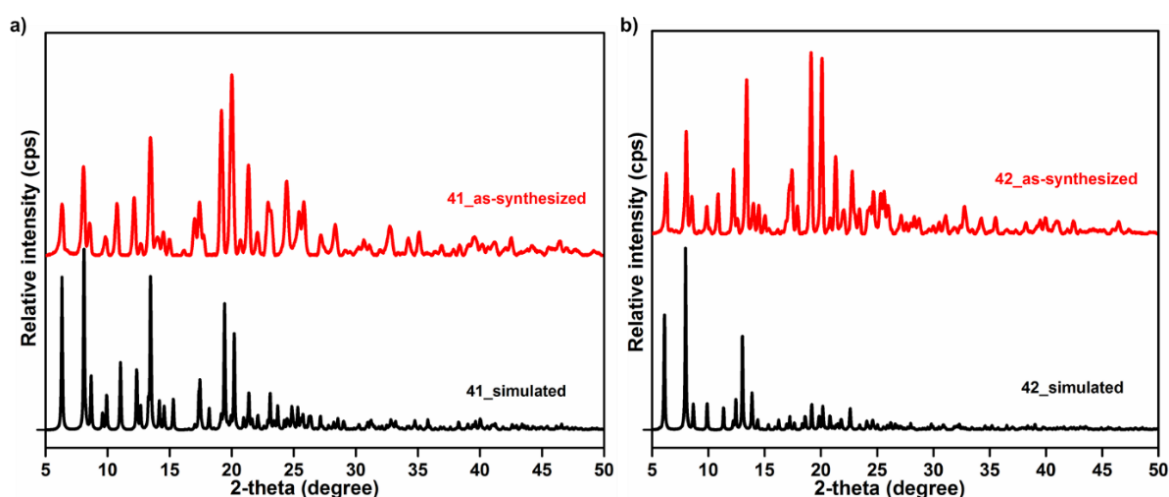


Figure 3.76. Powder X-ray diffraction patterns for the as-synthesized samples of (a) **41** and (b) **42** compared with their respective simulated powder patterns obtained from the single crystal data.

Framework stabilities and thermal properties. The thermal stability and structural variation as a function of temperature for **41** and **42** was studied by their thermogravimetric analysis (TGA). Single phase polycrystalline samples of **41** and **42** was heated between 30–500 °C, under a dinitrogen atmosphere and corresponding weight loss was plotted with respect to temperature. As shown in Figure 3.77a and b, the as-synthesized sample of **41** exhibits an initial weight loss of about 9 % in the temperature range of 50 °C to 150 °C, which is in good agreement due to the loss of one DMF and two water molecules (calculated 8.4 %) present in the crystal lattice, whereas no such weight loss was observed in the case of desolvated sample indicating the removal of highly disordered lattice solvents generating the framework with available pores. Similarly, the initial weight loss of about 18 % in the temperature range of 50 °C to 200 °C in case of **42**, can be attributed to the loss of four DMF

and one water molecule (calculated 19 %) present in the crystal lattice. Furthermore, as seen in case of **41**, no such weight loss was observed after framework activation/desolvation in case of **42** also. In both the cases the compounds were found to be stable up to 350 °C and 325 °C, respectively. In addition to study their thermal stability by thermogravimetric analysis, the retention of crystallinity and phase purity at higher temperature was also studied by in-situ variable temperature powder X-ray diffraction analysis. Their PXRD patterns indicates that both the samples **41** and **42**, maintains their crystallinity and phase purity up to 350 °C and 325 °C, respectively (Figure 3.77 c and d).

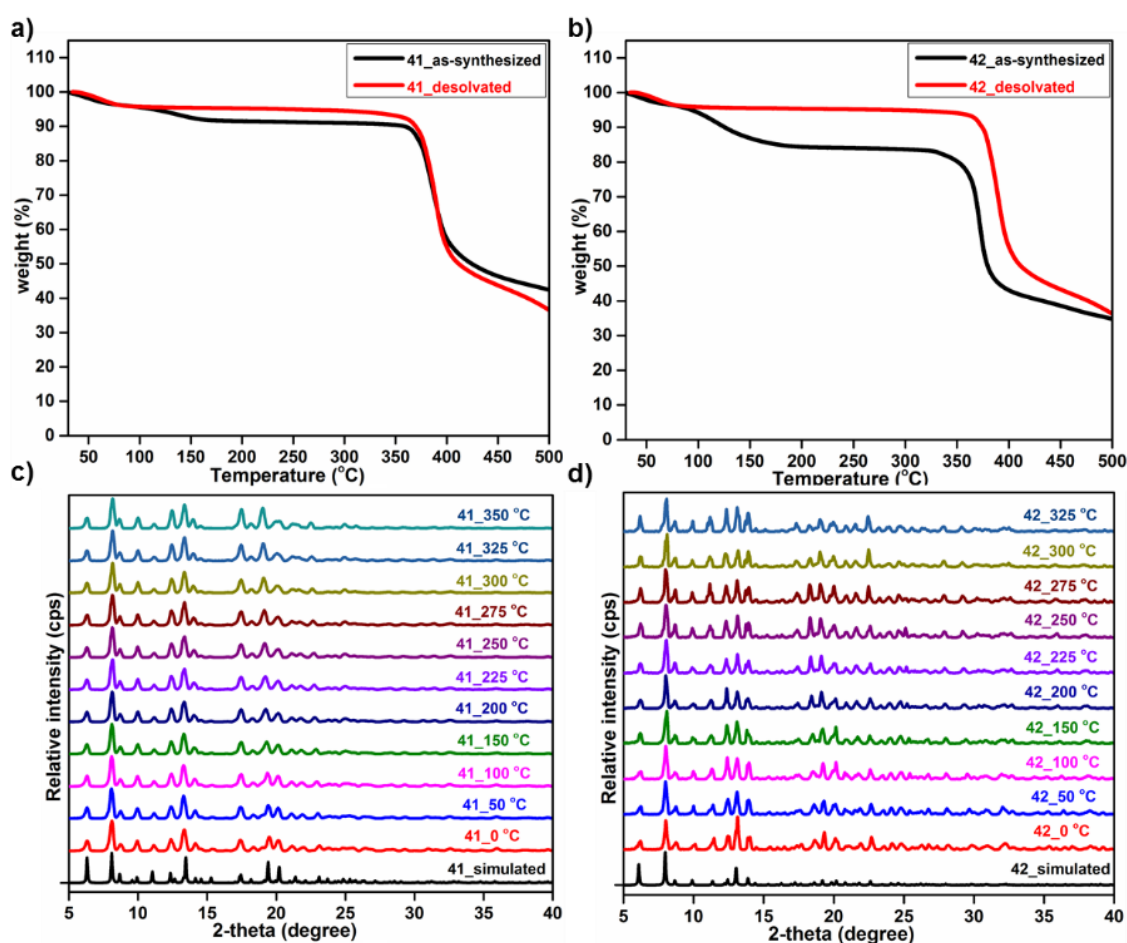


Figure 3.77. Thermogravimetric profile and variable temperature powder X-ray diffraction patterns for (a and c) **41** and (b and d) **42**, indicating their thermal stability and retention of crystallinity and phase purity at higher temperatures.

Gas sorption studies. The presence of open channels and potential solvent-accessible voids in **41** and **42** (*vide-supra*), has encouraged us to examine permanent porosity in both the compounds by gas sorption properties. Prior to adsorption measurements, the sample (~100 mg) was activated by degassing at an elevated temperature of 393 K under vacuum conditions (20 mTorr) for 24 hours to generate the desolvated frameworks. The loss of

lattice solvents was confirmed by thermogravimetric and analysis (Figure 3.77a and b). Due to the similar void volumes in their structures both the compounds show similar sorption properties. The low temperature gas sorption measurements reveal that both the samples adsorb appreciable amount of CO₂ but very less amount of N₂ at low temperatures. The Brunauer-Emmett-Teller (BET) and the Langmuir surface area was estimated to be 257 m²g⁻¹ and 323 m²g⁻¹ for **41** and 283 m²g⁻¹ and 391 m²g⁻¹ for **42** respectively, based on the CO₂ adsorption isotherms (Figure 3.78).

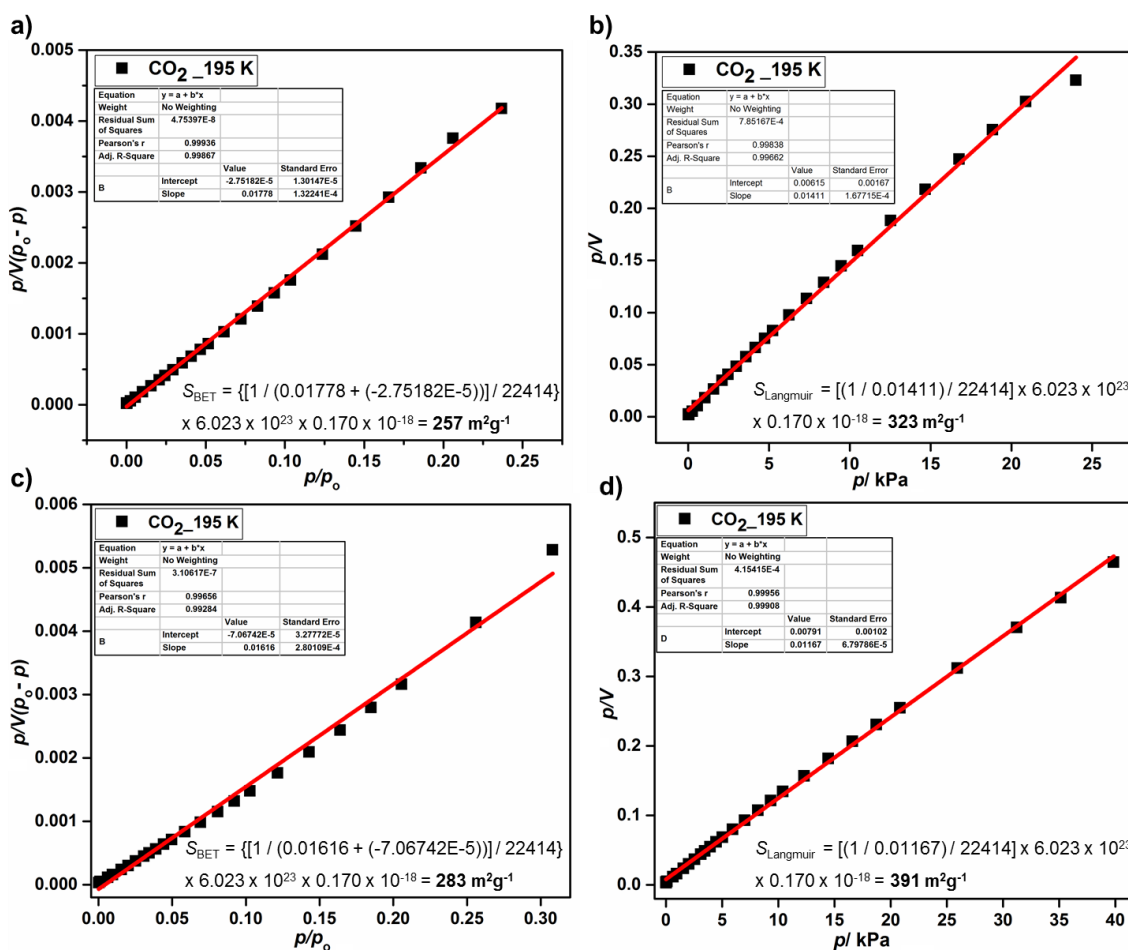


Figure 3.78. BET and Langmuir surface area of obtained from the CO₂ adsorption isotherm for (a and c) **41** and (b and d) **42**, respectively.

In order to determine the quantitative binding strength of CO₂ molecules with the framework, the isosteric adsorption enthalpy (Q_{st}) was calculated based on the Clausius-Clapeyron equation, and virial method. Pure-component isotherms for CO₂ collected at different temperatures were used for the estimation of Q_{st} by either methods. The CO₂ sorption isotherms for **41** and **42** at different temperatures are shown in Figure 3.79.

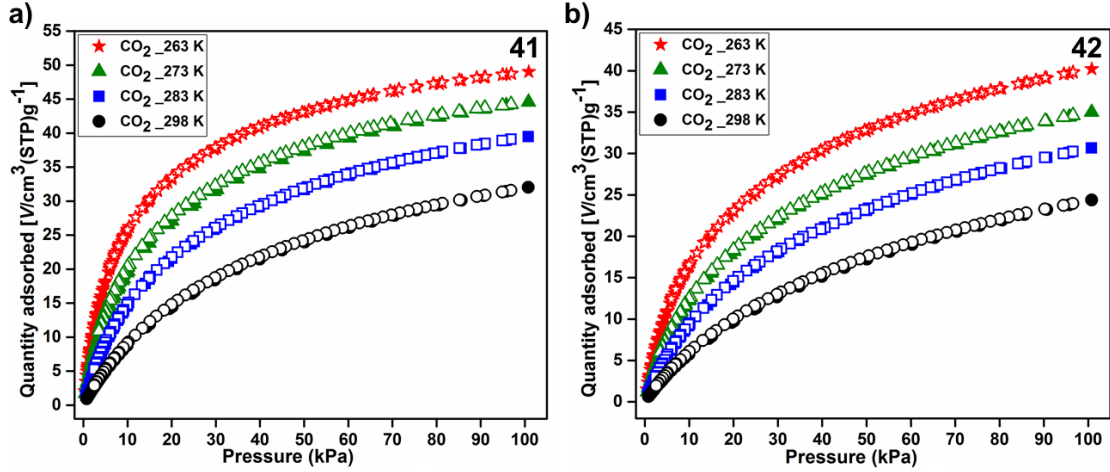


Figure 3.79. CO₂ sorption isotherms at different temperatures for (a) **41** and (b) **42**, respectively.

According to Clausius-Clapeyron equation, Q_{st} is defined as:

$$Q_{st} = - (\partial \ln x / \partial (1/T))_y$$

where, x is the pressure, T is the temperature, R is the gas constant and y is the adsorption amount. These calculations were done through the “Heat of Adsorption” function embedded in the Belsorp Adsorption/Desorption Data Analysis software version 6.3.1.0.

For the estimation of Q_{st} by virial method, a virial-type expression consisting of the temperature dependent virial parameters a_i and b_i were employed to calculate the enthalpy of absorption for CO₂. The virial type expression is given below:

$$\ln(P) = \ln(N) + \frac{1}{T} \sum_{i=0}^m a_i N^i + \sum_{j=0}^n b_j N^j$$

where, P is the pressure expressed in Torr, N is the amount adsorbed in mmol/g, T is the temperature in K, a_i and b_i is the virial coefficients, and m , n represent the number of coefficients required to adequately describe the isotherms (m and n were gradually increased until the contribution of a and b coefficients added further were negligible towards the overall final fit, and the average value of the squared deviations from the experimental values was minimized). The values of the virial coefficient a_0 to a_i were taken to calculate the isosteric heat of adsorption using the following expression.

$$Q_{st} = -R \sum_{i=0}^m a_i N^i$$

Where, Q_{st} is the coverage dependent isosteric heat of adsorption and R is the universal gas constant. The pure component CO₂ isotherms at different temperatures were fitted into virial-type expression at the pressure range 1 to 100 kPa (Figure 3.80a and b).

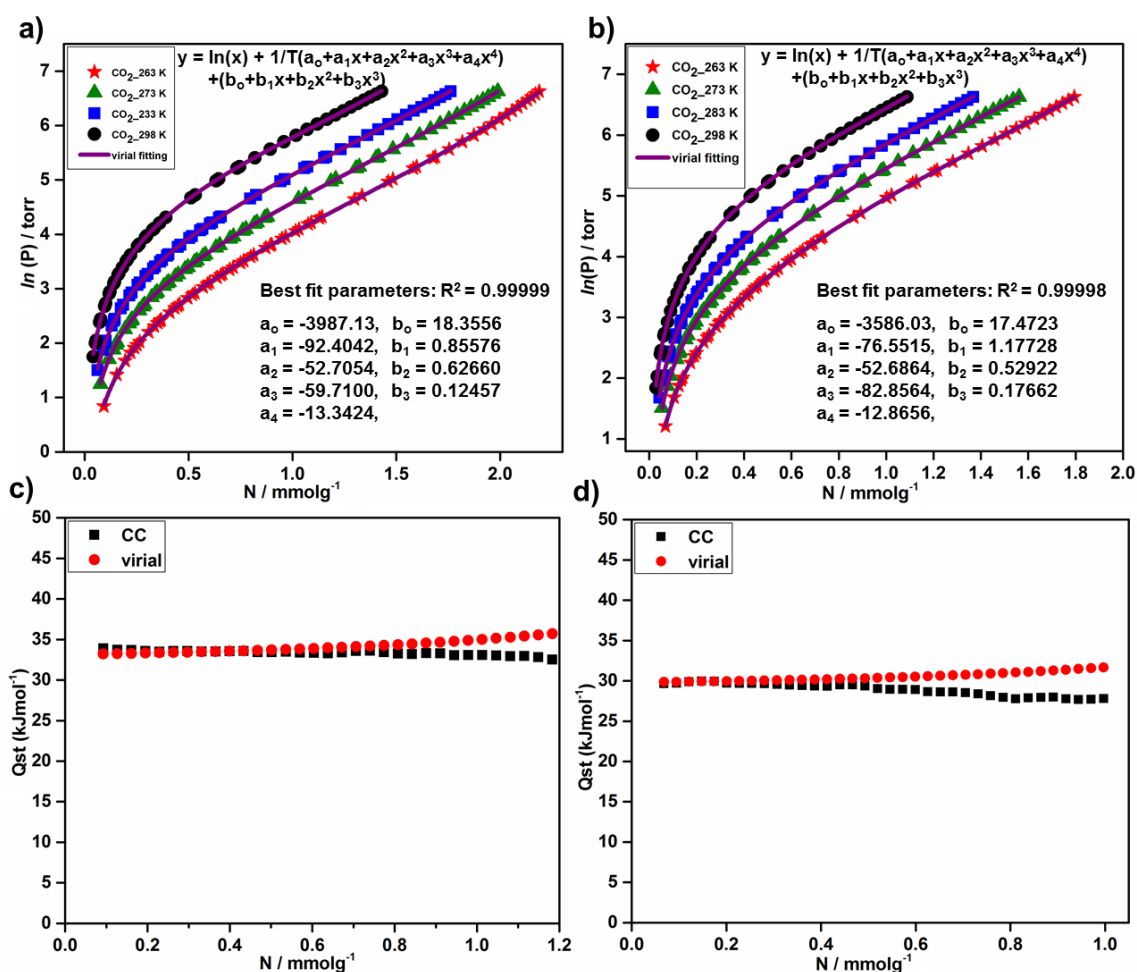


Figure 3.80. Fitting (purple solid lines) of the CO₂ adsorption isotherms for (a) **41** and (b) **42**, measured at different temperatures using the virial method and (c and d) represents the variation of isosteric heat of adsorption with respect to surface coverage for **41** and **42**, respectively.

At zero loading, the isosteric heat of adsorption (Q_{st}) for **41** and **42** was found to be 33.2 kJmol⁻¹ and 29.7 kJmol⁻¹, respectively. The variation of heat of adsorption with respect to the surface coverage for **41** and **42** is presented in Figure 3.80c and d, respectively. The Q_{st} values at zero coverage for both **41** and **42** are comparable with values for M' MOF-20 (28.4 kJmol⁻¹), {Cd₂(L)(2,6-NDC)₂}_n (28.1 kJmol⁻¹), {Cu(bc ppm)H₂O}_n and JUC-199 (29 kJmol⁻¹), MIL-53(Cr) and Hpip@ZnPC-2 (32 kJmol⁻¹) but higher than values for UCMC-1 (12 kJmol⁻¹), MOF-5 (17 kJmol⁻¹), CuBTTri (21 kJmol⁻¹), IITKGP-5 (22.6 kJmol⁻¹), IITKGP-6 (23 kJmol⁻¹) and NOTT-40 (25 kJmol⁻¹) (Table A67).

Inspired from the very low uptake of large sized nitrogen gas molecules (diameter: 3.64 Å) compared to the smaller CO₂ molecules (diameter: 3.30 Å) in both the cases, both **41** and **42** were further tested for the selective carbon dioxide adsorption properties. It is well-known that the separation of CO₂ from CH₄ in the pre-combustion process of natural gas and separation of CO₂ from N₂ in the post-combustion process is very essential. Therefore,

the small pore spaces and the establishment of permanent porosity within **41** and **42** motivated us to examine its CO₂, CH₄ and N₂ sorption isotherms and potential for gas separations.

Single component gas sorption isotherm was measured at different temperatures under 1 bar pressure. As shown in Figure 3.81, both **41** and **42** takes up moderate amount of carbon dioxide 44.5 cm³g⁻¹ and 34.9 cm³g⁻¹ at 273 K and 32.1 cm³g⁻¹, and 24.3 cm³g⁻¹ at 298 K, respectively. In comparison both these takes up very less amount of N₂ and CH₄ when compared to the CO₂ uptake at both temperatures. The higher CO₂ affinity can be attributed to the smaller kinetic diameter of CO₂ (diameter: 3.30 Å) compared to those of N₂ (diameter: 3.64 Å) and CH₄ (diameter: 4.09 Å) as well as the difference of quadrupole moment, thus allowing CO₂ molecules to diffuse easily into the pores.³⁰⁴

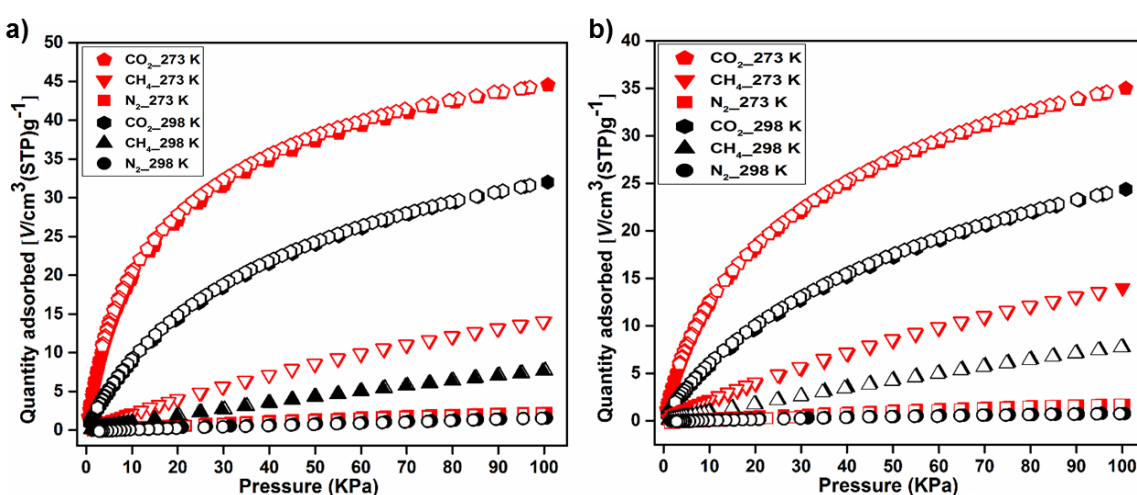


Figure 3.81. CO₂ adsorption isotherms compared with the adsorption isotherms of N₂ and CH₄ at 273 K and 298 K for (a) **41** and (b) **42**.

The hydrogen sorption isotherm for **41** and **42** indicates an uptake of 0.83 wt% and 0.85 wt%, respectively at 77 K and 1 bar pressure (Figure 3.82). The uptake amount is found to be moderate among the well-known MOF materials in the literature. For example, ZIF-8 (BET: 1630 m²g⁻¹) absorbs 1.27 wt%, IRMOF 9 (BET: 1904 m²g⁻¹) absorbs 1.27 wt%, PCN-17 (BET: 820 m²g⁻¹) absorbs 0.94 wt% under 1 bar and 77 K.³⁰⁵ Both the frameworks exhibit very fast rise in H₂ uptake, indicating the highest affinity toward H₂ at low pressures. This kind of phenomenon is known for coordination polymers with crowded pore environment.

Catalysis Studies. Carbon dioxide (CO₂), the most abundant waste gas from anthropogenic emissions has been cited as the leading culprit, causing global warming and subsequent climate changes. However, in contrast to the toxic nature of the currently used C1 sources

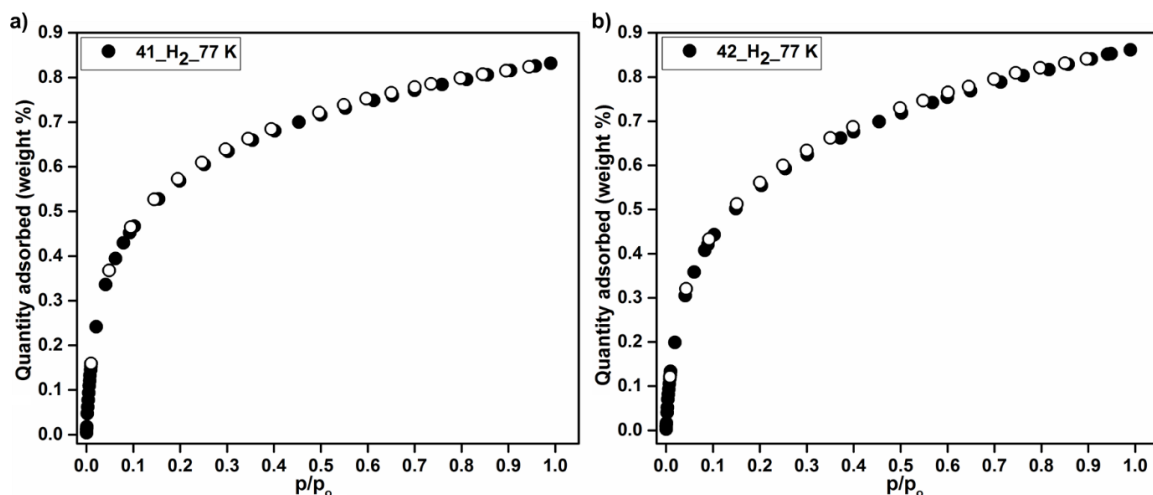
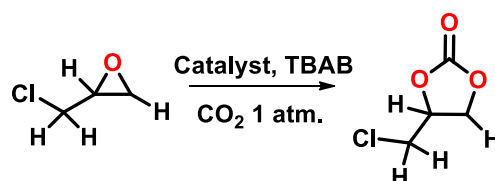


Figure 3.82. H₂ sorption isotherms for (a) **41** and (b) **42** at 77 K and 1 bar pressure.

such as phosgene and CO, CO₂ as a cheap, nontoxic, nonflammable and abundant carbon resource, can be considered as C1 feed stock. Therefore, in addition of utilization of porous coordination polymers as landfill material for carbon dioxide capture and sequestration (CCS), the utilization of such materials for chemical transformation of CO₂, into value-added industrial products turns into an alternative yet sustainable means of effective CO₂ elimination. However, many metal organic frameworks and other materials are known to catalyze such transformations, but the reactions generally require high temperature and high CO₂ pressure. There are a limited number of reports for chemical conversion of CO₂ into cyclic carbonates at ambient conditions,^{183,192,200} Therefore, together with significant and highly selective CO₂ uptake and due to the presence of unsaturated metal coordination in **41**, it was further studied for the catalytic activity towards cycloaddition reaction of CO₂ with epoxides to generate cyclic carbonates at ambient conditions. For a typical reaction, epichlorohydrin was chosen as a standard substrate with **41** as a catalyst in conjunction with tert-butylammoniumbromide (TBAB) as a co-catalyst. The reaction was carried out in a solvent free condition and 1 bar pressure of CO₂. The progress of the reaction was monitored by ¹H NMR spectroscopy. The reaction conditions were optimized over different parameters (Table 3.9).

With increase in the amount of catalyst **41** (0.25 to 1 mol %) or co-catalyst TBAB (0.25 to 2 mol %), increase in the product conversion was obtained (entries 1-7, Table 3.9). The progress of the reaction was also studied for reaction temperature and it was found that the progress of the reaction was much faster at higher temperature while a very low product conversion was obtained at room temperature (25-30 °C) (entries 8-10, Table 3.9). In order to find the most suitable reaction condition, a test reaction was carried out at 40 °C with 0.5

Table 3.9. Optimization for the cycloaddition of CO₂ with epichlorohydrin, catalyzed by **41**^a

Entry	41 (mol%)	TBAB (mol%)	Temperature (°C)	Time (h)	conversion (%) ^b	TON ^c
1	0.5	0.25	40	16	34	68
2	0.5	0.5	40	16	72	144
3	0.5	1.0	40	16	92	184
4	0.5	2.0	40	16	96	192
5	0.25	1.0	40	16	56	224
6	0.75	1.0	40	16	94	125
7	1.0	1.0	40	16	97	97
8	0.5	1.0	25-30	16	25	50
9	0.5	1.0	60	16	94	188
10	0.5	1.0	80	16	>99	200
11	0.5	1.0	40	04	69	138
12	0.5	1.0	40	08	79	158
13	0.5	1.0	40	12	82	164
14	0.5	1.0	40	16	95	190
15	0.5	1.0	40	20	>99	200
16	1	----	40	20	10	20
17	----	2	40	20	18	----
18	42 ^d	1.0	40	20	18	18
19	Zn(OAc) ₂ ^e	1.0	40	20	15	15

^aReaction conditions: Epichlorohydrin (0.2 mmol) was reacted with CO₂ under 1 atmospheric pressure maintained with a balloon filled with CO₂ gas, in the presence of co-catalyst *tert.* butyl ammonium bromide (TBAB) in a solvent free condition. ^bCalculated by ¹H NMR of the crude products. ^cNumber of moles of product per mole of catalyst. ^d1 mol % of **42** and ^e1 mol % of zinc acetate dihydrate was used instead of **41**.

mol % of **41** and 1 mol % of TBAB and the progress of the reaction was studied with time (entries 11-15, Table 3.9). It was found that after 20 h almost 100 % product conversion was obtained (Figure 3.83). The progress of the reaction was further studied in the absence of either of **41** or TBAB (entries 16-17, Table 3.9). A very less product conversion was obtained in both cases, indicating the requirement of both **41** and TBAB in the catalytic process. The corresponding metal salt and compound **42**, were also tested for the same reaction under identical reaction conditions. In both cases very less product conversion was

obtained (entries 18-19, Table 3.9). The results further support the fact that the catalytic activity of **41**, is due to the presence of unsaturated metal sites in the framework.

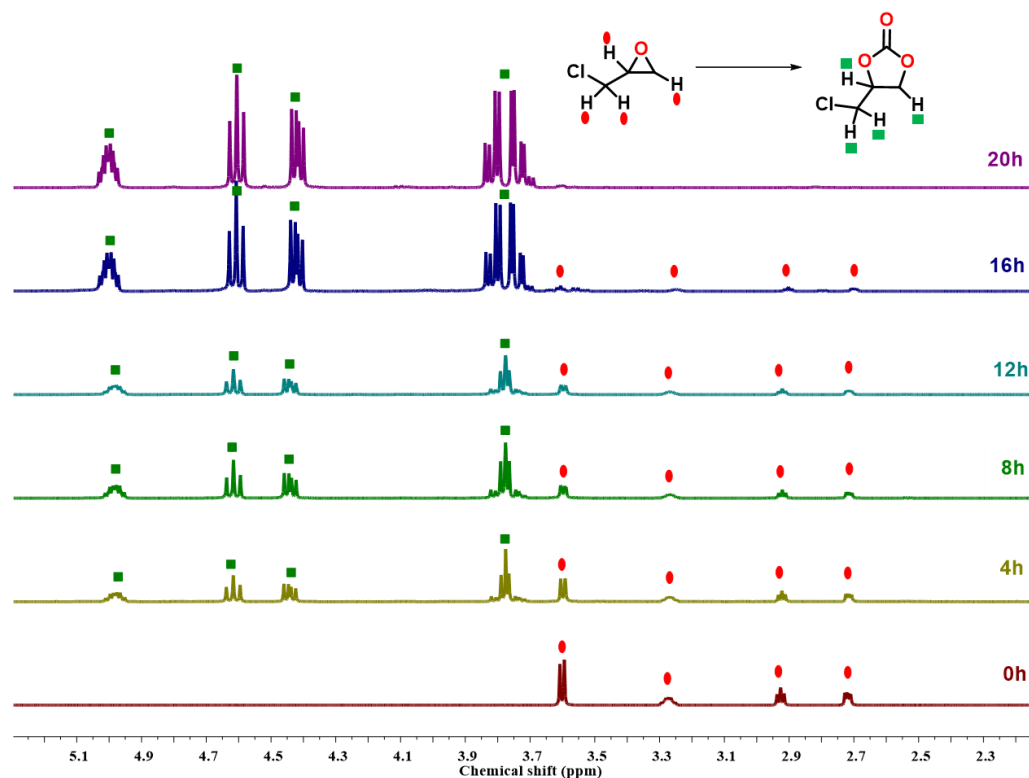
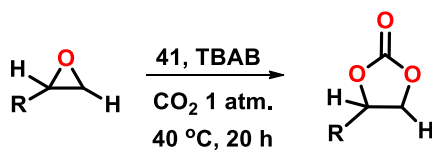


Figure 3.83. Progress of the cycloaddition reaction of CO₂ with epichlorohydrin, catalyzed by **41**, monitored by ¹H NMR spectroscopy.

After having the optimized conditions in hand, the catalytic activity of **41** was further examined for different functional group substituted epoxides under the same reaction conditions. A good product conversion was obtained for epoxides substituted with aliphatic groups, whereas a decrease in product conversion was observed for styrene oxide and its derivatives. The results are summarized in Table 3.10.

To determine the recyclability of the catalyst, it was isolated after the reaction by filtration, washed with DCM and dried under vacuum. The catalyst was recycled in three consecutive experiments. No significant loss of catalytic activity was observed even after three cycles of reaction (Figure 3.84a). Based on the PXRD data of the catalyst recorded before and after the reaction, no loss of crystallinity or the phase purity of the catalyst was observed (Figure 3.84b). Furthermore, to check any leaching of the catalyst into the product stream, the catalyst was separated from the reaction mixture by centrifugation and the reaction mixture was subjected to similar reaction conditions. The progress of the reaction did not increase significantly (Figure 3.84c), indicating the active role of the catalyst for cycloaddition reaction.

Table 3.10. Substrate scope for cycloaddition of CO₂ with epoxides, catalyzed by **41**^a

Entry	Reactants	Products	conversion (%) ^b	TON ^c
1			>99	200
2			>99	200
3			96	192
4			93	186
5			85	170
6			83	166
7			87	174
8			56	112

^aReaction conditions: 0.2 mmol of epoxide was reacted with CO₂ under 1 atmospheric pressure maintained with a balloon filled with CO₂ gas in the presence of 0.5 mol % of **41** and 1 mol % of co-catalyst *tert.* butyl ammonium bromide (TBAB) in a solvent free condition. ^bCalculated by ¹H NMR of the crude products. ^cNumber of moles of product per mole of catalyst.

Based on the aforementioned experiments and previous reports,^{183,192,200} a plausible mechanism for the catalytic cycloaddition of epoxide and CO₂ into cyclic carbonate is presented in Figure 3.85. The reaction generally requires a binary catalytic system involving a Lewis acid catalytic site and a nucleophilic cocatalyst (TBAB) required for ring opening of epoxide. As illustrated in Figure 3.85, the unsaturated Zn(II) centers provides Lewis acidic sites for the O atom of epoxide molecules to coordinates to the Lewis acidic centers and hence leading to the activation of the epoxy ring.

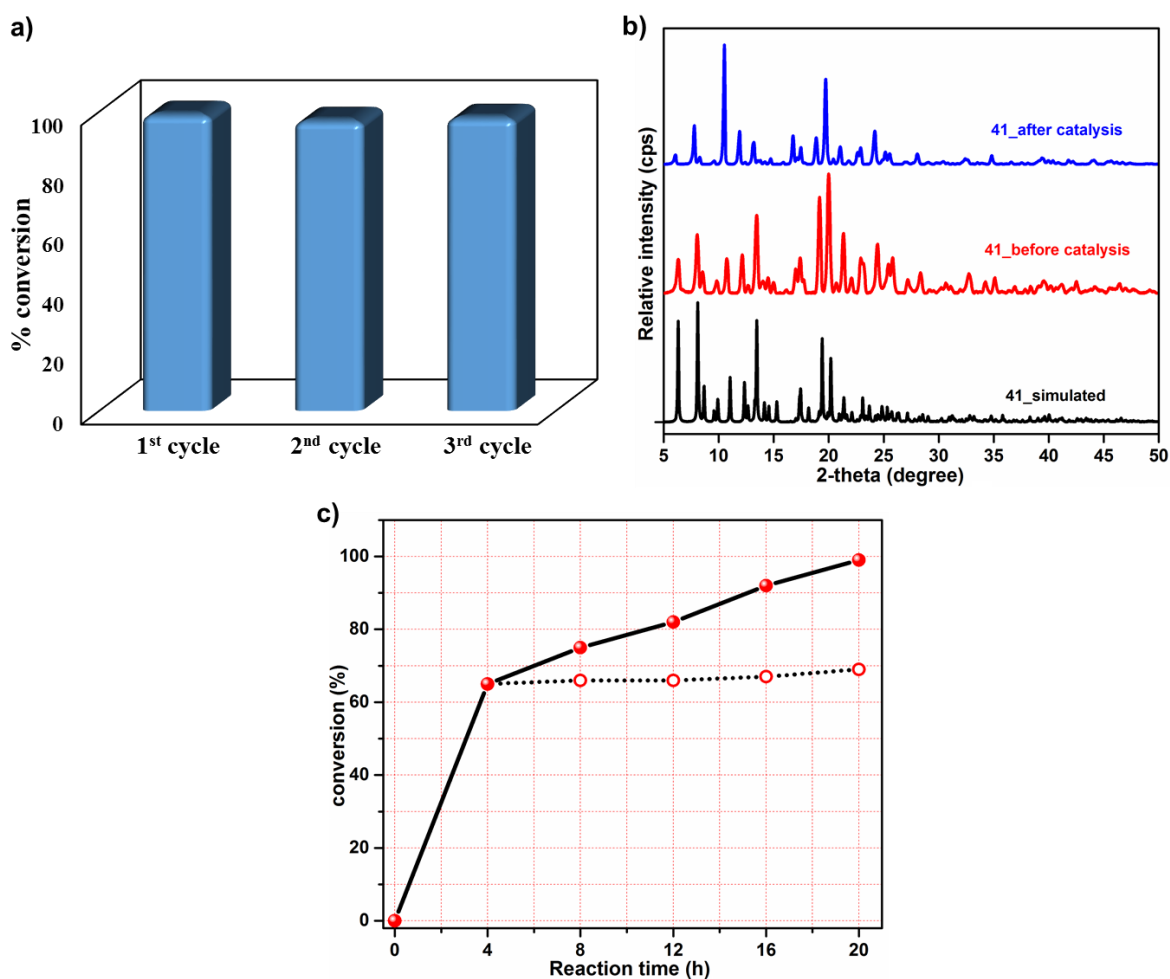


Figure 3.84. (a) conversion for three consecutive cycles for the cycloaddition reaction of CO₂ with epichlorohydrin, (b) PXRD pattern of **41** before and after catalysis experiments and of (c) progress of the reaction with time in presence of catalysts (solid lines) and after separating the catalyst from the reaction mixture (dotted lines) for cycloaddition reaction of CO₂ with epichlorohydrin.

The second step involves the ring opening of the epoxide from the less hindered C atom by nucleophilic attack of the Br⁻ from TBAB to form a metal-coordinated bromoalkoxide. The next step involves the polarization of the CO₂ and its interaction with the opened epoxy ring to form the metal carbonate species which immediately undergoes an intramolecular ring-closure reaction to generate cyclic carbonate and, simultaneously, TBAB and catalyst are regenerated. The use of nucleophiles as co-catalysts is essential for ring opening of epoxides, and the catalysts, which lack a nucleophilic anion, require high temperatures to achieve ring opening of epoxides. Therefore, it can be deduced that the synergistic effect of the Lewis acidic sites and TBAB along with highly selective CO₂ capture in the confined pores of **41** promotes the cycloaddition reaction.

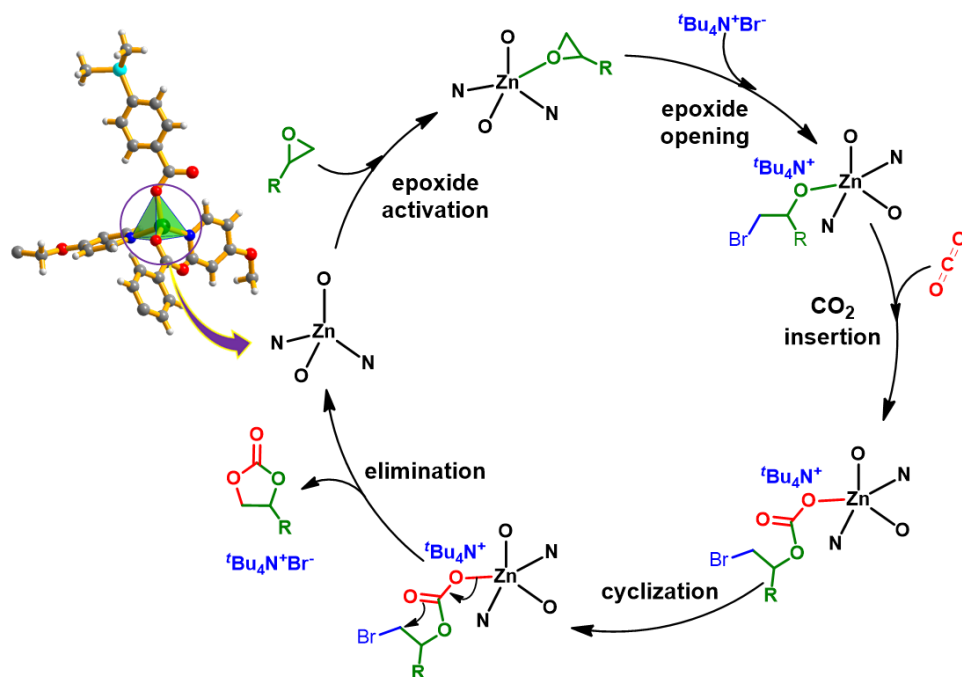


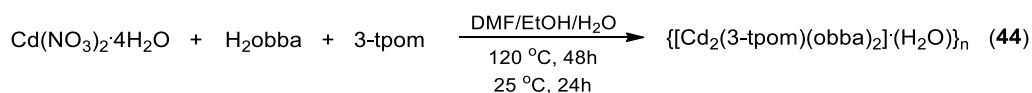
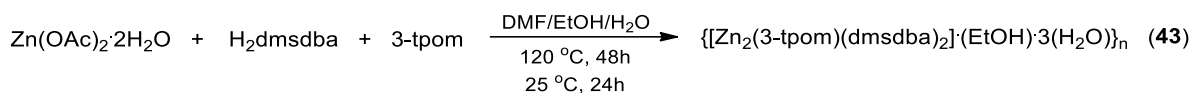
Figure 3.85. Proposed reaction mechanism for the cycloaddition of CO₂ with epoxides catalyzed by **41**.

The present study thus illustrates the utilization of flexible tetradentate tetrapyridyl ligand (**4-tpom**) in combination with bent dicarboxylate linker (**H₂dmsdba**) in the syntheses of two isostructural 3D coordination polymers with narrow pores, functionalized with oxygen atoms present in the tetradentate ligand structure. The compounds exhibit a 4-connected uninodal net NbO topology and are highly stable as indicated by their thermogravimetric and temperature dependent powder X-ray diffraction analysis. Gas sorption analysis reveals that both the compounds are highly selective for CO₂ capture over N₂ and CH₄. In addition, due to the presence of coordinatively unsaturated metal sites in **41**, it shows very good heterogeneous catalytic activity towards chemical transformation of CO₂ with epoxides into value added cyclic carbonates under ambient conditions. The catalyst can be easily separated and reused successively for three cycles. The catalyst framework did not degrade and, promisingly, no significant fall in the product conversion of the cycloaddition occurred, indicating chemical stability of the framework.

Inspired from the above results for the coordination polymers fabricated from the flexible tetradentate ligand (**4-tpom**), we have further expanded this study using another tetradentate ligand (**3-tpom**) in combination with dicarboxylate linkers (**H₂dmsdba**) and (**H₂obba**), respectively. The ligand **3-tpom** is a structural isomer of **4-tpom** where the N-donor coordination site of the pyridyl ring has been shifted from fourth to third position in order to systematically investigate the influence of the coordination site shifting of the ligand

structure to the final architecture and their properties. A set of two coordination polymers $\{[\text{Zn}_2(3\text{-tpom})(\text{dmsdba})_2]\cdot\text{EtOH}\cdot 3\text{H}_2\text{O}\}_n$ (**43**) and $\{[\text{Cd}_2(3\text{-tpom})(\text{obba})_2]\cdot\text{H}_2\text{O}\}_n$ (**44**) have been synthesized (Scheme 3.20) and the effect of coordination site shifting for the structural diversity has been discussed.

Scheme 3.20. Synthesis of **43** and **44**.



The solvothermal reactions of zinc(II) acetate or cadmium(II) nitrate with **3-tpom** in combination with dicarboxylate linkers **H₂dmsdba** or **H₂obba** have resulted in the formation of **43** and **44**, respectively. Both compounds have been structurally characterized by single crystal X-ray diffraction analysis and their molecular formulas has been established by a combination of elemental analysis, thermogravimetric and single crystal X-ray diffraction analysis.

Single crystal structure analysis Single crystal suitable for X-ray diffraction analysis in both cases were obtained by solvothermal reaction at 120 °C. Compound **43** crystallizes in the monoclinic crystal system with *Cc* space group. The asymmetric unit in **43** contains two Zn(II) ion, two **dmsdba**²⁻ and one of the tetradentate ligand 3-tpom along with three water and one ethanol molecule in the crystal lattice. The coordination environment around the Zn(II) center is similar to **41**. The carboxylate linker is fully deprotonated and the asymmetric unit is expanded by the full span of the carboxylate linker **dmsdba**²⁻ and the tetrapyrindyl ligand **3-tpom** to generate an overall 3D framework (Figure 3.86) similar to **41**. All the structural features are also similar to **41**. All the crystallographic information pertaining to data collection and structure refinement parameters, selected bond lengths and bond angles are listed in Table A16, A38 and A60, respectively. The total potential solvent-accessible void volume was estimated to be 13 % (764/5834 Å³ per unit cell volume) per unit cell volume by the PLATON software.²⁷⁵

Compound **44** crystallizes in a triclinic crystal system with *P* $\bar{1}$ space group. The asymmetric unit contains two Cd(II), two carboxylate linkers **obba**²⁻, one tetrapyrindyl ligand **3-tpom** and one water molecule occupying the lattice site. The coordination environment around each Cd(II) is N2O4 type distorted octahedral, where the six coordination sites of the

octahedral geometry around the Cd(II) are occupied by two nitrogen atoms of the two pyridyl groups of the tetradentate ligand 3-tpom and four oxygen atoms of the carboxyl group of two different **obba**²⁻, which are coordinated to the metal center in a chelated bidentate fashion (Figure 3.87a).

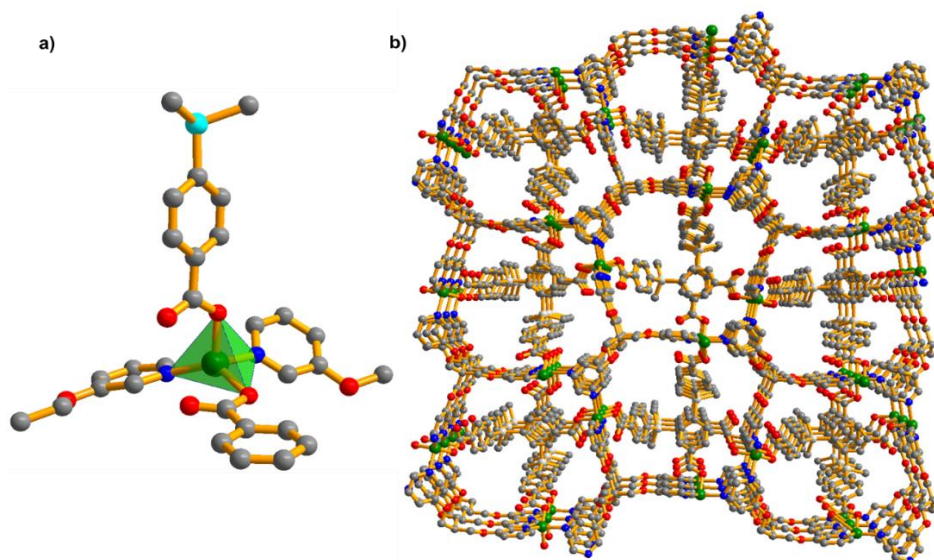


Figure 3.86. Perspective view of the (a) coordination environment around the Zn(II) center and (b) overall 3D framework in **43**.

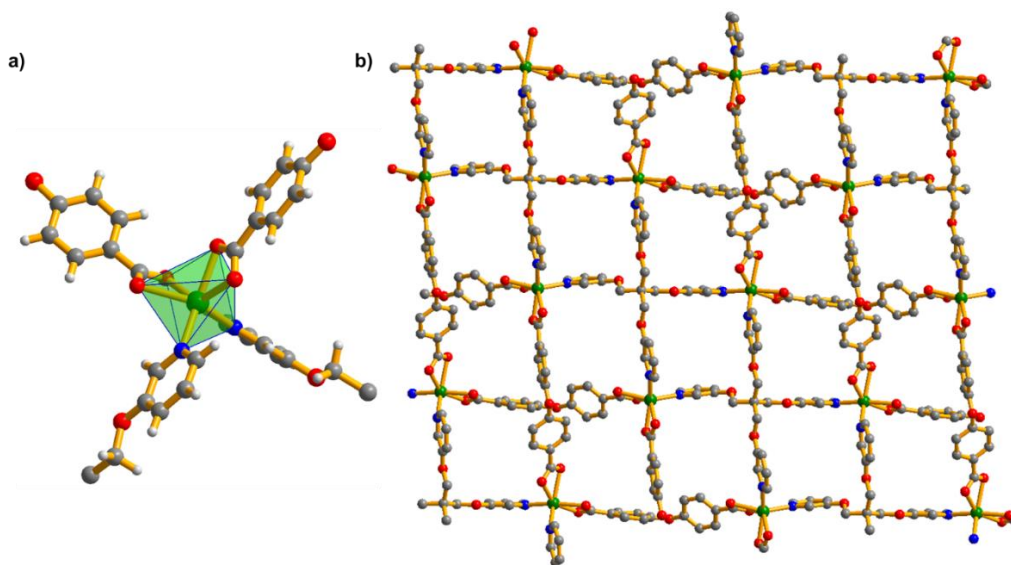


Figure 3.87. Perspective view of the (a) coordination environment around the Cd(II) center and (b) overall 2D framework in **44**.

Prominent distortions from the regular octahedral geometry is reflected from the cisoid angles [56.87° - 112.02°] and [56.25° - 125.46°] around Cd1 and Cd2, respectively. The asymmetric unit is further expanded by full span of **obba**²⁻ and 3-tpom, resulting in the formation of an overall 2D framework (Figure 87b). The Cd-O bond lengths in **44** lies in the range of 2.243 Å to 2.471 Å for Cd1 and 2.252 Å to 2.446 Å for Cd2, whereas the Cd-

N bond lengths are found to be 2.276 Å and 2.327 Å for Cd1 and 2.274 Å and 2.304 Å, respectively. These values are within the usual range for this kind of complexes. All the crystallographic information pertaining to data collection and structure refinement parameters, selected bond lengths and bond angles are listed in Table A16, A38 and A60, respectively.

Structural diversity due to coordination site shifting. As can be seen in Figure 3.73 and 3.86, the geometry and coordination environment around the Zn(II) in **41** and **43** are same using either **4-tpom** or **3-tpom**, respectively. Both the compounds forms 3D frameworks and their simplified node and linker representation reveals that both the frameworks exhibit different network topologies. However, both the tetrapyridyl ligand and the metal center acts as 4-connected nodes and organic dicarboxylate as a bent linker (Figure 3.88), but the relative position of the coordination site into the N-donor ligand plays an important role in directing the overall framework topology. A shift in the coordination site from fourth position to third position has resulted in a change in the relative conformation of the dicarboxylate linker. However, no significant difference into the bite angle at the silicon center has been observed in both the cases but a prominent increase in the dihedral angle (74.10° in **41** and 105.64° in **43**) between the two phenyl rings containing the carboxylic acid groups has been observed. The change in the dihedral angle and relative orientation can be attributed to the diversity in the final structures of **41** to **43**. Similarly, the effect of coordination site shifting in the tetrapyridyl ligand in the Cd(II)-obba system can be understood by comparison of **44** with the already reported Cd(II) coordination polymer, $\{[\text{Cd}_2(4\text{-tpom})(\text{obba})_2(\text{H}_2\text{O})_2] \cdot (\text{H}_2\text{O})_4(\text{DMF})_{1.5}\}_n$ where in contrast to **44**, the Cd-4tpom-obba system exhibits a 3D framework. In order to understand the effect of coordination site shifting on the resulting architectures, the structures can be simplified as node and linker representation (Figure 3.89) where the Cd(II) and the ligands **3-tpom** and **4-tpom** can be considered as 4-connected nodes and the dicarboxylate ligand **obba**²⁻ as bent linkers, respectively.

More insights into the structures reveal that the ligand **3-tpom** in **44** acts as almost planer 4-connected node whereas the ligand **4-tpom** in Cd-4tpom-obba system acts as a tetrahedral 4-connecting node as indicated by the respective cisoid angles into the two nodes. A significant difference in the dihedral angles between the two phenyl rings containing the carboxylic acid groups has also been observed in both cases. Therefore, from these observations it can be deduced that respective geometries of the ligands **3-tpom** and **4-tpom**

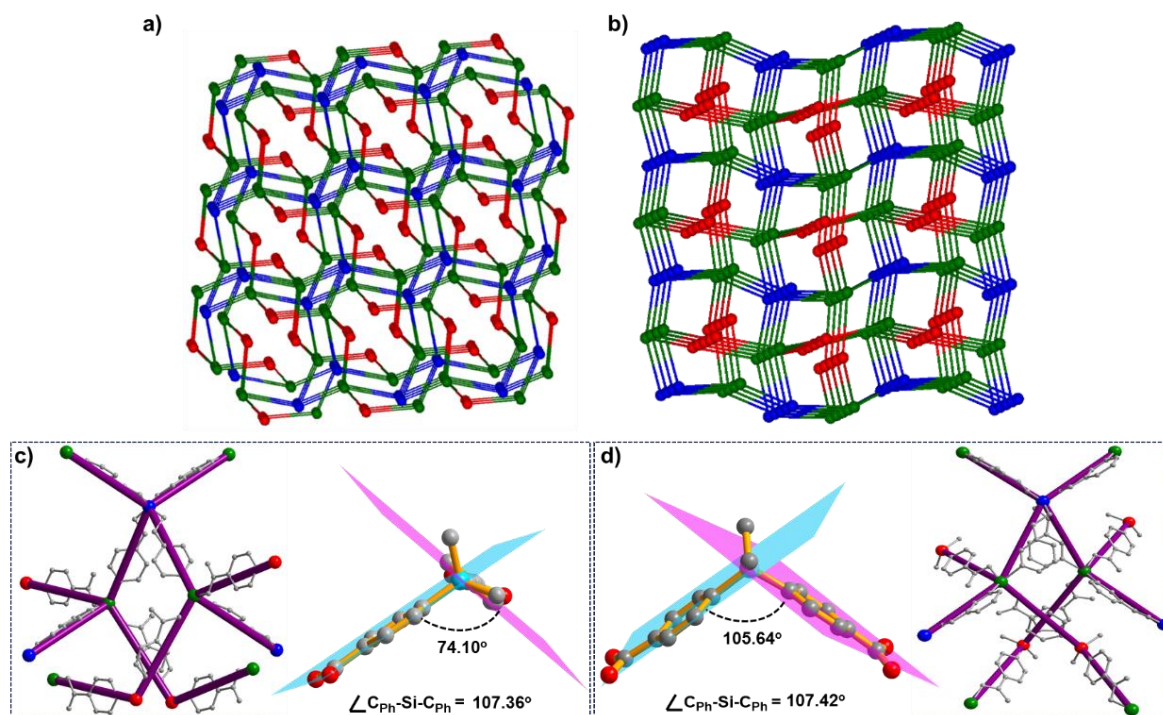


Figure 3.88. Simplified node and linker representation for (a) **41** and (b) **43** and (c and d) shows Zn(II) and 4-tpom or 3-tpom as 4-connected nodes and relative orientations and dihedral angles between the phenyl rings containing carboxylic acid groups in **dmsdba**²⁻ in case of **41** and **43**, respectively.

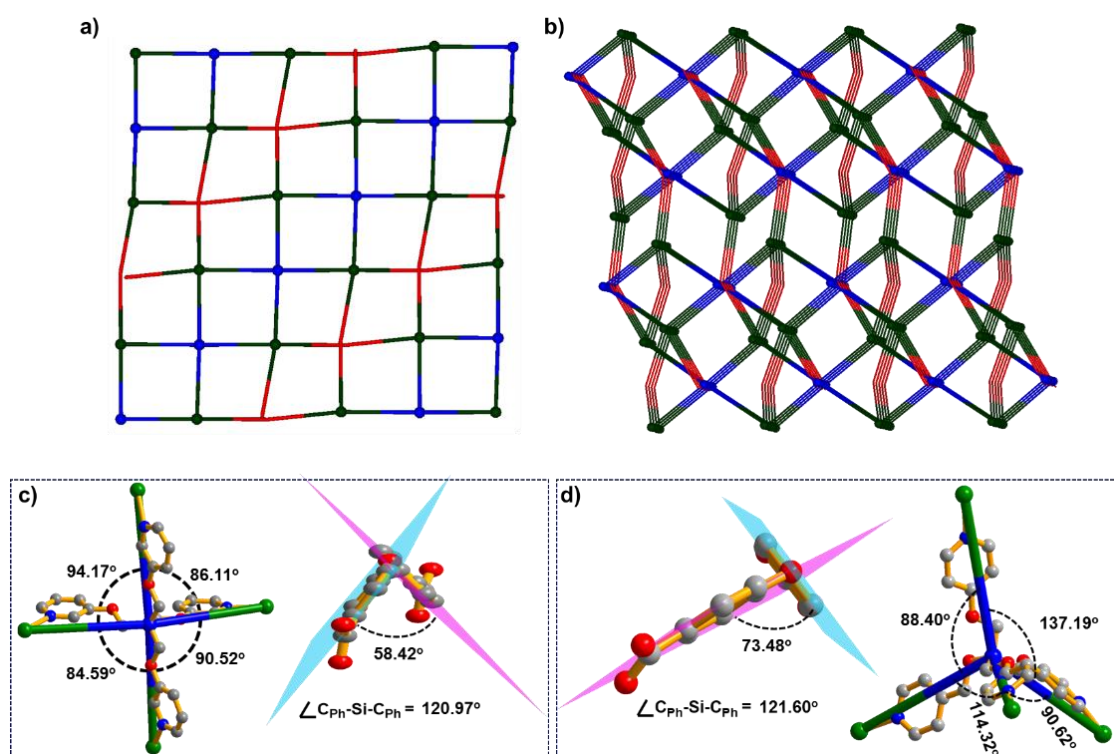


Figure 3.89. Simplified node and linker representation for (a) **44** and (b) Cd-4-tpom-obba complex and (c and d) shows the 3-tpom and 4-tpom ligands as 4-connected nodes and dihedral angles between the phenyl rings containing carboxylic acid groups in **obba**²⁻ in case of **44** and Cd-4-tpom-obba complex, respectively.

after binding to the metal atoms and the relative conformations of the dicarboxylate linker **obba**²⁻ simultaneously directs the structure and topology of the final architectures.

FTIR and PXRD analysis. FTIR spectra of **43** and **44** show sharp peaks at 1624 cm⁻¹ and 1390 cm⁻¹ and at 1597 cm⁻¹ and 1401 cm⁻¹, respectively. These peaks can be ascribed due to the asymmetric (ν_{asym}) and symmetric (ν_{sym}) stretching vibrations of the carboxylates. The difference in the asymmetric and symmetric stretching ($\Delta\nu = 234 \text{ cm}^{-1}$ and 196 cm^{-1}) indicates the monodentate and chelated bidentate binding of the carboxylates to the metal centers in **43** and **44**, respectively. This further supports the respective binding modes of carboxylates seen in their single crystal structures. Further, the shift from the asymmetric and symmetric -C=O stretch for free ligands, indicates strong binding of the carboxylates to the metal center in both cases. In order to the phase purity of the as-synthesized materials, powder X-ray diffraction patterns were recorded for **43** and **44** at room temperature. As shown in Figure 3.90, the experimentally obtained powder patterns for as-synthesized compounds were in good agreement with the simulated powder patterns (obtained from the single crystal data). This confirms the crystallinity and phase purity of the as-synthesized **43** and **44**, respectively.

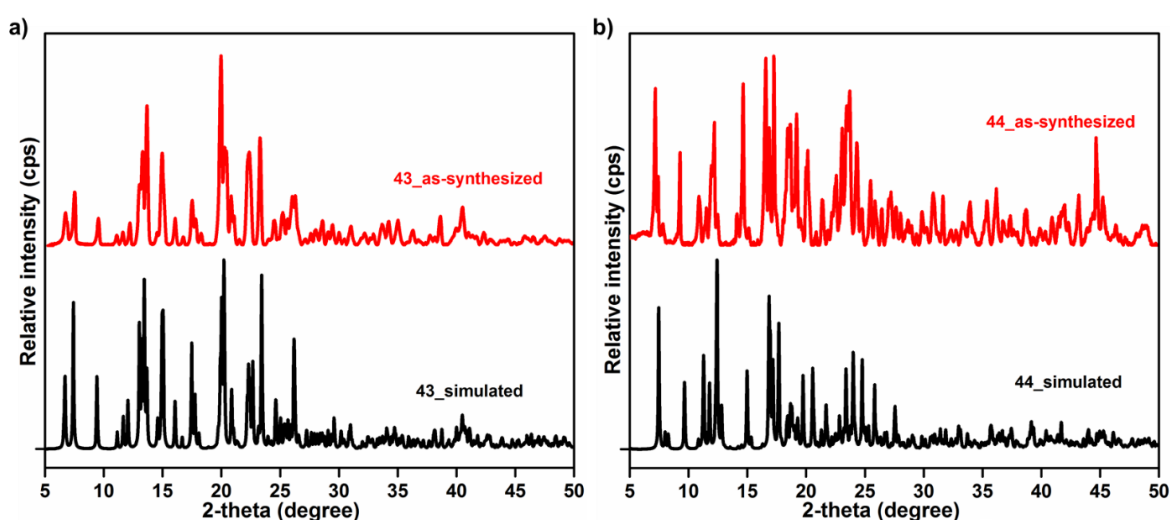


Figure 3.90. Powder X-ray diffraction patterns for the as-synthesized samples of (a) **43** and (b) **44** compared with their respective simulated powder patterns obtained from the single crystal data.

Framework stabilities and thermal properties. The thermal stability and structural variation as a function of temperature for **43** and **44** was studied by their thermogravimetric analysis (TGA). Single phase polycrystalline samples of **43** and **44** was heated between 30-500 °C, under a dinitrogen atmosphere and corresponding weight loss was plotted with respect to temperature. As shown in Figure 3.91 the as-synthesized sample of **43** exhibits an initial weight loss of about 7 % in the temperature range of 50 °C to 120 °C, which is in

good agreement due to the loss of one ethanol and three water molecules (ca. 7.8 %) present in the crystal lattice. After that no weight loss could be seen up to 320 °C, before the framework decomposition, indicating good thermal stability of **43**. The compound **44** also exhibits similar thermogravimetric profile. It shows excellent stability up to 350 °C after initial weight loss due to lattice water molecule.

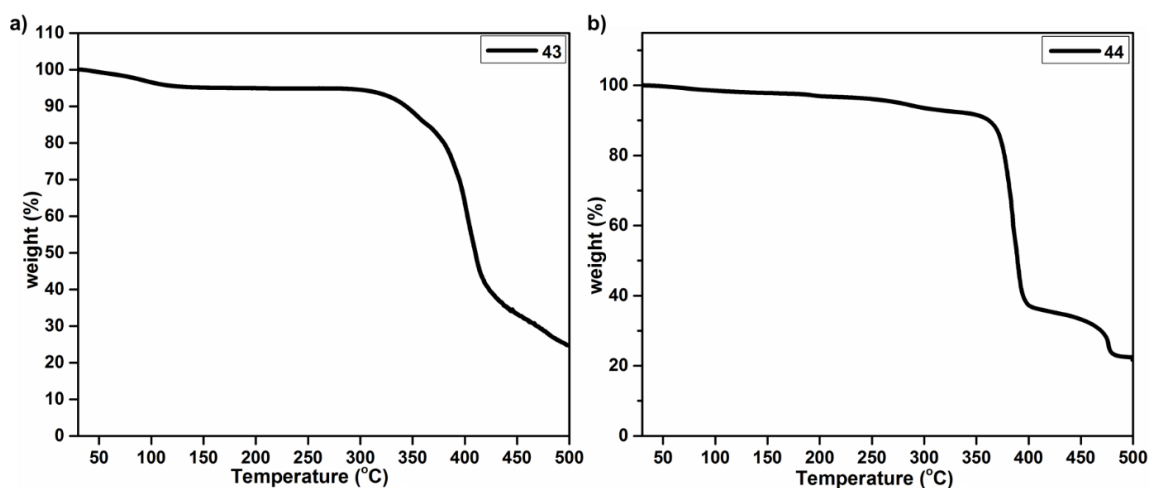


Figure 3.91. Thermogravimetric profile for (a) **43** and (b) **44**, respectively.

Gas sorption studies. The presence of open channels in the 3D structure and potential solvent-accessible voids in **43** has encouraged us to examine the permanent porosity and the effect of coordination site shifting on the gas sorption properties. Prior to adsorption measurements, the sample (~100 mg) was activated by degassing at an elevated temperature of 393 K under vacuum conditions (20 mTorr) for 24 hours to generate the desolvated frameworks. A similar result was obtained when low temperature sorption isotherms of CO₂ and N₂ were compared. As shown in Figure 3.92a, **43** takes up appreciable amount of CO₂ but very less amount of N₂ at low temperatures. The Brunauer-Emmett-Teller (BET) and the Langmuir surface area was estimated to be 135 m²g⁻¹ and 180 m²g⁻¹, respectively, based on the CO₂ adsorption isotherm at 195 K (Figure 3.92b and c). Inspired from the comparatively high CO₂ adsorption into **43**, we further investigated CO₂ sorption properties of **43** at higher temperatures. Single component CO₂ sorption isotherm measured at different temperatures (298 - 263 K) under 1 bar pressure are presented in Figure 3.93a. **43** takes up comparatively less amount of CO₂ (20.3 cm³g⁻¹, 25.4 cm³g⁻¹, 28.7 cm³g⁻¹, and 31.8 cm³g⁻¹ at 298 K, 283 K, 273 K and 263 K, respectively) than **41**. In order to determine the quantitative binding strength of CO₂ molecules with the framework, the isosteric adsorption enthalpy (Q_{st}) was calculated based on the Clausius-Clapeyron equation, and virial method. Pure-component isotherms for CO₂ collected at different temperatures were used for the

estimation of Q_{st} by either methods (*vide-supra*). At zero loading, the isosteric heat of adsorption (Q_{st}) was found to be 32.6 kJ mol^{-1} . The value is comparable with the values for some well-known MOF materials (Table A67).

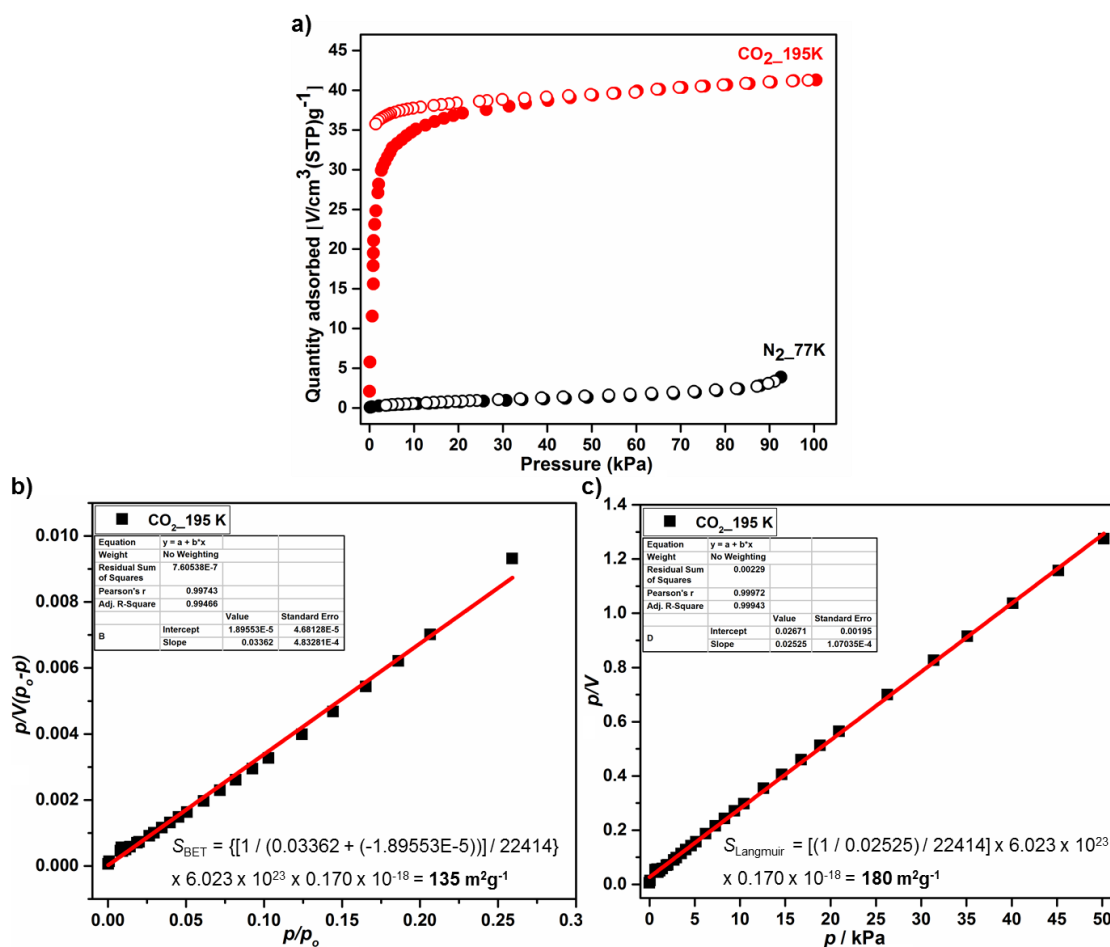


Figure 3.92. (a) Comparison of N₂ (77 K) and CO₂ (195 K) sorption isotherms at low temperatures and (b and c) BET and Langmuir surface area of obtained from the CO₂ adsorption isotherm for **43**.

The variation of heat of adsorption with respect to the surface coverage is presented in Figure 3.93c. Inspired from the comparatively higher CO₂ uptake in **43**, it was further tested for the selective carbon dioxide adsorption properties. It is well-known that the separation of CO₂ from CH₄ in the pre-combustion process of natural gas and separation of CO₂ from N₂ in the post-combustion process is very essential. Single component gas sorption isotherm was measured at different temperatures under 1 bar pressure. As shown in Figure 3.93d the uptake capacity of **43** is very less for N₂ and CH₄ compared to the uptake capacity for CO₂ molecules. The higher CO₂ affinity can be attributed to the smaller kinetic diameter of CO₂ (diameter: 3.30 \AA) compared to that of N₂ (diameter: 3.64 \AA) and CH₄ (diameter: 4.09 \AA) as well as the difference of quadrupole moment, thus allowing CO₂ molecules to diffuse easily into the pores.³⁰⁴

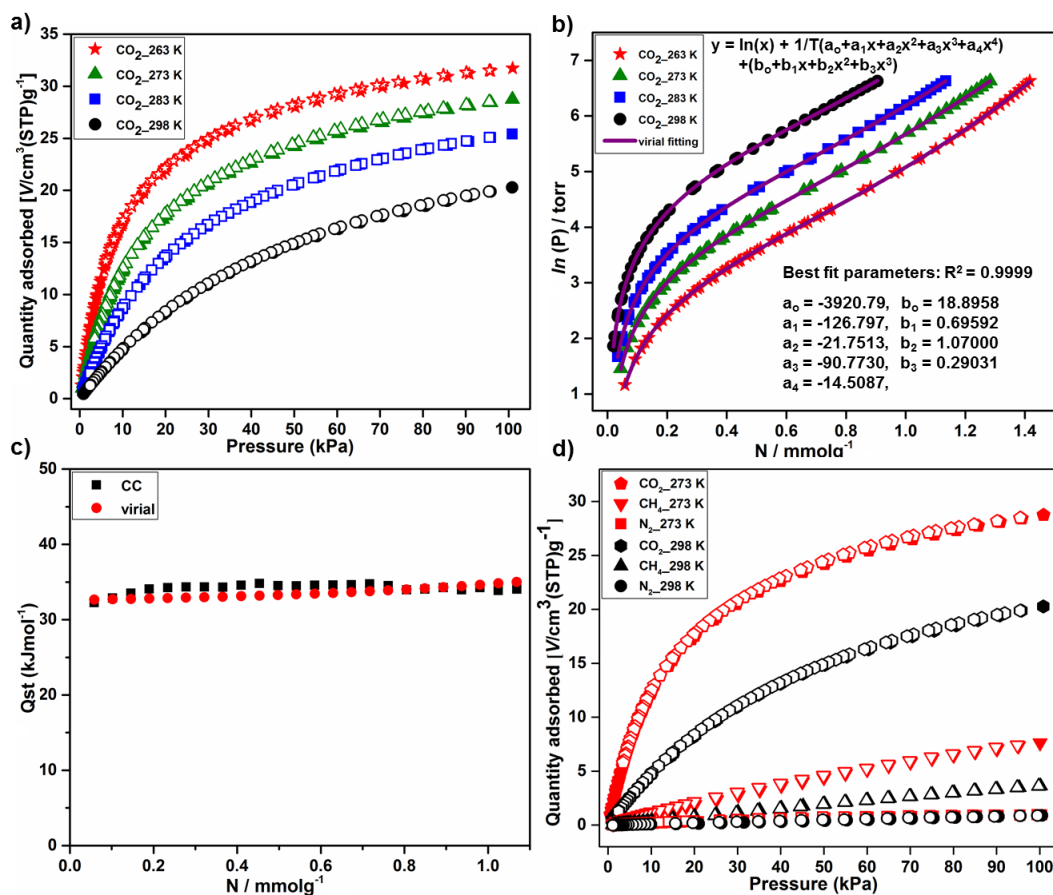
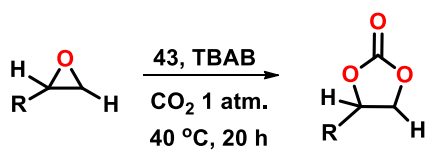


Figure 3.93. (a) CO₂ sorption isotherms for **43** collected at different temperatures, (b) Fitting (purple solid lines) of the CO₂ adsorption isotherms using the virial method, (c) variation of isothermic heat of adsorption with respect to surface coverage and CO₂ adsorption isotherms for **43** compared with the adsorption isotherms of N₂ and CH₄ at 273 K and 298 K, respectively.

Catalysis Studies. Inspired from the highly selective carbon dioxide (CO₂) adsorption and presence of unsaturated active meta sites, similar to **41**, **43** was also tested for its catalytic activity towards the cycloaddition reaction of CO₂ with epoxides to generate cyclic carbonates at ambient conditions. The catalytic activity was tested under similar reaction conditions. Epichlorohydrin was chosen as a standard substrate with **43** as a catalyst in conjunction with tert-butylammoniumbromide (TBAB) as a co-catalyst. The reaction was carried out in a solvent free condition and at 1 bar pressure of CO₂. The progress of the reaction was monitored by ¹H NMR spectroscopy. However, **43** exhibits lower CO₂ uptake compared to **41**, but showed similar catalytic activity towards cycloaddition reaction. The catalytic activity of **43** was further explored for different functional group substituted epoxides under the same reaction conditions. A similar trend in the catalytic activity was observed for **43** also. Epoxides substituted with aliphatic groups exhibited very good product conversion, whereas a decrease in product conversion was observed for styrene oxide and its derivatives. The results are summarized in Table 3.11.

Table 3.11. Substrate scope for cycloaddition of CO₂ with epoxides, catalyzed by **43**^a

Entry	Reactants	Products	conversion (%) ^b	TON ^c
1			>99	200
2			>99	200
3			95	190
4			96	192
5			88	176
6			88	176
7			85	170
8			62	124

^aReaction conditions: 0.2 mmol of epoxide was reacted with CO₂ under 1 atmospheric pressure maintained with a balloon filled with CO₂ gas in the presence of 0.5 mol % of **43** and 1 mol % of co-catalyst *tert.* butyl ammonium bromide (TBAB) in a solvent free condition. ^bCalculated by ¹H NMR of the crude products.

^cNumber of moles of product per mole of catalyst.

In addition to the catalytic activity towards cycloaddition of CO₂ with epoxides, the catalytic activity of **43** was also tested for Lewis-acid catalyzed Strecker reaction. The three component Strecker reaction is an important C-N bond forming reaction which provides a direct and viable method for the synthesis of α -aminonitriles, which are versatile building blocks for the synthesis of α -amino acids and their derivatives.³⁰⁶ The reaction of benzaldehyde with trimethylsilyl cyanide (TMSCN) and aniline was used as the test reaction, where 2 mol % of **43** was taken in a Schlenk tube followed by the addition of all the reactants. The reaction was carried out under a solvent free condition at room

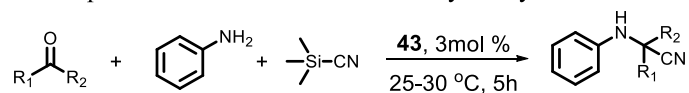
temperature under N₂ atmosphere. The progress of the reaction was monitored by TLC and the final conversion was calculated by ¹H NMR spectroscopy. A very good product conversion (about 94%) was observed after 5 h of reaction, indicating very good catalytic activity of **43**. The catalytic activity of **43** was further tested for different substrates, especially for the more reluctant ketone derivatives. The results are summarized in Table 3.12.

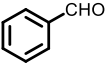
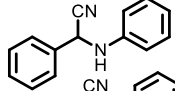
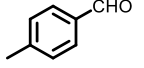
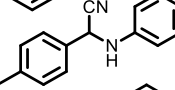
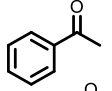
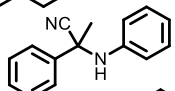
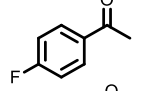
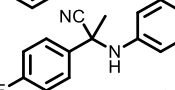
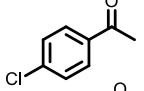
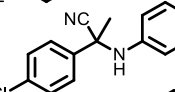
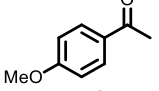
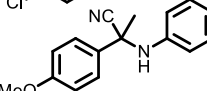
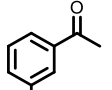
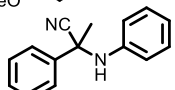
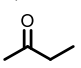
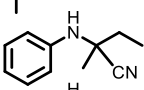
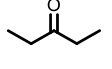
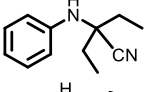
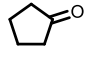
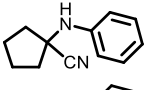
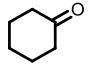
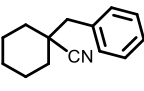
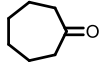
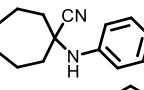
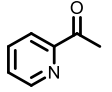
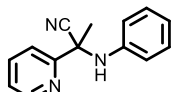
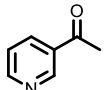
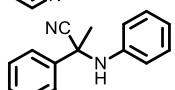
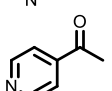
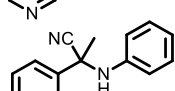
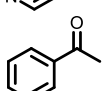
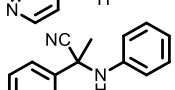
The results obtained reveal that the substrates with electron withdrawing group gave the maximum conversion while a drop in the product conversion was obtained for the substrates with electron donating substituents. This trend is similar to the results obtained for the reactions involving nucleophilic attack at electrophilic carbon of carbonyl or imine groups. The electron withdrawing groups tends to increase the nucleophilicity at the carbonyls or imines carbon and hence enhances the rate of reaction. In all cases, products were isolated and characterized by ¹H and ¹³C NMR spectroscopy to confirm their identity and purity. For control experiment, a blank reaction was carried out in the absence of catalyst for both the reactions. In each case very little product conversions indicates the active role of the catalyst.

In order to check the utility of **43** as a reusable catalyst for both conversions, the catalyst was isolated after the reaction by filtration, washed with DCM, dried under vacuum and reused for next catalytic experiment. The catalyst was recycled in three consecutive experiments in each case. No significant loss of catalytic activity was observed even after three cycles of reaction (Figure 3.94a). Based on the PXRD data of the catalyst recorded before and after the reaction, no loss of crystallinity or the phase purity of the catalyst was observed (Figure 3.94b). Furthermore, any possibility of catalyst leaching into the product stream was investigated by hot filtration method. The catalyst was separated from the reaction mixture after certain time by centrifugation and the reaction mixture was subjected to similar reaction conditions. In each case the progress of the reaction did not increase significantly (Figure 3.94 c and d), indicating no leaching of the catalyst into the product stream during catalytic reactions.

Plausible mechanisms for both the catalytic reactions can be proposed similar to that of **39** for the Lewis-acid catalyzed Strecker reaction and **41** for the Lewis-acid catalyzed cycloaddition reaction of carbon dioxide with epoxides in the presence of co-catalyst TBAB (Figure 3.71 and 3.85, respectively).

Table 3.12. Substrate scope for the Strecker reaction catalysed by **43**^a



Entry	Reactant	Product	Yield (%) ^b	TON ^c
1			94	188
2			81	162
3			68	136
4			92	184
5			89	178
6			58	116
7			65	130
8			88	176
9			86	172
10			89	178
11			88	176
12			82	164
13			72	144
14			76	152
15			85	170
16			17 ^d	34

^aReaction conditions: Aldehyde/ketone (0.1 mmol), amine (0.1 mmol), TMSCN (0.12 mmol) and reaction time: 5 h. ^bAverage percent yield for a set of triplicate runs, calculated by ¹H NMR of the crude products.

^cNumber of moles of product per mole of catalyst. ^dBlank reaction.

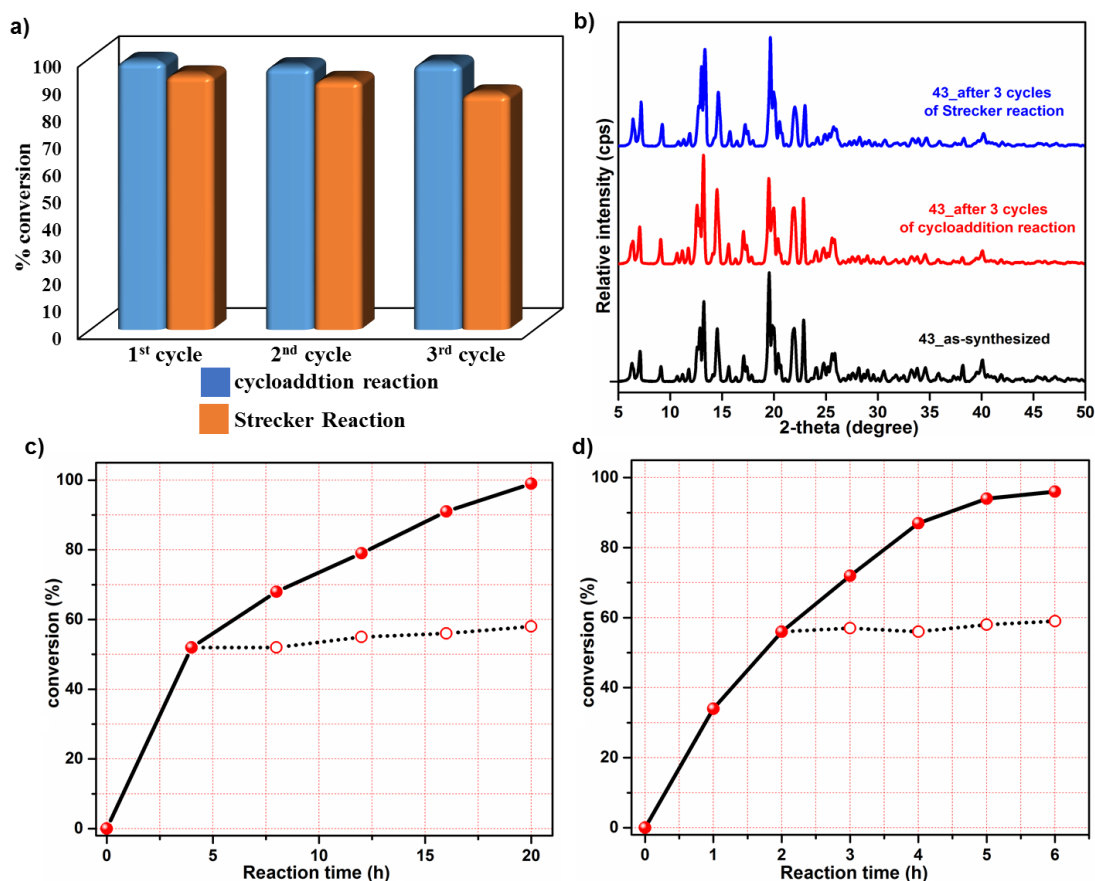


Figure 3.94. (a) conversion for three consecutive cycles for the cycloaddition reaction of CO₂ with epichlorohydrin and three component Strecker reaction of benzaldehyde, aniline and trimethylsilyl cyanide, catalyzed by **43**, (b) PXRD pattern of **43** before and after catalysis experiments and of (c and d) progress of the reaction with time in presence of catalysts (solid lines) and after separating the catalyst from the reaction mixture (dotted lines) for cycloaddition reaction of CO₂ with epichlorohydrin and Strecker reaction of benzaldehyde with aniline and trimethylsilyl cyanide, respectively.

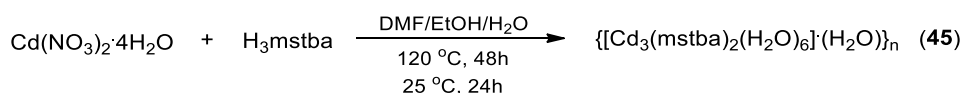
3.2 COORDINATION ARCHITECTURES DERIVED FROM TRICARBOXYLATE

As seen in the previous section, the use of tetrahedral tetrapyridyl ligands instead of bis-pyridyl ligands for the fabrication of coordination polymers has resulted in the formation of 3D porous architectures with open channels (except in case of **44**). Therefore, inspired from the interesting properties they exhibit, in an attempt to synthesize such porous coordination architecture, the thought of increasing the denticity of the carboxylate linker instead of neutral pyridyl ligands in the multi-component self-assembly process came and executed. In this section the tricarboxylate linker (**H₃mstba**) was utilized in combination with neutral N-donor pillar ligands to synthesize such coordination polymers. However, the carboxylate linker (**H₃mstba**) is known in the literature, but has not been explored much for the synthesis of such architectures.²³²

Therefore, in an attempt to synthesize coordination polymers based on **H₃mstba** and Cd(II) as the metal center, three coordination polymers namely $\{[\text{Cd}_3(\text{mstba})_2(\text{H}_2\text{O})_6] \cdot (\text{H}_2\text{O})\}_n$ (**45**), $\{((\text{NH}_2(\text{CH}_3)_2)_2) \cdot [\text{Cd}_2(\text{bpy})(\text{mstba})_2] \cdot 8\text{DMF} \cdot 2(\text{H}_2\text{O})\}_n$ (**46**) and $\{((\text{NH}_2(\text{CH}_3)_2)_2) \cdot [\text{Cd}_2(\text{azopy})(\text{mstba})_2] \cdot 4\text{DMF} \cdot 2(\text{H}_2\text{O})\}_n$ (**47**), where in order to understand the role of bis(pyridyl) pillar ligands a metal carboxylate system (**45**) have been synthesized with no pillar ligand.

The solvothermal reaction of cadmium(II) nitrate and **H₃mstab** in a solvent mixture of DMF/EtOH/H₂O (1/1/3) has resulted in the formation of **45** (Scheme 3.21).

Scheme 3.21. Synthesis of **45**.



Single crystal structure analysis Single crystals suitable for X-ray diffraction analysis was obtained by solvothermal reaction at 120 °C. Structural analysis reveals that **45** crystallizes in the cubic crystal system with *Pn-3* space group. The asymmetric unit consists of two Cd(II) ion (each with half occupancies), two-third of **mstba**³⁻ and two water molecules coordinated to Cd₂. The metal center Cd1 is octacoordinated by eight oxygen atoms all from the carboxylate group of **mstba**³⁻, whereas Cd2 is hexacoordinated in a distorted octahedral environment. The coordination environment around the Cd(II) is completed by two carboxyl oxygen atoms and four oxygen atoms of the water molecule coordinated to the Cd2 (Figure 3.95a). The two metal centers are bridged by carboxyl oxygen atoms forming a Cd₂O₂ core as the secondary building unit (SBU). The carboxylate linker is fully deprotonated and the dimetallic SBU is further expanded by full span

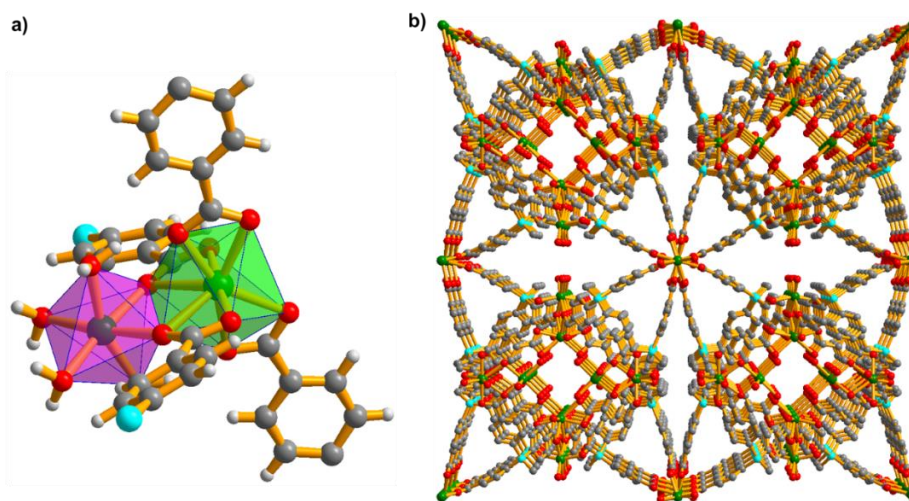


Figure 3.95. (a) Coordination environment around the metal centers and (b) perspective view of the overall 3D framework in **45**.

of mstba^{3-} to form the overall 3D framework (Figure 3.95b). The structure is further interpenetrated into each other to form a doubly interpenetrated framework. Upon simplification of the structure into node and linker representation each dimetallic SBU can be considered as a 4-connected node (Figure 3.96a) and the tricarboxylate linker mstba^{3-} as a 3-connected node (Figure 3.96b), respectively. Further examination of the simplified node and linker representation reveal that the framework exhibits a 3,4-connected bi-nodal net pt_3O_4 ; $\text{sqc}5591$ (topos & RCSR.ttd) topology as determined by the TOPOS program (Figure 3.96c).²⁷⁴ The total potential solvent-accessible void volume was estimated to be 12% ($1113/9263 \text{ \AA}^3$ per unit cell volume) per unit cell volume by the PLATON software.²⁷⁵ The Cd-O bond lengths for octacoordinated Cd1 lies in the range of 2.226 Å to 2.439 Å, whereas the Cd-O bond lengths for hexacoordinated Cd2 are in the range of 2.117 Å to 2.214 Å, respectively. The Cd1-Cd2 distance for the dimetallic Cd_2O_2 SBU is found to be 3.619 Å. The metal-oxygen bond lengths are in the usual range for this kind of complexes. Usual distortions from the regular geometries around each metal center is evident from the respective bond angle values. The cisoids angles around Cd1 and Cd2 lies in the range of $[54.22^\circ - 97.21^\circ]$ and $[54.22^\circ - 97.21^\circ]$, respectively. All the crystallographic information pertaining to data collection and structure refinement parameters, selected bond lengths and bond angles are listed in Table A17, A39 and A61, respectively.

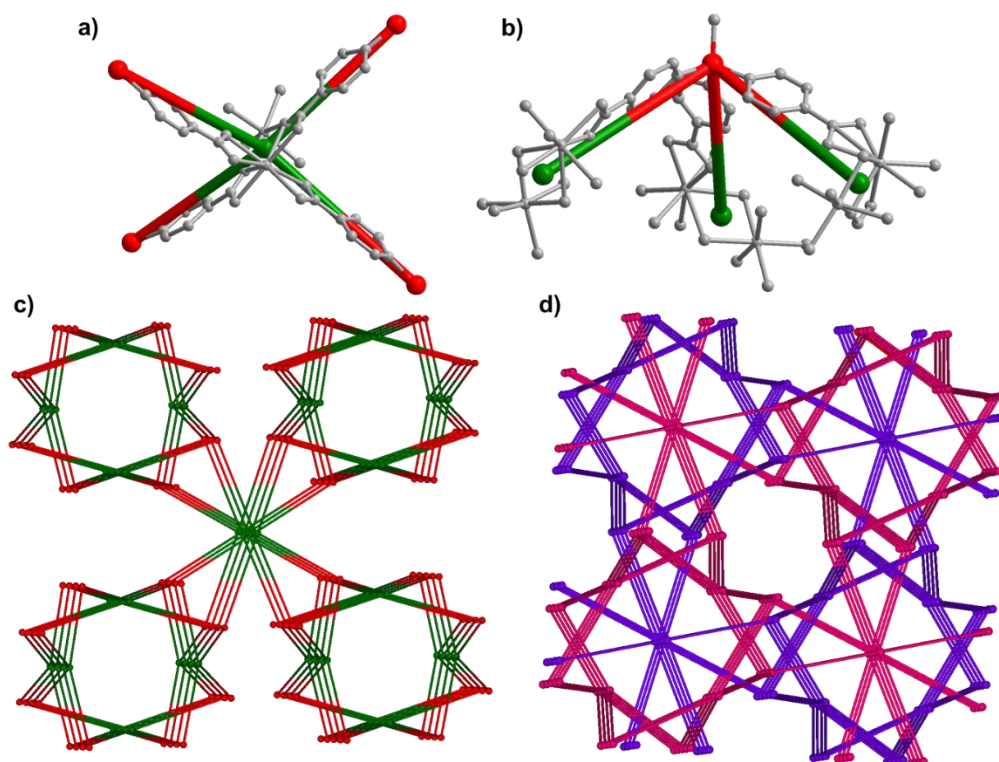
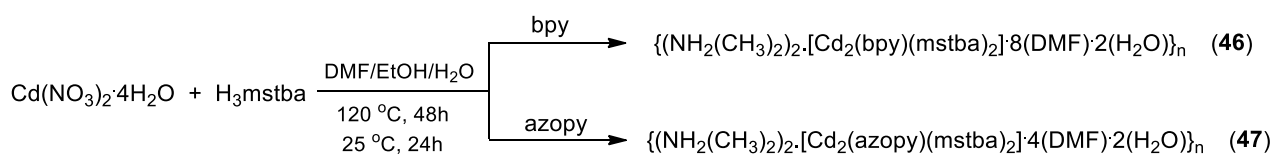


Figure 3.96. Simplified node and linker type representation for (a) the dimetallic Cd₂O₂ SBU and (b) H₃mstba as 4-connected and 3-connected node, respectively, (c and d) represents the overall 3,4-connected bi-nodal net sqc5591 topology without and with twofold interpenetration into the framework of **45**.

The introduction of linear bis(pyridyl) pillar ligands **bpy** or **azopy** into the metal carboxylate system has resulted in the formation of two iso-structural coordination polymers, **46** and **47**, respectively (Scheme 3.22).

Scheme 3.22. Synthesis of **46** and **47**.



Single crystal structure analysis. Single crystal suitable for X-ray diffraction analysis were obtained by solvothermal reaction at 120 °C in each case. Both **46** and **47** crystallizes in a triclinic crystal system with $P\bar{1}$ space group. The asymmetric unit in **46** consists of two Cd(II) ion, two **mstba**³⁻ and one bpy molecule, whereas the asymmetric unit in **47** consists of one Cd(II), one **mstba**³⁻ and one-half of the pillar ligand azopy along with one molecule of DMF, present in crystal lattice. The metal center in each case is in similar coordination geometry. The metal center in each case is heptacoordinated by six carboxyl oxygen atoms and one nitrogen atom from the pillar ligand **bpy** or **azopy** (Figure 3.97a and b). Both **46**

and **47** forms an overall double layered anionic framework (Figure 3.97c), where it is charge balanced by dimethyl ammonium cations formed by the dissociation of DMF molecules during the solvothermal reaction. The structure in each case contains guest solvent molecules into the pores along with the dimethyl ammonium cations, which are highly disordered and could not be modelled. The diffused electron density due to the highly disordered guest molecules in each case was squeezed out using the solvent mask in olex2 software. The total potential solvent-accessible void volume was estimated to be 54% (2433/4460 Å³) and 32% (610/1906 Å³) per unit cell volume for **46** and **47**, respectively.

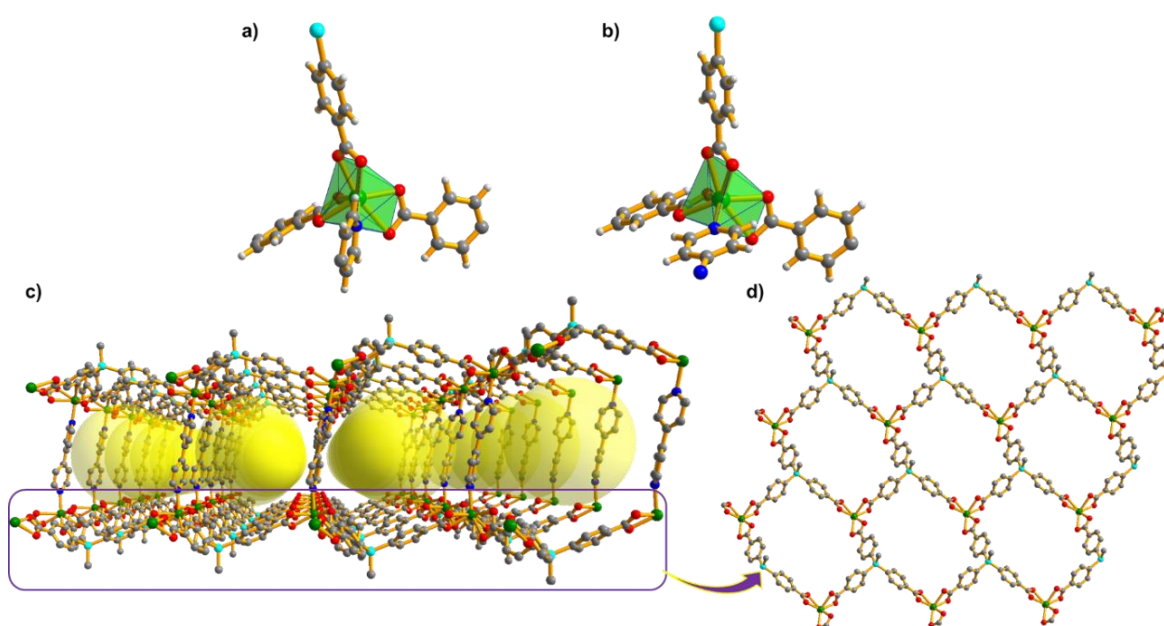


Figure 3.97. Structural description for **46** and **47**; (a and b) coordination environment around the metal center in **46** and **47**, respectively, (c) double layered sheet structure in **46** and **47** and (d) view of 2D metal carboxylate sheet structure in both the frameworks.

The overall frameworks in both cases can be simplified in node and linker type representation, where the metal center, carboxylate linker and the pillar ligands can be considered 4- and 3-connected nodes and linear linker, respectively (Figure 3.98). Further examination reveals that the framework in each case exhibits 3,4-connected bi-nodal network topology with 2-fold interpenetration into the framework. The Cd-O bond lengths lies in the range of 2.238 Å to 2.554 Å and 2.269 Å to 2.539 Å, whereas the Cd-N bond lengths are found to be 2.290 Å and 2.290 Å for **46** and **47**, respectively, which are in the usual range for this kind of complexes. All the crystallographic information pertaining to data collection and structure refinement parameters, selected bond lengths and bond angles are listed in Table A17, A39 and A61, respectively.

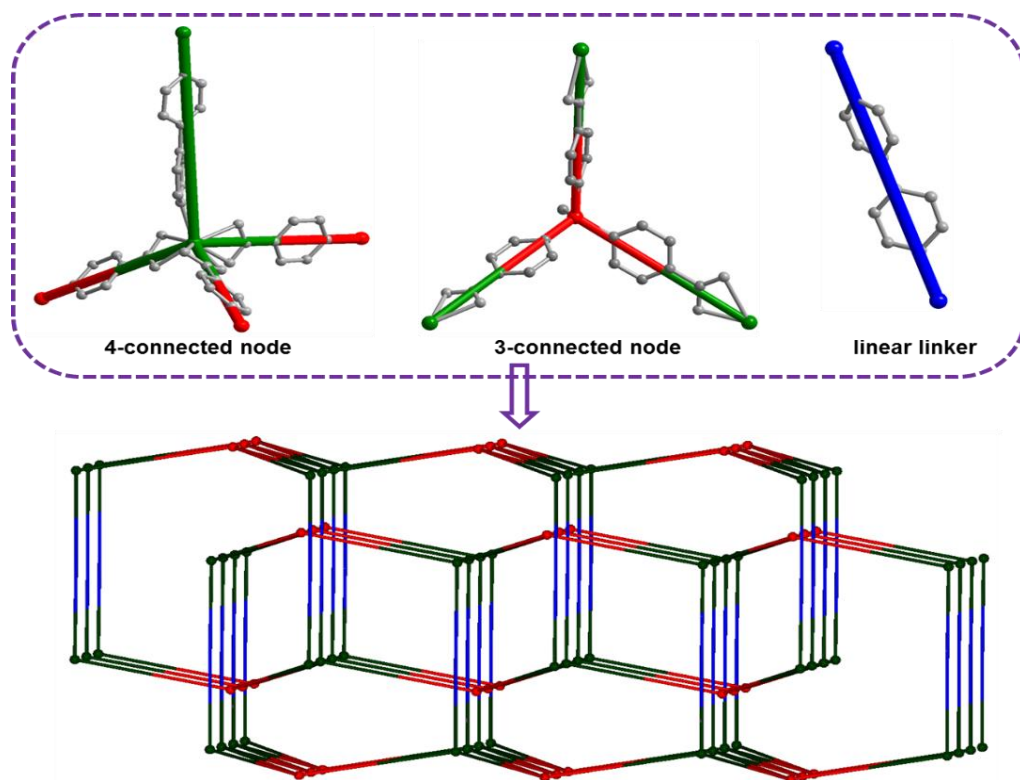


Figure 3.98. Simplified representation of the metal center, H₃mstba and linear pillar ligand as 4- and 3-connected nodes and a linear linker, respectively and the overall 3,4-connected bi-nodal network topology with two-fold interpenetration into the framework of **46** and **47**.

FTIR and PXRD analysis. FTIR spectra in each case was recorded in the solid state at room temperature as KBr pellets. The sharp peaks due to asymmetric (ν_{asym}) and symmetric (ν_{sym}) stretching vibrations of the carboxylates for **45-47** appeared at 1594 cm^{-1} and 1415 cm^{-1} , 1595 cm^{-1} and 1413 cm^{-1} and 1592 cm^{-1} and 1413 cm^{-1} , respectively. The difference in the asymmetric and symmetric stretching ($\Delta\nu = 179 \text{ cm}^{-1}$, 182 cm^{-1} and 179 cm^{-1} for **45-47**), further supports the chelated bidentate binding mode of the carboxylates²⁵¹ in all cases as seen in their respective single crystal structures. In addition, the sharp peaks at 1660 cm^{-1} in **46** and **47** can be ascribed due to the presence of lattice DMF molecules in the open channels. In order to check whether the bulk samples represent the same compound as obtained from the single crystal analysis, powder X-ray diffraction patterns were recorded in each case at room temperature. As shown in Figure 3.99, the experimental powder patterns for as-synthesized compounds were in good agreement with the simulated powder patterns (obtained from the single crystal data). This confirms the crystallinity and phase purity of the as-synthesized samples in each case.

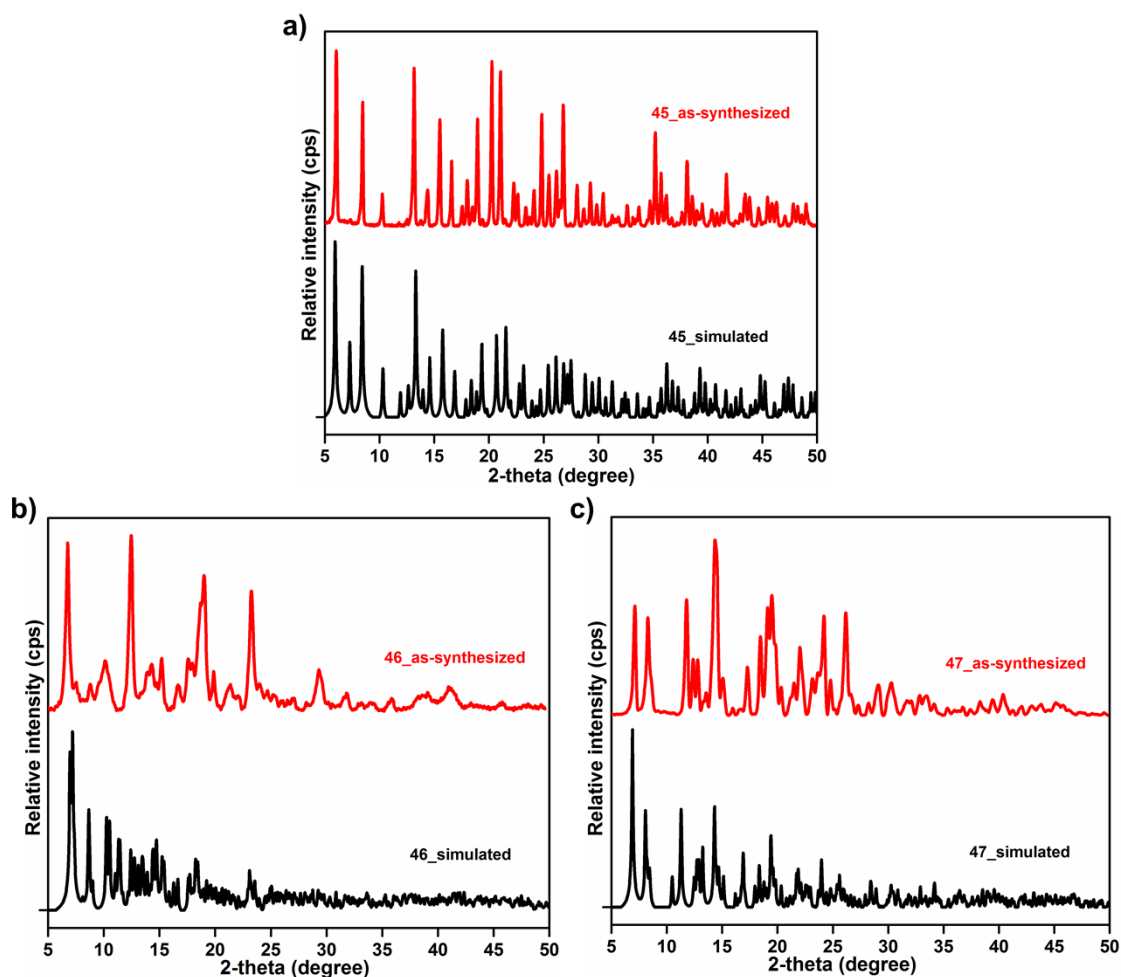


Figure 3.99. Powder X-ray diffraction patterns for the as-synthesized samples of (a) **45**, (b) **46** and (c) **47** compared with their respective simulated PXRD patterns obtained from their single crystal data.

Framework stabilities and thermal properties. The thermal stability in each case was tested by thermogravimetric analysis (TGA). Single phase polycrystalline samples in each case was heated between 30-500 °C, under a dinitrogen atmosphere and corresponding weight loss was plotted with respect to temperature. As shown in Figure 3.100, the as-synthesized sample of **45** exhibits an initial weight loss of about 9% in the temperature range of 70 °C-200 °C, which can be ascribed due to the loss of lattice solvent molecules upon heating. After which it exhibits stability up to 350 °C before framework degradation. A similar thermogravimetric profile was obtained in case of **46** and **47**. Both exhibits continuous weight loss up to 320 °C after which a sudden weight loss in each case indicates the framework degradation. The continuous weight loss in both cases can be ascribed due to the large number of lattice solvents and dimethyl ammonium cations present in the open pores. The similar TG profile further supports the isostructural frameworks of **46** and **47**.

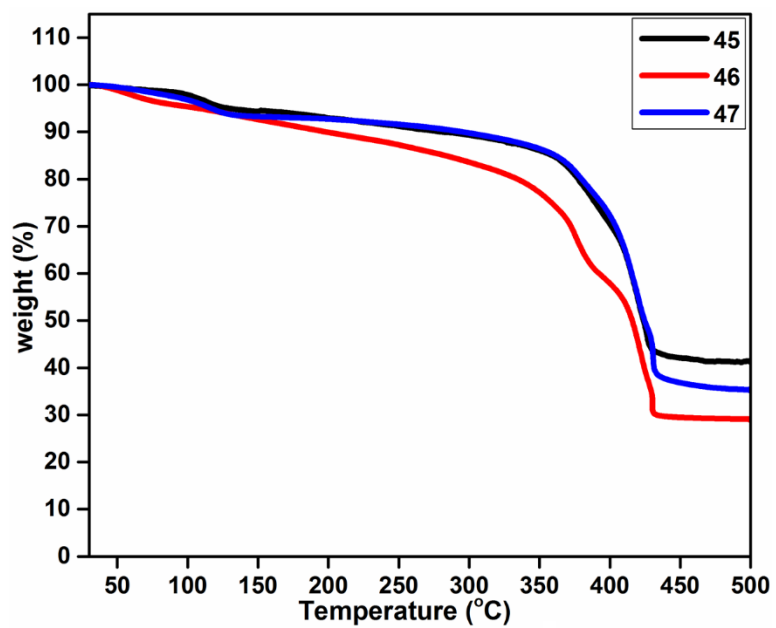


Figure 3.100. Thermogravimetric profile for 45-47.

3.3 COORDINATION ARCHITECTURES DERIVED FROM TETRACARBOXYLATE

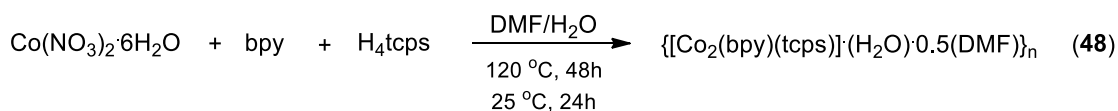
In addition to the tricarboxylate linker, the carboxylate structure has been further modified to a tetrahedral tetracarboxylate linker (**H4tcps**) in order to design porous coordination polymers. As seen in the previous sections that such porous coordination polymers exhibit interesting adsorption properties and also their properties can be modulated by fine tuning into their structures by judicious ligand selections. However, various strategies have been developed for the construction of coordination polymers based on tri- and tetradentate linkers which are found to be relatively more stable and exhibits interesting properties for different applications, the use of tetrahedral tetracarboxylates in making such MOFs is very limited.¹²⁶ Furthermore, such porous coordination polymers ligated with N-coordination exhibit better stability toward aqueous conditions, than their carboxylate counterparts.^{307,308} Therefore, the present section illustrates the utilization of tetrahedral tetracarboxylate linker (**H4tcps**) in combination with multidentate multidentate nitrogen linkers for the construction of highly stable porous coordination architectures for different applications. The section 3.3 is further subdivided into two subsections (3.3.1 and 3.3.2, respectively) based on the denticity of the neutral polypyridyl ligands used.

3.3.1 bis(pyridyl) pillar ligands

In this section, five coordination polymers have been reported based on the tetrahedral carboxylate linker (**H4tcps**) in combination with neutral N-donor bis(pyridyl) ligands. In all cases the compounds have been well characterized by different analytical techniques and their properties have been studied for selective gas adsorption/separation and sensing applications.

The solvothermal reaction of cobalt nitrate hexahydrate and **H4tcps** in combination with neutral ligand bpy has resulted in the formation of a doubly interpenetrated 3D coordination polymer $\{[\text{Co}_2(\text{bpy})(\text{tcps})]\cdot\text{H}_2\text{O}\cdot 0.5\text{DMF}\}_n$ (**48**) (Scheme 3.23). It has been structurally characterized by single crystal X-ray diffraction analysis and the molecular formula was established by a combination of elemental analysis, TGA and single crystal X-ray diffraction.

Scheme 3.23. Synthesis of **48**.



Single crystal structure analysis. Single crystal X-ray diffraction reveals that **48** crystallizes in a tetragonal crystal system, with $P4_2/mcm$ space group (space group no. 132) and the asymmetric unit contains one Co(II) atom (occupancy 0.25), one eighth of the **tcps**⁴⁻ ligand, and a quarter of the **bpy** molecule. As shown in Figure 3.101a the title molecule, $\{[\text{Co}_2(\text{bpy})(\text{tcps})] \cdot (\text{H}_2\text{O}) \cdot 0.5(\text{DMF})\}_n$, contains two Co(II) centres bridged by four carboxylates from four different **tcps**⁴⁻ ligands in syn-syn bridging modes. Square-pyramidal five-coordination of each cobalt is completed by a N-donor pyridine of 4,4'-bipyridine. The ligand, **H₄tcps** is fully deprotonated, coordinating to eight cobalt atoms (Figure 3.101b). The structure consist of Co(II)-paddlewheel as SBU, which is connected to twelve other $\{\text{Co}_2(\text{OCO})_4\}$ paddlewheel dimers, ten are connected by full span of the four **tcps**⁴⁻, two other $\{\text{Co}_2(\text{OCO})_4\}$ paddlewheel dimers by two bpy (Figure 3.101c), resulting to form a doubly interpenetrated 3D framework (Figure 3.101d). To simplify the rather intricate structure of compound **48**, the $\{\text{Co}_2(\text{OCO})_4\}$ paddle wheel SBU can be considered as a six connected node, ligand **tcps**⁴⁻ as a four connected node and 4,4'-bipyridine as a linear linker, respectively (Figure 3.102).

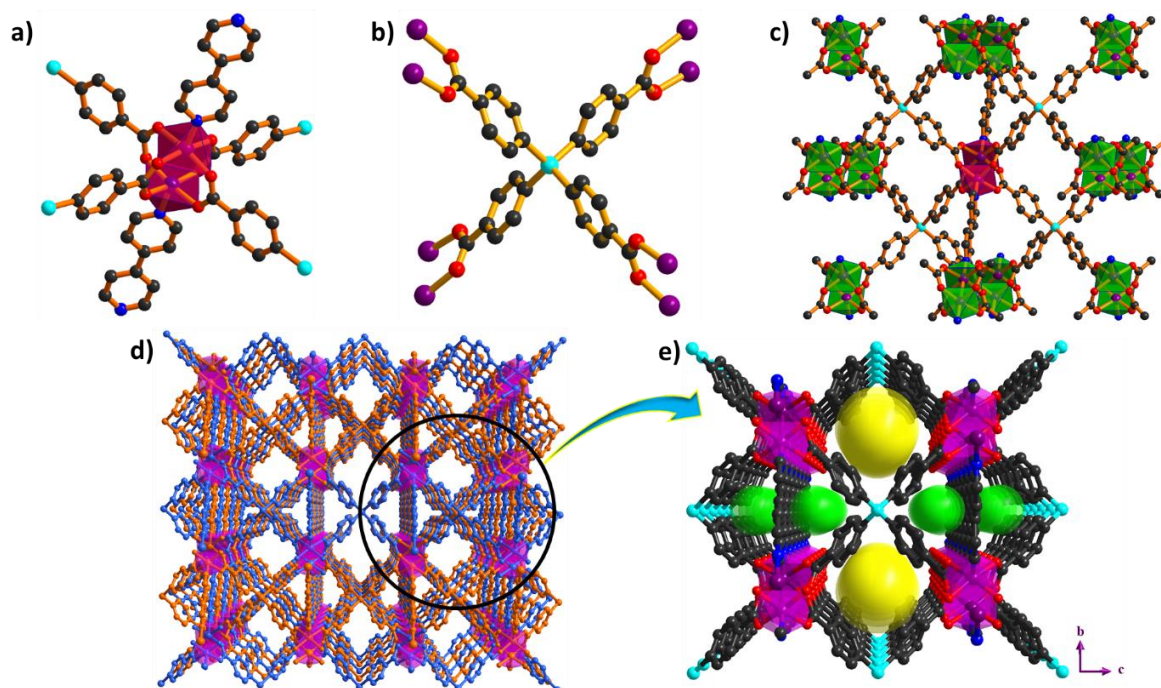


Figure 3.101. Structure description for **48**; (a) The coordination environment around the Co(II) center showing the paddle-wheel secondary building unit (SBU), (b) fully deprotonated ligand **tcps**⁴⁻ coordinated to the eight cobalt atoms, (c) connections of a paddle wheel SBU, via **tcps**⁴⁻ and 4,4'-bipyridine linker, (d) a perspective view of the doubly interpenetrated 3D porous framework along the a-axis and (e) an enlarged view of the rhombus and triangular channels shown with the help of dummy balls of different colors.

Further examination of the node and linker representation reveals that the framework exhibits a (4,6)-connected 2-nodal net, sqc422 topology, with Schläfli point symbol $\{4^2.5^{10}.7^2.8\}\{4^2.5^4\}$ as determined by the TOPOS program.²⁷⁴ The notable feature of **48** is the presence of two types of open channels, which runs along all three axes makes it a porous network. The two types of channels: the rhombic channels are about 9.6×11.0 (5.4×7.0) Å², and the trigonal channels are about 5.5×6.2 (1.7×2.5) Å² and are filled with disordered solvent molecules which were removed using solvent masking option in Olex2 software²⁰³ during the structure refinement. The total solvent-accessible volume for **48** was estimated to be 19 % ($382/2030$ Å³ per unit cell volume) using PLATON software.²⁷⁵

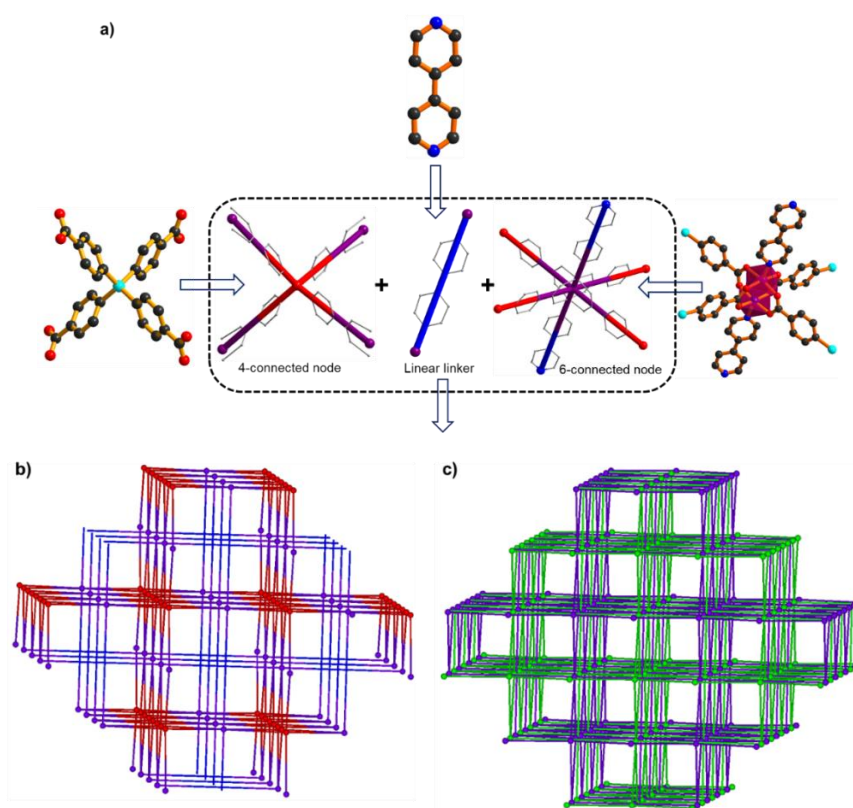


Figure 3.102. (a) simplified node and linker representation of the ligands H₄tpps, bpy and Co₂(COO)₄ cluster, (b) the overall (4,6)-connected 2-nodal net, sqc422 topology and (c) view of the two fold interpenetration into the framework.

The τ parameter, which is an indicator for the deviation from the ideal square-pyramidal ($\tau = 0$) and trigonal bipyramidal ($\tau = 1$) geometries for five coordinated metal centers, is found to be 0.19 for **48**. While the average Co-O (bond length 2.013 Å) and the Co-N (bond length 2.014 Å) bond distances are within the range reported for the similar structures, the Co---Co distance 2.572(4) Å is shorter than the reported paddle wheel complexes but is longer than the Co-Co single bonds (Co---Co 2.3 Å) reported in dicobalt tetrakis(formamidinate)

complexes.²⁹⁶ Prominent distortions around the Co(II) center are evident from the bond angles as well as the distance (2.173 Å) between the oxygen atoms of the bridging carboxylate group. All the crystallographic information pertaining to data collection and structure refinement parameters, selected bond lengths and bond angles are listed in Table A18, A40 and A62, respectively. The phase purity of bulk material was confirmed by recording the powder X-ray diffraction pattern of the as synthesized compound, which shows a good agreement with the corresponding simulated pattern obtained from the single-crystal data (Figure 3.103a).

Spectroscopic characterization. FTIR spectrum of **48** was recorded in solid state at room temperature in the form of KBr pellets. A sharp peak at 1681 cm⁻¹ corresponds to the free DMF molecules present in the lattice. The sharp peaks due to asymmetric and symmetric stretching modes of the -C=O group of H₄tcps at 1690 and 1416 cm⁻¹ were shifted to 1618 and 1399 cm⁻¹ in **48**, indicating strong binding of the carboxylates to the metal center and are in good agreement with the spectroscopic data for NCoO5 square planar complexes.³⁰⁹ The UV-vis diffuse reflectance spectra of **48** and H₄tcps are shown in Figure 3.103b. As shown in figure H₄tcps absorbs only in the UV-region at 251 nm, which is slightly red shifted to 283 nm in case of **48**. In addition to the strong peak in UV-region at 283 nm, **48** also shows characteristic peaks in the visible region at 433 and 577 nm which can be assigned on the basis of a square pyramidal NCoO4 chromophore with C_{4v} symmetry and the transitions arise from the 4A₂ ground state to 4B₁, 4E and 4A₂ excited states.³⁰⁹ The band gap (E_g) calculated using the Kubelka–Munk function was found to be 3.23 eV.

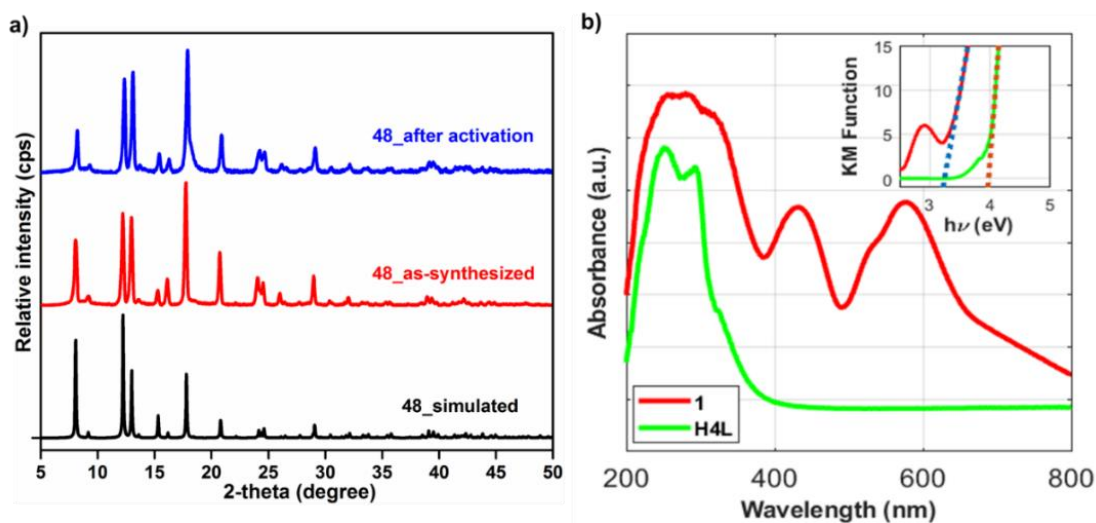


Figure 3.103. (a) Powder X-ray diffraction of the as-synthesized and activated sample of **48**, compared with the simulated powder pattern, (b) Diffuse reflectance UV-Vis spectra of **48** (red line) and H₄tcps (green line); inset: KM function vs. energy (eV) of **48** and H₄tcps.

Framework stabilities and thermal properties. In order to understand its thermal stability and structural variation as a function of temperature, thermogravimetric analysis (TGA) was carried out for the single-phase polycrystalline samples of **48** between 30-500 °C, under a dinitrogen atmosphere. The TGA showed ~7.8 % weight loss until 300 °C, which is ascribed to the release of lattice solvent molecules; calculated 6.5 % (Figure 3.104a). No weight loss in the temperature range of 300 to 350 °C could be seen before degradation of the framework indicating its good thermal stability. The robustness and thermal stability of the framework of **48** were further checked by in-situ variable temperature powder X-ray diffraction (VT-PXRD) (Figure 3.104b). In addition to the thermal stability, the compound was also tested for its stability towards water. In order to assess the water stability, **48** was taken in water and left for stirring at room temperature. The PXRD pattern of **1** was recorded at regular intervals after filtration and drying of the sample. The PXRD pattern obtained even after 30 days of stirring in water reveals exact similarity with as synthesized pattern of **48**, confirming its water stability. Further, the stability of **48** in water at high temperature was confirmed by recording its powder pattern after soaking in boiling water for 2 days (Figure 3.104c). The presence of N-coordination to the paddle-wheel $\{Co_2(COO)_4\}$ SBU and interpenetrating nature of **48** possibly makes it a water stable material as demonstrated by Walton et al.³¹⁰

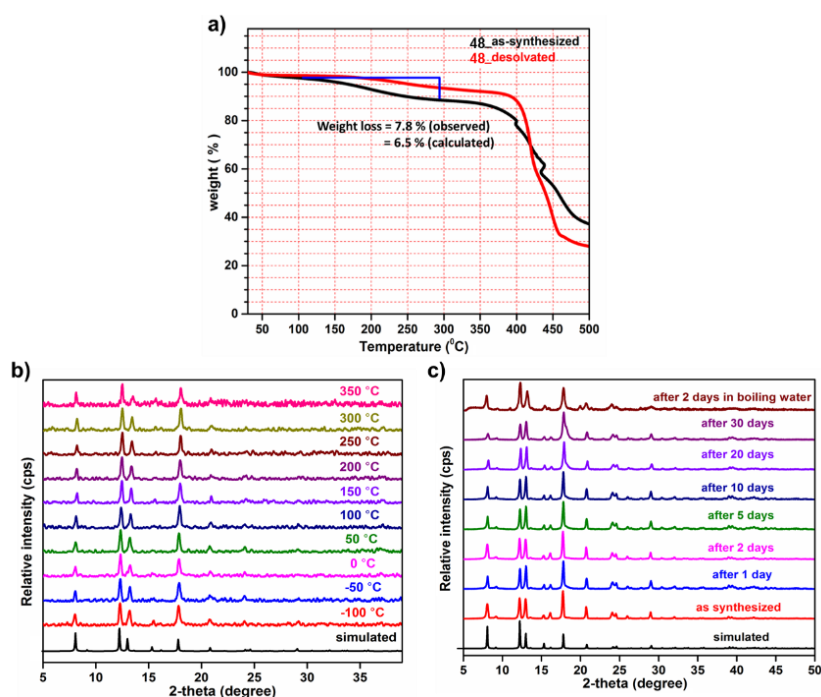


Figure 3.104. (a) Thermogravimetric profiles of **48** (as-synthesized and desolvated). (b) In-situ variable temperature powder pattern of the as synthesized sample of **48** and (b) the powder X-ray diffraction pattern of the as synthesized sample after soaking in water at room temperature and in boiling water, indicating the thermal robustness and water stability of **48**.

Gas sorption studies. The presence of open channels in **48** encouraged us to examine permanent porosity in **48**. Like in other cases, the sample (~100 mg) was activated by degassing at an elevated temperature of 393 K under vacuum conditions (20 mTorr) for 24 hours prior to adsorption measurements. The loss of lattice solvents was confirmed by thermogravimetric analysis (Figure 3.104a). Furthermore, the PXRD pattern of the activated sample revealed that the original framework structure is retained after the activation process (Figure 3.103a). The CO₂ gas sorption isotherm for activated sample of **48** at 195 K and 1 bar pressure (Figure 3.105a) clearly indicates its microporous nature. Based on the CO₂ adsorption data at 195 K, the Brunauer–Emmett–Teller (BET) surface area and the Langmuir surface area were estimated to be 224 m²g⁻¹ and 343 m²g⁻¹, respectively (Figure 3.105c and d). The BET surface area of **48** is smaller than those in MOF-2 {Zn₃(BDC)₃}_n (270 m²g⁻¹),³¹¹ SNU-15 {Co₄(μ-OH₂)₄(MTB)₂}_n (356 m²g⁻¹),³¹² and ZIF-97 {Zn(hymeIm)₂}_n (564 m²g⁻¹)³¹³ but comparable with those for {Zn(DHBP)(DMF)₂}_n, {Cd₆(CPOM)₃(H₂O)₆}_n and {Cu₂(TP)₃(OH)}_n having surface area of 209 m²g⁻¹, 231 m²g⁻¹ and 258 m²g⁻¹, respectively.⁹⁶

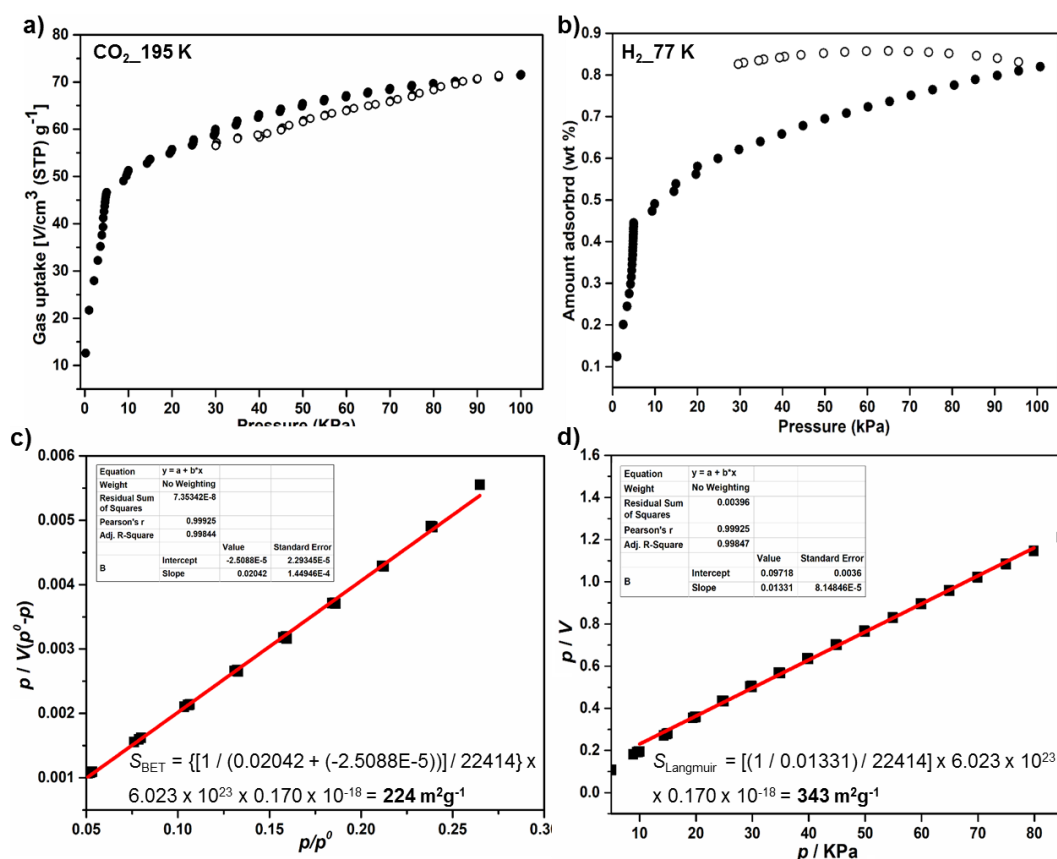


Figure 3.105. (a and b) CO₂ and H₂ sorption isotherm for **48** at 195 K and 77 K. Filled circles and open circles indicate the adsorption and desorption points, respectively, (c and d) BET and Langmuir surface area of obtained from the CO₂ adsorption isotherm.

The hydrogen sorption isotherm indicates an uptake of 0.82 wt% at 77 K and 1 bar pressure (Figure 3.105b). A large sorption hysteresis loop observed in the H₂ sorption isotherm can be explained by the kinetic trap effect where the adsorbed H₂ was trapped into the framework. The uptake amount is found to be moderate among the well-known MOF materials in the literature.⁹⁷

It is well-known that the separation of CO₂ from CH₄ in the pre-combustion process of natural gas and separation of CO₂ from N₂ in the post-combustion process is very essential. Therefore, the small pore spaces and the establishment of permanent porosity within **48** motivated us to examine its CO₂, CH₄ and N₂ sorption isotherms and potential for gas separations. Single component CO₂ sorption isotherm was measured at different temperatures (298 - 263 K) under 1 bar pressure. As shown in Figure 3.106a, **48** takes up moderate amount of carbon dioxide 36.4 cm³g⁻¹, 44.2 cm³g⁻¹, 51.3 cm³g⁻¹, and 59.2 cm³g⁻¹ at 298 K, 283 K, 273 K and 263 K, respectively. It is of particular interest to note that the uptake capacity of **48** at 273K is comparable to the uptake capacities (50-55 cm³g⁻¹) of well-known MOFs, such as for {Co₂(SDB)₂(L)}_n (IITKGP-6), for {[Cu₂₄(TPBTM)₈]}_n, JUC-141 and for activated carbon. When the adsorption values of N₂ (3.6 cm³g⁻¹ and 4.1 cm³g⁻¹) and CH₄ (11.4 cm³g⁻¹ and 17.6 cm³g⁻¹) at 298 K and at 273 K, respectively, at 1 bar pressure are compared with those of CO₂ under the same conditions, it clear that **48** takes up much higher amount of CO₂ (Figure 3.106b). The higher CO₂ affinity can be attributed to the smaller kinetic diameter of CO₂ (diameter: 3.30 Å) compared to those of N₂ (diameter: 3.64 Å) and CH₄ (diameter: 4.09 Å) as well as the difference of quadrupole moment, thus allowing CO₂ molecules to diffuse easily into the pores.³¹

Before the evaluation of gas selectivity, the quantitative binding strengths of CO₂ molecules with **48** was calculated based on the virial method, a well-established and reliable methodology, from fits of their adsorption isotherms at different temperatures (Figure 3.106c). The Q_{st} value of **48** at zero coverage was 30.4 kJmol⁻¹. The variation of isosteric heat of adsorption is shown in Figure 3.106d. It slightly increases at high loading and can be due to the increase in quadrupole-quadrupole interaction.³¹⁴ This trend for Q_{st} is similar to that observed for the interpenetrated MOF NOTT-202a.³¹⁵ The Q_{st} value of **48** at zero coverage is comparable with values for M'MOF-20 (28.4 kJmol⁻¹), {Cd₂(L)(2,6-NDC)₂}_n (28.1 kJmol⁻¹), {Cu(bc ppm)H₂O}_n and JUC-199 (29 kJmol⁻¹), MIL-53(Cr) and Hpip@ZnPC-2 (32 kJmol⁻¹) but higher than values for UMCM-1 (12 kJmol⁻¹), MOF-5 (17 kJmol⁻¹), CuBTtri (21kJmol⁻¹), IITKGP-5 (22.6 kJmol⁻¹), IITKGP-6 (23 kJmol⁻¹) and

NOTT-40 (25 kJmol^{-1}) and lower than the extra high values of 60 kJmol^{-1} for MIL-10035 and 90 kJmol^{-1} for $\text{HCu}-[(\text{Cu}_4\text{Cl})_3(\text{BTri})_8(\text{en})_5]$ (Table A67).

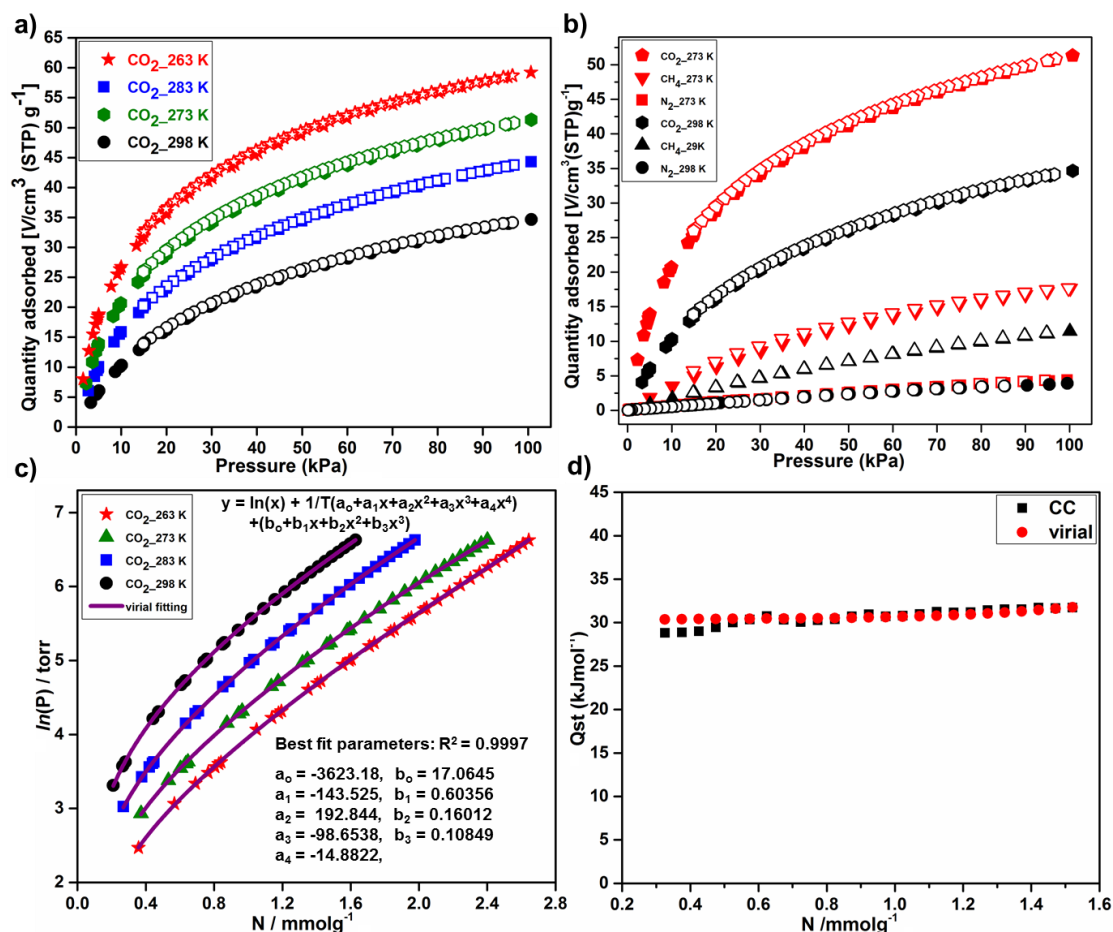


Figure 3.106. (a) CO₂ sorption isotherms for **48** collected at different temperatures, (b) comparison of CO₂ sorption isotherm with that of CH₄ and N₂ at 273 K and 298 K, respectively. (c) Fitting (purple solid lines) of the CO₂ adsorption isotherms using the virial method and (d) variation of isosteric heat of adsorption with respect to surface coverage.

In the interest of evaluating the gas separation ability of **48**, we further studied the mixture selectivity at different temperatures for CO₂-CH₄ and CO₂-N₂ mixtures at a general feed composition of landfill gas (CO₂/CH₄ = 50:50) and flue gas (CO₂/N₂ = 15:85) with pressure up to 1 bar. The well-known ideal adsorbed solution theory (IAST) developed by Myers and Prausnitz for binary mixtures was applied to our system.³¹⁶ The pure component adsorption data at a particular temperature were taken as input to the IAST calculation, and the output predicts the mixture adsorption equilibrium over a desired pressure range. The precision of the IAST calculations for the estimation of loading of components in a binary gas mixture has already been well established by comparison with the Configuration-Bias Monte Carlo (CBMC) simulations for a diverse range of zeolites and MOFs.³¹⁷ The IAST theory assumes that the adsorbed phase is a two-dimensional solution in equilibrium with

the gas phase. Both the components in the mixture behave as ideal adsorbed solution and conform to the rule analogous to Raoult's law. In order to calculate the selective sorption performance of **48** toward the separation of binary mixed gases, the parameters fitted from the single-component CO₂, CH₄ and N₂ adsorption isotherms based on the single-site Langmuir-Freundlich equation as given below.

$$Q = Q_{sat} \left(\frac{Kc^n}{1 + Kc^n} \right)$$

where Q is the adsorbed amount (mmolg⁻¹), Q_{sat} is the saturation capacity (mmolg⁻¹), c is the equilibrium pressure (kPa), and K and $1/n$ are the Langmuir and Freundlich constants. Then the fitted parameters were used to predict the molar fraction of A in the adsorbed phase using following equation:

$$Q_{sat,a} \ln \left(1 + \frac{K_a c^{n_a} y}{x} \right) - Q_{sat,b} \ln \left(1 + \frac{K_b c^{n_b} (1-y)}{(1-x)} \right) = 0$$

where $Q_{sat,a}$, K_a and n_a are the Langmuir-Freundlich fitting parameters of adsorption equilibrium of pure A, $Q_{sat,b}$, K_b and n_b are Langmuir-Freundlich parameters of adsorption equilibrium of pure B, and x and y are the molar fractions of A in the adsorbed phase and in bulk phase, respectively.

The predicted adsorption selectivity is defined as

$$S = \left(\frac{x_1/y_1}{x_2/y_2} \right)$$

where x_i is the mole fractions of component i in the adsorbed and y_i is the mole fractions of component i in bulk phase. The IAST calculations were carried out for a binary mixture containing 15% CO₂ (y_1) and 85% N₂ (y_2), which is typical of flue gases and for a binary mixture containing 50% CO₂ (y_1) and 50% CH₄ (y_2), which is typical of landfill gases.

The mixture adsorption isotherms and adsorption selectivity for **48** at different temperatures and pressures calculated by IAST (based on the single site Langmuir-Freundlich model) for CO₂/N₂ and CO₂/CH₄ mixtures as a function of total bulk pressure are shown in Figure 3.107. The results indicate that under 1 bar pressure the selectivity for CO₂/N₂ and CO₂/CH₄ are 194.7 and 19.3 at 273 K and 70.5 and 9.9 at 298 K, respectively.

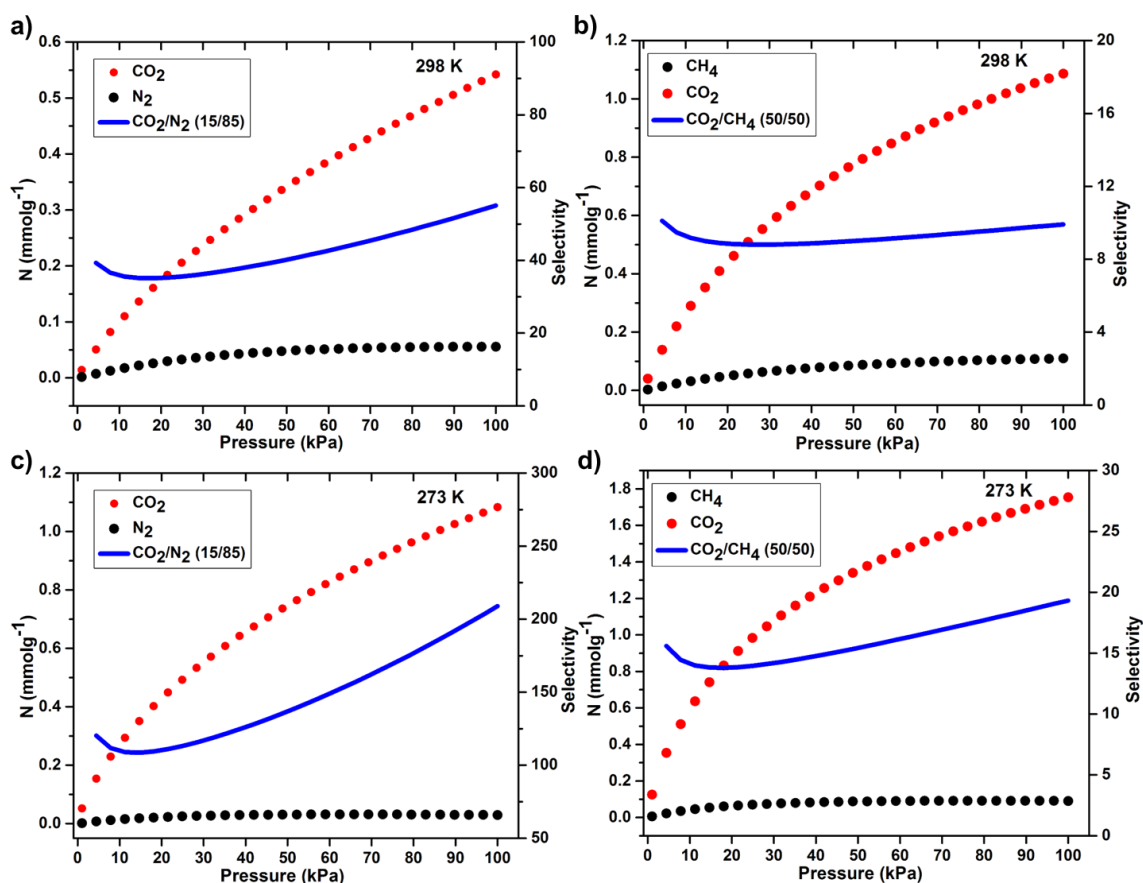
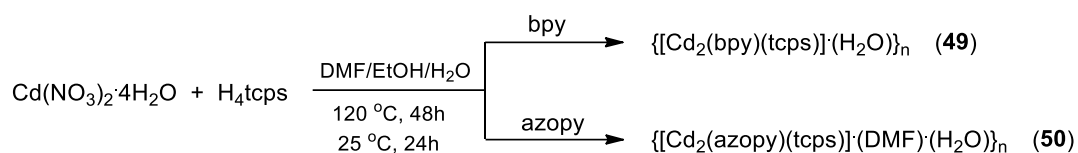


Figure 3.107. Binary mixture adsorption isotherms and selectivities for CO_2/N_2 (15/85) mixture and CO_2/CH_4 (50/50) mixtures at 298 K (a and b) and 273 K (c and d), respectively.

The CO_2/N_2 selectivities with 0.15 bar of CO_2 and 0.85 bar of N_2 (which is a typical composition of flue gas mixture from power plants) at 273 K is higher than some of the well-known MOF materials. The selectivity values at different temperatures and pressures for some well-known MOFs such as HKUST-1, PCN-88, PCN-61, UTSA-49a, UTSA-72a, UTSA-85a, MIL-101, SNU-M10, MAF-66 and many ZIF materials are summarized in Table A68. Therefore, it is notable that **48** exhibiting moderate CO_2 uptake capacity but showing very high CO_2/N_2 selectivity and moderate CO_2/CH_4 selectivity. Along with very good thermal and water stability even at elevated temperature, the uniqueness of 2-fold interpenetrated **48** for CO_2 capture and separation from flue gas as well as landfill gas entitles it as a good candidate for practical applications in gas separation and purification processes. Since the industrial gas streams contains lot of moisture and are escaped at high temperatures. It is very difficult to get rid of water from industrial gas streams. Therefore, while considering the materials for adsorption based separation and purification applications, the stability of MOFs in humid environment most importantly at elevated temperatures must be taken into account.

The study with bis(pyridyl) ligands has been further extended with Cd(II) as metal center in combination with different rigid, flexible and functionalized pillar ligands for the construction of functionalized coordination polymers based on tetrahedral tetracarboxylate linker **H₄tcps**. The solvothermal reaction of cadmium(II) nitrate and **H₄tcps** in combination with neutral ligand bpy or azopy has resulted in the formation of a non-interpenetrated 3D coordination polymer $\{[\text{Cd}_2(\text{bpy})(\text{tcps})]\cdot\text{H}_2\text{O}\}_n$ (**49**) and $\{[\text{Cd}_2(\text{azopy})(\text{tcps})]\cdot\text{H}_2\text{O}\cdot\text{DMF}\}_n$ (**50**) (Scheme 3.24). Both the compounds have been structurally characterized by single crystal X-ray diffraction analysis and the molecular formula was established by a combination of elemental analysis, TGA and single crystal X-ray diffraction.

Scheme 3.24. Synthesis of **49** and **50**.



Single crystal structure analysis. Single crystal suitable for X-ray diffraction analysis in both cases were obtained by solvothermal reaction at 120 °C. Both **49** and **50** are isostructural and crystallizes in a monoclinic crystal system with *C2/c* space group. Both the structures consists of similar asymmetric units, which contains two crystallographically independent Cd(II) ions (each with 0.5 occupancies), one-half of the tetracarboxylate linker (**tcps⁴⁻**) and one-half of **bpy** or **azopy** molecule in **49** and **50**, respectively. Both the Cd(II) centers in each case are in distorted octahedral environment, where six coordination sites around one of the metal centers are occupied by six oxygen atoms of the carboxyl group of four different **tcps⁴⁻**. The other metal center is in N₂O₄ type environment, where six coordination sites are fulfilled by four carboxyl oxygen atoms from four different **tcps⁴⁻** and two nitrogen atoms from two **bpy** (in case of **49**) or two **azopy** (in case of **50**) ligands (Figure 3.108a and b). The metal centers are bridged by the carboxylate linkers to form a 1D chain of metal carboxylate clusters (Figure 3.108c). These 1D chains of metal carboxylate clusters are bridged by the neutral N-donor linear linkers to form 2D sheet structures (Figure 3.108d) which are further extended by the carboxylate linkers to form an overall non-interpenetrating 3D framework (Figure 3.108e). The average Cd-O bond distance in **49** and **50** are 2.324 Å and 2.324 Å whereas the Cd-N distances are 2.543 Å and 2.278 Å, respectively. The prominent distortions from the regular octahedral geometries around the metal centers are evident from the bond angle values around the metal centers. All the crystallographic information pertaining to data collection and structure refinement

parameters, selected bond lengths and bond angles for both **49** and **50** are listed in Table A19, A41 and A63, respectively.

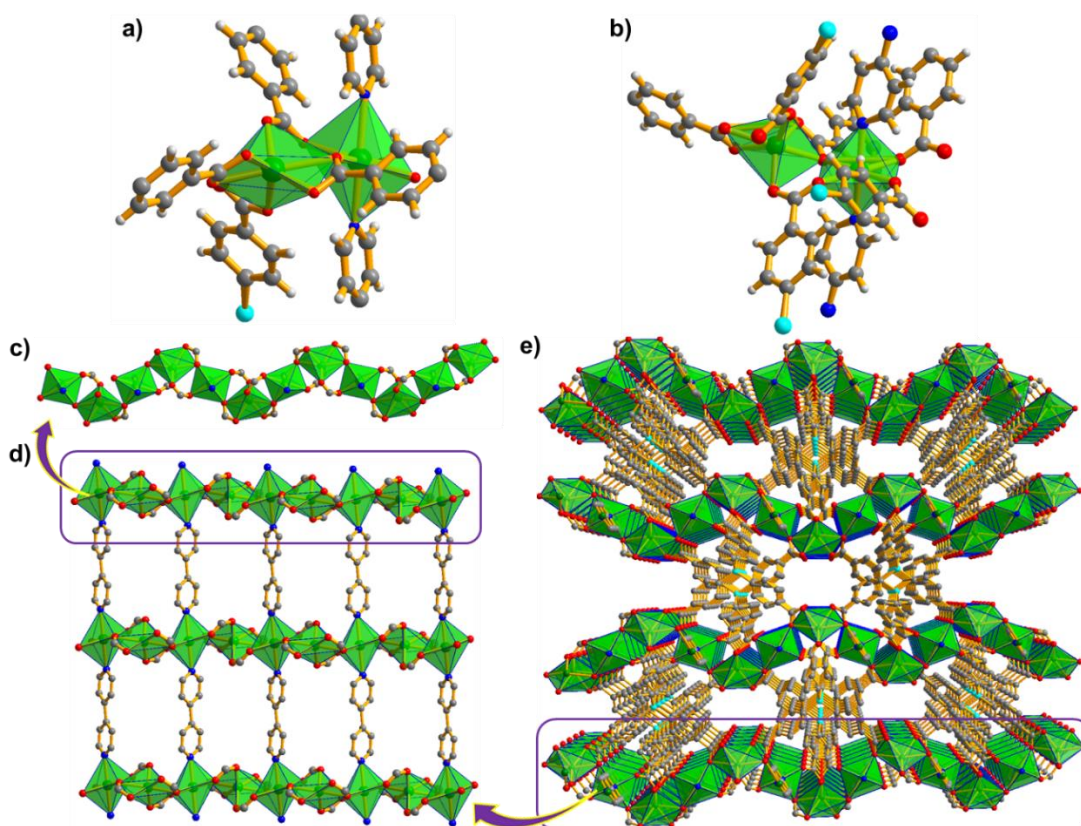


Figure 3.108. Coordination environment around the metal centers in (a) **49** and (b) **50**, (c) view of the metal carboxylate clusters forming 1D linear chain in **49**, (d) metal carboxylate clusters bridged by the neutral bpy ligands and (e) representation of overall 3D structure formed in **49**. The structural features of **50** are similar to that of **49**.

FTIR and PXRD analysis. FTIR spectra of **49** and **50** were recorded in the solid state at room temperature as KBr pellets. The characteristic peaks due to asymmetric (ν_{asym}) (1580 cm^{-1} for **49** and 1578 cm^{-1} for **50**) and symmetric (ν_{sym}) (1393 cm^{-1} in each case) stretching vibrations of the carboxylates indicates a strong binding of the carboxylates to the metal center in both the cases, which is evident from the significant shifts from the asymmetric and symmetric -C=O stretch for free **H4tcps** (1690 cm^{-1} and 1416 cm^{-1}). In addition, the difference in their ν values ($\Delta\nu = 187\text{ cm}^{-1}$ and 185 cm^{-1} for **49** and **50**, respectively) further supports the chelated and bridging bidentate binding of the carboxylates to the metal centers as seen in their respective single crystal structures. A sharp peak at 1654 cm^{-1} in **50** can be assigned due to the -C=O stretch of the DMF molecule present in the crystal lattice. In order to establish the phase purity of the as-synthesized materials, powder X-ray diffraction patterns were recorded for **49** and **50** at room temperature. As shown in Figure 3.109a and

b, the experimental powder patterns for as-synthesized compounds were in good agreement with the simulated powder patterns (obtained from the single crystal data). This confirms the crystallinity and phase purity of the as-synthesized **49** and **50**, respectively.

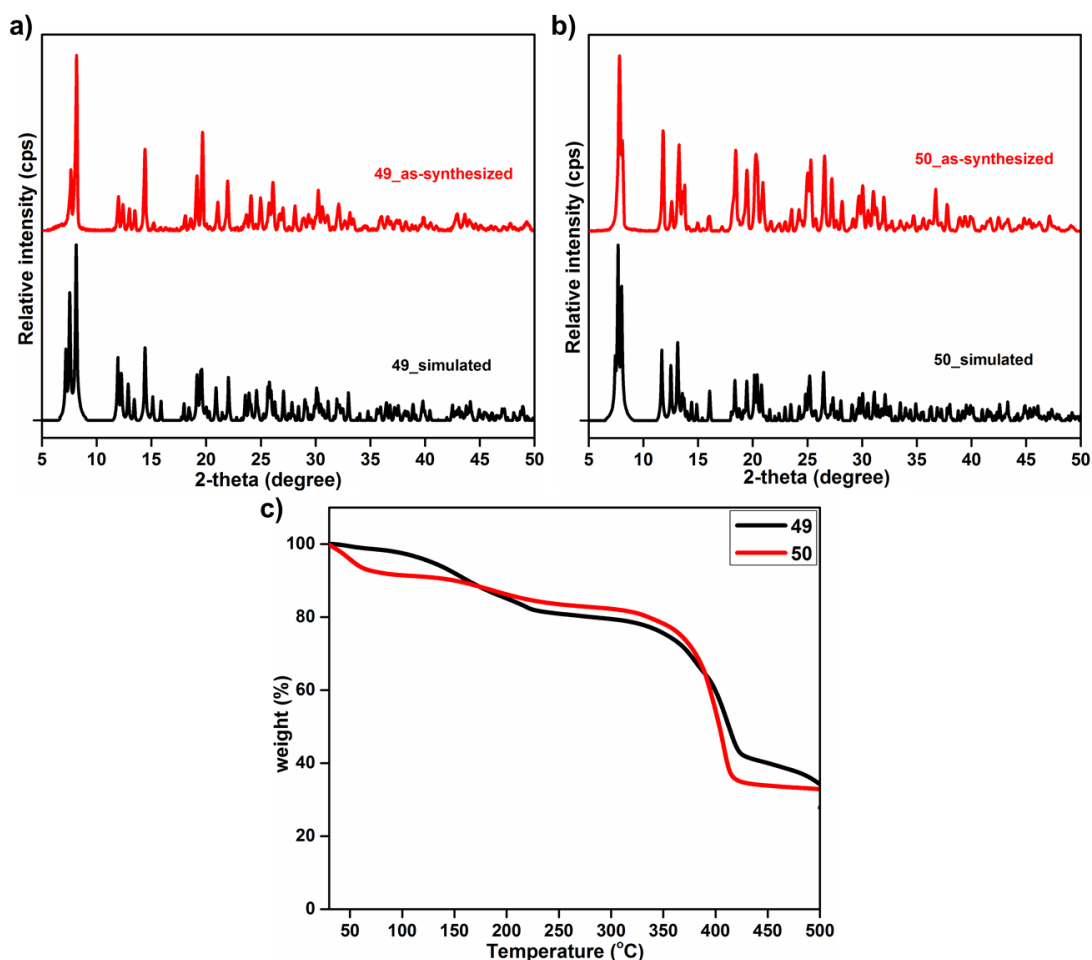
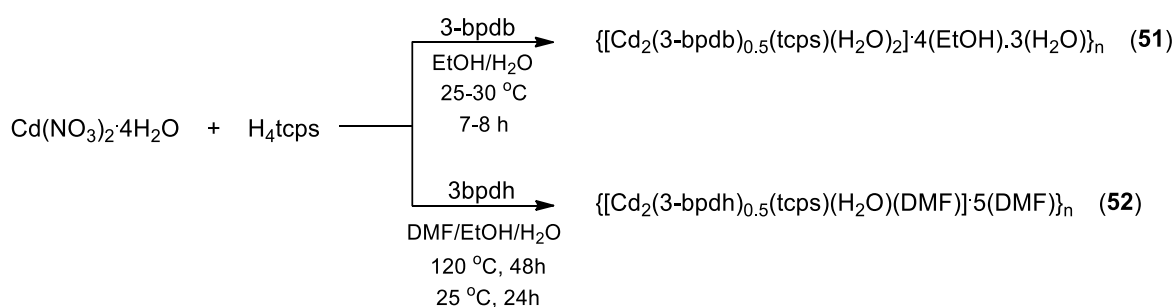


Figure 3.109. Powder X-ray diffraction of the as-synthesized samples of (a) **49**, (b) **50** compared with their respective simulated powder patterns and (c) thermogravimetric profiles for **49** and **50**.

Framework stabilities and thermal properties. The thermal stability and structural variation as a function of temperature for **49** and **50** was studied by their thermogravimetric analysis (TGA). Single phase polycrystalline samples of **49** and **50** was heated between 30-500 °C, under a dinitrogen atmosphere and corresponding weight loss was plotted with respect to temperature. As shown in Figure 3.109c, the as-synthesized samples in both cases exhibit continuous weight loss up to 220 °C, which can be ascribed due to the loss of lattice solvent molecules present into the pores of the 3D framework. After the initial weight loss due to the lattice solvent molecules both compounds show stability up to 350 °C as no weight loss could be seen in the TG profiles. After that sudden weight loss in each case indicates the framework decomposition at higher temperatures.

In order to study any effect on the final architectures due to the extended pillar ligands and any steric hindrance on the ligand structure, another set of coordination polymers, namely $\{[\text{Cd}_2(3\text{-bpdb})(\text{tcps})(\text{H}_2\text{O})_2]\cdot 4\text{EtOH}\cdot 3\text{H}_2\text{O}\}_n$ (**51**) and $\{[\text{Cd}_2(3\text{-bpdh})(\text{tcps})(\text{H}_2\text{O})(\text{DMF})]\cdot 4\text{DMF}\}_n$ (**52**) have been synthesized using the azine functionalized pillar ligands **3-bpdb** and **3-bpdh** in combination with the same metal carboxylate ($\text{Cd}(\text{II})\text{-tcps}^{4-}$) system. The solvothermal reactions of cadmium(II) nitrate and **H₄tcps** along with the pillar ligands **3-bpdb** or **3-bpdh** has resulted in the formation of **51** and **52** (Scheme 3.25). Their structures have been characterized by single crystal X-ray diffraction analysis and the respective molecular formulas have been established by a combination of elemental analysis, thermogravimetric and single crystal X-ray diffraction analysis.

Scheme 3.25. Synthesis of **51** and **52**.



Single crystal structure analysis. Single crystal X-ray diffraction analysis for **51** and **52** reveals that both are isostructural and forms a doubly interpenetrated 3D framework. Both crystallizes in a monoclinic crystal system with $P2_1/c$ space group having similar unit cell parameters. Since the structure in both the cases is same, the structure of only **51** is described here. The asymmetric unit contains two crystallographically independent $\text{Cd}(\text{II})$ ions, one tcps^{4-} , one-half of the ligand **3-bpdb** and two water molecules coordinated to $\text{Cd}1$ (Figure 3.110a). The only difference in **52** is the neutral N-donor ligand and instead of two water coordinated to one of the metal center it has one water and one DMF molecule coordinated to one of the metal center (Figure 3.110). Both the metal centers are in distorted octahedral coordination environment. The six coordination sites around $\text{Cd}1$ are occupied by three oxygen atoms from the carboxyl group of the carboxylate linker tcps^{4-} , two oxygen atoms from water molecules and one nitrogen atom of the neutral ligand **3-bpdb**, whereas in case of $\text{Cd}2$ all six coordination sites are occupied by six carboxyl oxygen atoms from four different carboxylate linkers.

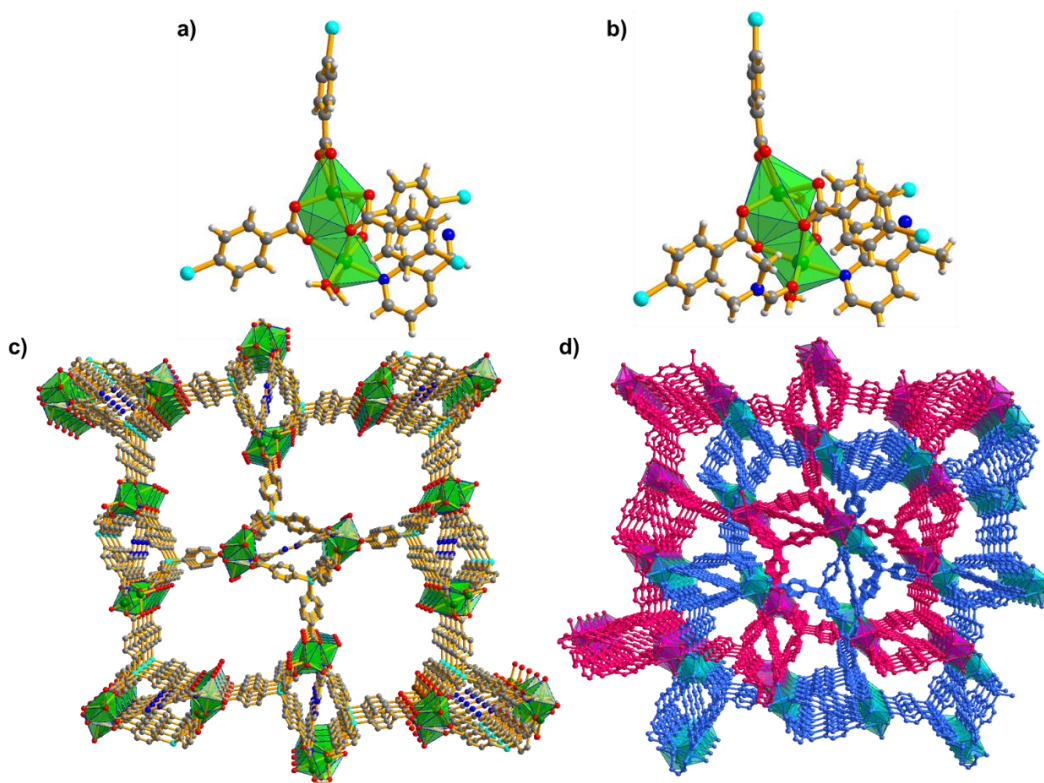


Figure 3.110. Coordination environment around the metal centers in (a) **51** and (b) **52**, (c) perspective view of the overall 3D framework and (d) two-fold interpenetration into the framework of **51**. Two different networks are shown in different colors.

The two metal centers are bridged by the three carboxylate groups to form a dimetallic $\text{Cd}_2(\text{COO})_3$ core as a secondary building unit (SBU) which is further expanded by full span of the carboxylate linker and neutral N-donor ligand to form the overall 3D framework (Figure 3.110c), where two of such networks are interpenetrated into each other to form a doubly interpenetrated structure (Figure 3.110d). Even after interpenetration, the structures consist of potential solvent accessible voids. The total potential solvent-accessible volumes were estimated to be 40% ($1969/4874 \text{ \AA}^3$ per unit cell volume) for **51** and 32% ($1595/4935 \text{ \AA}^3$ per unit cell volume) for **52** using PLATON software.²⁷⁵ The decrease in void volume in **52** is due to the presence of methyl groups (steric crowding) on the ligand **3-bpdh**. The rather intricate structure can be simplified as node and linker representation where the dimetallic $\text{Cd}_2(\text{COO})_3$ SBU can be considered as a five connected node, ligand **tcps**⁴⁻ as a four connected node and **3-bpdb** or **3-bpdh** as a linear linker, respectively (Figure 3.111a). Further examination of the node and linker representation reveals that the framework exhibits a (4,5)-connected 2-nodal network topology with two-fold interpenetration (Figure 3.111b and c) as determined by the TOPOS program.²⁷⁴

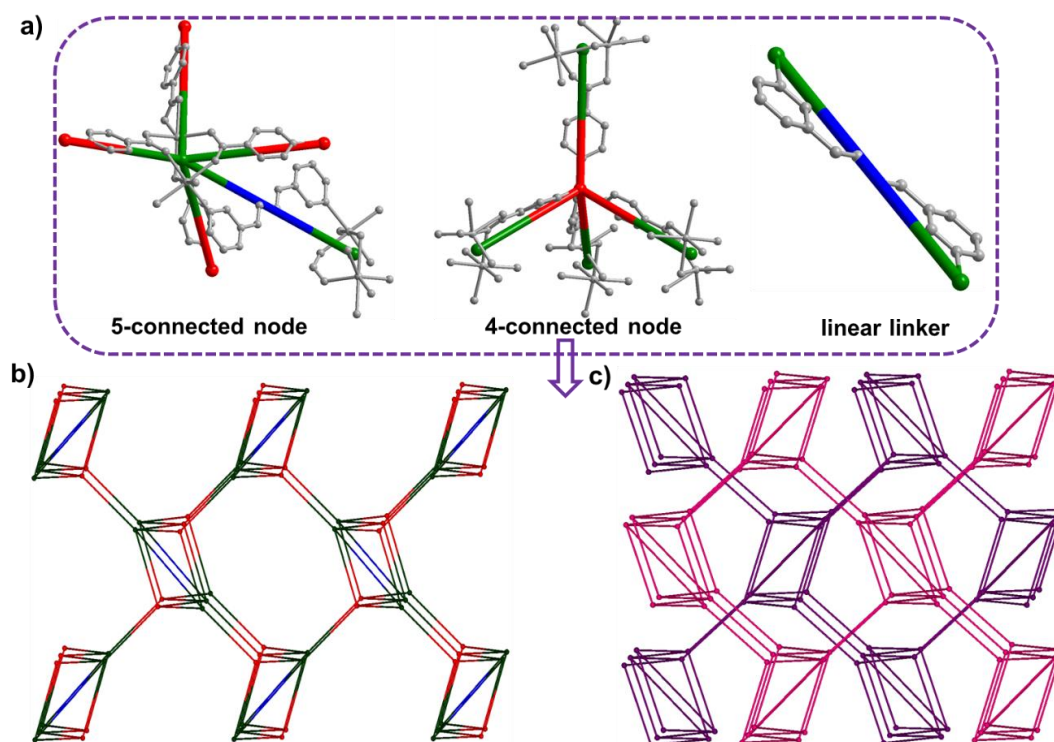


Figure 3.111. (a) simplified node and linker representation of the dimetallic SBU, ligands H_4tcps and 3-bpdb, (b) representation of the (4,5)-connected 2-nodal network topology without and (c) with two-fold interpenetration into the framework of **51**.

The average Cd-O bond distance in **51** and **52** are 2.290 Å and 2.295 Å whereas the Cd-N distances are 2.3277 Å and 2.335 Å, respectively. The prominent distortions from the regular octahedral geometries around the metal centers are evident from the bond angle values around the metal centers. All the crystallographic information pertaining to data collection and structure refinement parameters, selected bond lengths and bond angles for both **51** and **52** are listed in Table A20, A42 and A64, respectively.

FTIR and PXRD analysis. FTIR spectra of **51** and **52** were recorded in the solid state at room temperature as KBr pellets. In both cases a similar spectrum was obtained. The characteristic peaks due to asymmetric (ν_{asym}) and symmetric (ν_{sym}) stretching vibrations of the carboxylates were appeared at 1580 cm^{-1} and 1397 cm^{-1} for **51** and 1578 cm^{-1} and 1391 cm^{-1} for **52**. Difference in their ν values ($\Delta\nu = 183\text{ cm}^{-1}$ and 187 cm^{-1} for **51** and **52**, respectively) indicated the chelated and bridging bidentate binding of the carboxylates to the metal centers as seen in their respective single crystal structures. Further, significant shifts from the asymmetric and symmetric -C=O stretch for free H_4tcps (1690 cm^{-1} and 1416 cm^{-1}) indicates a strong binding of the carboxylates to the metal center in both the cases. In order to establish the phase purity and to confirm whether the bulk material represents the same compound as obtained from single crystal structure analysis, powder

X-ray diffraction patterns were recorded for the as-synthesized samples of **51** and **52** at room temperature. As shown in Figure 3.112 and b, the experimental powder patterns for as-synthesized compounds were in good agreement with the simulated powder patterns (obtained from the single crystal data). This confirms the crystallinity and phase purity of the as-synthesized **51** and **52**, respectively.

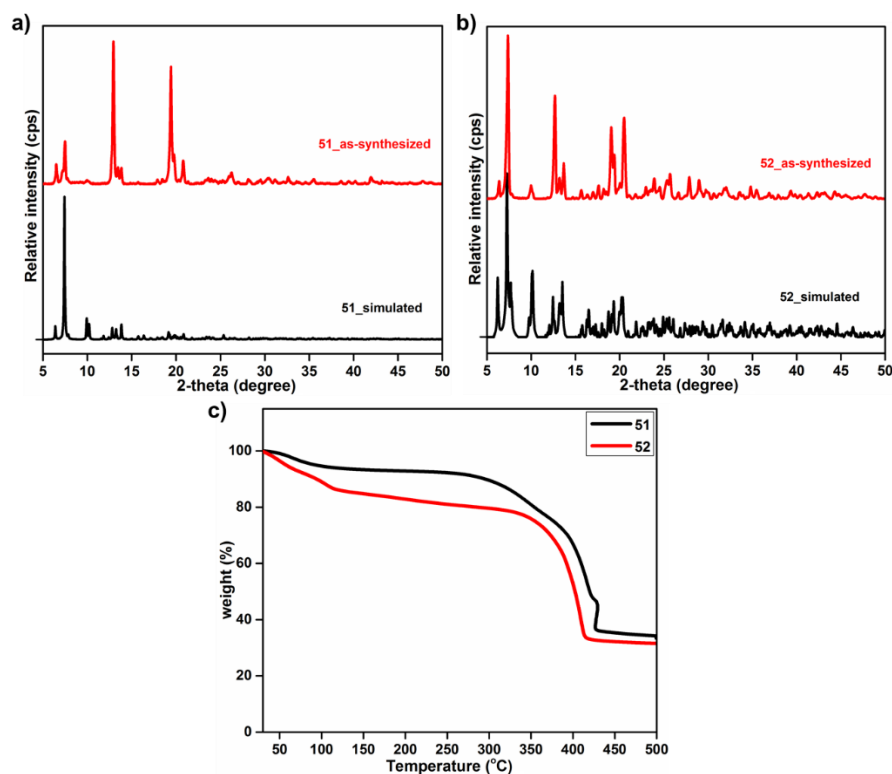


Figure 3.112. Powder X-ray diffraction of the as-synthesized samples of (a) **51**, (b) **52** compared with their respective simulated powder patterns and (c) thermogravimetric profiles for **51** and **52**.

Framework stabilities and thermal properties. The thermal stability and structural variation as a function of temperature for **51** and **52** was studied by their thermogravimetric analysis (TGA). Single phase polycrystalline samples of **51** and **52** was heated between 30-500 °C, under a dinitrogen atmosphere and corresponding weight loss was plotted with respect to temperature. As shown in Figure 3.112c, the as-synthesized samples in both cases exhibit thermal stability up to 300 °C and 350 °C, respectively. The initial weight loss at lower temperatures in both the cases can be assigned due to the solvent molecules present in the crystal lattice.

Gas sorption studies. The microporous nature of **51** and **52** was established with the help of gas sorption studies. Both compounds exhibit very low nitrogen sorption compared to carbon dioxide at lower temperatures. This might be due to the interpenetration and the pore walls functionalized with nitrogen rich azine-functionalized ligands. The

Brunauer–Emmett–Teller (BET) surface area and the Langmuir surface area were estimated to be $100 \text{ m}^2\text{g}^{-1}$ and $150 \text{ m}^2\text{g}^{-1}$ for **51** and $90 \text{ m}^2\text{g}^{-1}$ and $132 \text{ m}^2\text{g}^{-1}$ for **52**, respectively, based on the CO_2 adsorption measurement (Figure 3.113).

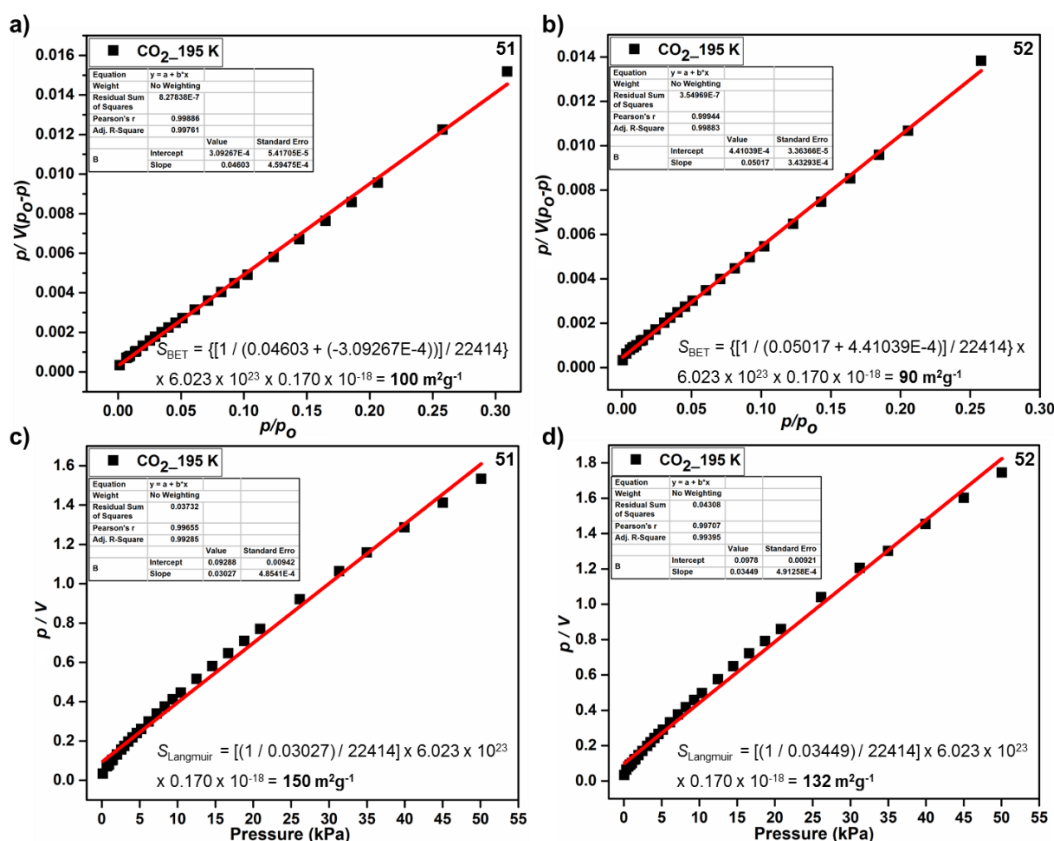


Figure 3.113. (a and b) BET and (c and d) Langmuir surface area obtained from the CO_2 adsorption isotherms for **51** and **52**, respectively.

In order to determine the quantitative binding strength of CO_2 molecules with the frameworks, the isosteric adsorption enthalpy (Q_{st}) was calculated based on the Clausius–Clapeyron equation and well-known virial equation, using the CO_2 adsorption isotherms collected at different temperatures (Figure 3.114). The Q_{st} value at zero loading was found to be $\sim 29 \text{ kJ mol}^{-1}$ and $\sim 25 \text{ kJ mol}^{-1}$, for **51** and **52**, respectively, are comparable to some MOF materials (Table A67) and indicates good binding affinity of CO_2 with the framework in both cases.

Luminescence properties. After establishment of permanent porosity in **51** and **52** by CO_2 adsorption, the azine functionalized coordination polymers have been further studied for their luminescence properties. In order to study the luminescence properties of **51** and **52**, their solid-state reflectance spectra were first recorded at room temperature. **H4tcps** and **1-4** exhibited a strong and broad absorption with λ_{max} 260 nm corresponding to $\pi-\pi^*$ transitions. On the basis of these data, emission properties were studied.

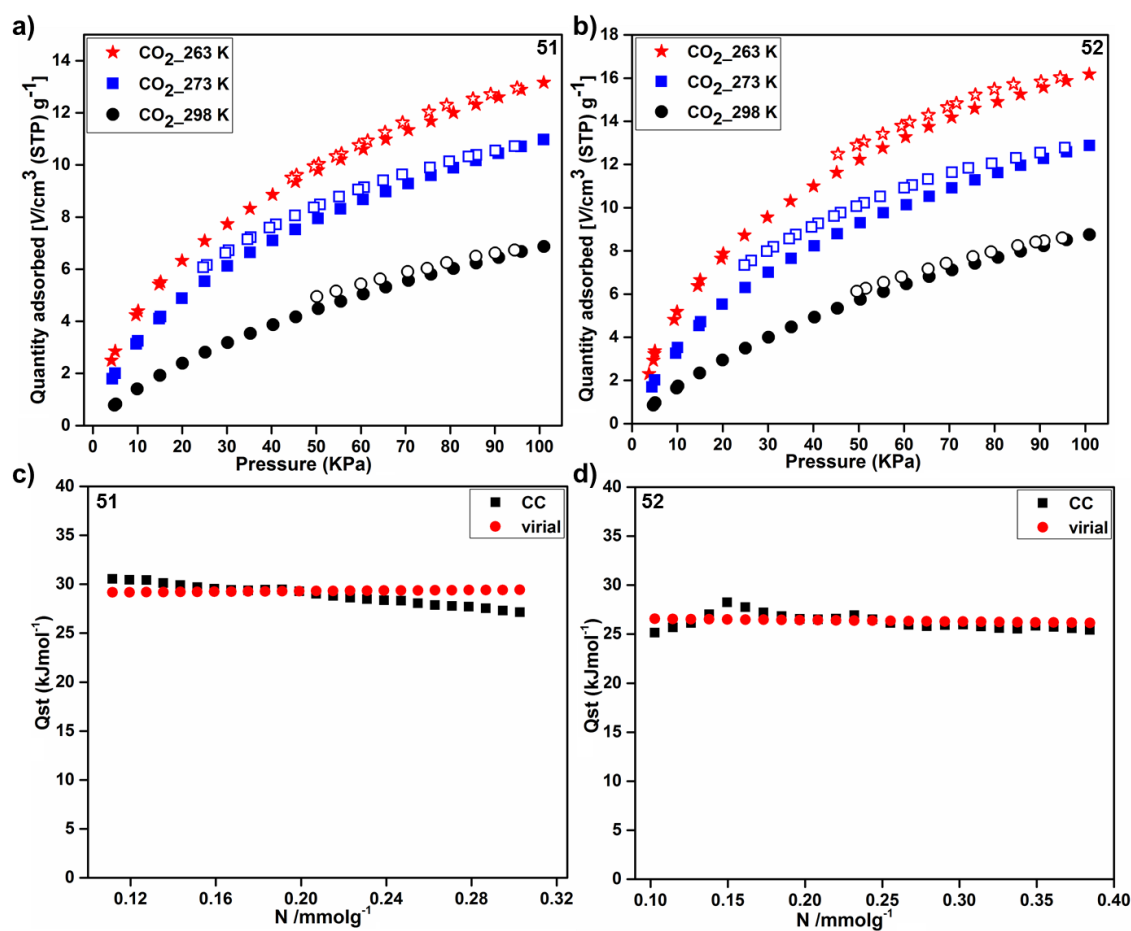


Figure 3.114. (a and b) CO₂ sorption isotherms collected at different temperatures and (c and d) variation of isosteric heat of adsorption with respect to surface coverage for **51** and **52**, respectively.

In order to understand the effect of organic solvents on their emission properties, emission spectra of **51** and **52** were recorded in different solvents such as water (H₂O), ethanol (EtOH), acetonitrile (CH₃CN), chloroform (CHCl₃), acetone, dimethylformamide (DMF) and nitrobenzene upon excitation at 270 nm. It is significant to observe that both **51** and **52** show different emission intensities in different solvents; with shifts in the emission wavelength due to change in polarity of the solvents.²⁶² The maximum intensity in both cases was obtained in methanol. Although a variation in the luminescence response was observed for different solvents, both **51** and **52** exhibit very strong emission intensities in aqueous methanol (3:1 mixture) and are therefore suitable for sensing studies in this solvent. Among all the solvents, the emission intensities were totally quenched in nitrobenzene (NB). This can be attributed due to the electron-withdrawing ability of the nitro group which facilitates an electron transfer from the excited state to the electron-deficient nitrobenzene, restricting the self-relaxation to the ground state.²⁶³ The quenching of the fluorescence intensities of **51** and **52** was further studied for different nitro aromatic derivatives. For each

experiment, a suspension of 1mg in 2mL MeOH/water mixture (1/3) was taken and the fluorescence response was measured after addition of indicated amount of a stock solution (0.5 mM) of nitroaromatic in MeOH/water mixture (1/3). Almost all the nitro-analytes moderately quench the emission intensities of **51** and **52**, it is noteworthy to observe that hydroxyl substituted NACs, such as 4-NP, 2,4-DNP, and especially TNP, preferentially quench the emission intensities over the others and show an order based on the increase in the number of nitro groups (Figure 3.115). The luminescence intensities of **51** and **52** decrease gradually as the concentration of TNP increases and at 15 ppm of TNP, the fluorescence intensity was almost completely quenched (96 % for both **51** and **52**) (Figure 3.116). A similar trend in the quenching of the emission intensities was obtained in both the cases with incremental addition of TNP. The quenching efficiency, defined by $(I_0 - I)/I_0 \times 100\%$, where I_0 and I are the luminescence intensities of **51** or **52** before and after the addition of TNP, respectively, was estimated to be about 50% for 1 ppm of TNP, 80% for 3 ppm of TNP and 90% for 8 ppm of TNP for both compounds. In order to compare the quenching efficiencies of different nitro-analytes, the quenching of emission intensities for both **51** and **52** was also studied for different nitro-analytes and the result were analyzed using the Stern-Volmer (SV) equation: $I_0/I = 1 + K_{SV}[A]$, where I_0 and I are the luminescent intensities of the compound before and after addition of the nitro-analytes, $[A]$ is the molar concentration of NB, and K_{SV} is the quenching constant (mM^{-1}). A similar value of the quenching constants (K_{SV}) for TNP was found for both **51** and **52** ($2.19 \times 10^5 \text{ M}^{-1}$ and $2.14 \times 10^5 \text{ M}^{-1}$ for **51** and **52**, respectively).

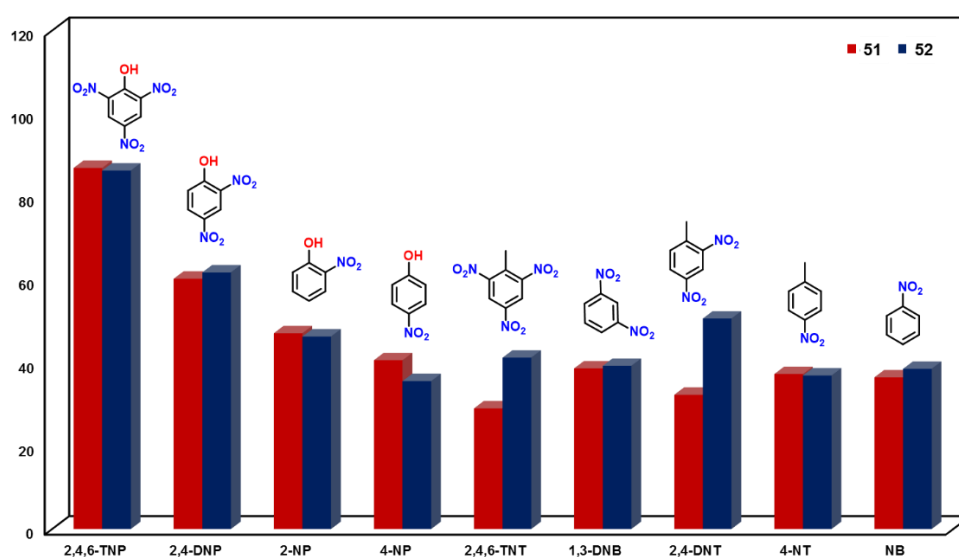


Figure 3.115. Comparison of quenching percentages of different nitroanalytes (upon addition to 100 mL in each case) by **51** and **52**, respectively.

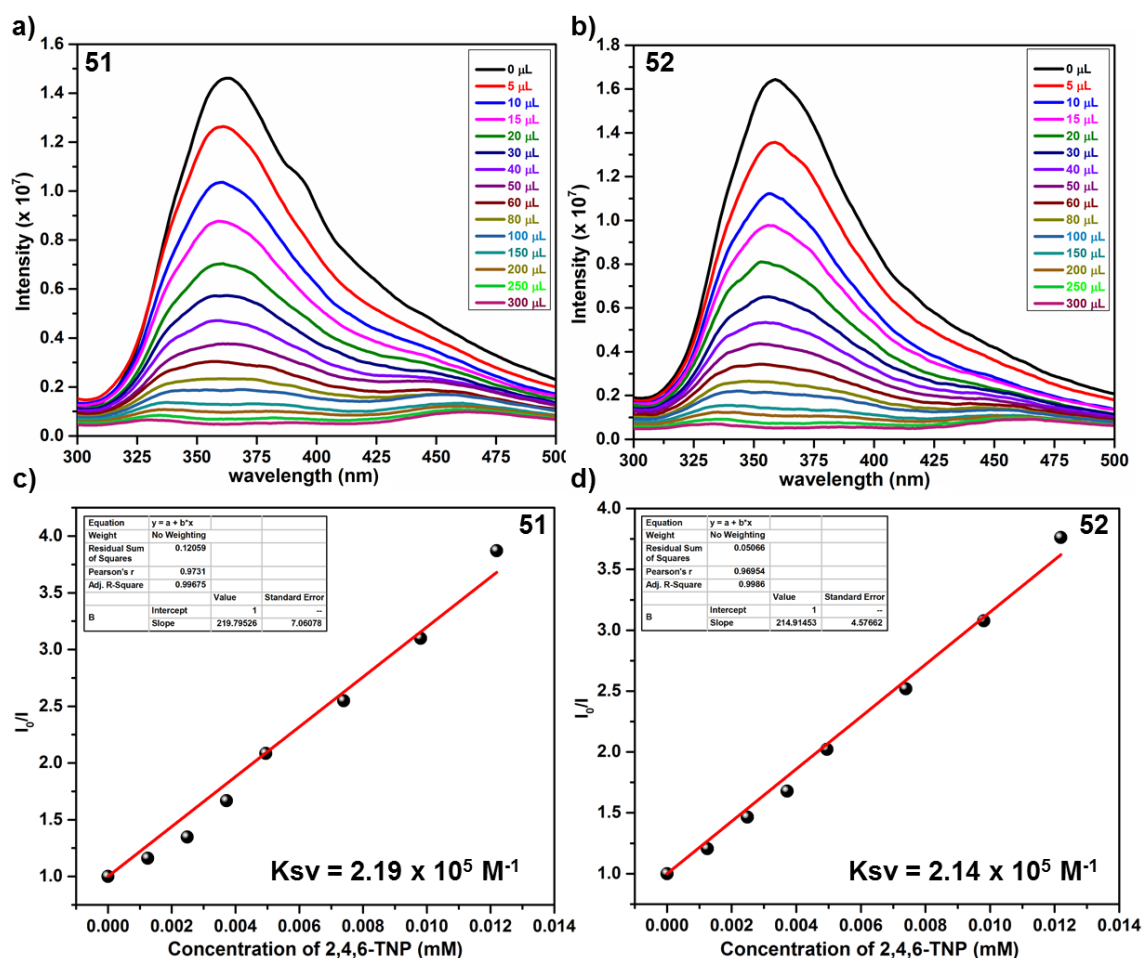


Figure 3.116. Change in emission intensities of (a) **51** and (b) **52** dispersed in aqueous methanol upon incremental addition of TNP solution and (c and d) linear fitting of Stern-Volmer plots for **51** and **52** in the low concentration region.

The high K_{SV} values in each case indicates stronger electrostatic interaction between TNP and the azine functionalized frameworks **51** and **52**. These K_{SV} values are much higher than some of the reported MOF materials (Table A69). A comparison of Stern-Volmer plots for different nitro-analytes is shown in Figure 3.117, which shows that both **51** and **52** are highly sensitive towards TNP compared to the other nitroanalytes. The K_{SV} values for different nitro-analytes was found to be in the following order: TNP \gg 2,4-DNP $>$ 2-NP \approx 4-NP $>$ 1,3-DNB $>$ NB $>$ 2,4-DNT $>$ 4-NT $>$ 2,4,6-TNT for **51** and TNP \gg 2,4-DNP $>$ 2-NP \approx 4-NP $>$ 2,4-DNT $>$ NB $>$ 4-NT $>$ 1,3-DNB $>$ 2,4,6-TNT for **52**. The very high sensitivity towards the TNP molecules in both the cases is further reflected by their detection limit values. The detection limits for **51** and **52** was estimated to be 98 ppb and 74 ppb, respectively, which is comparable with the values reported for other MOF materials (Table A69).

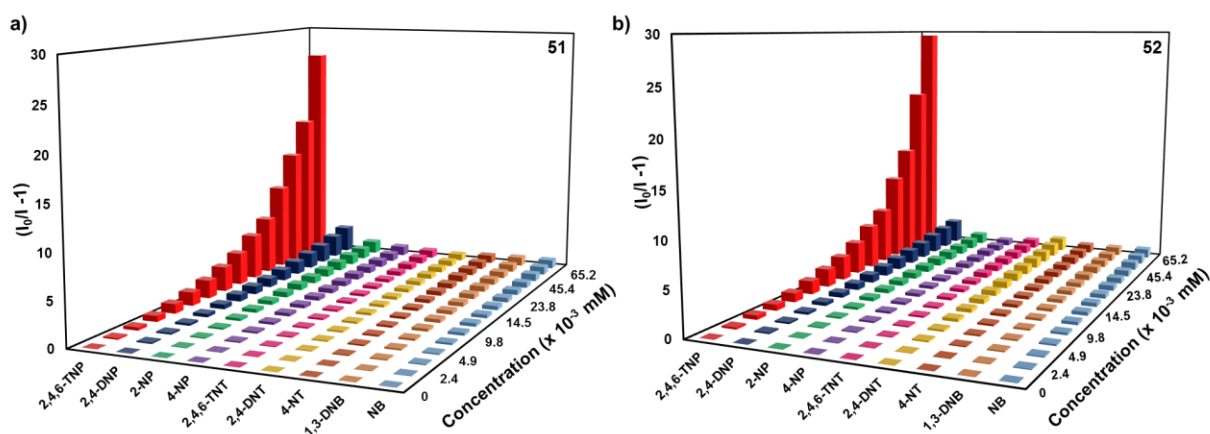


Figure 3.117. 3D-Stern-Volmer plot of different nitro-analytes for (a) **51** and (b) **52** showing high selectivity for TNP in each case.

Inspired from the highly sensitivity detection of TNP by **51** and **52**, we further investigated the selectivity of **51** and **52** for TNP in the presence of other nitro analytes. For each experiment a suspension of 1 mg of **51** or **52** was made as described before and the emission intensity was recorded before and after the addition of 40 μ L of the nitro-analyte. The percent quenching of emission intensity was calculated using the equation $(I_0 - I)/I_0 \times 100\%$. The quenching of emission intensity was finally calculated after the addition of same amount of TNP. As shown in Figure 3.118a and b, the quenching of emission intensity by TNP remains unaffected due to the presence of other nitro-analytes for both **51** and **52**. These results indicate that in addition to the highly sensitive detection of TNP by **51** and **52**, both the compounds exhibits highly selective sensing of TNP in the presence of other nitro-analytes. This can be attributed due to the non-covalent interactions of the acidic TNP molecules with the basic azine functionalities embedded into the frameworks of **51** and **52**. It is clear that the nitrophenols shows comparatively good interaction with the framework. This can be ascribed due to the presence of Lewis basic azine functionality into the frameworks of **51** and **52**, which interacts with the acidic phenol derivatives. Further, 2,4,6-trinitrophenol (TNP) being the most acidic among all the analytes due to the presence of three electron withdrawing nitro groups interacts strongly with the framework and hence shows highest quenching, which is further supported by the order of quenching efficiencies by hydroxyl substituted NACs. The quenching efficiency follows the order $TNP \gg 2,4-DNP > 2-NP \approx 4-NP$, which correlates well with the order of their acidity.

In order to study the stability of both **51** and **52**, during sensing experiments, the as-synthesized samples of **51** and **52** were immersed in the stock solution of TNP for 24 h and after separation and drying of the samples their powder X-ray diffraction data was recorded

at room temperature. It was found that both the samples retain their crystallinity and phase purity, which indicates very good stability of both the samples under the experimental conditions.

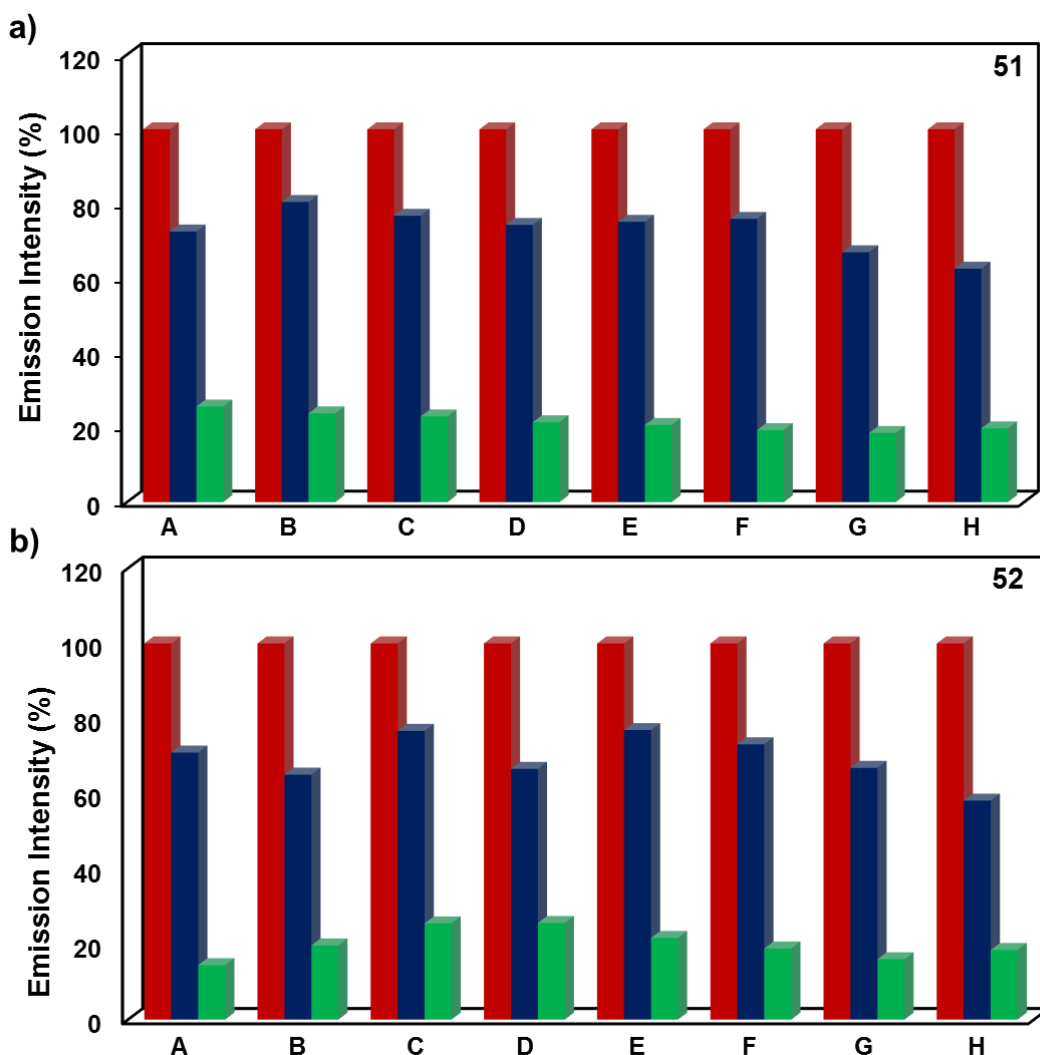


Figure 3.118. Bar plot of percentage decrease in emission intensity of (a) **51** and (b) **52** before and after the addition of different analytes (40 μ L) followed by same amount of 2,4,6-TNP (40 μ L). (Red bar represent the emission intensity by pristine **51** or **52**, blue bar represents the percent emission intensity after addition of different analytes (**51** or **52** + analyte) and green bar represents the percent emission intensity after TNP addition (**51** or **52** + analyte + 2,4,6-TNP); A: NB; B: 4-NT; C: 1,3-DNB; D: 2,4-DNT; E: 2,4,6-TNT; F: 4-NP; G: 2-NP; H: 2,4-DNP).

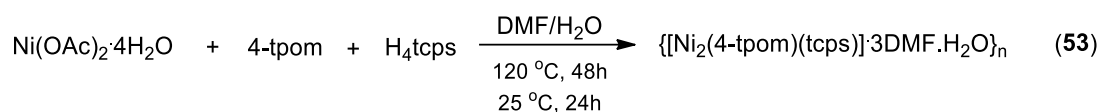
3.3.2 Semi-flexible tetra(pyridyl) ligands

As explained in the previous sections that the polymers with flexible ligands exhibit more complex and unusual structures due to variable configurations adopted by the flexible ligands during crystallization. The tetra(pyridyl) ligand 4-tpom is one of such semi-flexible tetrahedral ligand which serves as four connecting node and the four pyridyl arms can twist around the central quaternary carbon atom randomly. However, various coordination

polymers with different structures and functions have been reported using this ligand, but to the best of our knowledge, there have been only few mixed-ligand polymers containing TPOM and the carboxylate linker (linear vs. bent or aromatic vs. aliphatic carboxylates) and no mixed-ligand polymers containing tetrahedral 4-tpom and tetrahedral carboxylate linker have been reported.¹²⁶ Therefore, the present section illustrates the syntheses of coordination polymers using tetrahedral tetracarboxylate linker **H4tcps** and tetrahedral tetrapyrindyl ligands **4-tpom** or **3-tpom** with an aim to get the coordination polymers with diamondoid topology.

The solvothermal reaction of nickel(II) acetate with tetracarboxylate linker (**H4tcps**) and **4-tpom** ligand has resulted in the formation of coordination polymer **53** (Scheme 3.26), which has been characterized as a doubly interpenetrated 3D framework with diamondoid topology by single crystal X-ray diffraction analysis and the molecular formula has been established as $\{[\text{Ni}_2(4\text{-tpom})(\text{tcps})]\cdot 3\text{DMF}\cdot\text{H}_2\text{O}\}_n$ by a combination of elemental analysis, thermogravimetric and single crystal analysis.

Scheme 3.26. Synthesis of **53**.



Single crystal structure analysis. Single crystals suitable for X-ray diffraction analysis were obtained by the solvothermal reaction at 120 °C for 48 h in a solvent mixture of 1:1 DMF and water. Single crystal X-ray diffraction analysis for **53** reveals that it forms a doubly interpenetrated 3D framework. It crystallizes in a monoclinic crystal system with C_2 space group. The asymmetric unit contains two Ni(II) ions, one tcps^{4-} and one 4-tpom ligand. Each metal center is in a N_2O_4 type distorted octahedral coordination environment. The six coordination sites around the metal centers are occupied by four oxygen atoms from two carboxyl groups from two different tcps^{4-} , which are coordinated to the metal center in a chelated bidentate fashion. The other two sites are occupied by two nitrogen atoms from two different **4-tpom** ligands (Figure 3.119a). The carboxylate linker **H4tcps** is fully deprotonated and the structure is expanded by the full span of carboxylate linker and the tetra(pyridyl) linker to form an overall neutral 3D framework with open channels (Figure 3.119b). The open channels are further blocked due to the two-fold interpenetration into the framework (Figure 3.119c). Even after interpenetration into the framework the structure consists of potential voids which are filled with highly disordered solvent molecules. The diffused electron density due to the lattice solvent molecules was squeezed out using the

solvent mask option in Olex2 software, during the refinement of the structure. The total potential solvent-accessible volumes were estimated to be 42% ($3061/7177 \text{ \AA}^3$ per unit cell volume) using PLATON software.²⁷⁵

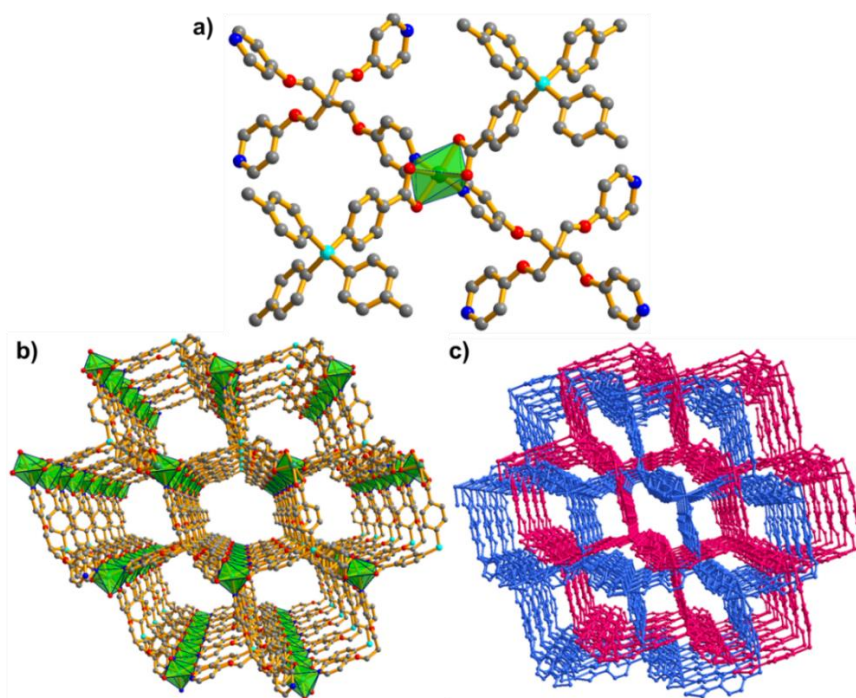


Figure 3.119. Structure description for **53**; (a) coordination environment around the metal center and perspective view of the overall 3D framework (b) without interpenetration and (c) with two-fold interpenetration into the framework.

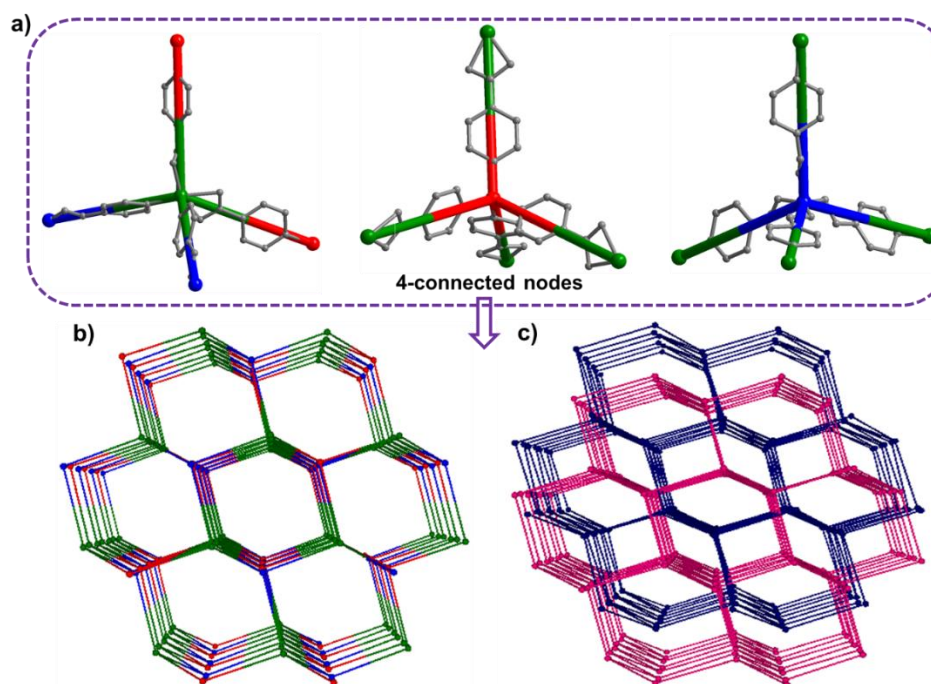


Figure 3.120. Simplified node and linker type representation for **53**; (a) the metal center, carboxylate linker tpcs^4 and 4-topm shown as 4-connected nodes and overall 4-connected uni-nodal dia; sqc6 network topology (b) without interpenetration and (c) with two-fold interpenetration.

The structure can be simplified as node and linker representation. The metal centers is expanded by two carboxylate linkers and two 4-tpom ligands and hence can be considered as a 4-connected node. Similarly, the carboxylate linker tcps4- and 4-tpom ligands can also be considered as 4-connected nodes (Figure 3.120a). Therefore, the structure is composed of only 4-connected tetrahedral nodes which expands to give a diamond like framework. Further examination of the node and linker type representation reveal that the framework exhibits a 4-connected uninodal net dia Diamond; 4/6/c1; sqc6 (topos&RCSR.ttd) topology as determined using the TOPOS program (Figure 3.120b and c).²⁷⁴ The point symbol for net is {6^6}. The average Ni-O and Ni-N bond distances are found to be 2.217 Å and 2.029 Å, respectively, which are in the usual range for this kind of complexes. The prominent distortions from the regular octahedral geometries around the metal centers are evident from the cisoid angles in the range of [62.60°-103.48°] for Ni1 and [62.01°-100.87°] for Ni2. All the crystallographic information pertaining to data collection and structure refinement parameters, selected bond lengths and bond angles for both **51** and **52** are listed in Table A21, A43 and A65, respectively.

FTIR and PXRD analysis. FTIR spectra for **53** was recorded in the solid state at room temperature as KBr pellets. The characteristic peaks due to asymmetric (ν_{asym}) and symmetric (ν_{sym}) stretching vibrations of the carboxylates were observed at 1576 cm^{-1} and 1388 cm^{-1} . The difference in their ν values ($\Delta\nu = 188 \text{ cm}^{-1}$) indicates the chelated bidentate binding of the carboxylates to the metal centers. Further, the significant shifts from the asymmetric and symmetric -C=O stretch for free **H4tcps** (1690 cm^{-1} and 1416 cm^{-1}) indicates a strong binding of the carboxylates to the metal center. The phase purity of the as-synthesized compound was established with the help of powder X-ray diffraction analysis. The repeated powder X-ray diffraction experiment with different batches, resulted in the same diffraction pattern. As shown in Figure 3.121a, the experimentally obtained powder patterns for as-synthesized compound was in good agreement with the simulated powder patterns (obtained from the single crystal data). Most of the peak positions matches with the simulated diffraction pattern, some of them differ only in the relative peak intensities. This confirms the crystallinity and phase purity of the as-synthesized sample of **53**.

Framework stabilities and thermal properties. The thermal stability and structural variation as a function of temperature for **53** was studied by their thermogravimetric analysis (TGA). Single phase polycrystalline samples of **53** was heated between 30-500 °C,

under a dinitrogen atmosphere and corresponding weight loss was plotted with respect to temperature. As shown in Figure 3.121b, the as-synthesized samples exhibit moderate thermal stability up to 250 °C. The initial weight loss in the temperature range of 50 °C to 150 °C can be ascribed due to the loss of lattice solvent molecules. After which no weight loss up to 250 °C indicates the framework stability and continuous weight loss after 250 °C indicates framework degradation at higher temperatures.

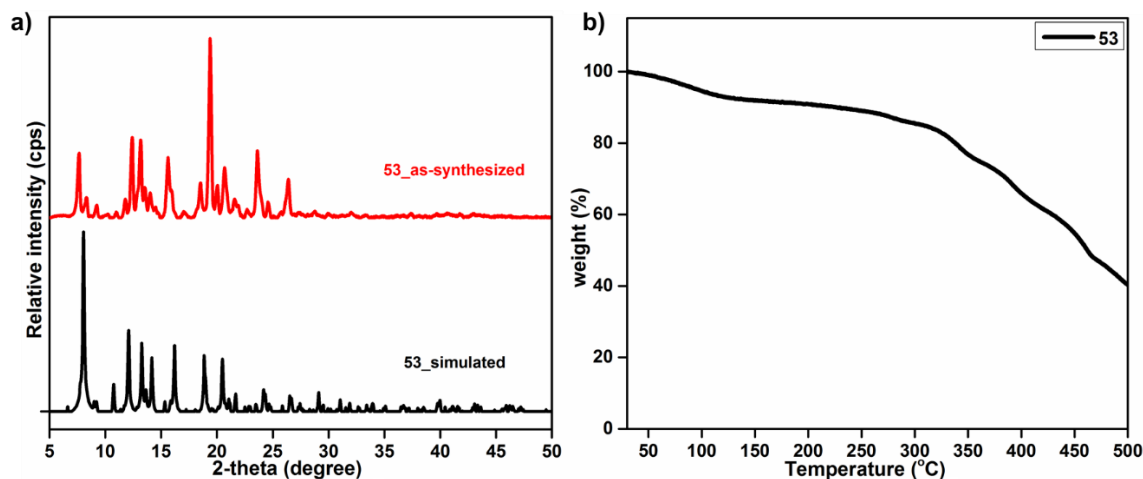


Figure 3.121. (a) Powder X-ray diffraction pattern of the as-synthesized samples of **53** compared with their respective simulated powder patterns and (b) thermogravimetric profiles for **53**.

Gas sorption studies. The permanent porosity in **53** was established with the help of gas sorption experiments. Before any sorption experiment, the sample (~100 mg) was activated by degassing at an elevated temperature of 393 K under vacuum conditions (20 mTorr) for 24 hours to remove the lattice solvent molecules present in voids. The nitrogen sorption isotherm at 77 K shows a type I adsorption isotherm indicating the microporous nature of **53**. The Brunauer–Emmett–Teller (BET) surface area and the Langmuir surface area were estimated to be 585 m²g⁻¹ and 758 m²g⁻¹, respectively, based on the N₂ adsorption measurement. After establishing the permanent porosity, the oxygen functionalized pores in **53** were further tested for their ability for carbon dioxide capture. Single component CO₂ sorption isotherm was measured at different temperatures (298–263 K) under 1 bar pressure. As shown in Figure 3.122a, **53** takes up moderate amount of carbon dioxide 28.4 cm³g⁻¹, 37.1 cm³g⁻¹, 42.8 cm³g⁻¹, and 50.7 cm³g⁻¹ at 298 K, 283 K, 273 K and 263 K, respectively. It is of particular interest to note that the uptake capacity of **53** at 273K is comparable to the uptake capacities of well-known MOFs (vide-supra). Further to test the ability of **53** for selective CO₂ capture, N₂ and CH₄ adsorption isotherms were collected at 298 K and 273 K, under 1 bar pressure. When the adsorption values of N₂ (1.3 cm³g⁻¹ and 2.7 cm³g⁻¹) and

CH₄ (3.9 cm³g⁻¹ and 5.8 cm³g⁻¹) at 298 K and at 273 K, respectively are compared with those of CO₂ under the same conditions, it clear that **53** takes up much higher amount of CO₂ (Figure 3.122b) than N₂ or CH₄. The higher CO₂ affinity can be attributed to the smaller kinetic diameter of CO₂ (diameter: 3.30 Å) compared to those of N₂ (diameter: 3.64 Å) and CH₄ (diameter: 4.09 Å) as well as the difference of quadrupole moment, thus allowing CO₂ molecules to diffuse easily into the pores.³¹

Before the evaluation of gas selectivity, the quantitative binding strengths of CO₂ molecules with **53** was calculated based on the virial method, a well-established and reliable methodology, from fits of their adsorption isotherms at different temperatures (Figure 3.122c). For the estimation of Q_{st} by virial method, a virial-type expression consisting of the temperature dependent virial parameters (vide supra) were employed to calculate the enthalpy of absorption for CO₂. The Q_{st} value of **53** at zero coverage was 27.5 kJmol⁻¹. The variation of isosteric heat of adsorption is shown in Figure 3.122d. It slightly increases at

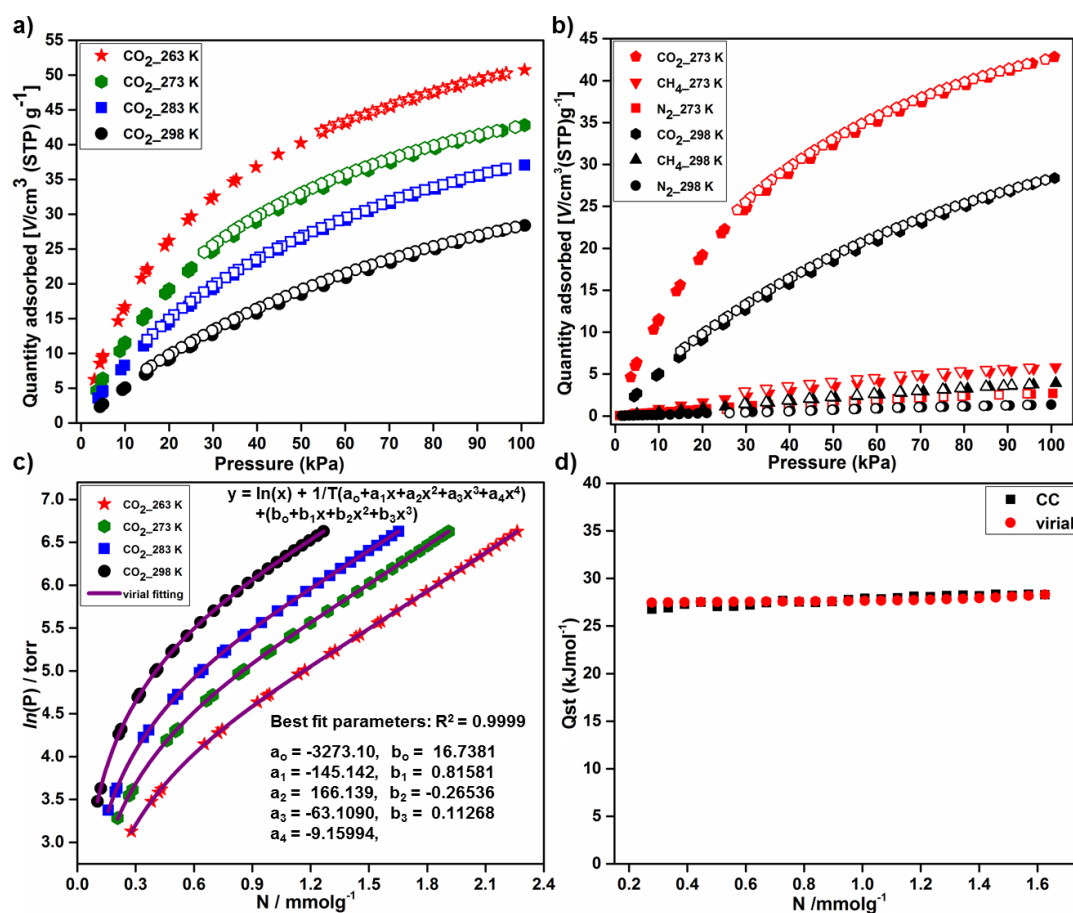


Figure 3.122. (a) CO₂ sorption isotherms for **53** collected at different temperatures, (b) comparison of CO₂ sorption isotherm with that of CH₄ and N₂ at 273 K and 298 K, respectively. (c) Fitting (purple solid lines) of the CO₂ adsorption isotherms using the virial method and (d) variation of isosteric heat of adsorption with respect to surface coverage.

high loading and can be due to the increasing in quadrupole-quadrupole interaction.³¹² This trend for Qst is similar to that observed for the interpenetrated MOF NOTT-202a. A comparison of the Qst value of **53** at zero coverage with other MOF materials is shown in Table A67.

In the interest of evaluating the gas separation ability of **53**, we further studied the mixture selectivity at different temperatures for CO₂-CH₄ and CO₂-N₂ mixtures at a general feed composition of landfill gas (CO₂/CH₄ = 50:50) and flue gas (CO₂/N₂ = 15:85) with pressure up to 1 bar. We applied the well-known ideal adsorbed solution theory (IAST) developed by Myers and Prausnitz for binary mixtures.³¹⁶ The pure component adsorption data at a particular temperature were taken as input to the IAST calculation, and the output predicts the mixture adsorption equilibrium over a desired pressure range. In order to calculate the selective sorption performance of **53** toward the separation of binary mixed gases, the parameters fitted from the single-component CO₂, CH₄ and N₂ adsorption isotherms based on the single-site Langmuir-Freundlich equation (*vide supra*). The IAST calculations were carried out for a binary mixture containing 15% CO₂ (y₁) and 85% N₂ (y₂), which is typical of flue gases and for a binary mixture containing 50% CO₂ (y₁) and 50% CH₄ (y₂), which is typical of landfill gases.

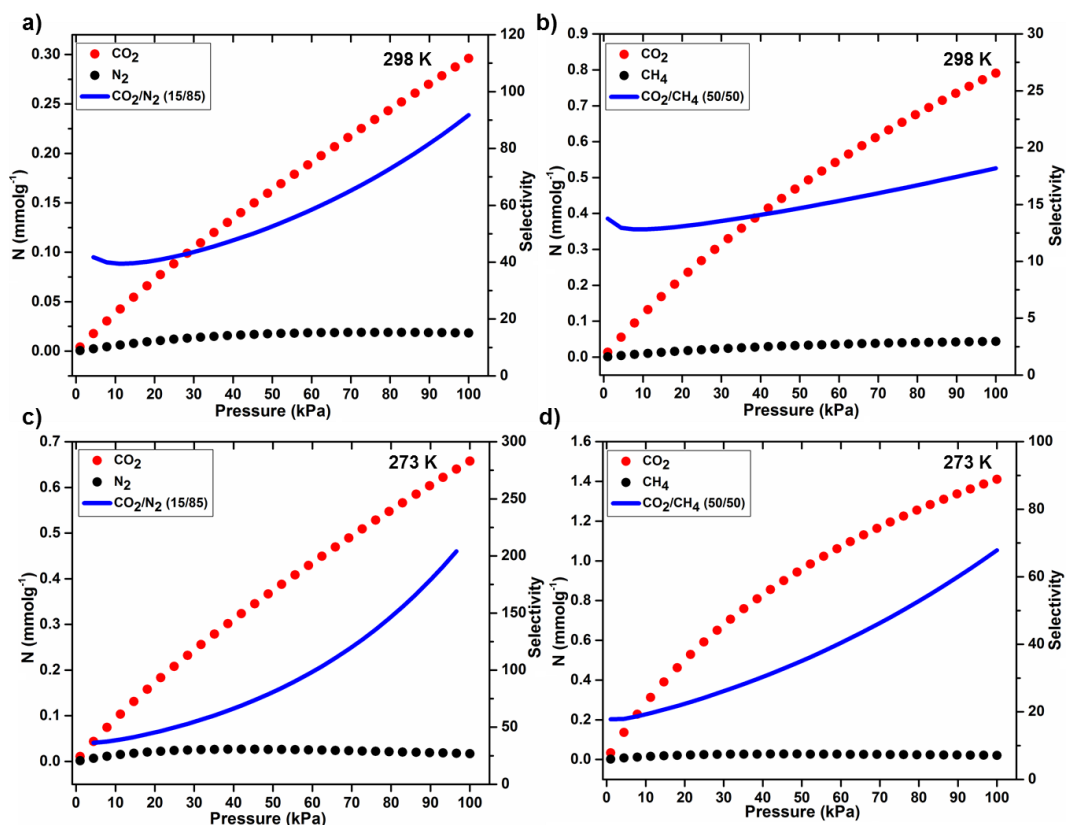
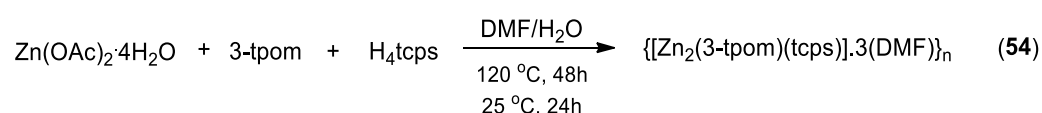


Figure 3.123. Binary mixture adsorption isotherms and selectivities for CO₂/N₂ (15/85) mixture and CO₂/CH₄ (50/50) mixtures at 298 K (a and b) and 273 K (c and d), respectively for **53**.

The mixture adsorption isotherms and adsorption selectivity for **53** at different temperatures and pressures calculated by IAST (based on the single site Langmuir-Freundlich model) for CO₂/N₂ and CO₂/CH₄ mixtures as a function of total bulk pressure are shown in Figure 3.123. The results indicated that under 1 bar pressure the selectivity for CO₂/N₂ and CO₂/CH₄ are 218.4 and 67.8 at 273 K and 91.7 and 18.2 at 298 K, respectively. The CO₂/N₂ selectivities with 0.15 bar of CO₂ and 0.85 bar of N₂ (which is a typical composition of flue gas mixture from power plants) at 273 K is higher than some of the well-known MOF materials. The selectivity values at different temperatures and pressures for some well-known MOFs and many ZIF materials are tabulated in Table A68. Therefore, it is notable that **53** exhibiting moderate CO₂ uptake capacity but showing very high CO₂/N₂ selectivity and moderate CO₂/CH₄ selectivity.

In order to study the effect of coordination site shifting on to the structure and properties of coordination polymers, we report the synthesis of another coordination polymer {[Zn₂(3-tpom)(tcps)]·3DMF}_n (**54**), based on Zn(II) metal center, same tetracarboxylate linker and 3-tpom ligand which is a positional isomer of the tetrapyriddy ligand 4-tpom. The solvothermal reaction of zinc acetate, 3-tpom and H₄tcps has resulted in the formation of **54** (Scheme 3.27). The compound has been structurally characterized by single crystal X-ray diffraction analysis and the molecular formula has been established as {[Zn₂(3-tpom)(tcps)]·3DMF}_n based on a combination of elemental analysis, thermogravimetric and single crystal X-ray diffraction analysis.

Scheme 3.27. Synthesis of **54**.



Single crystal structure analysis. Single crystals suitable for X-ray diffraction analysis were obtained by the solvothermal reaction at 120 °C for 48 h in a solvent mixture of 1:1 DMF and water. Single crystal X-ray diffraction analysis for **54** reveals that it forms a non-interpenetrated 3D framework. It crystallizes in a monoclinic crystal system with *Pc* space group. The asymmetric unit consists of two crystallographically independent Zn(II) ions, one tcps⁴⁻ and one 3-tpom ligand. The coordination sites around Zn1 are occupied by two oxygen atoms from the carboxylate groups of two tcps⁴⁻, where the carboxylates are coordinated to the metal center in a monodentate fashion and two nitrogen atoms from two 3-tpom ligand, giving an N₂O₂ type tetrahedral coordination environment around Zn1 (Figure 3.124a). The coordination environment around the Zn2 is distorted octahedral,

where four coordination sites are occupied by four oxygen atoms from the carboxylate groups of two tcps^{4-} , where the carboxylates are coordinated to the metal center in a chelated bidentate fashion. The other two sites are occupied by two nitrogen atoms from two 3-tpom ligand, giving an N_2O_4 type octahedral coordination environment around Zn^{2+} (Figure 3.124b). The carboxylate linker H_4tcps is fully deprotonated and the structure is expanded by the full span of carboxylate linker and the tetra(pyridyl) ligand to form an overall neutral 3D framework (Figure 3.124c). The open channels in **54** contain highly disordered solvent molecules, entrapped during the process of crystallization. The diffused electron density due to the lattice solvent molecules was squeezed out using the solvent mask option in Olex2 software, during the refinement of the structure. The total potential solvent-accessible volumes were estimated to be 29% ($885/3068 \text{ \AA}^3$ per unit cell volume) using PLATON software.²⁷⁵

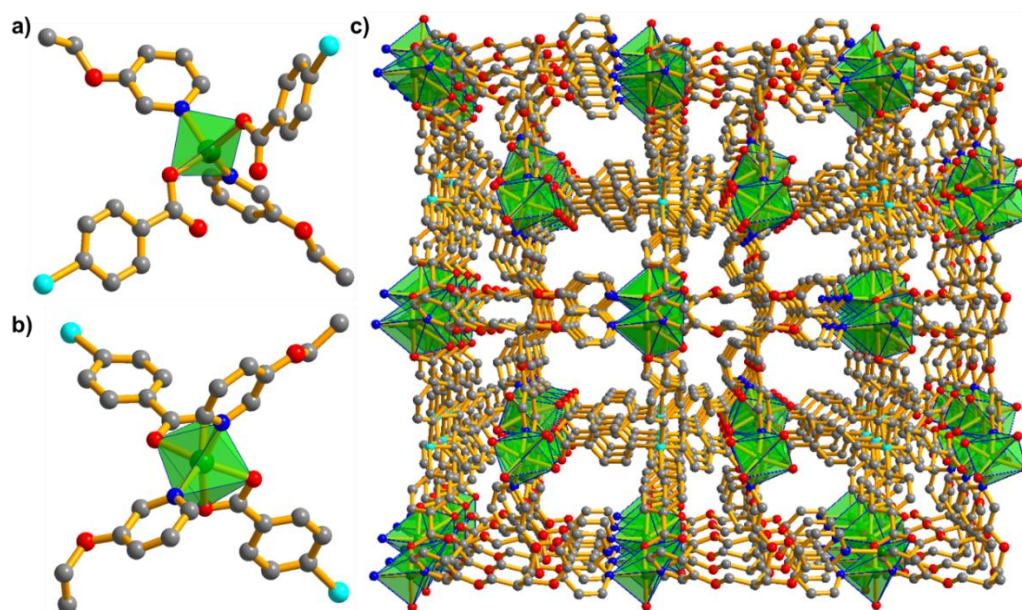


Figure 3.124. (a) coordination environment around the metal center (a) $\text{Zn}1$, (b) $\text{Zn}2$ and (c) perspective view of the overall 3D framework in **54**.

The structure can be simplified as node and linker representation. Both the metal centers ($\text{Zn}1$ and $\text{Zn}2$) are expanded by two carboxylate linkers and two 3-tpom ligands and hence can be considered as 4-connected nodes. Similarly, the carboxylate linker tcps^{4-} and 3-tpom ligands can also be considered as 4-connected nodes (Figure 3.125a). But unlike 4-tpom ligand in **53**, the ligand 3-tpom in **54**, doesn't work as a tetrahedral node instead it acts as a nearly planar 4-connected node, which is evident from the cisoid angles around the node. Therefore, however the structure is composed of only 4-connected tetrahedral nodes and exhibits a 4-connected uninodal network topology (Figure 3.125b); it does not give diamond

topology. The point symbol for net is $\{6^45.8\}$. The average Zn-O and Zn-N bond distances are found to be 2.118 Å and 2.059 Å, respectively, which are in the usual range for this kind of complexes. The prominent distortions from the regular tetrahedral and octahedral geometries around Zn1 and Zn2 are evident from the cisoid angles in the range of $[96.30^\circ-121.72^\circ]$ for Zn1 and $[58.39^\circ-117.99^\circ]$ for Zn2. All the crystallographic information pertaining to data collection and structure refinement parameters, selected bond lengths and bond angles for **54** are listed in Table A21, A43 and A65, respectively.

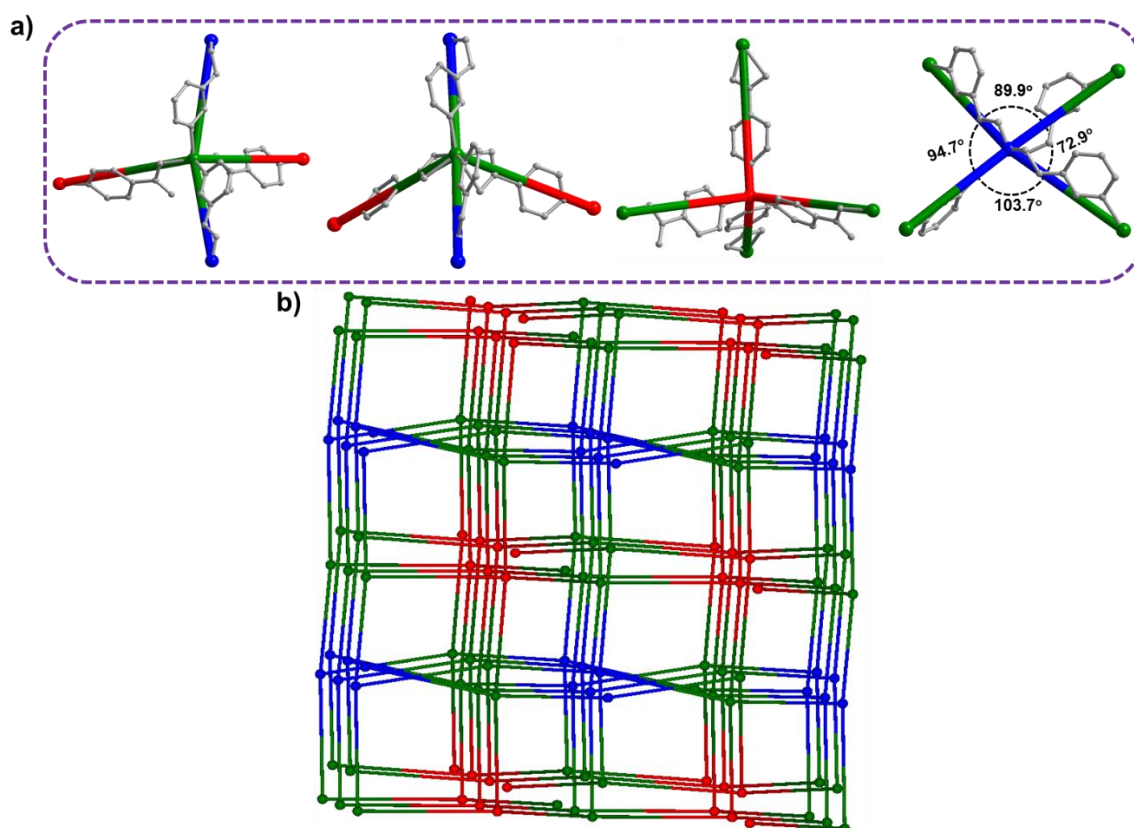


Figure 3.125. Simplified node and linker type representation for **54**; (a) the metal centers Zn1 and Zn2, carboxylate linker tcps⁺ and 3-tpom shown as 4-connected nodes and overall 4-connected unidodal network topology.

FTIR and PXRD analysis. FTIR spectra for **54** was recorded in the solid state at room temperature as KBr pellets. The characteristic peaks due to asymmetric (ν_{asym}) stretching vibrations of the carboxylates appeared at 1577 cm^{-1} and 1541 cm^{-1} whereas the symmetric (ν_{sym}) stretching vibrations of the carboxylates appeared at 1389 cm^{-1} and 1364 cm^{-1} . The difference in their ν values ($\Delta\nu = 208\text{ cm}^{-1}$ and 177 cm^{-1}) indicates monodentate and chelated bidentate binding of the carboxylates to the metal centers. Further, the prominent shifts from the asymmetric and symmetric -C=O stretch for free **H4tcps** (1690 cm^{-1} and 1416 cm^{-1}) indicates a strong binding of the carboxylates to the metal center. The phase

purity of the as-synthesized compound was established with the help of powder X-ray diffraction analysis. As shown in Figure 3.126a, the experimentally obtained powder patterns for as-synthesized compound was in good agreement with the simulated powder patterns (obtained from the single crystal data), which confirms the crystallinity and phase purity of the as-synthesized sample of **54**.

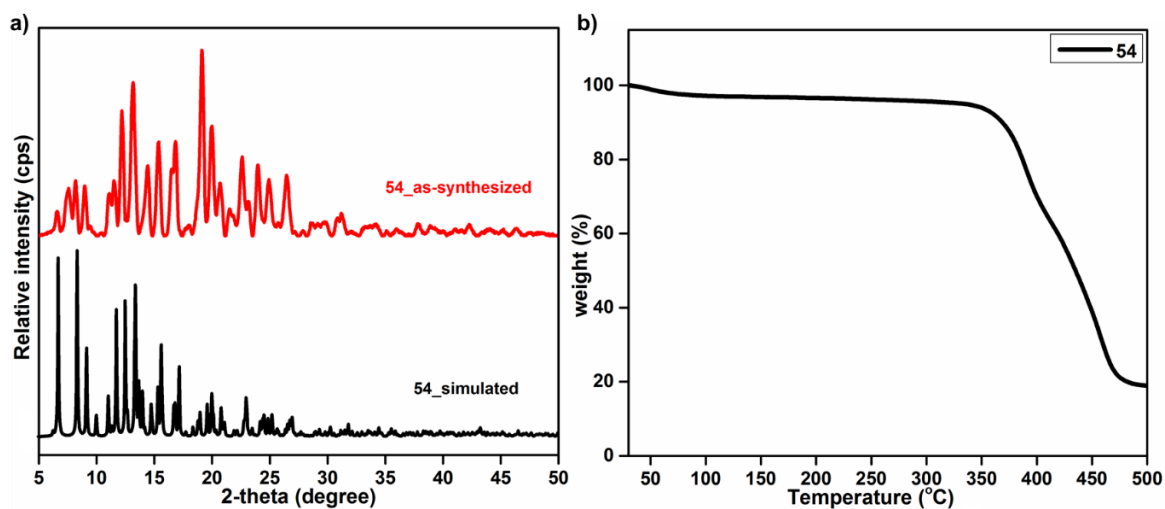


Figure 3.126. (a) Powder X-ray diffraction pattern of the as-synthesized samples of **54** compared with their respective simulated powder patterns and (b) thermogravimetric profiles for **54**.

Framework stabilities and thermal properties. The thermal stability and structural variation as a function of temperature for **54** was studied by their thermogravimetric analysis (TGA). Single phase polycrystalline samples of **54** was heated between 30-500 °C, under a dinitrogen atmosphere and corresponding weight loss was plotted with respect to temperature. As shown in Figure 3.126b, the as-synthesized samples exhibit very good thermal stability up to 350 °C as no weight loss could be seen up to 350 °C.

Gas sorption studies. In addition to the structural diversity due to coordination site shifting into the ligand structure, the effect of positional isomerization was also studied for the gas adsorption properties of these coordination polymers. The as-synthesized sample of **54** (~100 mg) was activated by degassing at an elevated temperature of 393 K under vacuum conditions (20 mTorr) for 24 hours, prior to any sorption experiment. The low temperature nitrogen sorption isotherm indicates that **54** takes up very less amount of gas than **53** under similar measurement conditions (Figure 3.127a). The sorption properties of **54** was also studied for carbon dioxide capture. Single component CO₂ sorption isotherm was measured at different temperatures (298 - 263 K) under 1 bar pressure. As shown in Figure 3.127b, **54** takes up very less amount of carbon dioxide (7.8 cm³g⁻¹, 12.2 cm³g⁻¹ and 23.2 cm³g⁻¹ at 298 K, 273 K and 263 K, respectively) when compared to the uptake capacity of **53**. The

Brunauer–Emmett–Teller (BET) surface area and the Langmuir surface area were estimated to be $104 \text{ m}^2\text{g}^{-1}$ and $140 \text{ m}^2\text{g}^{-1}$, respectively, based on the N_2 adsorption measurement (Figure 3.127c and d).

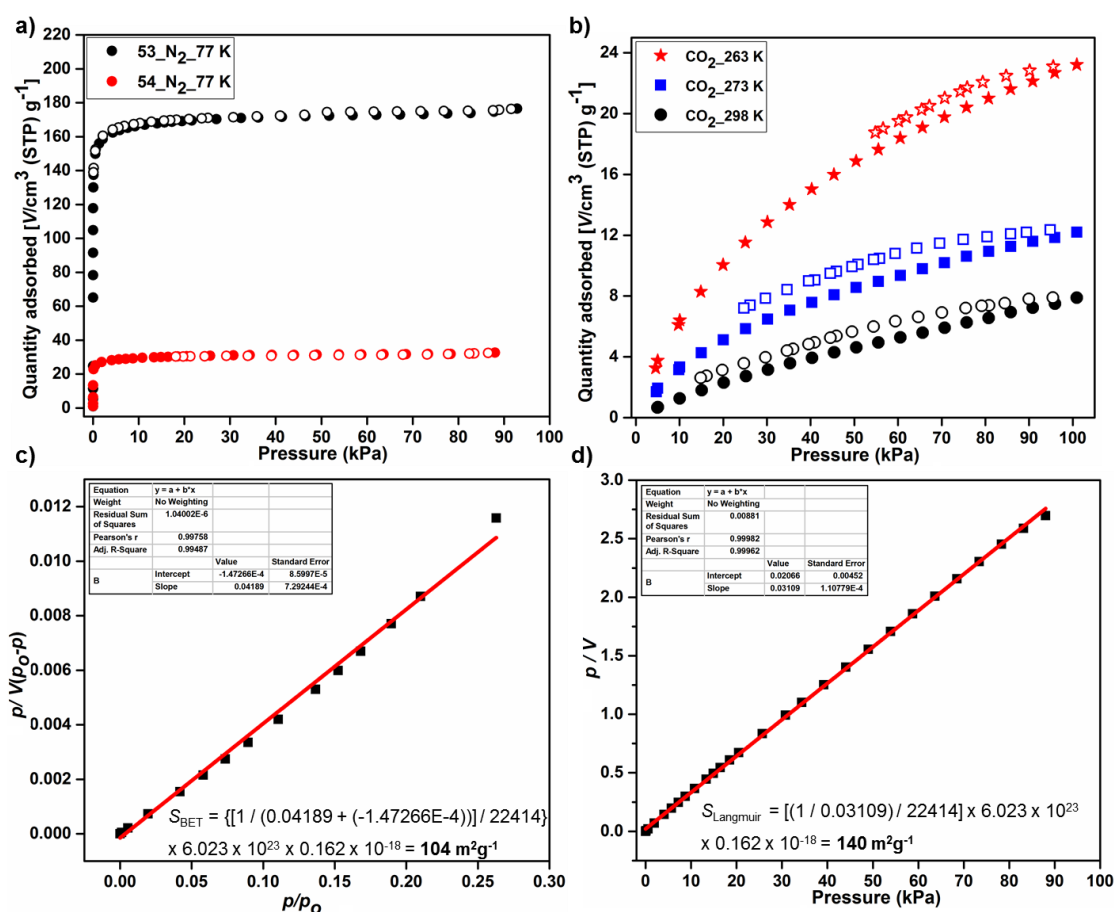


Figure 3.127. (a) Comparison of N_2 sorption isotherms for **53** and **54**, (b) CO_2 sorption isotherms for **54** at different temperatures and (c and d) BET and Langmuir surface area obtained from the N_2 adsorption isotherm for **54**.

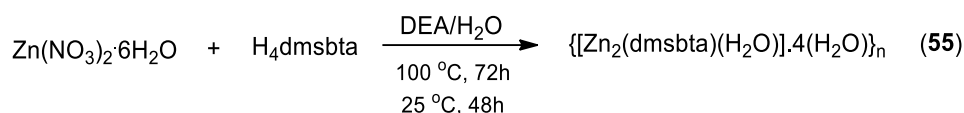
The low surface area and comparatively very less gas uptake in **54**, clearly illustrate the effect of coordination site shifting into the ligand structure. Due to the respective positions of the nitrogen donor sites in the ligands 4-tpom and 3-tpom, the ligands act as a 4-connected tetrahedral and almost planar building blocks, respectively. This accounts for the formation of a doubly interpenetrated porous diamondoid framework in **53** whereas a non-interpenetrated but less porous 3D framework in case of **54**.

3.4 CHEMISTRY WITH TRIAZOLE FUNCTIONALIZED TETRACARBOXYLATES

Aiming at CO₂ capture into the porous coordination polymers, current efforts are largely devoted to enhance the CO₂ binding affinity in such coordination polymers either by the incorporation of open metal or by the pore functionalization with polar functional groups such as –NO₂, –NH₂, –OH, –COOH, –CONH–, –SO₃H, –F, and –CF₃ etc. In addition, the introduction of additional N-donors and open metal sites into the framework is also known to enhance the CO₂ capture capacity and selectivity into such functionalized coordination polymers than the un-functionalized ones. The introduction of functional groups usually adds to the cost of available void volume as the functional groups may lead to some occupancy of space in pores. But while considering selective CO₂ capture/separation from other gases, like CO₂/N₂ (post-combustion), CO₂/H₂ (pre-combustion), CO₂/O₂ (air separation), and CO₂/CH₄ (natural gas purification), it has been found that high porosity of the framework is not a prerequisite. Instead, several factors like (a) suitable pore sizes for their size-exclusive effects, (b) functional sites and (c) parameters of gases like kinetic diameters and their electric properties (quadrupole moment and polarization) are even much more important. In this respect various Nitrogen rich MOFs containing triazolate and tetrazolate functionalized ligands have been synthesized, but the high affinity of these ligands towards the metal ions limits the no. of open donor sites responsible for CO₂ enhancement during adsorption process. There are only few examples of triazole functionalized porous coordination polymers where all the donor sites are available for interaction with the CO₂ molecules.

Based on the considerations and with the aim of incorporating accessible nitrogen-donor Lewis-basic sites into the polymeric architectures, 1,2,3-triazole functionalized tetracarboxylic acid ligands (**H₄dmsbta** and **H₄tpstba**) were synthesized via versatile click chemistry in good yields and utilized for the fabrication of coordination polymers with pore walls functionalized by nitrogen atoms of the triazole functional groups. As expected, the reaction of **H₄dmsbta** with zinc(II) nitrate under solvothermal conditions resulted in a thermally robust framework, {[Zn₂(dmsbta)(H₂O)]·4H₂O}_n (**55**) (Scheme 3.28) with Zn₄ cluster secondary building units (SBUs), having high density of exposed Lewis-acid metal sites and nitrogen-donor Lewis-basic sites accessible for the guest molecules. The compound has been structurally characterized by single crystal X-ray diffraction analysis and the molecular formula has been established by a combination of elemental analysis, thermogravimetric and single crystal analysis.

Scheme 3.28. Synthesis of **55**



Single crystal structure analysis. Single-crystal X-ray diffraction analysis reveals that **55** crystallizes in a monoclinic crystal system, with $P2_1/n$ space group (No. 14). As shown in Figure 3.128, the framework is assembled using the Zn_4 cluster secondary building units (SBUs) and organic ligands dmsbta^{4-} , which can be considered as 8-c node and as a pair of 3-c nodes, respectively. The asymmetric unit contains two crystallographically independent Zn(II) atoms, one dmsbta^{4-} ligand and five water molecules, one of which is coordinated to Zn2 atom and other four occupies the lattice positions.

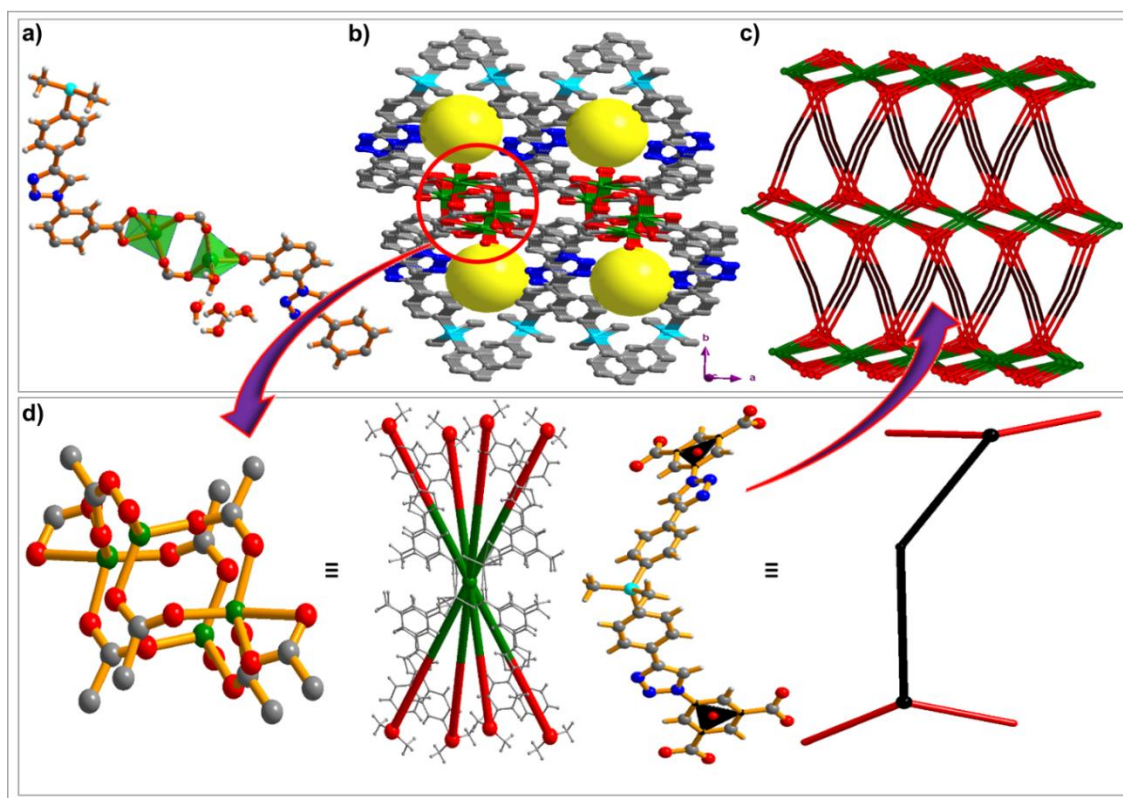


Figure 3.128. Structure description for **55**; (a) coordination environment around the metal centers, (b) perspective view of the 3D framework with open channels, (c) simplified node and linker type representation exhibiting a 3,8-connected 2-nodal : cut; sqc517 topology where (d) tetranuclear $\text{Zn}_4(\text{COO})_6$ cluster and organic ligand dmsbta^{4-} have been shown as an eight connected node and a pair of 3-connected node, respectively.

The metal centers, Zn1 is in distorted square pyramidal environment whereas the Zn2 is in a tetrahedral coordination environment. The coordination sites around Zn1 are occupied by five oxygen atoms from carboxyl groups of four different dmsbta^{4-} ligands and coordination sites around Zn2 are occupied by three carboxyl oxygen atoms from three

different **dmsbta**⁴⁻ ligands and one oxygen atom from coordinated water molecule (Figure 3.128a). The two metal centers are bridged by the carboxylate groups in the form of a Zn₄(COO)₆ cluster which can be considered as an eight connected SBU. Further the eight connected SBU is expanded by the full span of the carboxylate linker **dmsbta**⁴⁻ (a pair of 3-connected node) (Figure 3.128d) to form a 3D framework with open channels. The simplified node and linker type representation reveal that the framework exhibits a 3,8-connected 2-nodal: cut; sqc517 (epinet.ttd) topology with point symbol {4.6²}₄{4¹².6⁴.8¹²} as determined by the TOPOS program.²⁷⁴ The τ parameter,²⁷⁶ which is an indicator for the deviation from the ideal square-pyramidal ($\tau = 0$) and trigonal bipyramidal ($\tau = 1$) geometries for five coordinate metal centers, is found to be 0.2 for Zn1. The framework consists of open channels along the c-axis (Figure 3.128b), with an approximate diameter of 8.7 X 6.1 Å² along the c axis (regardless of the van der Waals radii). The total solvent-accessible volume for **55** was estimated to be 18% (692/3706 Å³ per unit cell volume) using PLATON software.²⁷⁵ The average Zn-O distance is found to be 1.962 Å, which is in the usual range for this kind of complexes. The prominent distortions from the regular square pyramidal and tetrahedral geometries around Zn1 and Zn2 are evident from the cisoid angles in the range of [56.07°-111.99°] for Zn1 and [97.28°-121.21°] for Zn2. All the crystallographic information pertaining to data collection and structure refinement parameters, selected bond lengths and bond angles for **55** are listed in Table A22, A44 and A66, respectively.

FTIR and PXRD analysis. FTIR spectra for **55** was recorded in the solid state at room temperature as KBr pellets. A broad band between 3400 – 3440 cm⁻¹ in the FTIR spectrum of **55** indicates the existence of coordinated and lattice water molecules, whereas the sharp peaks in the range of 1380–1630 cm⁻¹ can be assigned due to the asymmetric and symmetric stretching of the carboxylates coordinated to the metal centers. The $\Delta\nu$ ($\Delta\nu = \Delta\nu_{\text{asym}} - \nu_{\text{sym}}$) values of 209 cm⁻¹ and 180 cm⁻¹ indicates the monodentate and chelated bidentate binding of the carboxylates to the metal centers, respectively.²⁵¹ Further, the prominent shifts from the asymmetric and symmetric -C=O stretch for free **H₄dmsbta** (1722 cm⁻¹ and 1463 cm⁻¹) indicates a strong binding of the carboxylates to the metal center. The phase purity of the as-synthesized compound was established with the help of powder X-ray diffraction analysis. As shown in Figure 3.129a, the experimentally obtained powder patterns for as-synthesized compound was in good agreement with the simulated powder patterns (obtained

from the single crystal data), which confirms the crystallinity and phase purity of the as-synthesized sample of **55**.

Framework stabilities and thermal properties. The thermal stability and structural variation as a function of temperature for **55** was studied by their thermogravimetric analysis (TGA). Single phase polycrystalline samples of **55** was heated between 30-500 °C, under a dinitrogen atmosphere and corresponding weight loss was plotted with respect to temperature. As shown in Figure 3.129b, the as-synthesized samples **55** exhibits a weight loss of ~7% in the temperature range 50-150 °C followed by ~2% weight loss in the temperature range 180-250 °C, which can be ascribed to the loss of four lattice water (8%) and one coordinated water (2.2%) molecules, respectively. No further weight loss was observed until 325 °C, before the framework degradation, indicating very good thermal stability up to 325 °C. The robustness and thermal stability of **55** was further checked by in-situ variable temperature powder X-ray diffraction (VT-PXRD) (Figure 3.129c). In addition to the thermal stability, the chemical stability of **55** was also tested towards various solvents by powder X-ray diffraction analysis. It was found that the PXRD pattern of the compound remains the same after soaking in various solvents, which reflects the stability of **55** towards these solvents (Figure 3.129d).

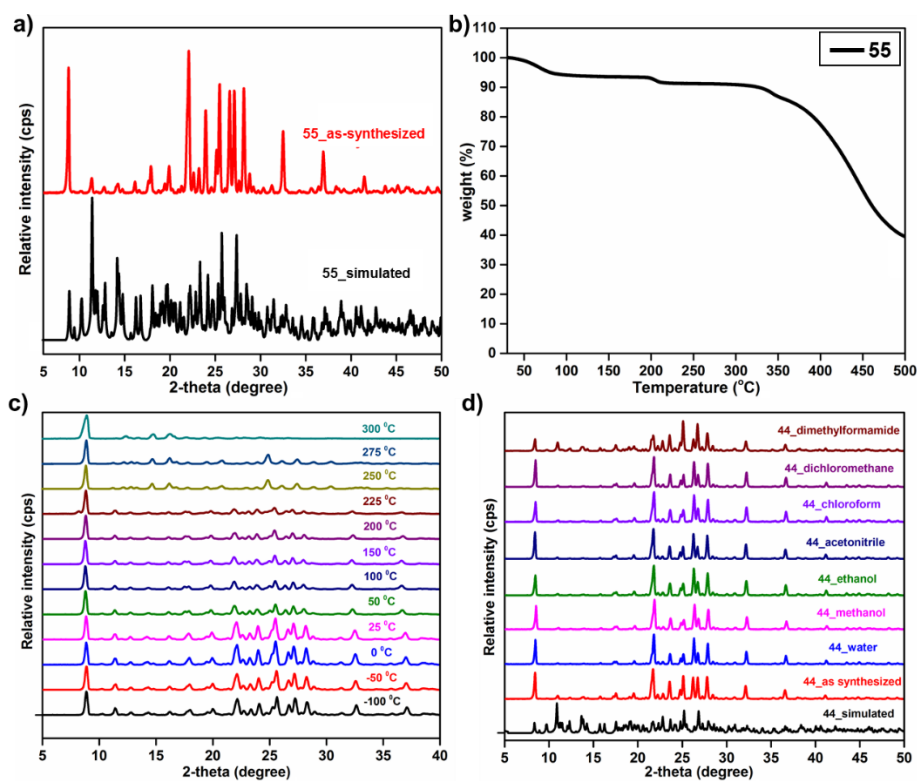


Figure 3.129. (a) Powder X-ray diffraction pattern of the as-synthesized samples of **55** compared with the simulated powder patterns and (b) thermogravimetric profiles for **55**, (c) temperature dependent powder X-ray diffraction and (d) PXRD pattern of **55** after soaking in different solvents.

Gas sorption studies. The establishment of permanent porosity in **1** was evaluated through N₂ adsorption isotherm at 77 K. The as-synthesized sample of **55** (~100 mg) was activated by degassing at an elevated temperature of 393 K under vacuum conditions (20 mTorr) for 24 hours, prior to any sorption experiment. Interesting enough that **55** takes similar amount of N₂ and CO₂ at low temperatures (N₂ at 77 K and CO₂ at 195 K). The Brunauer–Emmett–Teller (BET) and Langmuir surface area was estimated to be 314 m²g⁻¹ and 447 m²g⁻¹, respectively. The properly oriented accessible N-donor sites towards the pores and high CO₂ uptake by **55** at low temperature, inspired us to explore the potential of **55** for CO₂ capture and separation from a gas mixture under ambient conditions. Single component CO₂ sorption isotherm was measured at different temperatures (298 - 263 K) under 1 bar pressure. As shown in (Figure 3.130a), **55** takes up moderate amount of carbon dioxide (41.7 cm³g⁻¹), (46.6 cm³g⁻¹), (49.5 cm³g⁻¹), and (52.3 cm³g⁻¹) at 298 K, 283 K, 273 K and 263 K, respectively. The quantitative binding strengths of CO₂ molecules with the framework was calculated based on the virial method, a well-established and reliable methodology from fits of their adsorption isotherms at different temperatures. For the estimation of Q_{st} by virial method, a virial-type expression consisting of the temperature dependent virial parameters (vide supra) were employed to calculate the enthalpy of absorption for CO₂. The Q_{st} value of **55** at zero coverage was 32.5 kJmol⁻¹, which is higher than the values for M' MOF-20 (28.4 kJmol⁻¹), {Cd₂(L)(2,6-NDC)₂}_n (28.1 kJmol⁻¹), {Cu(bcppm)H₂O}_n and JUC-199 (29 kJmol⁻¹), MIL-53(Cr) and Hpip@ZnPC-2 (32 kJmol⁻¹), UMCM-1 (12 kJmol⁻¹), MOF-5 (17 kJmol⁻¹), CuBTTri (21 kJmol⁻¹), IITKGP-5 (22.6 kJmol⁻¹), IITKGP-6 (23 kJmol⁻¹) and NOTT-40 (25 kJmol⁻¹) but is lower than the extra high values of 60 kJmol⁻¹ for MIL-10035 and 90 kJmol⁻¹ for HCu-[(Cu₄Cl)₃(BTTri)₈(en)₅] (Table A67).

Since **55** takes up very less N₂ and CH₄ compared to CO₂ (Figure 3.130b), the gas mixture selectivity was studied for CO₂-N₂ and CO₂-CH₄ mixture at a general feed composition of flue gas (CO₂/N₂ = 15:85) and landfill gas (CO₂/CH₄ = 50:50) with pressure up to 1 bar, by applying well-known ideal adsorbed solution theory (IAST) developed by Myers and Prausnitz for binary mixtures.³¹⁶ Mixture adsorption isotherms and adsorption selectivities at 298 K and up to 1 bar pressures calculated by IAST (based on the single site Langmuir-Freundlich model) for mixed CO₂/N₂ and CO₂/CH₄ in **55** as a function of total bulk pressure are shown in Figure 3.130c and d. The results indicate that under 1 bar pressure the selectivity values for CO₂/N₂ (161.5) and CO₂/CH₄ (29.4) are much higher than the values reported for some well-known examples (Table A68). The highly selective CO₂ capture

further suggests the positive effect of dual functionalities into the framework. The applicability of **55** for selective CO₂ capture was further studied by recycling experiments; it was found that even after 3 cycles, it still maintains about 100% adsorption capacity.

Grand Canonical Monte Carlo Simulations. The highly selective and efficient CO₂ capture performance of **55** under ambient conditions has motivated us to examine the accurate interactions between the framework and CO₂ molecules. To understand the sorption behaviour of **55**, Grand Canonical Monte Carlo (GCMC) simulations have been implemented using Material Studio program. As shown in Figure 3.131, the CO₂ molecules

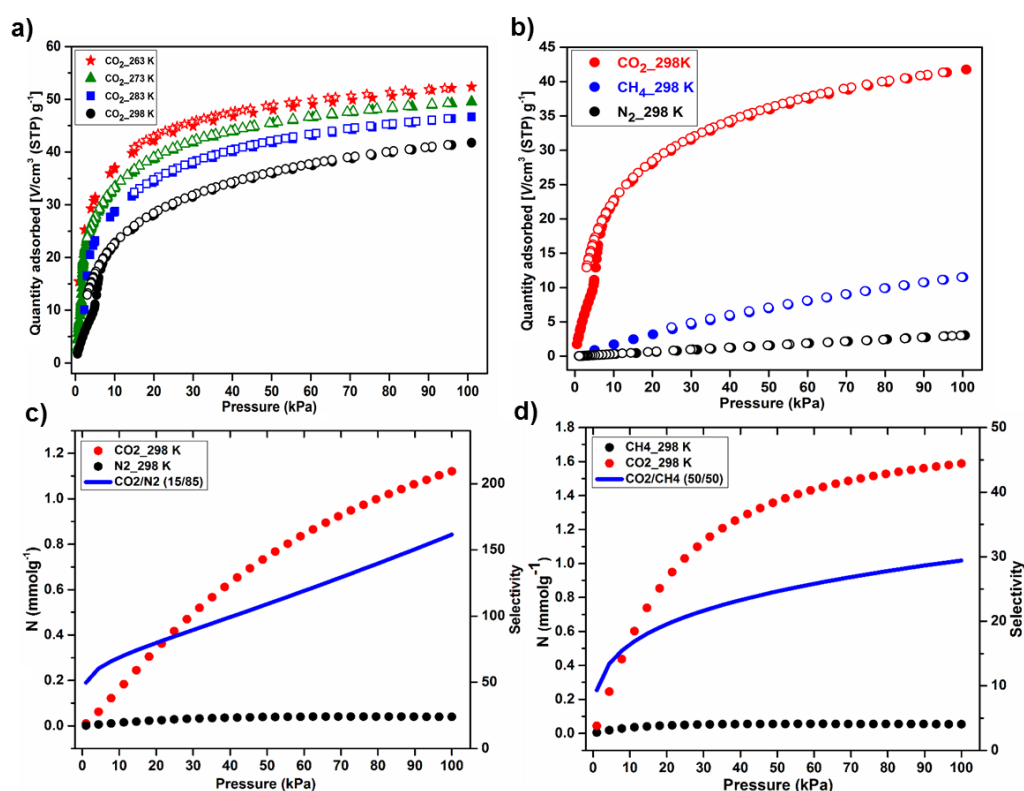


Figure 3.130. (a) CO₂ sorption isotherms for **55** collected at different temperatures, (b) comparison of CO₂ sorption isotherm with that of N₂ and CH₄ and (c and d) Binary mixture adsorption isotherms and selectivities for CO₂/N₂ (15/85) mixture and CO₂/CH₄ (50/50) mixtures, respectively at 298 K.

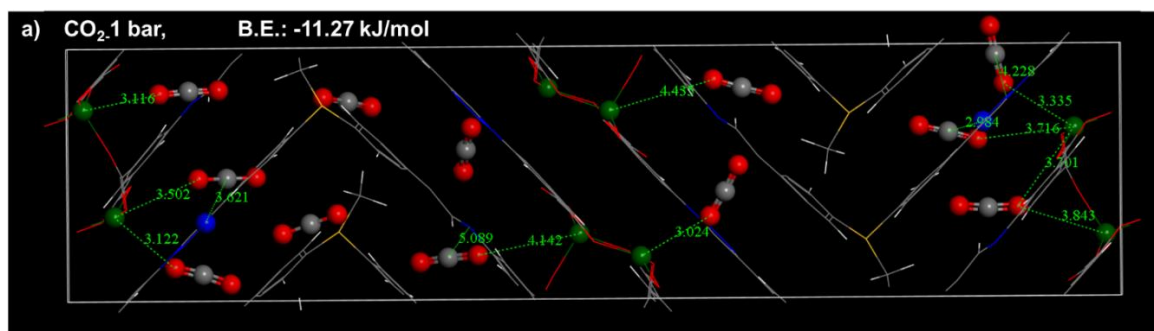


Figure 3.131. The snapshot of CO₂ adsorption for **55** at 1 bar and 298 K, calculated using GCMC method. The green dashed line represents the interaction between the CO₂ molecule and the preferential binding sites into the framework. Color codes: blue, N; gray, C; red, O; green, Zn.

prefer to coordinate with open Zn(II) sites through Zn-O interaction. Also the uncoordinated nitrogen atoms of the triazole group interact as Lewis base with the CO₂ molecules. The shortest Zn...O_{CO2} separation of 3.024 Å is very close to the sum of van der Waals radii of Zn (1.39 Å) and O (1.52 Å) atoms, whereas the shortest N...C_{CO2} separation of 2.984 Å is significantly shorter than the sum of van der Waals radii of N (1.55 Å) and C (1.7 Å) atoms, indicating strong interactions of the CO₂ molecules with the framework.

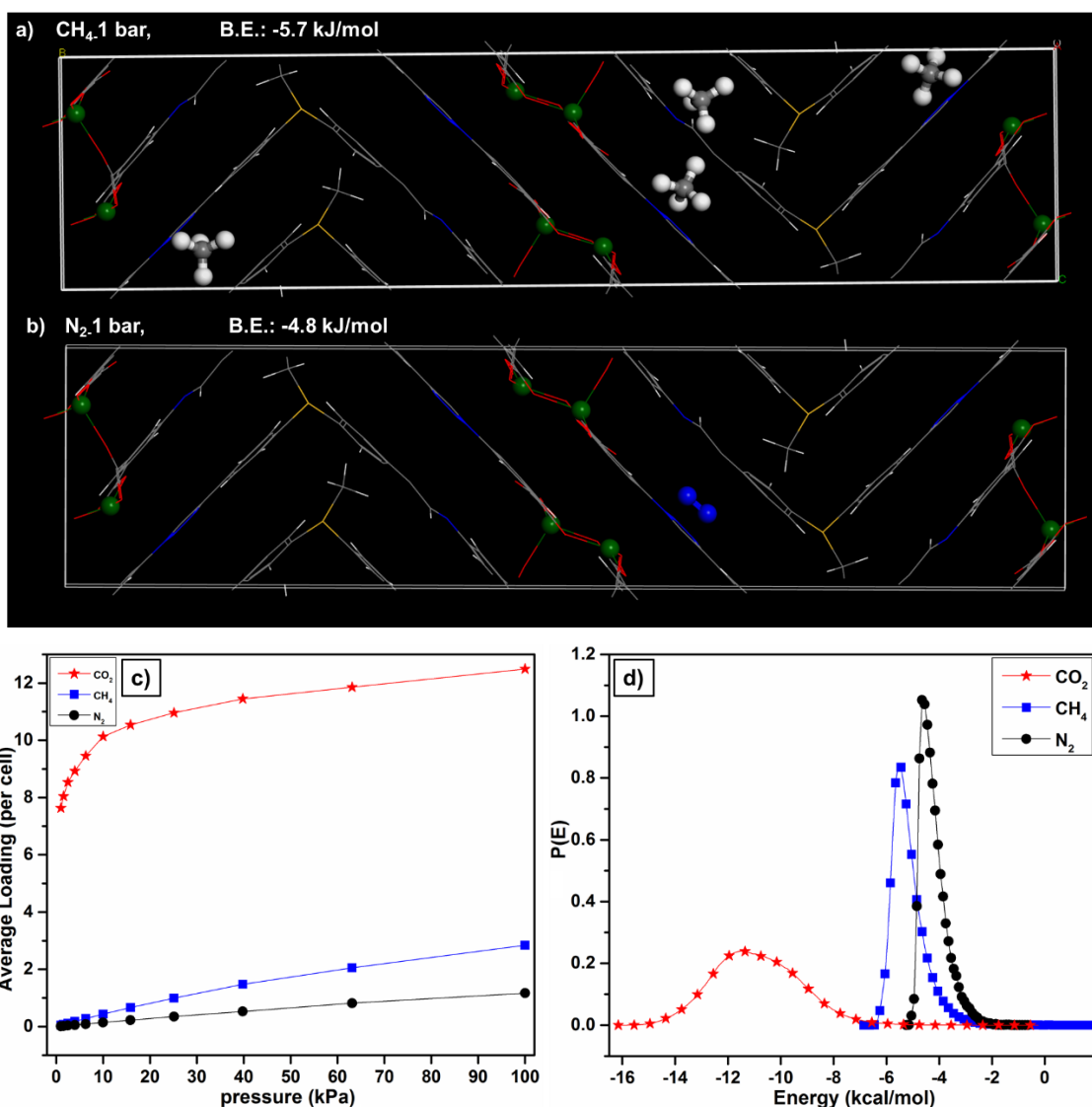


Figure 3.132. The snapshot of (a) CH₄ and (b) N₂ adsorption for **55** at 1 bar and 298 K, calculated using GCMC method. Color codes: blue, N; gray, C; red, O; white, H; green, Zn, (c) simulated adsorption isotherms for CO₂, CH₄ and N₂ on **55** at 298 K and 1 bar and (d) energy histogram for **55** in presence of CO₂, CH₄ and N₂.

From the simulation experiments, it is also evident that **55** takes up comparatively high CO₂ than N₂ and CH₄ (Figure 3.132), which is in accordance with the experimental results. Further, the very strong interaction of the CO₂ with the framework was established by evaluating the binding energies of CO₂ (-11.27 kJ/mol), N₂ (-4.8 kJ/mol) and CH₄ (-

5.7kJ/mol) (Figure 3.132). Moreover, the GCMC simulation was also accomplished for binary CO₂/N₂ (1:1) and CO₂/CH₄ (1:1) mixtures at 298 K and 1 bar pressure. As shown in Figure 3.133, the highly selective CO₂ uptake in the framework over N₂ and CH₄ in the mixed gas compositions further corroborates to the IAST selectivity obtained from the experimental adsorption isotherms.

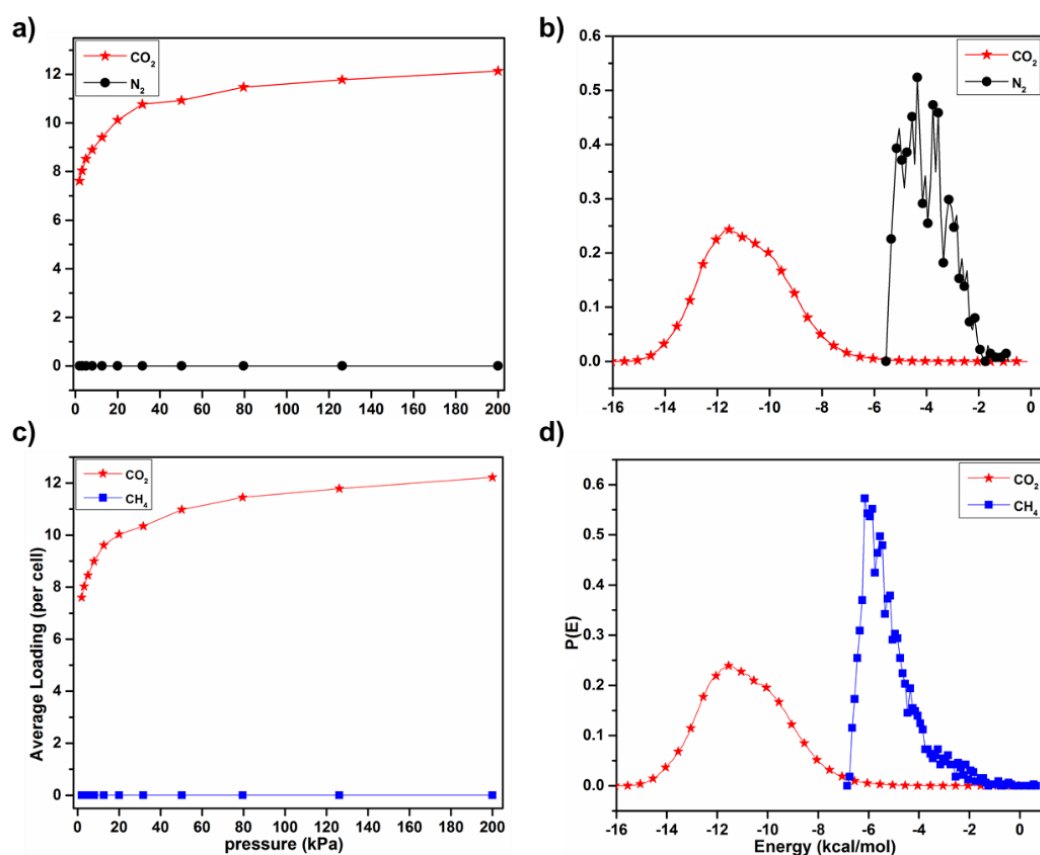


Figure 3.133 Simulated adsorption isotherms for (a) CO₂/N₂ (50/50) and (c) CO₂/CH₄ (50/50) binary mixtures at 298 K and their energy histograms (b and d, respectively).

In addition to the selective CO₂ capture, another attractive means of effective CO₂ elimination is the direct chemical conversion of CO₂ into value added chemicals (e.g. dimethyl carbonates, cyclic carbonates, N,N'-disubstituted ureas or formic acid). Therefore, after establishment of permanent porosity, chemical stability and highly selective CO₂ capture, the existence of high density of Lewis-acid metal sites was further examined for the catalytic activity of **55**, towards chemical conversion of CO₂ to cyclic carbonates. Although several MOFs as heterogeneous catalysts for chemical conversion of CO₂ into cyclic carbonates have been demonstrated but under the conditions of high pressure and high temperature.^{193,197,199,304,307} Together with significant uptake and limited reports for chemical conversion of CO₂ into cyclic carbonates at ambient conditions,^{183,192,200} the

catalytic activity of **55** for this conversion was explored under mild conditions (30-40 °C and 1 atm. pressure). Epichlorohydrin was taken as a standard substrate with **55** as a catalyst in conjunction with tetra-*n*-tert-butyl ammonium bromide (TBAB) as a co-catalyst. The progress of the reaction was monitored by ¹H NMR experiments; a complete conversion (>99%) was obtained over 24 h, which indicates excellent catalytic activity of **55**. The catalytic activity is much higher than the previously reported MOF materials. Furthermore, the catalytic performance of **55** was also examined for different functional group substituted epoxides under the same conditions. The results are summarized in Table 3.13.

Table 3.13. Cyclic carbonates obtained from the reaction of epoxides with CO₂, catalysed by **55**^a

Entry	Catalyst	R	Conversion ^b (%)	TON ^c
1	55	-CH ₂ Cl	10	20
2	TBAB	-CH ₂ Cl	30	60
3	55 , TBAB	-CH ₂ Cl	>99	200
4	55 , TBAB	-CH ₃	>99	200
5	55 , TBAB	-CH ₂ CH ₃	>99	200
6	55 , TBAB	-CH ₂ CH ₂ CH ₂ CH ₃	84.7	169.4
7	55 , TBAB	-CH ₂ OCH ₂ CHCH ₂	78.7	157.4
8	55 , TBAB	-CH ₂ OCH ₂ CH ₂ CH ₂ CH ₃	71.4	142.8
9	55 , TBAB	-Ph	67.6	135.2
10	55 , TBAB	-CH ₂ OPh	50.2	100.4

^aReaction conditions: epoxide (5 mmol), catalyst **55** (0.5 mol%), TBAB (1 mol%), reaction time 24 h and temperature 30-40 °C. ^bAverage conversion for a set of triplicate experiments calculated by ¹H NMR experiment. ^cTON is the turnover number (No. of moles of product per mole of the catalyst).

The high catalytic activity of **55** was also obtained for the larger-sized 1,2-epoxyhexane substrate with a conversion of 84.7% (Table 3.13, entry 6); but the efficiency drops dramatically for the bigger bulky styrene oxide and phenyl glycidyl ether (Table 3.13, entry 9 and 10). This is perhaps due to, on the one hand, the limited diffusion of bulky epoxide substrates into the channels of **1a** and, on the other hand, the low reactivity at the β-carbon atom of large size substrates. The recyclability of **55**, was assessed by taking the cycloaddition of CO₂ with epichlorohydrin as an example. After each catalytic run, it was separated, washed with DCM, dried under vacuum and reused for five consecutive experiments. A very little drop (8-10%) in the catalytic activity was observed even after five catalytic cycles (Figure 3.134a). Based on PXRD data of the catalyst recorded before and after five cycles, no loss of crystallinity or phase purity of the catalyst was observed

(Figure 3.134b). The hot filtration test reflects the requisite role of **55** as a heterogeneous catalyst (Figure 3.134c).

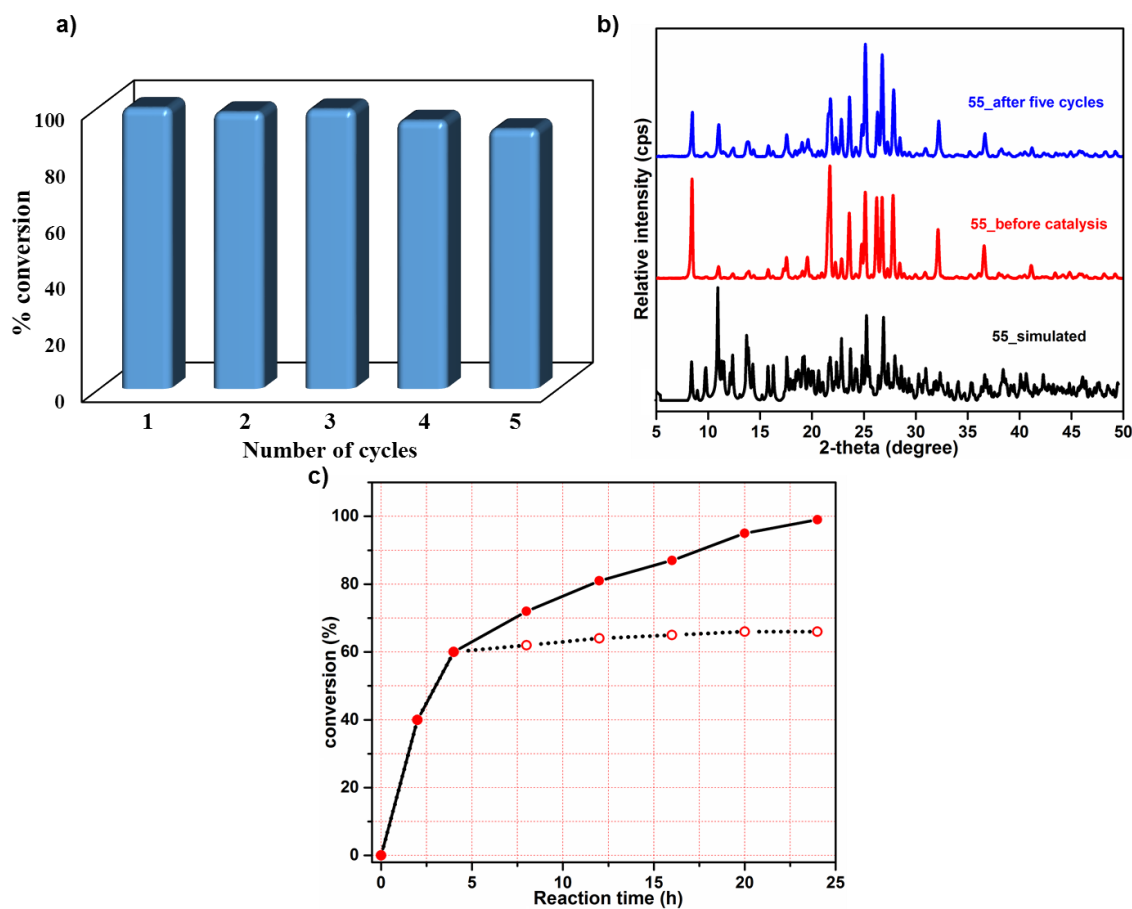


Figure 3.134. (a) conversion for five consecutive cycles for the cycloaddition reaction of CO₂ with epichlorohydrin, catalyzed by **55**, (b) PXRD pattern of **55** before and after catalysis experiments and of (c) progress of the reaction with time in presence of catalyst (solid lines) and after separating the catalyst from the reaction mixture (dotted lines) for cycloaddition reaction of CO₂ with epichlorohydrin.

Based on the studies described above, a possible mechanism for cycloaddition of CO₂ with epoxides is presented in Figure 3.135. First, epoxides are activated by the Lewis-acid metal sites, when O atom of epoxide interacts with the Lewis-acid metal site. Second, the less-hindered C atoms of the epoxides are attacked by Br⁻ nucleophiles from TBAB to open the epoxy ring. Finally, the opened epoxy ring adds up with CO₂ to produce the cycloaddition product. The mechanism can be further supported by GCMC simulations (Figure 3.136).

Therefore **55** presents a dual functionalized Zn (II) organic framework with exposed Lewis-acid metal sites and accessible nitrogen-donor Lewis basic sites which exhibits highly selective CO₂ capture and its chemical conversion under ambient conditions. The GCMC simulations further supports the contributions of dual active sites for preferential strong interactions with the CO₂ as well as epoxide molecules.

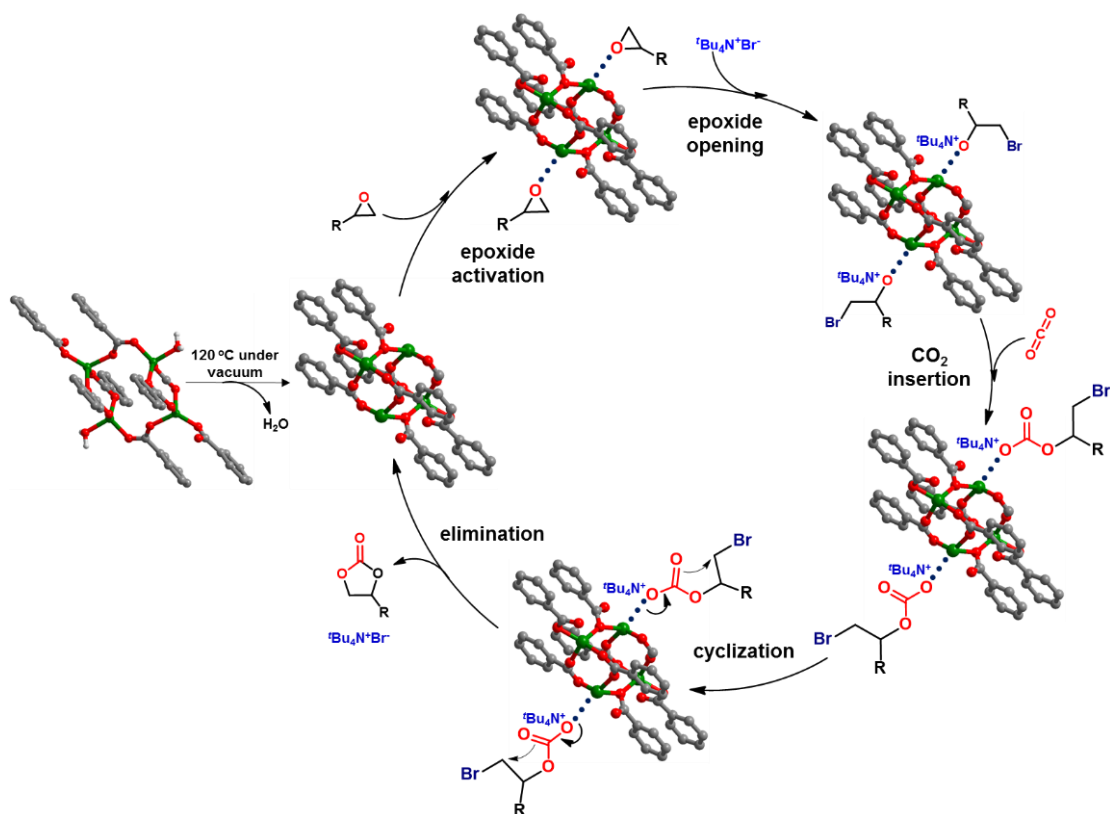


Figure 3.135. Plausible mechanism for the cycloaddition reactions of CO₂ with epoxides catalyzed by **55**.

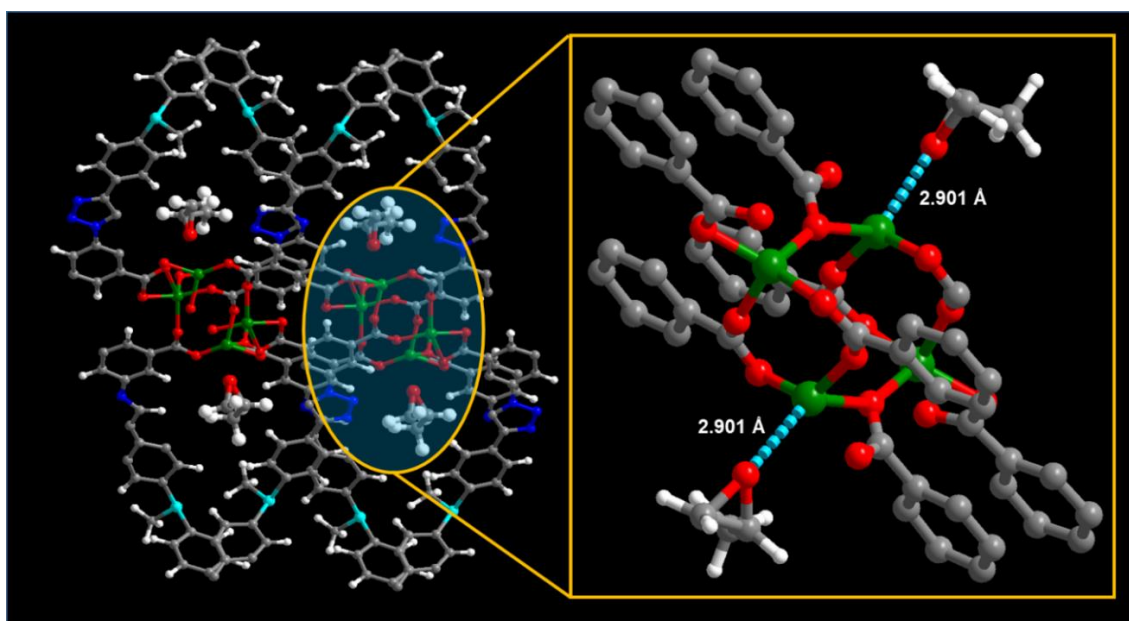
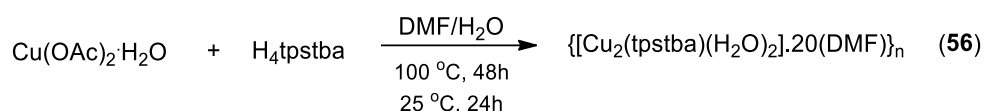


Figure 3.136. Propylene oxide position in **55** generated from GCMC simulation using locate method.

The very high CO₂ capture capacity and selectivity followed by very good thermal stability and catalytic activity towards cycloaddition of carbon dioxide to cyclic carbonates has motivated us to design such triazole functionalized porous coordination polymers with open

metal sites. For this purpose, we have designed another triazole functionalized tetracarboxylic acid (**H₄tpstba**) and used it in combination with Cu(II), which is known to form dimetallic paddle wheel clusters as SBUs, where the axial positions of the paddle wheel SBUs are generally occupied by the coordinating solvent molecules. These coordinating solvents can be removed to generate catalytically active metal centers into the resulting framework structures. As per our expectations, the solvothermal reaction of H₄tpstba with copper acetate has resulted in the construction of a highly interpenetrated 3D porous framework with Cu₂(COO)₄ dimetallic paddle wheel core as SBU (Scheme 3.29). The compound has been structurally characterized by single crystal X-ray diffraction analysis and the molecular formula has been established by a combination of elemental analysis, thermogravimetric and single crystal analysis.

Scheme 3.29. Synthesis of **56**



Single crystal structure analysis. Single crystals suitable for X-ray diffraction analysis were obtained by the solvothermal reaction at 100 °C for 48h in a solvent mixture of 1:1 DMF and water. It crystallizes in a tetragonal crystal system with *P4₂/n* space group and forms an eight-fold interpenetrated 3D framework. The asymmetric unit contains two Cu(II) ions, one tpsbta⁴⁻ and two water molecules coordinated to the metal centers.

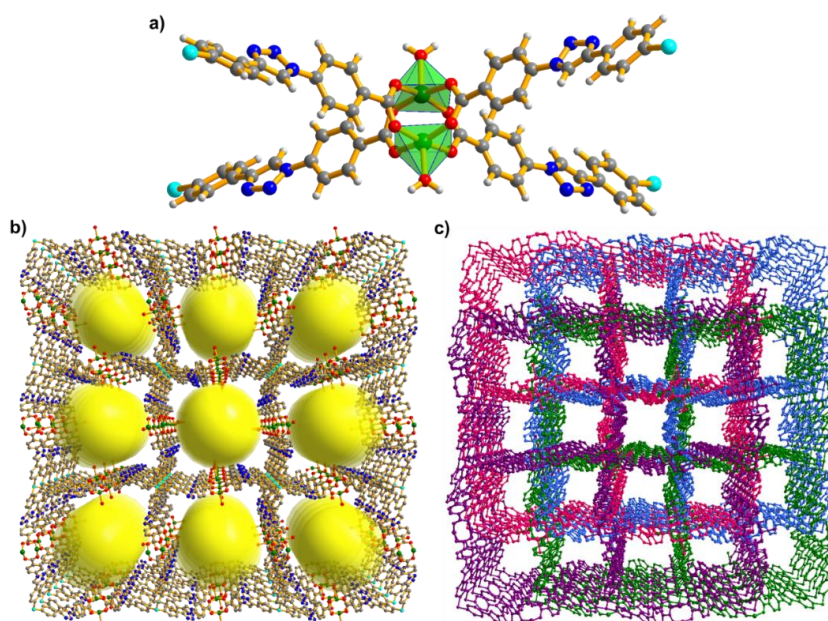


Figure 3.137. Structure description of **56**; (a) coordination environment around the metal center, (b) perspective view of the 3D framework with open channels and (c) fourfold interpenetration into the framework.

The coordination environment around each metal center is distorted square pyramidal, where the five coordination sites are occupied by four oxygen atoms from the carboxylate group of four different tpsbta⁴⁻ at equatorial positions and the axial position is occupied by the oxygen atom of the coordinated water molecule (Figure 3.137a). Each carboxylate group is coordinated to the metal centers in a bridging monodentate fashion resulting in the formation of a Cu₂(COO)₄ paddle wheel dimetallic core as secondary building unit. The carboxylate linker tpsbta⁴⁻ is fully deprotonated and structure is expanded by the full span of tetrahedral linker to form a 3D network with open channels with dimensions 31.6 × 31.6 Å² (27.4 × 27.4 Å² without van der Waals radii) (Figure 3.137b), which are filled with highly disordered DMF molecules. The diffused electron density due to the highly disordered solvent molecules was squeezed out using the solvent mask option in Olex2 software,²⁰³ during the refinement of the structure. The channel size is further reduced to 17.8 × 17.8 Å² (13.6 × 13.6 Å² without van der Waals radii) due to fourfold interpenetration into the framework (Figure 3.137c). The total potential solvent-accessible void volume for **56** was estimated to be 62% (14567/23362 Å³ per unit cell volume) using PLATON software.²⁷⁵

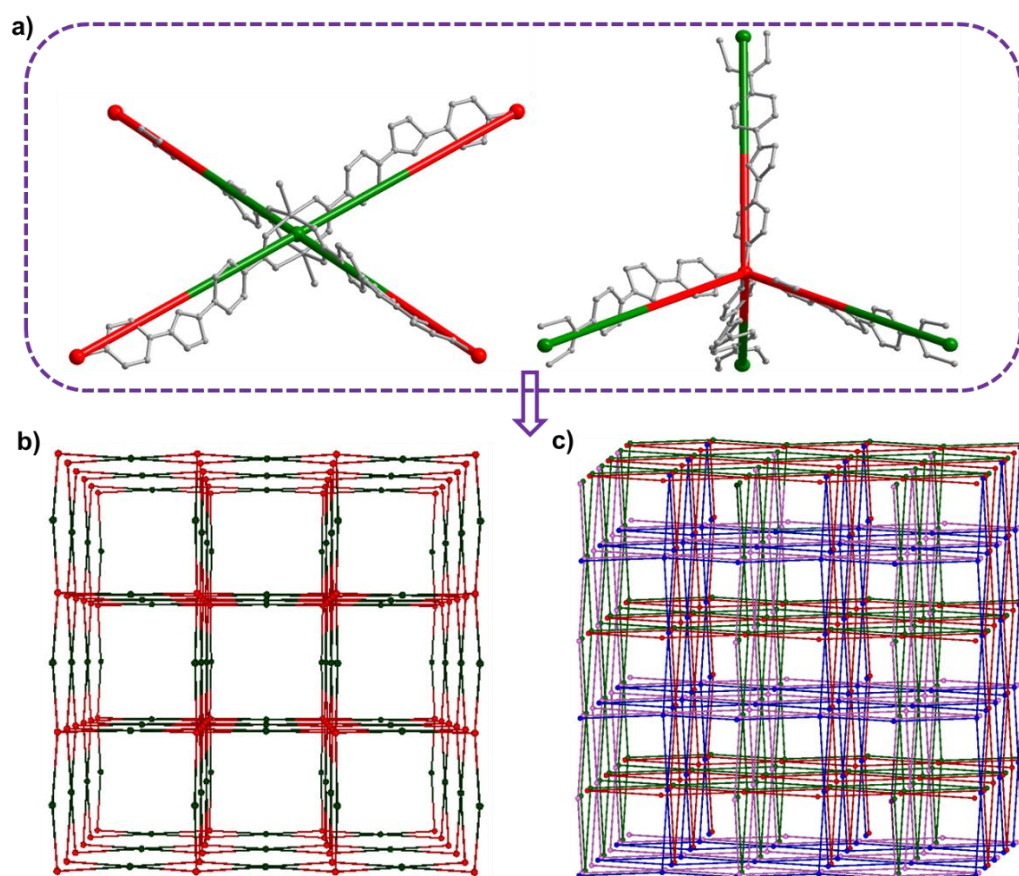


Figure 3.138. Simplified node and linker type representation for **56**; (a) paddle wheel SBU and the ligand H₄tpstba shown as 4-connected nodes and overall 4,4-connected 2-nodal PtS topology (b) without interpenetration and (c) with fourfold interpenetration.

The structure can be simplified in the form of node and linker type representation, where the paddle wheel SBU can be considered as a planar 4-connected node and the ligand tpsbta⁴⁻ as a tetrahedral 4-connected node (Figure 3.138a). Further examination of the node and linker type representation reveal that the framework exhibits a 4,4-connected 2-nodal : PtS, Cooperite; sqc183 (topos&RCSR.ttd) topology with point symbol {4².8⁴} as determined by the TOPOS program (Figure 3.138b and c).²⁷⁴

The average Cu-O bond length 1.994 Å, in **56**, is in the usual range for this kind of complexes. The prominent distortions from the regular square pyramidal geometries around Cu1 and Cu2 are evident from the bond angle value around the metal centers. All the crystallographic information pertaining to data collection and structure refinement parameters, selected bond lengths and bond angles for **56** are listed in Table A22, A44 and A66, respectively. The DMF molecules present in the crystal lattice are highly disordered and could not be modelled. The diffused electron density due to the disordered DMF molecules was squeezed out during structure refinement and number of solvent molecules was calculated based on the electron counts squeezed out.

Calculation of determining solvent molecules squeezed out:

Number of electrons squeezed out (N: Electron Count / Cell) = 6556 - To be included in D(calc), F000 & Mol.Wght.

$$Z = 8$$

Therefore number of electron per formula unit = 6556/8 = 819

Number of electrons in (20 DMF) molecule = (40 x 20) = 800; this is in good agreement with the number of electrons squeezed out (819).

FTIR and PXRD analysis. FTIR spectrum for **56** was recorded in the solid state at room temperature as KBr pellets. A broad band in the range of 3350 – 3400 cm⁻¹ indicates the presence of coordinated water molecules, whereas the sharp peaks at 1604 cm⁻¹ and 1406 cm⁻¹ can be assigned due to the asymmetric and symmetric stretching of the carboxylates coordinated to the metal centers. The Δν values of 198 cm⁻¹ indicates that the carboxylates are coordinated to the metal center in a bridging monodentate fashion.²⁵¹ Further, the prominent shifts from the asymmetric and symmetric -C=O stretch for free **H4dmsbta** (1722 cm⁻¹ and 1463 cm⁻¹) indicates a strong binding of the carboxylates to the metal center. The phase purity of the as-synthesized compound was established with the help of powder X-ray diffraction analysis. As shown in Figure 3.139a, the experimentally obtained powder patterns for as-synthesized compound was in good agreement with the simulated powder

patterns (obtained from the single crystal data), which confirms the crystallinity and phase purity of the as-synthesized sample of **56**.

Framework stabilities and thermal properties. The thermal stability and structural variation as a function of temperature for **56** was studied by their thermogravimetric analysis (TGA). Single phase polycrystalline samples of **56** was heated between 30-500 °C, under a dinitrogen atmosphere and corresponding weight loss was plotted with respect to temperature. As shown in Figure 3.139b, the as-synthesized samples **56** exhibits continuous weight loss up to 250 °C, which can be ascribed to the loss of lattice solvent molecules. The framework shows stability up to 250 °C, after which sudden weight loss indicates the framework degradation.

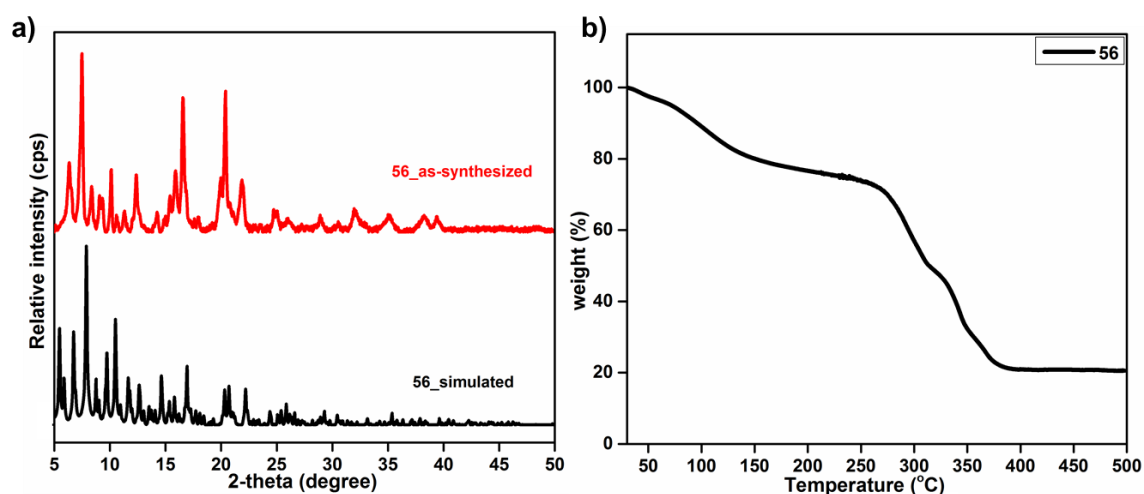


Figure 3.139. (a) Powder X-ray diffraction pattern of the as-synthesized samples of **56** compared with the simulated powder patterns and (b) thermogravimetric profiles for **56**.

Owing to the large volume of solvent accessible voids functionalized with Lewis-basic nitrogen atoms of the triazole group along with high density of open metal sites, **56** can be a potential candidate for selective carbon dioxide capture and its chemical conversion into value added chemicals.

CHAPTER IV

Conclusions

1. For a systematic combination of various polypyridyl ligands (tridentate, *bis*-tridentate, *bis*-pyridyl and tetra-pyridyl), carboxylate linkers (di-, tri- and tetracarboxylates) and divalent metal ions, a set of over sixty coordination architectures with varied dimensionalities (0D, 1D, 2D and 3D) have been synthesized and well characterized by a combination of different analytical techniques. In most of the cases, the compounds have been structurally characterized by single crystal X-ray diffraction analysis and bulk phase purity of the as-synthesized compounds have been established by powder X-ray diffraction analysis.
2. A new strategy has been developed for the coordination driven self-assembly of molecular squares in a [2+2+2] self-assembly process, without using the pre-synthesized precursors. The self-assembly of M(II) acetates with a tridentate capping ligand and a bent dicarboxylate linker at ambient conditions has resulted in the formation of molecular squares in a highly selective manner. The synthetic strategy used to construct the molecular squares have been generalized with the synthesis of molecular squares with different metal ions and another bent dicarboxylate linker. Further, the presence of Lewis-acidic open metal sites along with very good thermal and chemical stability of these molecular squares has enabled their use as an efficient heterogeneous catalyst towards Lewis-acid catalysed Knoevenagel condensation reaction. On the other hand, the blue emitting nature of the cadmium analogous have been explored for the detection of nitrobenzene.
3. The chemistry of the tridentate polypyridyl capping ligands and bent dicarboxylate linkers with divalent transition metal ions have been further extended to synthesize polymeric structures through connected polygons. The structure of polypyridyl capping ligand was modified to have two capping sites, which are separated either by a flexible alkyl chain or a rigid xylyl spacer. The effect of spacer chain length and rigidity or flexibility of the xylyl or alkyl spacers on the structural diversity of the final architectures has been studied for the Mn(II) or Cd(II)-dicarboxylate systems. By varying the reaction conditions and the spacer chain length of the polypyridyl ligands, optimized reaction conditions have been presented for the isolation of both possible structural isomers.

4. By employing the well-known pillar layer strategy, a series of coordination polymers with varied dimensionalities has been synthesized for the Zn(II)-dicarboxylate system. Through strategic modifications of different neutral N-donor pillar ligands, the control over the dimensionality and structural interpenetration has been established for Zn(II) coordination polymers with a similar dinuclear ($\text{Zn}_2(\text{COO})_4$) paddle wheel core as an SBU.
5. The pillar layer strategy has been further extended for the Mn(II)-dicarboxylate system in constructing magnetically active pillared-layer frameworks. By varying the length and rigidity/flexibility of the pillar ligands, a series of Mn(II) coordination polymers with different types of dinuclear or tetranuclear cores have been synthesized in good yields. The introduction of a rigid pillar ligand bpy has resulted in the formation of a 2D robust pillared-layer framework based on the rare paddlewheel subunit $[\text{Mn}_2^{\text{II}}(\mu\text{-O}_2\text{CR})_4]$. Whereas, the introduction of relatively flexible ligands bpee or azopy has resulted in the frameworks with the paddle wheel core along with mononuclear Mn(II) center as the repeat units. Similarly, the introduction of conformationally flexible ligand bpe and longer bpy analogue, dpb, has resulted in the formation a 3D coordination polymer with ($\mu\text{-aqua}$)bis($\mu\text{-carboxylato}$)- dimanganese core $[\text{Mn}_2^{\text{II}}(\mu\text{-OH}_2)(\mu\text{-O}_2\text{CR})_2]$ and a 2D framework with carboxylato bridged tetranuclear Mn_4 cluster as an SBU, respectively. The coordination polymer with ($\mu\text{-aqua}$)bis($\mu\text{-carboxylato}$)-dimanganese core, $[\text{Mn}_2^{\text{II}}(\mu\text{-OH}_2)(\mu\text{-O}_2\text{CR})_2]$, represents a unique example because of its relevance to biological systems.
6. The effect of rigidity/flexibility of the pillar ligands has been further studied for the Co(II)-dicarboxylate system, where a set of six Co(II) coordination polymers has been synthesized with the same dinuclear paddlewheel SBU and the effect of conformational flexibility or rigidity on the dimensionality of final architectures has been presented. The use of rigid and conformationally locked pillar ligands has resulted in the formation of 2D coordination polymers, whereas the introduction of conformationally flexible ligands has resulted in the formation of 3D porous frameworks. The frameworks exhibit very good thermal stability as confirmed by their thermogravimetric analysis.
7. The structural diversity due to the coordination preferences of different metal ions has been observed for the same carboxylate linker. The self-assembly of the

dicarboxylate linker and bpe ligand with Cd(II) acetate has resulted in the formation of 1D coordination polymer. Due to the presence of open metal sites, it has been utilized as a reusable heterogeneous catalyst for the Knoevenagel condensation reaction. Further, the incorporation of an azine functionalized pillar ligand 4-bpdb instead of bpy has resulted in the formation of an isostructural framework with dual catalytic sites, which allowed its use in acid catalyzed Knoevenagel condensation reaction and base catalyzed Biginelli reaction.

8. The synthesis and structural characterization of a chiral Cd(II) coordination polymer based on a relatively simple bent dicarboxylate linker and conformationally flexible bpp ligand has been reported without the need of any chiral auxiliaries such as enantiopure solvents, additives, catalysts or a template. The chirality induction has occurred due to the helical arrangement of the polymeric chain around a twofold screw-axis. The microporous nature and the presence of open metal sites in the activated framework has been utilized for its catalytic activity towards Lewis acid catalyzed C-C and C-N bond forming Knoevenagel condensation and Strecker reactions, respectively. The structural integrity of the catalyst during the reaction was retained and thus provided its heterogeneous nature. Further, the incorporation of a naphthyl based pillar ligand 1,5-ND-4-Py into the Cd(II)-dicarboxylate system has resulted in the formation of 3D porous framework. This kind of 3D porous frameworks with fluorophore-based ligands can impart interesting luminescence properties.
9. By utilizing the flexible tetradentate ligand 4-tpom in combination of a bent dicarboxylate linker, two highly stable 3D porous coordination polymers of Zn(II) and Cd(II) have synthesized and their excellent thermal stability and robustness have been established by temperature dependent powder X-ray diffraction analysis. The highly selective carbon dioxide adsorption property of both frameworks along with the excellent stability and presence of unsaturated metal sites in the Zn(II) framework have allowed its use as an efficient heterogeneous catalyst for the chemical conversion of CO₂ into value added cyclic carbonates.
10. A systematic investigation has been carried out to study the influence of the coordination site shifting into the ligand structure to the final architecture and their properties. The use of 3-tpom instead of 4-tpom in Zn(II)-dicarboxylate system has resulted in a coordination polymer with an entirely different framework architecture

and topology. Further, a decrease in the gas adsorption capacity has also been observed.

11. Two isostructural double layered anionic coordination polymers of Cd(II) have been fabricated by utilizing a tricarboxylate linker in combination with pillar ligands bpy and azopy. These anionic polymers can be good candidates for cationic guest adsorption and separation applications.
12. A new twofold interpenetrated 3D coordination polymer, based on a tetrahedral tetracarboxylate and the rigid pillar ligand bpy, has been synthesized under solvothermal conditions. The gas adsorption studies revealed the role of interpenetration for comparatively higher uptake for smaller sized CO₂ molecules than larger sized (N₂ and CH₄) gas molecules. In addition, the framework exhibits moderately high selectivity for separation of CO₂/N₂ and CO₂/CH₄ gas mixtures based on the IAST. With high thermal and water stability, this selectivity entitles the framework as a good candidate for practical applications in gas separation and purification processes.
13. The chemistry of tetrahedral tetracarboxylate linker with rigid pillar ligands has been further extended to Cd(II) and a set of four 3D coordination polymers has been reported. The introduction of bpy or azopy has resulted into the construction of isostructural frameworks whereas the introduction of 3-bpdb or 3-bpdh has resulted into another set of isostructural coordination polymers. The photoluminescence properties of the azine functionalized coordination polymers have been further utilized for highly selective and sensitive detection of TNP at the ppb level.
14. A porous coordination polymer with diamondoid network topology has been synthesized by the self-assembly of tetrahedral tetracarboxylate linker and tetrahedral tetradentate ligand 4-tpom with Ni(II) metal center. The doubly interpenetrated framework exhibits moderate CO₂ uptake capacity with very good IAST selectivity. Further, the coordination site shifting in the N-donor ligand has resulted into a change in network topology and CO₂ uptake capacity of the framework indicating the important role of judicious ligand selection for the fabrication of such porous coordination polymers.
15. For enhanced CO₂ uptake capacity and selectivity, 1,2,3-triazole functionalized tetracarboxylic acid ligands have been designed and synthesized in good yields. The utilization of these ligands for the fabrication of polymeric architectures has resulted into the coordination polymers having high density of exposed Lewis-acid metal

sites and nitrogen-donor Lewis-basic sites accessible for the guest molecules. The Zn(II) compound **55**, exhibits very good CO₂ uptake capacity with very high selectivity over N₂ and CH₄. Further, the high density of open metal sites makes it an efficient heterogeneous catalyst for cycloaddition reaction of CO₂ with epoxides to generate value-added cyclic carbonates.

REFERENCES

- (1) Pedersen, C. J. *Science* **1988**, *241*, 536–540.
- (2) Cram, D. *Science* **1988**, *240*, 760–767.
- (3) Lehn, J. - M. *Angew. Chemie Int. Ed. English* **1988**, *27*, 89–112.
- (4) Leonard R. MacGillivray; Jerry L. A. *Angew. Chemie Int. Ed.* **1999**, *38*, 1018–1033.
- (5) Fujita, M.; Yazaki, J.; Ogura, K. *J. Am. Chem. Soc.* **1990**, *112*, 5645–5647.
- (6) Fujita, D.; Ueda, Y.; Sato, S.; Yokoyama, H.; Mizuno, N.; Kumasaka, T.; Fujita, M. *Chem* **2016**, *1*, 91–101.
- (7) Chan, A. K.-W.; Lam, W. H.; Tanaka, Y.; Wong, K. M.-C.; Yam, V. W.-W. *Proc. Natl. Acad. Sci.* **2015**, *112*, 690–695.
- (8) Holliday, B. J.; Mirkin, C. A. *Angew. Chemie Int. Ed.* **2001**, *40*, 2022–2043.
- (9) Leininger, S.; Olenyuk, B.; Stang, P. J. *Chem. Rev.* **2000**, *100*, 853–908.
- (10) Cook, T. R.; Stang, P. J. *Chem. Rev.* **2015**, *115*, 7001–7045.
- (11) Sun, Q.-F.; Sato, S.; Fujita, M. *Nat. Chem.* **2012**, *4*, 330–333.
- (12) Chakrabarty, R.; Mukherjee, P. S.; Stang, P. J. *Chem. Rev.* **2011**, *111*, 6810–6918.
- (13) Sun, Q.-F.; Iwasa, J.; Ogawa, D.; Ishido, Y.; Sato, S.; Ozeki, T.; Sei, Y.; Yamaguchi, K.; Fujita, M. *Science* **2010**, *328*, 1144–1147.
- (14) Northrop, B. H.; Zheng, Y.; Chi, K.; Stang, P. J. *Acc. Chem. Res.* **2009**, *42*, 1554–1563.
- (15) Lee, S. J.; Hupp, J. T. *Coord. Chem. Rev.* **2006**, *250*, 1710–1723.
- (16) Gianneschi, N. C.; Masar, M. S.; Mirkin, C. A. *Acc. Chem. Res.* **2005**, *38*, 825–837.
- (17) Lehn, J.-M. *Wiely-VCH: Weinheim, Germany*, 1995.
- (18) Sauvage, J. -P; Dietrich-Buchecker, C. *Wiely-VCH: Weinheim, Germany*, 1999.
- (19) Beves, J. E.; Leigh, D. A. *Nat. Chem.* **2010**, *2*, 708–710.
- (20) Fang, L.; Olson, M. A.; Benítez, D.; Tkatchouk, E.; Goddard, W. A.; Stoddart, J. F. *Chem. Soc. Rev.* **2010**, *39*, 17–29.
- (21) Durot, S.; Reviriego, F.; Sauvage, J. P. *Dalt. Trans.* **2010**, *39*, 10557–10570.
- (22) Faiz, J. A.; Heitz, V.; Sauvage, J. P. *Chem. Soc. Rev.* **2009**, *38*, 422–442.
- (23) Crowley, J. D.; Goldup, S. M.; Lee, A. L.; Leigh, D. A.; McBurney, R. T. *Chem. Soc. Rev.* **2009**, *38*, 1530–1541.
- (24) L. Caulder, D.; N. Raymond, K. *J. Chem. Soc. Dalt. Trans.* **1999**, *8*, 1185–1200.
- (25) Caulder, D. L.; Raymond, K. N. *Acc. Chem. Res.* **1999**, *32*, 975–982.
- (26) Caulder, D. L.; Brückner, C.; Powers, R. E.; König, S.; Parac, T. N.; Leary, J. A.; Raymond, K. N. *J. Am. Chem. Soc.* **2001**, *123*, 8923–8938.
- (27) Fujita, M.; Tominaga, M.; Hori, A.; Therrien, B. *Acc. Chem. Res.* **2005**, *38*, 369–378.
- (28) Oliveri, C.G.; Ulmann, P.A.; Wiester, M. J.; Mirkin, C. A. *Acc. Chem. Res.* **2008**, *41*, 1618–

1629.

- (29) Cotton, F. A.; Lin, C.; Murillo, C. A. *Proc. Natl. Acad. Sci.* **2002**, *99*, 4810–4813.
- (30) Cotton, F. A.; Lin, C.; Murillo, C. A. *Acc. Chem. Res.*, **2001**, *34*, 759–771.
- (31) De, S.; Mahata, K.; Schmittel, M. *Chem. Soc. Rev.* **2010**, *39*, 1555–1575.
- (32) Nitschke, J. R. *Acc. Chem. Res.* **2007**, *40*, 103–112.
- (33) Safont-Sempere, M. M.; Fernández, G.; Würthner, F. *Chem. Rev.* **2011**, *111*, 5784–5814.
- (34) Fujita, M.; Yazaki, J.; Ogura, K. *Chem. Lett.* **1991**, *20*, 1031–1032.
- (35) Stang, P. J.; Cao, D. H. *J. Am. Chem. Soc.* **1994**, *116*, 4981–4982.
- (36) Mishra, A.; Gupta, R. *Dalt. Trans.* **2014**, *43*, 7668–7682.
- (37) Debata, N. B.; Tripathy, D.; Chand, D. K. *Coord. Chem. Rev.* **2012**, *256*, 1831–1945.
- (38) Palma, C. A.; Cecchini, M.; Samorì, P. *Chem. Soc. Rev.* **2012**, *41*, 3713–3730.
- (39) Avram, L.; Cohen, Y. *Chem. Soc. Rev.* **2015**, *44*, 586–602.
- (40) Young, N. J.; Hay, B. P. *Chem. Commun.* **2013**, *49*, 1354–1379.
- (41) Mukherjee, S.; Mukherjee, P. S. *Chem. Commun.* **2014**, *50*, 2239–2248.
- (42) Tanaka, S.; Tsurugi, H.; Mashima, K. *Coord. Chem. Rev.* **2014**, *265*, 38–51.
- (43) Smulders, M. M. J.; Riddell, I. A.; Browne, C.; Nitschke, J. R. *Chem. Soc. Rev.* **2013**, *42*, 1728–1754.
- (44) Ward, M. D.; Raithby, P. R. *Chem. Soc. Rev.* **2013**, *42*, 1619–1636.
- (45) Bilbeisi, R. A.; Olsen, J. C.; Charbonnière, L. J.; Trabolssi, A. *Inorganica Chim. Acta* **2014**, *417*, 79–108.
- (46) Housecroft, C. E. *Dalt. Trans.* **2014**, *43*, 6594–6604.
- (47) Schmidt, A.; Casini, A.; Kühn, F. E. *Coord. Chem. Rev.* **2014**, *275*, 19–36.
- (48) Kumar, G.; Gupta, R. *Chem. Soc. Rev.* **2013**, *42*, 9403–9453.
- (49) Kraft, S.; Hanuschek, E.; Beckhaus, R.; Haase, D.; Saak, W. *Chem. - A Eur. J.* **2005**, *11*, 969–978.
- (50) Theilmann, O.; Saak, W.; Haase, D.; Beckhaus, R. *Organometallics* **2009**, *28*, 2799–2807.
- (51) Shanmugaraju, S.; Bar, A. K.; Chi, K. W.; Mukherjee, P. S. *Organometallics* **2010**, *29*, 2971–2980.
- (52) Janzen, D. E.; Patel, K. N.; VanDerveer, D. G.; Grant, G. J. *Chem. Commun.* **2006**, *9*, 3540–3542.
- (53) Würthner, F.; Sautter, A. *Chem. Commun.* **2000**, *2*, 445–446.
- (54) Lee, S. J.; Lin, W. *Acc. Chem. Res.* **2008**, *41*, 521–537.
- (55) Janka, M.; Anderson, G. K.; Rath, N. P. *Organometallics* **2004**, *23*, 4382–4390.
- (56) Hall, B. C.; Skelton, B. W.; White, A. H.; Bruce, M. I.; Low, P. J.; Nicholson, B. K.; Halet, J.-F.; Costuas, K. *J. Chem. Soc. Dalt. Trans.* **2002**, *3*, 383–398.
- (57) ALQaisi, S. M.; Galat, K. J.; Chai, M.; Ray, D. G.; Rinaldi, P. L.; Tessier, C. A.; Youngs,

- W. J. *J. Am. Chem. Soc.* **1998**, *120*, 12149–12150.
- (58) Jeong, K. S.; Cho, Y. L.; Song, J. U.; Chang, H. Y.; Choi, M. G. *J. Am. Chem. Soc.* **1998**, *120*, 10982–10983.
- (59) Slone, R. V.; Hupp, J. T.; Stern, C. L. *Inorg. Chem.* **1996**, *35*, 4096–4097.
- (60) Shiu, K.-B.; Lee, H.-C.; Lee, G.-H.; Wang, Y. *Organometallics* **2002**, *21*, 4013–4016.
- (61) Guzmán-Percástegui, E.; Vonlanthen, M.; Quiroz-García, B.; Flores-Alamo, M.; Rivera, E.; Castillo, I. *Dalt. Trans.* **2015**, *44*, 15966–15975.
- (62) Sathishkumar, R.; Manimaran, B.; Karthikeyan, S.; Velavan, K.; Varghese, B. *Organometallics* **2012**, *31*, 1953–1957.
- (63) Brechin, E. K.; Meally, S. T.; Jones, L. F.; Ryder, A. G.; McArdle, P.; Mason, K. *Chem. Commun.* **2009**, *45*, 7024.
- (64) Kabir, S. E.; Alam, J.; Ghosh, S.; Kundu, K.; Hogarth, G.; Tocher, D. A.; Hossain, G. M. G.; Roesky, H. W. *J. Chem. Soc. Dalt. Trans.* **2009**, *23*, 4458–4467.
- (65) Sautter, A.; Kaletaş, B. K.; Schmid, D. G.; Dobraua, R.; Zimine, M.; Jung, G.; Van Stokkum, I. H. M.; De Cola, L.; Williams, R. M.; Würthner, F. *J. Am. Chem. Soc.* **2005**, *127*, 6719–6729.
- (66) Robson, R. *J. Chem. Soc. Dalt. Trans.* **2008**, *38*, 5113–5131.
- (67) Robin, A. Y.; Fromm, K. M. *Coord. Chem. Rev.* **2006**, *250*, 2127–2157.
- (68) Kitagawa, S.; Uemura, K. *Chem. Soc. Rev.* **2005**, *34*, 109–119.
- (69) Janiak, C. *Dalt. Trans.* **2003**, *14*, 2781.
- (70) Irie, M. *Chem. Rev.* **2000**, *100*, 3483–3537.
- (71) Blake, A. J.; Champness, N. R.; Hubberstey, P.; Li, W.-S.; Withersby, M. A.; Schröder, M. *Coord. Chem. Rev.* **1999**, *183*, 117–138.
- (72) Hagrman, P. J.; Hagrman, D.; Zubieta, J. *Angew. Chemie Int. Ed.* **1999**, *38*, 2638–2684.
- (73) Buser, H. J.; Ludi, A.; Schwarzenbach, D.; Petter, W. *Inorg. Chem.* **1977**, *16*, 2704–2710.
- (74) Rayner, J. H.; Powell, H. M. *J. Chem. Soc.* **1952**, 319–328.
- (75) Kinoshita, Y.; Matsubara, I.; Saito, Y. *Bull. Chem. Soc. Jpn.* **1959**, *32*, 741–747.
- (76) Kinoshita, Y.; Matsubara, I.; Saito, Y. *Bull. Chem. Soc. Jpn.* **1959**, *32*, 1216–1221.
- (77) Kinoshita, Y.; Matsubara, I.; Higuchi, T.; Saito, Y. *Bull. Chem. Soc. Jpn.* **1959**, *32*, 1221–1226.
- (78) Hoskins, B. F.; Robson, R. *J. Am. Chem. Soc.* **1989**, *111*, 5962–5964.
- (79) Iwamoto, T. *J. Mol. Struct.* **1981**, *75*, 51–65.
- (80) Fujita, M.; Kwon, Y. J.; Washizu, S.; Ogura, K. *J. Am. Chem. Soc.* **1994**, *116*, 1151–1152.
- (81) Kitagawa, S.; Kitaura, R.; Noro, S. I. *Angew. Chemie - Int. Ed.* **2004**, *43*, 2334–2375.
- (82) Subramanian, S.; Zaworotko, M. J. *Angew. Chemie Int. Ed.* **1995**, *34*, 2127–2129.
- (83) Yaghi, O. M.; Li, H. *J. Am. Chem. Soc.* **1995**, *117*, 10401–10402.
- (84) Li, H.; Eddaoudi, M.; Groy, T. L.; Yaghi, O. M. *J. Am. Chem. Soc.* **1998**, *120*, 8571–8572.

- (85) Yaghi, O. M.; O’Keeffe, M.; Eddaoudi, M.; Li, H. *Nature* **1999**, *402*, 276–279.
- (86) Yaghi, O. M.; O’Keeffe, M.; Ockwig, N. W.; Chae, H. K.; Eddaoudi, M.; Jaheon K. *Nature* **2003**, *423*, 705–714.
- (87) Furukawa, H.; Cordova, K. E.; O’Keeffe, M.; Yaghi, O. M. *Science* **2013**, *341*, 1230444–1230444.
- (88) Eddaoudi, M.; Kim, J.; Rosi, N.; Vodak, D.; Wachter, J.; O’Keeffe, M.; Yaghi, O. M. *Science* **2002**, *295*, 469–472.
- (89) Guillerme, V.; Kim, D.; Eubank, J. F.; Luebke, R.; Liu, X.; Adil, K.; Lah, M. S.; Eddaoudi, M. *Chem. Soc. Rev.* **2014**, *43*, 6141–6172.
- (90) Li, M.; Li, D.; O’Keeffe, M.; Yaghi, O. M. *Chem. Rev.* **2014**, *114*, 1343–1370.
- (91) Cook, T. R.; Zheng, Y. R.; Stang, P. J. *Chem. Rev.* **2013**, *113*, 734–777.
- (92) Stock, N.; Biswas, S. *Chem. Rev.* **2012**, *112*, 933–969.
- (93) Cui, Y.; Li, B.; He, H.; Zhou, W.; Chen, B.; Qian, G. *Acc. Chem. Res.* **2016**, *49*, 483–493.
- (94) DeCoste, J. B.; Peterson, G. W. *Chem. Rev.* **2014**, *114*, 5695–5727.
- (95) Li, J.-R.; Sculley, J.; Zhou, H.-C. *Chem. Rev.* **2012**, *112*, 869–932.
- (96) Sumida, K.; Rogow, D. L.; Mason, J. A.; McDonald, T. M.; Bloch, E. D.; Herm, Z. R.; Bae, T.-H.; Long, J. R. *Chem. Rev.* **2012**, *112*, 724–781.
- (97) Suh, M. P.; Park, H. J.; Prasad, T. K.; Lim, D.-W. *Chem. Rev.* **2012**, *112*, 782–835.
- (98) Lustig, W. P.; Mukherjee, S.; Rudd, N. D.; Desai, A. V.; Li, J.; Ghosh, S. K. *Chem. Soc. Rev.* **2017**, *46*, 3242–3285.
- (99) Cui, Y.; Yue, Y.; Qian, G.; Chen, B. *Chem. Rev.* **2012**, *112*, 1126–1162.
- (100) Kreno, L. E.; Leong, K.; Farha, O. K.; Allendorf, M.; Van Duyne, R. P.; Hupp, J. T. *Chem. Rev.* **2012**, *112*, 1105–1125.
- (101) Coghlan, C. J.; Sumby, C. J.; Doonan, C. J. *CrystEngComm* **2014**, *16*, 6364–6371.
- (102) Kurmoo, M. *Chem. Soc. Rev.* **2009**, *38*, 1353–1379.
- (103) Wang, L.; Zheng, M.; Xie, Z. *J. Mater. Chem. B* **2018**, *6*, 707–717.
- (104) Chen, W.; Wu, C. *Dalton Trans.* **2018**, *47*, 2114–2133.
- (105) Gu, J.; Liang, A.; Yang, J.; Li, Y.; Zhuang, Q.; Wang, Z.; Hu, S. *Adv. Funct. Mater.* **2018**, *28*, 1707356.
- (106) Wu, M. X.; Yang, Y. W. *Adv. Mater.* **2017**, *29*, 1–20.
- (107) Teplensky, M. H.; Fantham, M.; Li, P.; Wang, T. C.; Mehta, J. P.; Young, L. J.; Moghadam, P. Z.; Hupp, J. T.; Farha, O. K.; Kaminski, C. F.; Fairen-Jimenez, D. *J. Am. Chem. Soc.* **2017**, *139*, 7522–7532.
- (108) He, C.; Liu, D.; Lin, W. *Chem. Rev.* **2015**, *115*, 11079–11108.
- (109) Maurin, G.; Serre, C.; Allan, P. K.; Couvreur, P.; Férey, G.; Gref, R.; Baati, T.; Horcajada, P.; Morris, R. E. *Chem. Rev.* **2011**, *112*, 1232–1268.
- (110) Zhao, X.; Liu, S.; Tang, Z.; Niu, H.; Cai, Y.; Meng, W.; Wu, F.; Giesy, J. P. *Sci. Rep.* **2015**, *5*, 1–10.

- (111) Huang, Y. B.; Liang, J.; Wang, X. S.; Cao, R. *Chem. Soc. Rev.* **2017**, *46*, 126–157.
- (112) Sun, L. B.; Liu, X. Q.; Zhou, H. C. *Chem. Soc. Rev.* **2015**, *44*, 5092–5147.
- (113) Chughtai, A. H.; Ahmad, N.; Younus, H. A.; Laypkov, A.; Verpoort, F. *Chem. Soc. Rev.* **2015**, *44*, 6804–6849.
- (114) Liu, J.; Chen, L.; Cui, H.; Zhang, J.; Zhang, L.; Su, C. Y. *Chem. Soc. Rev.* **2014**, *43*, 6011–6061.
- (115) García-García, P.; Müller, M.; Corma, A. *Chem. Sci.* **2014**, *5*, 2979–3007.
- (116) Gascon, J.; Corma, A.; Kapteijn, F.; Llabrés I Xamena, F. X. *ACS Catal.* **2014**, *4*, 361–378.
- (117) Shaabani, A.; Mohammadian, R.; Hashemzadeh, A.; Afshari, R.; Amini, M. M. *New J. Chem.* **2018**, *42*, 4167–4174.
- (118) Szilágyi, P.; Rogers, D. M.; Zaiser, I.; Callini, E.; Turner, S.; Borgschulte, A.; Züttel, A.; Geerlings, H.; Hirscher, M.; Dam, B. *J. Mater. Chem. A* **2017**, *5*, 15559–15566.
- (119) Zheng, Z.; Xu, H.; Xu, Z.; Ge, J. *Small* **2018**, *14*, 1–8.
- (120) Falaise, C.; Volkringer, C.; Giovine, R.; Prelot, B.; Huve, M.; Loiseau, T. *Dalton Trans.* **2017**, *46*, 12010–12014.
- (121) Falcaro, P.; Ricco, R.; Yazdi, A.; Imaz, I.; Furukawa, S.; Maspoch, D.; Ameloot, R.; Evans, J. D.; Doonan, C. J. *Coord. Chem. Rev.* **2016**, *307*, 237–254.
- (122) Choi, K. M.; Na, K.; Somorjai, G. A.; Yaghi, O. M. *J. Am. Chem. Soc.* **2015**, *137*, 7810–7816.
- (123) Lu, G.; Li, S.; Guo, Z.; Farha, O. K.; Hauser, B. G.; Qi, X.; Wang, Y.; Wang, X.; Han, S.; Liu, X.; DuChene J. S.; Zhang, H.; Zhang, Q.; Chen, X.; Ma, J.; Loo, S. C. J.; Wei, W. D.; Yang, Y.; Hupp, J. T.; Huo, F. *Nat. Chem.* **2012**, *4*, 310–316.
- (124) Ferguson, A.; Liu, L.; Tapperwijn, S. J.; Perl, D.; Coudert, F. X.; Van Cleuvenbergen, S.; Verbiest, T.; Van Der Veen, M. A.; Telfer, S. G. *Nat. Chem.* **2016**, *8*, 250–257.
- (125) Lin, Z. J.; Lü, J.; Hong, M.; Cao, R. *Chem. Soc. Rev.* **2014**, *43*, 5867–5895.
- (126) Lu, W.; Wei, Z.; Gu, Z. Y.; Liu, T. F.; Park, J.; Park, J.; Tian, J.; Zhang, M.; Zhang, Q.; Gentle, T.; Bosch, M.; Zhou, H. -C. *Chem. Soc. Rev.* **2014**, *43*, 5561–5593.
- (127) Schneemann, A.; Bon, V.; Schwedler, I.; Senkovska, I.; Kaskel, S.; Fischer, R. A. *Chem. Soc. Rev.* **2014**, *43*, 6062–6096.
- (128) Morris, R. E.; Bu, X. *Nat. Chem.* **2010**, *2*, 353–361.
- (129) Howlader, P.; Das, P.; Zangrando, E.; Mukherjee, P. S. *J. Am. Chem. Soc.* **2016**, *138*, 1668–1676.
- (130) Vivekananda, K. V.; Dey, S.; Maity, D. K.; Bhuvanesh, N.; Jain, V. K. *Inorg. Chem.* **2015**, *54*, 10153–10162.
- (131) Brown, C. J.; Toste, F. D.; Bergman, R. G.; Raymond, K. N. *Chem. Rev.* **2015**, *115*, 3012–3035.
- (132) Germain, M. E.; Knapp, M. J. *Chem. Soc. Rev.* **2009**, *38*, 2543–2555.
- (133) Salinas, Y.; Martínez-Máñez, R.; Marcos, M. D.; Sancenón, F.; Costero, A. M.; Parra, M.; Gil, S. *Chem. Soc. Rev.* **2012**, *41*, 1261–1296.
- (134) Nagarkar, S. S.; Joarder, B.; Chaudhari, A. K.; Mukherjee, S.; Ghosh, S. K. *Angew. Chemie*

- *Int. Ed.* **2013**, *52*, 2881–2885.
- (135) Joarder, B.; Desai, A. V.; Samanta, P.; Mukherjee, S.; Ghosh, S. K. *Chem. - A Eur. J.* **2015**, *21*, 965–969.
- (136) Wang, B.; Lv, X. L.; Feng, D.; Xie, L. H.; Zhang, J.; Li, M.; Xie, Y.; Li, J. R.; Zhou, H. C. *J. Am. Chem. Soc.* **2016**, *138*, 6204–6216.
- (137) Lin, J.-B.; Chen, Q.; Qi, X.-L.; Zhang, J.-P.; Chen, X.-M.; Lin, R.-B. *Chem. Sci.* **2011**, *2*, 2214.
- (138) Chen, L.; Ye, J. W.; Wang, H. P.; Pan, M.; Yin, S. Y.; Wei, Z. W.; Zhang, L. Y.; Wu, K.; Fan, Y. N.; Su, C. Y. *Nat. Commun.* **2017**, *8*, 1–10.
- (139) Wu, Y.; Yang, G. P.; Zhang, Y.; Shi, N.; Han, J.; Wang, Y. Y. *RSC Adv.* **2015**, *5*, 90772–90777.
- (140) Lu, Y.; Yan, B. *Chem. Commun.* **2014**, *50*, 13323–13326.
- (141) Hu, Z.; Deibert, B. J.; Li, J. *Chem. Soc. Rev.* **2014**, *43*, 5815–5840.
- (142) Liu, L.; Zhou, Y.; Liu, S.; Xu, M. *ChemElectroChem* **2018**, *5*, 6–19.
- (143) Kim, K.-H.; Ok, Y. S.; Deep, A.; Vikrant, K.; Kumar, V. *Trends Anal. Chem.* **2018**, *105*, 263–281.
- (144) Fang, X.; Zong, B.; Mao, S. *Nano-Micro Lett.* **2018**, *10*, 1–19.
- (145) Yi, F. Y.; Chen, D.; Wu, M. K.; Han, L.; Jiang, H. L. *Chempluschem* **2016**, *81*, 675–690.
- (146) Ahmad, N.; Younus, H. A.; Chughtai, A. H.; Verpoort, F. *Chem. Soc. Rev.* **2015**, *44*, 9–25.
- (147) Shanmugaraju, S.; Mukherjee, P. S. *Chem. - A Eur. J.* **2015**, *21*, 6656–6666.
- (148) Arakawa, H.; Aresta, M.; Armor, J. N.; Barteau, M. A.; Beckman, E. J.; Bell, A. T.; Bercaw, J. E.; Creutz, C.; Dinjus, E.; Dixon, D. A.; Domen, K.; DuBois, D. L.; Eckert, J.; Fujita, E.; Gibson, D. H.; Goddard, W. A.; Goodman, D. W.; Keller, J.; Kubas, G. J.; Kung, H. H.; Lyons, J. E.; Manzer, L. E.; Marks, T. J.; Morokuma, K.; Nicholas, K. M.; Periana, R.; Que, L.; Rostrup-Nielsen, J.; Sachtler, W. M. H.; Schmidt, L. D.; Sen, A.; Somorjai, G. A.; Stair, P. C.; Stults, B. R.; Tumas, W. *Chem. Rev.* **2001**, *101*, 953–996.
- (149) Lindzen, R. S. *Proc. Natl. Acad. Sci.* **2002**, *94*, 8335–8342.
- (150) World Meteorological Organization. *Greenhouse Gas Bulletin* **2017**, *13*, 2.
- (151) D’Alessandro, D. M.; Smit, B.; Long, J. R. *Angew. Chemie - Int. Ed.* **2010**, *49*, 6058–6082.
- (152) Keskin, S.; van Heest, T. M.; Sholl, D. S. *ChemSusChem* **2010**, *3*, 879–891.
- (153) Choi, H. S.; Suh, M. P. *Angew. Chemie - Int. Ed.* **2009**, *48*, 6865–6869.
- (154) Bui, M.; Adjiman, C. S.; Bardow, A.; Anthony, E. J.; Boston, A.; Brown, S.; Fennell, P. S.; Fuss, S.; Galindo, A.; Hackett, L. A.; Hallet, J. P.; Herzog, H. J.; Jackson, G.; Kemper, J.; Krevor, S.; Maitland, G. C.; Matuszewski, M.; Metcalfe, I. S.; Petit, C.; Puxty, G.; Reimer, J.; Rubin, E. S.; Scott, S. A.; Shah, N.; Smit, B.; Trusler, J. P. M.; Webley, P.; Wilcox, J.; MacDowell, N.; *Energy Environ. Sci.* **2018**, *11*, 1062–1176.
- (155) Berger, A. H.; Bhowan, A. S. *Energy Procedia* **2011**, *4*, 562–567.
- (156) House, K. Z.; Harvey, C. F.; Aziz, M. J.; Schrag, D. P. *Energy Environ. Sci.* **2009**, *2*, 193–205.
- (157) Rubin, E. S.; Chen, C.; Rao, A. B. *Energy Policy* **2007**, *35*, 4444–4454.

- (158) Liu, J.; Thallapally, P. K.; McGrail, B. P.; Brown, D. R.; Liu, J. *Chem. Soc. Rev.* **2012**, *41*, 2308–2322.
- (159) Makal, T. A.; Li, J. R.; Lu, W.; Zhou, H. C. *Chem. Soc. Rev.* **2012**, *41*, 7761–7779.
- (160) International Energy Agency, *CO₂ Emission from Fuel Combustions Highlights*, **2015**.
- (161) Schoedel, A.; Ji, Z.; Yaghi, O. M. *Nat. Energy* **2016**, *1*, 16034.
- (162) Zhang, Z.; Yao, Z.-Z.; Xiang, S.; Chen, B. *Energy Environ. Sci.* **2014**, *7*, 2868–2899.
- (163) Forse, A. C.; Gonzalez, M. I.; Siegelman, R. L.; Witherspoon, V. J.; Jawahery, S.; Mercado, R.; Milner, P. J.; Martell, J. D.; Smit, B.; Blümich, B.; Long, J. R.; Reimer, J. A.; *J. Am. Chem. Soc.* **2018**, *140*, 1663–1673.
- (164) Zhang, J.; Wu, H.; Emge, T. J.; Li, J. *Chem. Commun.* **2010**, *46*, 9152–9154.
- (165) Demessence, A.; D’Alessandro, D. M.; Foo, M. L.; Long, J. R. *J. Am. Chem. Soc.* **2009**, *131*, 8784–8786.
- (166) Ramsahye, N. A.; Maurin, G.; Bourrelly, S.; Llewellyn, P. L.; Loiseau, T.; Serre, C.; Férey, G. *Chem. Commun.* **2007**, *31*, 3261–3263.
- (167) Milner, P. J.; Siegelman, R. L.; Forse, A. C.; Gonzalez, M. I.; Runčevski, T.; Martell, J. D.; Reimer, J. A.; Long, J. R. *J. Am. Chem. Soc.* **2017**, *139*, 13541–13553.
- (168) Gómora-Figueroa, A. P.; Mason, J. A.; Gonzalez, M. I.; Bloch, E. D.; Meihaus, K. R. *Inorg. Chem.* **2017**, *56*, 4308–4316.
- (169) Feng, G.; Peng, Y.; Liu, W.; Chang, F.; Dai, Y.; Huang, W. *Inorg. Chem.* **2017**, *56*, 2363–2366.
- (170) Su, X.; Bromberg, L.; Martis, V.; Simeon, F.; Huq, A.; Hatton, T. A. *ACS Appl. Mater. Interfaces* **2017**, *9*, 11299–11306.
- (171) Wang, Q.; Bai, J.; Lu, Z.; Pan, Y.; You, X. *Chem. Commun.* **2016**, *52*, 443–452.
- (172) Nugent, P.; Belmabkhout, Y.; Burd, S. D.; Cairns, A. J.; Luebke, R.; Forrest, K.; Pham, T.; Ma, S.; Space, B.; Wojtas, L.; Eddaoudi, M.; Zaworotko, M. J. *Nature* **2013**, *495*, 80–84.
- (173) Li, B.; Zhang, Z.; Li, Y.; Yao, K.; Zhu, Y.; Deng, Z.; Yang, F.; Zhou, X.; Li, G.; Wu, H.; Nijem, N.; Chabal, Y. J.; Lai, Z.; Han, Y.; Shi, Z.; Feng, S.; Li, J. *Angew. Chemie Int. Ed.* **2012**, *51*, 1412–1415.
- (174) Elsaidi, S. K.; Mohamed, M. H.; Wojtas, L.; Chanthapally, A.; Pham, T.; Space, B.; Vittal, J. J.; Zaworotko, M. J. *J. Am. Chem. Soc.* **2014**, *136*, 5072–5077.
- (175) Zhang, Z.; Zhao, Y.; Gong, Q.; Li, Z.; Li, J. *Chem. Commun.* **2013**, *49*, 653–661.
- (176) Furukawa, H.; Müller, U.; Yaghi, O. M. *Angew. Chemie Int. Ed.* **2015**, *54*, 3417–3430.
- (177) Liu, Y.; Wang, Z. U.; Zhou, H.-C. *Greenh. Gases Sci. Technol.* **2012**, *2*, 239–259.
- (178) Das, A.; D’Alessandro, D. M. *CrystEngComm* **2015**, *17*, 706–718.
- (179) You, X.; Liu, W.; Pan, Y.; Lu, Z.; Meng, F.; Bai, J.; Hang, C. *Chem. - A Eur. J.* **2016**, *22*, 6277–6285.
- (180) Lanzafame, P.; Centi, G.; Perathoner, S. *Chem. Soc. Rev.* **2014**, *43*, 7562–7580.
- (181) Gao, W.-Y.; Sun, Y.; Wu, H.; Ma, S.; Leng, K. *Angew. Chemie Int. Ed.* **2016**, *55*, 5472–5476.

- (182) Cao, C.-Y.; Dou, Z.-F.; Li, P.; Song, W.-G.; Liu, H.; Yu, Y.; Qu, J. *ChemSusChem* **2012**, *5*, 652–655.
- (183) Ma, R.; He, L.-N.; Zhou, Y.-B. *Green Chem.* **2016**, *18*, 226–231.
- (184) Wang, X.; Zhou, Y.; Guo, Z.; Chen, G.; Li, J.; Shi, Y.; Liu, Y.; Wang, J. *Chem. Sci.* **2015**, *6*, 6916–6924.
- (185) Kuruppathparambil, R. R.; Babu, R.; Jeong, H. M.; Hwang, G. Y.; Jeong, G. S.; Kim, M.; Kim, D. W.; Park, D. W. *Green Chem.* **2016**, *18*, 6349–6356.
- (186) Miralda, C. M.; MacÍas, E. E.; Zhu, M.; Ratnasamy, P.; Carreon, M. A. *ACS Catal.* **2012**, *2*, 180–183.
- (187) Yamaguchi, K.; Ebitani, K.; Yoshida, T.; Yoshida, H.; Kaneda, K. *J. Am. Chem. Soc.* **1999**, *121*, 4526–4527.
- (188) Gao, W.-Y.; Chen, Y.; Niu, Y.; Williams, K.; Cash, L.; Perez, P. J.; Wojtas, L.; Cai, J.; Chen, Y.-S.; Ma, S. *Angew. Chemie Int. Ed.* **2014**, *53*, 2615–2619.
- (189) Beyzavi, M. H.; Vermeulen, N. A.; Howarth, A. J.; Tussupbayev, S.; League, A. B.; Schweitzer, N. M.; Gallagher, J. R.; Platero-Prats, A. E.; Hafezi, N.; Sarjeant, A. A.; Miller, J. T.; Chapman, K. W.; Stodart, J. F.; Cramer, C. J.; Hupp, J. T.; Farha, O. K. *J. Am. Chem. Soc.* **2015**, *137*, 13624–13631.
- (190) Feng, D.; Chung, W.-C.; Wei, Z.; Gu, Z.-Y.; Jiang, H.-L.; Chen, Y.-P.; Darensbourg, D. J.; Zhou, H.-C. *J. Am. Chem. Soc.* **2013**, *135*, 17105–17110.
- (191) Li, P.-Z.; Wang, X.-J.; Liu, J.; Lim, J. S.; Zou, R.; Zhao, Y. *J. Am. Chem. Soc.* **2016**, *138*, 2142–2145.
- (192) Lu, B.-B.; Jiang, W.; Yang, J.; Liu, Y.-Y.; Ma, J.-F. *ACS Appl. Mater. Interfaces* **2017**, *9*, 39441–39449.
- (193) Gao, W.-Y.; Tsai, C.-Y.; Wojtas, L.; Thiounn, T.; Lin, C.-C.; Ma, S. *Inorg. Chem.* **2016**, *55*, 7291–7294.
- (194) Liu, L.; Wang, S.-M.; Han, Z.-B.; Ding, M.; Yuan, D.-Q.; Jiang, H.-L. *Inorg. Chem.* **2016**, *55*, 3558–3565.
- (195) Zou, R.; Li, P.-Z.; Zeng, Y.-F.; Liu, J.; Zhao, R.; Duan, H.; Luo, Z.; Wang, J.-G.; Zou, R.; Zhao, Y. *Small* **2016**, *12*, 2334–2343.
- (196) Tang, L.; Zhang, S.; Wu, Q.; Wang, X.; Wu, H.; Jiang, Z. *J. Mater. Chem. A* **2018**, *6*, 2964–2973.
- (197) Liang, J.; Xie, Y.-Q.; Wang, X.-S.; Wang, Q.; Liu, T.-T.; Huang, Y.-B.; Cao, R. *Chem. Commun.* **2018**, *54*, 342–345.
- (198) Zhou, H.-F.; Liu, B.; Hou, L.; Zhang, W.-Y.; Wang, Y.-Y. *Chem. Commun.* **2018**, *54*, 456–459.
- (199) Han, Y.-H.; Zhou, Z.-Y.; Tian, C.-B.; Du, S.-W. *Green Chem.* **2016**, *18*, 4086–4091.
- (200) Ma, D.; Li, B.; Liu, K.; Zhang, X.; Zou, W.; Yang, Y.; Li, G.; Shi, Z.; Feng, S. *J. Mater. Chem. A* **2015**, *3*, 23136–23142.
- (201) Ugale, B.; Dhankhar, S. S.; Nagaraja, C. M. *Inorg. Chem.* **2016**, *55*, 9757–9766.
- (202) *APEX2, SADABS and SAINT*; Bruker AXS Inc, Madison, WI, USA, 2008.
- (203) Dolomanov, O. V.; Bourhis, L. J.; Gildea, R. J.; Howard, J. A. K.; Puschmann, H. *J. Appl.*

- Crystallogr.* **2009**, *42*, 339–341.
- (204) Sheldrick, G. M. *Acta Crystallogr. Sect. A Found. Adv.* **2015**, *71*, 3–8.
- (205) Macrae, C. F.; Bruno, I. J.; Chisholm, J. A.; Edgington, P. R.; McCabe, P.; Pidcock, E.; Rodriguez-Monge, L.; Taylor, R.; van de Streek, J.; Wood, P. A. *J. Appl. Crystallogr.*, **2008**, *41*, 466–470.
- (206) Putz, H.; Brandenburg, K. Diamond - Crystal and Molecular Structure Visualization. <http://www.crystalimpact.com/diamond>.
- (207) Spek, A. L. *J. Appl. Crystallogr.* **2003**, *36* (1), 7–13.
- (208) Spek, A. L. *PLATON, Version 1.62*; University of Utrecht, 1999.
- (209) Khullar, S.; Mandal, S. K. *Dalt. Trans.* **2015**, *44*, 1203–1210.
- (210) Khullar, S.; Gupta, V.; Mandal, S. K. *CrystEngComm* **2014**, *16*, 5705–5715.
- (211) Bisht, K. K.; Patel, P.; Rachuri, Y.; Eringathodi, S. *Acta Crystallogr. Sect. B Struct. Sci. Cryst. Eng. Mater.* **2014**, *70*, 63–71.
- (212) Bisht, K. K.; Suresh, E. *J. Am. Chem. Soc.* **2013**, *135*, 15690–15693.
- (213) Ciurtin, D. M.; Dong, Y. B.; Smith, M. D.; Barclay, T.; Zur Loye, H. C. *Inorg. Chem.* **2001**, *40*, 2825–2834.
- (214) Dong, Y. B.; Smith, M. D.; Layland, R. C.; Zur Loye, H. C. *Chem. Mater.* **2000**, *12*, 1156–1161.
- (215) Dong, Y. B.; Smith, M. D.; Zur Loye, H. C. *Inorg. Chem.* **2000**, *39*, 4927–4935.
- (216) Tripathy, D.; Ramkumar, V.; Chand, D. K. *Cryst. Growth Des.* **2013**, *13*, 3763–3772.
- (217) Pocic, D.; Planeix, J. M.; Kyritsakas, N.; Jouaiti, A.; Hosseini, M. W. *CrystEngComm* **2005**, *7*, 624–628.
- (218) Niu, Y.; Hou, H.; Wei, Y.; Fan, Y.; Zhu, Y.; Du, C.; Xin, X. *Inorg. Chem. Commun.* **2001**, *4*, 358–361.
- (219) Azhdari Tehrani, A.; Ghasempour, H.; Morsali, A.; Makhloufi, G.; Janiak, C. *Cryst. Growth Des.* **2015**, *15*, 5543–5547.
- (220) Min, D.; Cho, B. Y.; Lee, S. W. *Inorganica Chim. Acta* **2006**, *359*, 577–584.
- (221) Mok, H. J.; Davis, J. A.; Pal, S.; Mandal, S. K.; Armstrong, W. H. *Inorganica Chim. Acta* **1997**, *263*, 385–394.
- (222) Zhang, Q.; Bu, X.; Lin, Z.; Wu, T.; Feng, P. *Inorg. Chem.* **2008**, *47*, 9724–9726.
- (223) Pal, S.; Chan, M. K.; Armstrong, W. H. *J. Am. Chem. Soc.* **1992**, *114*, 6398–6406.
- (224) Chakraborty, G.; Mandal, S. K. *Inorg. Chem.* **2017**, *56*, 14556–14566.
- (225) Khullar, S.; Mandal, S. K. *Cryst. Growth Des.* **2014**, *14*, 6433–6444.
- (226) Khullar, S.; Mandal, S. K. *Cryst. Growth Des.* **2013**, *13*, 3116–3125.
- (227) Pal, T. K.; Neogi, S.; Bharadwaj, P. K. *Chem. - A Eur. J.* **2015**, *21*, 16083–16090.
- (228) Culp, J. T.; Madden, C.; Kauffman, K.; Shi, F.; Matranga, C. *Inorg. Chem.* **2013**, *52*, 4205–4216.
- (229) Kudo, N.; Perseghini, M.; Fu, G. C. *Angew. Chem. - Int. Ed.* **2006**, *45*, 1282–1284.

- (230) Gupta, V.; Mandal, S. K. *Dalton Trans.* **2019**, *48*, 415–425.
- (231) Gupta, V.; Khullar, S.; Kumar, S.; Mandal, S. K. *Dalton Trans.* **2015**, *44*, 16778–16784.
- (232) Davies, R. P.; Less, R. J.; Lickiss, P. D.; Robertson, K.; White, A. J. P. *Inorg. Chem.* **2008**, *47*, 9958–9964.
- (233) Fournier, J.-H.; Wang, X.; Wuest, J. D. *Can. J. Chem.* **2003**, *81*, 376–380.
- (234) Liu, J.; Zhao, Y.; Zou, R.; Li, P.-Z.; Wang, X.-J.; Lim, J. S. *J. Am. Chem. Soc.* **2016**, *138*, 2142–2145.
- (235) Li, P. Z.; Wang, X. J.; Tan, S. Y.; Ang, C. Y.; Chen, H.; Liu, J.; Zou, R.; Zhao, Y. *Angew. Chem. - Int. Ed.* **2015**, *54*, 12748–12752.
- (236) Wang, X. J.; Li, P. Z.; Chen, Y.; Zhang, Q.; Zhang, H.; Chan, X. X.; Ganguly, R.; Li, Y.; Jiang, J.; Zhao, Y. *Sci. Rep.* **2013**, *3*, 1–5.
- (237) Pandey, P.; Farha, O. K.; Spokoyny, A. M.; Mirkin, C. A.; Kanatzidis, M. G.; Hupp, J. T.; Nguyen, S. T. *J. Mater. Chem.* **2011**, *21*, 1700–1703.
- (238) Plietzsch, O.; Schilling, C. I.; Tolev, M.; Nieger, M.; Richert, C.; Muller, T.; Bräse, S. *Org. Biomol. Chem.* **2009**, *7*, 4734–4743.
- (239) Zhao, M.; Huang, Y.; Peng, Y.; Huang, Z.; Ma, Q.; Zhang, H. *Chem. Soc. Rev.* **2018**, *47*, 6267–6295.
- (240) Bai, Y.; Dou, Y.; Xie, L. H.; Rutledge, W.; Li, J. R.; Zhou, H. C. *Chem. Soc. Rev.* **2016**, *45*, 2327–2367.
- (241) Jiang, H. L.; Xu, Q. *Chem. Commun.* **2011**, *47*, 3351–3370.
- (242) McGuire, C. V.; Forgan, R. S. *Chem. Commun.* **2015**, *51*, 5199–5217.
- (243) Liu, X. W.; Sun, T. J.; Hu, J. L.; Wang, S. D. *J. Mater. Chem. A* **2016**, *4*, 3584–3616.
- (244) Sun, D.; Xu, M.-Z.; Liu, S.-S.; Yuan, S.; Lu, H.-F.; Feng, S.-Y.; Sun, D.-F. *Dalt. Trans.* **2013**, *42*, 12324.
- (245) Chan, A. K.-W.; Lam, W. H.; Tanaka, Y.; Wong, K. M.-C.; Yam, V. W.-W. *Proc. Natl. Acad. Sci.* **2015**, *112*, 690–695.
- (246) Fujita, M.; Tominaga, M.; Hori, A.; Therrien, B. *Acc. Chem. Res.* **2005**, *38*, 369–378.
- (247) Cotton, F. A.; Daniels, L. M.; Lin, C.; Murillo, C. A. *J. Am. Chem. Soc.* **1999**, *121*, 4538–4539.
- (248) Angaridis, P.; Berry, J. F.; Cofton, F. A.; Murillo, C. A.; Wang, X. *J. Am. Chem. Soc.* **2003**, *125*, 10327–10334.
- (249) Khullar, S.; Mandal, S. K. *Cryst. Growth Des.* **2012**, *12*, 5329–5337.
- (250) Wikstrom, J. P.; Filatov, A. S.; Mikhalyova, E. A.; Shatruk, M.; Foxman, B. M.; Rybak-Akimova, E. V. *Dalt. Trans.* **2010**, *39*, 2504.
- (251) Nakamoto, K. *Infrared Spectra of Inorganic and Coordination Compounds Part B*, John Wiley & Sons, New York, 6th edn, 2009.
- (252) Zhu, L.; Liu, X.-Q.; Jiang, H.-L.; Sun, L.-B. *Chem. Rev.* **2017**, *117*, 8129–8176.
- (253) Rogge, S. M. J.; Bavykina, A.; Hajek, J.; Garcia, H.; Olivos-Suarez, A. I.; Sepúlveda-Escribano, A.; Vimont, A.; Clet, G.; Bazin, P.; Kapteijn, F.; Daturi, M.; Ramos-Fernandez, E. V.; Llabrés i Xamena, F. X.; Van Speybroeck, V.; Gascon, J. *Chem. Soc. Rev.* **2017**, *46*,

3134–3184.

- (254) Murase, T.; Nishijima, Y.; Fujita, M. *J. Am. Chem. Soc.* **2012**, *134*, 162–164.
- (255) Zhu, L.; Liu, X. Q.; Jiang, H. L.; Sun, L. B. *Chem. Rev.* **2017**, *117*, 8129–8176.
- (256) Hu, Z.; Zhao, D. *CrystEngComm* **2017**, *19*, 4066–4081.
- (257) Liu, J.; Chen, L.; Cui, H.; Zhang, J.; Zhang, L.; Su, C. Y. *Chem. Soc. Rev.* **2014**, *43*, 6011–6061.
- (258) Karmakar, A.; Rúbio, G. M. D. M.; Guedes da Silva, M. F. C.; Hazra, S.; Pombeiro, A. J. L. *Cryst. Growth Des.* **2015**, *15*, 4185–4197.
- (259) Karmakar, A.; Paul, A.; Mahmudov, K. T. *New J. Chem.* **2016**, *40*, 1535–1546.
- (260) Almáši, M.; Zeleňák, V.; Opanasenko, M.; Čejka, J. *Dalt. Trans.* **2014**, *43*, 3730–3738.
- (261) Panchenko, V. N.; Matrosova, M. M.; Jeon, J.; Jun, J. W.; Timofeeva, M. N.; Jhung, S. H. *J. Catal.* **2014**, *316*, 251–259.
- (262) Chen, M.; Zhou, X.; Li, H.; Yang, X.; Lang, J. *Cryst. Growth Des.* **2015**, *15*, 2753–2760.
- (263) Tian, D.; Li, Y.; Chen, R. Y.; Chang, Z.; Wang, G. Y.; Bu, X. H. *J. Mater. Chem. A* **2014**, *2*, 1465–1470.
- (264) Zhang, X. T.; Chen, H. T.; Li, B.; Liu, G. Z.; Liu, X. Z. *Dalt. Trans.* **2018**, *47*, 1202–1213.
- (265) Zhang, J.; Huo, L.; Wang, X.; Fang, K.; Fan, L.; Hu, T. *Cryst. Growth Des.* **2017**, *17*, 5887–5897.
- (266) Duan, W. L.; Wang, H. C.; Martí-Rujas, J.; Guo, F. *CrystEngComm* **2018**, *20*, 323–327.
- (267) Song, W.-C.; Cui, X.-Z.; Liu, Z.-Y.; Yang, E.-C.; Zhao, X.-J. *Sci. Rep.* **2016**, *6*, 34870.
- (268) Bai, J.; Zhou, H.-L.; Liao, P.-Q.; Zhang, W.-X.; Chen, X.-M. *CrystEngComm* **2015**, *17*, 4462–4468.
- (269) Kuai, H. W.; Cheng, X. C.; Zhu, X. H. *J. Coord. Chem.* **2011**, *64*, 1636–1644.
- (270) Khullar, S.; Mandal, S. K. *RSC Adv.* **2014**, *4*, 39204–39213.
- (271) Yaghi, O. M.; Sun, Z.; Richardson, D. A.; Groy, T. L. *J. Am. Chem. Soc.* **1994**, *116*, 807–808.
- (272) Zheng, Y. Q.; Lin, J. L.; Kong, Z. P. *Inorg. Chem.* **2004**, *43*, 2590–2596.
- (273) Dybtsev, D. N.; Chun, H.; Kim, K. *Angew. Chem. - Int. Ed.* **2004**, *43*, 5033–5036.
- (274) Blatov, V. A.; Shevchenko, A. P.; Proserpio, D. M. *Cryst. Growth Des.* **2014**, *14*, 3576–3586.
- (275) Spek, A. L. *Acta Crystallogr. Sect. D Biol. Crystallogr.* **2009**, *65*, 148–155.
- (276) Addison, A. W.; Rao, T. N.; Reedijk, J.; van Rijn, J.; Verschoor, G. C. *J. Chem. Soc., Dalt. Trans.* **1984**, *18*, 1349–1356.
- (277) Fu, Z.; Yi, J.; Chen, Y.; Liao, S.; Guo, N.; Dai, J.; Yang, G.; Lian, Y.; Wu, X. *Eur. J. Inorg. Chem.* **2008**, *2008*, 628–634.
- (278) van Niekerk, J. N.; Schoening, F. R. L. *Acta Crystallogr.* **1953**, *6*, 227–232.
- (279) Brown, G. M.; Chidambaram, R. *Acta Crystallogr. Sect. B Struct. Crystallogr. Cryst. Chem.* **1973**, *29*, 2393–2403.

- (280) Vogiatzis, K. D.; Klopper, W.; Mavrandonakis, A.; Fink, K. *ChemPhysChem* **2011**, *12*, 3307–3319.
- (281) Hill, S.; Datta, S.; Liu, J.; Inglis, R.; Milios, C. J.; Feng, P. L.; Henderson, J. J.; del Barco, E.; Brechin, E. K.; Hendrickson, D. N. *Dalt. Trans.* **2010**, *39*, 4693.
- (282) Grirrane, A.; Pastor, A.; Galindo, A.; Ienco, A.; Mealli, C.; Rosa, P. *Chem. Commun.* **2003**, *304*, 512–513.
- (283) Fohlmeister, L.; Liu, S.; Schulten, C.; Moubaraki, B.; Stasch, A.; Cashion, J. D.; Murray, K. S.; Gagliardi, L.; Jones, C. *Angew. Chemie Int. Ed.* **2012**, *51*, 8294–8298.
- (284) Evans, S. R.; Tiana, D.; Simoncic, P.; Casati, N.; Macchi, P.; Gozzo, F. *Chem. Commun.* **2014**, *50*, 12824–12827.
- (285) Caneschi, A.; Ferraro, F.; Gatteschi, D.; Melandri, M. C.; Rey, P.; Sessoli, R. *Angew. Chem. Int. Ed.* **1989**, *28*, 1365–1367.
- (286) Fontanet, M.; Rodríguez, M.; Fontrodona, X.; Romero, I.; Teixidor, F.; Viñas, C.; Aliaga-Alcalde, N.; Matějček, P. *Chem. - A Eur. J.* **2014**, *20*, 13993–14003.
- (287) Dai, F.; He, H.; Xie, A.; Chu, G.; Sun, D.; Ke, Y. *CrystEngComm* **2009**, *11*, 47–49.
- (288) Yu, S. B.; Lippard, S. J.; Shweky, I.; Bino, A. *Inorg. Chem.* **1992**, *31*, 3502–3504.
- (289) Cañadillas-Delgado, L.; Fabelo, O.; Pasán, J.; Delgado, F. S.; Lloret, F.; Julve, M.; Ruiz-Pérez, C. *Inorg. Chem.* **2007**, *46*, 7458–7465.
- (290) Chen, L.-F.; Zhang, J.; Song, L.-J.; Ju, Z.-F. *Inorg. Chem. Commun.* **2005**, *8*, 555–558.
- (291) Society, R. *Proc. R. Soc. London. Ser. A. Math. Phys. Sci.* **1952**, *214*, 451–465.
- (292) Nakashima, M.; Maruo, H.; Hata, T.; Tokii, T. *Chem. Lett.* **1999**, *28*, 1277–1278.
- (293) Kiskin, M. A.; Fomina, I. G.; Aleksandrov, G. G.; Sidorov, A. A.; Novotortsev, V. M.; Rakitin, Y. V.; Dobrokhotova, Z. V.; Ikorskii, V. N.; Shvedenkov, Y. G.; Eremenko, I. L.; Moiseev, I. *Inorg. Chem. Commun.* **2005**, *8*, 89–93.
- (294) Rardin, R. L.; Poganiuch, P.; Bino, A.; Goldberg, D. P.; Tolman, W. B.; Liu, S.; Lippard, S. J. *J. Am. Chem. Soc.* **1992**, *114*, 5240–5249.
- (295) Benbellat, N.; Gavrilenko, K. S.; Le Gal, Y.; Cador, O.; Golhen, S.; Gouasmia, A.; Fabre, J.-M.; Ouahab, L. *Inorg. Chem.* **2006**, *45*, 10440–10442.
- (296) Cotton, F. A.; Murilo, C. A.; Walton, R. A. Multiple Bonds Between Metal Atoms, *Springer Science & Business Media Inc.* New York, 3rd edn, 2005.
- (297) Freeman, F. *Chem. Rev.* **1980**, *80*, 329–350.
- (298) Kamath, S.; Buolamwini, J. K. *J. Med. Chem.* **2003**, *46*, 4657–4668.
- (299) Rogge, S. M. J.; Bavykina, A.; Hajek, J.; Garcia, H.; Olivos-Suarez, A. I.; Sepúlveda-Escribano, A.; Vimont, A.; Clet, G.; Bazin, P.; Kapteijn, F.; *Chem. Soc. Rev.* **2017**, *46*, 3134–3184.
- (300) Pal, T. K.; De, D.; Senthilkumar, S.; Neogi, S.; Bharadwaj, P. K. *Inorg. Chem.* **2016**, *55*, 7835–7842.
- (301) Verma, A.; Tomar, K.; Bharadwaj, P. K. *Inorg. Chem.* **2017**, *56*, 13629–13633.
- (302) Gupta, M.; De, D.; Tomar, K.; Bharadwaj, P. K. *Inorg. Chem.* **2017**, *56*, 14605–14611.
- (303) Aguirre-Díaz, L. M.; Gándara, F.; Iglesias, M.; Snejko, N.; Gutiérrez-Puebla, E.; Monge, M.

- Á. *J. Am. Chem. Soc.* **2015**, *137*, 6132–6135.
- (304) Li, X. Y.; Li, Y. Z.; Yang, Y.; Hou, L.; Wang, Y. Y.; Zhu, Z. *Chem. Commun.* **2017**, *53*, 12970–12973.
- (305) Suh, M. P.; Park, H. J.; Prasad, T. K.; Lim, D.-W. *Chem. Rev.* **2012**, *112*, 782–835.
- (306) Nájera, C.; Sansano, J. M. *Chem. Rev.* **2007**, *107*, 4584–4671.
- (307) Wang, H. H.; Hou, L.; Li, Y. Z.; Jiang, C. Y.; Wang, Y. Y.; Zhu, Z. *ACS Appl. Mater. Interfaces* **2017**, *9*, 17969–17976.
- (308) Cychosz, K. A.; Matzger, A. J. *Langmuir* **2010**, *26*, 17198–17202.
- (309) Little, I. R.; Straughan, B. P.; Thornton, P. J. *Chem. Soc. Dalt. Trans.* **1986**, *10*, 2211–2214.
- (310) Jasuja, H.; Walton, K. S. *Dalt. Trans.* **2013**, *42*, 15421.
- (311) Li, H.; Eddaoudi, M.; Groy, T. L.; Yaghi, O. M. *J. Am. Chem. Soc.* **1998**, *120*, 8571–8572.
- (312) Cheon, Y. E.; Suh, M. P. *Chem. Commun.* **2009**, *17*, 2296.
- (313) Yaghi, O. K.; Morris, W.; Hayashi, H.; Asta, M.; Laird, B. B.; Leung, B.; He, N.; Furukawa, H.; Yaghi, O. M.; Houndonougbo, Y. A. *J. Am. Chem. Soc.* **2010**, *132*, 11006–11008.
- (314) Vaidhyanathan, R.; Iremonger, S. S.; Dawson, K. W.; Shimizu, G. K. H. *Chem. Commun.* **2009**, *35*, 5230.
- (315) Yang, S.; Lin, X.; Lewis, W.; Suyetin, M.; Bichoutskaia, E.; Parker, J. E.; Tang, C. C.; Allan, D. R.; Rizkallah, P. J.; Hubberstey, P. *Nat. Mater.* **2012**, *11*, 710–716.
- (316) Myers, A. L.; Prausnitz, J. M. *AIChE J.* **1965**, *11*, 121–127.
- (317) Krishna, R.; Van Baten, J. M. *Phys. Chem. Chem. Phys.* **2011**, *13*, 10593–10616.

APPENDIX

Table A1. Crystallographic data and structure refinement parameters for **1** and **4**.

Compound	1	4
Empirical formula	C ₆₄ H ₇₄ Mn ₂ N ₆ O ₁₀ Si ₂	C ₆₄ H ₇₄ N ₆ O ₁₀ Si ₂ Cd ₂
Formula weight	1253.35	1368.27
Temperature/K	296.15	296.15
Crystal system	triclinic	triclinic
Space group	<i>P</i> $\bar{1}$	<i>P</i> $\bar{1}$
a/Å	8.7239(2)	8.2227(10)
b/Å	13.9878(4)	13.2417(17)
c/Å	14.5801(4)	13.6655(18)
α /°	98.608(2)	98.980(2)
β /°	100.9110(10)	102.437(2)
γ /°	104.0960(10)	104.636(2)
Volume/Å ³	1658.23(8)	1370.5(3)
Z	1	1
$\rho_{\text{calc}}/\text{cm}^3$	1.255	1.658
μ/mm^{-1}	0.475	0.891
F(000)	658	704
Crystal size/mm ³	0.2 × 0.2 × 0.2	0.2 × 0.15 × 0.15
Radiation	MoK α (λ = 0.71073)	MoK α (λ = 0.71073)
2 θ range for data collection/°	2.906 to 50.136	3.13 to 50.164
Index ranges	-10 ≤ h ≤ 10, -16 ≤ k ≤ 16, -17 ≤ l ≤ 17	-9 ≤ h ≤ 9, -15 ≤ k ≤ 15, -16 ≤ l ≤ 16
Reflections collected	44511	18002
Independent reflections	5899 [R _{int} = 0.0397, R _{sigma} = 0.0206]	4872 [R _{int} = 0.0362, R _{sigma} = 0.0377]
Data/restraints/parameters	5899/0/385	4872/0/385
Goodness-of-fit on F ²	1.026	1.057
Final R indexes [I ≥ 2 σ (I)]	R ₁ = 0.0301, wR ₂ = 0.0805	R ₁ = 0.0336, wR ₂ = 0.0713
Final R indexes [all data]	R ₁ = 0.0350, wR ₂ = 0.0849	R ₁ = 0.0442, wR ₂ = 0.0752
Largest diff. peak/hole / e Å ⁻³	0.28/-0.30	0.34/-0.49

^aR₁ = $\Sigma ||F_o| - |F_c|| / \Sigma |F_o|$, ^bwR₂ = $[\Sigma w(F_o^2 - F_c^2)^2 / \Sigma w(F_o^2)^2]^{1/2}$, where $w = 1 / [\sigma^2(F_o^2) + (aP)^2 + bP]$, $P = (F_o^2 + 2F_c^2) / 3$

Table A2. Crystallographic data and structure refinement parameters for **5**, **9** and **10**.

Compound	5	9	10
Empirical formula	C ₆₀ H ₆₂ Mn ₂ N ₆ O ₁₂	C ₆₀ H ₆₂ N ₆ O ₁₂ Zn ₂	C ₆₀ H ₆₂ Cd ₂ N ₆ O ₁₂
Formula weight	1169.03	1189.89	1283.95
Temperature/K	296.15	296.15	296.15
Crystal system	triclinic	triclinic	triclinic
Space group	<i>P</i> $\bar{1}$	<i>P</i> $\bar{1}$	<i>P</i> $\bar{1}$
<i>a</i> /Å	9.061(3)	9.017(4)	9.2466(16)
<i>b</i> /Å	9.991(3)	10.047(5)	10.1167(18)
<i>c</i> /Å	17.405(5)	17.543(10)	17.518(3)
α /°	73.892(4)	73.400(6)	73.518(2)
β /°	87.146(4)	87.639(7)	86.683(2)
γ /°	63.605(4)	63.565(5)	63.544(2)
Volume/Å ³	1351.0(7)	1357.0(12)	1402.4(4)
<i>Z</i>	1	1	1
ρ_{calc} /cm ³	1.437	1.456	1.52
μ /mm ⁻¹	0.539	0.955	0.827
F(000)	610	620	656
Crystal size/mm ³	0.2 × 0.2 × 0.2	0.15 × 0.15 × 0.15	0.2 × 0.15 × 0.15
Radiation	MoK α (λ = 0.71073)	MoK α (λ = 0.71073)	MoK α (λ = 0.71073)
2 θ range for data collection/°	2.444 to 50.24	2.434 to 50.332	2.432 to 50
Index ranges	-10 ≤ <i>h</i> ≤ 10, -11 ≤ <i>k</i> ≤ 11, -20 ≤ <i>l</i> ≤ 20	-10 ≤ <i>h</i> ≤ 10, -12 ≤ <i>k</i> ≤ 11, -20 ≤ <i>l</i> ≤ 20	-10 ≤ <i>h</i> ≤ 10, -12 ≤ <i>k</i> ≤ 12, -20 ≤ <i>l</i> ≤ 20
Reflections collected	19882	18708	14344
Independent reflections	4793 [<i>R</i> _{int} = 0.0366, <i>R</i> _{sigma} = 0.0339]	4811 [<i>R</i> _{int} = 0.0299, <i>R</i> _{sigma} = 0.0255]	4870 [<i>R</i> _{int} = 0.0260, <i>R</i> _{sigma} = 0.0283]
Data/restraints/parameters	4793/0/365	4811/3/370	4870/0/365
Goodness-of-fit on <i>F</i> ²	1.069	1.166	1.121
Final <i>R</i> indexes [<i>I</i> ≥ 2 σ (<i>I</i>)]	<i>R</i> ₁ = 0.0341, <i>wR</i> ₂ = 0.0804	<i>R</i> ₁ = 0.0386, <i>wR</i> ₂ = 0.1145	<i>R</i> ₁ = 0.0255, <i>wR</i> ₂ = 0.0767
Final <i>R</i> indexes [all data]	<i>R</i> ₁ = 0.0424, <i>wR</i> ₂ = 0.0910	<i>R</i> ₁ = 0.0417, <i>wR</i> ₂ = 0.1206	<i>R</i> ₁ = 0.0291, <i>wR</i> ₂ = 0.0854
Largest diff. peak/hole / e Å ⁻³	0.30/-0.44	0.86/-0.35	0.32/-0.35

^a*R*₁ = $\Sigma||F_o| - |F_c||/\Sigma|F_o|$. ^b*wR*₂ = $[\Sigma w(F_o^2 - F_c^2)^2/\Sigma w(F_o^2)^2]^{1/2}$, where $w = 1/[\sigma^2(F_o^2) + (aP)^2 + bP]$, $P = (F_o^2 + 2F_c^2)/3$

Table A3. Crystallographic data and structure refinement parameters for **11** and **11a**.

Compound	11	11a
Empirical formula	C ₃₀ H ₃₂ MnN ₃ O ₅ Si ·C ₃ H ₇ NO	C ₃₀ H ₃₂ MnN ₃ O ₅ Si
Formula weight	670.71	597.61
Temperature/K	100.15	296.15
Crystal system	triclinic	triclinic
Space group	<i>P</i> $\bar{1}$	<i>P</i> $\bar{1}$
a/Å	9.17(2)	8.537(3)
b/Å	14.46(3)	12.938(4)
c/Å	14.84(3)	14.713(5)
α /°	100.33(3)	104.535(4)
β /°	103.91(3)	94.021(4)
γ /°	99.75(3)	102.967(4)
Volume/Å ³	1833(7)	1519.1(8)
Z	2	2
ρ_{calc} /cm ³	1.215	1.306
μ /mm ⁻¹	0.437	0.516
F(000)	704	624
Crystal size/mm ³	0.15 × 0.15 × 0.15	0.1 × 0.1 × 0.1
Radiation	MoK α (λ = 0.71073)	MoK α (λ = 0.71073)
2 θ range for data collection/°	2.906 to 51.506	2.886 to 50.014
Index ranges	-11 ≤ h ≤ 11, -17 ≤ k ≤ 17, -18 ≤ l ≤ 18	-10 ≤ h ≤ 10, -15 ≤ k ≤ 15, -17 ≤ l ≤ 17
Reflections collected	40751	14419
Independent reflections	6924 [<i>R</i> _{int} = 0.2652, <i>R</i> _{sigma} = 0.1964]	5176 [<i>R</i> _{int} = 0.0274, <i>R</i> _{sigma} = 0.0370]
Data/restraints/parameters	6924/0/395	5176/0/364
Goodness-of-fit on F ²	0.925	1.025
Final R indexes [<i>I</i> ≥ 2 σ (<i>I</i>)]	<i>R</i> ₁ = 0.0840, <i>wR</i> ₂ = 0.1931	<i>R</i> ₁ = 0.0364, <i>wR</i> ₂ = 0.0873
Final R indexes [all data]	<i>R</i> ₁ = 0.2011, <i>wR</i> ₂ = 0.2525	<i>R</i> ₁ = 0.0492, <i>wR</i> ₂ = 0.0937
Largest diff. peak/hole / e Å ⁻³	0.61/-0.76	0.60/-0.28

^a*R*₁ = $\sum ||F_o| - |F_c|| / \sum |F_o|$. ^b*wR*₂ = $[\sum w(F_o^2 - F_c^2)^2 / \sum w(F_o^2)^2]^{1/2}$, where $w = 1/[\sigma^2(F_o^2) + (aP)^2 + bP]$, $P = (F_o^2 + 2F_c^2)/3$

Table A4. Crystallographic data and structure refinement parameters for **12** and **13**.

Compound	12	13
Empirical formula	C ₃₁ H ₃₄ MnN ₃ O ₅ Si ·C ₃ H ₇ NO	C ₃₂ H ₃₂ MnN ₃ O ₄ Si ·1.5CH ₄ O
Formula weight	684.74	653.67
Temperature/K	100	100.15
Crystal system	triclinic	monoclinic
Space group	<i>P</i> $\bar{1}$	<i>C</i> 2/ <i>c</i>
<i>a</i> /Å	9.116(3)	29.443(4)
<i>b</i> /Å	13.296(4)	14.253(2)
<i>c</i> /Å	15.134(4)	15.491(2)
α /°	106.697(7)	90
β /°	98.174(8)	99.570(4)
γ /°	95.093(7)	90
Volume/Å ³	1722.7(8)	6410.1(16)
Z	2	8
ρ_{calc} /cm ³	1.32	1.348
μ /mm ⁻¹	0.467	0.496
F(000)	720	2720
Crystal size/mm ³	0.15 × 0.15 × 0.1	0.2 × 0.2 × 0.2
Radiation	MoK α (λ = 0.71073)	MoK α (λ = 0.71073)
2 Θ range for data collection/°	2.854 to 50	2.806 to 50.158
Index ranges	-10 ≤ <i>h</i> ≤ 10, -15 ≤ <i>k</i> ≤ 15, -14 ≤ <i>l</i> ≤ 17	-34 ≤ <i>h</i> ≤ 34, -16 ≤ <i>k</i> ≤ 16, -18 ≤ <i>l</i> ≤ 17
Reflections collected	23099	43767
Independent reflections	6013 [<i>R</i> _{int} = 0.0966, <i>R</i> _{sigma} = 0.1156]	5686 [<i>R</i> _{int} = 0.0617, <i>R</i> _{sigma} = 0.0426]
Data/restraints/parameters	6013/0/420	5686/0/407
Goodness-of-fit on F ²	0.912	1.111
Final R indexes [<i>I</i> ≥ 2 σ (<i>I</i>)]	<i>R</i> ₁ = 0.0589, <i>wR</i> ₂ = 0.1324	<i>R</i> ₁ = 0.0647, <i>wR</i> ₂ = 0.1616
Final R indexes [all data]	<i>R</i> ₁ = 0.1178, <i>wR</i> ₂ = 0.1677	<i>R</i> ₁ = 0.0843, <i>wR</i> ₂ = 0.1797
Largest diff. peak/hole / e Å ⁻³	0.66/-0.60	0.96/-0.66

^a*R*₁ = $\sum ||F_o| - |F_c|| / \sum |F_o|$. ^b*wR*₂ = $[\sum w(F_o^2 - F_c^2)^2 / \sum w(F_o^2)^2]^{1/2}$, where $w = 1/[\sigma^2(F_o^2) + (aP)^2 + bP]$, $P = (F_o^2 + 2F_c^2)/3$

Table A5. Crystallographic data and structure refinement parameters for **14**, **15** and **16**.

Compound	14	15	16
Empirical formula	C ₂₈ H ₂₄ MnN ₃ O ₅	C ₂₉ H ₂₈ MnN ₃ O ₆	C ₃₀ H ₂₈ MnN ₃ O ₇ ·3H ₂ O·C ₂ H ₆ O
Formula weight	537.44	569.48	697.61
Temperature/K	100.15	296.15	100.15
Crystal system	monoclinic	triclinic	triclinic
Space group	<i>P</i> 2 ₁ / <i>c</i>	<i>P</i> $\bar{1}$	<i>P</i> $\bar{1}$
<i>a</i> /Å	13.7464(17)	9.181(3)	9.879(4)
<i>b</i> /Å	11.1242(14)	9.845(3)	12.369(4)
<i>c</i> /Å	15.5064(19)	17.095(6)	14.629(5)
α /°	90	94.855(6)	69.652(7)
β /°	98.587(2)	102.083(6)	87.876(7)
γ /°	90	115.960(5)	71.709(7)
Volume/Å ³	2344.6(5)	1331.0(8)	1586.2(10)
<i>Z</i>	4	2	2
ρ_{calc} /cm ³	1.523	1.421	1.461
μ /mm ⁻¹	0.61	0.545	0.483
<i>F</i> (000)	1112	592	732
Crystal size/mm ³	0.2 × 0.2 × 0.2	0.2 × 0.2 × 0.2	0.2 × 0.2 × 0.2
Radiation	MoK α (λ = 0.71073)	MoK α (λ = 0.71073)	MoK α (λ = 0.71073)
2 θ range for data collection/°	2.996 to 50.572	2.486 to 50.282	2.978 to 50.302
Index ranges	-16 ≤ <i>h</i> ≤ 16, -13 ≤ <i>k</i> ≤ 13, -18 ≤ <i>l</i> ≤ 18	-10 ≤ <i>h</i> ≤ 10, -11 ≤ <i>k</i> ≤ 11, -20 ≤ <i>l</i> ≤ 20	-11 ≤ <i>h</i> ≤ 11, -14 ≤ <i>k</i> ≤ 14, -17 ≤ <i>l</i> ≤ 17
Reflections collected	31311	19683	21791
Independent reflections	4237 [<i>R</i> _{int} = 0.0287, <i>R</i> _{sigma} = 0.0176]	4735 [<i>R</i> _{int} = 0.0210, <i>R</i> _{sigma} = 0.0168]	5647 [<i>R</i> _{int} = 0.0386, <i>R</i> _{sigma} = 0.0326]
Data/restraints/parameters	4237/0/338	4735/4/358	5647/5/456
Goodness-of-fit on <i>F</i> ²	1.055	1.091	1.1
Final <i>R</i> indexes [<i>I</i> ≥ 2 σ (<i>I</i>)]	<i>R</i> ₁ = 0.0332, <i>wR</i> ₂ = 0.0794	<i>R</i> ₁ = 0.0258, <i>wR</i> ₂ = 0.0670	<i>R</i> ₁ = 0.0454, <i>wR</i> ₂ = 0.1257
Final <i>R</i> indexes [all data]	<i>R</i> ₁ = 0.0391, <i>wR</i> ₂ = 0.0843	<i>R</i> ₁ = 0.0299, <i>wR</i> ₂ = 0.0768	<i>R</i> ₁ = 0.0516, <i>wR</i> ₂ = 0.1336
Largest diff. peak/hole / e Å ⁻³	0.94/-0.87	0.27/-0.21	1.55/-0.90

^a*R*₁ = $\Sigma ||F_o| - |F_c|| / \Sigma |F_o|$. ^b*wR*₂ = $[\Sigma w(F_o^2 - F_c^2)^2 / \Sigma w(F_o^2)^2]^{1/2}$, where $w = 1/[\sigma^2(F_o^2) + (aP)^2 + bP]$, $P = (F_o^2 + 2F_c^2)/3$

Table A6. Crystallographic data and structure refinement parameters for **17**, **18** and **19**.

Compound	17	18	19
Empirical formula	C ₅₈ H ₅₈ Cd ₂ N ₆ O ₉ Si ₂ ·6H ₂ O	C ₃₀ H ₃₀ CdN ₃ O ₄ Si·H ₂ O	C ₂₈ H ₂₄ CdN ₃ O ₅
Formula weight	1372.13	655.07	594.9
Temperature/K	100.15	100.15	100.15
Crystal system	triclinic	triclinic	monoclinic
Space group	<i>P</i> $\bar{1}$	<i>P</i> $\bar{1}$	<i>P</i> 2 ₁ / <i>c</i>
<i>a</i> /Å	12.7350(18)	8.133(8)	13.9336(8)
<i>b</i> /Å	14.644(2)	13.810(14)	11.1454(6)
<i>c</i> /Å	20.253(3)	15.225(15)	15.6711(9)
α /°	93.692(2)	65.005(10)	90
β /°	103.780(2)	78.268(12)	98.689(2)
γ /°	114.824(2)	81.345(12)	90
Volume/Å ³	3270.8(8)	1513(3)	2405.7(2)
<i>Z</i>	2	2	4
ρ_{calc} /cm ³	1.387	1.438	1.643
μ /mm ⁻¹	0.752	0.803	0.954
F(000)	1396	670	1204
Crystal size/mm ³	0.2 × 0.2 × 0.2	0.2 × 0.2 × 0.2	0.2 × 0.2 × 0.2
Radiation	MoK α (λ = 0.71073)	MoK α (λ = 0.71073)	MoK α (λ = 0.71073)
2 θ range for data collection/°	2.108 to 50.348	2.988 to 50.35	2.956 to 49.836
Index ranges	-15 ≤ <i>h</i> ≤ 15, -17 ≤ <i>k</i> ≤ 17, -24 ≤ <i>l</i> ≤ 24	-9 ≤ <i>h</i> ≤ 9, -16 ≤ <i>k</i> ≤ 14, -18 ≤ <i>l</i> ≤ 18	-16 ≤ <i>h</i> ≤ 16, -13 ≤ <i>k</i> ≤ 11, -18 ≤ <i>l</i> ≤ 18
Reflections collected	38926	9883	13375
Independent reflections	11723 [R _{int} = 0.0238, R _{sigma} = 0.0233]	4664 [R _{int} = 0.0434, R _{sigma} = 0.0793]	4201 [R _{int} = 0.0272, R _{sigma} = 0.0291]
Data/restraints/parameters	11723/3/774	4664/0/366	4201/0/334
Goodness-of-fit on F ²	1.104	1.064	1.082
Final R indexes [I >= 2 σ (I)]	R ₁ = 0.0367, wR ₂ = 0.1258	R ₁ = 0.0539, wR ₂ = 0.1246	R ₁ = 0.0325, wR ₂ = 0.0830
Final R indexes [all data]	R ₁ = 0.0438, wR ₂ = 0.1345	R ₁ = 0.0902, wR ₂ = 0.1407	R ₁ = 0.0418, wR ₂ = 0.0969
Largest diff. peak/hole / e Å ⁻³	1.26/-0.63	1.19/-0.88	0.95/-0.38

$${}^a R_1 = \sum |F_o| - |F_c| / \sum |F_o|, {}^b wR_2 = [\sum w(F_o^2 - F_c^2)^2 / \sum w(F_o^2)^2]^{1/2}, \text{ where } w = 1 / [\sigma^2(F_o^2) + (aP)^2 + bP], P = (F_o^2 + 2F_c^2) / 3$$

Table A7. Crystallographic data and structure refinement parameters for **20**, **21** and **22**.

Compound	20	21	22
Empirical formula	C ₁₆ H ₁₆ O ₅ SiZn .2H ₂ O	C ₂₁ H ₁₈ NO ₄ SiZn	C ₄₄ H ₃₈ N ₄ O ₈ Si ₂ Zn ₂ ·C ₃ H ₇ NO·2H ₂ O
Formula weight	417.79	441.82	1046.87
Temperature/K	296.15	296.15	100.15
Crystal system	monoclinic	triclinic	triclinic
Space group	C2/m	P $\bar{1}$	P $\bar{1}$
a/Å	13.4779(10)	8.1804(3)	13.261(5)
b/Å	22.9307(16)	10.7252(4)	13.274(5)
c/Å	13.9851(10)	12.2049(5)	17.946(7)
α /°	90	70.453(2)	68.981(5)
β /°	118.536(2)	79.290(2)	70.475(5)
γ /°	90	87.263(2)	60.524(5)
Volume/Å ³	3797.1(5)	991.40(7)	2518.2(17)
Z	8	2	2
ρ calc/gcm ³	1.332	1.48	1.237
μ /mm ⁻¹	1.375	1.326	1.049
F(000)	1560	454	964
Crystal size/mm ³	0.15 × 0.15 × 0.15	0.2 × 0.2 × 0.2	0.2 × 0.2 × 0.2
Radiation	MoK α (λ = 0.71073)	MoK α (λ = 0.71073)	MoK α (λ = 0.71073)
2 θ range for data collection/°	3.314 to 50.048	3.6 to 50.018	2.478 to 50.376
Index ranges	-16 ≤ h ≤ 14, -27 ≤ k ≤ 22, -11 ≤ l ≤ 16	-9 ≤ h ≤ 9, -12 ≤ k ≤ 12, -14 ≤ l ≤ 14	-15 ≤ h ≤ 15, -15 ≤ k ≤ 15, -21 ≤ l ≤ 21
Reflections collected	8907	15387	30118
Independent reflections	2772 [R _{int} = 0.0349, R _{sigma} = 0.0632]	3499 [R _{int} = 0.0229, R _{sigma} = 0.0201]	8918 [R _{int} = 0.0469, R _{sigma} = 0.0558]
Data/restraints/parameters	2772/0/209	3499/0/255	8918/0/545
Goodness-of-fit on F ²	1.265	1.054	0.977
Final R indexes [I ≥ 2 σ (I)]	R1 = 0.0806, wR2 = 0.2783	R1 = 0.0393, wR2 = 0.1058	R1 = 0.0362, wR2 = 0.0916
Final R indexes [all data]	R1 = 0.1384, wR2 = 0.3198	R1 = 0.0432, wR2 = 0.1090	R1 = 0.0542, wR2 = 0.1041
Largest diff. peak/hole / e Å ⁻³	1.58/-1.00	0.77/-0.59	0.35/-0.30

^aR₁ = $\Sigma||F_o| - |F_c||/\Sigma|F_o|$. ^bwR₂ = $[\Sigma w(F_o^2 - F_c^2)^2/\Sigma w(F_o^2)^2]^{1/2}$, where $w = 1/[\sigma^2(F_o^2) + (aP)^2 + bP]$, $P = (F_o^2 + 2F_c^2)/3$

Table A8. Crystallographic data and structure refinement parameters for **23**, **24** and **25**.

Compound	23	24	25
Empirical formula	C ₄₈ H ₄₈ N ₄ O ₈ Si ₂ Zn ₂ ·2C ₃ H ₇ NO·2H ₂ O	C ₄₆ H ₄₂ N ₄ O ₈ Si ₂ Zn ₂ ·3C ₂ H ₆ O·3H ₂ O	C ₄₅ H ₄₂ N ₂ O ₈ Si ₂ Zn ₂ ·C ₃ H ₇ NO·H ₂ O
Formula weight	1178.08	1158.05	1016.88
Temperature/K	100.15	296.15	296.15
Crystal system	triclinic	triclinic	monoclinic
Space group	<i>P</i> $\bar{1}$	<i>P</i> $\bar{1}$	<i>C</i> 2/ <i>c</i>
<i>a</i> /Å	13.080(2)	13.486(3)	23.003(3)
<i>b</i> /Å	13.143(2)	14.415(4)	13.1853(18)
<i>c</i> /Å	19.188(4)	16.827(4)	31.317(4)
α /°	76.109(3)	68.298(3)	90
β /°	75.530(3)	76.898(3)	91.559(2)
γ /°	61.060(2)	72.661(3)	90
Volume/Å ³	2767.5(9)	2876.0(12)	9495(2)
Z	2	2	8
ρ_{calc} /cm ³	1.137	1.115	1.294
μ /mm ⁻¹	0.956	0.92	1.111
F(000)	936	996	3816
Crystal size/mm ³	0.1 × 0.1 × 0.1	0.2 × 0.2 × 0.2	0.2 × 0.2 × 0.2
Radiation	MoK α (λ = 0.71073)	MoK α (λ = 0.71073)	MoK α (λ = 0.71073)
2 θ range for data collection/°	2.214 to 50.158	2.628 to 49.96	2.602 to 50.11
Index ranges	-15 ≤ <i>h</i> ≤ 15, -15 ≤ <i>k</i> ≤ 15, -22 ≤ <i>l</i> ≤ 22	-15 ≤ <i>h</i> ≤ 15, -17 ≤ <i>k</i> ≤ 17, -19 ≤ <i>l</i> ≤ 19	-27 ≤ <i>h</i> ≤ 27, -15 ≤ <i>k</i> ≤ 15, -37 ≤ <i>l</i> ≤ 37
Reflections collected	37035	38892	54651
Independent reflections	9742 [R _{int} = 0.0952, R _{sigma} = 0.1141]	9931 [R _{int} = 0.0433, R _{sigma} = 0.0485]	8400 [R _{int} = 0.0710, R _{sigma} = 0.0577]
Data/restraints/parameters	9742/0/577	9931/0/565	8400/0/536
Goodness-of-fit on F ²	0.973	1.006	1.138
Final R indexes [I ≥ 2 σ (I)]	R ₁ = 0.0691, wR ₂ = 0.1812	R ₁ = 0.0476, wR ₂ = 0.1420	R ₁ = 0.0776, wR ₂ = 0.1790
Final R indexes [all data]	R ₁ = 0.1222, wR ₂ = 0.2125	R ₁ = 0.0636, wR ₂ = 0.1506	R ₁ = 0.0975, wR ₂ = 0.1921
Largest diff. peak/hole / e Å ⁻³	0.89/-0.59	0.93/-0.36	0.72/-0.58

$${}^a R_1 = \sum ||F_o| - |F_c|| / \sum |F_o|, {}^b wR_2 = [\sum w(F_o^2 - F_c^2)^2 / \sum w(F_o^2)^2]^{1/2}, \text{ where } w = 1/[\sigma^2(F_o^2) + (aP)^2 + bP], P = (F_o^2 + 2F_c^2)/3$$

Table A9. Crystallographic data and structure refinement parameters for **26** and **27**.

Compound	26	27
Empirical formula	C ₂₁ H ₁₈ MnNO ₄ Si	C ₄₀ H ₃₆ Mn ₂ NO ₉ Si ₂
Formula weight	431.39	840.76
Temperature/K	296.15	100.15
Crystal system	triclinic	triclinic
Space group	<i>P</i> $\bar{1}$	<i>P</i> $\bar{1}$
a/Å	8.540(8)	12.5263(5)
b/Å	10.782(10)	13.1229(6)
c/Å	11.338(10)	13.2481(6)
α /°	73.360(12)	62.821(2)
β /°	82.601(13)	80.312(2)
γ /°	87.137(12)	79.025(2)
Volume/Å ³	991.8(16)	1893.59(15)
Z	2	2
$\rho_{\text{calc}}/\text{cm}^3$	1.444	1.475
μ/mm^{-1}	0.753	0.787
F(000)	444	866
Crystal size/mm ³	0.15 × 0.15 × 0.15	0.2 × 0.2 × 0.2
Radiation	MoK α ($\lambda = 0.71073$)	MoK α ($\lambda = 0.71073$)
2 θ range for data collection/°	3.944 to 50.032	3.326 to 50.136
Index ranges	-10 ≤ h ≤ 10, -12 ≤ k ≤ 12, -13 ≤ l ≤ 13	-14 ≤ h ≤ 14, -15 ≤ k ≤ 15, -15 ≤ l ≤ 15
Reflections collected	10602	23472
Independent reflections	3454 [<i>R</i> _{int} = 0.1445, <i>R</i> _{sigma} = 0.1838]	6654 [<i>R</i> _{int} = 0.0393, <i>R</i> _{sigma} = 0.0398]
Data/restraints/parameters	3454/0/255	6654/0/492
Goodness-of-fit on <i>F</i> ²	1.067	1.191
Final <i>R</i> indexes [<i>I</i> ≥ 2 σ (<i>I</i>)]	<i>R</i> ₁ = 0.0942, <i>wR</i> ₂ = 0.2527	<i>R</i> ₁ = 0.0702, <i>wR</i> ₂ = 0.2368
Final <i>R</i> indexes [all data]	<i>R</i> ₁ = 0.1795, <i>wR</i> ₂ = 0.2968	<i>R</i> ₁ = 0.0799, <i>wR</i> ₂ = 0.2413
Largest diff. peak/hole / e Å ⁻³	0.85/-0.92	1.84/-0.68

^a*R*₁ = $\sum ||F_o| - |F_c|| / \sum |F_o|$, ^b*wR*₂ = $[\sum w(F_o^2 - F_c^2)^2 / \sum w(F_o^2)^2]^{1/2}$, where $w = 1/[\sigma^2(F_o^2) + (aP)^2 + bP]$, $P = (F_o^2 + 2F_c^2)/3$

Table A10. Crystallographic data and structure refinement parameters for **28**, **29** and **30**.

Compound	28	29	30
Empirical formula	C ₆₀ H ₅₅ Mn ₃ N ₂ O ₁₄ Si ₃ ·C ₆ H ₅ N·C ₃ H ₇ NO ·H ₂ O	C ₅₉ H ₅₄ Mn ₃ N ₄ O ₁₄ Si ₃ ·C ₄ H ₄ N ₂ ·C ₃ H ₇ NO ·2H ₂ O	C ₄₄ H ₄₂ Mn ₂ N ₂ O ₉ Si ₂
Formula weight	1459.37	1481.34	908.85
Temperature/K	100.15	100.15	100.15
Crystal system	monoclinic	monoclinic	orthorhombic
Space group	<i>P2₁/n</i>	<i>P2₁/n</i>	<i>Pbcn</i>
<i>a</i> /Å	13.5567(8)	13.5144(9)	26.813(3)
<i>b</i> /Å	22.6042(13)	22.7241(15)	12.2970(12)
<i>c</i> /Å	22.3840(13)	21.9784(13)	12.297
α /°	90	90	90
β /°	97.390(3)	96.200(4)	90
γ /°	90	90	90
Volume/Å ³	6802.3(7)	6710.1(7)	4054.5(6)
<i>Z</i>	4	4	4
ρ_{calc} /cm ³	1.425	1.462	1.489
μ /mm ⁻¹	0.672	0.684	0.742
F(000)	3024	3052	1880
Crystal size/mm ³	0.2 × 0.2 × 0.2	0.2 × 0.2 × 0.2	0.2 × 0.2 × 0.2
Radiation	MoK α (λ = 0.71073)	MoK α (λ = 0.71073)	MoK α (λ = 0.71073)
2 θ range for data collection/°	2.572 to 50	2.586 to 50.3	3.038 to 50.212
Index ranges	-10 ≤ <i>h</i> ≤ 16, -26 ≤ <i>k</i> ≤ 24, -26 ≤ <i>l</i> ≤ 26	-16 ≤ <i>h</i> ≤ 16, -24 ≤ <i>k</i> ≤ 27, -26 ≤ <i>l</i> ≤ 25	-31 ≤ <i>h</i> ≤ 31, -12 ≤ <i>k</i> ≤ 14, -14 ≤ <i>l</i> ≤ 14
Reflections collected	63447	49077	21726
Independent reflections	11971 [R _{int} = 0.0447, R _{sigma} = 0.0395]	11917 [R _{int} = 0.0612, R _{sigma} = 0.0578]	3610 [R _{int} = 0.0714, R _{sigma} = 0.0455]
Data/restraints/parameters	11971/4/874	11917/0/870	3610/0/273
Goodness-of-fit on F ²	1.009	1.023	1.004
Final R indexes [I ≥ 2 σ (I)]	R ₁ = 0.0416, wR ₂ = 0.0897	R ₁ = 0.0680, wR ₂ = 0.1742	R ₁ = 0.0331, wR ₂ = 0.0801
Final R indexes [all data]	R ₁ = 0.0571, wR ₂ = 0.0985	R ₁ = 0.0926, wR ₂ = 0.1942	R ₁ = 0.0466, wR ₂ = 0.0852
Largest diff. peak/hole / e Å ⁻³	1.41/-1.65	1.79/-1.14	0.47/-0.44

$${}^a R_1 = \Sigma ||F_o| - |F_c|| / \Sigma |F_o|. {}^b wR_2 = [\Sigma w(F_o^2 - F_c^2)^2 / \Sigma w(F_o^2)^2]^{1/2}, \text{ where } w = 1 / [\sigma^2(F_o^2) + (aP)^2 + bP], P = (F_o^2 + 2F_c^2) / 3$$

Table A11. Crystallographic data and structure refinement parameters for **32**, **33** and **34**.

Compound	32	33	34
Empirical formula	C ₄₄ H ₃₈ Co ₂ N ₂ O ₈ Si ₂	C ₄₄ H ₃₈ Co ₂ N ₄ O ₈ Si ₂	C ₄₈ H ₄₈ Co ₂ N ₄ O ₈ Si ₂ ·H ₂ O
Formula weight	896.8	924.82	1000.94
Temperature/K	100.15	100.15	100.15
Crystal system	triclinic	triclinic	triclinic
Space group	<i>P</i> $\bar{1}$	<i>P</i> $\bar{1}$	<i>P</i> $\bar{1}$
a/Å	13.057(12)	13.337(4)	13.1470(7)
b/Å	13.191(12)	13.377(5)	13.3667(7)
c/Å	14.987(13)	17.602(5)	19.1424(11)
α /°	67.092(11)	88.932(5)	77.439(2)
β /°	76.754(11)	69.032(4)	81.379(2)
γ /°	62.357(10)	60.311(3)	60.593(2)
Volume/Å ³	2103(3)	2498.2(14)	2856.7(3)
Z	2	2	2
ρ_{calc} /cm ³	1.417	1.229	1.161
μ /mm ⁻¹	0.901	0.761	0.672
F(000)	924	952	1036
Crystal size/mm ³	0.2 × 0.2 × 0.2	0.2 × 0.2 × 0.15	0.2 × 0.2 × 0.1
Radiation	MoK α (λ = 0.71073)	MoK α (λ = 0.71073)	MoK α (λ = 0.71073)
2 θ range for data collection/°	3.528 to 49.998	2.526 to 49.996	4.366 to 50.166
Index ranges	-15 ≤ h ≤ 15, -15 ≤ k ≤ 15, -17 ≤ l ≤ 17	-15 ≤ h ≤ 15, -15 ≤ k ≤ 14, -20 ≤ l ≤ 20	-15 ≤ h ≤ 15, -15 ≤ k ≤ 15, -22 ≤ l ≤ 22
Reflections collected	19193	26853	46536
Independent reflections	6748 [R _{int} = 0.0543, R _{sigma} = 0.0784]	8776 [R _{int} = 0.0613, R _{sigma} = 0.0763]	10113 [R _{int} = 0.1885, R _{sigma} = 0.1006]
Data/restraints/parameters	6748/135/527	8776/0/540	10113/66/634
Goodness-of-fit on F ²	1.194	1.037	1.039
Final R indexes [I ≥ 2 σ (I)]	R ₁ = 0.0716, wR ₂ = 0.1863	R ₁ = 0.0491, wR ₂ = 0.1187	R ₁ = 0.0774, wR ₂ = 0.1872
Final R indexes [all data]	R ₁ = 0.1134, wR ₂ = 0.1996	R ₁ = 0.0905, wR ₂ = 0.1443	R ₁ = 0.1081, wR ₂ = 0.2051
Largest diff. peak/hole / e Å ⁻³	0.97/-1.08	0.42/-0.36	0.73/-0.84

$${}^a R_1 = \frac{\sum ||F_o| - |F_c||}{\sum |F_o|}, {}^b wR_2 = \frac{[\sum w(F_o^2 - F_c^2)^2 / \sum w(F_o^2)^2]^{1/2}}{P}, \text{ where } w = 1/[\sigma^2(F_o^2) + (aP)^2 + bP], P = (F_o^2 + 2F_c^2)/3$$

Table A12. Crystallographic data and structure refinement parameters for **35** and **36**.

Compound	35	36
Empirical formula	C ₈₄ H ₇₂ C ₀₄ N ₈ O ₁₆ Si ₄	C ₄₅ H ₄₂ C ₀₂ N ₂ O ₈ Si ₂
Formula weight	1797.57	912.84
Temperature/K	100.15	100.15
Crystal system	triclinic	monoclinic
Space group	<i>P</i> $\bar{1}$	<i>C</i> 2/ <i>c</i>
<i>a</i> /Å	13.136(8)	23.1212(12)
<i>b</i> /Å	13.359(8)	13.1905(6)
<i>c</i> /Å	27.021(17)	31.4802(15)
α /°	83.745(7)	90
β /°	90	90.365(3)
γ /°	60.55	90
Volume/Å ³	4097(4)	9600.6(8)
<i>Z</i>	2	8
ρ_{calc} /cm ³	1.457	1.263
μ /mm ⁻¹	0.926	0.79
F(000)	1848	3776
Crystal size/mm ³	0.2 × 0.2 × 0.1	0.2 × 0.2 × 0.2
Radiation	MoK α (λ = 0.71073)	MoK α (λ = 0.71073)
2 Θ range for data collection/°	1.52 to 49.962	2.588 to 50.078
Index ranges	-15 ≤ <i>h</i> ≤ 10, -15 ≤ <i>k</i> ≤ 15, -31 ≤ <i>l</i> ≤ 32	-27 ≤ <i>h</i> ≤ 27, -15 ≤ <i>k</i> ≤ 15, -36 ≤ <i>l</i> ≤ 37
Reflections collected	27745	35779
Independent reflections	13541 [<i>R</i> _{int} = 0.1624, <i>R</i> _{sigma} = 0.2751]	8474 [<i>R</i> _{int} = 0.0442, <i>R</i> _{sigma} = 0.0472]
Data/restraints/parameters	13541/126/1053	8474/13/524
Goodness-of-fit on <i>F</i> ²	0.957	1.056
Final <i>R</i> indexes [<i>I</i> ≥ 2 σ (<i>I</i>)]	<i>R</i> ₁ = 0.0846, <i>wR</i> ₂ = 0.1417	<i>R</i> ₁ = 0.0821, <i>wR</i> ₂ = 0.2281
Final <i>R</i> indexes [all data]	<i>R</i> ₁ = 0.2407, <i>wR</i> ₂ = 0.2002	<i>R</i> ₁ = 0.0964, <i>wR</i> ₂ = 0.2374
Largest diff. peak/hole / e Å ⁻³	0.52/-0.63	1.91/-1.05

$$^a R_1 = \frac{\sum |F_o| - |F_c|}{\sum |F_o|}, ^b wR_2 = \frac{[\sum w(F_o^2 - F_c^2)^2 / \sum w(F_o^2)^2]^{1/2}}{P}, \text{ where } w = 1/[\sigma^2(F_o^2) + (aP)^2 + bP], P = (F_o^2 + 2F_c^2)/3$$

Table A13. Crystallographic data and structure refinement parameters for **37** and **38**.

Compound	37	38
Empirical formula	C ₂₅ H ₂₇ CdN ₂ O ₅ Si	C ₂₂ H ₂₁ CdN ₂ O ₅ Si·H ₂ O
Formula weight	575.97	551.91
Temperature/K	100.15	100.15
Crystal system	triclinic	triclinic
Space group	<i>P</i> $\bar{1}$	<i>P</i> $\bar{1}$
a/Å	9.1392(2)	8.5396(4)
b/Å	10.5368(2)	10.9546(6)
c/Å	14.4085(3)	13.6566(7)
α /°	108.7600(10)	110.933(3)
β /°	94.8480(10)	103.766(3)
γ /°	96.5280(10)	92.567(2)
Volume/Å ³	1294.42(5)	1147.03(10)
Z	2	2
$\rho_{\text{calc}}/\text{cm}^3$	1.478	1.598
μ/mm^{-1}	0.926	1.045
F(000)	586	558
Crystal size/mm ³	0.2 × 0.2 × 0.2	0.2 × 0.2 × 0.2
Radiation	MoK α (λ = 0.71073)	MoK α (λ = 0.71073)
2 θ range for data collection/°	3.01 to 50.062	3.318 to 50.088
Index ranges	-10 ≤ h ≤ 10, -12 ≤ k ≤ 12, -17 ≤ l ≤ 17	-10 ≤ h ≤ 10, -13 ≤ k ≤ 13, -16 ≤ l ≤ 15
Reflections collected	13237	14121
Independent reflections	4584 [R _{int} = 0.0119, R _{sigma} = 0.0126]	4049 [R _{int} = 0.0248, R _{sigma} = 0.0217]
Data/restraints/parameters	4584/0/311	4049/0/295
Goodness-of-fit on F ²	1.079	1.099
Final R indexes [I ≥ 2 σ (I)]	R ₁ = 0.0259, wR ₂ = 0.0736	R ₁ = 0.0457, wR ₂ = 0.1179
Final R indexes [all data]	R ₁ = 0.0265, wR ₂ = 0.0741	R ₁ = 0.0484, wR ₂ = 0.1206
Largest diff. peak/hole / e Å ⁻³	0.92/-0.42	2.76/-1.41

$$^a R_1 = \sum ||F_o| - |F_c|| / \sum |F_o|, ^b wR_2 = [\sum w(F_o^2 - F_c^2)^2 / \sum w(F_o^2)^2]^{1/2}, \text{ where } w = 1/[\sigma^2(F_o^2) + (aP)^2 + bP], P = (F_o^2 + 2F_c^2)/3$$

Table A14. Crystallographic data and structure refinement parameters for **39** and **40**.

Compound	39	40
Empirical formula	C ₂₉ H ₃₀ CdN ₂ O ₅ Si.C ₃ H ₇ NO	C ₃₁ H ₃₀ CdN ₂ O ₅ Si.2C ₄ H ₈ O
Formula weight	700.13	795.29
Temperature/K	100.15	100.15
Crystal system	orthorhombic	monoclinic
Space group	<i>P</i> 2 ₁ 2 ₁ 2	<i>C</i> 2/ <i>c</i>
<i>a</i> /Å	21.4397(6)	27.621(6)
<i>b</i> /Å	24.0514(5)	10.303(2)
<i>c</i> /Å	6.25270(10)	29.476(6)
α /°	90	90
β /°	90	112.316(2)
γ /°	90	90
Volume/Å ³	3224.23(12)	7760(3)
<i>Z</i>	4	8
ρ_{calc} /cm ³	1.442	1.111
μ /mm ⁻¹	0.761	0.624
F(000)	1440	2648
Crystal size/mm ³	0.2 × 0.15 × 0.15	0.2 × 0.2 × 0.2
Radiation	MoK α (λ = 0.71073)	MoK α (λ = 0.71073)
2 Θ range for data collection/°	2.544 to 50.112	2.988 to 50.15
Index ranges	-25 ≤ <i>h</i> ≤ 17, -28 ≤ <i>k</i> ≤ 28, -7 ≤ <i>l</i> ≤ 7	-32 ≤ <i>h</i> ≤ 32, -12 ≤ <i>k</i> ≤ 12, -34 ≤ <i>l</i> ≤ 34
Reflections collected	30641	48129
Independent reflections	5730 [<i>R</i> _{int} = 0.0282, <i>R</i> _{sigma} = 0.0231]	6890 [<i>R</i> _{int} = 0.0309, <i>R</i> _{sigma} = 0.0214]
Data/restraints/parameters	5730/0/393	6890/42/373
Goodness-of-fit on <i>F</i> ²	1.072	1.004
Final <i>R</i> indexes [<i>I</i> ≥ 2 σ (<i>I</i>)]	<i>R</i> ₁ = 0.0298, <i>wR</i> ₂ = 0.0670	<i>R</i> ₁ = 0.0399, <i>wR</i> ₂ = 0.1082
Final <i>R</i> indexes [all data]	<i>R</i> ₁ = 0.0318, <i>wR</i> ₂ = 0.0678	<i>R</i> ₁ = 0.0477, <i>wR</i> ₂ = 0.1121
Largest diff. peak/hole / e Å ⁻³	0.50/-0.32	1.06/-0.66
Flack parameter	0.001(7)	-----

$$^a R_1 = \sum ||F_o| - |F_c|| / \sum |F_o|. \quad ^b wR_2 = [\sum w(F_o^2 - F_c^2)^2 / \sum w(F_o^2)^2]^{1/2}, \text{ where } w = 1/[\sigma^2(F_o^2) + (aP)^2 + bP], \quad P = (F_o^2 + 2F_c^2)/3$$

Table A15. Crystallographic data and structure refinement parameters for **41** and **42**.

Compound	41	42
Empirical formula	C ₅₇ H ₅₂ N ₄ O ₁₂ Si ₂ Zn ₂ ·C ₃ H ₇ NO·2H ₂ O	C ₁₇₁ H ₁₅₆ Cd ₆ N ₁₂ O ₃₆ Si ₆ ·12C ₃ H ₇ NO·3H ₂ O
Formula weight	1281.12	4729.24
Temperature/K	100.15	100.15
Crystal system	monoclinic	monoclinic
Space group	<i>C2/c</i>	<i>C2/c</i>
a/Å	18.342(5)	19.9143(7)
b/Å	21.595(6)	21.0635(7)
c/Å	16.290(4)	48.7192(18)
α/°	90	90
β/°	95.340(3)	93.399(2)
γ/°	90	90
Volume/Å ³	6424(3)	20400.0(12)
Z	4	4
ρ _{calc} /cm ³	1.212	1.237
μ/mm ⁻¹	0.84	0.714
F(000)	2424	7704
Crystal size/mm ³	0.2 × 0.2 × 0.15	0.2 × 0.15 × 0.15
Radiation	MoKα (λ = 0.71073)	MoKα (λ = 0.71073)
2θ range for data collection/°	2.92 to 50.212	1.674 to 49.994
Index ranges	-21 ≤ h ≤ 21, -25 ≤ k ≤ 25, -19 ≤ l ≤ 19	-20 ≤ h ≤ 23, -24 ≤ k ≤ 24, -37 ≤ l ≤ 57
Reflections collected	33765	60492
Independent reflections	5702 [R _{int} = 0.0395, R _{sigma} = 0.0322]	17909 [R _{int} = 0.0773, R _{sigma} = 0.0963]
Data/restraints/parameters	5702/0/350	17909/0/1047
Goodness-of-fit on F ²	1.048	1.029
Final R indexes [I ≥ 2σ(I)]	R ₁ = 0.0622, wR ₂ = 0.1745	R ₁ = 0.0714, wR ₂ = 0.1978
Final R indexes [all data]	R ₁ = 0.0750, wR ₂ = 0.1836	R ₁ = 0.1054, wR ₂ = 0.2125
Largest diff. peak/hole / e Å ⁻³	1.42/-0.55	1.19/-1.10

$${}^a R_1 = \frac{\sum ||F_o| - |F_c||}{\sum |F_o|}, {}^b wR_2 = \frac{[\sum w(F_o^2 - F_c^2)^2 / \sum w(F_o^2)^2]^{1/2}}{P}, \text{ where } w = 1/[\sigma^2(F_o^2) + (aP)^2 + bP], P = (F_o^2 + 2F_c^2)/3$$

Table A16. Crystallographic data and structure refinement parameters for **43** and **44**.

Compound	43	44
Empirical formula	C ₅₇ H ₅₂ N ₄ O ₁₂ Si ₂ Zn ₂ ·C ₂ H ₆ O·3H ₂ O	C ₅₃ H ₄₀ Cd ₂ N ₄ O ₁₄ ·H ₂ O
Formula weight	1272.06	1199.7
Temperature/K	100.15	100.15
Crystal system	monoclinic	triclinic
Space group	Cc	$P\bar{1}$
a/Å	8.3003(5)	11.0310(9)
b/Å	26.7153(18)	11.9515(10)
c/Å	26.3110(17)	18.5131(15)
α/°	90	81.467(2)
β/°	90.138(2)	87.3840(10)
γ/°	90	88.3310(10)
Volume/Å ³	5834.3(6)	2410.6(3)
Z	4	2
ρ _{calc} /cm ³	1.448	1.653
μ/mm ⁻¹	0.936	0.959
F(000)	2648	1208
Crystal size/mm ³	0.15 × 0.15 × 0.15	0.2 × 0.2 × 0.2
Radiation	MoKα (λ = 0.71073)	MoKα (λ = 0.71073)
2θ range for data collection/°	3.048 to 50.072	2.226 to 50.068
Index ranges	-9 ≤ h ≤ 9, -31 ≤ k ≤ 31, -31 ≤ l ≤ 31	-13 ≤ h ≤ 13, -14 ≤ k ≤ 14, -22 ≤ l ≤ 22
Reflections collected	36720	38298
Independent reflections	9764 [R _{int} = 0.0461, R _{sigma} = 0.0621]	8497 [R _{int} = 0.0205, R _{sigma} = 0.0148]
Data/restraints/parameters	9764/11/772	8497/0/670
Goodness-of-fit on F ²	1.119	1.094
Final R indexes [I ≥ 2σ (I)]	R ₁ = 0.0420, wR ₂ = 0.0976	R ₁ = 0.0235, wR ₂ = 0.0572
Final R indexes [all data]	R ₁ = 0.0523, wR ₂ = 0.1169	R ₁ = 0.0251, wR ₂ = 0.0594
Largest diff. peak/hole / e Å ⁻³	0.54/-0.43	0.87/-0.99
Flack parameter	0.020(5)	

^aR₁ = Σ||F_o| - |F_c||/Σ|F_o|. ^bwR₂ = [Σw(F_o² - F_c²)²/Σw(F_o²)²]^{1/2}, where w = 1/[σ²(F_o²) + (aP)² + bP], P = (F_o² + 2F_c²)/3

Table A17. Crystallographic data and structure refinement parameters for **45**, **46** and **47**.

Compound	45	46	47
Empirical formula	C ₄₄ H ₄₂ Cd ₃ O ₁₈ Si ₂ ·H ₂ O	{[(NH ₂ (CH ₃) ₂)] ₂ · C ₅₄ H ₃₈ Cd ₂ N ₂ O ₁₂ Si ₂ ·8C ₃ H ₇ NO·2H ₂ O	{[(NH ₂ (CH ₃) ₂)]· C ₂₇ H ₁₉ CdN ₂ O ₆ Si ·2C ₃ H ₇ NO·H ₂ O
Formula weight	1270.17	1900.84	818.24
Temperature/K	100.15	100.15	100.15
Crystal system	cubic	triclinic	triclinic
Space group	<i>Pn</i> -3	<i>P</i> $\bar{1}$	<i>P</i> $\bar{1}$
a/Å	21.0021(5)	14.1230(5)	12.655(10)
b/Å	21.0021(5)	14.4916(6)	12.693(10)
c/Å	21.0021(5)	25.0292(9)	14.462(11)
α /°	90	100.146(2)	108.28(2)
β /°	90	97.120(2)	101.64(2)
γ /°	90	114.889(2)	112.02(2)
Volume/Å ³	9263.8(7)	4460.2(3)	1906(3)
Z	8	2	2
ρ_{calc} /cm ³	1.796	0.884	1.187
μ /mm ⁻¹	1.492	0.541	0.644
F(000)	4976	1192	690
Crystal size/mm ³	0.2 × 0.2 × 0.2	0.2 × 0.15 × 0.15	0.15 × 0.15 × 0.15
Radiation	MoK α (λ = 0.71073)	MoK α (λ = 0.71073)	MoK α (λ = 0.71073)
2 θ range for data collection/°	2.742 to 50.22	1.696 to 50.172	3.182 to 49.998
Index ranges	-23 ≤ h ≤ 25, -20 ≤ k ≤ 25, -24 ≤ l ≤ 24	-16 ≤ h ≤ 16, -17 ≤ k ≤ 16, -29 ≤ l ≤ 29	-15 ≤ h ≤ 15, -15 ≤ k ≤ 14, -17 ≤ l ≤ 15
Reflections collected	60896	68857	13457
Independent reflections	2776 [<i>R</i> _{int} = 0.0567, <i>R</i> _{sigma} = 0.0233]	15829 [<i>R</i> _{int} = 0.0388, <i>R</i> _{sigma} = 0.0358]	6661 [<i>R</i> _{int} = 0.0674, <i>R</i> _{sigma} = 0.1423]
Data/restraints/parameters	2776/0/207	15829/0/651	6661/24/382
Goodness-of-fit on <i>F</i> ²	1.503	0.987	0.879
Final <i>R</i> indexes [<i>I</i> ≥ 2 σ (<i>I</i>)]	<i>R</i> ₁ = 0.1044, <i>wR</i> ₂ = 0.3435	<i>R</i> ₁ = 0.0368, <i>wR</i> ₂ = 0.0979	<i>R</i> ₁ = 0.0654, <i>wR</i> ₂ = 0.1537
Final <i>R</i> indexes [all data]	<i>R</i> ₁ = 0.1228, <i>wR</i> ₂ = 0.3593	<i>R</i> ₁ = 0.0457, <i>wR</i> ₂ = 0.1006	<i>R</i> ₁ = 0.1065, <i>wR</i> ₂ = 0.1667
Largest diff. peak/hole / e Å ⁻³	6.52/-4.46	0.86/-0.31	1.04/-0.97

$$^a R_1 = \sum \|F_o\| - |F_c| / \sum \|F_o\|, ^b wR_2 = [\sum w(F_o^2 - F_c^2)^2 / \sum w(F_o^2)^2]^{1/2}, \text{ where } w = 1/[\sigma^2(F_o^2) + (aP)^2 + bP], P = (F_o^2 + 2F_c^2)/3$$

Table A18. Crystallographic data and structure refinement parameters for **48**.

Compound	48
Empirical formula	$C_{38}H_{24}Co_2N_2O_8Si \cdot H_2O \cdot 0.5C_3H_7NO$
Formula weight	836.60
Temperature/K	100
Crystal system	Tetragonal
Space group	$P4_2/mcm$
$a/\text{\AA}$	9.6299(5)
$b/\text{\AA}$	9.6299(5)
$c/\text{\AA}$	21.8959(12)
$\alpha/^\circ$	90
$\beta/^\circ$	90
$\gamma/^\circ$	90
Volume/ \AA^3	2030.5(2)
Z	2
$\rho_{\text{calc}}/\text{cm}^3$	1.28
μ/mm^{-1}	0.894
F(000)	796
Crystal size/ mm^3	$0.2 \times 0.1 \times 0.1$
Radiation	$\text{MoK}\alpha$ ($\lambda = 0.71073$)
2Θ range for data collection/ $^\circ$	5.634 to 50.164
Index ranges	$-11 \leq h \leq 11, -11 \leq k \leq 11, -26 \leq l \leq 26$
Reflections collected	34835
Independent reflections	1025 [$R_{\text{int}} = 0.0888, R_{\text{sigma}} = 0.0248$]
Data/restraints/parameters	1025/18/90
Goodness-of-fit on F^2	1.136
Final R indexes [$I \geq 2\sigma(I)$]	$R_1 = 0.0928, wR_2 = 0.2019$
Final R indexes [all data]	$R_1 = 0.0960, wR_2 = 0.2041$
Largest diff. peak/hole / $e \text{\AA}^{-3}$	0.46/-0.52

$${}^a R_1 = \sum ||F_o| - |F_c|| / \sum |F_o|. {}^b wR_2 = [\sum w(F_o^2 - F_c^2)^2 / \sum w(F_o^2)^2]^{1/2}, \text{ where } w = 1/[\sigma^2(F_o^2) + (aP)^2 + bP], P = (F_o^2 + 2F_c^2)/3$$

Table A19. Crystallographic data and structure refinement parameters for **49** and **50**.

Compound	49	50
Empirical formula	C ₃₈ H ₂₄ Cd ₂ N ₂ O ₈ Si ·H ₂ O	C ₃₈ H ₂₄ Cd ₂ N ₄ O ₈ Si ·C ₃ H ₇ NO·H ₂ O
Formula weight	907.48	1008.64
Temperature/K	100.15	100.15
Crystal system	monoclinic	Monoclinic
Space group	<i>C2/c</i>	<i>C2/c</i>
a/Å	18.5529(10)	18.418(3)
b/Å	23.4097(11)	22.052(4)
c/Å	12.2802(6)	13.571(2)
α/°	90	90
β/°	128.788(2)	129.921(7)
γ/°	90	90
Volume/Å ³	4157.3(4)	4227.4(12)
Z	4	4
ρ _{calc} /g/cm ³	1.447	1.442
μ/mm ⁻¹	1.102	1.084
F(000)	1792	1816
Crystal size/mm ³	0.2 × 0.2 × 0.2	0.2 × 0.2 × 0.2
Radiation	MoKα (λ = 0.71073)	MoKα (λ = 0.71073)
2θ range for data collection/°	3.31 to 50.022	3.544 to 50.692
Index ranges	-14 ≤ h ≤ 22, -27 ≤ k ≤ 23, -14 ≤ l ≤ 12	-21 ≤ h ≤ 21, -26 ≤ k ≤ 26, -16 ≤ l ≤ 16
Reflections collected	16460	28455
Independent reflections	3666 [R _{int} = 0.0203, R _{sigma} = 0.0160]	3828 [R _{int} = 0.0399, R _{sigma} = 0.0252]
Data/restraints/parameters	3666/0/230	3828/0/242
Goodness-of-fit on F ²	1.14	1.093
Final R indexes [I ≥ 2σ (I)]	R ₁ = 0.0736, wR ₂ = 0.2247	R ₁ = 0.0524, wR ₂ = 0.1515
Final R indexes [all data]	R ₁ = 0.0832, wR ₂ = 0.2400	R ₁ = 0.0584, wR ₂ = 0.1575
Largest diff. peak/hole / e Å ⁻³	1.58/-2.33	2.57/-0.83

$${}^a R_1 = \frac{\sum ||F_o| - |F_c||}{\sum |F_o|}, {}^b wR_2 = \frac{[\sum w(F_o^2 - F_c^2)^2 / \sum w(F_o^2)^2]^{1/2}}{P}, \text{ where } w = 1/[\sigma^2(F_o^2) + (aP)^2 + bP], P = (F_o^2 + 2F_c^2)/3$$

Table A20. Crystallographic data and structure refinement parameters for **51** and **52**.

Compound	51	52
Empirical formula	C ₃₄ H ₂₅ Cd ₂ N ₂ O ₁₀ Si ·4C ₂ H ₆ O·3H ₂ O	C ₃₈ H ₃₂ Cd ₂ N ₃ O ₁₀ Si ·5C ₃ H ₇ NO
Formula weight	1112.79	1309.02
Temperature/K	100.15	100.15
Crystal system	monoclinic	Monoclinic
Space group	<i>P</i> 2 ₁ / <i>c</i>	<i>P</i> 2 ₁ / <i>c</i>
<i>a</i> /Å	15.2629(11)	15.8382(15)
<i>b</i> /Å	23.5673(14)	23.600(2)
<i>c</i> /Å	14.9842(11)	14.7413(13)
α /°	90	90
β /°	115.271(3)	116.408(5)
γ /°	90	90
Volume/Å ³	4874.1(6)	4935.0(8)
<i>Z</i>	4	4
ρ_{calc} /cm ³	1.192	1.27
μ /mm ⁻¹	0.939	0.933
F(000)	1732	1884
Crystal size/mm ³	0.2 × 0.2 × 0.2	0.2 × 0.2 × 0.2
Radiation	MoK α (λ = 0.71073)	MoK α (λ = 0.71073)
2 Θ range for data collection/°	4.546 to 50	2.87 to 50.182
Index ranges	-18 ≤ <i>h</i> ≤ 18, -28 ≤ <i>k</i> ≤ 28, -17 ≤ <i>l</i> ≤ 17	-18 ≤ <i>h</i> ≤ 18, -25 ≤ <i>k</i> ≤ 28, -17 ≤ <i>l</i> ≤ 17
Reflections collected	92609	45856
Independent reflections	8571 [<i>R</i> _{int} = 0.1310, <i>R</i> _{sigma} = 0.1010]	8749 [<i>R</i> _{int} = 0.0295, <i>R</i> _{sigma} = 0.0211]
Data/restraints/parameters	8571/0/444	8749/0/491
Goodness-of-fit on <i>F</i> ²	1.043	1.105
Final <i>R</i> indexes [<i>I</i> ≥ 2 σ (<i>I</i>)]	<i>R</i> ₁ = 0.0931, <i>wR</i> ₂ = 0.2106	<i>R</i> ₁ = 0.0428, <i>wR</i> ₂ = 0.1273
Final <i>R</i> indexes [all data]	<i>R</i> ₁ = 0.1856, <i>wR</i> ₂ = 0.2499	<i>R</i> ₁ = 0.0493, <i>wR</i> ₂ = 0.1372
Largest diff. peak/hole / e Å ⁻³	1.31/-0.53	0.66/-0.83

$$^a R_1 = \frac{\sum |F_o| - |F_c|}{\sum |F_o|}, \quad ^b wR_2 = \frac{[\sum w(F_o^2 - F_c^2)^2 / \sum w(F_o^2)^2]^{1/2}}{P}, \quad \text{where } w = 1/[\sigma^2(F_o^2) + (aP)^2 + bP], \quad P = (F_o^2 + 2F_c^2)/3$$

Table A21. Crystallographic data and structure refinement parameters for **53** and **54**.

Compound	53	54
Empirical formula	C ₅₃ H ₄₀ N ₄ Ni ₂ O ₁₂ Si ·3C ₃ H ₇ NO·H ₂ O	C ₅₃ H ₄₀ N ₄ O ₁₂ SiZn ₂ ·3C ₃ H ₇ NO
Formula weight	1307.67	1303.04
Temperature/K	100.15	100.15
Crystal system	monoclinic	Monoclinic
Space group	C ₂	Pc
a/Å	22.751(3)	13.493(2)
b/Å	16.443(2)	14.168(2)
c/Å	19.187(3)	16.366(2)
α/°	90	90
β/°	90.366(9)	101.269(5)
γ/°	90	90
Volume/Å ³	7177.4(17)	3068.4(9)
Z	4	2
ρ _{calc} /cm ³	0.991	1.173
μ/mm ⁻¹	0.588	0.856
F(000)	2208	1112
Crystal size/mm ³	0.1 × 0.1 × 0.1	0.2 × 0.1 × 0.1
Radiation	MoKα (λ = 0.71073)	MoKα (λ = 0.71073)
2θ range for data collection/°	2.122 to 46.856	2.874 to 50.048
Index ranges	-25 ≤ h ≤ 25, -18 ≤ k ≤ 18, -21 ≤ l ≤ 21	-16 ≤ h ≤ 16, -16 ≤ k ≤ 16, -19 ≤ l ≤ 19
Reflections collected	19872	69643
Independent reflections	8698 [R _{int} = 0.0577, R _{sigma} = 0.1070]	10530 [R _{int} = 0.0617, R _{sigma} = 0.0658]
Data/restraints/parameters	8698/545/553	10530/2/625
Goodness-of-fit on F ²	1.147	0.997
Final R indexes [I ≥ 2σ (I)]	R ₁ = 0.1163, wR ₂ = 0.3088	R ₁ = 0.0678, wR ₂ = 0.1694
Final R indexes [all data]	R ₁ = 0.1306, wR ₂ = 0.3187	R ₁ = 0.0940, wR ₂ = 0.1805
Largest diff. peak/hole / e Å ⁻³	0.87/-0.63	0.57/-0.39
Flack parameter	0.179(12)	0.044(7)

^aR₁ = Σ||F_o| - |F_c||/Σ|F_o|, ^bwR₂ = [Σw(F_o² - F_c²)²/Σw(F_o²)²]^{1/2}, where w = 1/[σ²(F_o²) + (aP)² + bP], P = (F_o² + 2F_c²)/3

Table A22. Crystallographic data and structure refinement parameters for **55** and **56**.

Compound	55	56
Empirical formula	C ₃₄ H ₂₄ N ₆ O ₉ SiZn ₂ ·4H ₂ O	C ₆₀ H ₄₀ Cu ₂ N ₁₂ O ₁₀ Si ·20C ₃ H ₇ NO
Formula weight	891.48	2706.01
Temperature/K	100	100.15
Crystal system	monoclinic	Tetragonal
Space group	<i>P2₁/n</i>	<i>P4₂/n</i>
<i>a</i> /Å	9.6579(6)	22.4075(8)
<i>b</i> /Å	40.024(2)	22.4075(8)
<i>c</i> /Å	9.7499(7)	46.5308(16)
α /°	90	90
β /°	100.404(4)	90
γ /°	90	90
Volume/Å ³	3706.9(4)	23362.9(19)
Z	4	8
ρ_{calc} /cm ³	1.597	0.707
μ /mm ⁻¹	1.401	0.409
F(000)	1824	5088
Crystal size/mm ³	0.15 × 0.15 × 0.1	0.1 × 0.1 × 0.1
Radiation	MoK α (λ = 0.71073)	MoK α (λ = 0.71073)
2 Θ range for data collection/°	2.034 to 50.034	1.75 to 37.222
Index ranges	-9 ≤ <i>h</i> ≤ 11, -39 ≤ <i>k</i> ≤ 47, -11 ≤ <i>l</i> ≤ 10	-20 ≤ <i>h</i> ≤ 20, -20 ≤ <i>k</i> ≤ 14, -41 ≤ <i>l</i> ≤ 41
Reflections collected	25043	63015
Independent reflections	6537 [<i>R</i> _{int} = 0.0861, <i>R</i> _{sigma} = 0.0848]	8857 [<i>R</i> _{int} = 0.0928, <i>R</i> _{sigma} = 0.0736]
Data/restraints/parameters	6537/0/502	8857/699/672
Goodness-of-fit on <i>F</i> ²	1.119	1.07
Final <i>R</i> indexes [<i>I</i> ≥ 2 σ (<i>I</i>)]	<i>R</i> ₁ = 0.0611, <i>wR</i> ₂ = 0.1386	<i>R</i> ₁ = 0.0768, <i>wR</i> ₂ = 0.2017
Final <i>R</i> indexes [all data]	<i>R</i> ₁ = 0.1052, <i>wR</i> ₂ = 0.1633	<i>R</i> ₁ = 0.1447, <i>wR</i> ₂ = 0.2211
Largest diff. peak/hole / e Å ⁻³	0.67/-0.72	0.34/-0.43

$$^a R_1 = \frac{\sum |F_o| - |F_c|}{\sum |F_o|}, \quad ^b wR_2 = \frac{[\sum w(F_o^2 - F_c^2)^2 / \sum w(F_o^2)^2]^{1/2}}{P}, \quad \text{where } w = 1/[\sigma^2(F_o^2) + (aP)^2 + bP], \quad P = (F_o^2 + 2F_c^2)/3$$

Table A23. Selected Bond lengths (Å) for **1** and **4**.**1**

Mn1-O1	2.1395(12)	Mn1-O4 ¹	2.1354(12)
Mn1-O5	2.2371(12)	Mn1-N1	2.2809(14)
Mn1-N2	2.4091(13)	Mn1-N3	2.2647(14)

4

Cd1-O1	2.121(2)	Cd1-O3	2.117(2)
Cd1-O4	2.236(2)	Cd1-N1	2.314(3)
Cd1-N2	2.209(3)	Cd1-N3	2.219(3)

Table A24. Selected Bond lengths (Å) for **5**, **9** and **4**.**5**

Mn1-O1	2.1178(16)	Mn1-O4 ¹	2.1293(16)
Mn1-O6	2.2262(16)	Mn1-N1	2.268(2)
Mn1-N2	2.3927(19)	Mn1-N3	2.2398(19)

9

Zn1-O1	2.155(2)	Zn1-O2	2.075(2)
Zn1-O6	2.060(2)	Zn1-N1	2.127(3)
Zn1-N2	2.335(3)	Zn1-N3	2.183(3)

10

Cd1-O1	2.235(2)	Cd1-O4 ¹	2.238(2)
Cd1-O6	2.364(2)	Cd1-N1	2.348(2)
Cd1-N2	2.473(2)	Cd1-N3	2.327(2)

Table A25. Selected Bond lengths (Å) for **11** and **11a**.**11**

Mn1-O1	2.097(5)	Mn1-O3	2.110(6)
Mn1-O5	2.195(6)	Mn1-N1	2.367(7)
Mn1-N2	2.181(8)	Mn1-N3	2.268(7)

11a

Mn1-O1	2.1221(17)	Mn1-O4 ¹	2.1354(16)
Mn1-O5	2.2426(16)	Mn1-N1	2.3027(19)
Mn1-N2	2.359(2)	Mn1-N3	1.408(3)

Table A26. Selected Bond lengths (Å) for **12** and **13**.**12**

Mn1-O2	2.145(3)	Mn1-O4 ¹	2.129(4)
Mn1-O5	2.227(3)	Mn1-N1	2.266(5)
Mn1-N2	2.402(4)	Mn1-N3	2.257(3)

13

Mn1-O1 ¹	2.179(3)	Mn1-O2 ¹	2.407(4)
Mn1-O3	2.182(4)	Mn1-N1	2.431(3)
Mn1-N2	2.221(3)	Mn1-N3	2.236(3)

Table A27. Selected Bond lengths (Å) for **14**, **15** and **16**.**14**

Mn1-O1	2.1660(15)	Mn1-O4	2.2692(15)
Mn1-O5	2.2691(14)	Mn1-N1	2.3120(18)
Mn1-N2	2.4352(17)	Mn1-N3	2.2612

15

Mn1-O1	2.105(5)	Mn1-O2	2.232(5)
Mn1-O3 ¹	2.123(5)	Mn1-N1	2.240(6)
Mn1-N2	2.252(6)	Mn1-N3	2.376(6)

16

Mn1-O2	2.146(2)	Mn1-O6	2.2517(19)
Mn1-O9	2.145(2)	Mn1-N1	2.318(2)
Mn1-N2	2.416(2)	Mn1-N3	2.304(2)

Table A28. Selected Bond lengths (Å) for **17**, **18** and **19**.**17**

Cd1-O1	2.364(3)	Cd1-O4	2.377(3)
Cd1-O6	2.308(3)	Cd1-O7	2.453(3)
Cd1-O8	2.339(3)	Cd1-O8 ¹	2.562(3)
Cd1-O9 ¹	2.317(3)	Cd2-O5	2.283(3)
Cd2-N1	2.375(3)	Cd2-N2	2.471(3)
Cd2-N3	2.370(3)	Cd2-N4	2.474(3)
Cd2-N5	2.472(3)	Cd2-N6	2.481(4)

18

Cd1-O1	2.396(4)	Cd1-O3	2.344(5)
Cd1-O4	2.605(6)	Cd1-O5	2.399(5)
Cd1-N1	2.329(5)	Cd1-N2	2.537(6)
Cd1-N3	2.355(6)		

19

Cd1-O1	2.385(2)	Cd1-O2	2.399(2)
Cd1-O3	2.540(2)	Cd1-O4	2.330(2)
Cd1-N1	2.407(3)	Cd1-N2	2.515(3)
Cd1-N3	2.343(3)		

Table A29. Selected Bond lengths (Å) for **20**, **21** and **22**.**20**

Zn1-Zn1 ¹	2.921(3)	Zn2-Zn2 ⁵	2.953(4)
Zn1-O1 ²	2.019(7)	Zn2-O4 ⁵	2.110(10)
Zn1-O1 ¹	2.019(7)	Zn2-O4 ⁶	2.110(10)
Zn1-O2 ³	2.013(7)	Zn2-O5	2.052(10)
Zn1-O2	2.013(7)	Zn2-O5 ³	2.052(10)
Zn1-O3	1.946(9)	Zn2-O6	2.062(17)

21

Zn1-Zn1 ¹	2.9298(6)	Zn1-O1	2.034(2)
Zn1-O2	2.036(2)	Zn1-O3	2.043(2)
Zn1-O4 ¹	2.089(2)	Zn1-N1	2.027(2)

22

Zn1-Zn2	2.9352(12)	Zn1-O2	2.019(2)
Zn1-O4	2.076(2)	Zn1-O5	2.031(2)
Zn1-O7	2.0351(19)	Zn1-N2	2.050(2)
Zn2-O1	2.029(2)	Zn2-O3	2.0306(19)
Zn2-O6	2.032(2)	Zn2-O8	2.108(2)
Zn2-N1	2.023(2)	C11-C12	1.385(4)

Table A30. Selected Bond lengths (Å) for **23**, **24** and **25**.**23**

Zn1-Zn2	2.9443(10)	Zn1-O2	2.039(3)
Zn1-O3	2.020(3)	Zn1-O5 ¹	2.094(3)
Zn1-O7 ²	2.053(3)	Zn1-N2 ³	2.034(4)
Zn2-O1	2.027(3)	Zn2-O4	2.036(3)
Zn2-O6 ¹	2.034(3)	Zn2-O8 ²	2.141(4)
Zn2-N1	2.025(4)		

24

Zn1-Zn2 ¹	2.9223(9)	Zn1-O3 ²	2.058(2)
Zn1-O4	2.034(2)	Zn1-O5	2.023(2)
Zn1-O7 ³	2.060(2)	Zn1-N1	2.036(3)
Zn2-O1 ⁵	2.050(2)	Zn2-O2 ⁶	2.043(2)
Zn2-O6 ⁴	2.050(2)	Zn2-O8 ⁴	2.054(2)
Zn2-N2	2.035(3)		

25

Zn1-Zn2	2.9577(11)	Zn1-O1	2.093(4)
Zn1-O4	2.031(4)	Zn1-O7	2.020(4)
Zn1-O9	2.049(4)	Zn1-N1	2.024(5)
Zn2-O2	2.033(4)	Zn2-O3	2.052(4)
Zn2-O6	2.075(4)	Zn2-O8	2.037(4)
Zn2-N5	2.039(6)		

Table A31. Selected Bond lengths (Å) for **26** and **27**.**26**

Mn1-Mn1 ¹	2.992(3)	Mn1-O1 ¹	2.115(7)
Mn1-O2	2.160(7)	Mn1-O3	2.114(7)
Mn1-O4	2.146(7)	Mn1-N1	2.159(8)

27

Mn1-O2	2.102(6)	Mn1-O4	2.089(5)
Mn1-O5	2.483(5)	Mn1-O6	2.230(5)
Mn1-O7	2.163(5)	Mn1-N1	2.170(6)
Mn2-O1	2.100(6)	Mn2-O3	2.183(5)
Mn2-O5	2.136(5)	Mn2-O8	2.052(5)
Mn2-O9 ¹	2.210(5)	Mn1-Mn2	3.333(5)
Mn2-Mn2	4.309(5)		

Table A32. Selected Bond lengths (Å) for **28**, **29** and **30**.**28**

Mn1-Mn2	3.0298(6)	Mn1-O1	2.1376(19)
Mn1-O4	2.130(2)	Mn1-O6	2.164(2)
Mn1-O7	2.1629(19)	Mn1-O9	2.000(2)
Mn2-O2	2.1456(19)	Mn2-O3	2.131(2)
Mn2-O5	2.1261(19)	Mn2-O8	2.1185(19)
Mn2-O10	2.008(2)	Mn3-O11	2.156(2)
Mn3-O12	2.262(2)	Mn3-O13	2.150(2)
Mn3-O14	2.259(2)	Mn3-N1	2.244(2)
Mn3-N2 ¹	2.252(2)		

29

Mn1-Mn2 ¹	3.0330(9)	Mn1-O1 ²	2.143(3)
Mn1-O3	2.123(3)	Mn1-O6 ³	2.127(3)
Mn1-O8 ¹	2.128(3)	Mn1-O9	2.016(3)
Mn2-O2 ⁵	2.161(3)	Mn2-O4 ⁶	2.140(3)
Mn2-O7 ⁴	2.161(3)	Mn2-O11	2.123(3)
Mn2-O14	1.997(3)	Mn3-O5	2.152(3)
Mn3-O10	2.259(3)	Mn3-O12	2.234(3)
Mn3-O13 ⁶	2.147(3)	Mn3-N1 ⁴	2.270(4)
Mn3-N2	2.273(4)		

30

Mn1-O1 ¹	2.1501(14)	Mn1-O1 ²	2.2371(14)
Mn1-O2	2.3129(14)	Mn1-O3	2.0864(15)
Mn1-O4 ³	2.1417(15)	Mn1-N1	2.2734(19)

Table A33. Selected Bond lengths (Å) for **32**, **33** and **34**.**32**

Co1-O1	2.141(7)	Co1-O4	2.028(6)
Co1-O6	2.359(7)	Co1-O8	1.996(6)
Co1-N2	1.943(6)	Co2-O2	2.365(7)
Co2-O3	1.979(6)	Co2-O5	2.134(7)
Co2-O7	2.040(6)	Co2-N1	1.949(7)

33

Co1-O1	2.025(3)	Co1-O4	2.039(3)
Co1-O6	2.030(3)	Co1-O7	2.193(3)
Co1-N2	2.061(3)	Co2-O2	2.037(3)
Co2-O3	2.149(3)	Co2-O5	2.019(3)
Co2-O8	2.038(3)	Co2-N1	2.075(3)

34

Co1-O3 ¹	2.015(3)	Co1-O5	2.024(3)
Co1-O6 ¹	2.173(4)	Co1-O8	2.035(3)
Co1-N2 ²	2.072(4)	Co2-O1	2.018(3)
Co2-O2 ³	2.027(3)	Co2-O4	2.016(3)
Co2-O7 ³	2.213(4)	Co2-N1	2.049(4)

Table A34. Selected Bond lengths (Å) for **35** and **36**.**35**

Co1-O3	2.032(7)	Co1-O10 ¹	2.259(8)
Co1-O11	2.024(7)	Co1-O12 ²	2.065(7)
Co1-O13 ²	2.369(7)	Co1-N3	2.039(8)
Co2-O1	2.031(7)	Co2-O13 ²	2.284(8)
Co2-O14	2.039(7)	Co2-O15 ¹	2.039(7)
Co2-N2	2.048(9)	Co3-O2	2.032(7)
Co3-O4	2.039(7)	Co3-O5 ³	2.376(7)
Co3-O8 ⁴	2.253(7)	Co3-O16 ³	2.064(7)
Co3-N1 ⁵	2.050(9)	Co4-O5 ³	2.283(7)
Co4-O6	2.013(7)	Co4-O7	2.032(7)
Co4-O9 ⁴	2.030(7)	Co4-N4	2.056(9)

36

Co1-O1	2.028(4)	Co1-O3	2.114(4)
Co1-O5	2.025(4)	Co1-O7 ¹	2.039(4)
Co1-N2	2.079(4)	Co2-O2	2.133(4)
Co2-O4	2.007(4)	Co2-O6	2.034(4)
Co2-O8 ¹	2.021(4)	Co2-N1	2.060(4)

Table A35. Selected Bond lengths (Å) for **37** and **38**.**37**

Cd1-O1	2.306(2)	Cd1-O2	2.3606(18)
Cd1-O3	2.3901(19)	Cd1-O4	2.2571(19)
Cd1-O5	2.297(2)	Cd1-N1	2.255(2)

38

Cd1-O1	2.334(4)	Cd1-O2	2.350(3)
Cd1-O3	2.437(4)	Cd1-O4	2.340(4)
Cd1-O5	2.239(4)	Cd1-N1	2.315(3)

Table A36. Selected Bond lengths (Å) for **39** and **40**.**39**

Cd1-O1	2.350(3)	Cd1-O2	2.456(3)
Cd1-O3 ¹	2.410(3)	Cd1-O4 ¹	2.415(3)
Cd1-O5	2.307(3)	Cd1-N1	2.354(4)
Cd1-N2	2.324(5)		

40

Cd1-O1	2.196(2)	Cd1-O2 ¹	2.266(3)
Cd1-O3 ²	2.342(2)	Cd1-O4 ²	2.403(2)
Cd1-O5	2.367(3)	Cd1-N1	2.305(3)

Table A37. Selected Bond lengths (Å) for **41** and **42**.**41**

Zn1-O3	1.939(3)	Zn1-O4 ¹	1.979(3)
Zn1-N1	2.006(3)	Zn1-N22	2.051(3)

42

Cd1-O9	2.465(5)	Cd1-O10	2.297(5)
Cd1-O15	2.381(5)	Cd1-O16	2.316(6)
Cd1-N2 ¹	2.324(6)	Cd1-N3	2.257(5)
Cd2-O11 ²	2.353(5)	Cd2-O12	2.416(5)
Cd2-O13 ²	2.344(5)	Cd2-O14	2.270(6)
Cd2-N5 ³	2.300(6)	Cd2-N6	2.255(5)
Cd3-O6	2.261(5)	Cd3-O7	2.509(4)
Cd3-O17 ⁴	2.242(7)	Cd3-O18	2.728(4)
Cd3-N1 ⁵	2.286(6)	Cd3-N4	2.238(6)

Table A38. Selected Bond lengths (Å) for **43** and **44**.**43**

Zn1-O1	1.973(5)	Zn1-O3	1.921(5)
Zn1-N1	2.113(5)	Zn1-N2	2.022(5)
Zn2-O5	1.944(5)	Zn2-O7	1.924(6)
Zn2-N3	2.030(6)	Zn2-N4	2.079(6)

44

Cd1-O4	2.2436(17)	Cd1-O6	2.4088(17)
Cd1-O7 ¹	2.2719(17)	Cd1-O10 ¹	2.4716(17)
Cd1-N1	2.276(2)	Cd1-N4 ²	2.327(2)
Cd2-O11	2.4462(18)	Cd2-O12 ³	2.3840(18)
Cd2-O13	2.252(2)	Cd2-O15 ³	2.3495(18)
Cd2-N2	2.2744(19)	Cd2-N3 ²	2.304(2)

Table A39. Selected Bond lengths (Å) for **45**, **46** and **47**.**45**

Cd1-O1	2.375(7)	Cd1-O1 ¹	2.375(7)
Cd1-O2	2.439(7)	Cd1-O2 ¹	2.439(7)
Cd1-O3	2.226(7)	Cd1-O3 ¹	2.226(7)
Cd1-O4	2.244(7)	Cd1-O4 ¹	2.244(7)
Cd2-O2	2.214(7)	Cd2-O2 ¹	2.214(7)
Cd2-O5	2.117(9)	Cd2-O5 ¹	2.117(9)
Cd2-O6	2.191(9)	Cd2-O6 ¹	2.191(9)

46

Cd1-O1 ¹	2.3522(18)	Cd1-O2 ¹	2.3714(17)
Cd1-O5	2.277(2)	Cd1-O8 ²	2.326(2)
Cd1-O9	2.515(2)	Cd1-O10 ²	2.458(2)
Cd1-N1	2.290(2)	Cd2-O3 ³	2.4479(18)
Cd2-O4	2.5546(19)	Cd2-O6 ³	2.340(2)
Cd2-O7	2.2382(19)	Cd2-O11 ⁴	2.457(2)
Cd2-O12 ⁴	2.290(3)	Cd2-N2	2.291(2)

47

Cd1-O1 ¹	2.316(5)	Cd1-O2	2.269(5)
Cd1-O3 ¹	2.396(5)	Cd1-O4 ²	2.306(6)
Cd1-O5 ²	2.471(5)	Cd1-O6	2.539(6)
Cd1-N2	2.289(5)		

Table A40. Selected Bond lengths (Å) for **48**.**48**

Co1-Co1 ¹	2.566(3)	Co1-O1	2.007(4)
Co1-O1 ²	2.007(4)	Co1-O1 ³	2.007(4)
Co1-O1 ⁴	2.007(4)	Co1-N1	2.027(9)

Table A41. Selected Bond lengths (Å) for **49** and **50**.**49**

Cd1-O2	2.204(5)	Cd1-O2 ¹	2.203(5)
Cd1-O3 ²	2.324(6)	Cd1-O3 ³	2.324(6)
Cd1-O4 ²	2.461(6)	Cd1-O4 ³	2.461(6)
Cd2-O1	2.286(5)	Cd2-O1 ⁴	2.286(5)
Cd2-O4 ²	2.348(6)	Cd2-O4 ⁵	2.348(6)
Cd2-N1	2.543(7)	Cd2-N1 ⁴	2.543(7)

50

Cd1-O1 ¹	2.289(3)	Cd1-O1 ²	2.289(3)
Cd1-O2	2.288(3)	Cd1-O2 ³	2.288(3)
Cd1-N1	2.278(5)	Cd1-N1 ³	2.278(5)
Cd2-O1 ¹	2.411(3)	Cd2-O1 ⁴	2.411(3)
Cd2-O3	2.161(3)	Cd2-O3 ⁵	2.161(3)
Cd2-O4 ¹	2.364(4)	Cd2-O4 ⁴	2.364(4)

Table A42. Selected Bond lengths (Å) for **51** and **52**.**51**

Cd1-O1	2.193(8)	Cd1-O4 ¹	2.326(8)
Cd1-O5	2.272(11)	Cd1-O9	2.267(10)
Cd1-O10	2.251(8)	Cd1-N1	2.327(9)
Cd2-O2	2.209(12)	Cd2-O3 ¹	2.286(9)
Cd2-O4 ¹	2.486(8)	Cd2-O6	2.203(8)
Cd2-O7	2.382(9)	Cd2-O8	2.319(8)

52

Cd1-O1	2.465(4)	Cd1-O2	2.287(3)
Cd1-O3	2.224(4)	Cd1-O5 ¹	2.419(3)
Cd1-O6 ¹	2.317(4)	Cd1-O7	2.208(3)
Cd2-O4	2.213(4)	Cd2-O5 ¹	2.329(3)
Cd2-O8	2.282(3)	Cd2-O9	2.241(4)
Cd2-O10	2.267(4)	Cd2-N1	2.335(4)

Table A43. Selected Bond lengths (Å) for **53** and **54**.**53**

Ni1-O1 ¹	2.111(10)	Ni1-O2 ²	2.169(11)
Ni1-O6 ¹	2.187(10)	Ni1-O8 ²	2.069(12)
Ni1-N3 ³	2.08(7)	Ni1-N4	2.036(8)
Ni2-O3	2.073(11)	Ni2-O4	2.193(10)
Ni2-O5 ⁴	2.093(12)	Ni2-O7 ⁴	2.122(9)
Ni2-N1	1.991(7)	Ni2-N2 ⁵	2.01(8)

54

Zn1-O2	1.925(8)	Zn1-O6 ¹	1.978(7)
Zn1-N1	2.001(8)	Zn1-N3 ²	2.12(5)
Zn2-O3 ³	2.048(7)	Zn2-O4 ³	2.394(7)
Zn2-O7 ⁴	2.258(8)	Zn2-O8 ⁴	2.105(8)
Zn2-N2	2.035(8)	Zn2-N4 ¹	2.08(4)

Table A44. Selected Bond lengths (Å) for **55** and **56**.**55**

Zn1-O1	1.933(4)	Zn1-O3 ¹	1.956(4)
Zn1-O6 ²	1.979(4)	Zn1-O8 ³	1.988(4)
Zn2-O2	1.931(4)	Zn2-O5 ²	1.959(4)
Zn2-O7 ⁴	1.981(4)	Zn2-O9	1.972(5)

56

Cu1-Cu1 ¹	2.650(2)	Cu1-O1	1.954(6)
Cu1-O3 ²	1.973(6)	Cu1-O4 ¹	1.997(6)
Cu1-O5 ³	1.970(6)	Cu1-O10	2.112(6)
Cu2-Cu2 ⁴	2.638(2)	Cu2-O2	1.935(6)
Cu2-O6 ⁴	1.955(6)	Cu2-O7 ⁴	1.974(6)
Cu2-O8	1.918(6)	Cu2-O9	2.154(6)

Table A45. Selected Bond angles (°) for **1** and **4**.**1**

O5-Mn1-N2	155.35(5)	O5-Mn1-N1	86.62(5)
O5-Mn1-N3	92.18(5)	O4 ¹ -Mn1-O5	94.73(5)
O4 ¹ -Mn1-O1	89.92(5)	O4 ¹ -Mn1-N2	100.04(5)
O4 ¹ -Mn1-N1	89.71(5)	O4 ¹ -Mn1-N3	173.03(5)
O1-Mn1-O5	90.40(5)	O1-Mn1-N2	109.12(5)
O1-Mn1-N1	176.95(5)	O1-Mn1-N3	89.11(5)
N1-Mn1-N2	73.92(5)	N3-Mn1-N2	73.79(5)
N3-Mn1-N1	91.61(5)		

4

O1-Cd1-O4	90.52(9)	O1-Cd1-N1	110.30(10)
O1-Cd1-N2	88.91(10)	O1-Cd1-N3	177.31(10)
O3-Cd1-O1	89.13(10)	O3-Cd1-O4	96.60(9)
O3-Cd1-N1	101.13(9)	O3-Cd1-N2	172.06(10)
O3-Cd1-N3	90.52(10)	O4-Cd1-N1	152.62(9)
N2-Cd1-O4	91.11(9)	N2-Cd1-N1	72.39(9)
N2-Cd1-N3	91.80(10)	N3-Cd1-O4	86.86(10)
N3-Cd1-N1	72.39(10)		

Table A46. Selected Bond angles (°) for **5**, **9** and **10**.**5**

O1-Mn1-O4 ¹	88.27(7)	O1-Mn1-O6	91.33(6)
O1-Mn1-N1	86.84(7)	O1-Mn1-N2	98.75(6)
O1-Mn1-N3	172.13(6)	O4 ¹ -Mn1-O6	89.72(6)
O4 ¹ -Mn1-N1	174.78(7)	O4 ¹ -Mn1-N2	109.86(7)
O4 ¹ -Mn1-N3	89.52(7)	O6-Mn1-N1	88.56(7)
O6-Mn1-N2	158.10(6)	O6-Mn1-N3	96.22(6)
N1-Mn1-N2	72.75(7)	N3-Mn1-N1	95.57(7)
N3-Mn1-N2	74.92(7)		

9

O1-Zn1-N2	160.76(9)	O1-Zn1-N3	88.44(10)
O2-Zn1-O1	91.41(10)	O2-Zn1-N1	89.77(11)
O2-Zn1-N2	106.25(10)	O2-Zn1-N3	173.07(10)
O6-Zn1-O1	93.77(10)	O6-Zn1-O2	86.54(11)
O6-Zn1-N1	170.50(10)	O6-Zn1-N2	94.84(9)
O6-Zn1-N3	86.55(11)	N1-Zn1-O1	95.08(10)
N1-Zn1-N2	77.78(10)	N1-Zn1-N3	97.14(11)
N3-Zn1-N2	74.96(10)		

10

O1-Cd1-O4 ¹	87.20(10)	O1-Cd1-O6	89.55(8)
O1-Cd1-N1	174.15(9)	O1-Cd1-N2	109.99(8)
O1-Cd1-N3	90.10(10)	O4 ¹ -Cd1-O6	89.99(8)
O4 ¹ -Cd1-N1	86.97(9)	O4 ¹ -Cd1-N2	100.06(8)
O4 ¹ -Cd1-N3	171.38(9)	O6-Cd1-N2	158.28(8)
N1-Cd1-O6	89.96(8)	N1-Cd1-N2	71.58(8)
N3-Cd1-O6	98.18(8)	N3-Cd1-N1	95.75(9)
N3-Cd1-N2	73.20(8)		

Table A47. Selected Bond angles (°) for **11** and **11a**.**11**

O1-Mn1-O3	103.4(3)	O1-Mn1-O5	86.7(2)
O1-Mn1-N1	96.4(3)	O1-Mn1-N2	84.2(2)
O1-Mn1-N3	166.3(2)	O3-Mn1-O5	93.05(19)
O3-Mn1-N1	153.55(18)	O3-Mn1-N2	89.2(2)
O3-Mn1-N3	90.2(3)	O5-Mn1-N1	105.6(2)
O5-Mn1-N3	91.2(2)	N2-Mn1-O5	170.88(19)
N2-Mn1-N1	75.4(2)	N2-Mn1-N3	97.6(2)
N3-Mn1-N1	71.2(3)		

11a

O1-Mn1-O4 ¹	98.46(7)	O1-Mn1-O5	95.43(7)
O1-Mn1-N1	91.93(7)	O1-Mn1-N2	159.21(7)
O1-Mn1-N3	95.98(7)	O4 ¹ -Mn1-O5	87.36(6)
O4 ¹ -Mn1-N1	81.83(7)	O4 ¹ -Mn1-N2	95.73(7)
O4 ¹ -Mn1-N3	163.74(6)	O5-Mn1-N1	167.72(6)
O5-Mn1-N2	100.34(7)	O5-Mn1-N3	83.86(7)
N1-Mn1-N2	75.11(7)	N3-Mn1-N1	105.17(7)
N3-Mn1-N2	72.53(7)		

Table A48. Selected Bond angles (°) for **12** and **13**.**12**

O2-Mn1-O5	91.61(10)	O2-Mn1-N1	93.42(13)
O2-Mn1-N2	152.08(16)	O2-Mn1-N3	87.53(11)
O4 ¹ -Mn1-O2	106.96(12)	O4 ¹ -Mn1-O5	86.86(13)
O4 ¹ -Mn1-N1	158.66(13)	O4 ¹ -Mn1-N2	91.3(2)
O4 ¹ -Mn1-N3	86.06(13)	O5-Mn1-N1	86.27(13)
O5-Mn1-N2	110.73(12)	O5-Mn1-N3	172.28(14)
N1-Mn1-N2	72.4(2)	N3-Mn1-N1	101.44(14)
N3-Mn1-N2	72.51(13)		

13

O1 ¹ -Mn1-O2 ¹	57.02(13)	O1 ¹ -Mn1-O3	96.16(14)
O1 ¹ -Mn1-N1	85.69(11)	O1 ¹ -Mn1-N2	129.57(13)
O1 ¹ -Mn1-N3	94.26(14)	O2 ¹ -Mn1-N1	105.17(11)
O3-Mn1-O2 ¹	87.34(12)	O3-Mn1-N1	165.94(13)
O3-Mn1-N2	116.30(16)	O3-Mn1-N3	93.28(14)
N2-Mn1-O2 ¹	85.59(12)	N2-Mn1-N1	71.86(11)
N2-Mn1-N3	119.36(12)	N3-Mn1-N1	72.67(11)
N3-Mn1-O2 ¹	151.10(12)		

Table A49. Selected Bond angles (°) for **14**, **15** and **16**.**14**

O1-Mn1-O4	101.60(6)	O1-Mn1-O5	125.50(6)
O1-Mn1-N1	82.37(6)	O1-Mn1-N2	148.56(6)
O1-Mn1-N3	97.69(5)	O4-Mn1-N1	86.76(6)
O4-Mn1-N2	92.39(6)	O5-Mn1-O4	58.05(5)
O5-Mn1-N1	136.83(6)	O5-Mn1-N2	85.78(5)
N1-Mn1-N2	70.35(6)	N3-Mn1-O4	160.39(5)
N3-Mn1-O5	107.22(5)	N3-Mn1-N1	99.35(5)
N3-Mn1-N2	72.52(5)		

15

O1-Mn1-O2	89.53(18)	O1-Mn1-O3 ¹	90.14(19)
O1-Mn1-N1	172.30(18)	O1-Mn1-N2	87.6(2)
O1-Mn1-N3	98.3(2)	O2-Mn1-N1	98.12(19)
O2-Mn1-N2	91.54(19)	O2-Mn1-N3	161.62(17)
O3 ¹ -Mn1-O2	93.81(19)	O3 ¹ -Mn1-N1	88.5(2)
O3 ¹ -Mn1-N2	174.16(18)	O3 ¹ -Mn1-N3	102.71(19)
N1-Mn1-N2	93.1(2)	N1-Mn1-N3	74.6(2)
N2-Mn1-N3	72.35(19)		

16

O2-Mn1-O4	84.18(7)	O2-Mn1-O6	90.87(7)
O2-Mn1-N1	90.66(8)	O2-Mn1-N2	95.08(8)
O2-Mn1-N3	87.89(8)	O6-Mn1-O4	54.49(6)
O6-Mn1-N1	136.29(8)	O6-Mn1-N2	152.17(8)
O6-Mn1-N3	81.84(7)	O9-Mn1-O2	175.08(8)
O9-Mn1-O4	91.06(7)	O9-Mn1-O6	87.35(7)
O9-Mn1-N1	87.47(8)	O9-Mn1-N2	88.61(8)
O9-Mn1-N3	96.39(8)	N1-Mn1-O4	82.26(8)
N1-Mn1-N2	70.92(9)	N2-Mn1-O4	153.17(7)
N3-Mn1-O4	135.31(7)	N3-Mn1-N1	141.87(8)
N3-Mn1-N2	71.27(8)		

Table A50. Selected Bond angles (°) for **17**, **18** and **19**.**17**

O1-Cd1-O4	54.51(11)	O1-Cd1-O7	119.67(11)
O1-Cd1-O8 ¹	96.10(11)	O4-Cd1-O7	87.89(11)
O4-Cd1-O8 ¹	146.73(11)	O6-Cd1-O1	163.55(12)
O6-Cd1-O4	109.04(12)	O6-Cd1-O7	54.51(10)
O6-Cd1-O8 ¹	99.48(11)	O6-Cd1-O8	86.28(11)
O6-Cd1-O9 ¹	111.08(12)	O7-Cd1-O8 ¹	123.37(11)
O8-Cd1-O1	93.62(12)	O8-Cd1-O4	92.87(12)
O8-Cd1-O7	138.24(10)	O8-Cd1-O8 ¹	71.83(11)
O9 ¹ -Cd1-O1	82.67(11)	O9 ¹ -Cd1-O4	126.48(11)
O9 ¹ -Cd1-O7	87.73(11)	O9 ¹ -Cd1-O8 ¹	52.70(10)
O9 ¹ -Cd1-O8	123.35(10)	O5-Cd2-N1	102.80(14)

17 (continued)

O5-Cd2-N2	82.23(12)	O5-Cd2-N3	88.31(13)
O5-Cd2-N4	138.90(12)	O5-Cd2-N5	147.45(12)
O5-Cd2-N6	82.28(13)	N1-Cd2-N2	82.71(13)
N1-Cd2-N4	100.67(12)	N1-Cd2-N5	70.84(12)
N1-Cd2-N6	97.48(12)	N2-Cd2-N4	67.84(11)
N2-Cd2-N5	126.67(11)	N2-Cd2-N6	164.14(13)
N3-Cd2-N1	168.88(13)	N3-Cd2-N2	99.39(13)
N3-Cd2-N4	70.42(12)	N3-Cd2-N5	99.58(12)
N3-Cd2-N6	83.49(13)	N4-Cd2-N6	127.27(12)

18

O1-Cd1-O4	99.58(19)	O1-Cd1-O5	54.81(16)
O1-Cd1-N2	91.87(17)	O3-Cd1-O1	98.53(18)
O3-Cd1-O4	52.38(19)	O3-Cd1-O5	121.8(2)
O3-Cd1-N2	152.4(2)	O3-Cd1-N3	84.9(2)
O5-Cd1-O4	79.72(18)	O5-Cd1-N2	84.93(18)
N1-Cd1-O1	159.75(18)	N1-Cd1-O3	101.49(19)
N1-Cd1-O4	90.3(2)	N1-Cd1-O5	110.57(17)
N1-Cd1-N2	71.58(18)	N1-Cd1-N3	96.2(2)
N2-Cd1-O4	150.34(18)	N3-Cd1-O1	88.56(18)
N3-Cd1-O4	137.13(19)	N3-Cd1-O5	135.11(16)
N3-Cd1-N2	69.86(18)		

19

O1-Cd1-O2	55.07(8)	O1-Cd1-O3	81.61(8)
O1-Cd1-N1	134.84(9)	O1-Cd1-N2	86.05(8)
N3-Cd1-N2	71.26(9)	O2-Cd1-O3	101.35(8)
O2-Cd1-N1	87.54(9)	O2-Cd1-N2	91.69(9)
O4-Cd1-O1	126.41(8)	O4-Cd1-O2	101.64(9)
O4-Cd1-O3	54.10(8)	O4-Cd1-N1	81.20(9)
O4-Cd1-N2	146.86(9)	O4-Cd1-N3	99.80(9)
N1-Cd1-O3	135.29(8)	N1-Cd1-N2	69.08(8)
N3-Cd1-N1	98.07(9)	N2-Cd1-O3	152.14(8)
N3-Cd1-O1	109.10(8)	N3-Cd1-O2	158.43(9)
N3-Cd1-O3	89.31(9)		

Table A51. Selected Bond angles (°) for **20**, **21** and **22**.**20**

O1 ¹ -Zn1-O1 ²	86.5(4)	O4 ⁵ -Zn2-O4 ⁶	78.7(11)
O2-Zn1-O1 ¹	159.4(3)	O5 ³ -Zn2-O4 ⁶	159.8(5)
O2-Zn1-O1 ²	89.4(3)	O5-Zn2-O4 ⁶	91.0(6)
O2 ³ -Zn1-O1 ²	159.4(3)	O5 ³ -Zn2-O4 ⁵	91.0(6)
O2 ³ -Zn1-O1 ¹	89.4(3)	O5-Zn2-O4 ⁵	159.8(5)
O2-Zn1-O2 ³	87.4(5)	O5 ³ -Zn2-O5	93.3(7)
O5-Zn2-O6	99.1(4)	O3-Zn1-O1 ¹	100.0(3)
O5 ³ -Zn2-O6	99.1(4)	O3-Zn1-O1 ²	100.0(3)
O3-Zn1-O2	100.6(3)	O6-Zn2-O4 ⁶	99.7(4)
O3-Zn1-O2 ³	100.6(3)	O6-Zn2-O4 ⁵	99.7(4)

21

O1-Zn1-O2	88.17(9)	O1-Zn1-O3	160.57(9)
O1-Zn1-O4 ¹	87.65(8)	O2-Zn1-O3	90.81(9)
O2-Zn1-O4 ¹	160.30(9)	O3-Zn1-O4 ¹	86.80(9)
N1-Zn1-O1	101.03(9)	N1-Zn1-O2	108.82(10)
N1-Zn1-O3	97.65(9)	N1-Zn1-O4 ¹	90.88(9)

22

O2-Zn1-O4	87.49(9)	O2-Zn1-O5	161.03(8)
O2-Zn1-O7	91.38(9)	O2-Zn1-N2	98.69(9)
O5-Zn1-O4	86.76(9)	O5-Zn1-O7	88.52(9)
O5-Zn1-N2	99.47(9)	O7-Zn1-O4	161.90(9)
O7-Zn1-N2	107.08(9)	N2-Zn1-O4	90.93(9)
O1-Zn2-O3	88.75(9)	O1-Zn2-O6	159.08(8)
O1-Zn2-O8	86.70(9)	O3-Zn2-O6	91.06(8)
O3-Zn2-O8	157.61(8)	O6-Zn2-O8	85.55(9)
N1-Zn2-O1	99.57(9)	N1-Zn2-O3	110.08(9)
N1-Zn2-O6	100.13(9)	N1-Zn2-O8	92.30(9)

Table A52. Selected Bond angles (°) for **23**, **24** and **25**.**23**

O2-Zn1-O5 ¹	87.54(13)	O2-Zn1-O7 ²	87.57(12)
O3-Zn1-O2	160.03(14)	O3-Zn1-O5 ¹	87.21(13)
O3-Zn1-O7 ²	92.62(12)	O3-Zn1-N2 ³	106.82(15)
O7 ² -Zn1-O5 ¹	165.02(14)	N2 ³ -Zn1-O2	92.47(15)
N2 ³ -Zn1-O5 ¹	90.47(15)	N2 ³ -Zn1-O7 ²	103.88(16)
O1-Zn2-O4	160.16(14)	O1-Zn2-O6 ¹	93.35(12)
O1-Zn2-O8 ²	85.20(13)	O4-Zn2-O8 ²	86.61(13)
O6 ¹ -Zn2-O4	86.84(12)	O6 ¹ -Zn2-O8 ²	155.95(14)
N1-Zn2-O1	100.42(14)	N1-Zn2-O4	97.78(14)
N1-Zn2-O6 ¹	112.64(15)	N1-Zn2-O8 ²	91.17(15)

24

O3 ¹ -Zn1-O7 ³	160.50(10)	O4-Zn1-O3 ¹	87.35(10)
O4-Zn1-O7 ³	86.51(9)	O4-Zn1-N1	101.24(10)
O5-Zn1-O3 ¹	88.95(10)	O5-Zn1-O4	156.89(10)
O5-Zn1-O7 ³	89.47(9)	O5-Zn1-N1	101.81(10)
N1-Zn1-O3 ¹	95.32(10)	N1-Zn1-O7 ³	104.03(10)
O1 ⁴ -Zn2-O6 ⁵	90.65(10)	O1 ⁴ -Zn2-O8 ⁵	86.36(10)
O2 ⁶ -Zn2-O1 ⁴	158.77(10)	O2 ⁶ -Zn2-O6 ⁵	87.34(10)
O2 ⁶ -Zn2-O8 ⁵	89.39(10)	O6 ⁵ -Zn2-O8 ⁵	162.93(10)
N2-Zn2-O1 ⁴	99.36(10)	N2-Zn2-O2 ⁶	101.83(10)
N2-Zn2-O6 ⁵	98.88(10)	N2-Zn2-O8 ⁵	98.19(10)

25

O1-Zn1-Zn2	66.55(13)	O4-Zn1-Zn2	84.95(14)
O4-Zn1-O1	86.07(18)	O4-Zn1-O9	160.0(2)
O7-Zn1-Zn2	91.12(14)	O7-Zn1-O1	157.66(19)
O7-Zn1-O4	91.97(17)	O7-Zn1-O9	87.18(17)
O7-Zn1-N1	111.5(2)	O9-Zn1-Zn2	75.08(14)
O9-Zn1-O1	87.17(18)	N1-Zn1-Zn2	155.71(15)
N1-Zn1-O1	90.62(19)	N1-Zn1-O4	102.36(19)
N1-Zn1-O9	96.52(19)	O2-Zn2-Zn1	92.78(14)
O2-Zn2-O3	86.84(18)	O2-Zn2-O6	160.9(2)
O2-Zn2-O8	90.71(18)	O2-Zn2-N5	105.1(2)
O3-Zn2-Zn1	74.82(13)	O3-Zn2-O6	88.13(18)
O6-Zn2-Zn1	68.16(14)	O8-Zn2-Zn1	84.85(14)
O8-Zn2-O3	159.36(19)	O8-Zn2-O6	87.55(18)
O8-Zn2-N5	102.6(2)	N5-Zn2-Zn1	160.36(15)
N5-Zn2-O3	97.8(2)	N5-Zn2-O6	93.8(2)

Table A53. Selected Bond angles (°) for **26** and **27**.**26**

O1 ¹ -Mn1-Mn1 ¹	77.34(18)	O1 ¹ -Mn1-O2	86.5(3)
O1 ¹ -Mn1-O4	87.2(3)	O1 ¹ -Mn1-N1	98.3(3)
O2-Mn1-Mn1 ¹	61.5(2)	O3-Mn1-Mn1 ¹	82.13(19)
O3-Mn1-O1 ¹	159.4(2)	O3-Mn1-O2	85.7(3)
O3-Mn1-O4	93.1(3)	O3-Mn1-N1	101.1(3)
O4-Mn1-Mn1 ¹	96.7(2)	O4-Mn1-O2	158.1(3)
O4-Mn1-N1	109.0(3)	N1-Mn1-Mn1 ¹	153.8(2)
N1-Mn1-O2	92.7(3)		

27

O2-Mn1-O5	97.9(2)	O2-Mn1-O6	152.0(2)
O2-Mn1-O7	82.4(2)	O2-Mn1-N1	108.3(3)
O4-Mn1-O2	89.8(2)	O4-Mn1-O5	82.47(19)
O4-Mn1-O6	94.1(2)	O4-Mn1-O7	163.4(2)
O4-Mn1-N1	90.9(2)	O6-Mn1-O5	55.37(17)
O7-Mn1-O5	84.09(19)	O7-Mn1-O6	86.2(2)
O7-Mn1-N1	105.4(2)	N1-Mn1-O5	153.0(2)
N1-Mn1-O6	99.4(2)	O1-Mn2-O3	87.2(2)
O1-Mn2-O5	137.3(2)	O1-Mn2-O9 ¹	90.5(2)
O3-Mn2-O9 ¹	152.63(19)	O5-Mn2-O3	83.62(19)
O5-Mn2-O9 ¹	79.73(19)	O8-Mn2-O1	109.3(2)
O8-Mn2-O3	98.5(2)	O8-Mn2-O5	113.3(2)
O8-Mn2-O9 ¹	108.0(2)		

Table A54. Selected Bond angles (°) for **28**, **29** and **30**.**28**

O1-Mn1-Mn2	72.42(5)	O1-Mn1-O6	85.25(8)
O1-Mn1-O7	157.08(7)	O4-Mn1-Mn2	68.51(6)
O4-Mn1-O1	89.44(8)	O4-Mn1-O6	159.40(8)
O4-Mn1-O7	89.75(7)	O6-Mn1-Mn2	90.93(6)
O7-Mn1-Mn2	86.00(5)	O7-Mn1-O6	87.50(7)
O9-Mn1-Mn2	170.86(7)	O9-Mn1-O1	102.34(8)
O9-Mn1-O4	104.44(9)	O9-Mn1-O6	96.14(9)
O9-Mn1-O7	100.04(8)	O2-Mn2-Mn1	84.96(5)
O3-Mn2-Mn1	89.38(6)	O3-Mn2-O2	86.91(8)

28 (continued)

O5-Mn2-Mn1	66.53(6)	O5-Mn2-O2	89.81(7)
O5-Mn2-O3	155.89(8)	O8-Mn2-Mn1	71.90(5)
O8-Mn2-O2	155.23(7)	O8-Mn2-O3	84.19(8)
O8-Mn2-O5	88.98(8)	O10-Mn2-Mn1	164.64(6)
O10-Mn2-O2	94.92(8)	O10-Mn2-O3	105.96(8)
O10-Mn2-O5	98.12(8)	O10-Mn2-O8	109.74(8)
O11-Mn3-O12	90.88(7)	O11-Mn3-O14	159.25(7)
O11-Mn3-N1	108.52(8)	O11-Mn3-N2 ¹	81.17(8)
O13-Mn3-O11	81.98(8)	O13-Mn3-O12	160.83(8)
O13-Mn3-O14	99.99(8)	O13-Mn3-N1	80.32(9)
O13-Mn3-N2 ¹	107.31(9)	O14-Mn3-O12	92.99(7)
N1-Mn3-O12	85.19(9)	N1-Mn3-O14	92.13(8)
N1-Mn3-N2 ¹	168.72(9)	N2 ¹ -Mn3-O12	88.98(8)
N2 ¹ -Mn3-O14	78.52(8)		

29

O1 ¹ -Mn1-Mn2 ²	83.98(9)	O3-Mn1-Mn2 ²	64.71(9)
O3-Mn1-O1 ¹	89.86(12)	O3-Mn1-O6 ³	88.73(13)
O3-Mn1-O8 ²	154.78(13)	O6 ³ -Mn1-Mn2 ²	72.88(9)
O6 ³ -Mn1-O1 ¹	154.99(12)	O6 ³ -Mn1-O8 ²	83.90(13)
O8 ² -Mn1-Mn2 ²	90.07(10)	O8 ² -Mn1-O1 ¹	86.85(13)
O9-Mn1p-Mn2 ²	162.52(10)	O9-Mn1-O1 ¹	93.59(13)
O9-Mn1-O3	98.04(14)	O9-Mn1-O6 ³	111.33(13)
O9-Mn1-O8 ²	107.12(14)	O2 ⁴ -Mn2-Mn1 ⁵	85.10(8)
O4 ⁶ -Mn2-Mn1 ⁵	73.40(9)	O4 ⁶ -Mn2-O2 ⁴	157.23(12)
O4 ⁶ -Mn2-O7 ⁵	85.66(13)	O7 ⁵ -Mn2-Mn1 ⁵	92.32(9)
O7 ⁵ -Mn2-O2 ⁴	87.84(13)	O11-Mn2-Mn1 ⁵	67.59(10)
O11-Mn2-O2 ⁴	89.14(13)	O11-Mn2-O4 ⁶	89.51(13)
O11-Mn2-O7 ⁵	159.88(13)	O14-Mn2-Mn1 ⁵	170.47(12)
O14-Mn2-O2 ⁴	99.54(13)	O14-Mn2-O4 ⁶	102.84(14)
O14-Mn2-O7 ⁵	96.15(15)	O14-Mn2-O11	103.97(16)
O5-Mn3-O10	158.44(13)	O5-Mn3-O12	91.96(12)
O5-Mn3-N1 ⁵	80.92(14)	O5-Mn3-N2	108.65(14)
O10-Mn3-N1 ⁵	78.00(14)	O10-Mn3-N2	92.75(14)
O12-Mn3-O10	92.34(13)	O12-Mn3-N1 ⁵	89.43(14)
O12-Mn3-N2	85.37(15)	O13 ⁶ -Mn3-O5	82.70(13)
O13 ⁶ -Mn3-O10	99.43(13)	O13 ⁶ -Mn3-O12	160.71(14)
O13 ⁶ -Mn3-N1 ⁵	107.87(15)	O13 ⁶ -Mn3-N2	78.88(15)
N1 ⁵ -Mn3-N2	169.22(16)		

30

O1 ¹ -Mn1-O1 ²	75.89(6)	O1 ² -Mn1-O2	103.80(5)
O1 ¹ -Mn1-O2	88.63(5)	O1 ¹ -Mn1-N1	97.67(6)
O1 ² -Mn1-N1	86.87(6)	O3-Mn1-O1 ¹	167.93(6)
O3-Mn1-O1 ²	93.30(5)	O3-Mn1-O2	88.78(5)
O3-Mn1-O4 ³	104.09(6)	O3-Mn1-N1	86.92(6)
O4 ³ -Mn1-O1 ¹	87.69(6)	O4 ³ -Mn1-O1 ²	158.21(6)
O4 ³ -Mn1-O2	89.79(5)	O4 ³ -Mn1-N1	81.16(6)
N1-Mn1-O2	168.72(7)		

Table A55. Selected Bond angles (°) for **32**, **33** and **34**.**32**

O1-Co1-O6	165.3(2)	O4-Co1-O1	100.3(2)
O4-Co1-O6	81.7(2)	O8-Co1-O1	90.7(2)
O8-Co1-O4	161.6(3)	O8-Co1-O6	84.1(2)
N2-Co1-O1	102.6(3)	N2-Co1-O4	101.9(3)
N2-Co1-O6	91.1(3)	N2-Co1-O8	89.9(3)
O3-Co2-O2	85.4(2)	O3-Co2-O5	91.4(2)
O3-Co2-O7	162.1(3)	O5-Co2-O2	165.7(2)
O7-Co2-O2	80.1(2)	O7-Co2-O5	100.0(2)
N1-Co2-O2	93.1(3)	N1-Co2-O3	87.7(3)
N1-Co2-O5	100.7(3)	N1-Co2-O7	103.6(2)

33

O1-Co1-O4	95.18(11)	O1-Co1-O6	162.62(10)
O1-Co1-O7	83.99(11)	O1-Co1-N2	97.76(11)
O4-Co1-O7	161.76(11)	O4-Co1-N2	108.25(12)
O6-Co1-O4	91.26(11)	O6-Co1-O7	84.86(11)
O6-Co1-N2	95.51(11)	N2-Co1-O7	89.88(12)
O2-Co2-O3	84.72(11)	O2-Co2-O8	90.98(11)
O2-Co2-N1	96.79(11)	O5-Co2-O2	164.40(10)
O5-Co2-O3	85.79(11)	O5-Co2-O8	95.23(11)
O5-Co2-N1	95.05(11)	O8-Co2-O3	165.72(11)
O8-Co2-N1	107.05(12)	N1-Co2-O3	87.01(12)

34

O3 ¹ -Co1-Co2 ¹	83.38(10)	O3 ¹ -Co1-O5	163.55(14)
O3 ¹ -Co1-O6 ¹	85.72(13)	O3 ¹ -Co1-O8	95.50(14)
O3 ¹ -Co1-N2 ²	96.82(15)	O5-Co1-Co2 ¹	80.30(10)
O5-Co1-O6 ¹	84.51(13)	O5-Co1-O8	90.83(14)
O5-Co1-N2 ²	95.98(15)	O6 ¹ -Co1-Co2 ¹	60.61(11)
O8-Co1-Co2 ¹	105.45(12)	O8-Co1-O6 ¹	165.85(16)
O8-Co1-N2 ²	106.03(17)	N2 ² -Co1-Co2 ¹	148.34(13)
N2 ² -Co1-O6 ¹	87.78(16)	O1-Co2-Co1 ³	79.41(10)
O1-Co2-O2 ³	161.60(14)	O1-Co2-O7 ³	84.36(13)
O1-Co2-N1	95.68(14)	O2 ³ -Co2-Co1 ³	82.48(10)
O2 ³ -Co2-O7 ³	83.40(13)	O2 ³ -Co2-N1	97.75(14)
O4-Co2-Co1 ³	102.93(11)	O4-Co2-O1	91.98(14)
O4-Co2-O2 ³	95.22(14)	O4-Co2-O7 ³	161.29(16)
O4-Co2-N1	109.80(16)	O7 ³ -Co2-Co1 ³	58.36(11)
N1-Co2-Co1 ³	147.07(11)	N1-Co2-O7 ³	88.85(15)

Table A56. Selected Bond angles (°) for **35** and **36**.**35**

O3-Co1-O10 ¹	83.3(3)	O3-Co1-O12 ²	100.7(3)
O3-Co1-O13 ²	88.2(3)	O3-Co1-N3	102.0(3)
O10 ¹ -Co1-O13 ²	108.2(3)	O11-Co1-O3	162.5(3)
O11-Co1-O10 ¹	84.2(3)	O11-Co1-O12 ²	89.0(3)
O11-Co1-O13 ²	84.2(3)	O11-Co1-N3	90.5(3)
O12 ² -Co1-O10 ¹	166.7(3)	O12 ² -Co1-O13 ²	59.6(3)
N3-Co1-O10 ¹	91.3(3)	N3-Co1-O12 ²	100.2(3)
N3-Co1-O13 ²	159.1(3)	O1-Co2-O13 ²	82.3(3)
O1-Co2-O14	162.1(3)	O1-Co2-O15 ¹	92.2(3)
O1-Co2-N2	93.3(3)	O14-Co2-O13 ²	84.6(3)
O14-Co2-O15 ¹	96.1(3)	O14-Co2-N2	97.9(3)
O15 ¹ -Co2-O13 ²	160.1(3)	O15 ¹ -Co2-N2	113.0(3)
N2-Co2-O13 ²	86.5(3)	O2-Co3-O4	162.1(3)
O2-Co3-O5 ³	84.7(3)	O2-Co3-O8 ⁴	84.0(3)
O2-Co3-O16 ³	89.3(3)	O2-Co3-N1 ⁵	90.7(3)
O4-Co3-O5 ³	88.0(3)	O4-Co3-O8 ⁴	82.8(3)
O4-Co3-O16 ³	100.9(3)	O4-Co3-N1 ⁵	101.7(3)

35 (continued)

O8 ⁴ -Co3-O5 ³	108.2(3)	O16 ³ -Co3-O5 ³	59.0(3)
O16 ³ -Co3-O8 ⁴	166.2(3)	N1 ⁵ -Co3-O5 ³	158.9(3)
N1 ⁵ -Co3-O8 ⁴	91.7(3)	N1 ⁵ -Co3-O16 ³	100.4(3)
O6-Co4-O5 ³	82.7(3)	O6-Co4-O7	162.3(3)
O6-Co4-O9 ⁴	92.0(3)	O6-Co4-N4	93.2(3)
O7-Co4-O5 ³	85.0(3)	O7-Co4-N4	98.7(3)
O9 ⁴ -Co4-O5 ³	160.2(3)	O9 ⁴ -Co4-O7	95.3(3)
O9 ⁴ -Co4-N4	112.9(3)	N4-Co4-O5 ³	86.6(3)

36

O1-Co1-O3	164.81(19)	O1-Co1-O7 ¹	88.59(14)
O1-Co1-N2	103.93(19)	O5-Co1-O1	94.65(15)
O5-Co1-O3	86.77(16)	O5-Co1-O7 ¹	165.41(16)
O5-Co1-N2	98.46(17)	O7 ¹ -Co1-O3	86.45(15)
O7 ¹ -Co1-N2	94.54(16)	N2-Co1-O3	90.8(2)
O4-Co2-O2	163.1(2)	O4-Co2-O6	89.35(15)
O4-Co2-O8 ¹	95.02(15)	O4-Co2-N1	109.13(19)
O6-Co2-O2	85.86(16)	O6-Co2-N1	94.42(15)
O8 ¹ -Co2-O2	85.27(15)	O8 ¹ -Co2-O6	163.10(17)
O8 ¹ -Co2-N1	99.52(14)	N1-Co2-O2	87.44(16)

Table A57. Selected Bond angles (°) for **37** and **38**.**37**

O1-Cd1-O2	56.42(7)	O1-Cd1-O3	148.74(7)
O2-Cd1-O3	106.57(7)	O4-Cd1-O1	98.07(7)
O4-Cd1-O2	100.19(7)	O4-Cd1-O3	56.45(7)
O4-Cd1-O5	97.84(8)	O5-Cd1-O1	87.11(7)
O5-Cd1-O2	141.07(7)	O5-Cd1-O3	112.17(7)
N1-Cd1-O1	113.38(8)	N1-Cd1-O2	90.70(7)
N1-Cd1-O3	91.03(7)	N1-Cd1-O4	147.40(7)
N1-Cd1-O5	92.34(8)		

38

O1-Cd1-O2	55.06(13)	O1-Cd1-O3	125.02(14)
O1-Cd1-O4	108.27(16)	O2-Cd1-O3	85.50(13)
O4-Cd1-O2	117.20(15)	O4-Cd1-O3	53.88(12)
O5-Cd1-O1	118.55(18)	O5-Cd1-O2	96.71(16)
O5-Cd1-O3	100.89(15)	O5-Cd1-O4	132.49(18)
O5-Cd1-N1	88.40(15)	N1-Cd1-O1	88.43(13)
N1-Cd1-O2	140.79(13)	N1-Cd1-O3	131.76(13)
N1-Cd1-O4	85.15(13)	C4-C5-Si1	123.7(3)

Table A58. Selected Bond angles (°) for **39** and **40**.**39**

O1-Cd1-O2	53.97(11)	O1-Cd1-O3 ¹	135.84(11)
O1-Cd1-O4 ¹	165.87(13)	O1-Cd1-N1	86.22(13)
O3 ¹ -Cd1-O2	82.33(10)	O3 ¹ -Cd1-O4 ¹	54.18(12)
O4 ¹ -Cd1-O2	136.22(11)	O5-Cd1-O1	85.91(12)
O5-Cd1-O2	139.41(11)	O5-Cd1-O3 ¹	138.16(12)
O5-Cd1-O4 ¹	84.33(12)	O5-Cd1-N1	88.09(17)
O5-Cd1-N2	91.17(19)	N1-Cd1-O2	94.39(14)
N1-Cd1-O3 ¹	91.72(14)	N1-Cd1-O4 ¹	83.27(12)
N2-Cd1-O1	91.54(14)	N2-Cd1-O2	84.75(16)
N2-Cd1-O3 ¹	90.30(16)	N2-Cd1-O4 ¹	98.84(12)
N2-Cd1-N1	177.68(15)		

40

O1-Cd1-O2 ¹	118.70(9)	O1-Cd1-O3 ²	144.55(8)
O1-Cd1-O4 ²	91.11(8)	O1-Cd1-O5	83.74(10)
O1-Cd1-N1	104.30(10)	O2 ¹ -Cd1-O3 ²	92.82(8)
O2 ¹ -Cd1-O4 ²	147.80(8)	O2 ¹ -Cd1-O5	79.43(11)
O2 ¹ -Cd1-N1	92.23(10)	O3 ² -Cd1-O4 ²	55.29(8)
O3 ² -Cd1-O5	86.91(11)	O5-Cd1-O4 ²	93.08(12)
N1-Cd1-O3 ²	89.14(10)	N1-Cd1-O4 ²	91.70(10)
N1-Cd1-O5	170.57(11)		

Table A59. Selected Bond angles (°) for **41** and **42**.**41**

O3-Zn1-O4 ¹	110.73(15)	O3-Zn1-N1	111.02(14)
O3-Zn1-N2 ²	99.28(15)	O4 ¹ -Zn1-N1	127.14(14)
O4 ¹ -Zn1-N2 ²	98.91(13)	N1-Zn1-N2 ²	104.82(14)

42

O10-Cd1-O9	55.15(17)	O10-Cd1-O15	103.46(18)
O10-Cd1-O16	111.8(2)	O10-Cd1-N2 ¹	90.81(18)
O15-Cd1-O9	129.0(2)	O16-Cd1-O9	166.3(2)
O16-Cd1-O15	53.9(3)	O16-Cd1-N2 ¹	83.2(2)
N2 ¹ -Cd1-O9	92.41(17)	N2 ¹ -Cd1-O15	137.1(2)
N3-Cd1-O9	86.95(18)	N3-Cd1-O10	140.38(19)
N3-Cd1-O15	91.3(2)	N3-Cd1-O16	106.7(2)
N3-Cd1-N2 ¹	103.06(19)	O11 ² -Cd2-O12	131.92(19)
O13 ² -Cd2-O11 ²	55.42(19)	O13 ² -Cd2-O12	152.8(2)
O14-Cd2-O11 ²	97.0(2)	O14-Cd2-O12	55.51(18)
O14-Cd2-O13 ²	100.0(2)	O14-Cd2-N5 ³	100.8(2)
N5 ³ -Cd2-O11 ²	137.5(2)	N5 ³ -Cd2-O12	89.4(2)
N5 ³ -Cd2-O13 ²	83.4(2)	N6-Cd2-O11 ²	90.24(19)
N6-Cd2-O12	87.29(19)	N6-Cd2-O13 ²	119.9(2)
N6-Cd2-O14	135.06(19)	N6-Cd2-N5 ³	103.2(2)
O6-Cd3-O7	55.08(16)	O6-Cd3-N1 ⁴	91.99(19)
O17 ⁵ -Cd3-O6	107.7(2)	O17 ⁵ -Cd3-O7	162.0(2)
O17 ⁵ -Cd3-N1 ⁴	83.8(3)	N1 ⁴ -Cd3-O7	91.11(18)
N4-Cd3-O6	139.80(19)	N4-Cd3-O7	87.40(18)
N4-Cd3-O17 ⁵	110.6(2)	N4-Cd3-N1 ⁴	103.8(2)

Table A60. Selected Bond angles (°) for **43** and **44**.**43**

O1-Zn1-N1	96.4(2)	O1-Zn1-N2	130.4(2)
O3-Zn1-O1	110.4(2)	O3-Zn1-N1	93.4(2)
O3-Zn1-N2	113.0(2)	N2-Zn1-N1	103.8(2)
O5-Zn2-N3	110.1(2)	O5-Zn2-N4	94.2(2)
O7-Zn2-O5	113.6(2)	O7-Zn2-N3	126.4(2)
O7-Zn2-N4	97.5(3)	N3-Zn2-N4	108.7(2)

44

O4-Cd1-O6	56.87(6)	O4-Cd1-O7 ¹	146.67(6)
O4-Cd1-O10 ¹	96.41(6)	O4-Cd1-N1	112.02(7)
O4-Cd1-N4 ²	102.74(7)	O6-Cd1-O10 ¹	83.99(6)
O7 ¹ -Cd1-O6	98.77(6)	O7 ¹ -Cd1-O10 ¹	55.49(6)
O7 ¹ -Cd1-N1	92.92(7)	O7 ¹ -Cd1-N4 ²	93.25(7)
N1-Cd1-O6	168.27(6)	N1-Cd1-O10 ¹	102.00(6)
N1-Cd1-N4 ²	101.02(7)	N4 ² -Cd1-O6	79.41(7)
N4 ² -Cd1-O10 ¹	141.71(6)	O12 ³ -Cd2-O11	115.22(7)
O13-Cd2-O11	55.25(7)	O13-Cd2-O12 ³	94.15(9)
O13-Cd2-O15 ³	81.21(8)	O13-Cd2-N2	145.13(8)
O13-Cd2-N3 ²	102.70(10)	O15 ³ -Cd2-O11	135.77(7)
O15 ³ -Cd2-O12 ³	55.15(6)	N2-Cd2-O11	93.08(6)
N2-Cd2-O12 ³	86.48(6)	N2-Cd2-O15 ³	125.45(7)
N2-Cd2-N3 ²	100.44(7)	N3 ² -Cd2-O11	107.16(7)
N3 ² -Cd2-O12 ³	136.62(7)	N3 ² -Cd2-O15 ³	88.06(7)

Table A61. Selected Bond angles (°) for **45**, **46** and **47**.**45**

O1-Cd1-O1 ¹	97.2(4)	O1-Cd1-O2	119.4(2)
O1 ¹ -Cd1-O2 ¹	119.4(2)	O1-Cd1-O2 ¹	124.6(3)
O1 ¹ -Cd1-O2	124.6(3)	O2-Cd1-O2 ¹	73.5(3)
O3 ¹ -Cd1-O1	151.4(3)	O3 ¹ -Cd1-O1 ¹	54.2(3)
O3-Cd1-O1 ¹	151.4(3)	O3-Cd1-O1	54.2(3)
O3 ¹ -Cd1-O2 ¹	78.2(3)	O3 ¹ -Cd1-O2	81.3(3)
O3-Cd1-O2 ¹	81.3(3)	O3-Cd1-O2	78.2(3)
O3-Cd1-O3 ¹	154.4(4)	O3-Cd1-O4	87.0(3)
O3-Cd1-O4 ¹	93.5(3)	O3 ¹ -Cd1-O4	93.5(3)
O3 ¹ -Cd1-O4 ¹	87.0(3)	O4-Cd1-O1	85.0(2)
O4 ¹ -Cd1-O1	93.5(3)	O4 ¹ -Cd1-O1 ¹	85.0(2)
O4-Cd1-O1 ¹	93.5(2)	O4 ¹ -Cd1-O2	127.9(2)
O4-Cd1-O2	54.3(2)	O4 ¹ -Cd1-O2 ¹	54.4(2)
O4-Cd1-O2 ¹	127.9(2)	O4 ¹ -Cd1-O4	177.8(3)
O2 ¹ -Cd2-O2	82.5(4)	O5-Cd2-O2 ¹	83.7(3)
O5-Cd2-O2	80.3(3)	O5 ¹ -Cd2-O2	83.7(3)
O5 ¹ -Cd2-O2 ¹	80.3(4)	O5 ¹ -Cd2-O5	158.6(5)
O5 ¹ -Cd2-O6 ¹	90.7(4)	O5-Cd2-O6 ¹	104.6(4)
O5-Cd2-O6	90.7(4)	O5 ¹ -Cd2-O6	104.6(4)
O6 ¹ -Cd2-O2	174.0(3)	O6-Cd2-O2 ¹	174.0(3)
O6-Cd2-O2	94.5(3)	O6 ¹ -Cd2-O2 ¹	94.5(3)
O6 ¹ -Cd2-O6	89.0(5)		

46

O1 ¹ -Cd1-O2 ¹	55.41(6)	O1 ¹ -Cd1-O9	134.91(7)
O1 ¹ -Cd1-O10 ²	80.44(7)	O2 ¹ -Cd1-O9	134.62(7)
O2 ¹ -Cd1-O10 ²	92.92(8)	O5-Cd1-O1 ¹	87.27(7)
O5-Cd1-O2 ¹	91.26(7)	O5-Cd1-O8 ²	111.60(8)
O5-Cd1-O9	53.66(7)	O5-Cd1-O10 ²	161.62(8)
O5-Cd1-N1	113.77(8)	O8 ² -Cd1-O1 ¹	89.40(7)
O8 ² -Cd1-O2 ¹	137.70(7)	O8 ² -Cd1-O9	86.13(7)
O8 ² -Cd1-O10 ²	55.07(8)	O10 ² -Cd1-O9	129.84(8)
N1-Cd1-O1 ¹	139.94(7)	N1-Cd1-O2 ¹	88.97(7)
N1-Cd1-O8 ²	111.34(8)	N1-Cd1-O9	82.18(7)
N1-Cd1-O10 ²	84.20(7)	O3 ³ -Cd2-O4	82.66(6)
O3 ³ -Cd2-O11 ⁴	130.79(7)	O6 ³ -Cd2-O3 ³	54.72(6)
O6 ³ -Cd2-O4	93.01(7)	O6 ³ -Cd2-O11 ⁴	127.09(9)
O7-Cd2-O3 ³	91.24(7)	O7-Cd2-O4	54.34(7)
O7-Cd2-O6 ³	137.57(7)	O7-Cd2-O11 ⁴	93.59(9)
O7-Cd2-O12 ⁴	102.48(13)	O7-Cd2-N2	114.77(8)
O11 ⁴ -Cd2-O4	136.98(8)	O12 ⁴ -Cd2-O3 ³	78.59(8)
O12 ⁴ -Cd2-O4	149.86(12)	O12 ⁴ -Cd2-O6 ³	95.13(10)
O12 ⁴ -Cd2-O11 ⁴	52.56(9)	O12 ⁴ -Cd2-N2	124.54(12)
N2-Cd2-O3 ³	136.13(7)	N2-Cd2-O4	85.12(7)
N2-Cd2-O6 ³	84.22(8)	N2-Cd2-O11 ⁴	84.39(8)

47

O1 ¹ -Cd1-O3 ¹	55.09(17)	O1 ¹ -Cd1-O5 ²	133.0(2)
O1 ¹ -Cd1-O6	96.2(2)	O1 ¹ -Cd1-C7 ¹	27.73(19)
O2-Cd1-O1 ¹	139.17(18)	O2-Cd1-O3 ¹	91.1(2)
O2-Cd1-O4 ²	102.8(2)	O2-Cd1-O5 ²	85.8(2)
O2-Cd1-O6	52.92(19)	O2-Cd1-N2	110.9(2)
O3 ¹ -Cd1-O5 ²	132.5(2)	O3 ¹ -Cd1-O6	82.4(2)
O4 ² -Cd1-O1 ¹	94.24(19)	O4 ² -Cd1-O3 ¹	80.8(2)
O4 ² -Cd1-O5 ²	54.1(2)	O4 ² -Cd1-O6	150.1(2)
O5 ² -Cd1-O6	129.0(2)	N2-Cd1-O1 ¹	89.88(18)
N2-Cd1-O3 ¹	141.33(19)	N2-Cd1-O4 ²	121.7(2)
N2-Cd1-O5 ²	82.17(19)	N2-Cd1-O6	86.3(2)

Table A62. Selected Bond angles (°) for **48**.**48**

O1 ¹ -Co1-Co1 ²	84.56(12)	O1 ³ -Co1-Co1 ²	84.56(12)
O1 ⁴ -Co1-Co1 ²	84.56(12)	O1-Co1-Co1 ²	84.55(12)
O1 ¹ -Co1-O1 ³	87.7(3)	O1 ³ -Co1-O1 ⁴	91.3(3)
O1 ⁴ -Co1-O1	87.7(3)	O1 ¹ -Co1-O1	91.3(3)
O1 ³ -Co1-O1	169.1(2)	O1 ¹ -Co1-O1 ⁴	169.1(2)
O1 ¹ -Co1-N1	95.44(12)	O1 ³ -Co1-N1	95.44(12)
O1 ⁴ -Co1-N1	95.44(12)	O1-Co1-N1	95.45(12)
N1-Co1-Co1 ²	180.00(8)		

Table A63. Selected Bond angles (°) for **49** and **50**.**49**

O2 ¹ -Cd1-O2	102.6(3)	O2 ¹ -Cd1-O3 ²	102.8(2)
O2 ¹ -Cd1-O3 ³	136.7(2)	O2-Cd1-O3 ²	136.7(2)
O2-Cd1-O3 ³	102.7(2)	O2 ¹ -Cd1-O4 ²	101.9(3)
O2 ¹ -Cd1-O4 ³	86.7(2)	O2-Cd1-O4 ³	101.9(3)
O2-Cd1-O4 ²	86.7(2)	O3 ³ -Cd1-O3 ²	81.4(3)
O3 ³ -Cd1-O4 ²	114.1(2)	O3 ³ -Cd1-O4 ³	54.0(2)
O3 ² -Cd1-O4 ²	54.0(2)	O3 ² -Cd1-O4 ³	114.1(2)
O4 ³ -Cd1-O4 ²	166.4(3)	O1 ⁴ -Cd2-O1	180.0
O1 ⁴ -Cd2-O4 ²	98.8(2)	O1-Cd2-O4 ⁵	98.8(2)
O1 ⁴ -Cd2-O4 ⁵	81.2(2)	O1-Cd2-O4 ²	81.2(2)
O1-Cd2-N1	79.0(3)	O1-Cd2-N1 ⁴	101.0(3)
O1 ⁴ -Cd2-N1 ⁴	79.0(3)	O1 ⁴ -Cd2-N1	101.0(3)
O4 ⁵ -Cd2-O4 ²	180.0	O4 ⁵ -Cd2-N1 ⁴	84.2(3)
O4 ⁵ -Cd2-N1	95.8(3)	O4 ² -Cd2-N1	84.2(3)
O4 ² -Cd2-N1 ⁴	95.8(3)	N1-Cd2-N1 ⁴	180.0

50

O1 ¹ -Cd1-O1 ²	180.0	O2 ³ -Cd1-O1 ¹	82.28(12)
O2-Cd1-O1 ¹	97.72(12)	O2 ³ -Cd1-O1 ²	97.72(12)
O2-Cd1-O1 ²	82.28(12)	O2 ³ -Cd1-O2	180.0
N1 ³ -Cd1-O1 ¹	87.32(17)	N1 ³ -Cd1-O1 ²	92.68(17)
N1-Cd1-O1 ²	87.32(17)	N1-Cd1-O1 ¹	92.68(17)
N1-Cd1-O2 ³	97.64(18)	N1 ³ -Cd1-O2	97.63(18)

50 (continued)

N1-Cd1-O2	82.36(18)	N1 ³ -Cd1-O2 ³	82.37(18)
N1 ³ -Cd1-N1	180.0	O1 ² -Cd2-O1 ⁴	164.19(16)
O3-Cd2-O1 ²	86.94(13)	O3 ⁵ -Cd2-O1 ²	102.06(13)
O3 ⁵ -Cd2-O1 ⁴	86.95(13)	O3-Cd2-O1 ⁴	102.06(13)
O3-Cd2-O3 ⁵	111.0(2)	O3-Cd2-O4 ⁴	99.59(15)
O3 ⁵ -Cd2-O4 ²	99.59(15)	O3 ⁵ -Cd2-O4 ⁴	134.78(14)
O3-Cd2-O4 ²	134.78(14)	O4 ⁴ -Cd2-O1 ⁴	53.78(12)
O4 ² -Cd2-O1 ²	53.78(12)	O4 ² -Cd2-O1 ⁴	112.29(13)
O4 ⁴ -Cd2-O1 ²	112.29(13)	O4 ² -Cd2-O4 ⁴	79.4(2)

Table A64. Selected Bond angles (°) for **51** and **52**.**51**

O1-Cd1-O4 ¹	90.7(3)	O1-Cd1-O5	89.2(4)
O1-Cd1-O9	179.1(4)	O1-Cd1-O10	89.5(3)
O1-Cd1-N1	86.0(3)	O4 ¹ -Cd1-N1	94.8(3)
O5-Cd1-O4 ¹	81.1(3)	O5-Cd1-N1	173.6(4)
O9-Cd1-O4 ¹	88.9(4)	O9-Cd1-O5	91.6(4)
O9-Cd1-N1	93.2(4)	O10-Cd1-O4 ¹	174.1(3)
O10-Cd1-O5	93.0(4)	O10-Cd1-O9	91.0(4)
O10-Cd1-N1	91.1(3)	O2-Cd2-O3 ¹	92.5(6)
O2-Cd2-O4 ¹	98.3(4)	O2-Cd2-O7	122.0(4)
O2-Cd2-O8	84.2(4)	O3 ¹ -Cd2-O4 ¹	52.3(3)
O3 ¹ -Cd2-O7	80.2(4)	O3 ¹ -Cd2-O8	121.3(4)
O6-Cd2-O2	125.7(6)	O6-Cd2-O3 ¹	131.3(6)
O6-Cd2-O4 ¹	89.5(3)	O6-Cd2-O7	98.8(5)
O6-Cd2-O8	94.3(4)	O7-Cd2-O4 ¹	119.2(3)
O8-Cd2-O4 ¹	173.0(3)	O8-Cd2-O7	54.5(3)

52

O2-Cd1-O1	54.21(12)	O2-Cd1-O5 ¹	167.77(12)
O2-Cd1-O6 ¹	114.19(13)	O3-Cd1-O1	128.91(14)
O3-Cd1-O2	84.33(13)	O3-Cd1-O5 ¹	100.03(13)
O3-Cd1-O6 ¹	93.43(17)	O5 ¹ -Cd1-O1	115.68(12)
O6 ¹ -Cd1-O1	80.56(15)	O6 ¹ -Cd1-O5 ¹	54.44(12)
O7-Cd1-O1	87.06(15)	O7-Cd1-O2	98.64(13)
O7-Cd1-O3	132.14(16)	O7-Cd1-O5 ¹	86.94(12)
O7-Cd1-O6 ¹	126.68(16)	O4-Cd2-O5 ¹	91.44(15)

52 (continued)

O4-Cd2-O8	92.48(14)	O4-Cd2-O9	172.22(16)
O4-Cd2-O10	88.49(16)	O4-Cd2-N1	85.96(14)
O5 ¹ -Cd2-N1	94.25(13)	O8-Cd2-O5 ¹	81.21(12)
O8-Cd2-N1	175.17(13)	O9-Cd2-O5 ¹	87.30(15)
O9-Cd2-O8	94.92(15)	O9-Cd2-O10	93.93(16)
O9-Cd2-N1	86.48(15)	O10-Cd2-O5 ¹	171.20(13)
O10-Cd2-O8	90.00(14)	O10-Cd2-N1	94.53(14)

Table A65. Selected Bond angles (°) for **53** and **54**.**53**

O1 ¹ -Ni1-O2 ²	97.1(5)	O1 ¹ -Ni1-O6 ¹	62.6(4)
O2 ² -Ni1-O6 ¹	88.0(4)	O8 ² -Ni1-O1 ¹	157.2(5)
O8 ² -Ni1-O2 ²	63.0(5)	O8 ² -Ni1-O6 ¹	103.5(5)
O8 ² -Ni1-N3 ³	97(4)	N3 ³ -Ni1-O1 ¹	101(4)
N3 ³ -Ni1-O2 ²	158(4)	N3 ³ -Ni1-O6 ¹	88(2)
N4-Ni1-O1 ¹	96.8(4)	N4-Ni1-O2 ²	91.1(4)
N4-Ni1-O6 ¹	159.1(4)	N4-Ni1-O8 ²	94.7(5)
N4-Ni1-N3 ³	100(2)	O3-Ni2-O4	63.0(4)
O3-Ni2-O5 ⁴	153.1(5)	O3-Ni2-O7 ⁴	100.2(4)
O5 ⁴ -Ni2-O4	94.4(5)	O5 ⁴ -Ni2-O7 ⁴	62.0(4)
O7 ⁴ -Ni2-O4	87.1(4)	N1-Ni2O3	99.2(5)
N1-Ni2-O4	89.7(4)	N1-Ni2-O5 ⁴	94.9(5)
N1-Ni2-O7 ⁴	156.3(5)	N1-Ni2-N2 ⁵	97(3)
N2 ⁵ -Ni2-O3	100(5)	N2 ⁵ -Ni2-O4	163(5)
N2 ⁵ -Ni2-O5 ⁴	101(5)	N2 ⁵ -Ni2-O7 ⁴	93(3)

54

O2-Zn1-O6 ¹	121.7(4)	O2-Zn1-N1	116.7(4)
O2-Zn1-N3 ²	100.3(17)	O6 ¹ -Zn1-N1	114.1(3)
O6 ¹ -Zn1-N3 ²	96(2)	N1-Zn1-N3 ²	101.0(19)
O3 ³ -Zn2-O4 ³	58.4(3)	O3 ³ -Zn2-O7 ⁴	93.2(3)
O3 ³ -Zn2-O8 ⁴	135.0(3)	O3 ³ -Zn2-N4 ¹	96.0(17)
O7 ⁴ -Zn2-O4 ³	89.8(2)	O8 ⁴ -Zn2-O4 ³	84.2(3)
O8 ⁴ -Zn2-O7 ⁴	60.1(4)	N2-Zn2-O3 ³	105.7(3)
N2-Zn2-O4 ³	89.1(3)	N2-Zn2-O7 ⁴	157.0(3)
N2-Zn2-O8 ⁴	96.9(3)	N2-Zn2-N4 ¹	100.0(15)
N4 ¹ -Zn2-O4 ³	154.4(17)	N4 ¹ -Zn2-O7 ⁴	90.8(17)
N4 ¹ -Zn2-O8 ⁴	118.0(19)	C25-C26-C27	122.7(10)

Table A66. Selected Bond angles (°) for **55** and **56**.**55**

O1-Zn1-O3 ¹	131.55(18)	O1-Zn1-O6 ²	108.97(17)
O1-Zn1-O8 ³	101.35(17)	O3 ¹ -Zn1-O6 ²	97.66(18)
O3 ¹ -Zn1-O8 ³	111.98(16)	O6 ² -Zn1-O8 ³	101.94(17)
O2-Zn2-O5 ²	121.22(18)	O2-Zn2-O7 ⁴	100.41(18)
O2-Zn2-O9	111.9(2)	O5 ² -Zn2-O7 ⁴	116.40(17)
O5 ² -Zn2-O9	107.1(2)	O9-Zn2-O7 ⁴	97.27(18)

56

O1-Cu1-Cu1 ¹	86.70(19)	O1-Cu1-O3 ²	171.0(3)
O1-Cu1-O4 ¹	88.0(2)	O1-Cu1-O5 ³	90.1(2)
O1-Cu1-O10	92.6(3)	O3 ² -Cu1-Cu1 ¹	84.40(19)
O3 ² -Cu1-O4 ¹	92.1(2)	O3 ² -Cu1-O10	96.3(3)
O4 ¹ -Cu1-Cu1 ¹	80.71(19)	O4 ¹ -Cu1-O10	101.3(3)
O5 ³ -Cu1-Cu1 ¹	82.89(19)	O5 ³ -Cu1-O3 ²	87.2(2)
O5 ³ -Cu1-O4 ¹	163.6(3)	O5 ³ -Cu1-O10	95.1(3)
O10-Cu1-Cu1 ¹	177.9(2)	O2-Cu2-O9	99.1(3)
O6 ⁴ -Cu2-Cu2 ⁴	85.7(2)	O6 ⁴ -Cu2-O7 ⁴	88.9(3)
O7 ⁴ -Cu2-Cu2 ⁴	82.9(2)	O7 ⁴ -Cu2-O9	95.3(3)
O8-Cu2-Cu2 ⁴	85.3(2)	O8-Cu2-O2	90.0(3)
O8-Cu2-O6 ⁴	170.8(3)	O8-Cu2-O7 ⁴	88.2(3)
O8-Cu2-O9	94.9(3)	O9-Cu2-Cu2 ⁴	178.20(19)

Table A67. Q_{st} values of reported MOFs.

Compound	Q_{st} (kJmol ⁻¹)	Reference
39	25.4	This work
40	28.3	This work
41	33.2	This work
42	29.7	This work
43	32.6	This work
48	30.4	This work
51	29.3	This work
52	25.6	This work
53	27.5	This work
55	32.5	This work
UTSA-72a	34.6	<i>Cryst. Growth Des.</i> , 2014 , <i>14</i> , 2522–2526
IITKGP-8	35	<i>Chem. - A Eur. J.</i> , 2018 , 5982–5986
IITKGP-6	23	<i>Inorg. Chem.</i> , 2017 , <i>56</i> , 13991–13997
IITKGP-5	22.6	<i>Dalt. Trans.</i> , 2017 , <i>46</i> , 15280–15286
M' MOF-20a	28.4	<i>Inorg. Chem.</i> , 2012 , <i>51</i> , 4947–4953
ROD 6	20-21	<i>Chem. Commun.</i> , 2014 , <i>50</i> , 4047–4049
ROD 7	26-22	<i>Chem. Commun.</i> , 2014 , <i>50</i> , 4047–4049
NU 1000	17	<i>J. Am. Chem. Soc.</i> , 2013 , <i>135</i> , 16801–16804
PMF-NOTT-1	33.09	<i>J. Mater. Chem. A</i> , 2014 , <i>2</i> , 19889–19896
PMF- NOTT-2	31.86	<i>J. Mater. Chem. A</i> , 2014 , <i>2</i> , 19889–19896
[Zn ₂ (L)(2,6-NDC) ₂]	23.3	<i>Inorg. Chem.</i> , 2018 , <i>57</i> , 2695–2704
[Cd ₂ (L)(2,6-NDC) ₂]	28.1	<i>Inorg. Chem.</i> , 2018 , <i>57</i> , 2695–2704
ZnPC-2	32	<i>Chem. Commun.</i> , 2013 , <i>49</i> , 78–80
Cu-BCPPM	29	<i>J. Am. Chem. Soc.</i> , 2013 , <i>135</i> , 10441–10448
SIFSIX-3-Zn	45	<i>Nature</i> , 2013 , <i>495</i> , 80–84
[Co ₂ (tzpa)(OH)(H ₂ O) ₂]	38.5	<i>ACS Appl. Mater. Interfaces</i> , 2017 , <i>9</i> , 17969–17976
[Cu ₂ (L)(H ₂ O) ₂]	36.4	<i>Chem. Commun.</i> , 2016 , <i>52</i> , 11147–11150
SNU-77H	19.9	<i>Chem. - A Eur. J.</i> , 2011 , <i>17</i> , 7251–7260
NJU-Bai13	21.2	<i>CrystEngComm</i> , 2013 , <i>15</i> , 9348
CuBTTri	21	<i>J. Am. Chem. Soc.</i> , 2009 , <i>131</i> , 8784–8786
Cu-TDPAT	42.2	<i>Angew. Chemie - Int. Ed.</i> , 2012 , <i>51</i> , 1412–1415
[Cu(Me-4py-trz-ia)]	30	<i>Angew. Chemie - Int. Ed.</i> , 2011 , <i>50</i> , 10344–10348
[Zn(BTZ)]	31.2	<i>J. Am. Chem. Soc.</i> , 2012 , <i>134</i> , 18892–18895
Mg-DOBDC	47	<i>J. Am. Chem. Soc.</i> , 2008 , <i>130</i> , 10870–10871
Ni-DOBDC	41	<i>J. Am. Chem. Soc.</i> , 2008 , <i>130</i> , 10870–10871
Co-DOBDC	37	<i>J. Am. Chem. Soc.</i> , 2008 , <i>130</i> , 10870–10871
MOF-5	16.5	<i>Microporous Mesoporous Mater.</i> , 2008 , <i>116</i> , 727–731
UMCM-1	11.9	<i>J. Phys. Chem. C</i> , 2010 , <i>114</i> , 6464–6471
ZJNU-54a	24.7	<i>Dalton Trans.</i> , 2016 , <i>45</i> , 13373–13382
PCN 88	27	<i>Nat. Commun.</i> , 2013 , <i>4</i> , 1538
JUC-199	29	<i>J. Mater. Chem. A</i> , 2016 , <i>4</i> , 15240–15246
MIL-53 (Al)	20.1	<i>J. Phys. Chem. C</i> , 2008 , <i>112</i> , 1575–1581

Table A67 (continued)

HKUST-1	30	<i>Energy and Fuels</i> , 2009 , 2785–2789
NOTT 140a	24.7	<i>Chem. Commun.</i> , 2011 , 47, 4487
MIL-100	63	<i>Langmuir</i> , 2008 , 7245–7250
en-Cu-BTtri	90	<i>J. Am. Chem. Soc.</i> , 2009 , 131, 8784–8786
NOTT 202a	22	<i>Nat. Mater.</i> , 2012 , 11, 710–716

Table A68 Adsorption selectivity of reported MOFs for CO₂/N₂ (15:85) and CO₂/CH₄ (50:50) at 1 bar.

Compound	CO ₂ /N ₂ adsorption selectivity	CO ₂ /CH ₄ adsorption selectivity	Temperature (K)	Reference
48	70.5	9.9	298	This work
	194.7	19.0	273	This work
53	91.7	18.2	298	This work
	218.4	67.8	273	This work
55	161.5	29.4	298	This work
HKUST-1	101 ^b	7.4 ^{a,d}	293	<i>Energy and Fuels</i> , 2009 , 2785–2789
HKUST-1(hydrated)	28 ^a	7.5 ^a	298	<i>Chem. Mater.</i> , 2009 , 21, 1425–1430
PCN-88a	18 ^a	5 ^a	296	<i>Nat. Commun.</i> , 2013 , 4, 1538.
PCN-61a	15 ^a	NA	298	<i>J. Am. Chem. Soc.</i> , 2011 , 133, 748–751
UTSA-15a	NA	14.2 ^{a,d}	296	<i>Nat. Commun.</i> , 2012 , 3, 954–959
UTSA-16a	314.7 ^a	29.8 ^{a,d}	296	<i>Nat. Commun.</i> , 2012 , 3, 954–959
UTSA-20a	NA	8.3 ^{a,d}	296	<i>Nat. Commun.</i> , 2012 , 3, 954–959
UTSA-25a	NA	9.4 ^{a,d}	296	<i>Nat. Commun.</i> , 2012 , 3, 954–959
UTSA-33a	NA	7.0 ^{a,d}	296	<i>Nat. Commun.</i> , 2012 , 3, 954–959
UTSA-34a	NA	5.1 ^{a,d}	296	<i>Nat. Commun.</i> , 2012 , 3, 954–959
UTSA-49a	95.8 ^a	33.7 ^a	298	<i>Chem. Commun.</i> , 2014 , 50, 12101–12104
	197.7 ^a	34.8 ^a	273	
UTSA-72a	48.3 ^a	40.7 ^a	273	<i>Cryst. Growth Des.</i> , 2014 , 14, 2522–2526
	35.6 ^a	9.3 ^a	296	
UTSA-85a	55 ^a	11.4 ^a	273	<i>Chempluschem</i> , 2016 , 81, 764–769
	62.5 ^a	6.4 ^a	296	
ZIF-68	18.7 ^c	5 ^c	298	<i>Acc Chem Res</i> , 2010 , 43, 58–67
ZIF-69	19.9 ^c	5.1 ^c	298	<i>Acc Chem Res</i> , 2010 , 43, 58–67
ZIF-70	17.3 ^c	5.2 ^c	298	<i>Acc Chem Res</i> , 2010 , 43, 58–67
ZIF-78	41.4 ^a	10.4 ^{a,d}	296	<i>Acc Chem Res</i> , 2010 , 43, 58–67
	50.1 ^c	10.6 ^c	298	
ZIF-79	23.2 ^c	5.4 ^c	298	<i>Acc Chem Res</i> , 2010 , 43, 58–67
ZIF-81	23.8 ^c	5.7 ^c	298	<i>Acc Chem Res</i> , 2010 , 43, 58–67
ZIF-82	35.3 ^c	9.6 ^c	298	<i>Acc Chem Res</i> , 2010 , 43, 58–67
ZIF-95	18±1.7 ^c	4.3±0.4 ^c	298	<i>Acc Chem Res</i> , 2010 , 43, 58–67
ZIF-100	25±2.4 ^c	5.9±0.4 ^c	298	<i>Acc Chem Res</i> , 2010 , 43, 58–67
IITKGP-8	106 ^a	17.7 ^a	273	<i>Chem. - A Eur. J.</i> , 2018 , 5982–5986
	43.7 ^a	17.1 ^a	295	

Table A68 (continued)

IITKGP-7	57 ^a	8.4 ^a	273	<i>ChemistrySelect</i> , 2018 , 3, 917–921
	121.4 ^a	8.8 ^a	295	
IITKGP-6	51.3 ^a	36 ^a	273	<i>Inorg. Chem.</i> , 2017 , 56, 13991–13997
	42.8 ^a	5.1 ^a	295	
IITKGP-5	435.5 ^a	151.6 ^a	273	<i>Dalt. Trans.</i> , 2017 , 46, 15280–15286
	147.8 ^a	23.8 ^a	295	
SIFSIX-1-Cu	27 ^a	11 ^a	298	<i>Nature</i> , 2013 , 495, 80–84
SIFSIX-2-Cu	13.7 ^a	5.3 ^a	298	<i>Nature</i> , 2013 , 495, 80–84
SIFSIX-2-Cu-i	140 ^a	33 ^a	298	<i>Nature</i> , 2013 , 495, 80–84
TIFSIX-1-Cu	30 ^a	11 ^a	298	<i>Chem. Commun.</i> , 2013 , 49, 1606-1608
SNFSIX-1-Cu	22 ^a	12 ^a	298	<i>Chem. Commun.</i> , 2013 , 49, 1606-1608
Cu-BTTri	21 ^a	NA	298	<i>J. Am. Chem. Soc.</i> , 2009 , 131, 8784–8786
en-Cu-BTTri	25 ^a	NA	298	<i>J. Am. Chem. Soc.</i> , 2009 , 131, 8784–8786
mmen-Cu-BTTri	327 ^a	NA	298	<i>Chem. Sci.</i> , 2011 , 2, 2022-2028
mmen-Mg ₂ (dobpdc)	329 ^a	NA	298	<i>J. Am. Chem. Soc.</i> , 2012 , 134, 7056–7065
Cu ₂₄ (TPBTM) ₈	22 ^a	NA	298	<i>J. Am. Chem. Soc.</i> , 2011 , 133, 748–751
Cu-TDPAT	57.8 ^a	13.8 ^{a,d}	296	<i>Nat. Commun.</i> , 2012 , 3, 954–959
Mg-MOF-74	182.1 ^a	105.1 ^{a,d}	296	<i>Nat. Commun.</i> , 2012 , 3, 954–959
Zn-MOF-74	87.7 ^a	5 ^a	296	<i>Nat. Commun.</i> , 2012 , 3, 954–959
MOF-177	3.6 ^a	NA	296	<i>Nat. Commun.</i> , 2012 , 3, 954–959
Bio-MOF-11	79.5 ^a	NA	296	<i>Nat. Commun.</i> , 2012 , 3, 954–959
In ₂ X	250 ^a	6.4 ^a	273	<i>Inorg. Chem.</i> , 2013 , 52, 3127–3132
	NA	5.6 ^a	298	
[ZnLi(PTCA)]	126 ^a	26 ^a	298	<i>Inorg. Chem.</i> , 2017 , 56, 705–708
	277 ^a	35 ^a	273	
MIL-101	NA	9.6 ^{a,d}	296	<i>Nat. Commun.</i> , 2012 , 3, 954–959
	NA	5.6 ^a	298	
ZJNU-44a	15 ^a	5.5 ^a	296	<i>J. Mater. Chem. A</i> , 2015 , 3, 19417–19426
PMOF-3a	29.2 ^a	8 ^a	273	<i>Chempluschem</i> , 2016 , 81, 770–774
	23.4 ^a	5.1 ^a	296	
JUC-141	21.6 ^a	4.2 ^a	273	<i>Inorg. Chem.</i> , 2017 , 56, 6938–6942
	27.6 ^a	8.7 ^a	298	

Table A68 (continued)

MAF-66	403 ^b	7.5 ^b	273	<i>Inorg. Chem.</i> , 2012 , <i>51</i> , 9950–9955
	225 ^b	5.8 ^b	298	
Cu-SSZ13(zeolite)	67.4 ^a	NA	296	<i>Nat. Commun.</i> , 2012 , <i>3</i> , 954–959
H-SSZ13(zeolite)	71.3 ^a	NA	296	<i>Nat. Commun.</i> , 2012 , <i>3</i> , 954–959
Zeolite MF1	11.2 ^a	2.5 ^{a,d}	296	<i>Nat. Commun.</i> , 2012 , <i>3</i> , 954–959
NaX zeolite	145.9 ^a	60 ^{a,d}	296	<i>Nat. Commun.</i> , 2012 , <i>3</i> , 954–959
JBW zeolite	524.4 ^a	685.5 ^{a,d}	296	<i>Nat. Commun.</i> , 2012 , <i>3</i> , 954–959

a: IAST selectivity; b: selectivity from Henry's Law; c: from slopes of adsorption isotherms at low pressure; d: selectivity at 2 bar.

Table A69. Comparison of K_{sv} and Detection Limit for the sensing of TNP.

Compound	K _{sv} (M ⁻¹)	LOD	Medium	Reference
51	2.19 x 10 ⁵	98 ppb	MeOH/H ₂ O	This work
52	2.14 x 10 ⁵	74 ppb	MeOH/H ₂ O	This work
{[Cd(ATAIA)] .4H ₂ O} _n	1.59 x 10 ⁷	0.94 X 10 ⁻⁹ M (0.2 ppb)	H ₂ O	<i>ACS Appl. Mater. Interfaces</i> , 2018 , 10, 25360-25371
{Zn ₂ (tpbn)(2,6-NDC) ₂ } _n	5.907 x 10 ³ 2.19 x 10 ⁴ 2.89 x 10 ⁴	11 ppm 4 ppm 0.7 ppm	H ₂ O DMF/H ₂ O (1:1) DMF/H ₂ O (4:1)	<i>Inorg. Chem.</i> , 2017 , 56, 14556-14566
{[Zn ₂ (tphn)(2,6-NDC) ₂] .4H ₂ O} _n	2.464 x 10 ³ 7.25 x 10 ³ 2.2 x 10 ⁴	19 ppm 7 ppm 1.6 ppm	H ₂ O EtOH/H ₂ O (1:1) EtOH/H ₂ O (4:1)	<i>Inorg. Chem.</i> , 2017 , 56, 14556-14566
TB-Zn-CP	4.37 x10 ⁴	23 ppb	H ₂ O	<i>Chem. Sci.</i> , 2017 , 8, 1535–1546
[Pr ₂ (TATMA) ₂ .4DMF.4H ₂ O] _n	1.6 x 10 ⁴ M-1	NA	DMF	<i>RSC Adv.</i> , 2017 , 7, 38871-38876.
{[Cd(BIDPT)(oba)] .0.5H ₂ O} _n and {[Zn(BIDPT)(4,4'-sdb)] .2.25H ₂ O} _n	2.33 × 10 ⁴ and 2.78 × 10 ⁴	NA	DMF	<i>Inorganic Chemistry Communications</i> , 2016 , 66, 51–54
{[Cd ₄ (L) ₂ (L ₂) ₃ (H ₂ O) ₂].8DMF.8H ₂ O} _n	3.84 x10 ⁴	1.98 ppm	EtOH	<i>Inorg. Chem.</i> , 2016 , 55, 1741–1747
{[Cd ₅ Cl ₆ (L)(HL) ₂].7H ₂ O} _n	4.05 x 10 ⁴	1.87 X 10 ⁻⁷ M (42.84 ppb) ^a	EtOH	<i>Cryst. Growth Des.</i> 2016 , 16, 842–851
BUT-12 and BUT-13	3.1 x10 ⁵ and 5.1 x10 ⁵	23 ppb and 10 ppb	H ₂ O	<i>J. Am. Chem. Soc.</i> 2016 , 138, 6204–6216
{[Zr ₆ O ₄ (OH) ₄ (BTD B) ₆].8H ₂ O.6DMF} _n	2.49 x10 ⁴	1.63 x 10 ⁻⁶ M (37.3 ppm) ^a	MeOH	<i>CrystEngComm</i> , 2016 , 18, 3104–3113
{[Zn(C ₃₄ H ₁₈ O ₈)0.5(C ₂₀ N ₂ H ₁₆) _{0.5}][0.5(C ₂₀ N ₂ H ₁₆)]} _n	8.1 x 10 ⁴	NA	DMF	<i>Chem. Commun.</i> 2015 , 51, 6576-6579
{[Zn ₂ (L) ₂ (dpyb)]} _n and {[Zn(L)(dipb)] .2H ₂ O} _n	2.40 x 10 ⁴ and 2.46 x 10 ⁴	NA	DMA	<i>Chem. Commun.</i> , 2015 , 51, 8300
{[Cd(2,6-NDC)L] ₂ .H ₂ O} _n	3.7 x 10 ⁴	NA	H ₂ O	<i>Dalton Trans.</i> 2015 , 44, 18386–18394.

Table A69 (continued)

{[La(TPT)(DMSO) ₂] ·H ₂ O} _n	9.89 × 10 ⁴	NA	EtOH	<i>Dalton Trans.</i> , 2015 , 44, 13340–13346
{[Cd ₃ (TPT) ₂ (DMF) ₂] ·0.5H ₂ O} _n	6.56 × 10 ⁴	NA	EtOH	<i>Dalton Trans.</i> , 2015 , 44, 230–236
{[Zn ₈ (ad) ₄ (BPDC) ₆ 0.2Me ₂ NH ₂ ·G} _n	4.6 × 10 ⁴	12.9 × 10 ⁻⁹ M (2.9 ppb) ^a	H ₂ O	<i>Chem. Eur. J.</i> 2015 , 21, 965
[Zn ₄ (DMF)(Ur) ₂ (2,6- NDC) ₄] _n	10.83 × 10 ⁴	1.63 ppm	H ₂ O	<i>Cryst. Growth Des.</i> , 2015 , 15, 4627–4634
[Zr ₆ O ₄ (OH) ₆ (L) ₆] _n	5.8 × 10 ⁴	0.4 ppm	H ₂ O	<i>Dalton Trans.</i> 2015 , 44, 15175–15180
[Zn(NDC)H ₂ O] _n and [Cd(NDC)(H ₂ O)] _n	6 × 10 ⁴ and 2.38 × 10 ⁴	1 × 10 ⁻⁶ M (0.23 ppm) ^a and 4 × 10 ⁻⁶ M (0.92 ppm) ^a	H ₂ O	<i>Eur. J. Inorg. Chem.</i> 2015 , 2851–2857
{[Zn ₂ (NDC) ₂ (bpy)] ·Gx} _n	0.4 × 10 ⁴	NA	EtOH	<i>J. Mater. Chem. C</i> 2014 , 2, 10073
[Tb(1,3,5-BTC)] _n	3.4 × 10 ⁴	8.1 × 10 ⁻⁸ M	EtOH	<i>J. Mater. Chem. A</i> , 2013 , 1, 8745–8752
[Cd(NDC)0.5(PCA)] _n	3.5 × 10 ⁴	NA	CH ₃ CN	<i>Angew. Chem. Int.</i> <i>Ed.</i> 2013 , 52, 2881 – 2885

Where, NA = not available; ^athe value was calculated by us using information in the paper.

List of Publications

1) Sadhika Khullar, **Vijay Gupta** and Sanjay K. Mandal, "Tuning the formation of dicarboxylate linker-assisted supramolecular 1D chains and squares of Ni(II) using coordination and hydrogen bonds" *CrystEngComm.*, **2014**, *16*, 5705-5715.

<https://dx.doi.org/10.1039/C4CE00434E>

2) **Vijay Gupta**, Sadhika Khullar, Sandeep Kumar and Sanjay K. Mandal, "Construction of a robust pillared-layer framework based on the rare paddlewheel subunit [Mn^{II}₂(μ-O₂CR)₄L₂]: synthesis, crystal structure and magnetic properties" *Dalton Trans.*, **2015**, *44*, 16778-16784.

<http://dx.doi.org/10.1039/C5DT02354H>

3) **Vijay Gupta** and Sanjay K. Mandal, "Coordination driven self-assembly of [2 + 2 + 2] molecular squares: synthesis, crystal structures, catalytic and luminescence properties" *Dalton Trans.*, **2018**, *47*, 9742-9754.

<http://dx.doi.org/10.1039/c8dt01367e>

4) **Vijay Gupta** and Sanjay K. Mandal, "A robust and water-stable two-fold interpenetrated metal organic framework containing both rigid tetrapodal carboxylate and rigid bifunctional nitrogen linkers exhibiting selective CO₂ capture" *Dalton Trans.*, **2019**, *48*, 415-425. (Selected for cover page)

<http://dx.doi.org/10.1039/c8dt03844a>

5) **Vijay Gupta** and Sanjay K. Mandal, "Design and construction of a chiral Cd(II)-MOF from achiral precursors: synthesis, crystal Structure and catalytic activity towards C-C and C-N bond forming reactions" *Inorg. Chem.*, **2019**, *58*, 3219–3226.

<http://dx.doi.org/10.1021/acs.inorgchem.8b03307>

6) **Vijay Gupta** and Sanjay K. Mandal, "A highly stable triazole functionalized metal organic framework integrated with exposed metal sites for selective CO₂ capture and conversion" *manuscript to be submitted*.

7) **Vijay Gupta** and Sanjay K. Mandal, "A microporous metal organic framework catalyst for solvent-free Strecker reaction and CO₂ fixation at ambient conditions" *manuscript to be submitted*.

Vita

The author, Vijay Gupta, was born on May 08, 1988 in Yamuna Nagar (Haryana) in India. He earned his B.Sc. (Industrial Chemistry) from Guru Nanak Khalsa College Yamuna Nagar, affiliated from Kurukshetra University Kurukshetra (KUK), Haryana and M.Sc. (Inorganic Chemistry) from Kurukshetra University Kurukshetra (KUK), Haryana in 2009 and 2011, respectively. He joined Indian Institute of Science Education and Research Mohali (IISERM) with a research fellowship from University Grant Commission (UGC), New Delhi, India, to pursue his Ph.D. degree in Chemistry under the supervision of Professor Sanjay K. Mandal in August, 2013.